QA: NA

May 2004

Technical Basis Document No. 2: Unsaturated Zone Flow

Revision 1

Prepared for:
U.S. Department of Energy
Office of Civilian Radioactive Waste Management
Office of Repository Development
1551 Hillshire Drive
Las Vegas, Nevada 89134-6321

Prepared by:
Bechtel SAIC Company, LLC
1180 Town Center Drive
Las Vegas, Nevada 89144

Under Contract Number
DE-AC28-01RW12101

CONTENTS

Page

CONTENTS (Continued)

Page

CONTENTS (Continued)

Page

INTENTIONALLY LEFT BLANK

FIGURES

Page

FIGURES (Continued)

Page

FIGURES (Continued)

Page

INTENTIONALLY LEFT BLANK

TABLES

Page

INTENTIONALLY LEFT BLANK

ACRONYMS AND ABBREVIATIONS

AIN	additional information needed
DOE	U.S. Department of Energy
DST	Drift Scale Test
ECRB	Enhanced Characterization of the Repository Block
ESF	Exploratory Studies Facility
GEN	general agreement
GFM	geologic framework model
KTI	Key Technical Issue
LA	license application
LANL	Los Alamos National Laboratory
LLNL	Lawrence Livermore National Laboratory
NRC	U.S. Nuclear Regulatory Commission
PMR	process model report
RT	radionuclide transport
TSPA	total system performance assessment
TSPAI	total system performance assessment and integration
USFIC	unsaturated and saturated flow under isothermal conditions
USGS	U.S. Geological Survey

INTENTIONALLY LEFT BLANK

1. INTRODUCTION

This technical basis document summarizes the conceptual understanding of and the model development for water flow in the Yucca Mountain unsaturated zone, a process affecting the postclosure performance of the high-level radioactive waste repository at Yucca Mountain. This document is one in a series addressing each component of the repository system relevant to predicting its likely postclosure performance.

The repository is located in the unsaturated zone approximately 300 m below ground surface and at about the same distance above the water table (Bodvarsson et al. 1999, p. 5). The unsaturated zone is an important natural barrier to future radionuclide transport from the repository. Figure 1-1 illustrates the relationship between unsaturated zone flow paths and other components in Yucca Mountain.

Unsaturated zone flow is affected by processes described in *Technical Basis Document No. 1: Climate and Infiltration*, *Technical Basis Document No. 3: Water Seeping into Drifts*, *Technical Basis Document No. 4: Mechanical Degradation and Seismic Effects*, *Technical Basis Document No. 13: Volcanic Events*, and *Technical Basis Document No. 14: Low Probability Seismic Events*. Unsaturated zone flow directly relates to water seepage and, therefore, the in-drift environment discussed in *Technical Basis Document No. 5: In-Drift Chemical Environment*. The unsaturated zone flow paths affect the distribution and quantity of seepage water entering the waste emplacement drifts and potentially contacting waste canisters. Unsaturated zone flow impacts downstream repository system components, including corrosion, waste dissolution, and radionuclide and colloid transport through the engineered barrier system, the unsaturated and saturated zones, and the biosphere. Unsaturated zone flow is thus directly related to unsaturated zone transport, colloidal transport, and saturated zone flow and transport.

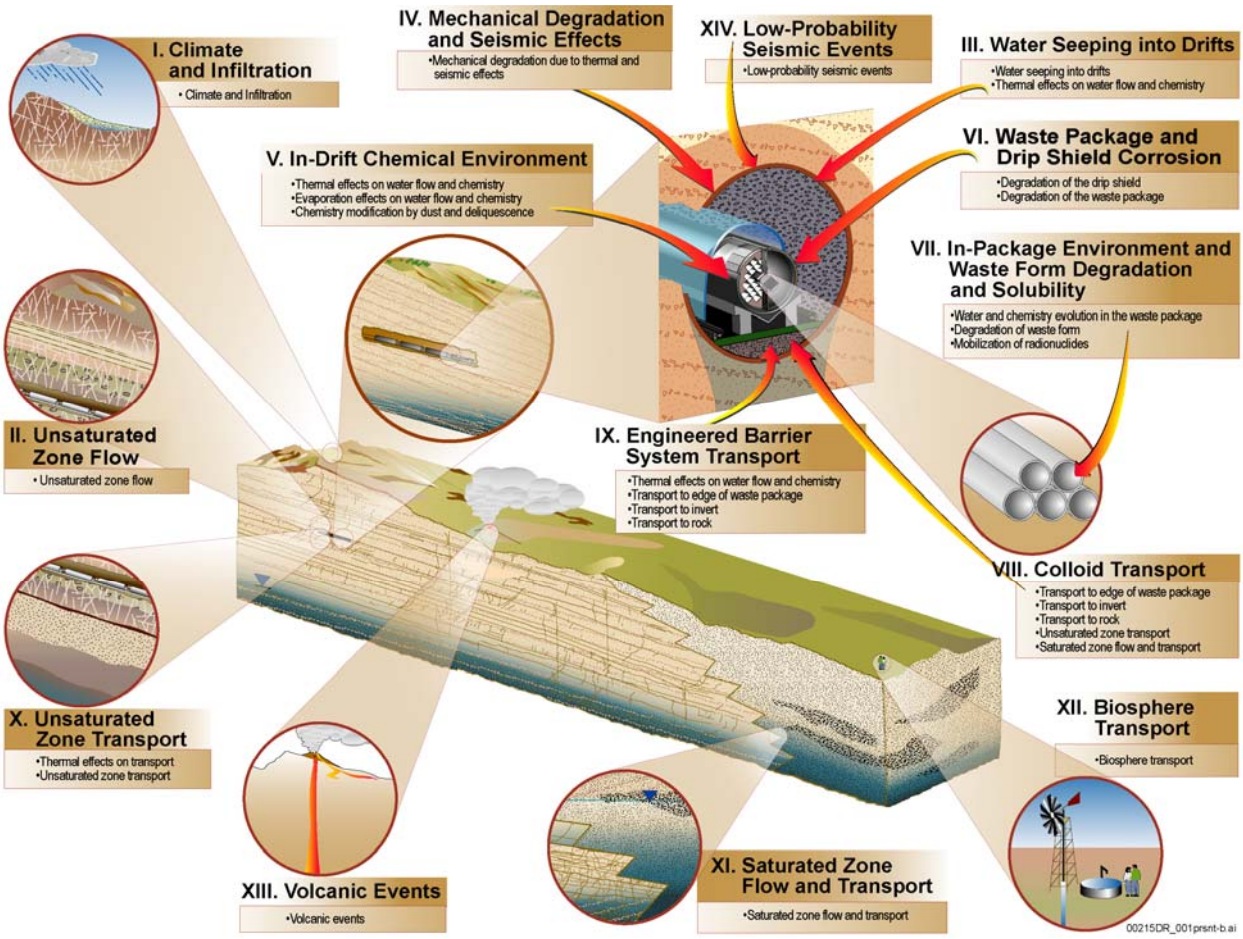

Figure 1-1. Components of the Postclosure Technical Basis for the License Application

This document provides a comprehensive review of the current understanding of flow paths in the unsaturated zone. It first reviews the geologic setting of the unsaturated zone and data collection activities related to flow processes in the unsaturated zone. It then presents the conceptual understanding of unsaturated zone flow paths (based mainly on the data that have been collected in the unsaturated zone) and discusses the development of the site-scale unsaturated zone flow model, including model uncertainties related to total system performance assessment (TSPA). This document also provides responses to the unsaturated zone flow-related Key Technical Issue (KTI) agreements (Table 1-1) between the U.S. Department of Energy (DOE) and the U.S. Nuclear Regulatory Commission (NRC) in the appendices of this report.

Table 1-1. Unsaturated Zone Flow–Related Key Technical Issue Agreements Addressed in This Document

KTI	Short Description	Appendix
ENFE 2.03[a]	Providing the technical basis for FEP 1.2.06.00 (Hydrothermal Activity)	H
RT 1.01	Providing the technical basis for the portion of fracture flow through the CHn unit (vitric)	A
RT 3.02	Providing the analysis of geochemical data used for support of flow field below the repository	B
TEF 2.11	Updating the calibrated properties model report, incorporating uncertainties from all significant sources	C
TEF 2.12	Providing Unsaturated Zone Flow and Transport PMR (REV.00, ICN 02), documenting the resolution of issues on page 5 of the Open Item 8 presentation	E
TEF 2.13 AIN-1	Providing AMR Conceptual and Numerical Models for Unsaturated Zone Flow and Transport (REV.01) and the AMR Analysis of Hydrologic Properties Data (REV.01)	F
TSPAI 3.22 AIN-1	Providing an analysis of uncertainties in predicting unsaturated zone flow under future climate conditions using unsaturated zone models calibrated for the current climate condition	D
TSPAI 3.24	Providing the analysis of geochemical and hydrologic data used for support of flow field below the repository	B
TSPAI 3.26	Calibrating the unsaturated zone flow model using the most recent data on saturation and water potentials	C
TSPAI 3.27	Providing an overview of water flow rates above and below the repository used in different models	G
USFIC 4.04[a]	Documenting the effectiveness of the PTn to dampen episodic flow, including reconciling the differences in ^{36}Cl studies	I

NOTE: [a]The responses to these agreements were submitted under separate cover.

Note Regarding the Status of Supporting Technical Information–This document was prepared using the most current information available at the time of its development. This technical basis document and appendices providing KTI agreement responses that were prepared using preliminary or draft information reflect the status of Yucca Mountain Project scientific and design bases at the time of submittal. In some cases this involved the use of draft analysis and model reports and other draft references whose contents may change with time. Information that evolves through subsequent revisions of the analysis model reports and other references will be reflected in the license application (LA) as the approved analyses of record at the time of LA submittal. Consequently, the project will not routinely update either this technical basis document or its KTI agreement appendices to reflect changes in the supporting references prior to submittal of the LA.

INTENTIONALLY LEFT BLANK

2. GEOLOGIC SETTING AND DATA COLLECTION

Yucca Mountain is located in an arid region with limited precipitation. Strong evaporation–transpiration processes limit the amount of water available for infiltration into the ground. Infiltrating water then percolates through the thick unsaturated zone at Yucca Mountain. Percolation represents the processes that redistribute the limited flow through alternating tuff layers with varying densities of fractures and through faults.

Subsurface heterogeneity has an important effect on flow paths in the Yucca Mountain unsaturated zone and is largely determined by the corresponding geologic setting (Figure 2-1). Data collected from the unsaturated zone form the basis for understanding unsaturated zone flow paths and for developing unsaturated zone flow models. This section briefly reviews the unsaturated zone geologic setting and the data collected from the unsaturated zone.

Source: BSC 2003a, Figure 1.2-4.

Figure 2-1. The Yucca Mountain Geologic Setting: Yucca Mountain Ridge, Fran Ridge, and Busted Butte, Viewed from the Southwest across the Solitario Canyon Fault

2.1 GEOLOGIC SETTING AND HYDROLOGIC UNITS

Subsurface formations in the unsaturated zone consist of heterogeneous layers of anisotropic, fractured volcanic tuffs, with alternating welded and nonwelded ash-flow and ash-fall deposits. The cooling history of these volcanic rocks determines their mechanical and hydrologic properties (Bodvarsson et al. 1999, p. 8). Syndepositional processes (such as welding, fracturing, and formation of lithophysal cavities) along with postdepositional activities (such as

hydrothermal alteration, faulting, and additional fracturing) control the heterogeneous distributions of hydrologic properties in the unsaturated zone.

The major lithostratigraphic units of the unsaturated zone beneath Yucca Mountain, from top to bottom, are the volcanic tuff formations of the Paintbrush (Tp) Group, the Calico Hills Formation (Tac), and the Crater Flat (Tc) Group. The lithostratigraphic nomenclature divides the Paintbrush Group into the Tiva Canyon (Tpc), Yucca Mountain (Tpy), Pah Canyon (Tpp), and Topopah Spring (Tpt) tuffs. The Crater Flat Group is divided into the Prow Pass (Tcp), Bullfrog (Tcb), and Tram tuffs (Tct). For purposes of hydrogeologic studies, a separate hydrogeologic nomenclature was developed based on the degree of welding and hydrologic property distributions (CRWMS M&O 2000a, Tables 4.7-1 and 8.10-1).

The major hydrogeologic units are divided into the Tiva Canyon welded (TCw), the Paintbrush nonwelded (PTn), (consisting primarily of the Yucca Mountain and Pah Canyon members and the interbedded tuffs), the Topopah Spring welded (TSw), the Calico Hills nonwelded (CHn), and the Crater Flat undifferentiated (CFu) units. Based on the hydrogeologic properties of the lithostratigraphic units, Flint (1998) developed a detailed hydrogeologic stratigraphy for use in numerical flow and transport modeling. The correlations between lithostratigraphic units, hydrogeologic units, and corresponding unsaturated zone flow model layers are presented in Table 2-1. Figure 2-2 shows the spatial relationship of the major hydrogeologic units of the unsaturated zone in both perspective and east–west cross-sectional views. Lithostratigraphic units from the geologic framework model (BSC 2002a) are shown in plan view through the repository horizon and along an east–west cross section of the repository in Figure 2-3.

The welded units typically have low matrix porosities (about 10%) and high fracture densities, whereas the nonwelded and bedded tuffs have relatively high matrix porosities (about 30%) and low fracture densities (BSC 2003b, Table 7). Portions of these units can be altered to zeolites or clays, depending on their cooling history and the presence of water. Such alteration does not affect porosities greatly, but it does decrease the permeabilities of formations where it occurs (BSC 2003b, Tables 7 and 8).

Table 2-1. Major Hydrogeologic Units, Lithostratigraphy, and Unsaturated Zone Model Layer Correlation

Major Hydrogeologic Units[a]	Lithostratigraphic Nomenclature [b]	Hydrogeologic Unit [c]	Unsaturated Zone Flow Model Layer [d]
Tiva Canyon welded (TCw)	Tpcr	CCR, CUC	tcw11
	Tpcp	CUL, CW	tcw12
	TpcLD		
	Tpcpv3	CMW	tcw13
	Tpcpv2		
Paintbrush nonwelded (PTn)	Tpcpv1	CNW	ptn21
	Tpbt4	BT4	ptn22
	Tpy (Yucca)	TPY	ptn23
		BT3	ptn24
	Tpbt3		
	Tpp (Pah)	TPP	ptn25
	Tpbt2	BT2	ptn26
	Tptrv3		
	Tptrv2		
Topopah Spring welded (TSw)	Tptrv1	TC	tsw31
	Tptrn		
		TR	tsw32
	Tptrl, Tptf	TUL	tsw33
	Tptpul, RHHtop		
	Tptpmn	TMN	tsw34
	Tptpll	TLL	tsw35
	Tptpl	TM2 (upper 2/3 of Tptpln)	tsw36
		TM1 (lower 1/3 of Tptpln)	tsw37
	Tptpv3	PV3	tsw38
	Tptpv2	PV2	tsw39 (vitric, zeolitic)

Table 2-1. Major Hydrogeologic Units, Lithostratigraphy, and Unsaturated Zone Model Layer Correlation (Continued)

Major Hydrogeologic Units[a]	Lithostratigraphic Nomenclature [b]	Hydrogeologic Unit [c]	Unsaturated Zone Flow Model Layer [d]
Calico Hills nonwelded (CHn)	Tptpv1	BT1 or BT1*a* (altered)	ch1 (vitric, zeolitic)
	Tpbt1		
	Tac (Calico)	CHV (vitric) or CHZ (zeolitic)	ch2 (vitric, zeolitic)
			ch3 (vitric, zeolitic)
			ch4 (vitric, zeolitic)
			ch5 (vitric, zeolitic)
	Tacbt (Calicobt)	BT	ch6 (vitric, zeolitic)
	Tcpuv (Prowuv)	PP4 (zeolitic)	pp4
	Tcpuc (Prowuc)	PP3 (devitrified)	pp3
	Tcpmd (Prowmd)	PP2 (devitrified)	pp2
	Tcplc (Prowlc)		
	Tcplv (Prowlv)	PP1 (zeolitic)	pp1
	Tcpbt (Prowbt)		
	Tcbuv (Bullfroguv)		
Crater Flat undifferentiated (CFu)	Tcbuc (Bullfroguc)	BF3 (welded)	bf3
	Tcbmd (Bullfrogmd)		
	Tcblc (Bullfroglc)		
	Tcblv (Bullfroglv)	BF2 (nonwelded)	bf2
	Tcbbt (Bullfrogbt)		
	Tctuv (Tramuv)		
	Tctuc (Tramuc)	Not Available	tr3
	Tctmd (Trammd)		
	Tctlc (Tramlc)		
	Tctlv (Tramlv)	Not Available	tr2
	Tctbt (Trambt) and below		

Source: Simmons 2004, Table 8-3.

NOTE: [a] Modified from Montazer and Wilson 1984, Table 1.
[b] BSC 2002a.
[c] Flint 1998.
[d] BSC 2003c.

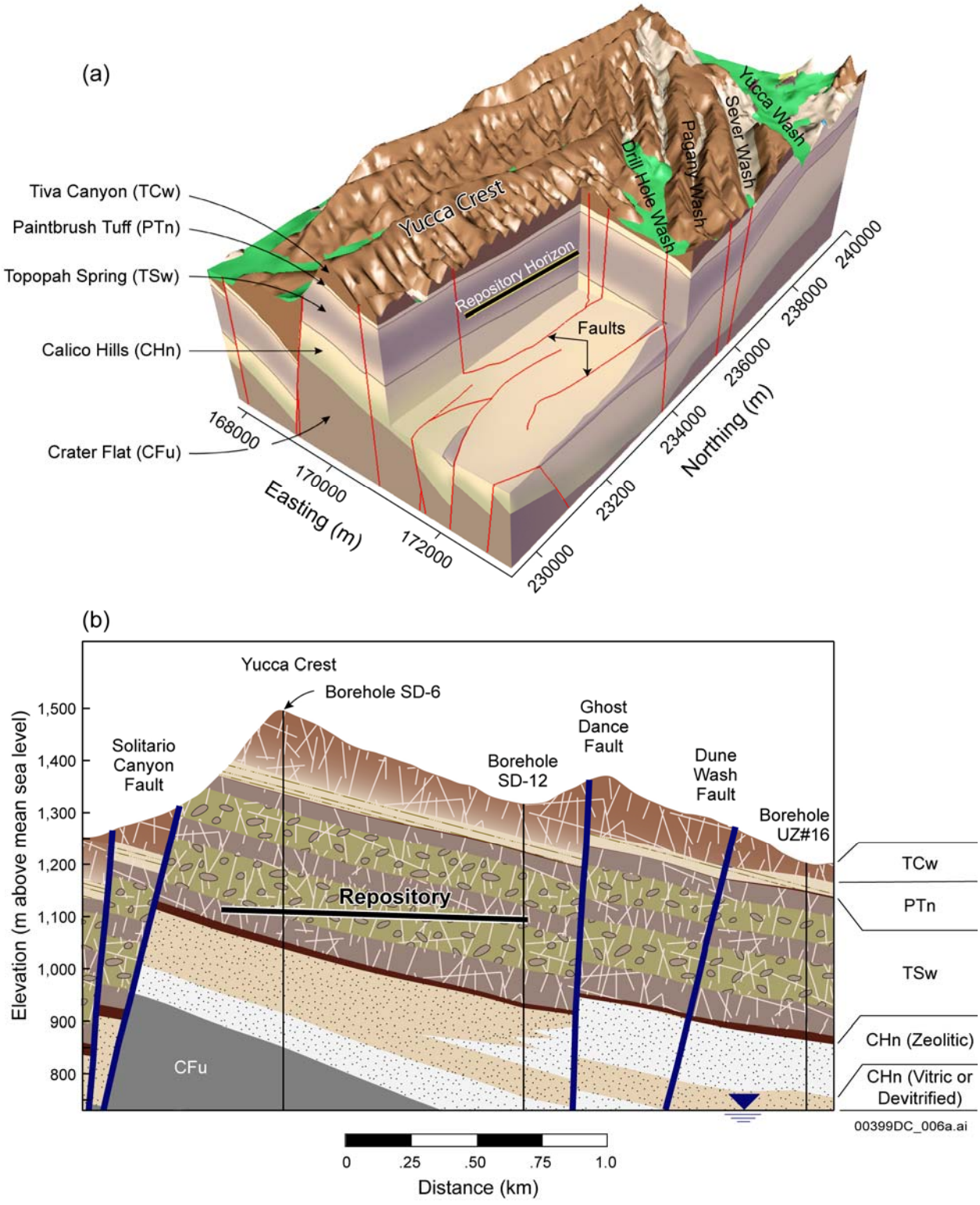

Source: CRWMS M&O 2000b, Figure 3.2-1.

Figure 2-2. Yucca Mountain Site-Scale Hydrogeology in Three-Dimensional Perspective (a) and along an East–West Cross Section (b)

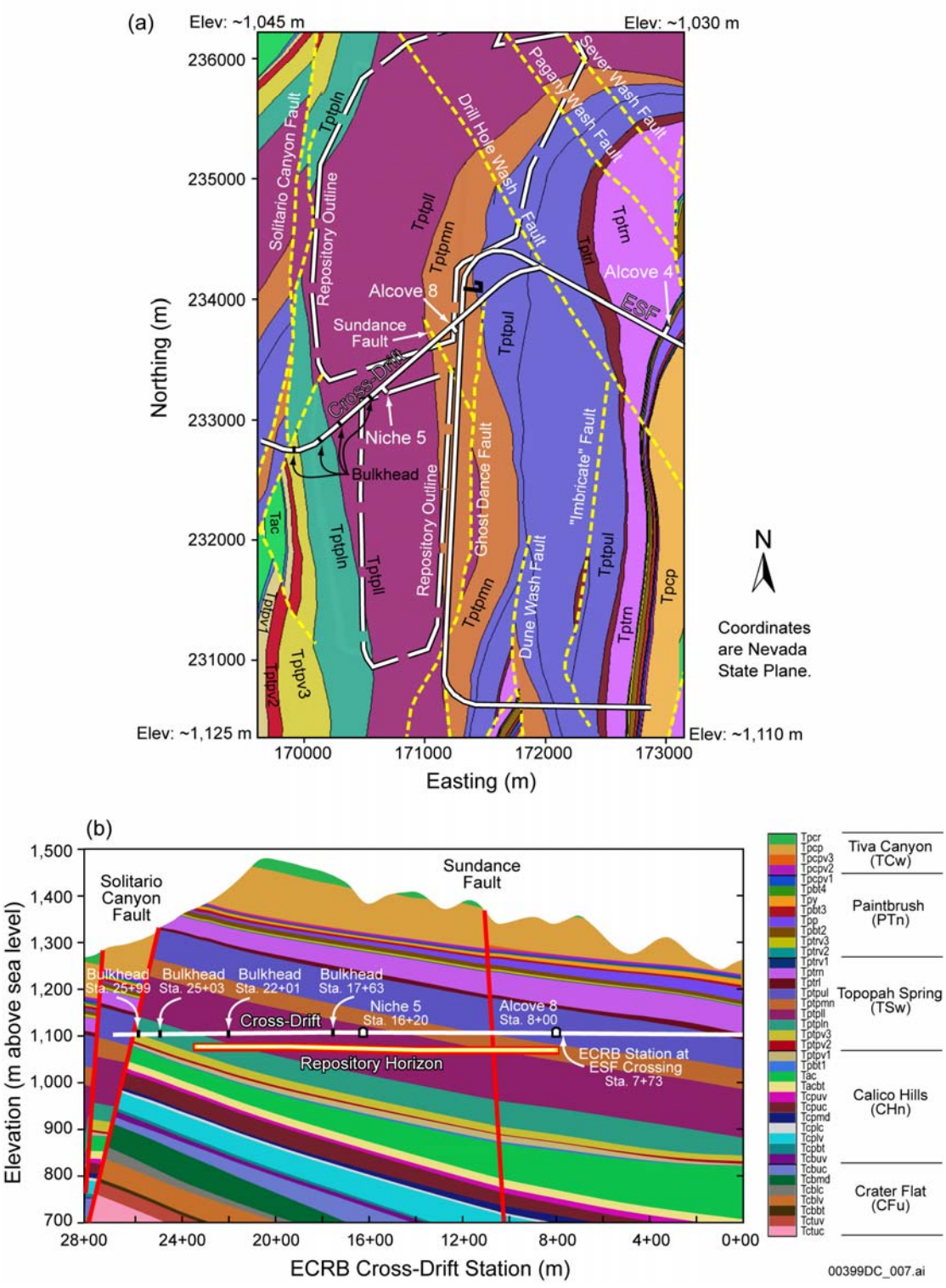

Source: BSC 2003a, Figure 1.2-3.

NOTE: ECRB = Enhanced Characterization of the Repository Block.

Figure 2-3. Yucca Mountain Lithostratigraphic Units and Major Hydrogeologic Units in Plan View through the Repository Horizon (a) and East–West Cross Section of Units Intersected by the Repository Horizon (Tptpul, Tptpmn, Tptpll, and Tptpln) (b)

2.2 HYDROGEOLOGIC DATA

The Yucca Mountain site has been characterized in the past two decades. The data, including hydrogeologic data, have been collected at multiple depths from surface-based boreholes and underground tunnels (i.e., the Exploratory Studies Facility (ESF) and Enhanced Characterization of the Repository Block (ECRB) Cross-Drift). Figure 2-4 illustrates the locations of deep boreholes, the ESF, and the ECRB Cross-Drift used in unsaturated zone flow studies (CRWMS M&O 2000b, Figure 2.1-2). Hydrogeologic data have been used for formulating, calibrating, and validating unsaturated zone flow models.

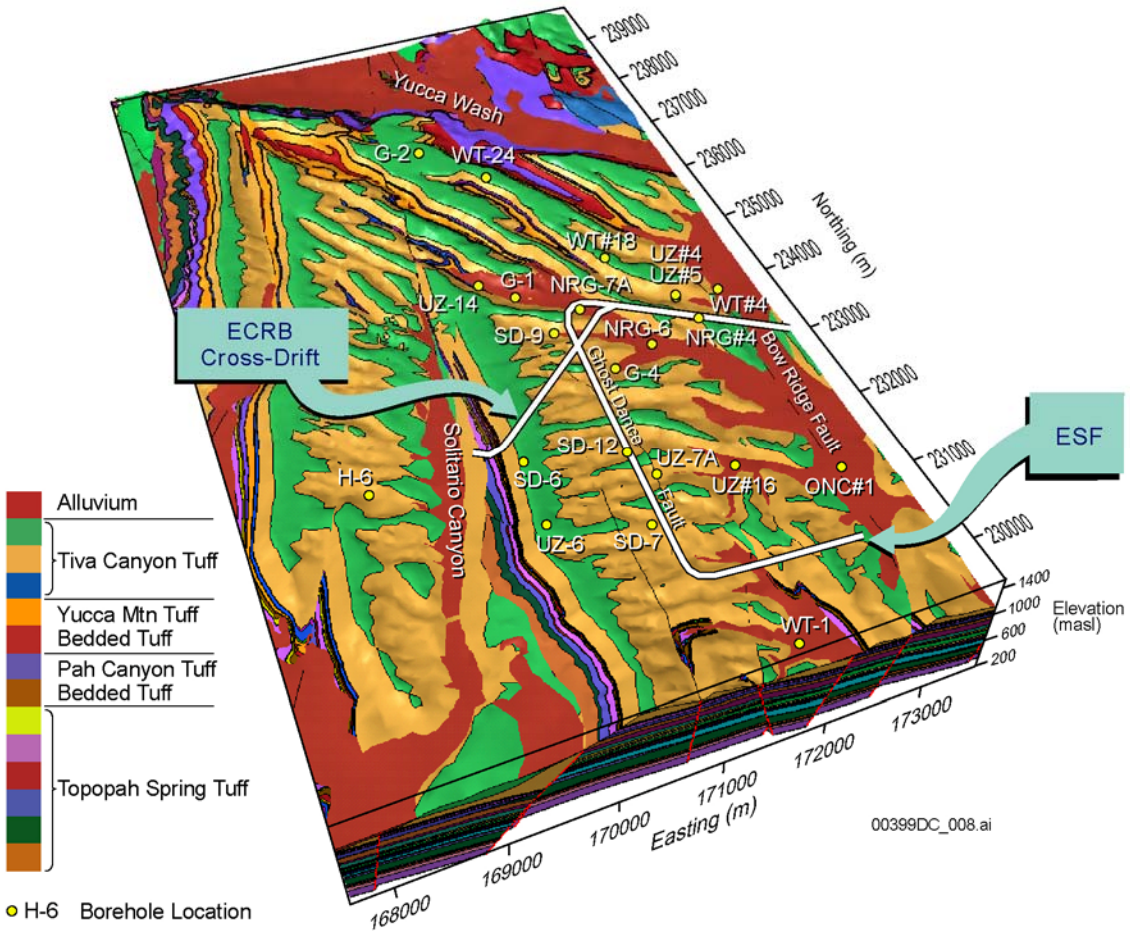

Source: CRWMS M&O 2000b, Figure 2.1-2.

Figure 2-4. Deep Boreholes and Underground Drifts of the ECRB Cross-Drift and the Exploratory Studies Facility and the Major Faults in the Vicinity of Yucca Mountain

2.2.1 Hydrogeologic Data for the Rock Matrix

Rock core samples collected from the unsaturated zone (Flint 1998, p. 11) were analyzed to determine matrix porosity, bulk density, particle density, and water content, with the number of samples used for different matrix properties in different units shown in Table 2-2. Subsets of samples were measured for water potential determination, saturated hydraulic conductivity (or

permeability), and moisture-retention relations. Matrix permeabilities in nonwelded units are orders of magnitude higher than those in welded units. Table 2-2 shows averaged matrix properties developed from core data for different hydrogeologic units.

Deep boreholes (USW NRG#4, USW NRG#5, USW NRG-6, USW NRG-7a, USW SD-7, USW SD-9, USW SD-12, USW UZ-1, USW UZ-4, UE-25 UZ#5, USW UZ-7a) were instrumented in the unsaturated zone to measure in situ matrix water potential using thermocouple psychrometers at multiple depths (Rousseau et al. 1999, p. 77; Rousseau et al. 1997, pp. 18 to 19). Monitoring in these boreholes began in October 1994 and continued to December 2001. As an example, Figure 2-5 shows stabilized in situ water potential measurements at different depths in borehole USW SD-12. The data indicate that matrix water potential is on the order of 1 bar (10^5 Pa) through the unsaturated zone. In situ matrix water potential data were also collected from the ECRB Cross-Drift (BSC 2004, Section 7.2).

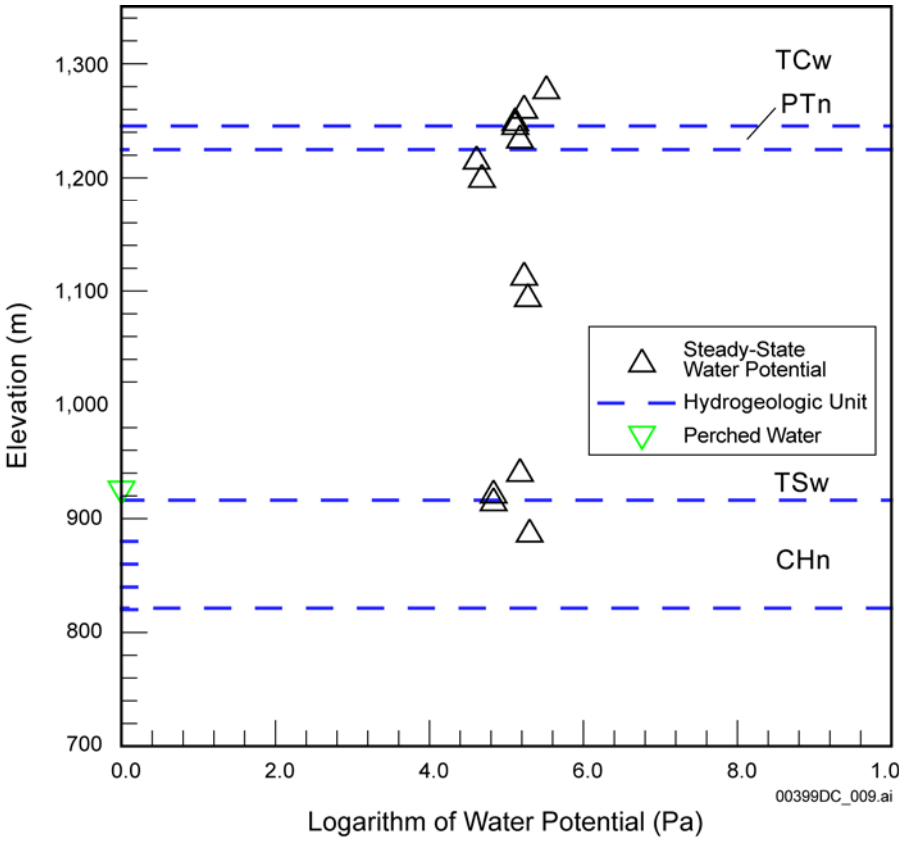

Source: BSC 2004, Figure 6.2-4.

NOTE: Simulation results are removed from the original figure.

Figure 2-5. Observed Water Potentials and Perched Water Elevations for Borehole USW SD-12

Table 2-2. Matrix Properties Developed from Core Data

Hydrogeologic Unit	ϕ	upscaled k [m^2]	upscaled log(k) [log(m^2)]	$\sigma_{log(k)}$	n	n_{nd}	$SE_{log(k)}$	$1/\alpha$ [Pa]	log($1/\alpha$) [log(Pa)]	$SE_{log(1/\alpha)}$	m	SE_m	S_r	η
CCR & CUC	0.241	4.7×10^{-15}	-14.33	0.47	3	0	0.27	8.27×10^{4}	4.918	0.279	0.388	0.085	0.02	3.47
CUL & CW	0.088	6.4×10^{-20}	-19.20	2.74	15	25	0.43	5.46×10^{5}	5.737	0.178	0.280	0.045	0.20	12.29
CMW	0.200	1.8×10^{-16}	-15.74	2.38	5	1	0.97	2.50×10^{5}	5.398	0.188	0.259	0.042	0.31	6.08
CNW	0.387	4.0×10^{-14}	-13.40	2.05	10	0	0.65	2.03×10^{4}	4.308	0.199	0.245	0.032	0.24	-2.58
BT4	0.428	4.1×10^{-13}	-12.39	1.41	11	0	0.43	4.55×10^{3}	3.658	0.174	0.219	0.019	0.13	-0.26
TPY	0.233	1.3×10^{-15}	-14.90	0.64	2	0	0.46	7.63×10^{4}	4.883	0.379	0.247	0.064	0.07	3.46
BT3	0.413	1.3×10^{-13}	-12.87	1.09	11	1	0.31	8.90×10^{3}	3.950	0.088	0.182	0.008	0.14	-0.56
TPP	0.498	1.1×10^{-13}	-12.96	0.39	11	0	0.12	2.12×10^{4}	4.325	0.104	0.300	0.023	0.06	0.26
BT2	0.490	6.7×10^{-13}	-12.17	1.12	21	0	0.24	1.74×10^{4}	4.239	0.170	0.126	0.013	0.05	-2.64
TC	0.054	4.4×10^{-17}	-16.36	3.02	6	5	0.91	2.71×10^{5}	5.432	0.310	0.218	0.054	0.21	6.14
TR	0.157	3.2×10^{-16}	-15.50	0.94	46	1	0.14	9.43×10^{4}	4.974	0.116	0.290	0.025	0.07	5.00
TUL	0.155	2.8×10^{-17}	-16.56	1.61	37	12	0.23	1.75×10^{5}	5.244	0.111	0.283	0.024	0.12	7.06
TMN	0.111	4.5×10^{-19}	-18.34	0.97	74	35	0.09	1.40×10^{6}	6.147	0.108	0.317	0.042	0.19	10.90
TLL	0.131	3.7×10^{-17}	-16.44	1.65	51	24	0.19	6.01×10^{4}	4.779	0.521	0.216	0.061	0.12	6.27
TM2 & TM1	0.103	2.3×10^{-20}	-19.63	3.67	21	42	0.46	3.40×10^{6}	6.532	0.097	0.442	0.073	0.20	14.48
PV3	0.043	2.9×10^{-18}	-17.54	1.57	16	2	0.37	1.00×10^{6}	6.000	0.278	0.286	0.065	0.42	9.04
PV2a	0.275	a	a	a	a	a	a	2.17×10^{5}	5.336	0.156	0.059	0.007	0.36	5.03
PV2v	0.229	4.3×10^{-13}	-12.37	1.38	16	0	0.34	1.94×10^{4}	4.287	0.042	0.293	0.011	0.13	-0.19
BT1a	0.285	3.5×10^{-17}	-16.45	2.74	9	1	0.87	4.72×10^{6}	6.674	0.183	0.349	0.073	0.38	7.39
BT1v	0.331	2.1×10^{-13}	-12.67	1.11	35	0	0.19	1.35×10^{4}	4.131	0.049	0.240	0.008	0.06	-2.07
CHV	0.346	1.6×10^{-12}	-11.81	1.62	46	0	0.24	3.39×10^{3}	3.530	0.094	0.158	0.008	0.06	-3.80
CHZ	0.322	5.2×10^{-18}	-17.28	0.91	99	17	0.08	4.45×10^{5}	5.649	0.094	0.257	0.022	0.26	8.30
BTa	0.271	8.2×10^{-19}	-18.08	2.05	9	8	0.50	6.42×10^{6}	6.808	0.043	0.499	0.036	0.36	11.87
BTv	b	b	b	b	b	b	b	5.04×10^{4}	4.703	0.207	0.147	0.020	b	-0.87
PP4	0.321	1.5×10^{-16}	-15.81	2.74	6	2	0.97	5.00×10^{5}	5.699	0.401	0.474	0.224	0.29	7.13
PP3	0.318	6.4×10^{-15}	-14.20	0.75	51	0	0.11	1.32×10^{5}	5.120	0.084	0.407	0.031	0.08	3.37
PP2	0.221	5.4×10^{-17}	-16.27	1.18	34	3	0.19	6.22×10^{5}	5.794	0.147	0.309	0.041	0.10	6.69
PP1	0.297	8.1×10^{-17}	-16.09	1.52	27	1	0.29	1.13×10^{5}	5.052	0.234	0.272	0.036	0.30	6.05
BF3/TR3	0.175	1.1×10^{-15}	-14.95	1.64	7	1	0.58	8.94×10^{4}	4.951	0.931	0.193	0.117	0.11	3.11
BF2	0.234	c	c	c	c	c	c	8.46×10^{6}	6.927	0.032	0.617	0.070	0.21	8.86

Source: BSC 2003b, Table 8.

NOTE: (a) BT1a was used as an analog for permeability because only one permeability data point is available for PV2a.
(b) BT1v was used as an analog for porosity, residual saturation, and permeability because only one sample is available for BTv.
(c) PP1 was used as an analog for permeability because only one measurable permeability data point is available for BF2.
k is permeability; σ is standard deviation; n is number of samples; ϕ is porosity; $_{nd}$ is number of samples with nondetected permeability measurements; α and m are fitting parameters for the van Genuchten water potential relationship; SE is standard error; S_r is residual liquid saturation; η and upscaled k are defined in Equations 29 and 34, respectively, in *Calibrated Properties Model* (BSC 2003b). The hydrogeologic units correspond to those given in Table 2-1.

In the 1980s, temperature measurements were made in numerous boreholes within the central block of Yucca Mountain and in the surrounding area (Sass et al. 1988) as part of a regional heat flow study. More recently, in situ temperature data were made as part of the Yucca Mountain instrumented borehole monitoring program (Rousseau et al. 1999, p. 77; Rousseau et al. 1997, pp. 18 to 19). Thermal properties (including rock grain density, dry and wet rock thermal conductivities, and rock grain specific heat capacity) were also measured for rock samples collected from surface-based boreholes (BSC 2003b, Section 6.3).

2.2.2 Permeability Data for Fractures

In order to compile data regarding matrix and fracture permeability, fracture geometry data (density, trace length, dips, and strikes) were obtained through detailed line surveys along the ESF tunnel walls. Fracture frequency data also has been collected from surface-based boreholes. As previously mentioned, fracture densities in welded units are much higher than those in nonwelded units (BSC 2003b, Table 7).

Air injection tests have been used to characterize fracture permeabilities from surface-based and underground boreholes associated with the ESF (LeCain et al. 2000; BSC 2003b, Section 6.1; BSC 2003a, Sections 6.1 and 6.11). In a welded unit, fracture permeability is orders of magnitude higher than the corresponding matrix permeabilities. Matrix and fracture permeabilities are roughly on the same order of magnitude for a nonwelded unit (BSC 2003b, Tables 7 and 8).

Temporal air pressure fluctuations on the ground surface propagate through the unsaturated zone (BSC 2003b, Section 4). Air pressure (pneumatic) data, as a function of time, were collected using sensors installed in a number of surface-based boreholes (including UE-25 NRG-5, USW NRG-6, USW NRG-7a, USW SD-7, USW SD-12, and USW UZ-7a) (Rousseau et al. 1999, p. 77; Rousseau et al. 1997, pp. 18 to 19). This data set is useful for understanding airflow in the unsaturated zone and for inferring large-scale fracture permeabilities.

Air permeabilities have been measured in ESF boreholes (BSC 2003a, Sections 6.1 and 6.11). More than 3,500 separate pneumatic injections have been undertaken to systematically characterize air permeability in locations throughout the ESF and ECRB Cross-Drift. Table 2-3 summarizes mean permeabilities and standard deviations in different areas of the underground facilities.

Table 2-3. Comparison of Geometric Means and Standard Deviations of Air Permeability Measurements Collected in Niches and Alcoves in the Yucca Mountain Exploratory Studies Facility

Borehole Cluster	Type of Site	log(*k*) (m^2)	
		Mean	Standard Deviation
Niche 1 Preexcavation	Intersects brecciated zone	−13.0	0.92
Niche 1 Radial	Predominantly within brecciated zone	−11.8	0.66
Niche 2 Preexcavation	Moderately fractured welded tuff	−13.4	0.81
Niche 2 Postexcavation	Postexcavation welded tuff	−11.8	0.88
Niche 3 Preexcavation	Moderately fractured welded tuff	−13.4	0.70
Niche 3 Postexcavation	Postexcavation welded tuff	−12.4	0.82
Niche 3 Radial	Moderately fractured welded tuff	−13.8	0.92
Niche 4 Preexcavation	Highly fractured welded tuff	−13.0	0.85
Niche 4 Postexcavation	Postexcavation welded tuff	−11.9	0.78
Niche 5 Preexcavation side	Highly porous lithophysal cavities; holes on side of excavation	−11.4	0.77
Niche 5 Postexcavation side	Highly porous lithophysal cavities; holes on side of excavation	−11.2	0.73
Niche 5 Preexcavation overhead	Highly porous lithophysal cavities; holes above of excavation	−11.4	1.14
Niche 5 Postexcavation overhead	Highly porous lithophysal cavities; holes above of excavation	−11.0	1.27
Alcove 4	Discretely faulted and fractured nonwelded tuff	−13.0	0.93
Alcove 6	Highly fractured postexcavation welded tuff	−11.9	0.67
Alcove 8	Transition from upper lithophysal to welded fractured nonlithophysal in near vertical boreholes	−13.1	1.29

Source: BSC 2003a, Table 6.1.2-5.

NOTE: Niche 1 is also referred to as Niche 3566; Niche 2 is also referred to as Niche 3650; Niche 3 is also referred to as Niche 3107; Niche 4 is also referred to as Niche 4788; Niche 5 is also referred to as Niche 1620.

2.2.3 Hydrologic Data for Faults

Although faults may serve as important flow paths within the unsaturated zone (Section 3), hydrologic data collected from the unsaturated zone for faults are limited. To obtain fault properties, air injection testing and tracer testing were conducted in the northern Ghost Dance fault alcove constructed off the ESF (LeCain et al. 2000, p. 2). The goals of the fault testing were to determine air permeability, porosity, and gaseous tracer transport characteristics (transport porosity and longitudinal dispersivity) in the volcanic rocks (tuff) that comprise the fault zone, footwall, and hanging wall of Ghost Dance fault. Permeability, porosity, and tracer transport characteristics of these tuffs control fluid movement in Yucca Mountain; quantified values of these parameters are needed for fluid flow numerical modeling in the unsaturated zone. Air injection testing was also conducted in southern Ghost Dance fault and Bow Ridge fault. In general, fracture permeabilities in fault zones are higher than nonfault zones (LeCain et al. 2000, Summary).

2.3 GEOCHEMICAL DATA

Geochemical analyses offer additional information over large scales, both spatially and temporally, for evaluating the flow processes of the Yucca Mountain unsaturated zone. Different fluid samples analyzed in Yucca Mountain studies include pore waters, gases from the unsaturated zone, and perched water. This section synthesizes available geochemical information within the unsaturated zone relevant to unsaturated zone flow paths. Figure 2-6 summarizes the available geochemical and isotopic information related to unsaturated zone flow and transport. Brief discussions on the data follow. This section does not present a comprehensive review of all available geochemical information, but rather focuses on those related to unsaturated zone flow processes.

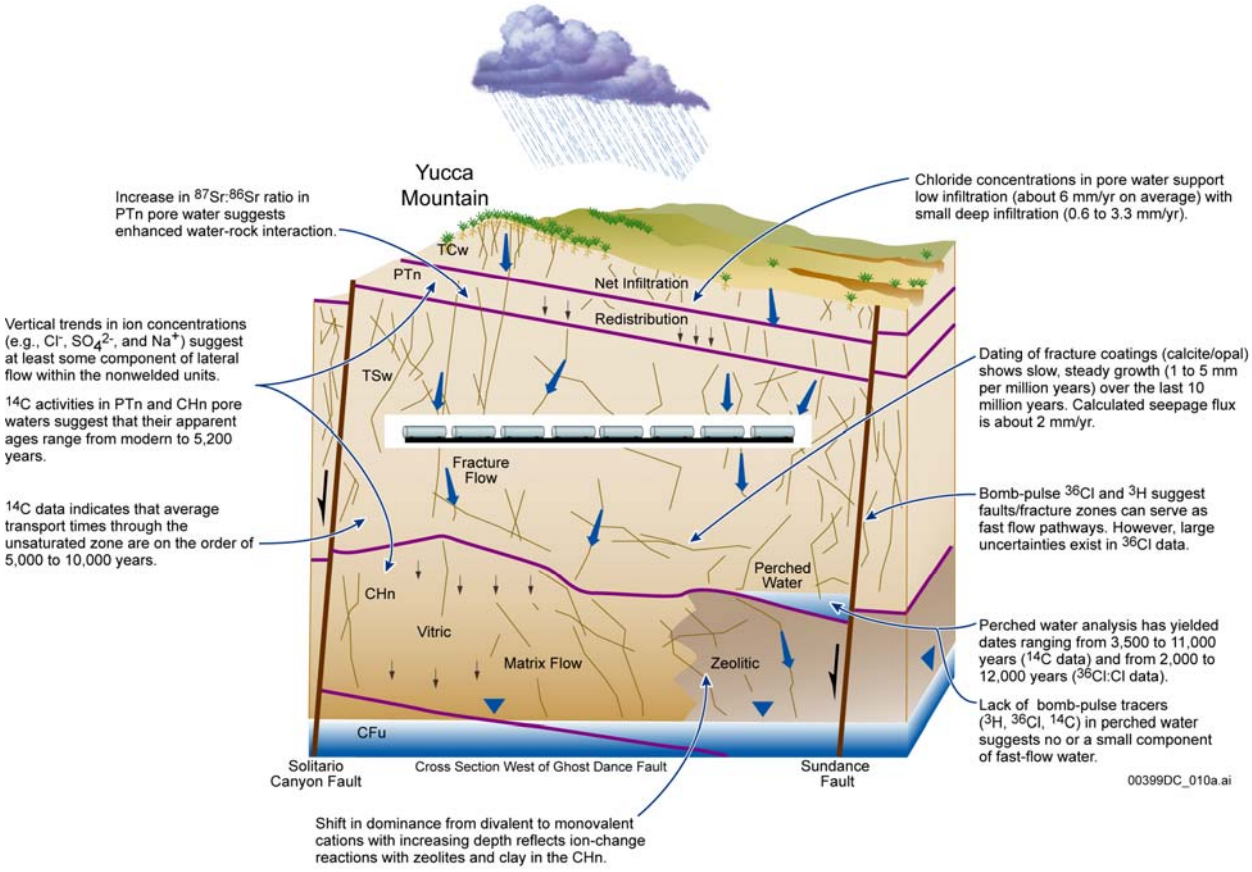

Source: BSC 2001, Figure 6.2-1.

Figure 2-6. Geochemical Information Related to Unsaturated Zone Flow Paths

2.3.1 Geochemical Composition of Pore Water

The chemical composition of unsaturated zone pore water provides corroborative evidence of water flow rates and pathways in the unsaturated zone. The pore water composition is determined by rock–water interactions. Pore water samples were extracted from unsaturated core samples recovered from dry drilled boreholes. Pore water extracted from the PTn are calcium chloride or calcium sulfate-type water. In terms of relative portions of anions, the chemical composition of TSw pore water falls between those of the PTn and CHn units. Pore water extracted from the CHn unit is sodium carbonate bicarbonate-type water. Sodium concentration increases as depth increases in the CHn. This shift in dominance from divalent to monovalent cations primarily reflects ion exchange reactions with zeolites in the CHn unit (Figure 2-6). Deviations from vertical trends in ion concentrations (chloride, sulfate, and sodium) suggest that at least some component of lateral flow exists within the unsaturated zone (BSC 2002b, pp. 121 to 122).

Pore water strontium data have been obtained from several boreholes. The data obtained from borehole USW SD-7 show that the ratio of $^{87}Sr/^{86}Sr$ increases with depth from ground surface to the repository horizon. This increase is steeper within the nonwelded units of the PTn (BSC 2002b, Figure 38), suggesting an enhanced water–rock interaction within the PTn (Figure 2-6). This is consistent with the current conceptual model in which water flow within the PTn occurs mainly in the matrix (Section 3.1.2). Observed pore water strontium concentrations from selected boreholes were also used to verify the site-scale unsaturated zone flow model (Section 4.3).

Chloride concentration data for pore water from the TCw, PTn, TSw, and CHn hydrogeologic units were compared against other available data to elucidate general trends (BSC 2002b, Section 6.5.3). The smaller concentration of chloride (which behaves as a conservative tracer) in perched water implies that pore water and perched water have distinctly different histories of geochemical evolution, undergoing different degrees of evaporation and water–rock interaction. This observation has been used for developing the conceptual understanding of fracture–matrix interaction in the TSw unit (Section 3.2.1).

Apparent infiltration rates were estimated by the chloride mass balance method, using chloride concentrations from pore water samples (BSC 2002b). PTn samples beneath deep alluvium had infiltration rates between 0.6 and 3.3 mm/yr. The overall average infiltration rate for pore water samples collected along the ESF main drift and the ECRB Cross-Drift is about 6 mm/yr. Observed pore water chloride concentration distribution along the ECRB Cross-Drift (Figure 2-7) is used to verify the site-scale unsaturated zone flow model (Section 4.3).

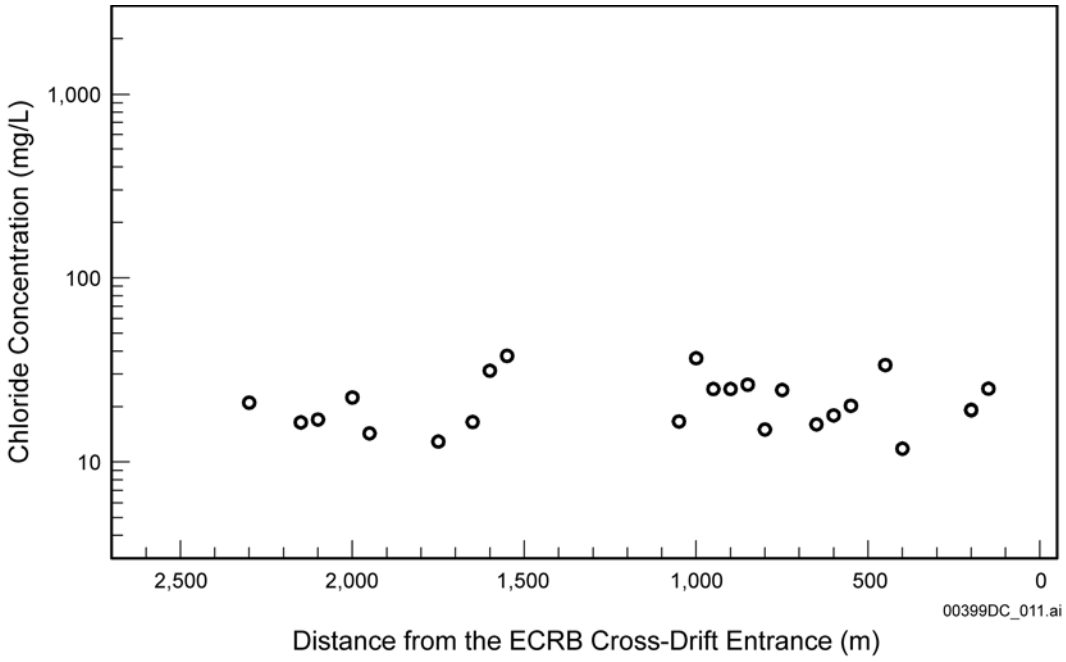

Source: BSC 2004, Figure 6.5-4.

NOTE: Simulation results were removed from the original figure.

Figure 2-7. Observed Pore Water Chloride Concentration Distribution along the ECRB Cross-Drift

2.3.2 Ages of Pore Water

The ^{14}C dating method was used to estimate the ages of pore water (BSC 2002b, Section 6.6.4.1). In general, ^{14}C activities in pore waters from both the PTn and CHn yield apparent ages ranging from present-day to 5,200 years (Figure 2-6). Apparent ages are based on the assumptions that the initial ^{14}C activity is 100 pmc (percent modern carbon) and that geochemical processes have not significantly altered the carbon isotopic composition of the sample. Changes relative to the initial atmospheric ^{14}C activity are assumed to be solely the result of radioactive decay.

To be accurate, radiocarbon age estimates must be corrected for contaminants like those potentially introduced to the pore water by CO_2 from drilling air. Contamination with this CO_2 would shift the isotopic signature to younger age estimates, causing the pore water to appear to have erroneously smaller residence times (Yang 2002, Section 4.1.2). The ^{14}C age estimates presented here were estimated based on the approach summarized by Yang (2002), which considered this correction for drilling air CO_2.

The ^{14}C values for perched water indicate an apparent age of 3,500 to 11,000 years (BSC 2002b, Section 6.9.3). ^{36}Cl analyses of perched water indicate that its age ranges from 2,000 to 12,000 years for the different perched water bodies sampled, which are in general agreement with ^{14}C–based ages (BSC 2002b, Section 6.6.3.6).

^{14}C age data are used for verifying the site-scale unsaturated zone flow model (Section 4.3).

2.3.3 ^{36}Cl and Tritium

^{36}Cl/Cl ratios and tritium data were used to provide evidence for potential fast path signals in unsaturated zone flow. There are ongoing ^{36}Cl validation studies being conducted by the U.S. Geological Survey (USGS), Lawrence Livermore National Laboratory (LLNL), and the Desert Research Institute (BSC 2003a, Section 6.14.2.1).

Elevated ^{36}Cl/Cl ratios were reported from Yucca Mountain at the depth of the repository horizon during the late 1990s (Fabryka-Martin et al. 1996; 1997; 1998). The ^{36}Cl/Cl values above $1{,}250 \times 10^{-15}$ (the upper limit for Pleistocene meteoric input) were attributed to atmospheric nuclear testing in the Pacific Ocean and interpreted as an indication that at least some meteoric water is capable of percolating rapidly through the unsaturated zone to depths of 300 m below the surface in the last 50 years (Fabryka-Martin et al. 1996; 1997; 1998; Levy et al. 1999).

Current flow and transport models used for TSPA include potential transport pathways that, under present-day climate conditions, result in a small fraction of the modeled flow paths acting as fast flow paths (BSC 2003d, Figure 6.9-1). The inclusion of these fast flow paths in unsaturated zone flow modeling is consistent with the results indicated by ^{36}Cl measurements reported by Fabryka-Martin et al. (1996).

Because of the fast path hydrologic implications for the repository, the validation study was initiated in late 1999 to independently verify the presence of bomb-pulse ^{36}Cl in the ESF. The study primarily entailed analyses of core from 50 new boreholes drilled across two zones, the Sundance fault and the Drill Hole Wash fault, where significant ^{36}Cl/Cl bomb-pulse ratios were identified by Fabryka-Martin et al. (1996).

Fabryka-Martin et al. (1996) reported numerous samples from the ESF with elevated levels of ^{36}Cl in a 165-m-wide zone associated with the Sundance fault (Figure 2-8). Ratios of ^{36}Cl/Cl near or above $1{,}250 \times 10^{-15}$ were obtained for 11 of 16 samples between ESF Stations 34+28 and 35+93 (^{36}Cl/Cl ratios from $1{,}339 \times 10^{-15}$ to $4{,}105 \times 10^{-15}$). Also, 9 of 15 samples from Niche 1, also associated with the Sundance fault, had ^{36}Cl/Cl values from $1{,}235 \times 10^{-15}$ to $2{,}038 \times 10^{-15}$. Validation study sampling targeted these zones to maximize the probability of reproducing the ^{36}Cl signal.

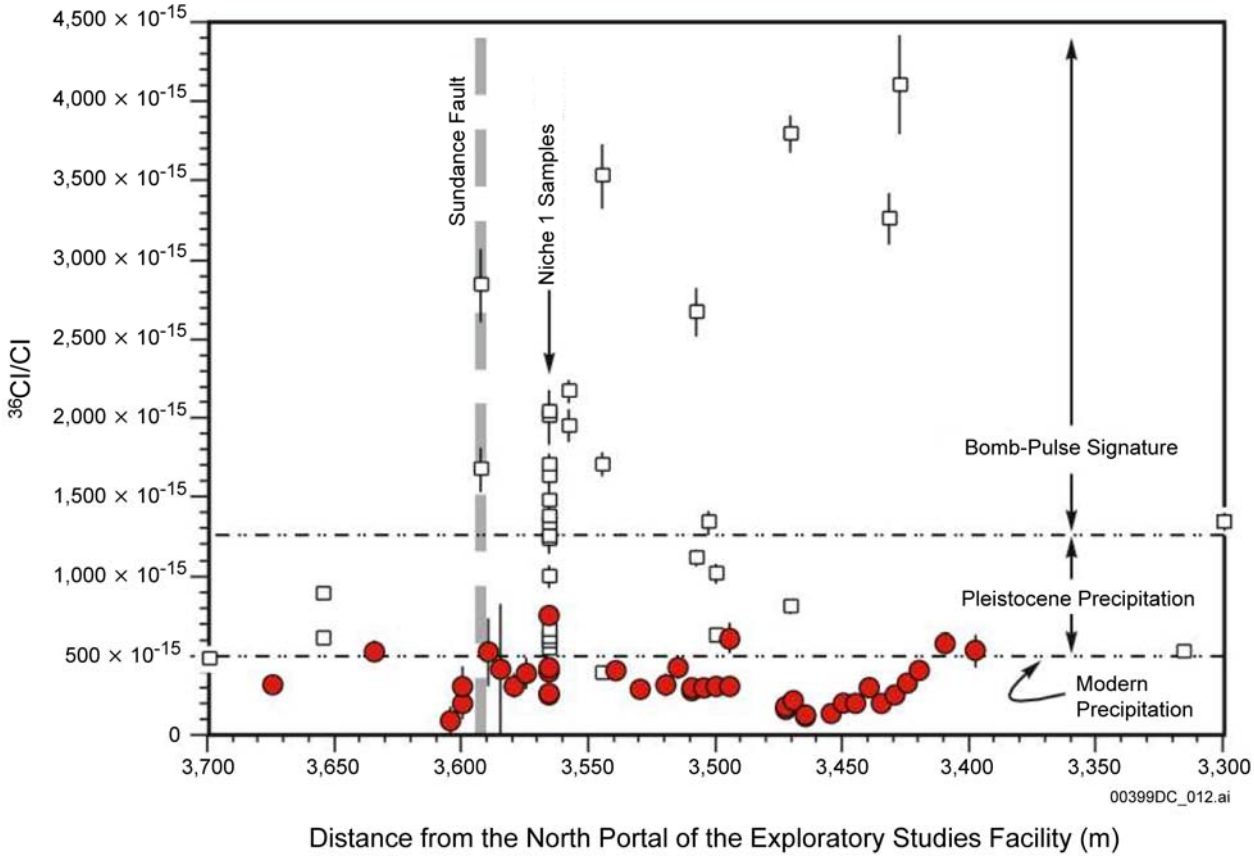

Source: BSC 2003a, 6.14.2-1.

NOTE: Although the main trace of the Sundance fault (shaded broad dashes) is exposed at a distance of 3,593 m from the ESF North Portal, the entire zone between about 3,400 and 3,650 m is pervasively fractured. Analytical errors (2σ) are shown as vertical lines if they are larger than the size of the symbol. USGS-LLNL validation study samples are shown as filled circles. Previously published LANL data are shown as open squares.

Figure 2-8. ^{36}Cl/Cl Ratio Plotted against Sample Location in the Exploratory Studies Facility

In addition to ^{36}Cl/Cl ratios, tritium was also used as a potential indicator of percolation rates. The analytical uncertainty for tritium analysis is 4 tritium units, based on counting statistics. All values above 25 tritium units lie outside the range of the population of background samples (BSC 2002b, Sections 6.2.6 and 6.6.2.2). The limitation of this approach is that background, in this case, includes postbomb waters that have decayed to prebomb tritium levels. This limitation contributes to uncertainty in tritium analyses. Bomb-pulse levels of tritium (greater than 25 tritium units) have been observed in the Bow Ridge fault zone in ESF Alcove 2 and in about 6% of the pore waters extracted from core samples from 11 surface-based boreholes. These detections occur within the TCw, PTn, and TSw, and also in some samples from the CHn as deep as the Prow Pass member of the CFu (BSC 2002b, Section 6.6.2.3).

In addition to the Bow Ridge fault location in the ESF above the PTn unit, samples with high tritium values are present in the south ramp of the ESF, where the PTn units are faulted and offset, and from 750 to 950 m in the ECRB in the upper lithophysal unit of the Topopah Spring Tuff. The occurrences in the Bow Ridge fault and in the south ramp of the ESF are clearly

linked to the absence of the PTn units or the inability of these units to impede downward percolation of young water at those locations. In the ECRB, it is unclear what features may provide the pathways for the percolation of young water. The investigation into the presence of tritium in pore water from the ECRB is in progress (BSC 2003a, Section 7.14.2.2).

2.3.4 Uranium Isotopes

At Yucca Mountain, uranium isotopic ratios have been used to evaluate the prevalence and frequency of fracture flow through the unsaturated zone and the issue of local recharge to the water table. Substantial differences in $^{234}U/^{238}U$ activity ratios between pore water and fracture water (from $^{234}U/^{238}U$ in fracture minerals as well as perched water) imply minimal liquid exchange between fracture and matrix flow pathways (BSC 2002b, Section 6.6.7).

Groundwater from the saturated zone beneath Yucca Mountain contains elevated $^{234}U/^{238}U$ activity ratios (between 6 and 8) compared to water from wells in adjacent areas to the south (between 1.5 and 4 (BSC 2002b, Figure 42)). Groundwater obtained from Paleozoic carbonate rocks at depth beneath Yucca Mountain (UE-25 p#1) has a much smaller $^{234}U/^{238}U$ ratio of 2.32, typical of the regional carbonate aquifer and is indicative of the stratification of shallow and deep aquifers at the site (Figure 2-6). The anomalous uranium isotopic compositions of shallow saturated zone water beneath Yucca Mountain are similar to the $^{234}U/^{238}U$ compositions measured for deep unsaturated zone fracture minerals and perched water bodies in the welded TSw. This similarity supports the concept of recharge through the thick unsaturated zone at Yucca Mountain and that much of the local recharge derives from flow through fracture pathways in the welded units of the unsaturated zone rather than from percolation through the matrix column in these units (BSC 2002b, Section 6.6.7).

Interpretations of the uranium isotopic data are used for developing a conceptual model of water flow within the unsaturated zone (Section 3).

2.3.5 Fracture-Lining Minerals

Deposits of calcite and opal lining fractures and cavities in the ESF contain spatial and temporal information on past water migration through the Yucca Mountain unsaturated zone. These mineral coatings provide a record of past water percolation through the connected fracture network in areas where solutions exceed chemical saturation with respect to various mineral phases. Calcite is abundant in the calcic soils at Yucca Mountain, leading to rapid saturation of infiltrating water with respect to calcite. The volcanic rocks are calcium-poor, so infiltrating water is essentially the only source of calcium available to form the calcite in the unsaturated zone. Therefore, the calcite that has formed in a cavity can be related directly to the amount of water required to transport that amount of calcium into the cavity. The calculated amount of water would be a minimum estimate of the amount of water that actually seeped into the cavity, unless the water evaporated completely within the cavity. The total percolation flux for the whole unsaturated zone, based on measurements of total calcite abundance in the ESF, indicates a flux of about 2 mm/yr, which is within an order of magnitude of the estimated long-term infiltration flux at the surface (BSC 2002b, Section 6.10.3.5). Field observations also indicate that less than 10% of all fractures and open spaces contain coatings of calcite and opal (BSC 2002b, Section 7.6).

Geochronological data indicate that calcite and opal have grown in the fractures of deep unsaturated zone at extremely slow and relatively uniform rates (1 to 5 mm per million years) over the last 10 million years (Neymark et al. 2002). This uniform mineral growth rate implies that fracture flow in the deep unsaturated zone at Yucca Mountain did not vary substantially despite climate variations. In addition, ^{230}Th/U ages do not show clustering that can be correlated with cycles of pluvial-interpluvial climate over the last 200,000 years. The ^{234}U/^{238}U ratios calculated for opal and calcite deposited within the repository horizon also imply that deep unsaturated zone fracture flow at Yucca Mountain was low in volume or infrequent (BSC 2002b, Section 7.6).

The fracture coating data are used for verifying the site-scale unsaturated zone flow model (Section 4.3).

2.4 IN SITU FIELD TESTING

This section briefly reviews selected in situ field tests that are important for understanding flow paths within the unsaturated zone, and for developing and verifying unsaturated zone flow models. More comprehensive discussions of in situ field tests can be found in *In Situ Field Testing of Processes* (BSC 2003a).

2.4.1 In Situ Borehole Testing

As discussed in Section 2.2, a number of deep boreholes were instrumented in the Yucca Mountain unsaturated zone to measure in situ pneumatic pressure, water potential, and temperature at multiple depths (Rousseau et al. 1999, p. 77; Rousseau et al. 1997, pp. 18 to 19). The data collection also included measurements of gas phase ^{14}C from selected boreholes. The data collected from in situ borehole testing are used for developing and validating the site-scale unsaturated zone flow model (Section 4).

2.4.2 Busted Butte Tests

The Busted Butte test facility is located 8 km southeast of the Yucca Mountain repository area. It was chosen as a test location because of its readily accessible exposure of the vitric CHn (Figure 2-9) (CRWMS M&O 2001, Sections 6.8.1.1 and 6.8.1.2).

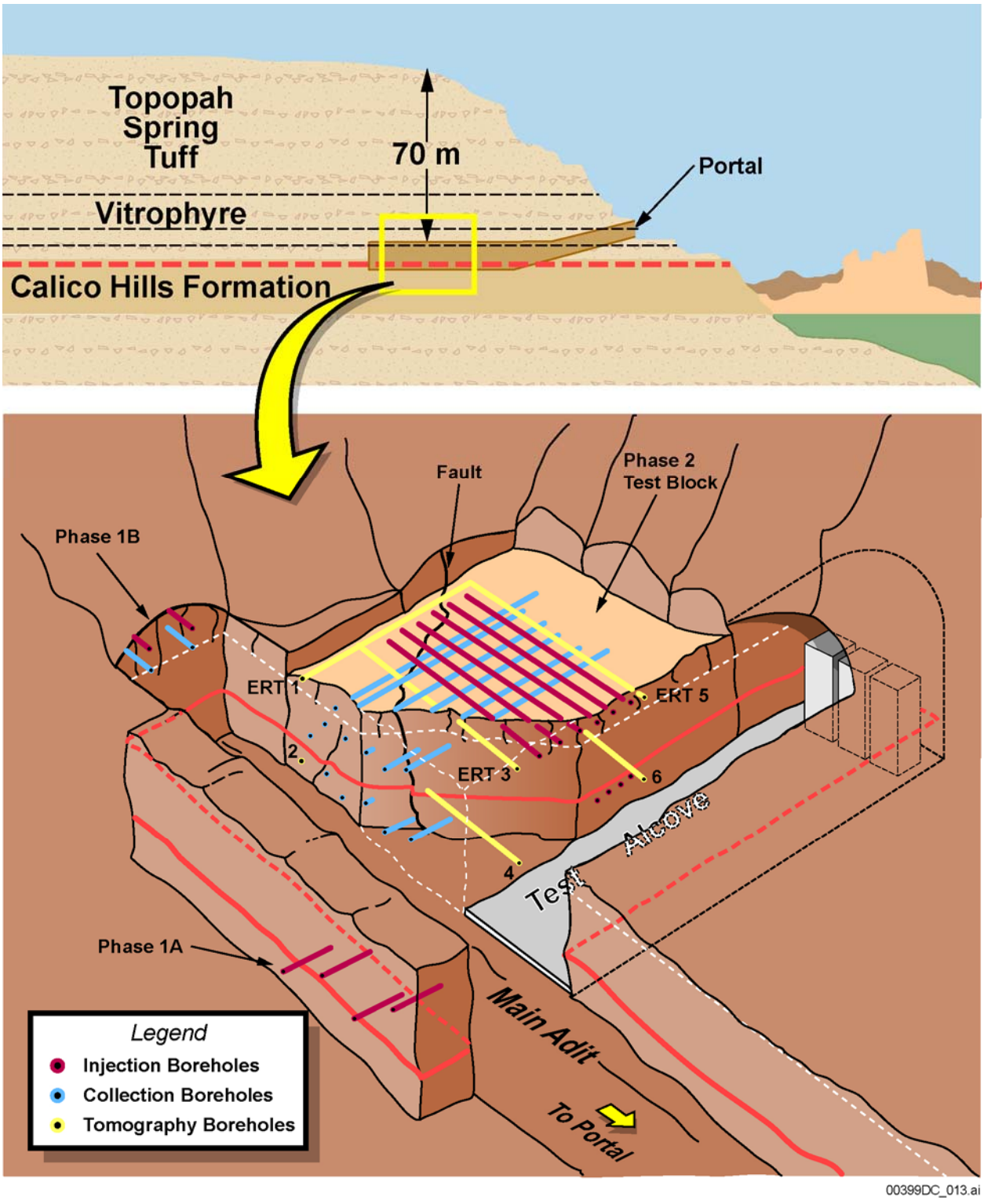

Source: BSC 2003a, Figure 6.13.1-1.

NOTE: This schematic of the Busted Butte unsaturated zone transport test site shows the relative locations of the different experiment phases and borehole locations. Figure not drawn to scale.

Figure 2-9. Busted Butte Unsaturated Zone Transport Test

Busted Butte tests include several phases. Tracer tests there indicate that strong capillary forces in the rock matrix of the vitric CHn are likely to modulate fracture flow from overlying units, thereby damping pulses of infiltrating water. This conclusion was partially derived from observed fluorescein tracer plumes (occurring in the matrix only) from phase 1A test (Figure 2-10). The phase 1B experiment of the Busted Butte tests also showed that, even when injection occurs immediately adjacent to a fracture, water appears to be imbibed quickly into the surrounding matrix. Under the injection rate of 10 mL/hr, the transport times for the nonsorbing tracers were observed to be on the order of 30 days over a distance of about 28 cm, whereas pure fracture flow would have resulted in transport times of minutes to hours at this flow rate.

Based on field observations from the Busted Butte site, water flow is considered to occur only in the matrix within the vitric CHn unit in the unsaturated zone flow models (BSC 2003b, p. 29).

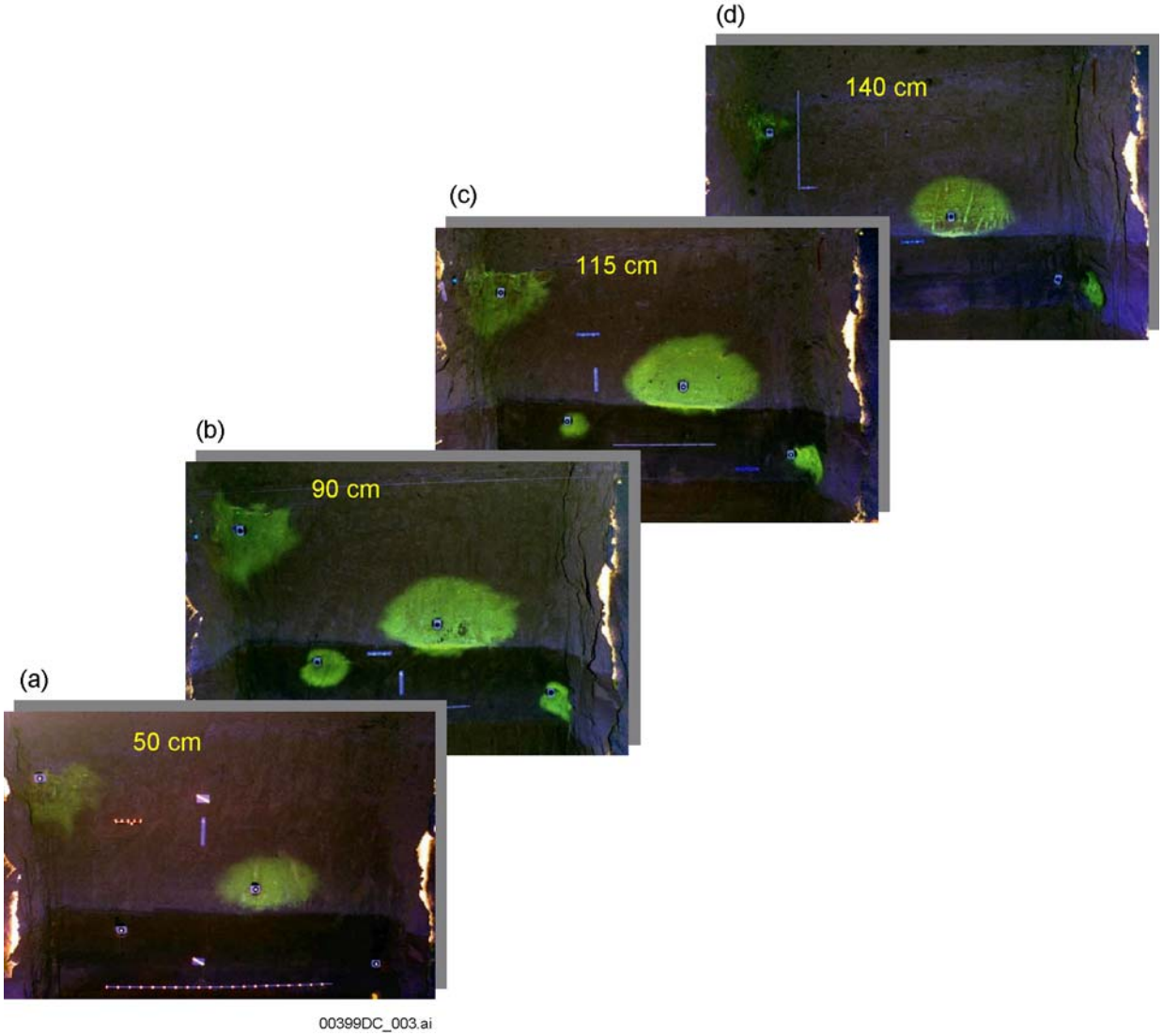

Source: BSC 2003a, Figure 6.13.2-1.

Figure 2-10. Fluorescein Plume at Each of the Four Phase 1A Mineback Faces at Busted Butte

2.4.3 Drift Scale Test

The Drift Scale Test (DST) is the second underground thermal test to be carried out in the ESF at Yucca Mountain, Nevada. The purpose of the test is to evaluate the coupled thermal, hydrologic, chemical, and mechanical processes that take place in unsaturated fractured tuff over a range of temperatures (approximately 25°C to 200°C). The DST provides important data for studying the coupled processes in the unsaturated zone. Data derived from the DST were used for developing models describing the coupled processes and their effects on water flow in the unsaturated zone (BSC 2003e, Section 7).

Details regarding the DST layout, borehole orientations, operation of the test, and measurements performed (as well as their uncertainties) are discussed in Section 6.3 of the *Thermal Testing Measurements Report* (BSC 2002c). In brief, the DST consists of an approximately 50-m-long drift that is 5 m in diameter. Nine electrical floor canister heaters were placed in this drift (the heated drift) to simulate nuclear waste-bearing containers. Electrical heaters were also placed in a series of horizontal boreholes (wing heaters) drilled perpendicularly outward from the central axis of the heated drift. These heaters were emplaced to simulate the effect of adjacent emplacement drifts. The DST heaters were activated on December 3, 1997, with a planned period of 4 years of heating, followed by 4 years of cooling. After just over 4 years, the heaters were switched off on January 14, 2002, and since that time the test area has been slowly cooling. Figure 2-11 shows a the test layout with the main heater tunnel, the wing heaters, and the array of observation boreholes for monitoring temperature as well as chemical, mechanical, and hydrologic variables. The data on the evolution of gas phase composition and aqueous speciation, isotopic composition, mineralogical alterations and associated porosity and permeability changes, pH evolution, changes in water content and air permeabilities, and rock deformations have been collected during the DST.

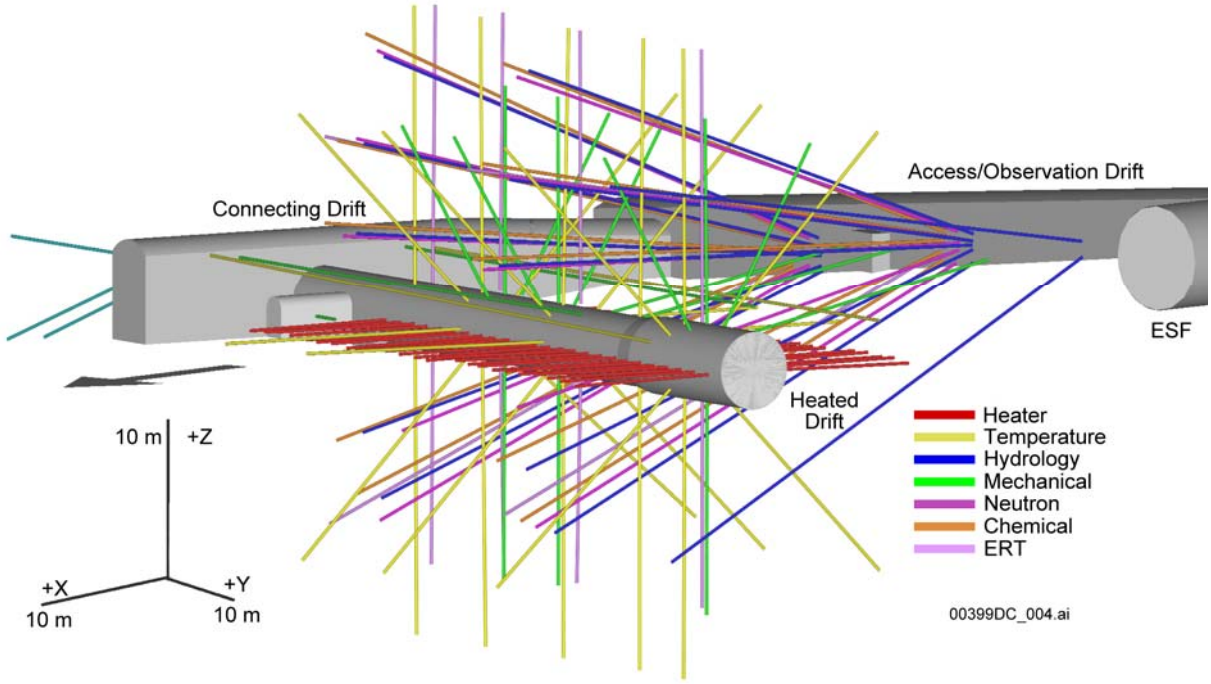

Source: BSC 2002c, Figure 6.3-2.

Figure 2-11. Three-Dimensional Perspective of the As-Built Borehole Configuration of the Drift Scale Test

2.4.4 Alcove 1 Tests and Alcove 8–Niche 3 Cross-Over Tests

The Alcove 1 test site is located near the North Portal of the ESF (Liu et al. 2003). Alcove 1 was constructed for measuring seepage originating from the surface infiltration. The alcove is about 5.5 m high and 5.8 m wide. Rocks between the ground surface and the alcove are within the intensely fractured TCw unit. A bulkhead was installed near the face of the alcove in order to isolate the end of the alcove from the ESF. The bulkhead was intended to raise the relative humidity in the end of the alcove and reduce evaporation from the wall of the alcove. This allowed observation of the wetting front arrival through observation of dripping from the alcove ceiling and walls. During the infiltration test, water was applied at the ground surface directly over the end of the alcove. The size of the infiltration plot was 7.9 m × 10.6 m. During the late stage of Alcove 1 tests, a tracer, bromide, was introduced into the infiltrating water. Seepage into the alcove was collected as a function of time. Tracer concentrations were obtained by analyzing the seepage water.

Infiltration and tracer transport tests have also been conducted at the cross-over test site, where Alcove 8 in the ECRB Cross-Drift is about 20 m directly above Niche 3 (also referred to as Niche 3107) in the ESF main drift (Figure 2-12) (BSC 2003a, Section 12). The test site is located in the upper lithophysal and middle nonlithophysal subunits of the TSw unit. The upper

lithophysal subunit contains lithophysal cavities. Liquid water both without and with tracers was released along a fault (line-release) and from a large 3 m by 4 m plot (areal release) on the floor of Alcove 8. Seepage rate and tracer concentration data are collected from Niche 3. The tests generate data sets that are useful for understanding flow behavior within a fault, the importance of the matrix diffusion within the unsaturated zone, and other important flow and transport processes.

These tests provide important data for studying seepage and water flow behavior in the unsaturated zone. Model results are compared with the experimental observations collected from both Alcove 1 and Alcove 8–Niche 3 tests to enhance understanding of flow and transport processes within the unsaturated zone and for validating the numerical approaches used in unsaturated zone models (BSC 2004, Section 7; Liu et al. 2003).

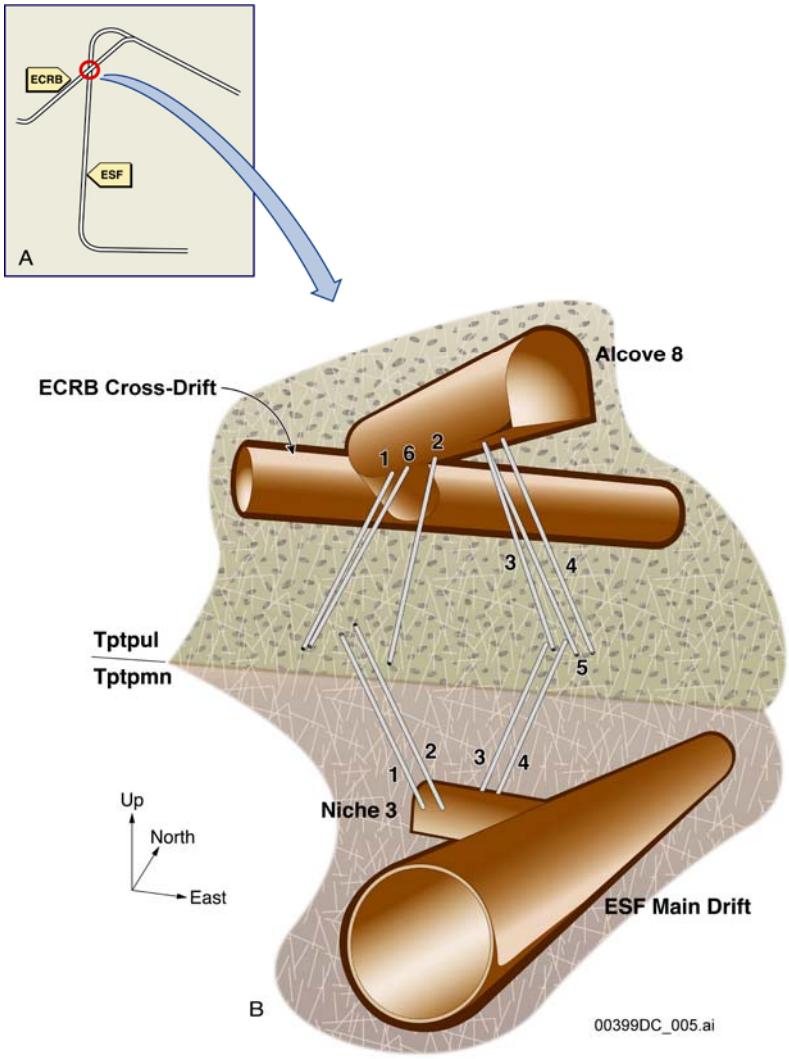

Source: BSC 2003a, Figure 6.12.1-2.

Figure 2-12. Location of Test Bed between the ECRB Cross-Drift and Exploratory Studies Facility Main Drift

INTENTIONALLY LEFT BLANK

3. CONCEPTUAL UNDERSTANDING OF UNSATURATED ZONE FLOW

A conceptual understanding of unsaturated zone flow processes is numerically modeled to predict flow paths under future conditions. The development of the models is based mainly on the geologic setting of the unsaturated zone and the variety of data collected from the unsaturated zone, in addition to theoretical and numerical studies conducted in the last two decades. This section briefly presents the model representations of unsaturated zone flow processes, as illustrated in Figure 3-1.

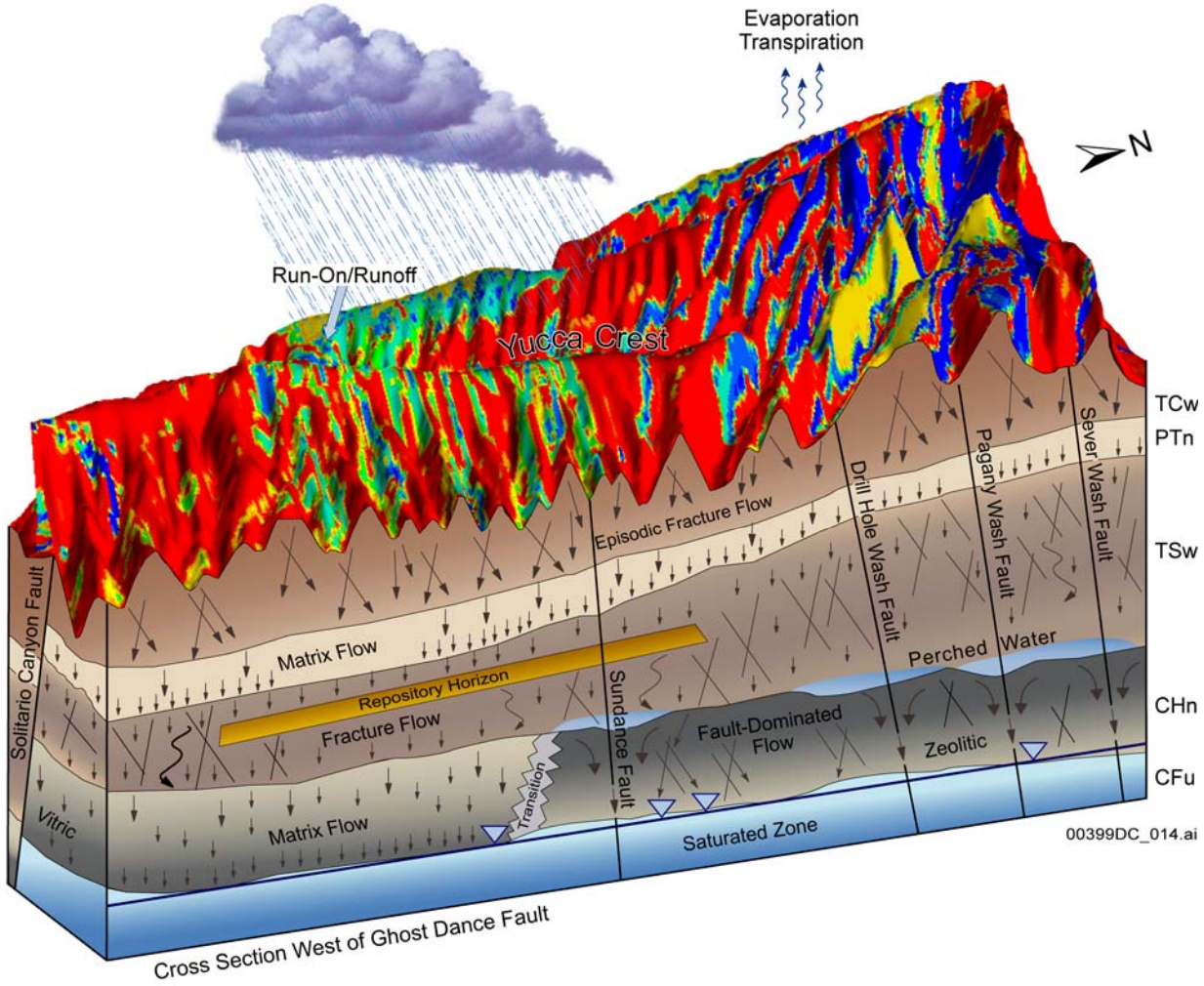

Figure 3-1. Overall Water Flow Behavior in the Unsaturated Zone, Including the Relative Flux Magnitudes of Fracture and Matrix Flow Components in the Different Hydrogeologic Units

3.1 OVERALL FLOW PATTERN WITHIN THE UNSATURATED ZONE

Figure 3-1 schematically shows the overall conceptualized water flow behavior in the unsaturated zone, including the relative importance of fracture and matrix flow components in the different hydrogeologic units, as described in Section 2. The characteristic flow behavior in each of the major hydrogeologic units is described in the following sections. Precipitation infiltrates through the soil and then percolates through the unsaturated zone, where this model

illustrates the geologic control over water flow. Water flows through the densely fractured Tiva Canyon welded (TCw) unit mainly through fractures. Within the more porous Paintbrush nonwelded (PTn) unit, most of the water flows through the matrix, where the high storage capacity promotes the dampening of infiltration pulses. Small amounts of flowing water preferentially pass through faults that cut through this unit. Accurate determination of the flow components is especially important for chemical transport processes. Flow in fractures (fracture flow) is typically much faster than flow in the matrix (matrix flow), leading to much shorter transport times for radionuclides and other chemicals in fractures compared to the matrix.

3.1.1 Flow through the TCw Unit

The high density of interconnected fractures and low matrix permeabilities in the TCw unit (BSC 2003b, Tables 7 and 8) are considered to give rise to significant water flow in fractures and limited matrix imbibition (water flow from fractures to the matrix). Thus, episodic infiltration pulses are expected to move rapidly through fracture networks, with little attenuation by the matrix. This is partially supported by pneumatic data in the TCw showing little attenuation of the barometric signal in monitoring boreholes relative to the barometric signal observed at the land surface (CRWMS M&O 2000c, Section 6.1.2).

3.1.2 Flow through the PTn Unit

The relatively high matrix permeabilities and porosities and low fracture densities of the PTn unit (BSC 2003b, Tables 7 and 8) convert the predominant fracture flow in the TCw to dominant matrix flow within the PTn (CRWMS M&O 2000c, Section 6.1) (Figure 3-2). The dominance of matrix flow is supported by field tests conducted in the PTn unit.

Salve et al. (2003) performed water release tests along a fault within the PTn unit. Water was released under constant-head conditions from a 0.3-m interval within a borehole that crosses the fault. A total of 193 L of water during seven distinct events was released over two weeks between October 21, 1998, and November 5, 1998. Between November 30, 1999, and December 2, 1999, an additional 136 L of water were introduced into the same interval during three distinct events lasting 4 to 7 hours (Salve et al. 2003). It was observed that during the first release test, the wetting front advanced slowly as a result of significant matrix imbibition. It was also found that water that imbibed into the matrix was retained for periods extending to at least a few months for the given test conditions. Based on these observations and considering that water release rates used in the tests were much larger than water percolation rates under ambient conditions, it is concluded that the dry porous PTn matrix is capable of attenuating episodic percolation fluxes in localized areas (such as around faults) where fast flow would otherwise be expected to dominate (Salve et al. 2003, p. 282). This conclusion is consistent with Busted Butte field observations of the vitric CHn, another nonwelded unit (Section 2.4.2).

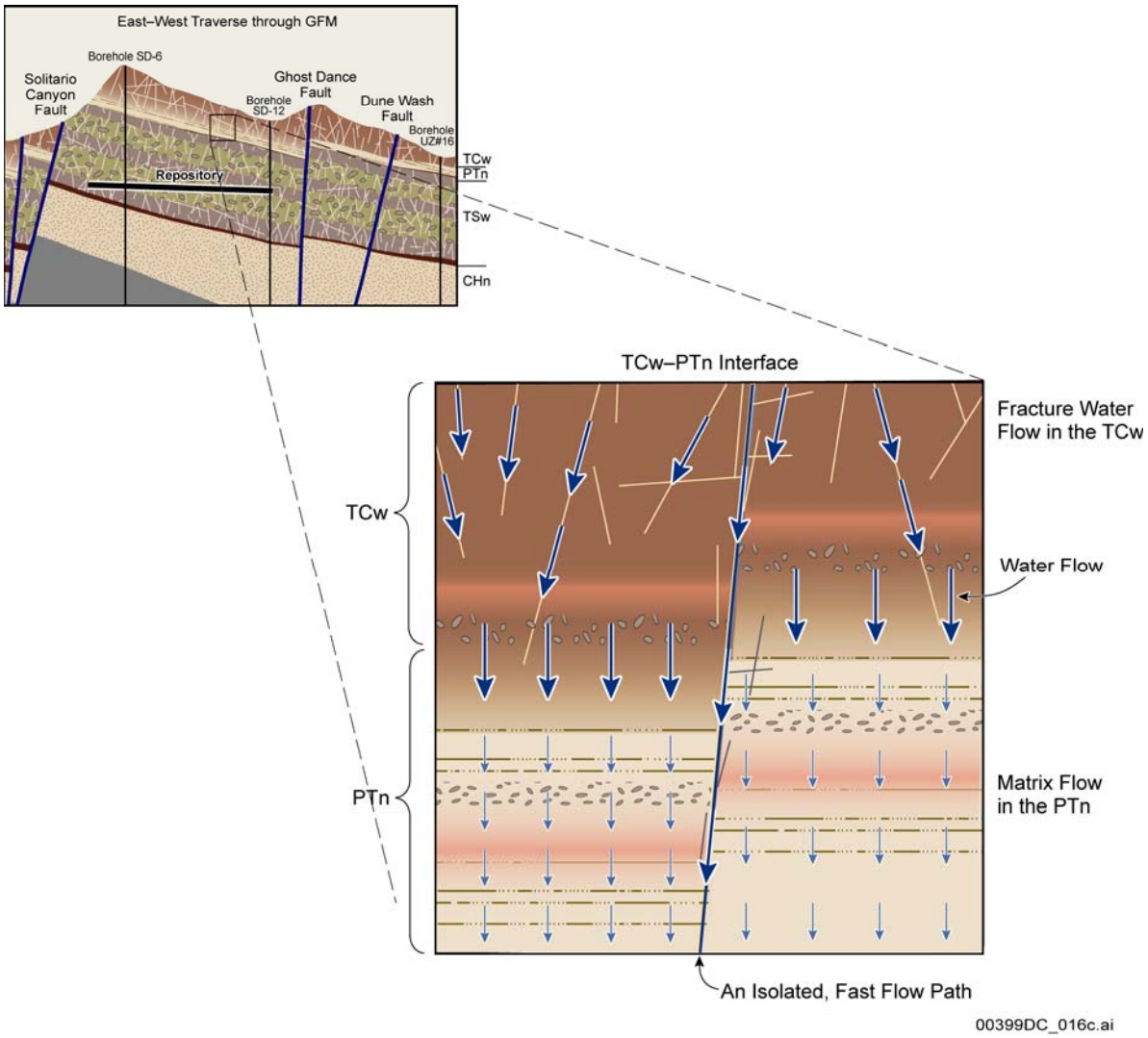

Figure 3-2. Water Flow Behavior within the PTn Characterized by Dominant Matrix Flow and a Few Fast Flow Paths

The PTn layer has the potential capacity to attenuate infiltration pulses, given that matrix flow dominates this layer and that the relatively low saturation (under ambient conditions) in this high-porosity layer provides available pore space for water storage. This is also consistent with the test results of Salve et al. (2003, p. 269) mentioned above. The modeling study of Wang and Narasimhan (1993, pp. 354 to 361) demonstrates that this will result in water flow below the PTn being approximately at steady state.

Faults (or geologic structures) may cut through the entire PTn unit at some locations, leading to potential fast flow paths when the localized tuff matrix is not dry enough. As will be discussed in Section 3.2.4, the fast flow paths, if existing, would only carry a small amount of water and should not affect the overall flow paths in the unsaturated zone significantly.

The issue regarding the effectiveness of the PTn to dampen episodic flow will be further addressed in the response to KTI USFIC 4.04.

In an early conceptual model of Yucca Mountain, Montazer and Wilson (1984, pp. 45 to 48) indicated that significant lateral flow occurs within the PTn unit. The contrast in hydraulic properties at internal layer contacts within the PTn could cause lateral flow. Furthermore, the transient flow of water from the TCw unit to the PTn unit promotes air entrapment, which could further reduce the vertical liquid flux into the PTn. Montazer and Wilson (1984, p. 47) also showed that vertical heterogeneities within the PTn unit may result in a much larger effective permeability of the unit in the direction of dip, compared with the effective permeability in the direction normal to the bedding plane. They argued that the combination of this factor and capillary barrier effects might introduce considerable lateral flow within the unit.

A fine grid simulation reported by Wu et al. (2002) supports the existence of lateral flow within the PTn resulting from capillary barrier effects. This conceptual model was further supported by the fact that the site-scale unsaturated zone flow model, considering lateral flow mechanisms within the PTn, better matches the observed chloride data within the unsaturated zone (BSC 2004, Section 6.5.2), as shown in Figure 3-3.

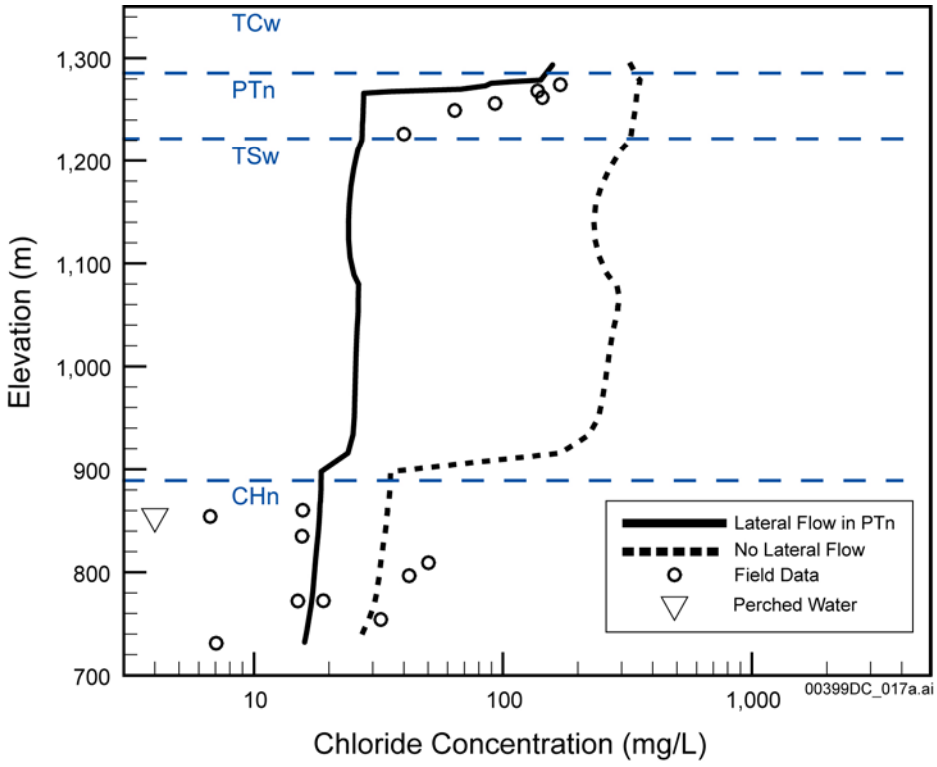

Source: BSC 2004, Figure 6.5-3.

NOTE: The simulations were performed with the site-scale unsaturated zone flow model with and without lateral flow mechanism in the PTn. Some simulation results were removed from the original figure.

Figure 3-3. Comparison between Observed and Simulated Chloride Concentration Distribution for Borehole USW SD-9

3.1.3 Flow through the TSw Unit

Unsaturated flow in the TSw unit occurs primarily through fractures (Figure 3-1). Supporting evidence for this comes from the magnitude of matrix hydraulic conductivity values of the TSw relative to the estimated average infiltration rate. The maximum matrix percolation rate is equal to the matrix hydraulic conductivity if the hydraulic gradient is assumed to be unity under unsaturated conditions. Because the matrix hydraulic conductivity is much lower than the average estimated infiltration rate (CRWMS M&O 2000c, Section 6.1.2), the remainder of the flow must be distributed in the fracture network (Pruess et al. 1999, p. 283).

Other evidence for fracture flow comes from calcite coating data, which are signatures of water flow history and indicate that most of the deposition is found within the fractures in the welded units (Paces et al. 1998, p. 37). As discussed in *Conceptual and Numerical Models for UZ Flow and Transport* (CRWMS M&O 2000c, Section 6.1.2), ^{14}C ages of the perched water bodies below the TSw unit also suggest fracture dominant flow within the TSw. These ages, ranging approximately from 3,500 to 11,000 years (Yang et al. 1996, p. 34), are much younger than if the matrix were the major water flow path within the TSw. Therefore, fracture flow is considered the dominant water flow mechanism within the TSw.

3.1.4 Flow below the Repository

Flow behavior below the repository is especially important for modeling radionuclide transport from the repository horizon to the water table, because transport paths follow the water flow pattern. The main hydrogeologic units below the repository are the CHn and CFu. Both of these units have vitric and zeolitic components that differ in their degree of hydrothermal alteration and subsequent hydrologic properties. The zeolitic rocks have low matrix permeability and some fracture permeability; consequently, a relatively small amount of water may flow through the zeolitic units, with most of the water flowing laterally in perched water bodies and then vertically down along faults (Figure 3-1).

One distinctive feature below the repository is the existence of perched water zones, which have been reported in a number of boreholes within the lower portion of the TSw unit and within the upper portion of the CHn unit (BSC 2004, Section 6.2). These perched water bodies were found primarily in the northern part of the repository area, where lower permeability, sparsely fractured zeolitic rock units predominate. The occurrence of perched water suggests that certain layers of the lower TSw (e.g., the basal vitrophyre) and the upper CHn (zeolitic portion) serve as barriers to vertical flow. Perched water is further discussed in Section 3.2.5.

On the other hand, similar to the PTn unit, the vitric units have relatively high matrix porosity and permeability; therefore, porous medium-type flow dominates (Figure 3-1). This is supported by the test results within the CHn at the Busted Butte underground facility, as previously discussed in Section 2.4. The results showed that water flow and tracer transport occur mainly within the matrix of the CHn, where fracture flow is believed to be limited.

As discussed in Section 2.3 of this chapter, different kinds of geochemical data have been collected below the repository. Perched water analysis has yielded residence ages ranging from 3,500 to 11,000 years (^{14}C data) (Figure 2-6). As previously indicated, this supports the idea that

water flow within the TSw unit (including its portion below the repository) is mainly vertical and occurs in fractures. As a result of ion exchange reactions with clays and zeolites along the flow paths, chemical compositions of pore water extracted from the CHn are generally found to be similar within a given stratigraphic unit and markedly different between different host lithologies in a given borehole, implying significant lateral flow within the zeolitic portion of the CHn unit (BSC 2002b, pp. 121 to 122). Chloride data and strontium concentration data below the repository were also collected from several deep surface-based boreholes. The consistency between concentration data and three-dimensional simulation results using the site-scale unsaturated zone flow model further supports the conceptual understanding of the flow pattern below the repository, as shown in Figure 3-1 (BSC 2004, Section 7).

The issue regarding the flow field below the repository will be further addressed in the responses to KTIs RT 1.01, RT 3.02, and TSPAI 3.24.

3.2 SPECIFIC ASPECTS OF UNSATURATED ZONE FLOW PATTERN

The overall flow pattern within the unsaturated zone was described in Section 3.1. The following section is devoted to some specific issues important for conceptual understanding of flow paths within the unsaturated zone.

3.2.1 Fracture–Matrix Interaction

Fracture–matrix interaction refers to flow and transport (or mass exchange) between fractures and the matrix. Owing to their different hydrologic properties, distinct flow and transport behavior occurs in each component. The extent of fracture–matrix interaction is a key factor in determining flow and transport processes in the unsaturated zone.

Modeling results and field observations show limited fracture–matrix interaction within welded units at Yucca Mountain (CRWMS M&O 2000c, Section 6.1.3). Chloride concentrations within the shallow TCw unit are generally lower than 10 mg/L; they range from 30 to 80 mg/L in the nonwelded PTn unit, and decline again to 5 to 10 mg/L in the deep perched water bodies. These chloride concentration data indicate that perched water is recharged mainly from water moving through fractures, with only a small degree of interaction (or mixing) with matrix water (Section 2.3.1 of this document; CRWMS M&O 2000c, Section 6.1.3; Yang et al. 1996, p. 55). Uranium isotopic ratios have been used to address the prevalence and frequency of fracture flow through the unsaturated zone and the issue of local recharge to the water table. Substantial differences in $^{234}U/^{238}U$ activity ratios between pore water and fracture water (from $^{234}U/^{238}U$ in fracture minerals as well as perched water) imply that there may be minimal liquid exchange between these two types of flow pathways (Section 2.3.4). Furthermore, studies by Ho (1997, pp. 401 to 412) show that the match between numerical simulations and observed matrix saturation and water potential data is improved by significantly reducing the amount of fracture–matrix interaction.

The occurrence of limited fracture–matrix interaction is also supported by observations from Rainier Mesa and other analog sites. The Rainier Mesa site is characterized by a thick sequence of alternating welded and nonwelded unsaturated tuffs, similar to those at Yucca Mountain. Thordarson (1965, pp. 6 to 7 and pp. 75 to 80) noted that typically only portions of fractures

carried water and that the chemical composition of water obtained from fractures was substantially different from that of water samples extracted from the nearby rock matrix at that site. At a field site in the Negev Desert in Israel, man-made tracers were observed to migrate with velocities of several meters per year across a 20- to 60-m-thick unsaturated zone of fractured chalk (Nativ et al. 1995, pp. 253 to 261). Such high velocities could only occur under conditions of limited fracture–matrix interaction.

The concept of limited fracture–matrix interaction at the Yucca Mountain site is further supported by many other independent laboratory tests as well as theoretical and numerical studies (CRWMS M&O 2000c, Section 6.1.3). In a number of laboratory experiments without considering matrix imbibition, Glass et al. (1996, pp. 6 to 7) and Nicholl et al. (1994, pp. 2533 to 2546) demonstrated that gravity-driven fingering flow is a common flow mechanism in individual fractures. This can reduce the wetted area in a single fracture to fractions as low as 0.01 to 0.001 of the total fracture area (Glass et al. 1996, pp. 6 to 7). However, consideration of matrix imbibition can increase wetted areas of fingering flow patterns in individual fractures (Abdel-Salam and Chrysikopoulos 1996, pp. 1537 to 1538). The wetted area in a fracture under unsaturated flow conditions is generally smaller than the geometric interface area between fractures and the matrix (Wang and Narasimhan 1993, pp. 329 to 335), even in the absence of fingering flow. This results from the observation that liquid water in an unsaturated fracture occurs as saturated segments that cover only a portion of the fracture–matrix interface area. Liu et al. (1998, p. 2645) suggested that in unsaturated, fractured rocks, fingering flow occurs at both a single fracture scale and a connected fracture network scale (Figure 3-4). This concept is supported by the field observations from the Rainier Mesa site, as discussed above, and by a numerical study of Kwicklis and Healy (1993, pp. 4097 to 4099). This study found that a large portion of the connected fracture network played no role in conducting water flow.

Studies have also shown that fracture coatings can either reduce or increase the extent of fracture–matrix interaction. Thoma et al. (1992, pp. 1357 to 1367) performed experiments on coated and uncoated tuff fractures and observed that the low-permeability coatings inhibited matrix imbibition considerably. In contrast, fracture coatings may in some cases increase the fracture–matrix interaction when microfractures develop in the coatings (Sharp et al. 1996, p. 1331). At this point, coating effects on fracture-matrix interaction are not totally clear. Therefore, the coating effects are not considered in the unsaturated zone flow models.

Based on the above discussion, it is believed that fingering flow in fractures is a common flow mechanism in unsaturated fractured rocks and a major reason for limiting fracture–matrix interaction (Figure 3-4). To incorporate the effects of fingering flow into modeling flow and transport in unsaturated fractured rocks, the active fracture model was developed (Liu et al. 1998, pp. 2633 to 2646; CRWMS M&O 2000c, Section 6.4). In the model, only a portion of connected fractures are considered to actively conduct liquid water as a result of fingering flow at a fracture network scale. Figure 3-5 shows the only observed in situ fracture flow under ambient conditions from the underground tunnels. While the scarcity of the observed fracture under ambient conditions partially results from the drying effects during and after the excavations, it is consistent with the conceptual idea that only a portion of fractures conducts water.

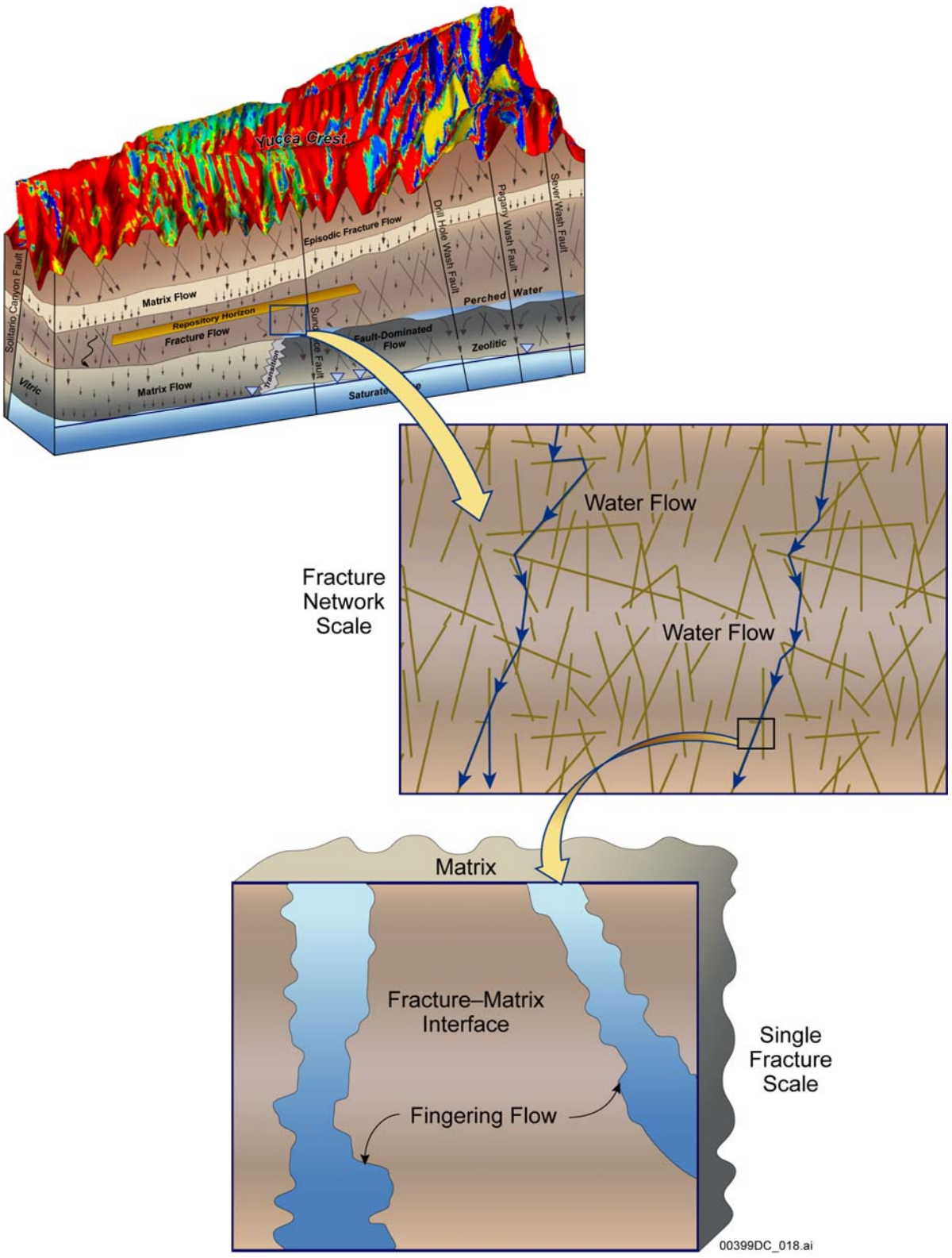

Figure 3-4. Water Flow in Fractures Characterized by Fingering Flow at Different Scales

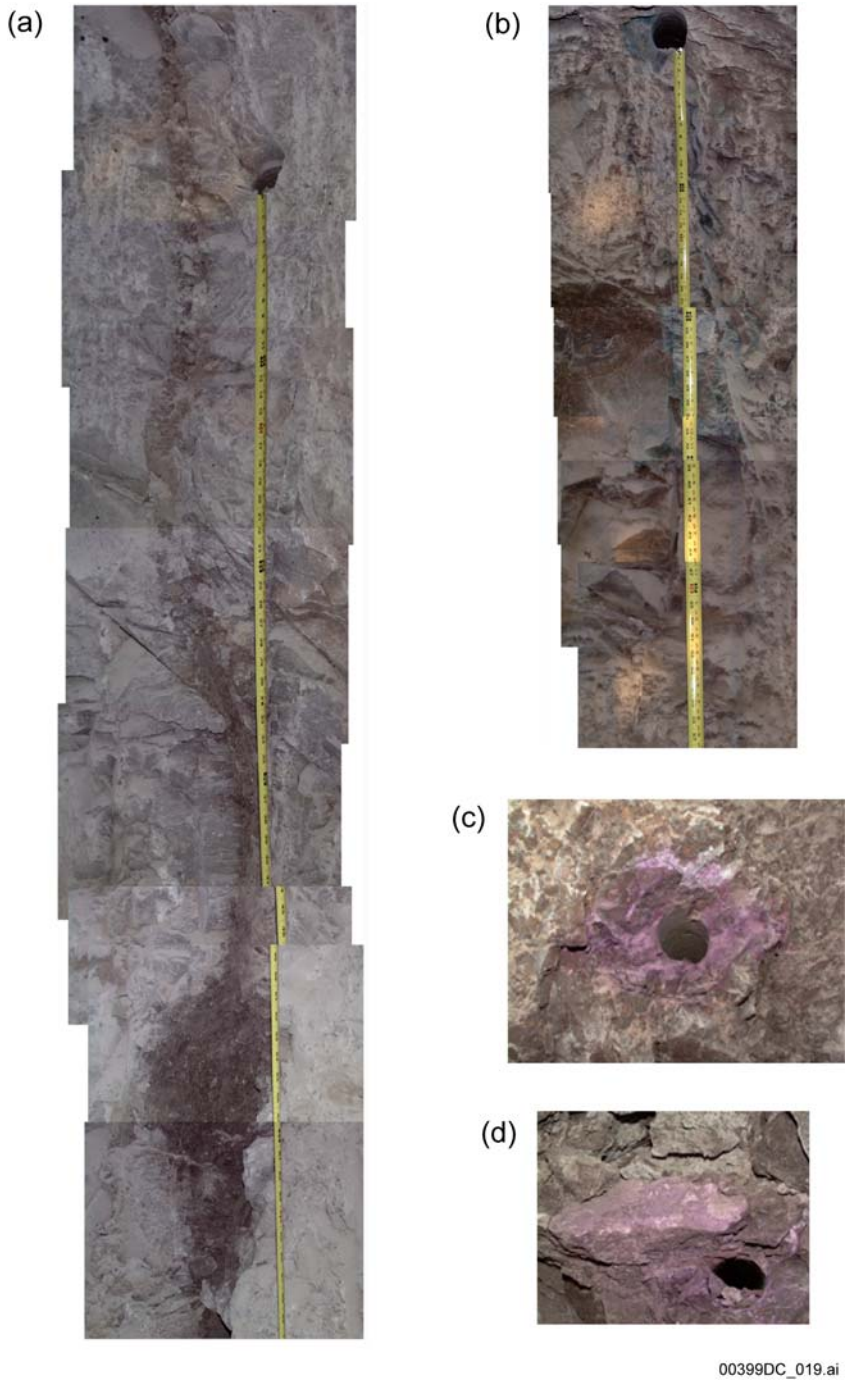

Source: BSC 2003a, Figure 6.2.1-1.

Figure 3-5. Flow Paths Observed During Niche Excavations: Ambient Flow Path at Niche 1 (a); Blue Dyed Flow Path at Niche 1 (b); Pink Dyed Flow Path at Niche 5 (c); and Pink Stain on the Floor of a Lithophysal Cavity at Niche 5 (d)

3.2.2 Effect of Major Faults

Different kinds of faults with varying amounts of displacement exist at Yucca Mountain. Fault properties are variable and generally controlled by rock type and stratigraphic displacement. Because major faults may have the potential to significantly affect the flow processes at Yucca Mountain, they are important features of the unsaturated zone.

A fault is considered to serve as a localized, fast flow conduit for liquid water, especially below the repository (Figure 3-1). Above the repository, transient water flow may occur within the fault as a result of temporally variable infiltration. At Yucca Mountain, major faults cut through the PTn unit, which may (in light of its high porosity and storage capacity) attenuate transient flow events within faults. Alternatively, the attenuating effect of the PTn on transient flow may be significantly reduced within the faults as a result of low-permeability mineral coatings along fracture walls within fault zones, or if the adjacent rock matrix has been altered to low-permeability clays or zeolites. However, fast flow along major faults above perched water bodies is expected to carry only a small amount of water and may not contribute significantly to the total liquid flow above the repository horizon in the unsaturated zone, as will be discussed in Section 3.2.4 of this chapter.

Below the repository, low-permeability layers (or perched water zones) at the base of the TSw and in the CHn may laterally divert a considerable amount of flow to major faults, which may vertically focus flow to the water table (BSC 2004, Section 6.2). However, it is also possible that alteration within or along faults in the CHn and CFu causes them to be of low permeability, slowing water transport times from the TSw to the water table. Nevertheless, to be conservative faults below the repository have been treated as localized fast flow paths in the current unsaturated zone flow model.

3.2.3 Transient Flow

Temporal variation in the infiltration rate drives the time-dependent or transient nature of flow in the unsaturated zone. The temporal variation of the infiltration may be short-term because of weather fluctuations that drive episodic flow, or long-term because of climate change. As discussed in Section 3.1.2, the PTn is believed to greatly attenuate episodic infiltration pulses such that water flow below the PTn is approximately steady. This is supported by the modeling studies of Wang and Narasimhan (1993, pp. 354 to 361) and Wu et al. (2000, pp. 30 to 32, and 39 to 41), and the test results of Salve et al. (2003, p. 269). However, water flow in the southern part of Solitario Canyon may be transient because the PTn is completely offset by the Solitario Canyon fault in this area. Some transience is also expected for liquid flow through isolated fast flow paths that cut through the PTn because of the lack of a significant attenuation mechanism.

3.2.4 Flow Focusing and Fast Flow Paths

Flow focusing refers to the occurrence of significant water flow through a very small area or zone. The potential for flow focusing below the PTn unit has been demonstrated using numerical studies by Bodvarsson et al. (2003), which support the conceptual model of unsaturated flow focusing illustrated in Figure 3-6. In this conceptual model, infiltration is dispersed in the near surface and also in the low effective permeability PTn layer. From there,

water begins to be focused in the TSw layer and continues into fewer discrete flow pathways on through the CHv and CHz layers. These discrete flow pathways, which likely occur in fractures, as shown in Figure 3-4, deliver percolating water to the groundwater. Whereas the focused flow pattern below the PTn unit has a critical impact on the percolation distribution above the repository and radionuclide transport from the repository to water table, details of this focused flow pattern are not very well understood.

While focused flow occurs in the TSw and below, the distribution of focused flow paths is relatively uniform and not limited to major faults, as supported by many field observations (CRWMS M&O 2000c, Section 6.1.7; Bodvarsson et al. 1999, p. 13). Average measured matrix saturations suggest relatively uniform values for most of the units, and in situ water potential measurements also show little variability within the TSw for different boreholes. It was also observed that temperatures within the TSw unit are fairly uniform (CRWMS M&O 2000c, Section 6.1.7). All these observations also support the use of the continuum approach in the unsaturated zone flow models.

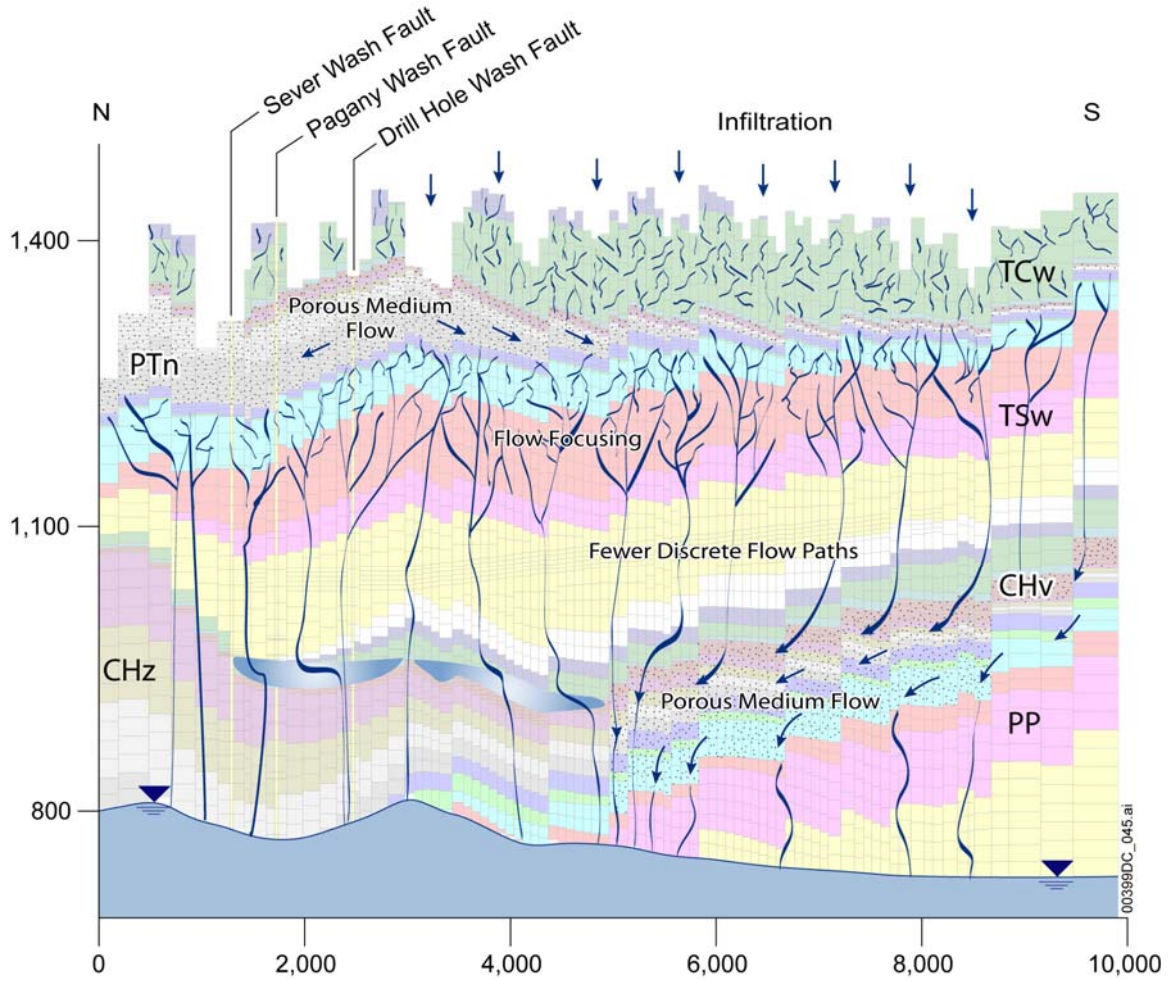

NOTE: Grey zones correspond to saturated zone and perched water bodies. Processes and geologic layers not represented to scale. Figure is an illustration only.

Figure 3-6. Schematic Conceptual Model of Unsaturated Zone Flow Focusing in Yucca Mountain

3.2.5 Perched Water

Perched water is defined as saturated zones that are above or not directly connected to the groundwater table. Such phenomena may occur when large permeability differences exist between geologic units. Perched water zones at Yucca Mountain have been detected in a number of boreholes (USW UZ-14, USW NRG-7a, SD-7, USW SD-9, UE-25 SD-12, and USW G-2), occurring in the lower portion of the TSw and the upper portion of the CHn (BSC 2004, Section 6.2) (Figure 3-7). Hydraulic testing indicates that the volume of the perched water bodies at Yucca Mountain varies greatly, depending on borehole location (CRWMS M&O 2000c, Section 6.1.4).

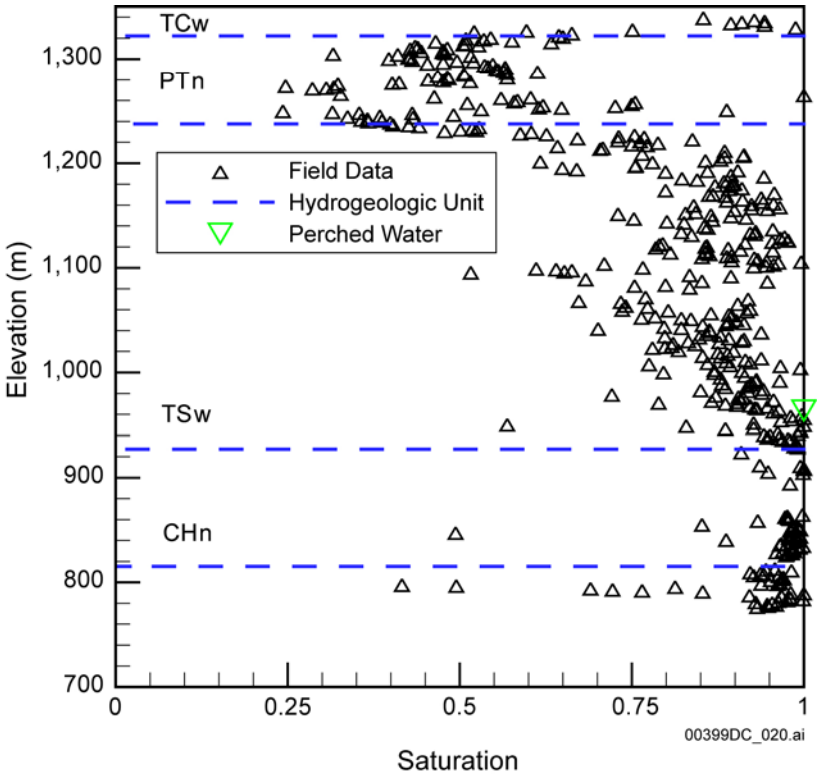

Source: BSC 2003a, Figure 6.2-2.

Figure 3-7. Observed Matrix Liquid Saturations and Perched Water Elevations for Borehole USW UZ-14

The presence of perched water has important implications for the transport times and flow paths of water through the Yucca Mountain unsaturated zone. First, ^{14}C age data for perched water suggest dominant fracture flow in the TSw unit (see Section 3.1.4). Second, the occurrence of perched water bodies indicates that certain layers of the TSw and the CHn serve as barriers to vertical flow and cause lateral flow diversion (Figure 3-8). These conceptual points are included in the unsaturated zone flow model.

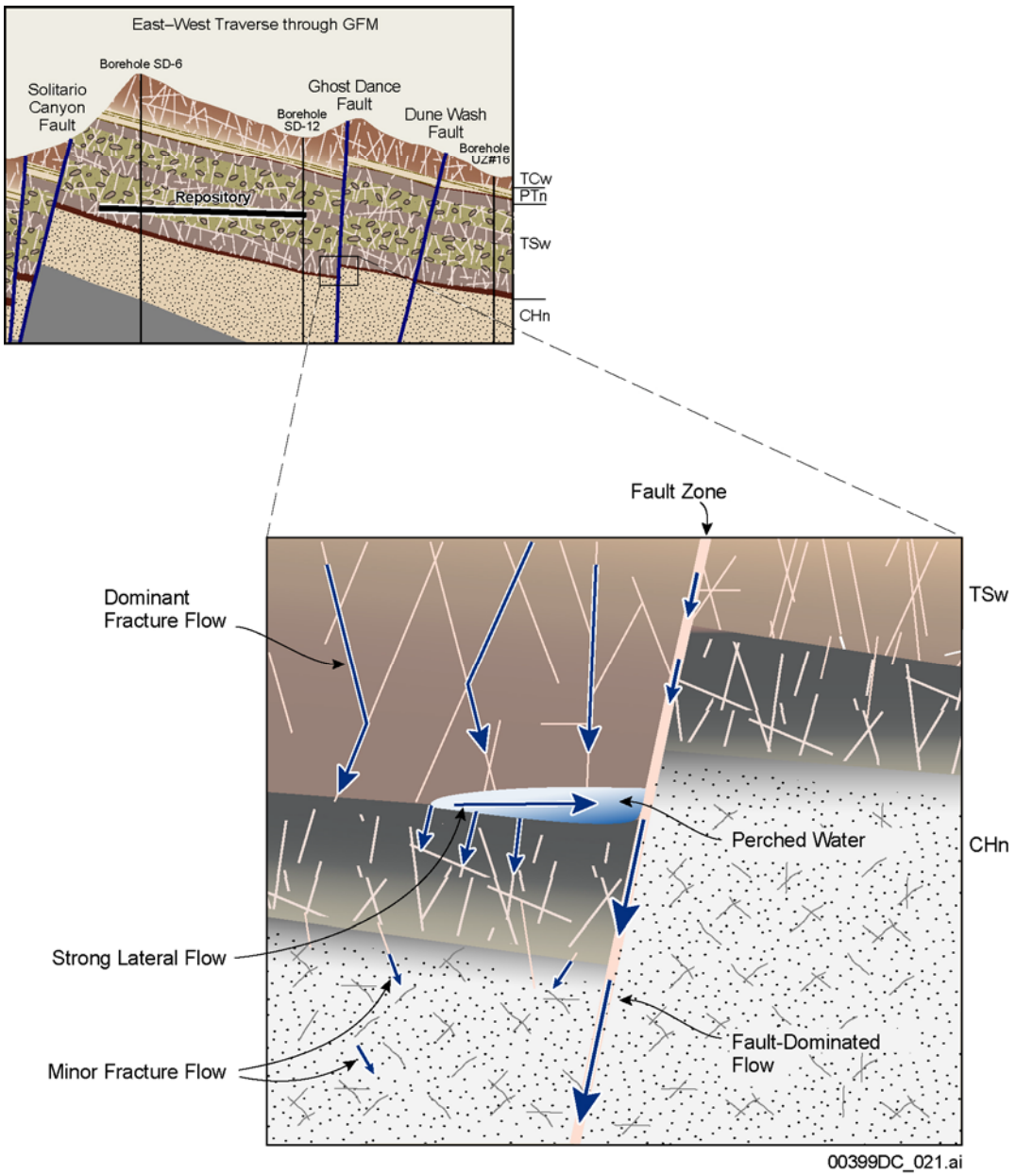

Figure 3-8. Flow Patterns within and near a Perched Water Body Characterized by Strong Lateral Flow within the Perched Water Body and the Associated Fault-Dominated Flow

3.2.6 Effects of Thermal Processes

The discussions above have focused on unsaturated zone flow under ambient conditions. After a geologic repository is constructed at Yucca Mountain, the emplaced radioactive wastes will emit a significant amount of heat as a result of the radioactive decay of the wastes (CRWMS M&O 2000c, Section 6.3). This heat will influence hydrologic, mechanical, and chemical conditions in both the near field (drift scale) and far field (mountain scale). This section discusses the potential effects of thermal processes and the corresponding coupled processes—thermal-hydrologic, thermal-mechanical, and thermal-chemical—on flow within the Yucca Mountain unsaturated zone.

The potential thermal-hydrologic response of the unsaturated, fractured tuff to decay heat involves a number of key processes (CRWMS M&O 2000c, Section 6.3.1). Conceptually, when formation temperatures increase sufficiently around the waste packages, pore water will boil and vaporize. Most of the vapor generated in the matrix will move into the fractures, where it will become highly mobile. When the vapor encounters cooler rock away from the repository drifts, it will condense, and fracture saturation will increase locally. Part of the condensate may then imbibe into the matrix. The amount of imbibition will depend on the fracture–matrix interaction. Some portion of the condensate will remain in the fractures, becoming mobile, and potentially flowing back toward the boiling zone. However, because capillary forces are relatively weak in the fractures, a substantial amount of liquid may drain by gravity (Figure 3-9). The stronger the vapor flux away from the drifts and the reflux toward the drifts, the more obvious the heat pipe conditions (vapor–liquid counterflow with phase change) in the temperature fields. Where heat pipe conditions exist, the temperature will remain at the nominal boiling point. Eventually, the heat output will decrease and become small enough so as not to affect the liquid flow field, and the flow field will return to steady state. Steady-state flow will not be reestablished until the dryout zones near the drifts are resaturated. The emplacement of heat-generating wastes in the repository likely will alter large-scale flow processes associated with the mountain as well (CRWMS M&O 2000c, Section 6.3.1). Heat-driven features at this scale potentially include the development of large-scale, gas phase, buoyant convection cells and thermally altered liquid phase flow fields, both above and below the repository.

Heat transfer from emplaced wastes will increase temperatures of the host rock surrounding the repository, resulting in mechanical changes to physical properties of the rock within the unsaturated zone (CRWMS M&O 2000c, Section 6.3.2). Expansion of the rock matrix caused by heating will create stress in the rock and induce changes in the fracture apertures. This may also change unsaturated zone flow pattern at different scales.

Chemical effects in response to a high thermal load in the repository may alter material hydrologic properties (CRWMS M&O 2000c, Section 6.3.3). Above the repository level, the temperature is projected to be sufficiently high to vaporize the water, resulting in precipitation of minerals in fractures. The condensate, being out of equilibrium with the rock, may dissolve mineral phases from the walls of fractures and then flow back into zones where chemical precipitation occurs. Below the repository, the processes are not completely the same because the liquid within the fractures, under the influence of gravity, can migrate away from the heat source and leave the two-phase flow system. This dissolution of minerals at one point in the fracture network and their redeposition at another, could lead to the formation of precipitate zones over the drifts. In a precipitate zone, the porosity and permeability of fractures and portions of the matrix near the fractures may be reduced. When thermal perturbation is considerably decreased, the precipitate may start to be dissolved by water from ambient, downward percolation. Because the process of chemical dissolution is much slower than the process of chemical precipitation, the precipitate zone may become virtually permanent after the thermal perturbation. Therefore, these changes will influence the flow field not only while the thermal process is active, but afterwards as well.

The effects of thermal processes and the resultant coupled processes on unsaturated zone flow will be further discussed in Section 4.4.

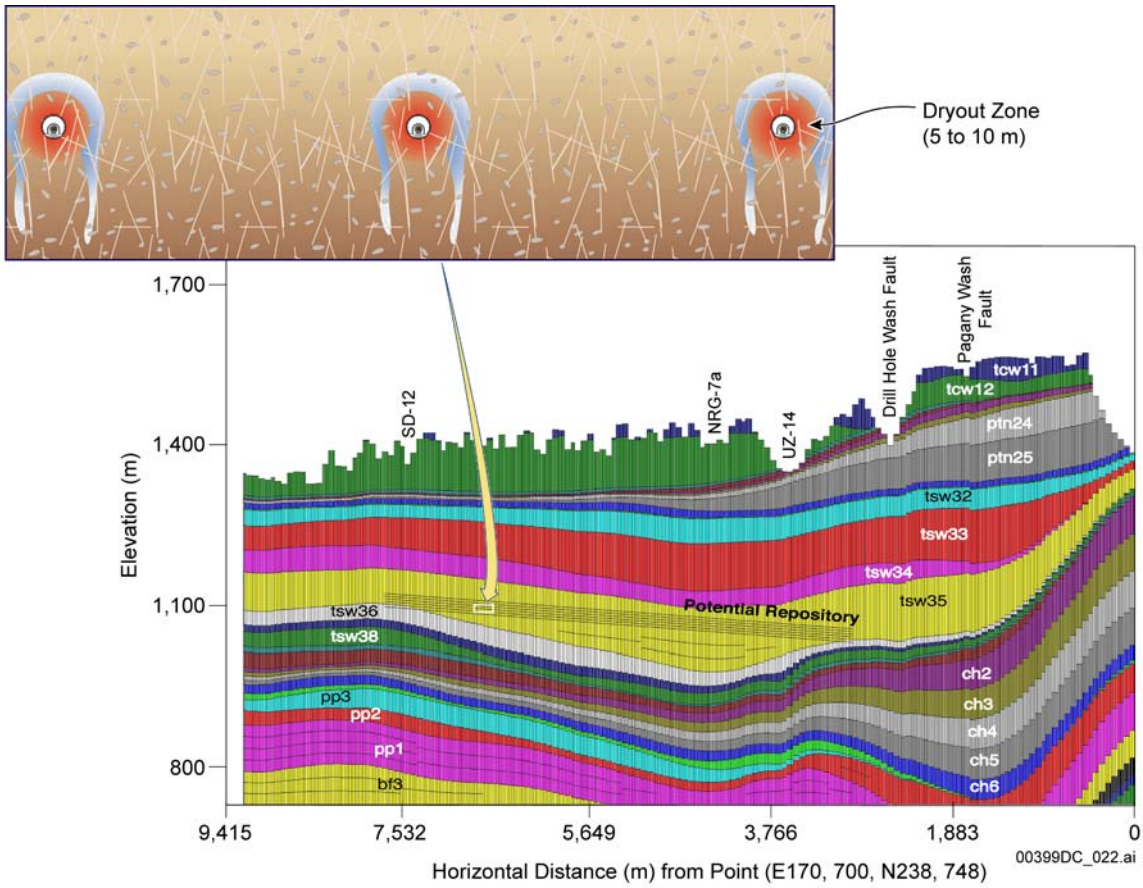

NOTE: For the current repository design concept, the dryout zone around drifts will extend to a distance of approximately 5 to 10 m from the drift wall.

Figure 3-9. Effects of Thermal Processes on Flow Pattern near Drifts

3.3 RELATIONS BETWEEN UNSATURATED ZONE FLOW AND OTHER PROCESSES

As indicated in Section 1, water flow process within the unsaturated zone is closely related to infiltration, water seepage into drifts, and radionuclide transport within the unsaturated zone. While detailed discussions of these related processes are given in the corresponding technical basis documents, this section provides a brief description of these related processes.

3.3.1 Climate and Infiltration

Net infiltration is the ultimate source of percolation flux within the unsaturated zone and provides the water for flow and transport mechanisms that may move radionuclides from the repository to the water table. Net infiltration is spatially and temporally variable because of the nature of the storm events that supply precipitation and the variation in soil cover and topography. Infiltration is believed to be high on side slopes and ridge tops where bedrock crops out, and fracture flow in the bedrock is able to move moisture away from zones of active evapotranspiration.

Net infiltration depends on precipitation. The global records show that climate is cyclic over 400,000-year periods. Sharpe (2003, Table 6-1) suggests the existence of a long-term, modern interglacial climate state for at least the last 9,000 years. Climatic data forecasting indicates that during the next 10,000 years at Yucca Mountain, the modern-day climate should persist for 400 to 600 years, followed by a warmer and much wetter monsoon climate for 900 to 1,400 years. The monsoon climate will be followed by a cooler and wetter glacial transition climate for the remaining 8,000 to 8,700 years of the regulatory period. The upper-bound precipitation values for the monsoon and glacial transition climates exceed the upper bounds of the region's modern-day climate by about 100 mm. The glacial transition climate's lower bound exceeds the modern lower bound values by about 150 mm. Thus the future climate is wetter, but not substantially wetter than the modern climate.

A detailed discussion of climate and infiltration process is provided in *Technical Basis Document No. 1: Climate and Infiltration*.

3.3.2 Water Seepage into Drifts

Water enters the unsaturated zone from above as net infiltration, then percolates downward through the host rock under the impetus of gravity. When the percolation encounters an opening such as an emplacement drift, capillary forces will tend to divert water around the opening. This phenomenon is known as the capillary barrier effect (BSC 2003f, Section 6.3.1) and is illustrated in Figure 3-10.

The barrier effect leads to a local saturation build up in the host rock immediately above, and adjacent to the drift opening. If capillary and permeability properties of the fracture network in this region are sufficiently large (or strong), some or all of the incident percolation is diverted around the drift. Locally, however, the saturation may increase (and capillarity decrease) such that water can enter the drift as seepage (BSC 2003f, Section 6.3.1).

Seepage is defined as the movement of liquid water into an underground opening, and does not include movement of water vapor or condensation within openings. The seepage threshold is the critical percolation flux below which seepage in the opening is unlikely to occur. Field tests have demonstrated the existence of a seepage threshold in the host rock.

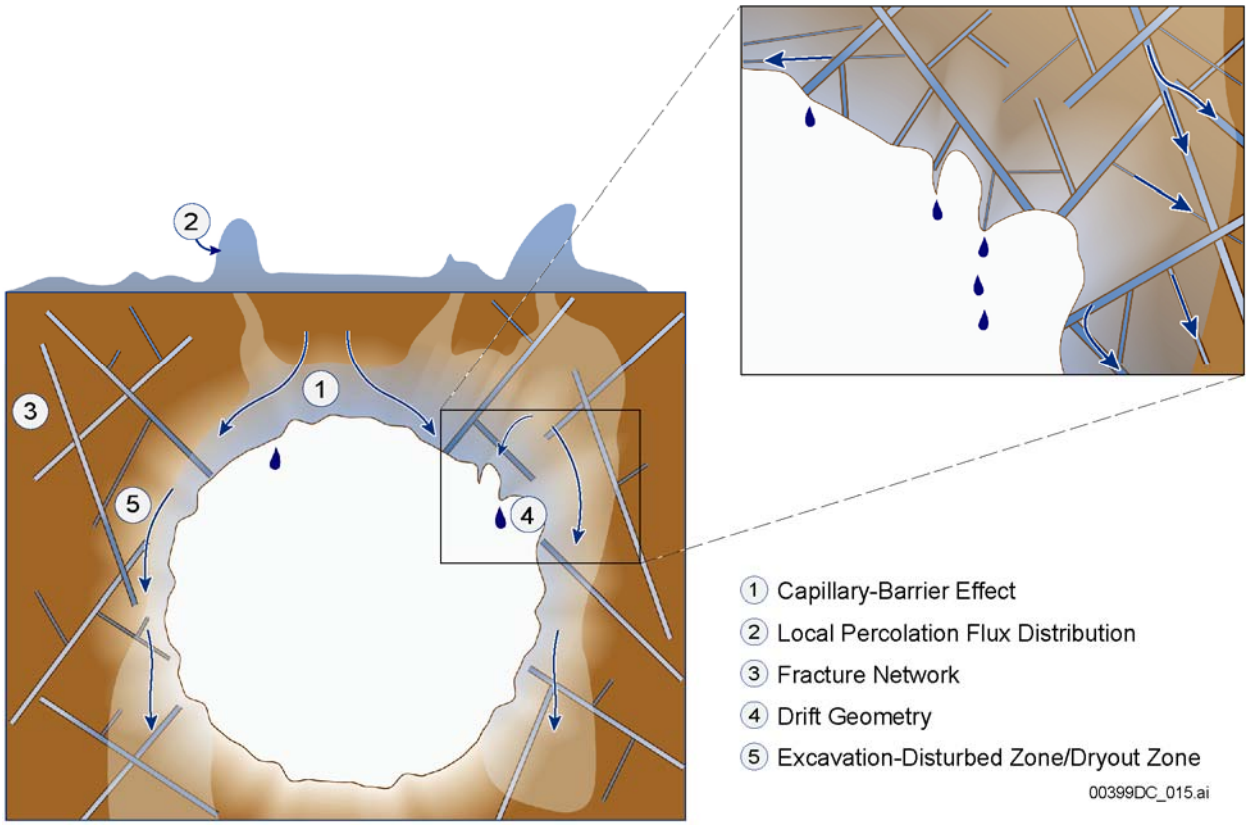

Source: BSC 2003f, Figure 6.3-1.

Figure 3-10. Phenomena and Processes Affecting Drift Seepage

For an emplacement drift of a given shape, the seepage threshold—and the amount of seepage once this threshold is exceeded—depend on the local flow conditions in the near field (Figure 3-10). These conditions are mainly influenced by the local percolation flux reaching the opening, and by the local hydrologic properties of the host rock (principally the capillary strength and relative permeability of the fracture network) (BSC 2003f, Section 6.3.1). Small-scale heterogeneity of hydrologic properties (i.e., fracture characteristics) increases the likelihood of seepage (Birkholzer et al. 1999). In addition, intermediate scale and mountain scale variability in hydrologic properties and flow paths within Yucca Mountain produces spatial variability in the percolation flux. The drift opening cross section shape and size affect seepage, in the manner originally discussed by Philip et al. (1989). As discussed in Section 3.2.6, seepage into drifts is also affected by thermal process and the resultant coupled processes.

A detailed discussion of seepage process is provided in *Technical Basis Document No. 3: Water Seeping into Drifts*.

3.3.3 Unsaturated Zone Transport

Radionuclide transport within the unsaturated zone is strongly related to unsaturated zone flow through the advection, and advective transport pathways are consistent with flow pathways discussed in Section 3.1. (Advective transport (advection) refers to the movement of dissolved or colloidal materials because of the bulk flow of fluid.) In the welded units, advection through

fractures is expected to dominate transport behavior, mainly because liquid water largely flows through fracture networks in these units. Advection is also an important mechanism for transport between fractures and matrix, especially at interfaces between nonwelded and welded units. At these interfaces, transitions occur between dominant fracture flow and dominant matrix flow. Liquid water flow paths below the repository horizon will be critical to the radionuclide transport resulting from advection, particularly in perched water bodies, where lateral transport of radionuclides is likely to occur. Dominant fault and fracture flow in the zeolitic part of the CHn provides relatively short transport times for transport to the water table, whereas dominant matrix flow in the vitric part of the CHn provides much longer transport times.

In addition to advection, radionuclide transport within the unsaturated zone is affected by several other mechanisms, such as matrix diffusion, sorption, colloid-facilitated transport, and decay. Matrix diffusion refers to solute transport from fracture networks to surrounding matrix blocks resulting from molecular diffusion (CRWMS M&O 2000c, Section 6.2.2). Mass transfer between fractures and tuff matrix may play an important role in transport within Yucca Mountain. Because flow velocity in the matrix is much slower than in fractures, transfer of radionuclides from fractures to the matrix can significantly retard the overall transport of radionuclides to the water table.

Sorption is an important mechanism in reactive chemical and radionuclide transport (CRWMS M&O 2000c, Section 6.2.3). It is used to describe a combination of chemical interactions between dissolved solutes and the solid phases (immobile rock matrix or colloids), including adsorption, ion exchange, surface complexation, and chemical precipitation.

Radionuclide transport in the unsaturated zone also involves a colloid-facilitated transport mechanism (CRWMS M&O 2000c, Section 6.2.4). Colloids are particles small enough to become suspended (and thus transportable) in a liquid. They can interact with radionuclides through sorption mechanisms. Unlike sorption of radionuclides to the rock matrix, however, radionuclides sorbed on colloids are potentially mobile. Therefore, colloids can facilitate radionuclide transport through the unsaturated zone at a faster rate than the aqueous phase alone.

Radioactive decay is a transformation process that affects the concentration of radionuclides during transport through the unsaturated zone (CRWMS M&O 2000c, Section 6.2.5). For simple decay, radionuclide concentration decreases exponentially with time, creating stable decay products. Chain decay adds additional complexity because of the ingrowth of new radionuclides created from the decay of a parent radionuclide. One aspect of potential significance with respect to chain decay is that daughter products may have significantly different sorption behavior than the parent radionuclide, therefore exhibiting different transport behavior.

A detailed discussion of radionuclide transport process is provided in *Technical Basis Document No. 10: Unsaturated Zone Transport*.

4. DEVELOPMENT OF THE SITE-SCALE FLOW MODEL

The site-scale unsaturated zone flow model has been developed based on the geology of the site, conceptual understanding of flow paths within the unsaturated zone, and field data. The unsaturated zone flow model is used to generate unsaturated zone flow fields used directly by TSPA. While the details of the unsaturated zone flow model are documented in *UZ Flow Models and Submodels* (BSC 2004), this section provides a brief introduction to development and validation of the site-scale unsaturated zone flow model.

4.1 NUMERICAL APPROACH AND RELATED ISSUES

In the site-scale unsaturated zone flow model, simulation of the complex flow and transport processes occurring within the unsaturated zone requires simplification of the real-world system. Among the many issues related to this simplification, this section discusses three important ones: selection of the numerical approach; treatment of heterogeneity; and the active fracture model used to deal with fingering flow in fracture networks.

4.1.1 Selection of the Numerical Approach

Several approaches are available in the literature for modeling flow and transport in unsaturated fractured rocks. When classified according to the manner in which fracture networks are treated in the model structure, these approaches mainly fall into one of two categories: the continuum approach and the discrete fracture network approach. Reviews on these approaches, which have been developed and used in different fields (including oil reservoir engineering, groundwater hydrology, geothermal engineering and soil physics), can be found in *Flow and Contaminant Transport in Fractured Rock* (Bear et al. 1993) and National Research Council (1996).

In the continuum approach, fractures are considered to be sufficiently ubiquitous and distributed in such a manner that they can be meaningfully described statistically (Bear et al. 1993). The role of individual fractures in fractured media is considered to be similar to that of individual pores in porous media. Therefore, one can describe average fracture properties as macroscopic and those associated with individual fractures as microscopic. In the continuum approach, connected fractures and rock matrix are viewed as two or more overlapped interacting continua. In other words, at a "point," two or more continua are considered to coexist. In this case, the continuum mechanics formulations, such as those used for porous media, can be used to describe flow and transport in each continuum. Coupling of processes between different continua is determined by their interaction mechanisms at a subgrid scale. Depending on the number of continua and the methodology used to treat fracture–matrix interaction, continuum models can be classified further as effective-continuum, dual-continuum, and multiple-interacting-continua models (Figure 4-1). (In Figure 4-1, solid lines between node points represent potential flow paths.) The effective-continuum model replaces fractures and rock matrix with a single effective continuum. Dual-continuum (dual-porosity and dual-permeability) models treat fractures and the matrix as two separate, yet interacting, continua. The multiple-interacting-continua model further subdivides the matrix into more than one continuum to consider the nonequilibrium of flow and transport within the matrix.

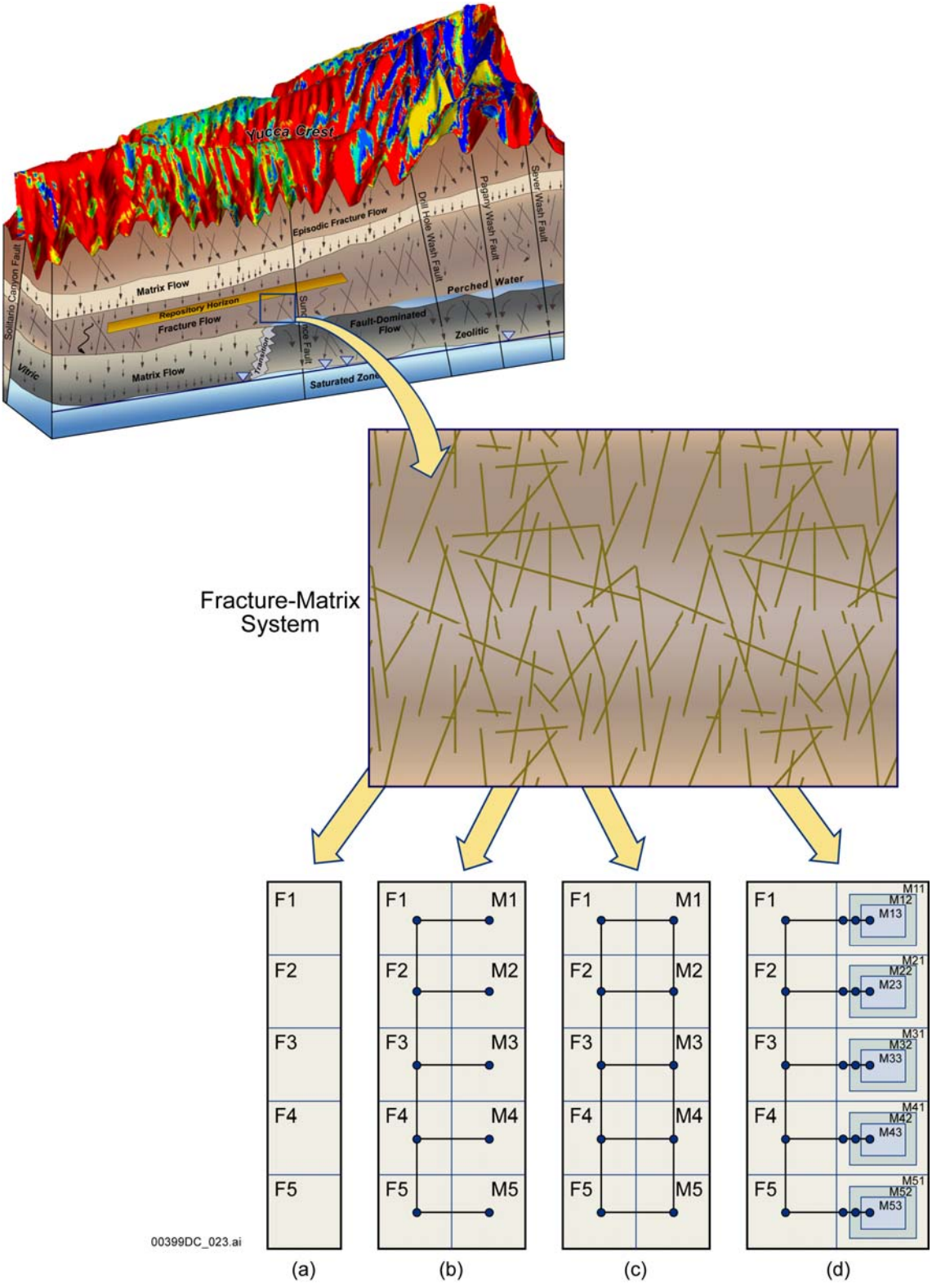

Figure 4-1. Effective-Continuum Model (a); Dual-Porosity with One Matrix Gridblock (b); Dual-Permeability with One Matrix Gridblock per Fracture Gridblock (c); and Multiple-Interacting-Continua Model with Three Matrix Gridblocks per Fracture Gridblock (d)

The discrete fracture network approach involves the generation, by computer simulation, of synthetic fracture networks and the subsequent modeling of flow and transport in these networks. The approach has been extensively used for single phase flow and transport, with deterministic, stochastic, artificial, or site-specific fracture networks (e.g., Bear et al. 1993; National Research Council 1996). This approach has been adapted for use in unsaturated zone studies at Yucca Mountain (CRWMS M&O 2000c, Section 6.4).

Both continuum and fracture network approaches have advantages and disadvantages. While the fracture network approach is useful as a tool for concept evaluation or model-based process studies, it has several limitations. First, the approach requires geometric parameters that may strongly impact flow and transport, such as fracture apertures and conductivity, but typically cannot be well constrained from field observations. Second, it is difficult to separate the conductive fracture geometry from the nonconductive fracture geometry. Third, flow and transport models based on the approach can be complex and computationally intensive for realistic fracture densities. Fourth, so far, studies based on the fracture network approach have rarely considered fracture–matrix interaction (flow and transport between fractures and the matrix), because of computational intensity for unsaturated flow and transport. Fracture–matrix interaction has important effects on flow and transport processes in unsaturated fractured rocks.

Because the continuum approach is relatively simple and straightforward to implement, it is preferred for most applications encountered in practice (National Research Council 1996). For example, because the number of fractures is estimated over the site on the order of 10^9 at Yucca Mountain (Doughty 1999), it is practically impossible to construct and calibrate a discrete fracture network site-scale model with so many fractures, considering data availability and computational feasibility. Therefore, the dual-continuum approach has been used as the baseline approach for modeling flow and transport within Yucca Mountain. The use of the continuum approach is also supported by the study of Finsterle (2000), who demonstrated that the continuum approach can capture flow behavior generated from a discrete feature model. A discussion of the other issues related to the selected numerical approach for the unsaturated zone flow model, such as integrated finite difference method, upstreaming, weighting, and grid refinement, can be found in *UZ Flow Models and Submodels* (BSC 2004).

4.1.2 Treatment of Subsurface Heterogeneity

Heterogeneities exist at different scales within both fracture and matrix continua in the unsaturated zone at Yucca Mountain. Treatment of subsurface heterogeneity is important for modeling flow and transport processes. A geology-based deterministic approach, in which an entire model layer is assigned uniform properties, is used mainly for representing subsurface heterogeneity.

The key justification for the above approach is that the overall behavior of site-scale flow and transport processes is determined mainly by relatively large-scale heterogeneities associated with the geologic stratification and tectonic features (e.g., faults) of the mountain. Within the same geologic unit, hydrologic properties are relatively uniformly distributed because of the intrastrata homogenization induced by tuff depositional environments. This justification is also consistent with a field observation that matrix saturation distribution is relatively uniform within a given geologic unit (CRWMS M&O 2000c, Section 6.4.3). Displacement of strata along faults can

result in units with different hydrologic properties being placed against each other across the fault, resulting in lateral heterogeneities within the unsaturated zone.

Zhou et al. (2003) recently demonstrated the validity of this approach in dealing with subsurface heterogeneity. They used a two-dimensional vertical cross section in the east–west direction through borehole USW UZ-14 to investigate the effect of multiscale heterogeneity on unsaturated flow and transport within the unsaturated zone. Specifically, they generated and used random fields of three selected properties: matrix permeability, k_m; matrix van Genuchten parameter, α_m; and fracture permeability, k_f (Zhou et al. 2003, Figure 13). For comparison, they employed different sets of rock property distributions in three cases. In these cases, mean rock properties for a given geological layer are the same. In Case A, the layered approach mentioned above was used. In Case B, stochastically generated k_f variability was considered within a geological layer. In Case C, variabilities of all the selected rock properties were included, with the variabilities determined from the measured hydrologic properties. Thus, Case A only considers large-scale heterogeneity, while Cases B and C include small-scale heterogeneity within a geological unit.

Figure 4-2 shows comparisons of vertical water fluxes within the matrix and fractures along the repository zone for three cases. Although relatively large differences exist for the water flux in the matrix, distributions of water fluxes in fractures are very similar for these three cases. Because the matrix flux corresponds to only a small percentage of total water flux, the three cases essentially provide similar water flow fields at the site scale. Zhou et al. (2003, Figure 17) also compared simulated results for tracer transport from the repository to water table, and again found that the results are similar for the three cases. In summary, the study of Zhou et al. (2003) demonstrates that heterogeneities within each geological unit have only a minor effect on the site-scale flow processes.

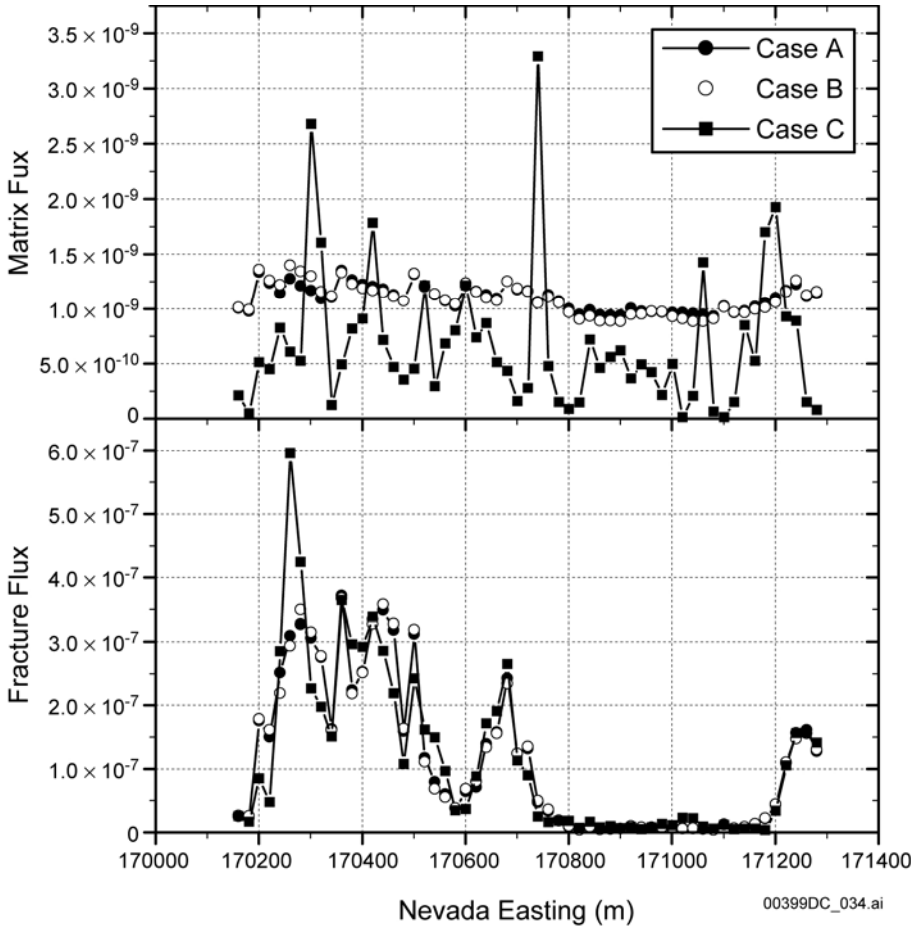

Source: Zhou et al. 2003, Figure 16.

Figure 4-2. Comparison of Simulated Matrix and Fracture Flux (m/s) at the Repository Horizon in Cases A, B, and C

4.1.3 Active Fracture Model

A traditional continuum approach assumes uniformly distributed flow patterns at a subgrid scale. Therefore, such an approach cannot be used for representing gravity driven fingering flow and transport in fracture networks, resulting from subsurface heterogeneities and nonlinearity involved in unsaturated flow. To incorporate this flow behavior into the continuum approach, the site-scale unsaturated zone flow model uses the active fracture model.

The active fracture model was developed within the context of the dual-continuum approach (Liu et al. 1998). While the details of the model can be found in Liu et al. (1998), a brief description of the model is provided here for convenience. The active fracture concept is based on the reasoning that, because of fingering flow, only a portion of fractures in a connected, unsaturated fracture network contribute to liquid water flow, while other fractures are simply bypassed. The connected fractures that actively conduct water are called active fractures. In other words, the active fracture model uses a combination of the volume-averaged method and a simple filter to deal with fracture flow and transport. Inactive fractures are filtered out in modeling fracture–matrix interaction, flow, and transport in the fracture continuum.

The conventional, capillary equilibrium-based, fracture water distribution model assumes that liquid water occupies first fractures with small apertures, and then fractures with relatively large apertures, as water potential (or water saturation) increases. In contrast, the active fracture model presumes gravity-dominated, nonequilibrium, preferential liquid water flow in fractures, which is expected to be similar to fingering flow in unsaturated porous media. A liquid finger can bypass a large portion of a porous medium, which does not necessarily correspond to large pores. The above discussion is valid for large-scale flow processes and not inconsistent with the possible validity of a capillary equilibrium-based fracture water distribution concept at relatively small scales, corresponding to an individual flow path or a single flow finger.

Flow and transport conditions and fractured rock properties determine the fraction of active fractures in a connected fracture network. In the active fracture model, this fraction is expressed as a power function of fracture saturation. *Analysis of Hydrologic Properties Data* (BSC 2003g, Section 6.7) showed that, in theory, this expression is consistent with fractal flow patterns often observed in unsaturated systems. It also demonstrated that the active fracture model-based simulation results are generally consistent with ^{14}C age and fracture coating data, although some uncertainty may exist in interpreting these data sets (BSC 2003g, Section 7). This study concludes that simulated distributions of large-scale water flux, matrix saturation, and water potential are not sensitive to active fracture model parameter values (BSC 2004, Section 6.8), although the water velocity distributions are (Liu et al 1998). A further discussion of effects of active-fracture-model parameter values on solute transport process may be found in *Technical Basis Document No. 10: Unsaturated Zone Transport*.

4.2 OVERVIEW OF THE SITE-SCALE UNSATURATED ZONE MODEL

The site-scale unsaturated zone flow model is a three-dimensional, dual-permeability unsaturated flow model. This section discusses some key elements of the unsaturated zone flow model, including the boundary conditions, property calibration, and simulation scenarios for TSPA.

4.2.1 Boundary Conditions

The three-dimensional unsaturated zone model domain and the numerical grid for this study is shown in plan view in Figure 4-3 and encompasses approximately 40 km^2 of the area over the mountain. This three-dimensional model grid uses a refined mesh in the vicinity of the repository, located near the center of the model domain, covering the region east of the Solitario Canyon fault through the Ghost Dance fault and north to beyond Pagany Wash fault. The model domain is selected to focus on the repository area and to investigate the effects of different infiltration scenarios and major faults on moisture flow around and below the repository. In the model grid, vertical or inclined 30-m-wide zones represent modeled faults.

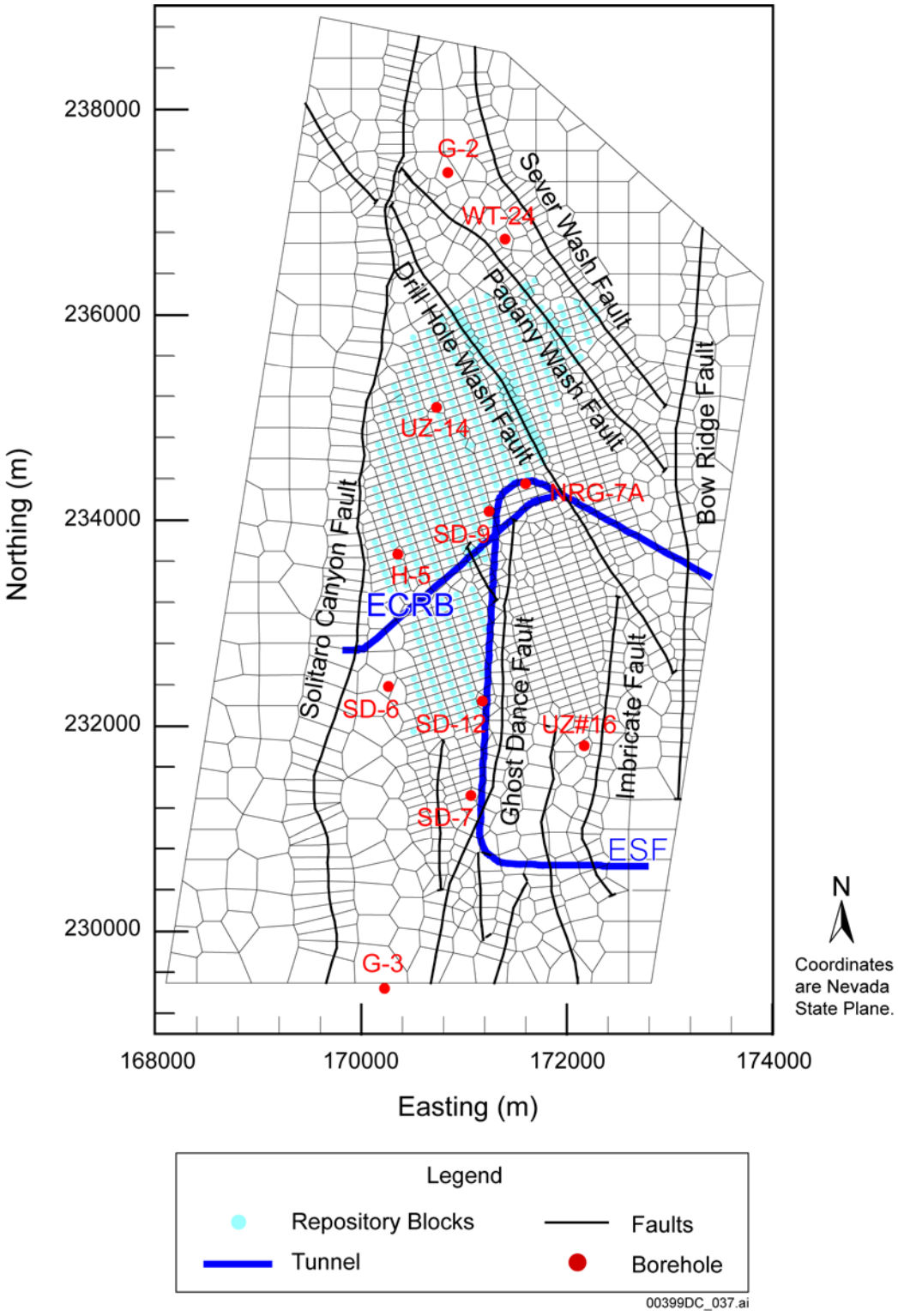

Source: BSC 2004, Figure 6.1-1.

Figure 4-3. Plan View of the Three-Dimensional Unsaturated Zone Flow Model Domain

The ground surface of the mountain with exposed tuff or the tuff–alluvium contact in areas with significant alluvial cover is taken as the top model boundary, and the water table is treated as the

bottom model boundary. Spatially variable surface infiltration is applied into fractures from the top boundary. All lateral boundaries (see Figure 4-3) are treated as no flow (closed) boundaries and allow flow only along vertical planes. This treatment should be reasonable for the eastern boundary, which is along or near the Bow Ridge fault, because high vertical permeability and lower capillary forces are expected within the faults (see fault properties estimated in *Calibrated Properties Model* (BSC 2003b, Section 6.3.4)). The southern, western, and northern lateral boundaries are farther away from the repository and, thus, have little effect on unsaturated flow within or near the repository. For simulations involving airflow and nonisothermal conditions, both the top and bottom boundaries of the model are treated as possessing Dirichlet-type conditions with specified constant but spatially varying gas pressure and or temperature.

4.2.2 Model Calibration and Uncertainties

The site-scale unsaturated zone flow model is a three-dimensional dual-permeability model. In the model, 32 layers with different hydrologic properties are used to represent the stratigraphic units encountered at the site. Each layer is assigned homogeneous hydrologic properties, with the exception of the layers in CHn, which are assigned hydrologic properties for either vitric or zeolitically altered rock types. Because field observations from the Busted Butte test sites (Section 2.4.1) clearly indicated that flow occurs in the matrix only within the vitric CHn, the fracture flow component within the vitric CHn is not considered in the site-scale unsaturated zone flow model.

Directly measured fracture permeability and matrix hydrologic properties are available for most of the model layers. However, the unsaturated zone flow model cannot directly use these properties. This is because measurement scales are generally inconsistent with the property resolution scales in the model. Also, not all the needed hydrologic properties (such as fracture van Genuchten parameters) are measured. Consequently, model calibration is needed to develop hydrologic properties for the site-scale unsaturated zone flow model.

Model calibration involves using numerical models for the unsaturated zone to predict unsaturated zone conditions and then comparing them to observations of these conditions from field measurements (such as saturation data and gas pressure data). Model parameters are adjusted (calibrated) so that the difference between the model predictions and the observed data is minimized.

Model calibration involves a series of increasingly complex models. Because model calibration needs a great number of forward simulation runs, computationally efficient one-dimensional models are used for developing preliminary calibrated hydrologic properties. Using one-dimensional models, data from multiple boreholes are inverted simultaneously to estimate layer average properties. Matrix saturation, in situ water potential data, and pneumatic pressure (barometric pumping response) data are used to estimate the hydrologic properties in one-dimensional calibrations. Two-dimensional cross-sectional models are employed for estimating fault properties. In a two-dimensional model, a fault is modeled perpendicular to the plane of the model. Again, matrix saturation, water potential, and pneumatic pressure data are inverted.

One major limitation of the one-dimensional models is that they can not capture the important three-dimensional flow behavior, such as lateral flow, because of capillary barrier effects in the PTn and effects of the perched water. To resolve this issue, three-dimensional models are used for limited trial-and-error calibrations and verification of simulation results against many different data sets, including data sets used for one- and two-dimensional calibrations (BSC 2004). Note that automatic calibrations have been used for one- and two-dimensional cases. Additional data sets used for model calibration at this stage include perched water elevations at several surface-based boreholes and pore water chloride concentration data from surface-based boreholes and the ECRB Cross-Drift. The latter data are closely related to spatial distribution of percolation within the unsaturated zone. The model is also calibrated against the temperature data observed from deep boreholes, which are also related to the percolation process. Property adjustments are needed to calibrate the three-dimensional unsaturated zone flow model against the data mentioned above. For example, Figures 4-4, 4-5, and 4-6 present some calibration (simulation) results compared to corresponding field observations.

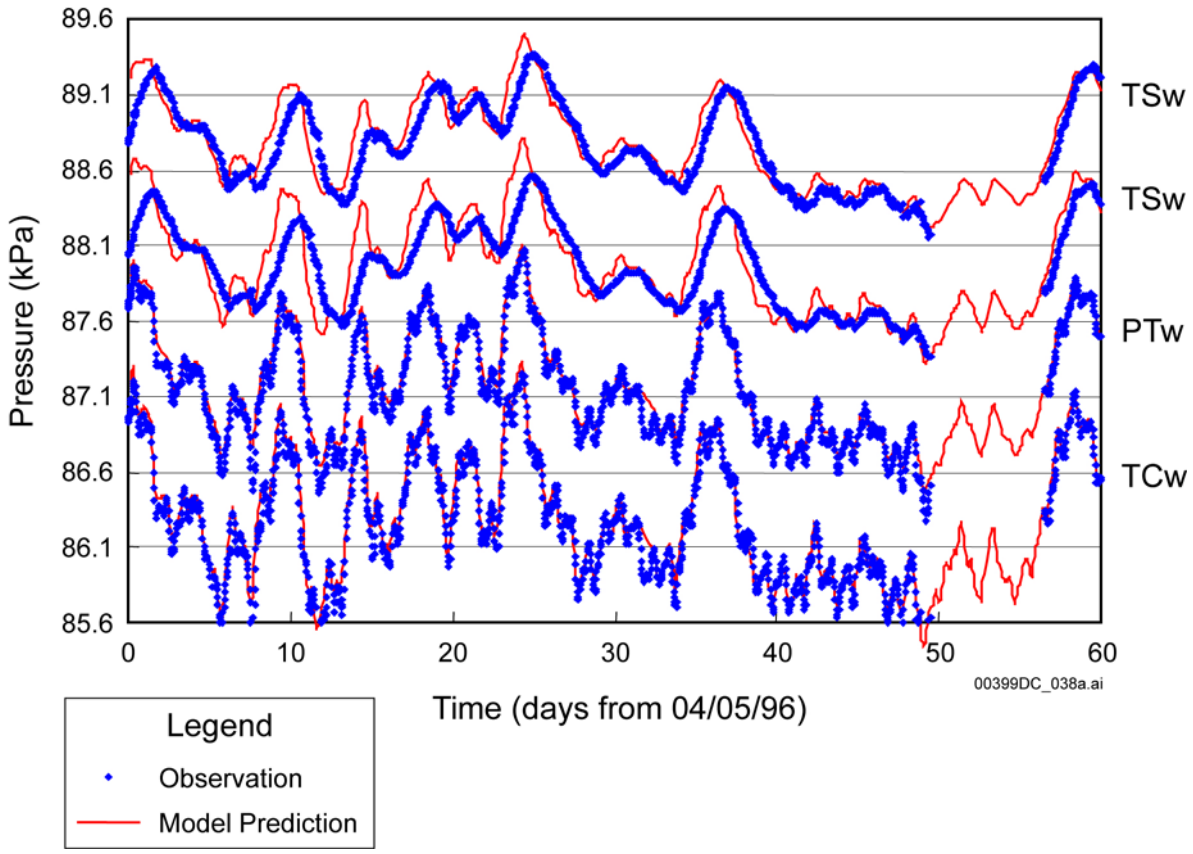

Source: BSC 2004, Figure 6.4-1.

Figure 4-4. Comparison of Simulated and Observed Gas Pressure at Borehole USW SD-7 in a 60-Day Period

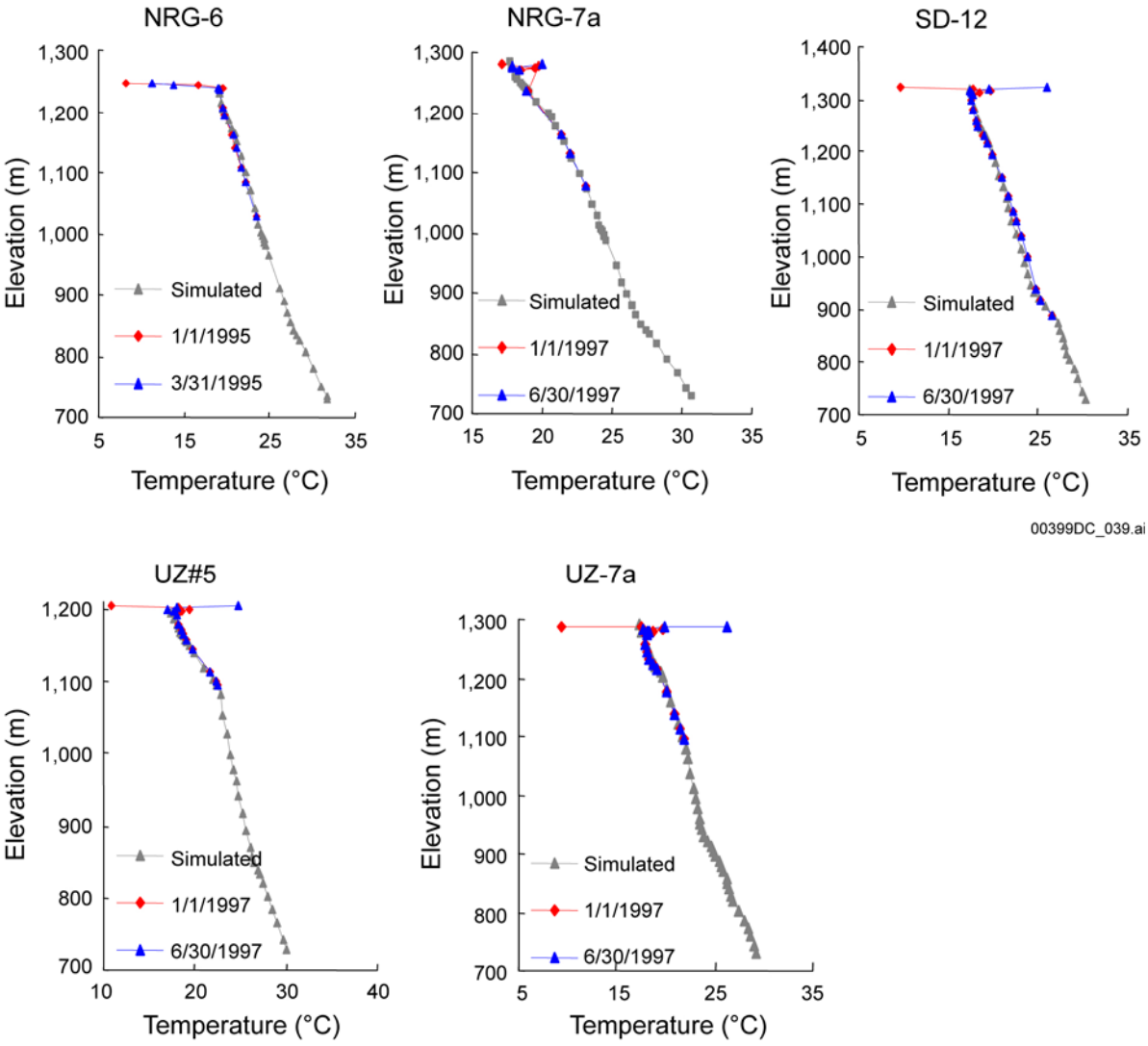

Source: BSC 2004, Figure 6.3-2.

Figure 4-5. Comparison of Simulated and Observed Ambient Temperature Profiles for the Five Boreholes under the Present-Day, Mean Infiltration Rate

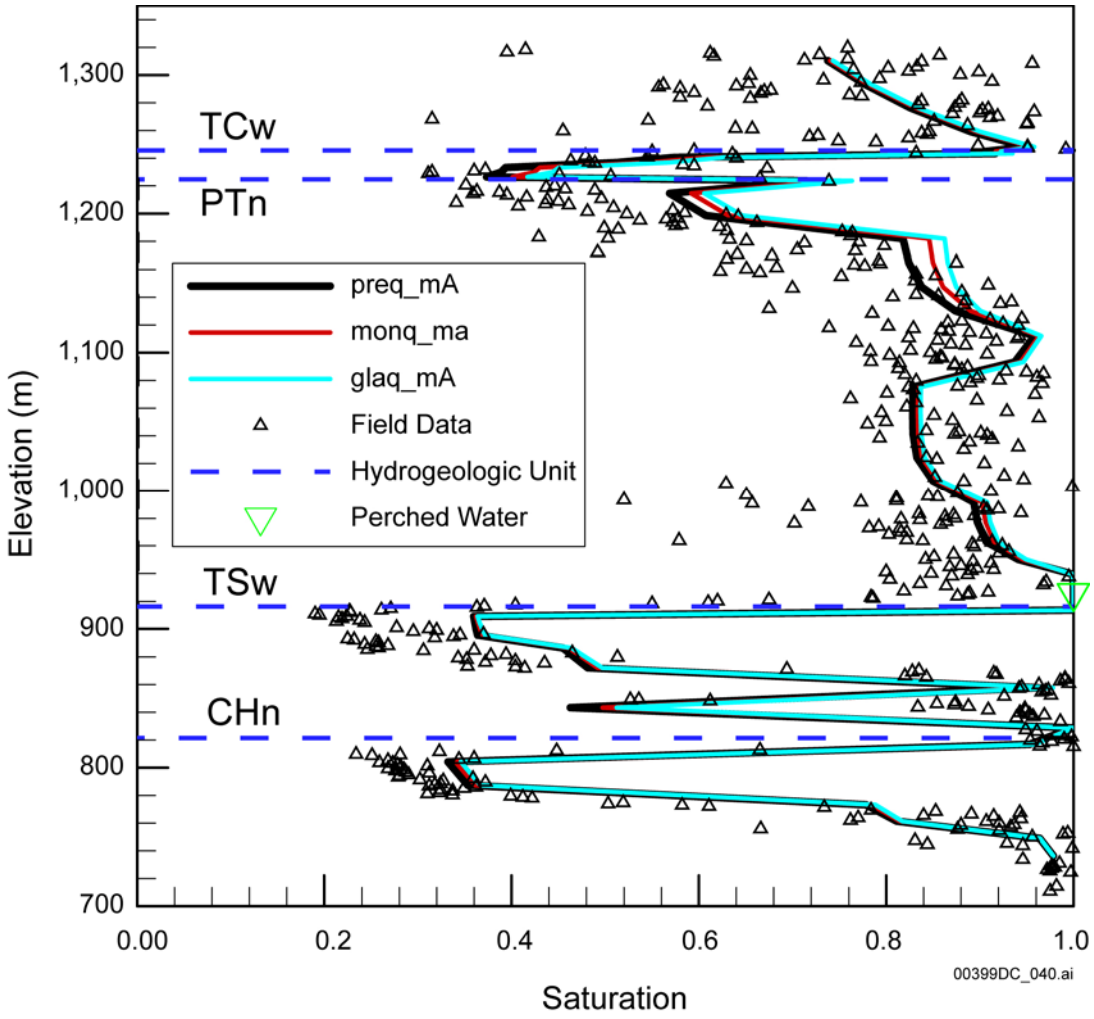

Source: BSC 2004, Figure 6.2-3.

NOTE: In the figure, preq_mA, monq_mA, and glad_mA correspond to present-day mean infiltration, monsoon mean infiltration, and glacial transition mean infiltration rates.

Figure 4-6. Comparison of Simulated and Observed Matrix Liquid Saturation and Perched Water Elevations for Borehole UE-25 SD-12, Using the Simulation Results for the Three Mean Infiltration Rates

Model calibration is subject to uncertainty. (The uncertainties are handled in the TSPA by considering a number of unsaturated zone flow fields generated by different property sets.) A major source of parameter uncertainty is the conceptual model described in Section 3. Infiltration rate uncertainty also contributes to parameter uncertainty, because flow processes in the unsaturated zone are largely determined by top boundary conditions. To capture this uncertainty, three infiltration scenarios (including present-day mean, upper-bound, and lower-bound infiltration maps) are used for the parameter calibration. In addition, scale effects are a well-known source of parameter uncertainty. This is especially true for determination of the unsaturated zone model parameters. For example, matrix parameters are measured in the unsaturated zone at core scale on the order of several centimeters, whereas in the unsaturated zone flow model, numerical gridblocks are on the order of a few meters to hundreds of meters. Scale-dependence of hydrologic parameters has been widely recognized in the scientific

community (e.g., Neuman 1994). Although upscaling is partially considered in developing uncalibrated matrix properties, the calibrated matrix permeabilities are, on average, higher than uncalibrated ones for the three infiltration scenarios, which is consistent with findings reported in the literature (e.g., Neuman 1994) and implies that the scale effects were captured by the model calibration. Fracture permeability values calibrated against pneumatic pressure data are also about two orders of magnitude higher than averaged permeability values measured from air injection tests with injection intervals of several meters. Furthermore, calibrated properties are not unique because of data limitation. Different property sets may match the data equally well.

Considering the difficulties in accurately quantifying parameter uncertainty, standard deviations of measured data are directly used for the parameter uncertainty of the calibrated parameter sets (BSC 2003h, Section 6.4). The parameter uncertainty of the uncalibrated property sets (measured data) is largely a result of small-scale spatial variability. Because the degree of spatial variability decreases with scale (subgrid scale (or high frequency) spatial variability is removed at a large scale), this treatment is likely to provide the upper limits of uncertainty on calibrated parameters for the given conceptual model and infiltration rates.

As previously discussed, the unsaturated zone flow model is based on the continuum (dual-permeability) approach that conceptualizes a fracture network as a continuum. The continuum approach is commonly used for modeling large-scale flow and transport problems (National Research Council 1996) and has been shown to be able to account for important flow and transport processes observed from a number of field tests in the ESF and the ECRB Cross-Drift at Yucca Mountain (e.g., Finsterle 2000). However, a continuum model is not designed to capture complex discrete-flow behavior in unsaturated fractured rock. In a discrete fracture-network study, Liu et al. (2002) suggest from the model results that the average spacing of active flow paths (in unsaturated fracture networks) within a layered system increases with depth, based on fracture network connectivity characteristics. Fracture network connectivity is not a characteristic considered by the current continuum approach.

The unsaturated zone flow model uses van Genuchten (1980) relationships, developed especially for porous media, for describing unsaturated flow in fractures. This constitutive relationship model largely determines the corresponding simulation results. However, the applicability of van Genuchten relationships for fractured rocks is questioned (Liu and Bodvarsson 2001, Glass et al. 1996). Liu and Bodvarsson (2001) reported that van Genuchten (1980) relationships underestimate fracture relative permeability for a large range of water saturation values and argued that an improved relationship model is needed for fractures. The uncertainty in the fracture constitutive relationship is fundamental to unsaturated zone models.

The unsaturated zone flow model uses the active fracture model of Liu et al. (1998) to deal with fingering flow and transport in unsaturated fractures. The active fracture model has been theoretically shown to be consistent with fractal flow patterns (common in different unsaturated systems), and simulation results based on the model can represent field-scale observations from different sources reasonably well (BSC 2003g, Sections 6.7 and 7). Considering the complexity of unsaturated flow in fractures at different scales, the tests for active fracture model validation require that detailed fracture–matrix interactions, partitioning of fracture flows from matrix flows, and water balances be taken into account (BSC 2003g, Sections 6.7 and 7).

The issues regarding model calibration and related uncertainties are further addressed in responses to KTIs TEF 2.11, and TSPAI 3.26.

4.3 CONFIDENCE BUILDING ACTIVITIES

In addition to being consistent with the conceptual understanding of water flow in the unsaturated zone, the unsaturated zone flow model is validated by checking for the consistency between modeling results with hydrologic and temperature data, geochemical data, and in situ field test data. These data are not used for model calibrations.

4.3.1 Consistency with Hydrologic and Temperature Data

Water potential data were collected from calibrated heat dissipation probes installed in the tunnel wall (at a depth of 2 m) along the ECRB Cross-Drift inside the ESF. As part of the three-dimensional flow and transport modeling validation process, modeled results of water potentials (for present-day, mean infiltration rates) were compared to field observations (Figure 4-7) (BSC 2004, Section 7.2). Most of the observed water potential data were distributed between 0.1 (10^4 Pa) and 1 (10^5 Pa) bars, with a maximum of 3.4 bar. The model predicted approximately 1 bar for the same section of tunnel. Even though the data available for comparison from the ECRB Cross-Drift are limited, the unsaturated zone model generally predicted the range of water potential data from in situ measurements.

Three-dimensional model simulation results (for the present-day, mean infiltration rates) were also compared with other sets of hydrologic and temperature data. The comparisons with perched water and matrix water potential data collected within the CHn hydrogeologic unit from borehole USW WT-24 are shown in Figure 4-8; the comparisons with gas pressure data from boreholes UE-25 SD-12 and USW UZ-7a are shown in Figure 4-9; and the comparisons with ambient temperature data from boreholes USW H-5, USW H-4, and UE-25 WT#18 are shown in Figure 4-10. The model was found to be consistent with these sets of data (BSC 2004, Section 7).

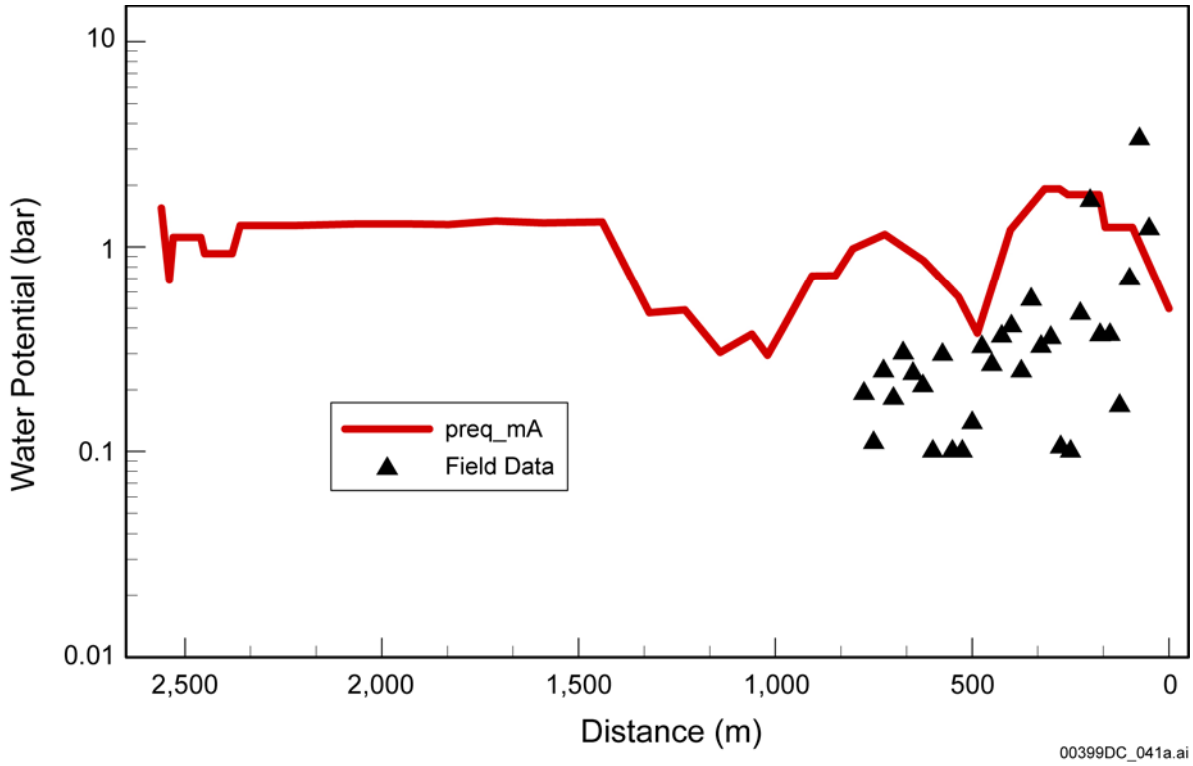

Source: BSC 2004, Figure 7.2-1.

NOTE: The preq_mA refers to simulation results for the present-day, mean infiltration rates.

Figure 4-7. Comparison of Predicted and Measured Water Potential along the ECRB Cross-Drift Using the Present-Day, Mean Infiltration Rates

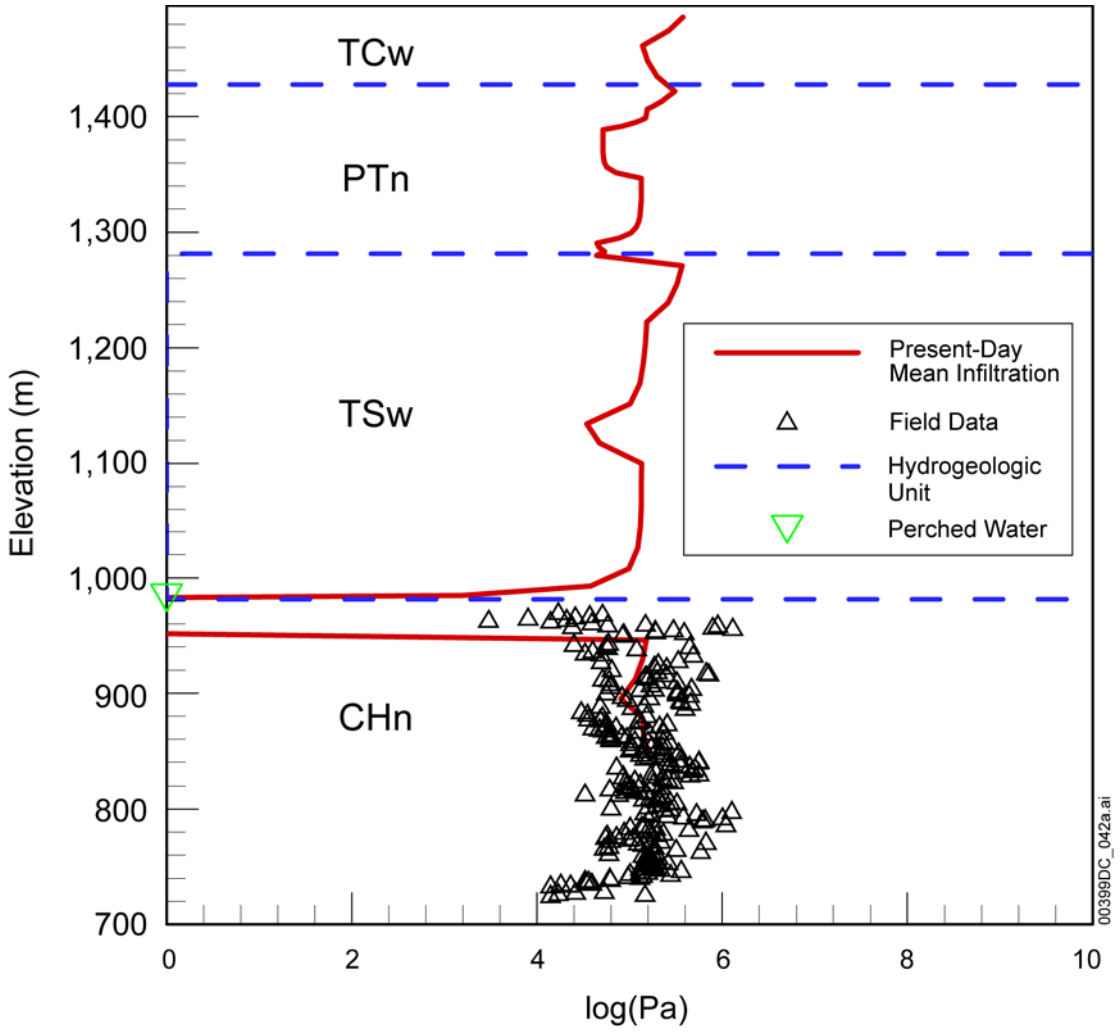

Source: BSC 2004, Figure 7.3-1.

NOTE: The preq mA refers to simulation results for the present-day, mean infiltration rates.

Figure 4-8. Comparison of Predicted and Measured Matrix Water Potentials and Perched Water Elevations at Borehole USW WT-24, Using the Present-Day, Mean Infiltration Rate (preq_mA)

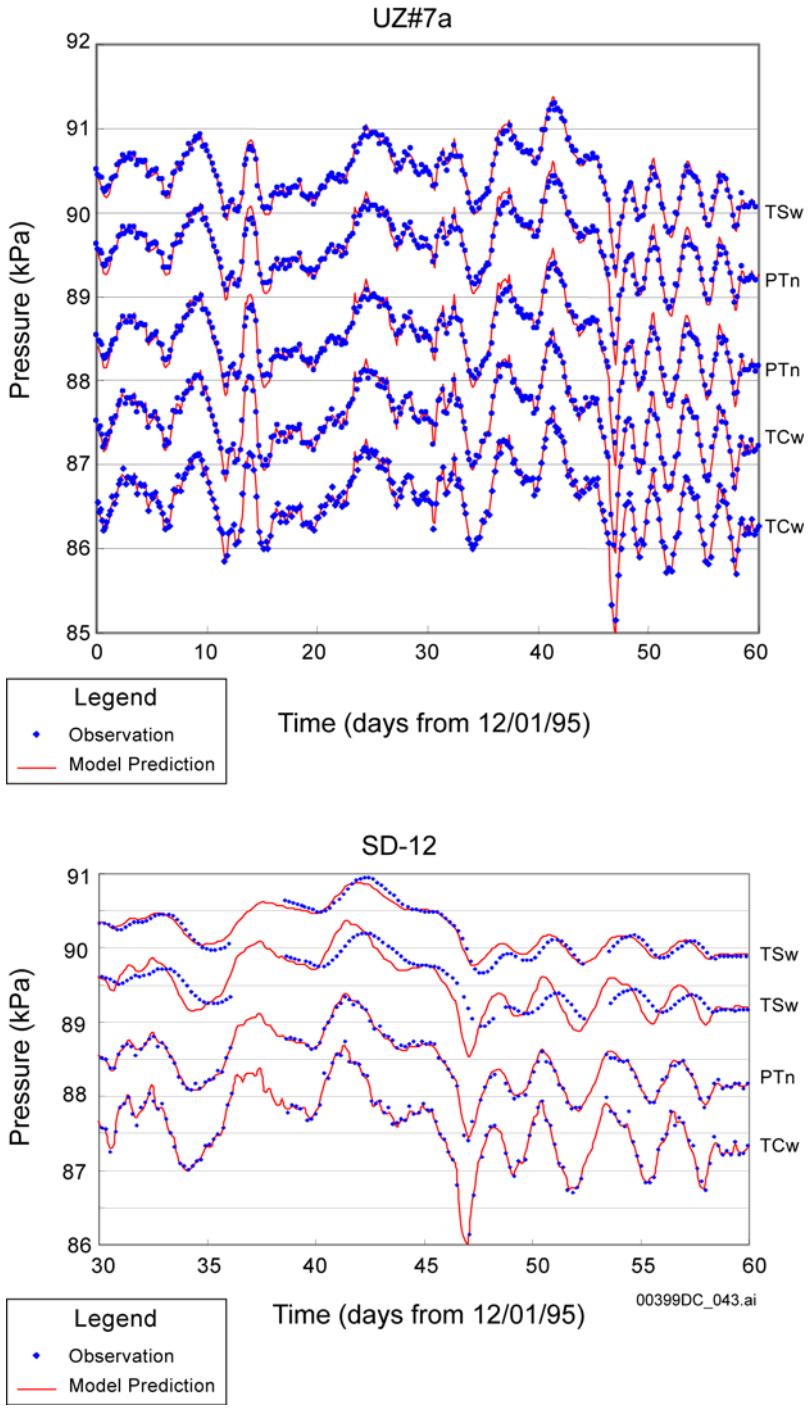

Source: BSC 2004, Figures 7.4-1 and 7.4-2.

Figure 4-9. Comparison of Three-Dimensional Pneumatic Prediction to Observation Data from Boreholes USW UZ-7a and UE-25 SD-12

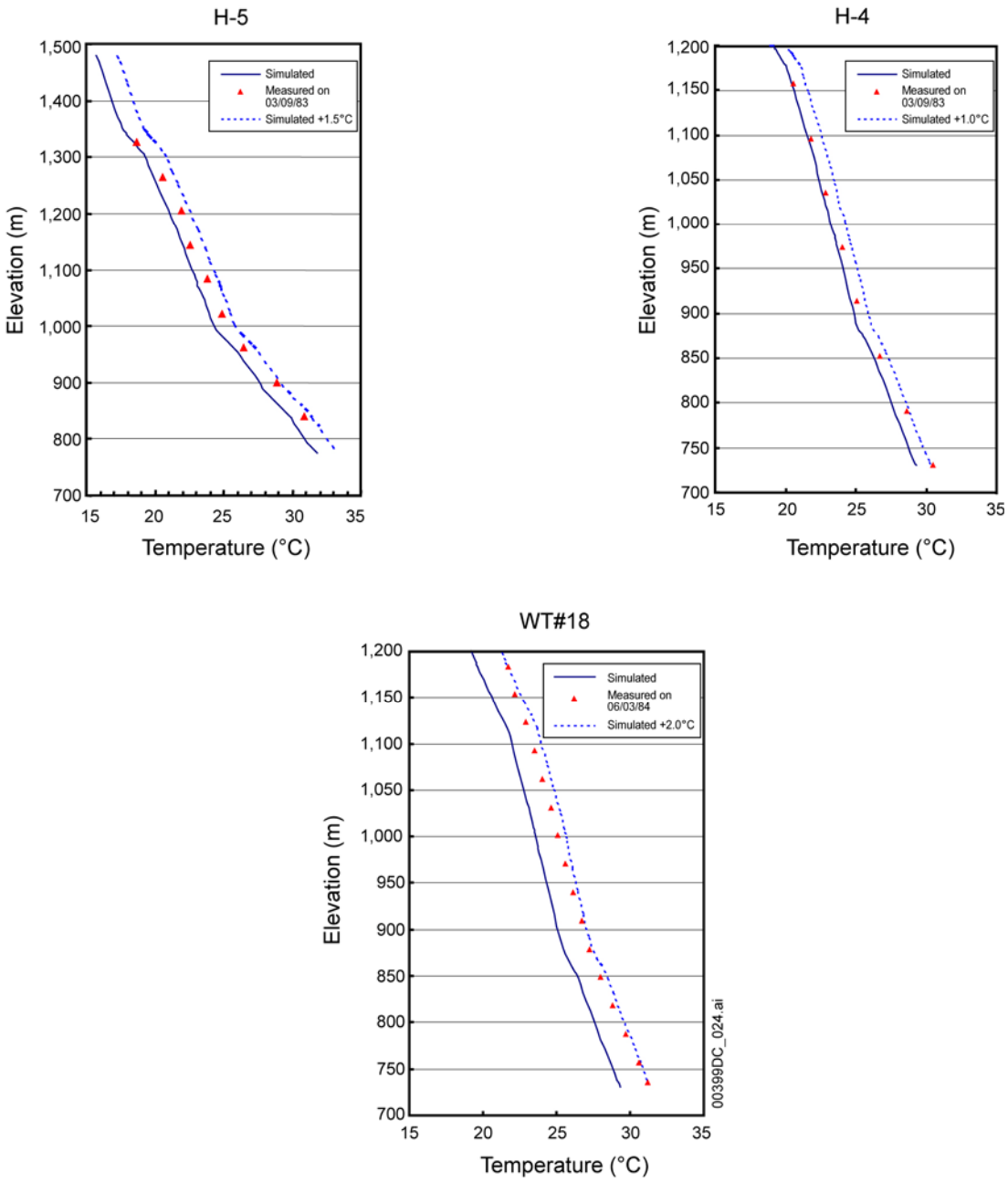

Source: BSC 2004, Figures 7.7-1 to 7.7-3.

Figure 4-10. Comparison of Simulated and Observed Temperature Profiles for Boreholes USW H-5, USW H-4, and UE-25 WT#18

4.3.2 Consistency with Geochemical Data

Because geochemical data provide independent insights into flow and transport processes in the unsaturated zone, various geochemical data sets are used for verifying the unsaturated zone flow model.

4.3.2.1 Model Validation with ^{14}C

^{14}C data were collected from perched water, pore water, and gas samples from the Yucca Mountain unsaturated zone (BSC 2002b, Section 6.6.4). ^{14}C data from gas samples are considered to be most representative of in situ conditions (Yang 2002, Section 4.1.2). ^{14}C is also considered to be the most sensitive isotope for measuring pore water age within the Yucca Mountain unsaturated zone, owing to its half-life time (which is in the same order of magnitude as the pore water age in the unsaturated zone) and its detectable abundance. Gas samples were collected from different kinds of boreholes, including open and instrumented surface-based boreholes. The data from instrumented boreholes, USW SD-12 and USW UZ-1, provide more reliable indicators of in situ matrix pore water ages (BSC 2002b, Section 6.6.4.3). ^{14}C ages (BSC 2002b, Table 20) calculated using the data from these two boreholes are used for validating the unsaturated zone model. Gas phase ^{14}C ages are interpreted to represent the ages of the in situ pore water. This interpretation is based on the rapid exchange of gas phase CO_2 (reaching equilibrium in hours to days) with dissolved CO_2 and HCO_3^- in pore water. Water transport times simulated with the site-scale unsaturated zone model are within the range of field observations, indicating the consistency between simulation results and the data (BSC 2004, Section 7.5). As an example, Figure 4-11 shows the simulation results compared to age data for borehole USW UZ-1.

4.3.2.2 Model Validation with Chloride

Chloride is hydrologically very mobile and chemically inert, and a nearly ideal natural tracer for the study of water movement in the liquid phase. A chloride model was developed to validate the unsaturated zone model by testing it with data not used in the development or calibration of the unsaturated zone model. The chloride model simulates large-scale unsaturated zone chloride transport processes. It uses the three-dimensional flow fields calculated by the unsaturated zone model and incorporates chloride-in-precipitation data to model advective and diffusive chloride transport in the unsaturated zone (BSC 2004, Section 7.8). The simulated pore water chloride concentration is compared with analysis of samples collected along the ESF. Chloride concentrations in the ESF using the three infiltration scenarios are plotted in Figure 4-12. The criterion for validation is that the range of the simulated chloride concentration falls within the range of measured concentrations (BSC 2002d, Attachment I-1-2-3, BSC 2004, Section 7.1). The range of the simulated chloride concentration of the base-case flow field (preq_mA) in the ESF generally fall within the range for measured concentrations. The figure also indicates that the trend of measured chloride concentrations in samples is preserved in the calculated chloride concentrations. Note that measured chloride data are clustered around three areas with distances of about 1,000, 3,600, and greater than 6,800 m. For the first two locations, at 1,000 and 3,600 m, the simulated (preq_mA) results are either within or at the range of measurements. For the last portion, however, the simulations are well within the range of measurement for greater than 7,000 m and are close to (but a little higher than) the measurement. The figure also shows simulation results for the present-day, upper-bound infiltration scenario (preq_uA), present-day, lower-bound infiltration scenario (preq_lA), and glacial transition mean infiltration scenario.

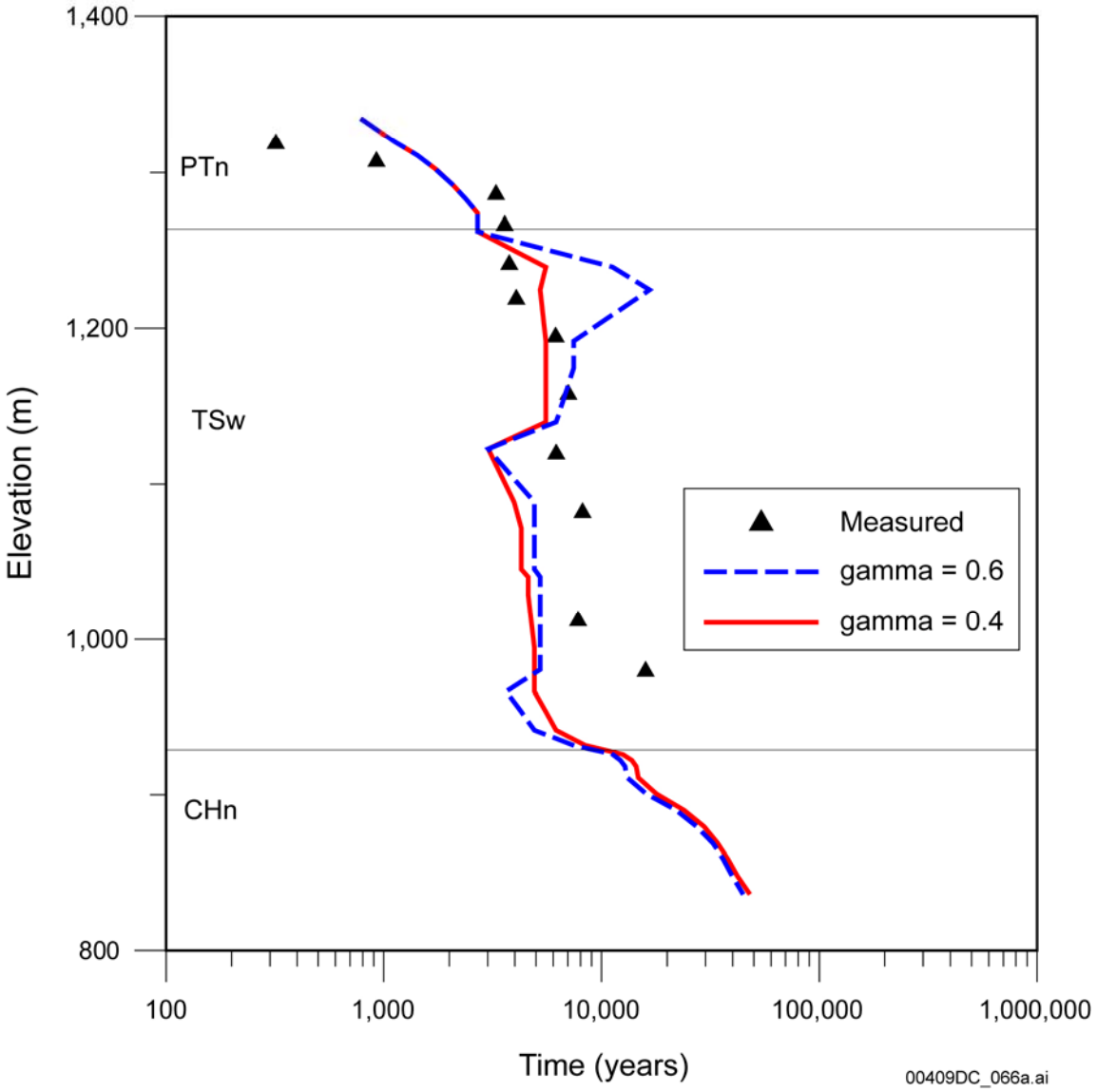

Source: BSC 2004, Figure 7.5-1.

Figure 4-11. Comparison between Simulated (the Curves with gamma = 0.6 and gamma = 0.4) and Observed Water Residence Ages in the Matrix for Borehole USW UZ-1

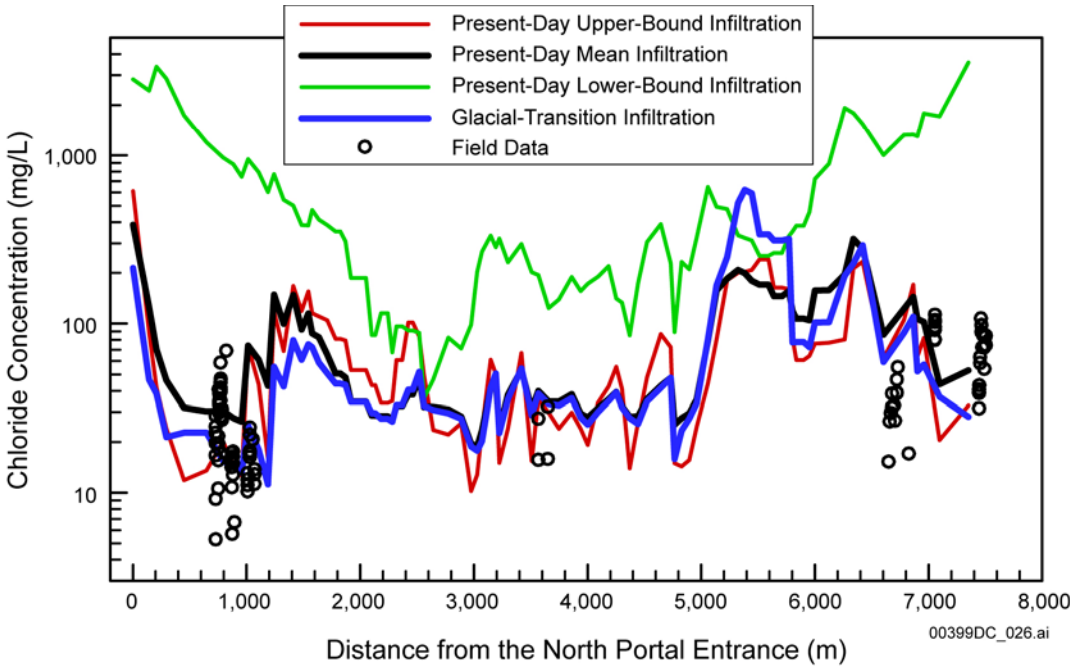

Source: BSC 2004, Figure 7.8.1.

Figure 4-12. Comparison of Chloride Concentration (mg/L) Profiles under Present-Day Infiltration Rates with Simulation Results for Mean (preq_mA), Upper (pre_uA), and Lower (preq_lA) Bounds, and Glacial Transition Infiltration Rates (glaq_pmA) at the Exploratory Studies Facility

4.3.2.3 Model Validation with Calcite

Modeling calcite deposition provides additional confidence for validation of the unsaturated zone flow model. A one-dimensional reactive transport model (an unsaturated zone submodel) is used to constrain the infiltration flux, by comparing the simulation results with calcite abundances from a deep surface-based borehole (USW WT-24). The percolation flux in the unsaturated zone is largely determined by infiltration rates corresponding to the top boundary conditions of the unsaturated zone flow model. Simulation results indicate that observed calcite abundance from USW WT-24 is consistent with a range of infiltration rates used in the unsaturated zone flow model near the borehole USW WT-24 (BSC 2004, Section 7.9) (Figure 4-13).

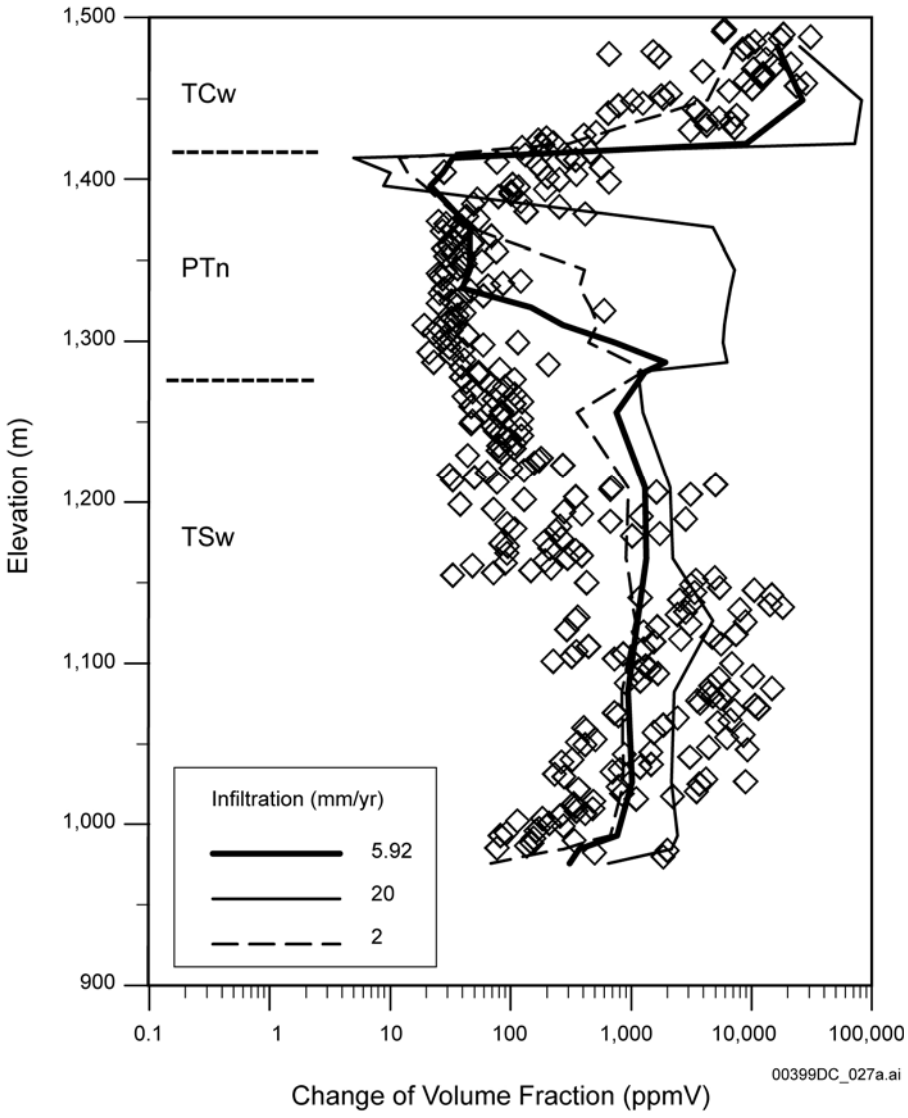

Source: BSC 2004, Figure 7.9-3.

Figure 4-13. Comparison between Measured and Simulated Total (Fracture plus Matrix) Calcite Abundances (in ppmV or 10^{-6} volume fraction) in the WT-24 Column for Different Infiltration Rates (Curves for Cases with Millimeters per Year)

Strontium concentrations and the $^{87}Sr/^{86}Sr$ ratio in pore fluids and secondary minerals can provide important constraints on infiltration rates, flow paths, residence times, and degrees of water rock and fracture–matrix interaction at Yucca Mountain. Simulation results based on three-dimensional flow fields from the unsaturated zone flow model are also found to be generally consistent with strontium concentrations observed from boreholes USW SD-9 and UE-25 SD-12 and from the ECRB Cross-Drift (BSC 2004, Section 7.10) (Figure 4-14).

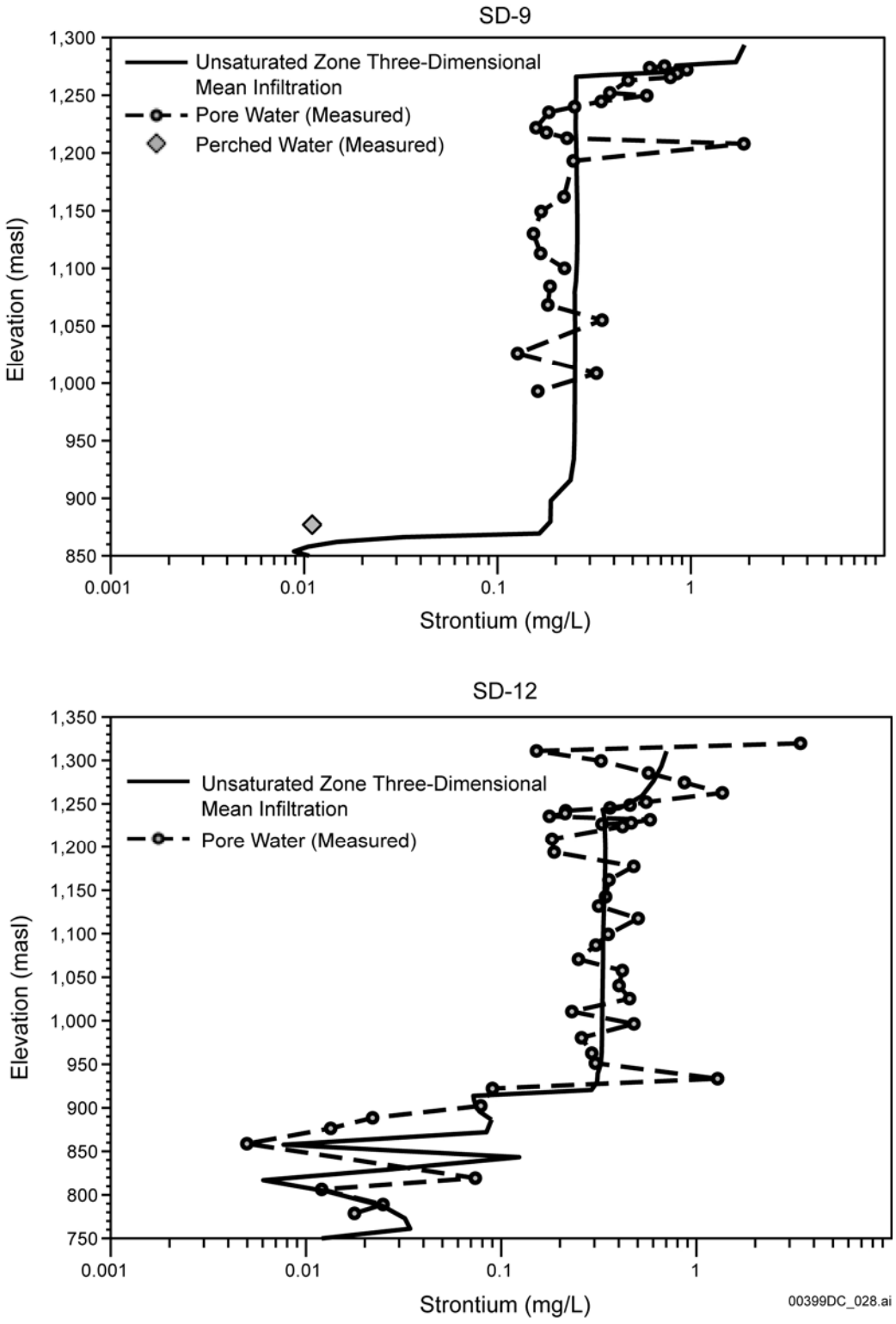

Source: BSC 2004, Figure 7.10-1.

Figure 4-14. Comparison of Measured and Modeled Strontium Concentrations as a Function of Elevation for the Surface-Based Boreholes USW SD-9 (a) and UE-25 SD-12 (b)

4.3.3 Consistency with In Situ Test Results

Comparisons between simulation results and field observations from Alcove 8–Niche 3 tests are used to evaluate the methodology (continuum approach) used in the site-scale unsaturated zone flow model. A three-dimensional submodel for the test site (based on the continuum modeling approaches used by the unsaturated zone flow model) is developed, and modeling analysis uses both model calibration and prediction (BSC 2004, Section 7.6). The Alcove 8-Niche 3 tests are briefly described in Section 2.3. Infiltration rate, seepage rate, and tracer concentration data from the tests are used to corroborate model simulations. It was found that the field observations are well represented by the modeling results. For example, Figure 4-15 shows a comparison between simulated and observed seepage rate as a function of time. A similar model evaluation approach was used for Alcove 1 tests (described in Section 2.3). Again, modeling results are found to be consistent with field observations (e.g., Figure 4-16). More detailed discussions of these model evaluation activities are given in *UZ Flow Models and Submodels* (BSC 2004, Section 7.6) and Liu et al. (2003).

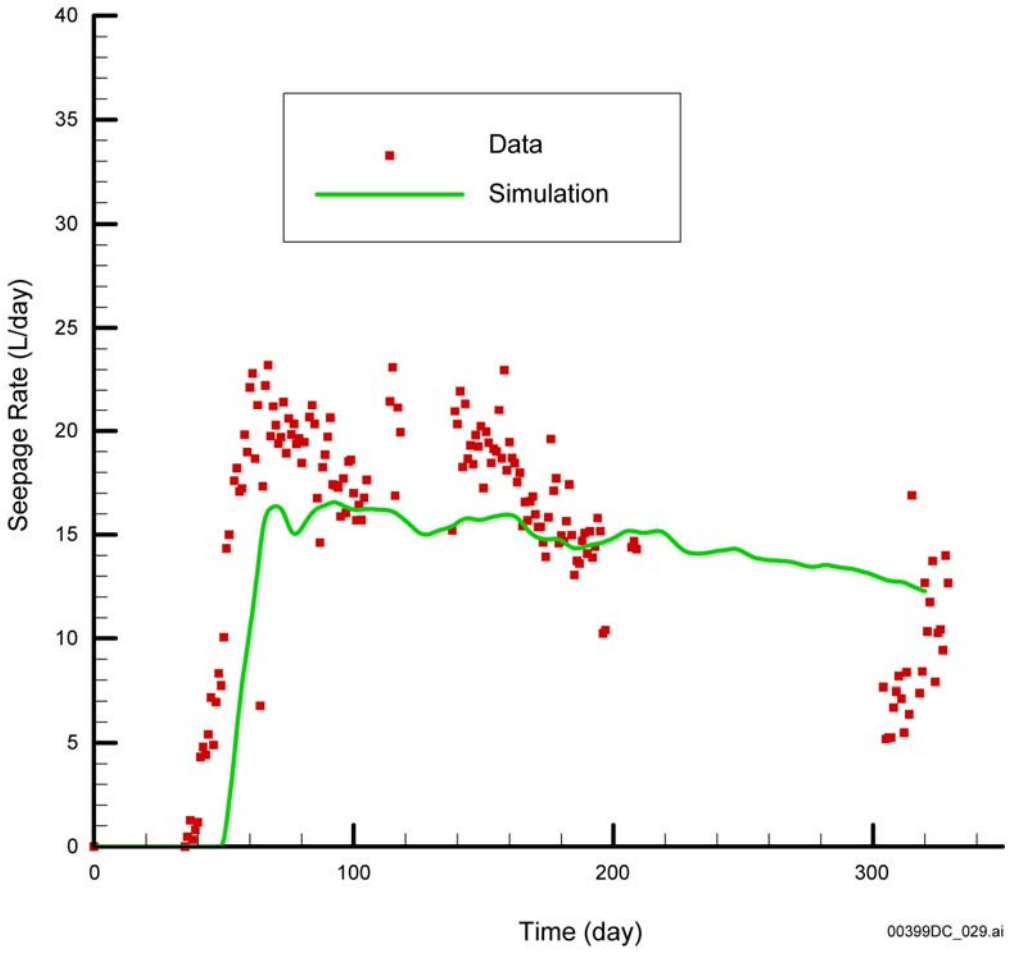

Source: BSC 2004, Figure 7.6-8.

Figure 4-15. Comparison between Simulated Seepage Rates as a Function of Time and Field Observations Collected from Alcove 8–Niche 3 Tests

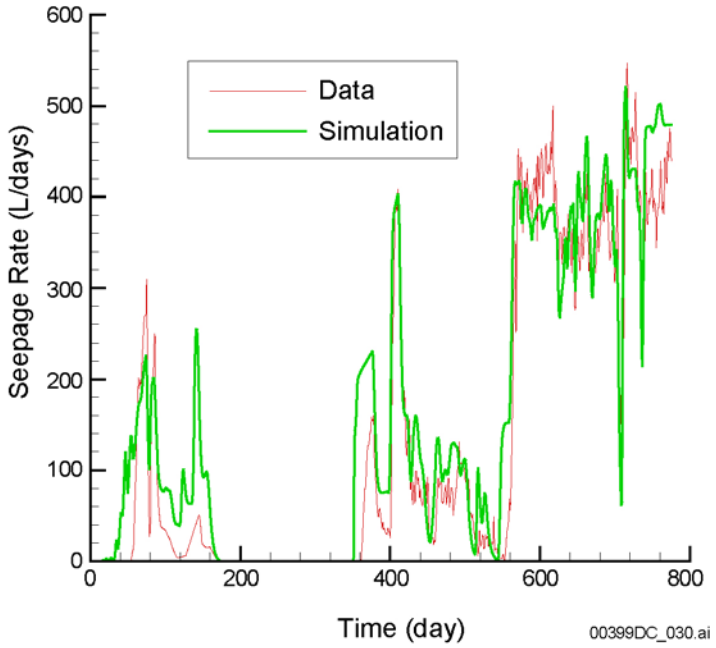

Source: Liu et al. 2003, Figure 4.

Figure 4-16. Comparison between Simulated Seepage Rates as a Function of Time and Field Observations Collected from Alcove 1 Tests

4.4 MODELING STUDIES OF THERMAL EFFECTS ON UNSATURATED ZONE FLOW

Heat released by the emplaced waste induces coupled changes in thermal, hydrologic, chemical, and mechanical processes both at the drift scale near the waste and at the site scale over Yucca Mountain. The site-scale thermal-hydrologic, thermal-hydrologic-chemical, and thermal-hydrologic-mechanical model results (BSC 2003e) are described in the following sections.

4.4.1 Site-Scale Thermal-Hydrologic Effects

The site-scale thermal-hydrologic model estimates the unsaturated zone responses to the repository thermal load in the Yucca Mountain unsaturated zone system under present and future climates, as well as the effect of ventilation (BSC 2003e, Sections 6.2 and 6.3). The dual-permeability model is used for all the site-scale coupled process models, including the thermal-hydrologic model. In general, thermal loading at the repository results in significant changes in the temperature conditions (Figure 4-17) and moisture distribution, both at the repository and in the zone directly above and below the repository, which have a large impact on fluid flow near repository drifts. The moisture conditions under repository heating become "drier" (experiencing reduced liquid saturation in fracture and matrix systems) than the ambient conditions. Both the base case with 50 years of ventilation and the alternative case without ventilation were evaluated (BSC 2003e, Sections 6.2.1 and 6.2.2). This drying effect with ventilation is found to reach its maximum between 100 and 500 years. Without ventilation, the drying effect lasts 1,000 years. At large mountain scales, the thermal-hydrologic models predict that no extensive dryout zones develop from the repository thermal load under the future

climates and the current thermal load scheme. The most significant dryout occurs in fractures within several meter regions immediately surrounding the drifts.

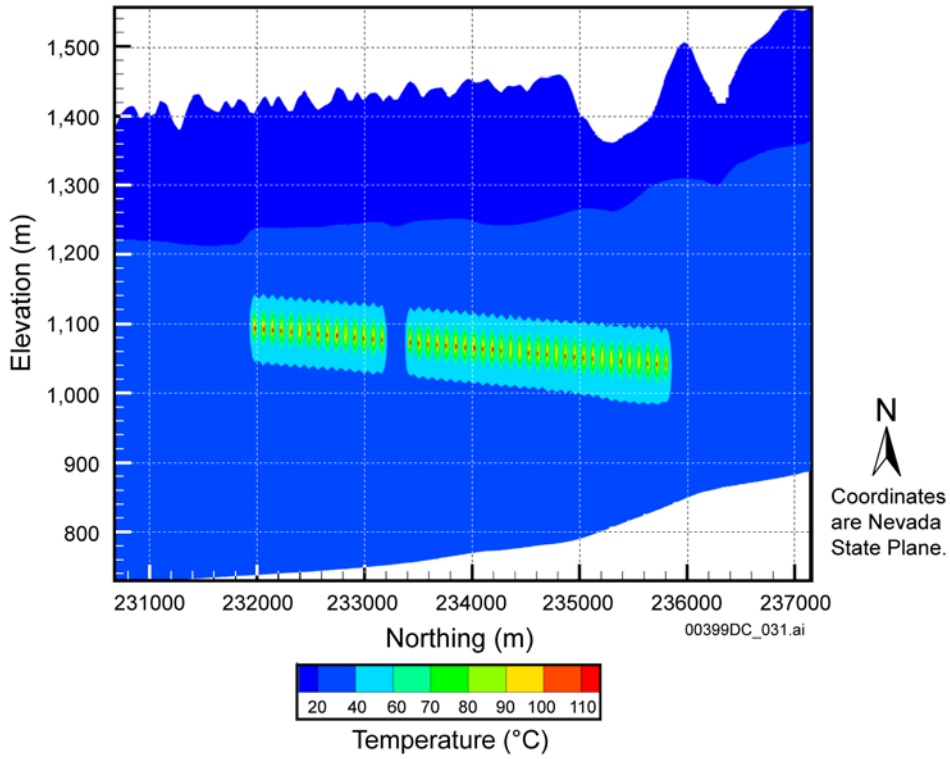

Source: BSC 2003e, Figure 6.2-1a.

Figure 4-17. Contours of Temperature in the Two-Dimensional North–South Cross Section of the Unsaturated Zone Model Grid at 100 Years with Base-Case Thermal Loading

Thermal loading at the repository has a significant impact on percolation fluxes near repository drifts for times less than 1,000 years. Strong liquid and gas flow fields, in particular for the nonventilation case, are developed in local areas surrounding repository drifts. These flow fields, especially flow through the fractures surrounding drifts, are enlarged many times (with ventilation) to one order of magnitude (without ventilation) higher than the ambient conditions at the repository drifts and at earlier times (100 to 500 years). Furthermore, simulation results indicate that no fracture or matrix liquid fluxes flow directly into drifts and that no seepage occurs during the entire thermal loading period, even with much higher infiltration rates imposed from climate changes. The thermal-hydrologic model results predict that repository heating will have only a small impact on flow through the pillar regions between two drifts. This is because boiling does not occur in these pillar areas, and moisture conditions there are not much changed from ambient status. Simulated vertical fluxes in the pillar regions show little variation in thermal activity at drifts. In fact, flow through the pillar regions is more affected by surface infiltration or climate changes than by repository heating.

The thermal-hydrologic model results also predict that repository heating with ventilation will have in general only a limited impact on far-field flow fields. In this case, thermally enhanced flux zones extend no more than 30 m in the regions directly above or below the repository blocks. Without ventilation, on the other hand, thermally impacted flux zones above the

repository grow to as thick as 100 m. In both modes of thermal operations, the thermal-hydrologic model predicts a much stronger thermal-hydrologic effect along highly permeable columns of faults that intersect repository blocks, because of the stronger vapor flow and condensation.

4.4.2 Site-Scale Thermal-Hydrologic-Chemical Effects

The site-scale thermal-hydrologic-chemical model was used to evaluate the coupled thermal-hydrologic-chemical processes and their effects on unsaturated zone flow (BSC 2003e, Section 6.4). A two-dimensional cross section of the repository was selected for a series of thermal-hydrologic and thermal-hydrologic-chemical calculations having increasing complexity in terms of processes and chemical components. The results of the simulations indicate that mineral precipitation and dissolution will not significantly affect the hydrologic properties and the percolation flux compared to the effects caused by thermal-hydrologic processes alone. Changes to water chemistry, mineralogy, and hydrologic properties in the ambient temperature regions are minimal. For example, Figure 4-18 shows a comparison of simulation results (for vertical water flux) with thermal-hydrologic and thermal-hydrologic-chemical models. Very little difference was found between the results from the two models.

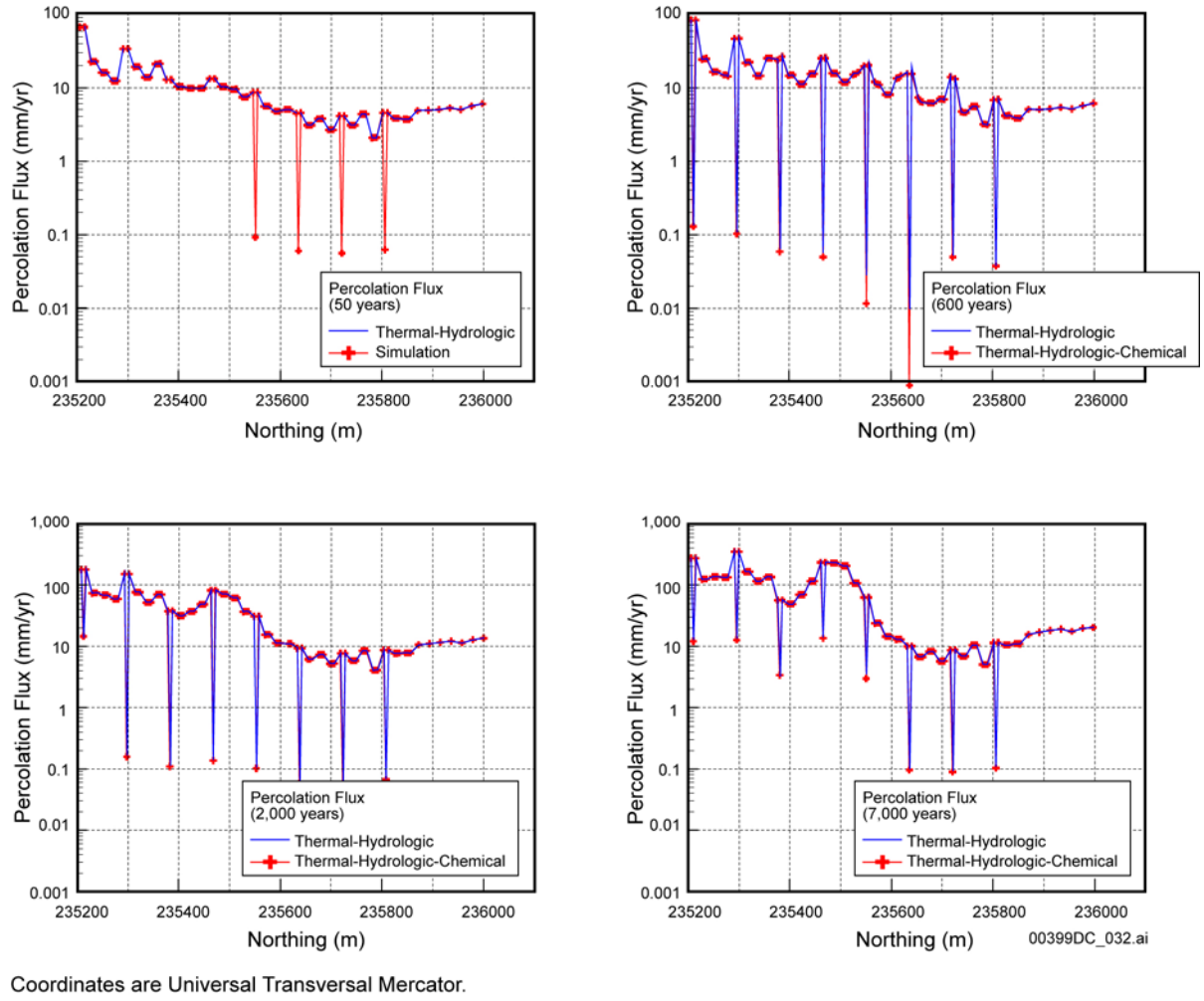

Source: BSC 2003e, Figure 6.4-27.

Figure 4-18. Percolation Fluxes at the Repository Horizon from the Thermal-Hydrologic and Thermal-Hydrologic-Chemical Models

4.4.3 Site-Scale Thermal-Hydrologic-Mechanical Effects

The site-scale thermal-hydrologic-mechanical model was developed for assessing the magnitude and distribution of changes in hydrologic properties and for analyzing the impact of such changes on the unsaturated zone flow (BSC 2003e, Section 6.5). The results show that maximum thermal-hydrologic-mechanical-induced changes in hydrologic properties occur at around 1,000 years after emplacement, when average temperature in the mountain reaches peak values. Near the repository level, thermal elastic stresses tend to tighten vertical fractures to smaller apertures, leading to reduced permeability and increased capillarity. The horizontal fractures near the repository level remain open with no significant thermal stress developed in the vertical direction because of the free-moving ground surface. At the ground surface, in a zone extending down about 100 m, compressive stresses are completely relieved into tension. In this zone, fractures will open elastically, and fracturing or shear slip along preexisting fractures is feasible.

Using estimates of input thermal-hydrologic-mechanical properties, changes in permeability by elastic closure or opening of preexisting fractures are within a factor of 0.3 to 5.0, whereas calculated changes in capillary pressure range between a factor of 0.7 to 1.2. In addition, a three-order-of-magnitude increase in permeability and one-order-of-magnitude reduction in capillary pressure were imposed for the zone of possible fracturing and shear slip near the ground surface. With these estimates of potential changes in hydrologic properties, the simulation results show that thermal-hydrologic-mechanical–induced changes in mountain-scale hydrologic properties have no significant impact on the vertical percolation flux through the repository horizon (Figure 4-19). Again, these results were obtained for estimates of the input thermal-hydrologic-mechanical properties, which are sufficient for bounding the possible impact of the thermal-hydrologic-mechanical processes on permeability and percolation flux at the mountain scale.

4.4.4 Summary of Site-Scale Thermally Induced Effects

In summary, the thermal process has a considerable effect on unsaturated zone flow, though largely limited to the repository horizon. The effects of resultant chemical and mechanical processes on unsaturated zone flow are minor; therefore, thermal effects on site-scale unsaturated zone flow are not considered in the TSPA.

4.5 SIMULATIONS SCENARIOS FOR TOTAL SYSTEM PERFORMANCE ASSESSMENT

The calibrated and verified site-scale unsaturated zone flow model is used to estimate percolation flux and its spatial distribution in the unsaturated zone. Percolation flux through the unsaturated zone is one of the most critical factors affecting overall repository performance in TSPA calculations. The quantity as well as the spatial and temporal variations in percolation flux will directly affect: (1) the amount of water flowing into waste emplacement drifts; (2) moisture conditions and the corrosion environment of waste packages within the drifts; (3) radionuclide release from the repository; and (4) radionuclide migration from the unsaturated zone to the saturated zone. The combinations of property sets and infiltration maps determine the total number of simulation scenarios for the TSPA. Three sets of calibrated properties are developed from model calibrations corresponding to three present-day (mean, lower bound, and upper bound) infiltration scenarios. Two conceptual models (or scenarios) for PTn flow (with and without lateral flow) are considered in the unsaturated zone flow model. The case with lateral flow corresponds to base case. For each conceptual model of PTn flow, three climates (present-day, monsoon, and glacial transition) are considered. Each climate corresponds to three infiltration scenarios (mean, lower bound, and upper bound). For each infiltration scenario and each conceptual model of PTn flow, three flow fields for the three climate states, respectively, are generated (Table 4-1).

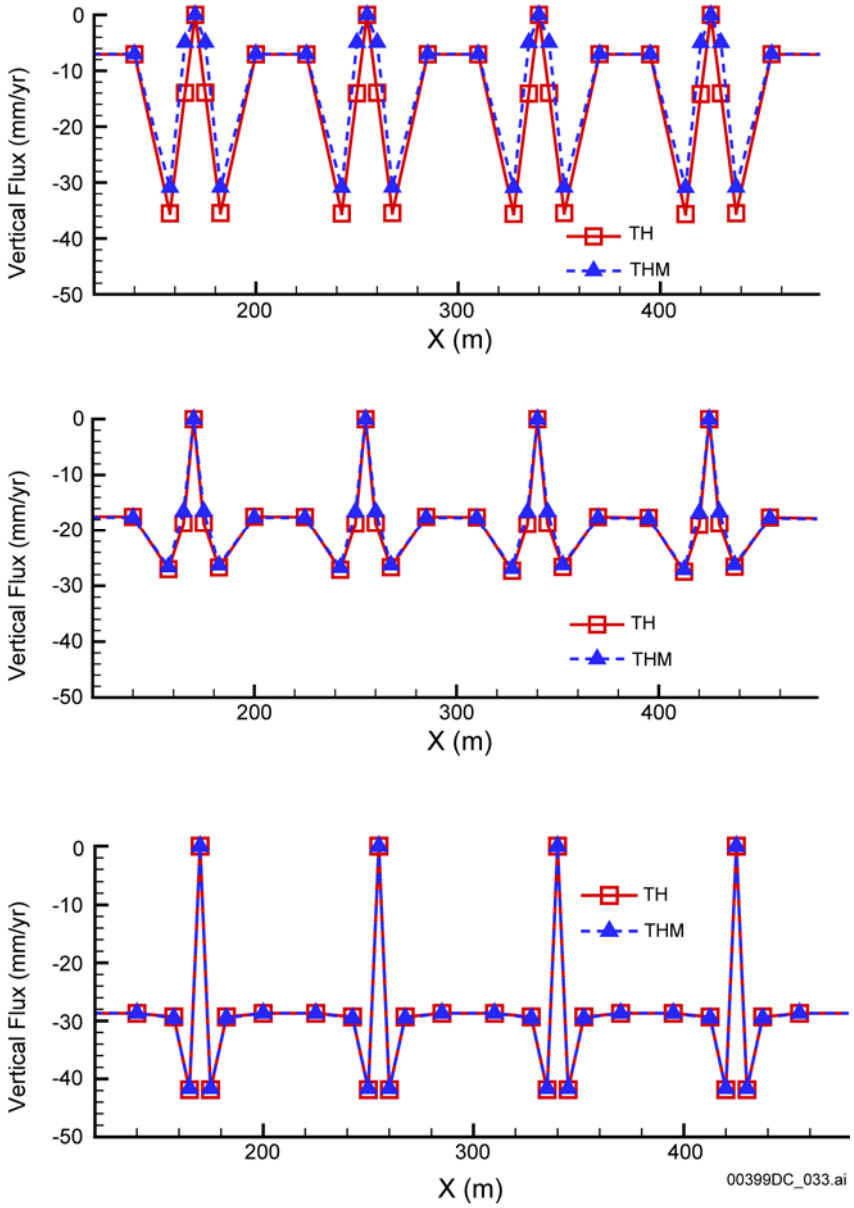

Source: BSC 2003e, Figure 6.5.13-7.

NOTE: Partially Coupled Thermal-Hydrologic Simulation = solid red lines; Fully Coupled Thermal-Hydrologic-Chemical Simulation = blue dashed lines.

Figure 4-19. Comparison of the Vertical Percolation Flux (across the Repository Horizon near Four Emplacement Drifts) for a Partially Coupled Thermal-Hydrologic Simulation to a Fully Coupled Thermal-Hydrologic-Chemical Simulation

Table 4-1. Simulation Scenarios of Unsaturated Zone Flow for the Total System Performance Assessment

Designation/ Simulation	PTn Flow Scenario	Infiltration Map
preq_lA	Lateral flow	Present-day, lower-bound infiltration
preq_lB	No lateral flow	
preq_mA	Lateral flow	Present-day, mean infiltration
preq_mB	No lateral flow	
preq_uA	Lateral flow	Present-day, upper-bound infiltration
preq_uB	No lateral flow	
monq_lA	Lateral flow	Monsoon, lower-bound infiltration
monq_lB	No lateral flow	
monq_mA	Lateral flow	Monsoon, mean infiltration
monq_mB	No lateral flow	
monq_uA	Lateral flow	Monsoon, upper-bound infiltration
monq_uB	No lateral flow	
glaq_lA	Lateral flow	Glacial transition, lower-bound infiltration
glaq_lB	No lateral flow	
glaq_mA	Lateral flow	Glacial transition, mean infiltration
glaq_mB	No lateral flow	
glaq_uA	Lateral flow	Glacial transition, upper-bound infiltration
glaq_uB	No lateral flow	

Source: BSC 2004, Sections 6.2 and 6.6.

For the PTn flow base case, simulation results indicate that percolation fluxes at the repository are very different from surface infiltration patterns. This result is, in part, due to the fact that surface infiltration rates and distributions are independent of faults. The major features in percolation flux at the repository level (Figure 4-20) are: (1) flow mainly through faults in the northernmost part of the model domain; (2) flow diverted into or near faults occurring within the entire model domain; and (3) an approximately 500 m lateral flow of the high infiltration zones from south to north along the crest located to the east. Note that the flow redistribution in the northernmost part of the model domain (far beyond the repository block) results from the repository grid layer horizon laterally intersecting the CHn zeolitic and perched water zones, with major flow paths being faults. Simulation results for the case without lateral flow within PTn differ from the base-case results in the extent of lateral flow in the model domain.

Percolation fluxes within the repository footprint are further analyzed using a frequency distribution plot. This plot displays the average percentage of the repository area subject to a particular percolation rate. Note that the normalized flux rates are determined by normalizing an infiltration value with respect to the averaged infiltration rate for the scenario. Figure 4-21 shows the frequency distribution of normalized percolation flux within the repository horizon for the three mean infiltration rates of the three climates.

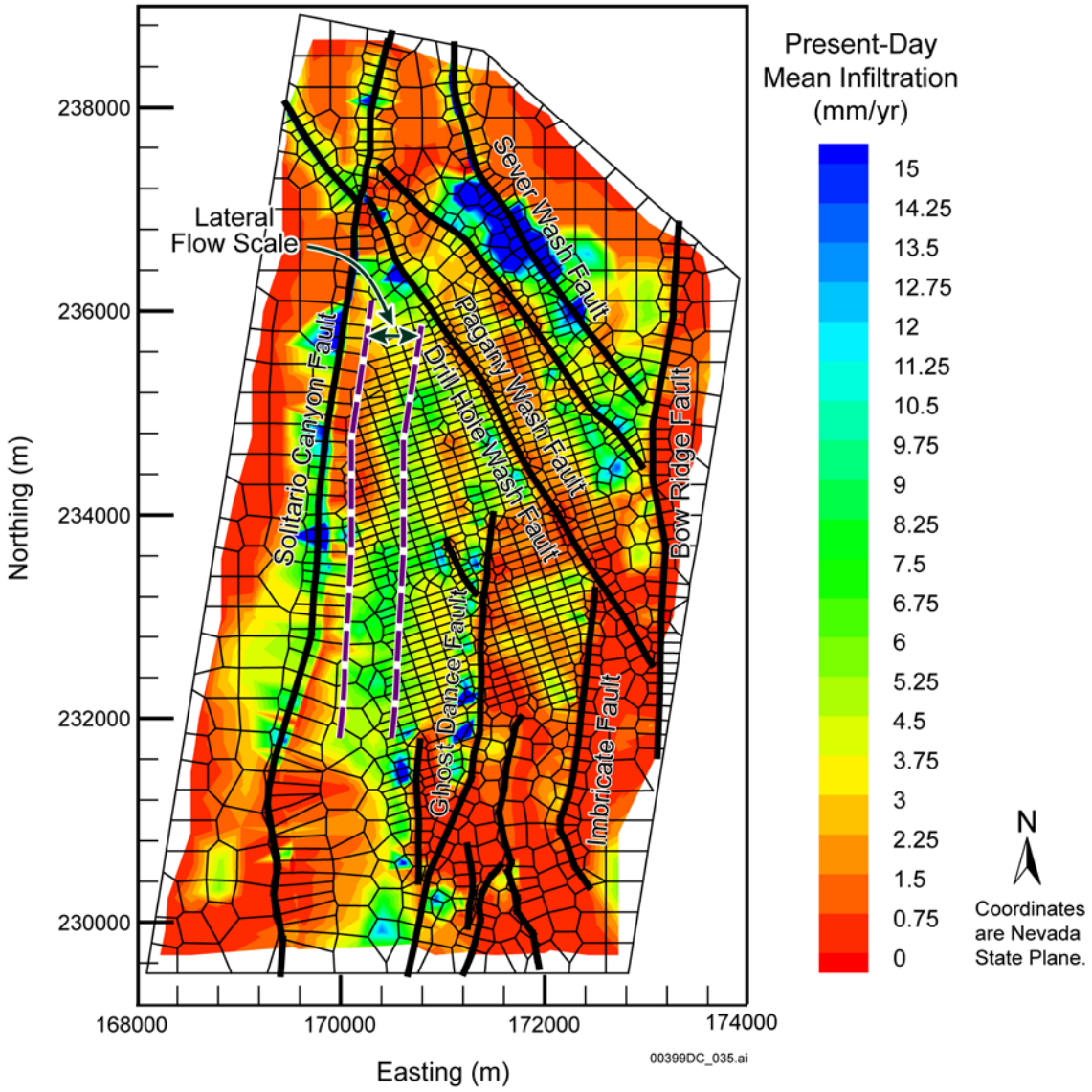

Source: BSC 2004, Figure 6.6-1.

Figure 4-20. Simulated Percolation Fluxes at the Repository Horizon under Present-Day, Mean Infiltration (preq_mA)

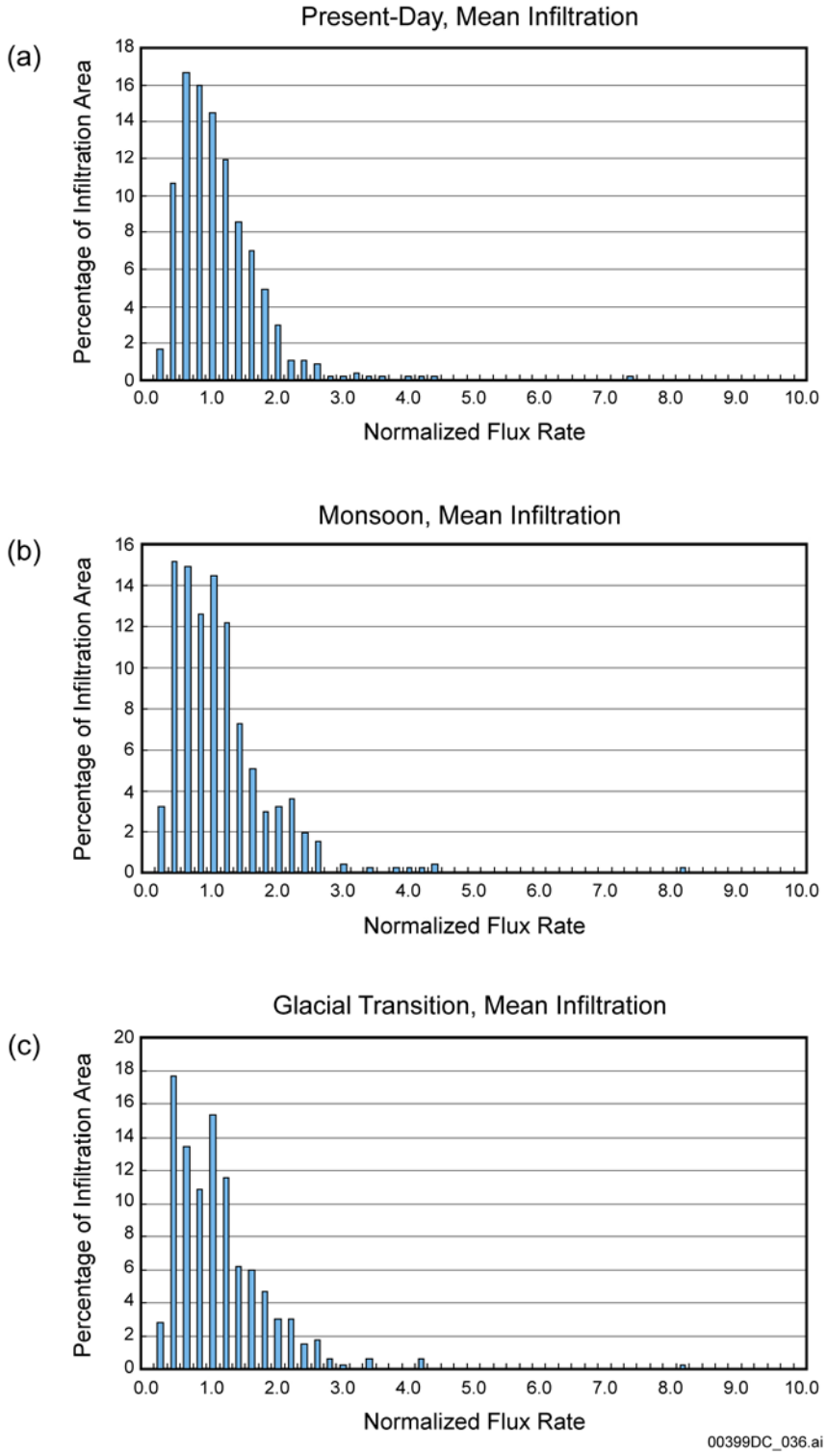

Source: BSC 2004, Figure 6.6-22.

Figure 4-21. Areal Frequency and Distribution of Simulated Percolation Fluxes within the Repository Domain Normalized to the Three Mean Infiltration Rates: Present-Day (a); Monsoon (b); and Glacial Transition (c)

Table 4-2 lists percentages of fracture–matrix flow components and fault flow at the repository horizon and the water table within the model domain for simulations with lateral flow in the PTn. Similar results are also obtained for simulations without lateral flow in the PTn. Table 4-2 contains two types of partition information: the partitioning between fault and nonfault gridblocks, and the partitioning between fracture and matrix flow components. Both fault and nonfault blocks have fracture and matrix flow components in the model. The fault flow percentages in Table 4-2 represent total vertical flux through fault blocks. Fracture and matrix percentages sum to 100% for both fault and nonfault blocks. These statistics indicate that fracture flow is dominant both at the repository horizon and at the water table. At the repository level, fracture flow consists of more than 90% to 95% of the total percolation fluxes. Fracture flow at the water table takes 70% to 80% of the total flow. On the other hand, fault flow percentage increases from about 30% to 40% at the repository to about 60% at the water table, except for the case of the present-day, lower-bound infiltration.

Table 4-2. Comparison of the Water Flux Through Matrix, Fractures, and Faults as a Percentage of the Total Flux at Two Different Horizons at the Repository and at the Water Table for the Nine Base-Case Flow Fields

Simulation Designation	Flux at Repository Horizon (%)			Flux at Water Table (%)		
	Fracture	Matrix	Fault	Fracture	Matrix	Fault
preq_lA	91.35	8.65	58.78	78.05	21.95	71.78
preq_mA	94.29	5.71	28.62	70.29	29.71	53.73
preq_uA	94.02	5.98	27.41	77.72	22.28	60.68
monq_lA	93.46	6.54	31.89	71.37	28.63	66.54
monq_mA	94.57	5.43	26.83	72.33	27.67	61.06
monq_uA	94.34	5.66	26.04	78.86	21.14	64.25
glaq_lA	92.11	7.89	36.71	70.37	29.63	65.40
glaq_mA	94.58	5.42	24.27	70.34	29.66	61.57
glaq_uA	94.53	5.47	23.81	76.44	23.56	65.37

Source: BSC 2004, Table 6.6-3.

Note that for a given climate, different simulation scenarios for TSPA are used to capture (or bound) uncertainties in the model results for unsaturated zone flow. These uncertainties result from the following:

1. Uncertainties in infiltration rates contribute to model uncertainties because unsaturated zone flow patterns are largely determined by infiltration rates and their spatial and temporal distributions. As indicated in Section 4.2, these uncertainties are captured by considering different infiltration scenarios.

2. Another source of model uncertainties is uncertainty in the conceptual model for unsaturated zone flow described in Section 3. Although this conceptual model has been supported by many field observations, some conceptual aspects of unsaturated zone flow related to focused flow at a smaller scale are not well understood. Effects of flow focusing on seepage into drifts are discussed in *Abstraction of Drift Seepage* (BSC 2003f, Section 6.6.4).

3. Unsaturated zone flow model is based on the continuum approach that conceptualizes a fracture network as a continuum, as discussed in Section 4.2.2. While the continuum approach is a practically reasonable approach for dealing with a large-scale, average unsaturated zone flow process, and generally supported by the previous studies (Section 4.2.2), it is uncertain that it is applicable for capturing effects of highly localized (or focused), subgrid-scale flow paths.

4. As discussed in Section 4.2.2, unsaturated zone flow models use van Genuchten (1980) relationships developed especially for porous media for describing unsaturated flow in fractures; these relationships have been questioned. Liu and Bodvarsson (2001) reported that van Genuchten (1980) relationships underestimate fracture relative permeability for a large range of relatively high water saturations and argued that an improved relationship model is needed for fractures to address this type of fundamental uncertainty.

5. As discussed in Section 4.2.2, the unsaturated zone flow models use the active fracture model to deal with fingering flow and transport in unsaturated fractures. The active fracture model is consistent with many field observations and theoretically related to fractal flow patterns often observed in unsaturated systems (Section 4.2.2). Considering the complexity of unsaturated flow in fractures at different scales, the tests for active fracture model validation require that detailed fracture–matrix interactions, partitioning of fracture flows from matrix flows, and water balances be taken into account (BSC 2003g, Sections 6.7 and 7).

6. Thermal effects on site-scale unsaturated zone flow discussed in Section 4.4 are not considered in simulation results for TSPA, because these effects may not be significant for far-field water flow. (The thermal effects on seepage have been studied in *Drift-Scale Coupled Processes (DST and TH Seepage) Models* (BSC 2003i).)

7. In the site-scale unsaturated zone flow model, a geology-based deterministic approach, in which an entire model layer is assigned uniform properties, is used for representing subsurface heterogeneity. This introduces a certain degree of uncertainty into modeling results by ignoring the small-scale heterogeneity, although this uncertainty may be minor for site-scale model results (Section 4.1.2).

5. SUMMARY

The Yucca Mountain unsaturated zone serves as an important natural barrier to radionuclide transport from the repository to the water table. This technical basis document briefly discusses a variety of issues related to flow paths within the unsaturated zone. The KTIs related to the unsaturated zone flow paths, and the responses to them, are documented in detail within the appendices of this report. The unsaturated zone flow model developed for Yucca Mountain has been calibrated and validated; moreover, the conceptual understanding of flow paths within the unsaturated zone has been corroborated with field observations.

5.1 GEOLOGIC SETTING AND DATA COLLECTION

The geologic setting and data collection activities related to unsaturated zone flow processes are reviewed (Section 2). The subsurface formations in the unsaturated zone consist of heterogeneous layers of fractured volcanic rock and are characterized by different degrees of welding, faulting, hydrothermal alteration, and formation of lithophysal cavities. The subsurface heterogeneity has important effects on flow paths in the unsaturated zone and is largely determined by the corresponding geologic setting. Based on the degree of welding and hydrologic property distributions, the unsaturated zone formations have been divided into several hydrologic units including TCw, PTn, TSw, CHn, and CFu. The geologic setting is used for developing numerical grids and property spatial distributions in the unsaturated zone flow models.

In the past two decades, a significant amount of data, including geologic, hydrologic, and geochemical data, and including data from in situ field tests, has been collected from the Yucca Mountain site. A brief review of these data is provided in Section 2. These data have been used for formulating, calibrating, and validating unsaturated zone flow models. However, data related to water flow in faults (especially below the repository) are relatively limited at this stage, considering that faults may serve as important flow paths in the unsaturated zone.

5.2 CONCEPTUAL UNDERSTANDING OF UNSATURATED ZONE FLOW

This document also presents a conceptual understanding of flow paths in the unsaturated zone (Section 3), largely based on a variety of field observations and modeling studies. Because of the attenuation effects of the PTn unit, percolation processes below this unit are approximately in steady state under ambient conditions. Fracture liquid water flow is dominant in the welded units and matrix flow in nonwelded units. Only a small portion of fractures actively conducts liquid water in the unsaturated zone. Isolated, transient, and fast flow paths may exist, but carry only a small amount of water. Fracture–matrix interaction in the welded units is limited. The existence of perched water bodies introduces three-dimensional lateral flow within the unsaturated zone. Below the repository, flow occurs mainly in the matrix within the vitric CHn, with some amount of lateral flow in the matrix contributing to the major faults in the mountain. The faults then serve as vertical focused flow paths toward the water table. This conceptual understanding has been used for developing the site-scale unsaturated zone flow model.

5.3 DEVELOPMENT OF THE SITE-SCALE UNSATURATED ZONE FLOW MODEL

The site-scale unsaturated zone flow model has been developed, calibrated and validation conducted based on the geology of the site, conceptual understanding of flow paths within the unsaturated zone, and field observations (Section 4). It is a three-dimensional dual-permeability model. A variety of data (including matrix saturation and water potential data, pneumatic data, perched water data, temperature data and geochemical data) has been used for calibrating the model. The model validation has also been conducted against substantial field data not used for model calibration. These validation activities include checking for consistency between modeling results with hydrologic data, geochemical data, and data collected from in situ tests. Effects of thermal processes and the resultant coupled processes on unsaturated zone flow are also discussed.

The site-scale unsaturated zone flow model is used for generating unsaturated zone flow fields used directly by TSPA.

5.4 MODEL UNCERTAINTIES

Because of the data limitation and complexity of unsaturated zone flow, the unsaturated zone flow models and their results are subject to uncertainties. These model uncertainties are related to infiltration rates, conceptual model of water flow, the continuum approach, the van Genuchten (1980) relationships for fractures, the active fracture model, effects of thermal processes, and small-scale heterogeneities within a model layer. A discussion of these model uncertainties and their treatment within the context of TSPA is provided in Section 4.5.

6. REFERENCES

Abdel-Salam, A. and Chrysikopoulos, C.V. 1996. "Unsaturated Flow in a Quasi-Three-Dimensional Fractured Medium with Spatially Variable Aperture." *Water Resources Research, 32*, (6), 1531-1540. Washington, D.C.: American Geophysical Union. TIC: 239861.

Bear, J.; Tsang, C.F.; and de Marsily, G., eds. 1993. *Flow and Contaminant Transport in Fractured Rock.* San Diego, California: Academic Press. TIC: 235461.

Birkholzer, J.; Li, G.; Tsang, C-F.; and Tsang, Y. 1999. "Modeling Studies and Analysis of Seepage into Drifts at Yucca Mountain." Journal of Contaminant Hydrology, 38, (1-3), 349-384. New York, New York: Elsevier. TIC: 244160.

Bodvarsson, G.S.; Boyle, W.; Patterson, R.; and Williams, D. 1999. "Overview of Scientific Investigations at Yucca Mountain—The Potential Repository for High-Level Nuclear Waste." *Journal of Contaminant Hydrology, 38*, (1-3), 3-24. New York, New York: Elsevier. TIC: 244160.

Bodvarsson, G.S.; Wu, Y-S.; and Zhang, K. 2003. "Development of Discrete Flow Paths in Unsaturated Fractures at Yucca Mountain." Journal of Contaminant Hydrology, 62-63, 23-42. New York, New York: Elsevier. TIC: 254205.

BSC (Bechtel SAIC Company) 2001. *Unsaturated Zone Flow Patterns and Analysis.* MDL-NBS-HS-000012 REV 00. Las Vegas, Nevada: Bechtel SAIC Company. ACC: MOL.20011029.0315.

BSC 2002a. *Geologic Framework Model (GFM2000).* MDL-NBS-GS-000002 REV 01. Las Vegas, Nevada: Bechtel SAIC Company. ACC: MOL.20020530.0078.

BSC 2002b. *Analysis of Geochemical Data for the Unsaturated Zone*. ANL-NBS-HS-000017 REV 00, ICN 02. Las Vegas, Nevada: Bechtel SAIC Company. ACC: MOL.20020314.0051.

BSC 2002c. *Thermal Testing Measurements Report*. ANL-NBS-HS-000041 REV 00. Las Vegas, Nevada: Bechtel SAIC Company. ACC: MOL.20021004.0314.

BSC 2002d. *Technical Work Plan for: Performance Assessment Unsaturated Zone.* TWP-NBS-HS-000003 REV 02. Las Vegas, Nevada: Bechtel SAIC Company. ACC: MOL.20030102.0108.

BSC 2003a. *In Situ Field Testing of Processes.* ANL-NBS-HS-000005 REV02. Las Vegas, Nevada: Bechtel SAIC Company. ACC: DOC.20031208.0001.

BSC 2003b. *Calibrated Properties Model*. MDL-NBS-HS-000003 REV 01. Las Vegas, Nevada: Bechtel SAIC Company. ACC: DOC.20030219.0001.

BSC 2003c. *Development of Numerical Grids for UZ Flow and Transport Modeling*. ANL-NBS-HS-000015 REV 01. Las Vegas, Nevada: Bechtel SAIC Company. ACC: DOC.20030404.0005.

BSC 2003d. *Radionuclide Transport Models Under Ambient Conditions.* MDL-NBS-HS-000008 REV 01. Las Vegas, Nevada: Bechtel SAIC Company. ACC: DOC.20031201.0002.

BSC 2003e. *Mountain-Scale Coupled Processes (TH/THC/THM).* MDL-NBS-HS-000007 REV 01. Las Vegas, Nevada: Bechtel SAIC Company. ACC: DOC.20031216.0003.

BSC 2003f. *Abstraction of Drift Seepage*. MDL-NBS-HS-000019 REV 00. Las Vegas, Nevada: Bechtel SAIC Company. ACC: DOC.20030826.0001.

BSC 2003g. *Analysis of Hydrologic Properties Data*. MDL-NBS-HS-000014 REV 00. Las Vegas, Nevada: Bechtel SAIC Company. ACC: DOC.20030404.0004.

BSC 2003h. *Analysis of Hydrologic Properties Data*. ANL-NBS-HS-000002 REV 00, ICN 01. Las Vegas, Nevada: Bechtel SAIC Company. ACC: MOL.20020429.0296.

BSC 2003i. *Drift-Scale Coupled Processes (DST and TH Seepage) Models.* MDL-NBS-HS-000015 REV 00C. Las Vegas, Nevada: Bechtel SAIC Company. ACC: MOL.20030910.0160.

BSC 2004. *UZ Flow Models and Submodels*. MDL-NBS-HS-000006 REV 01. Las Vegas, Nevada: Bechtel SAIC Company. ACC: DOC.20030818.0002; DOC.20040211.0008.

CRWMS M&O (Civilian Radioactive Waste Management System Management and Operating Contractor) 2000a. *Yucca Mountain Site Description.* TDR-CRW-GS-000001 REV 01 ICN 01. Las Vegas, Nevada: CRWMS M&O. ACC: MOL.20001003.0111.

CRWMS M&O 2000b. *Unsaturated Zone Flow and Transport Model Process Model Report.* TDR-NBS-HS-000002 REV 00, ICN 02. Las Vegas, Nevada: CRWMS M&O. ACC: MOL.20000831.0280.

CRWMS M&O 2000c. *Conceptual and Numerical Models for UZ Flow and Transport*. MDL-NBS-HS-000005 REV 00. Las Vegas, Nevada: CRWMS M&O. ACC: MOL.19990721.0526.

CRWMS M&O 2001. *Unsaturated Zone and Saturated Zone Transport Properties (U0100).* ANL-NBS-HS-000019 REV 00, ICN 1. Las Vegas, Nevada: CRWMS M&O. ACC: MOL.20010201.0026.

Doughty, C. 1999. "Investigation of Conceptual and Numerical Approaches for Evaluating Moisture, Gas, Chemical, and Heat Transport in Fractured Unsaturated Rock." *Journal of Contaminant Hydrology, 38*, (1-3), 69-106. New York, New York: Elsevier. TIC: 244160.

Fabryka-Martin, J.T.; Turin, H.J.; Wolfsberg, A.V.; Brenner, D.L.; Dixon, P.R.; and Musgrave, J.A. 1998. *Summary Report of Chlorine-36 Studies as of August 1996.* LA-13458-MS. Los Alamos, New Mexico: Los Alamos National Laboratory. ACC: MOL.20031119.0395.

Fabryka-Martin, J.; Wolfsberg, A.V.; Dixon, P.R.; Levy, S.S.; Musgrave, J.A.; and Turin, H.J. 1996. *Summary Report of Chlorine-36 Studies: Sampling, Analysis and Simulation of Chlorine-36 in the Exploratory Studies Facility.* Milestone 3783M. Los Alamos, New Mexico: Los Alamos National Laboratory. ACC: MOL.19970103.0047.

Fabryka-Martin, J.T.; Wolfsberg, A.V.; Dixon, P.R.; Levy, S.S.; Musgrave, J.A.; and Turin, H.J. 1997. *Summary Report of Chlorine-36 Studies: Sampling, Analysis, and Simulation of Chlorine-36 in the Exploratory Studies Facility.* LA-13352-MS. Los Alamos, New Mexico: Los Alamos National Laboratory. ACC: MOL.19980812.0254.

Finsterle, S. 2000. "Using the Continuum Approach to Model Unsaturated Flow in Fractured Rock." *Water Resources Research, 36*, (8), 2055-2066. Washington, D.C.: American Geophysical Union. TIC: 248769.

Flint, L.E. 1998. "Characterization of Hydrogeologic Units Using Matrix Properties, Yucca Mountain, Nevada." *Water-Resources Investigations Report 97-4243.* Denver, Colorado: U.S. Geological Survey. ACC: MOL.19980429.0512.

Glass, R.J.; Nicholl, M.J.; and Tidwell, V.C. 1996. *Challenging and Improving Conceptual Models for Isothermal Flow in Unsaturated, Fractured Rock Through Exploration of Small-Scale Processes*. SAND95-1824. Albuquerque, New Mexico: Sandia National Laboratories. ACC: MOL.19970520.0082.

Ho, C.K. 1997. "Models of Fracture-Matrix Interactions During Multiphase Heat and Mass Flow in Unsaturated Fractured Porous Media." *Proceedings of the ASME Fluids Engineering Division, November 16–21, 1997, Dallas, Texas. FED-Vol. 244*. Pages 401-412. New York, New York: American Society of Mechanical Engineers. TIC: 241082.

Kwicklis, E.M. and Healy, R.W. 1993. "Numerical Investigation of Steady Liquid Water Flow in a Variably Saturated Fracture Network." *Water Resources Research, 29*, (12), 4091-4102. Washington, D.C.: American Geophysical Union. TIC: 226993.

LeCain, G.D.; Anna, L.O.; and Fahy, M.F. 2000. *Results from Geothermal Logging, Air and Core-Water Chemistry Sampling, Air-Injection Testing, and Tracer Testing in the Northern Ghost Dance Fault, Yucca Mountain, Nevada, November 1996 to August 1998*. Water-Resources Investigations Report 99-4210. Denver, Colorado: U.S. Geological Survey. TIC: 247708.

Levy, S.; Chipera, S.; WoldeGabriel, G.; Fabryka-Martin, J.; Roach, J.; and Sweetkind, D. 1999. "Flow-Path Textures and Mineralogy in Tuffs of the Unsaturated Zone." *Faults and Subsurface Fluid Flow in the Shallow Crust.* Geophysical Monograph 113. 159–183. [Washington, D.C.]: American Geophysical Union. TIC: 254128.

Liu, H.H. and Bodvarsson, G.S. 2001. "Constitutive Relations for Unsaturated Flow in a Fracture Network." *Journal of Hydrology, 252*, (1-4), 116-125. New York, New York: Elsevier. TIC: 253269.

Liu, H.H.; Bodvarsson, G.S.; and Finsterle, S. 2002. "A Note on Unsaturated Flow in Two-Dimensional Fracture Networks." *Water Resources Research, 38*, (9), 15-1 to 15-9. Washington, D.C.: American Geophysical Union. TIC: 253307.

Liu, H.H.; Doughty, C.; and Bodvarsson, G.S. 1998. "An Active Fracture Model for Unsaturated Flow and Transport in Fractured Rocks." *Water Resources Research, 34*, (10), 2633-2646. Washington, D.C.: American Geophysical Union. TIC: 243012.

Liu, H-H.; Haukwa, C.B.; Ahlers, C.F.; Bodvarsson, G.S.; Flint, A.L.; and Guertal, W.B. 2003. "Modeling Flow and Transport in Unsaturated Fractured Rock: An Evaluation of the Continuum Approach." *Journal of Contaminant Hydrology, 62-63,* 173-188. New York, New York: Elsevier. TIC: 254205.

Montazer, P. and Wilson, W.E. 1984. *Conceptual Hydrologic Model of Flow in the Unsaturated Zone, Yucca Mountain, Nevada*. Water-Resources Investigations Report 84-4345. Lakewood, Colorado: U.S. Geological Survey. ACC: NNA.19890327.0051.

National Research Council. 1996. *Rock Fractures and Fluid Flow, Contemporary Understanding and Applications*. Washington, D.C.: National Academy Press. TIC: 235913.

Nativ, R.; Adar, E.; Dahan, O.; and Geyh, M. 1995. "Water Recharge and Solute Transport Through the Vadose Zone of Fractured Chalk Under Desert Conditions." *Water Resources Research, 31*, (2), 253-261. Washington, D.C.: American Geophysical Union. TIC: 233563.

Neuman, S.P. 1994. "Generalized Scaling of Permeabilities: Validation and Effect of Support Scale." *Geophysical Research Letters, 21*, (5), 349-352. Washington, D.C.: American Geophysical Union. TIC: 240142.

Neymark, L.A.; Amelin, Y.; Paces, J.B.; and Peterman, Z.E. 2002. "U-Pb Ages of Secondary Silica at Yucca Mountain, Nevada: Implications for the Paleohydrology of the Unsaturated Zone." *Applied Geochemistry, 17,* ([6]), 709–734. New York, New York: Elsevier. TIC: 252598.

Nicholl, M.J.; Glass, R.J.; and Wheatcraft, S.W. 1994. "Gravity-Driven Infiltration Instability in Initially Dry Nonhorizontal Fractures." *Water Resources Research, 30*, (9), 2533-2546. Washington, D.C.: American Geophysical Union. TIC: 243493.

Paces, J.B.; Neymark, L.A.; Marshall, B.D.; Whelan, J.F.; and Peterman, Z.E. 1998. "Inferences for Yucca Mountain Unsaturated-Zone Hydrology from Secondary Minerals." *High-Level Radioactive Waste Management, Proceedings of the Eighth International Conference, Las Vegas, Nevada, May 11-14, 1998*. Pages 36-39. La Grange Park, Illinois: American Nuclear Society. TIC: 237082.

Philip, J.R.; Knight, J.H.; and Waechter, R.T. 1989. "Unsaturated Seepage and Subterranean Holes: Conspectus, and Exclusion Problem for Circular Cylindrical Cavities." Water Resources Research, 25, (1), 16-28. Washington, D.C.: American Geophysical Union. TIC: 239117.

Pruess, K.; Faybishenko, B.; and Bodvarsson, G.S. 1999. "Alternative Concepts and Approaches for Modeling Flow and Transport in Thick Unsaturated Zones of Fractured Rocks." *Journal of Contaminant Hydrology, 38*, (1-3), 281-322. New York, New York: Elsevier. TIC: 244160.

Rousseau, J.P.; Kwicklis, E.M.; and Gillies, D.C., eds. 1999. *Hydrogeology of the Unsaturated Zone, North Ramp Area of the Exploratory Studies Facility, Yucca Mountain, Nevad*a. Water-Resources Investigations Report 98-4050. Denver, Colorado: U.S. Geological Survey. ACC: MOL.19990419.0335.

Rousseau, J.P.; Loskot, C.L.; Thamir, F.; and Lu, N. 1997. *Results of Borehole Monitoring in the Unsaturated Zone Within the Main Drift Area of the Exploratory Studies Facility, Yucca Mountain, Nevada*. Milestone SPH22M3. Denver, Colorado: U.S. Geological Survey. ACC: MOL.19970626.0351.

Salve, R.; Oldenburg, C.M.; and Wang, J.S.Y. 2003. "Fault-Matrix Interactions in Nonwelded Tuff of the Paintbrush Group at Yucca Mountain." *Journal of Contaminant Hydrology, 62-63*, 269-286. New York, New York: Elsevier. TIC: 254205.

Sass, J.H.; Lachenbruch, A.H.; Dudley, W.W., Jr.; Priest, S.S.; and Munroe, R.J. 1988. *Temperature, Thermal Conductivity, and Heat Flow Near Yucca Mountain, Nevada: Some Tectonic and Hydrologic Implications*. Open-File Report 87-649. [Denver, Colorado]: U.S. Geological Survey. TIC: 203195.

Sharp, J.M., Jr.; Kreisel, I.; Milliken, K.L.; Mace, R.E.; and Robinson, N.I. 1996. "Fracture Skin Properties and Effects on Solute Transport: Geotechnical and Environmental Implications." *Rock Mechanics, Tools and Techniques, Proceedings of the 2nd North American Rock Mechanics Symposium, NARMS '96, A Regional Conference of ISRM, Montreal, Quebec, Canada, 19-21 June 1996*. Aubertin, M.; Hassani, F.; and Mitri, H., eds. 2, 1329-1335. Brookfield, Vermont: A.A. Balkema. TIC: 239941.

Sharpe, S. 2003. Future Climate Analysis—10,000 Years to 1,000,000 Years After Present. MOD-01-001 REV 01. Reno, Nevada: Desert Research Institute. ACC: MOL.20030407.0055.

Simmons, A.M. 2004. *Yucca Mountain Site Description.* TDR-CRW-GS-000001 REV 02. Two volumes. Las Vegas, Nevada: Bechtel SAIC Company. ACC: DOC.20040120.0004.

Thoma, S.G.; Gallegos, D.P.; and Smith, D.M. 1992. "Impact of Fracture Coatings on Fracture/Matrix Flow Interactions in Unsaturated, Porous Media." *Water Resources Research, 28*, (5), 1357-1367. Washington, D.C.: American Geophysical Union. TIC: 237509.

Thordarson, W. 1965. *Perched Ground Water in Zeolitized-Bedded Tuff, Rainier Mesa and Vicinity, Nevada Test Site, Nevada*. TEI-862. Washington, D.C.: U.S. Geological Survey. ACC: NN1.19881021.0066.

van Genuchten, M.T. 1980. "A Closed-Form Equation for Predicting the Hydraulic Conductivity of Unsaturated Soils." *Soil Science Society of America Journal, 44*, (5), 892-898. Madison, Wisconsin: Soil Science Society of America. TIC: 217327.

Wang, J.S.Y. and Narasimhan, T.N. 1993. "Unsaturated Flow in Fractured Porous Media." Chapter 7 of *Flow and Contaminant Transport in Fractured Rock*. Bear, J.; Tsang, C-F.; and de Marsily, G., eds. San Diego, California: Academic Press. TIC: 235461.

Wu, Y-S.; Zhang, W.; Pan, L.; Hinds, J.; and Bodvarsson, G.S. 2000. *Capillary Barriers in Unsaturated Fractured Rocks of Yucca Mountain, Nevada*. LBNL-46876. Berkeley, California: Lawrence Berkeley National Laboratory. TIC: 249912.

Wu, Y-S.; Zhang, W.; Pan, L.; Hinds, J.; and Bodvarsson, G.S. 2002. "Modeling Capillary Barriers in Unsaturated Fractured Rock." *Water Resources Research, 38*, (11), 35-1 through 35-12. Washington, D.C.: American Geophysical Union. TIC: 253854.

Yang, I.C. 2002. "Percolation Flux and Transport Velocity in the Unsaturated Zone, Yucca Mountain, Nevada." *Applied Geochemistry, 17*, (6), 807-817. [New York, New York]: Elsevier. TIC: 253605.

Yang, I.C.; Rattray, G.W.; and Yu, P. 1996. *Interpretation of Chemical and Isotopic Data from Boreholes in the Unsaturated Zone at Yucca Mountain, Nevada*. Water-Resources Investigations Report 96-4058. Denver, Colorado: U.S. Geological Survey. ACC: MOL.19980528.0216.

Zhou, Q.; Liu, H-H.; Bodvarsson, G.S.; and Oldenburg, C.M. 2003. "Flow and Transport in Unsaturated Fractured Rock: Effects of Multiscale Heterogeneity of Hydrogeologic Properties." *Journal of Contaminant Hydrology, 60*, (1-2), 1-30. New York, New York: Elsevier. TIC: 253978.

APPENDIX A

FLOW IN THE CALICO HILLS NONWELDED VITRIC UNIT (RESPONSE TO RT 1.01 AND GEN 1.01 (COMMENT 26))

Note Regarding the Status of Supporting Technical Information

This document was prepared using the most current information available at the time of its development. This Technical Basis Document and its appendices providing Key Technical Issue Agreement responses that were prepared using preliminary or draft information reflect the status of the Yucca Mountain Project's scientific and design bases at the time of submittal. In some cases this involved the use of draft Analysis and Model Reports (AMRs) and other draft references whose contents may change with time. Information that evolves through subsequent revisions of the AMRs and other references will be reflected in the License Application (LA) as the approved analyses of record at the time of LA submittal. Consequently, the Project will not routinely update either this Technical Basis Document or its Key Technical Issue Agreement appendices to reflect changes in the supporting references prior to submittal of the LA.

APPENDIX A

FLOW IN THE CALICO HILLS NONWELDED VITRIC UNIT (RESPONSE TO RT 1.01 AND GEN 1.01 (COMMENT 26))

This appendix provides a response for Key Technical Issue (KTI) agreement Radionuclide Transport (RT) 1.01. This agreement relates to providing additional information on the technical basis for the proportion of fracture flow through the Calico Hills nonwelded (CHn) vitric units.

A.1 KEY TECHNICAL ISSUE AGREEMENT

A.1.1 RT 1.01 and GEN 1.01 (Comment 26)

Agreement RT 1.01 was reached during the U.S. Nuclear Regulatory Commission (NRC)/U.S. Department of Energy (DOE) Technical Exchange and Management Meeting on Radionuclide Transport on December 5 to 7, 2000 (Reamer and Williams 2000), in Berkeley, California. RT subissue 1, radionuclide transport through porous rock, was discussed at that meeting.

At that meeting the NRC expressed concern that the C-Wells tests provide an example that suggests a portion of the flow path is not acting as a single-continuum porous medium (Reamer and Gil 2001). Specifically, the NRC staff indicated that although the Calico Hills nonwelded vitric (CHnv) unit was considered a porous medium, due to its matrix permeability that was considered high enough to accommodate the percolation rates expected for Yucca Mountain, the Calico Hills nonwelded zeolitic (CHnz) unit has a matrix permeability that may accommodate only a relatively small portion of the percolation rate, and, consequently, most of the water may bypass the zeolitic unit in fractures. The NRC also stated that it remained to be demonstrated that the Calico Hills nonwelded unit behaves as a single-continuum porous medium. In response, the DOE pointed out that the current models represent flow and transport through all unsaturated zone units using a dual-continuum approach. Most, but not all, of the flow and transport occurs through the matrix of the CHnv unit. In the CHnz, most, but not all, of the flow and transport is through fractures. The DOE agreed to provide the technical basis for the proportion of fracture flow through the CHnv unit.

General agreement (GEN) 1.01 was reached during the NRC/DOE Technical Exchange and Management Meeting on Range of Thermal Operating Temperatures, held September 18 to 19, 2001 (Reamer and Gil 2001). At that meeting, the NRC provided additional comments, resulting in GEN 1.01 (Comment 26), which relates to RT 1.10. The specific section or page number referral cited below as part of GEN 1.01 (Comment 26) is from *FY01 Supplemental Science and Performance Analyses, Volume 1: Scientific Bases and Analyses* (BSC 2001).

The wording of the agreement is as follows:

RT 1.01

> Provide the basis for the proportion of fracture flow through the Calico Hills non-welded vitric. DOE will revise the AMR UZ Flow Models and Submodels and the AMR Calibrated Properties Model to provide the technical basis for the

proportion of fracture flow through the Calico Hills Nonwelded Vitric. These reports will be available to the NRC in FY 2002. In addition, the field data description will be documented in the AMR In Situ Field Testing of Processes in FY 2002.

GEN 1.01 (Comment 26)

The MINC is asserted to be better than the DKM and to produce "relatively conservative results". This has not been supported in the SSPA, nor does the referenced AMR provide any more detailed comparison of the two numerical approaches. Furthermore, the referenced AMR (*Conceptual and Numerical Models for UZ Flow and Transport*) indicates that "the dual-continua approach is expected to give conservative predictions of radionuclide transport in the unsaturated zone."

The matrix saturation levels beneath the repository identified in Subsection 11.3.5 seem to be much lower than those discussed in Subsection 11.3.1 (Compare Figures 11.3.1-6 and 11.3.5-2).

DOE Initial Response to GEN 1.01 (Comment 26):

It has been found in UZ flow and transport modeling that DKM produces more conservative results in terms of radionuclide travel times to the water table, while MINC provides a more realistic representation of the UZ flow and transport system.

TSPA-SR employed the DKM approach, thus yielding a more conservative estimate of UZ performance. DOE acknowledges the need to reconcile the differences should MINC be chosen as the modeling approach to be used in a potential LA.

A.1.2 Related Key Technical Issue Agreements

KTI agreement RT 1.01 and GEN 1.01 (Comment 26) is related to RT 3.02, Total System Performance Assessment and Integration (TSPAI) 3.24, and GEN 1.01 (Comment 106). While RT 3.02, TSPAI 3.24, and GEN 1.01 (Comment 106) concern the general use of geochemical and hydrologic data in the calibration and validation of the unsaturated zone flow field for all hydrostratigraphic units below the repository, RT 1.01 and GEN 1.01 (Comment 26) are specifically related to the justification of the approach for modeling flow through the CHnv unit (i.e., dominant matrix flow). Responses to agreements RT 3.02, TSPAI 3.24, and GEN 1.01 (Comment 106) are provided in Appendix B.

A.2 RELEVANCE TO REPOSITORY PERFORMANCE

Flow and transport through the unsaturated zone plays an important part in the assessment of total system performance, as the unsaturated zone is one of the key natural barriers upon which the repository will rely. The CHn unit is a major hydrogeologic unit underneath the repository. Since fractures are the main pathways for radionuclide transport in the CHnv unit (BSC 2003a,

Section 6), the determination of the relative flow proportion through fractures of the CHnv is, therefore, important for unsaturated zone transport calculations.

A.3 RESPONSE

KTI agreement RT 1.01 and GEN 1.01 (Comment 26) relate to the documentation and basis for conceptualization and modeling of the CHn vitric units as a single-porosity matrix in the unsaturated zone flow model (BSC 2003b). In the vitric portions of the CHn units, most of the liquid flow occurs in the matrix, whereas in all other CHn layers liquid flow occurs predominantly in the fractures. The dominance of matrix flow results from relatively high matrix permeabilities and low fracture densities in the CHn nonwelded vitric layers (BSC 2003c, Section 6.1).

Correspondingly, the vitric layers in the CHn units are conceptualized and handled as a single-porosity matrix only in the unsaturated zone flow model. The effect of fractures on flow and transport within Calico Hills vitric zones is considered negligible and is not modeled (BSC 2003b).

The above conceptual model of matrix-only flow in the CHn vitric unit is supported by the small proportion of fracture flow and dominance of matrix flow, which was qualitatively substantiated by field observation results. Field evidence was obtained from the tracer tests in Busted Butte (BSC 2003d, Section 6.13) at the vitric layer in the upper CHn. Observation showed that flow took place in the matrix and that a preferential (fracture) flow did not develop along a fracture present in the area of the developed fluorescein plume (BSC 2003d, Section 6.13). A detailed description of the Busted Butte tracer test is given in Section A.4.3.

Corroborative evidence is found in field testing along a fault at the Exploratory Studies Facility (ESF) Alcove 4 in the Paintbrush nonwelded (PTn) hydrologic unit. The PTn unit has properties similar to the CHn vitric units. Both the PTn units and the CHn vitric units have relatively high matrix permeability and low degree of fracturing, with the former having lower matrix permeability and smaller fracture spacing than the latter. The field test at the ESF Alcove 4 also reveals that the PTn unit has a significant dampening effect on fracture flow because of matrix imbibition of water flowing along the fault (BSC 2003d, Section 6.7). The ESF Alcove 4 test is described in Section A.4.4.

The above field observation results obtained at the Busted Butte and Alcove 4 tests provide qualitative evidence to support the conceptual model of matrix-only flow in the CHn units.

GEN 1.01 (Comment 26) concerns the use of the multiple interacting continua (MINC) method modeling approach to be used in the generation of flow fields, as opposed to the dual-permeability method. In fact, the unsaturated zone flow model adopts the dual-continuum approach for flows through both the fractures and matrix (BSC 2003b, Section 6.1.2). Because the dual-continuum approach produces results on the conservative side due to faster breakthrough of radionuclides (BSC 2004, Figure 7-9, Section 7.2), the unsaturated zone flow model is considered to have yielded relatively conservative flow fields. The technical basis for this response to the GEN 1.01 comment is given in Section A.4.5. A brief summary of the basis

for the KTI responses is given in Section A.4.6. The technical basis for all the above responses is provided in Section A.4.

The information in this report is responsive to agreement RT 1.01 and GEN 1.01 (Comment 26) made between the DOE and NRC. This report contains the information that DOE considers necessary for NRC review for closure of these agreements.

A.4 BASIS FOR THE RESPONSE

In the unsaturated zone flow model, matrix and fracture flow in the fractured tuffs was modeled using the dual-permeability method. However, the vitric portions in the CHn units were conceptualized and modeled as a single-porosity matrix unit. This approach is supported by the observation from tracer testing at Busted Butte and is substantiated by corroborative results from field testing at the ESF Alcove 4 in PTn units, which have properties similar to the CHn vitric units.

The following is a brief introduction of the dual-permeability model, a description of the vitric layers, and discussion of the relevant results from the Busted Butte tracer test and the ESF Alcove 4 test.

A.4.1 Dual-Permeability Modeling Approach

The dual-permeability modeling approach (also called dual-continuum approach) was chosen here for describing flow and transport in the unsaturated zone. It considers global flow occurring not only between fractures but also between matrix gridblocks, as well as interflow between fractures and matrix. Using this approach, each gridblock of the primary mesh is divided into two connected gridblocks, one for fracture and the other for matrix.

There are alternative modeling approaches, specifically including the discrete fracture-network and MINC approaches. Discrete fracture-network approaches generally involve computational generation of synthetic fracture networks and subsequent modeling of flow and transport in each individual fracture.

The MINC model has multiple subgriddings in all the matrix gridblocks to obtain the resolution of the driving pressure, temperature, and mass fraction gradients at the fracture-matrix interface. The concept behind this model is based on the notion that, because of the presence of sinks and sources, changes in fluid pressure, temperature, phase composition, and so on propagate rapidly through the fracture system but only slowly invade the tight matrix blocks. Therefore, changes in matrix conditions will be controlled locally by the distance from the fractures (Pruess and Narasimhan 1985).

While these alternative approaches have their advantages, both are too technically impractical or computationally burdensome to be effectively large-scale models for this study. The discrete fracture-network approaches are appealing scientifically, conceptually, and technically but impractical for both computation and matching the fracture systems. Similarly, the MINC model may be slightly more accurate in describing fracture–matrix interaction but computationally challenging. The dual-permeability model is consistently more conservative. This greater

conservatism, added to its computational straightforwardness, lead to the choice of the dual-permeability modeling approach (BSC 2003c, Section 6.1).

A.4.2 Distribution of the Vitric Layers in Calico Hills Nonwelded Tuff Units

Field observation shows that hydrologic properties are heterogeneous in nature at different scales within both the fracture and matrix continua in the Yucca Mountain unsaturated zone (e.g., matrix-saturation distributions) (BSC 2003c, Section 6.1). A geologically based, deterministic approach is primarily used for characterizing subsurface heterogeneity in the unsaturated zone (BSC 2003c, Section 6.1). The heterogeneity of hydrologic properties is treated as a function of geologic layering, so that any one geologic layer has homogeneous properties (referred to as layer average properties) except where faulting or variable alteration (e.g., zeolitization) is present. In addition, this layering representation of hydrologic properties is based on the considerations that (1) the overall behavior of large-scale flow and transport processes are mainly determined by relatively large-scale heterogeneities associated with the geologic structures of the mountain and (2) the heterogeneity model needs to be consistent with the availability of data (BSC 2003c, Section 6.1).

The vitric layers generally have high porosity and permeability and a low degree of fracturing (Table A-1). Portions of the CHn unit and the lower part of the Topopah Spring welded (TSw) unit occur as vitric tuffs below the repository in unsaturated zone model layers tsw39, ch1, ch2, ch3, ch4, ch5, and ch6. They are located in the southwest portion of the model domain (BSC 2003e, Section 6.6.3). This vitric region is complementary to the zeolitized area. Their relation is qualitatively shown in Figure A-1 as an example for the zeolitic and vitric regions in the unsaturated zone model layer ch2. Zeolite data are of a corroborative nature. The low content of zeolite in the lower left region of the figure is not directly interpolated from actual zeolite data points in that area; rather, it comes as a direct extrapolation from several data points to the east (BSC 2003e, Section 6.6.3). The white area within the purple vitric zone corresponds to the Solitario Canyon fault zone. The multiple faults in the fault zone were simplified into a single structural feature (BSC 2003e, Section 5.2, Assumption 7) in the unsaturated zone flow model. The width of the fault zone is on the same scale as the coarse grid spacing in this area. Distribution of the vitric layers in the CHn is plotted in Figures A-2 and A-3.

Table A-1. Summary of Rock Properties of Selected Unsaturated Zone Model Layers

Units	Unsaturated Zone Model Layers	Porosity	Matrix Permeability (m^2)	Fracture Frequency (m^{-1})[a]
PTn	ptn21 to ptn26 (nonwelded tuff)	0.233 to 0.498	1.3×10^{-15} to 6.7×10^{-13}	0.46 to 0.97
TSw	tsw31 to tsw38 (welded tuff)	0.043 to 0.157	2.3×10^{-20} to 3.2×10^{-16}	0.81 to 4.36
	tsw39 (vitric tuff)	0.229	4.3×10^{-13} [b]	0.96
CHn	ch1 to ch6 (vitric tuff)	0.331 to 0.346	2.1×10^{-13} to 1.6×10^{-12} [b]	0.10 to 0.14

Source: BSC 2003c, Tables 3, 4, and 6.

NOTE: Data are compiled from the average value of each unsaturated zone model layer.
[a]Fracture frequency is the inverse of fracture spacing.
[b]The layer-averaged permeabilities of all the zeolitic layers are 5.2×10^{-18} to 3.5×10^{-17} (m^2).

The vitric and zeolitic regions within the bottom TSw unit and the CHn units are not effectively determined by the absence or presence of zeolite because of the lack of sufficient zeolite X-ray diffraction data. The boundaries of vitric and zeolitic regions were selected using the results of saturated permeability data (BSC 2003e, Assumption 4), measured rock-property data from boreholes within the unsaturated zone model area (BSC 2003e, Assumption 5), and the location of faults with significant vertical offset (BSC 2003e, Assumption 6, Section 6.6.3). Vitric tuff has a saturated permeability several orders of magnitude greater than that of zeolitic tuff; for both vitric tuff and zeolitic tuff (Table A-1), there is more saturated permeability data available than mineralogic alteration data (e.g., percentage of zeolite). Altered (i.e., zeolitic) nonwelded tuffs have characteristic hydrous secondary minerals, such as zeolites and clays. This fact results in higher estimates of the matrix porosity by the oven-dried method than those by the relative-humidity method, with oven-dried porosities being typically more than 5% higher than relative-humidity porosities. The huge offsets of the CHn layers by major faults (i.e., the Solitario Canyon and Dune Wash faults) have caused enough disparity in elevation and in environment for mineral alteration, with resulting contrasting degrees of zeolitization on different sides of the fault (BSC 2003e, Sections 5.2 and 6.6.3).

A.4.3 Busted Butte Unsaturated Zone Transport Test

Busted Butte provides a rare exposure of a distal extension of the Calico Hills Formation below Yucca Mountain, located 8 km southeast of the repository. The site was chosen based on the presence and similarity of these units to those beneath the repository horizon. The test facility consists of an underground excavation along a lithostratigraphic contact between Topopah Spring Tuff (Tpt) and Calico Hills Formation (Tac) (i.e., the contact between the TSw and CHn units). Specifically, the contact is made between the nonwelded portion of the basal vitrophyre of Tpt (Tptpv2 (tsw39 (vit)) and Tac (Tptpv1 (ch1 (vit)) (Figure A-4) (BSC 2003b, Table 6.1-1; BSC 2003d, Section 6.13.1.1).

Busted Butte nonwelded vitric layers are exposed around the contact of the Tpt and Tac. These vitric layers have relatively high matrix permeabilities and low fracture densities (Table A-1). The tracer test performed on these vitric layers provides evidence of matrix flow dominance, which is the basis for approximating them as single-porosity matrices.

The principal objectives of the test were to address uncertainties associated with unsaturated zone flow and transport models, including a study of the effect of heterogeneity in unsaturated and partially saturated conditions near the TSw–CHn contact, particularly issues relevant to fracture-matrix interactions and permeability contrast boundaries.

The unsaturated zone transport test site consists of a 75-m-long main adit and a 19-m-long alcove. The configuration of the unsaturated zone transport test site is shown in Figure A-4.

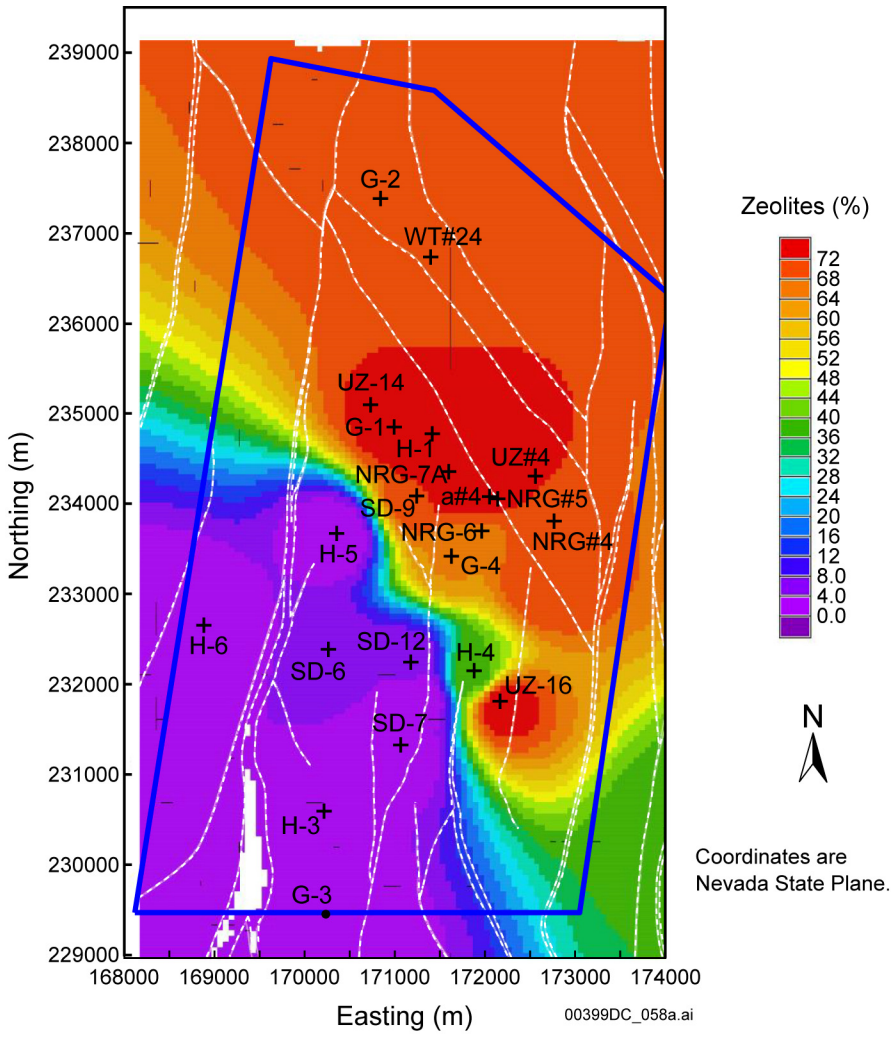

Source: BSC 2003e, Figure 5.

NOTE: The vitric region is denoted by purple. The white area within the purple region corresponds to the Solitario Canyon Fault zone. The thick blue line marks the unsaturated zone flow model domain boundary and white dash lines are traces of fault lines.

Figure A-1. Percent Zeolite Distribution of the Unsaturated Zone Model Layer ch2

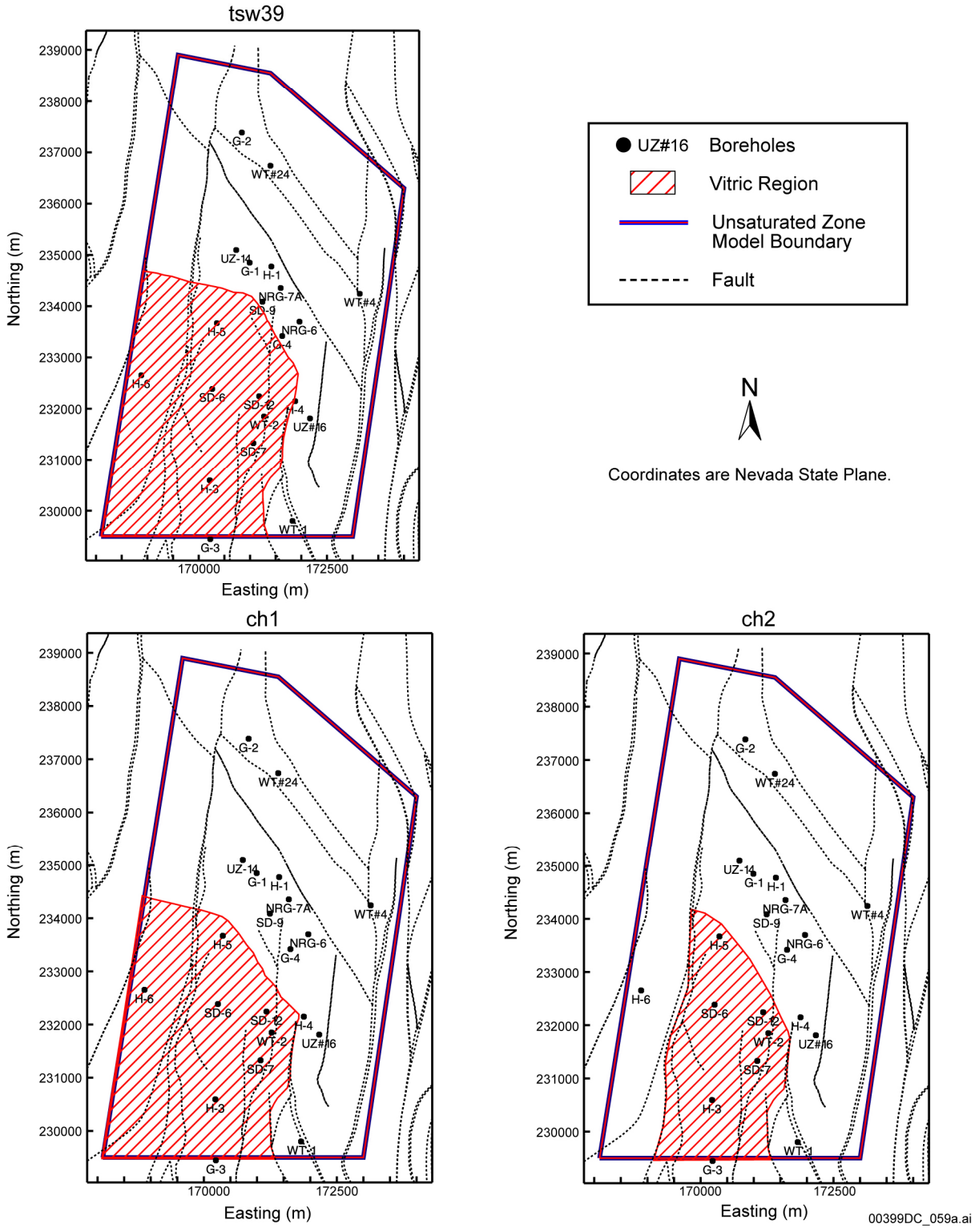

Source: BSC 2003e, Figure 6a.

Figure A-2. Extent of Vitric Region in Fiscal Year 2002 Unsaturated Zone Model Layers tsw39, ch1, and ch2

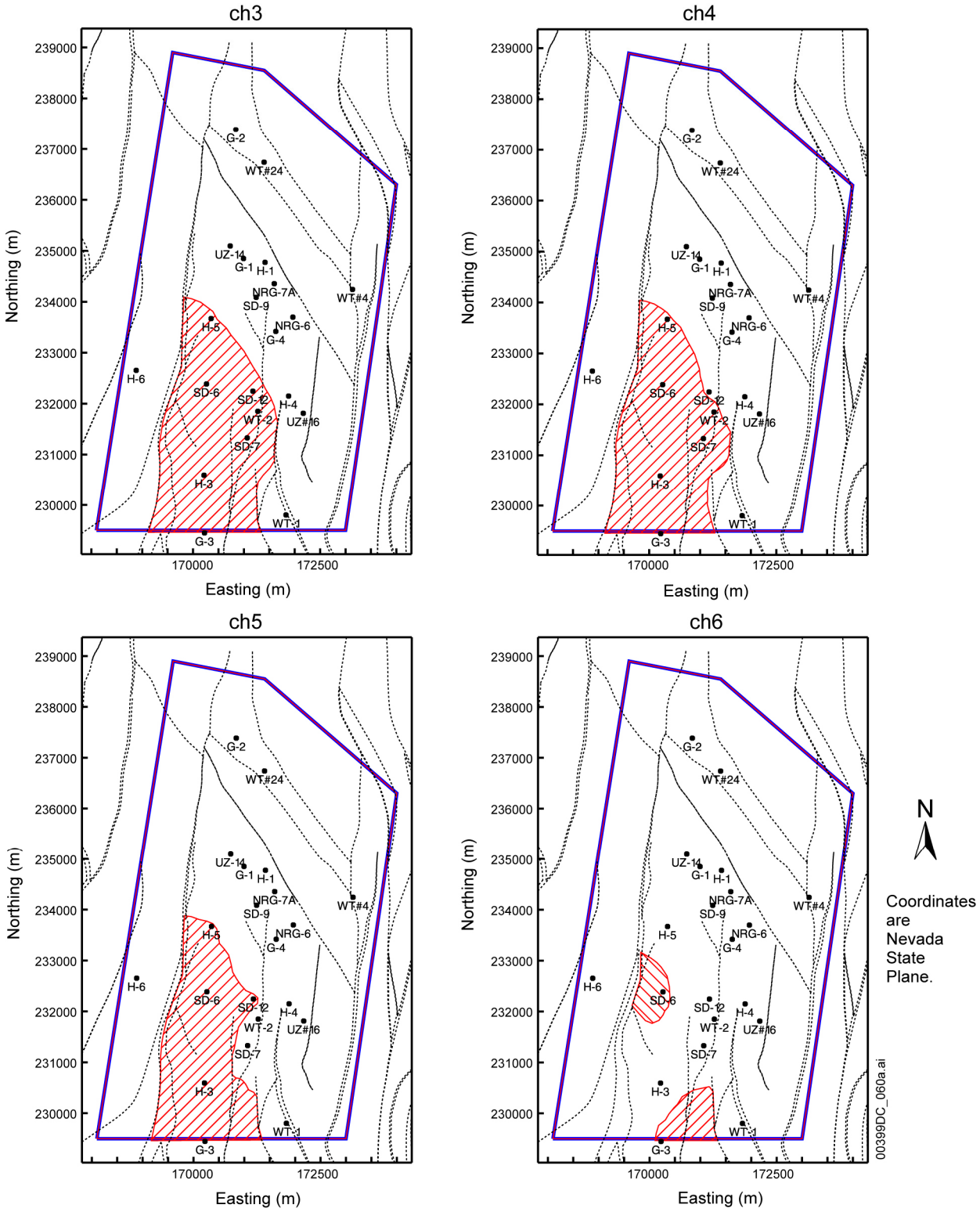

Source: BSC 2003e, Figure 6b.

Figure A-3. Extent of Vitric Region in Fiscal Year 2002 Unsaturated Zone Model Layers ch3, ch4, ch5 and ch6

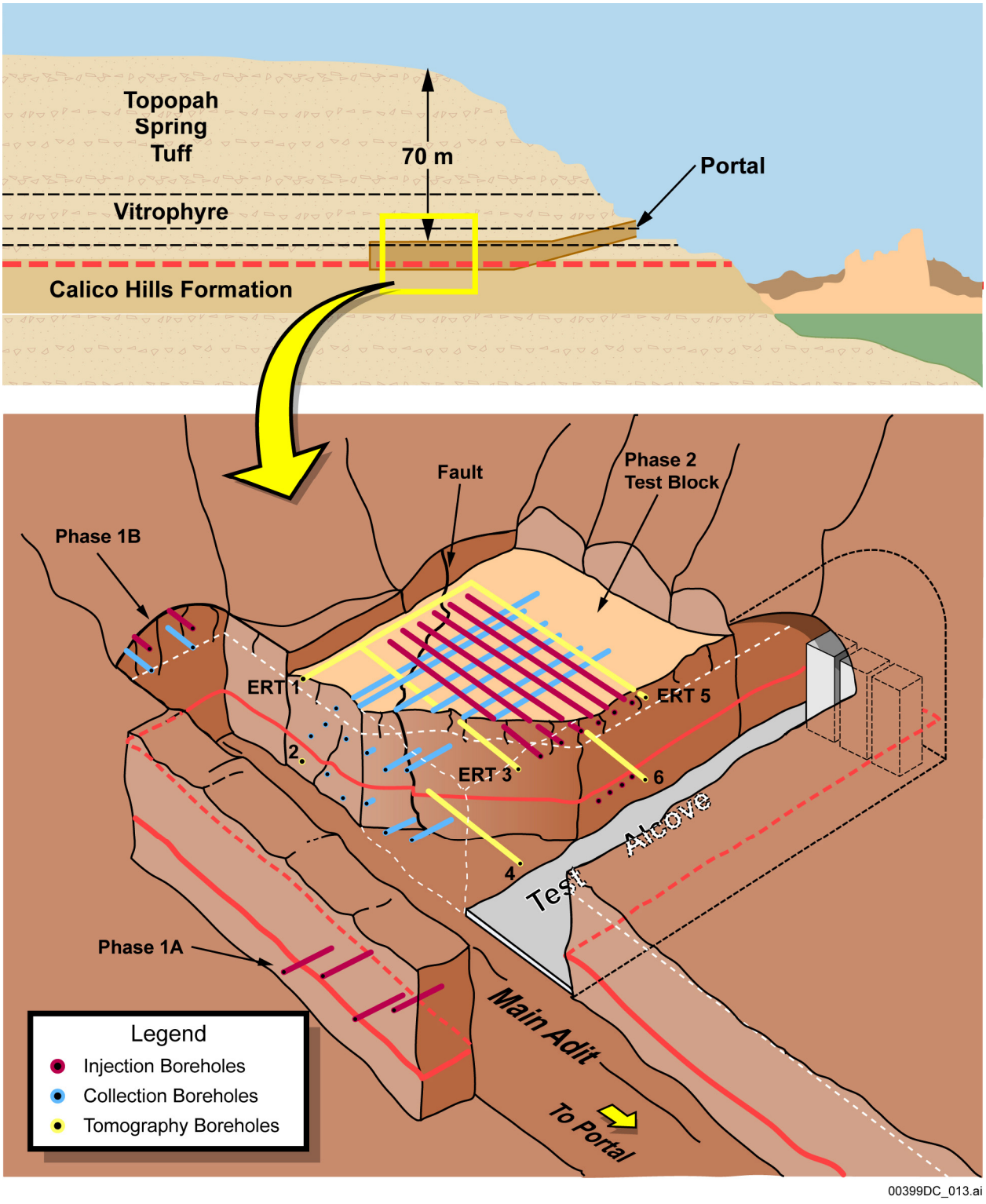

Source: BSC 2003d, Figure 6.13.1-1.

NOTE: This schematic of the Busted Butte unsaturated zone transport test shows the relative locations of the different experiment phases and borehole locations. Schematic is not drawn to scale.

Figure A-4. Busted Butte Unsaturated Zone Transport Test

The unsaturated zone transport test was designed in two test phases. The first phase, including test Phases 1A and 1B, was designed as a short-term experiment aimed at providing initial transport data on fractures near the contact of the Tpt (TSw) and Tac (CHn) and as a scoping study to assist in design and analysis of Phase 2. The second phase incorporated a larger region than Phase 1, with a broader, more complex scope of tracer injection, monitoring, and collection. Test Phase 1A provides results relevant to KTI RT 1.01 and is discussed here in detail. Other tests are documented in *In Situ Field Testing of Processes* (BSC 2003d, Section 6).

Phase 1A was in Tac (Tptpv1 (ch1 (vit)) and was a noninstrumented or blind single-point injection test using four boreholes (Figure A-5). Phase 1A used a few tracers, including nonreactive tracers (bromide, fluorescein, pyridone, and fluorinated benzoic acids), a reactive tracer (lithium), and fluorescent polystyrene microspheres (BSC 2003d, Section 6.13.2.1). The tracer of interest is sodium fluorescein, which was used to create images to investigate plume development following the injection. The sodium fluorescein initial concentration was set at 500 mg kg^{-1}. An injection rate of 10 mL/hr was applied at boreholes 1 and 3, and a 1 mL/hr rate was applied at boreholes 2 and 4. All the boreholes were 2 m in length and 10 cm in diameter. The injection point was located 90 cm in from the borehole collar. Continuous injection started on April 2, 1998, and ended on January 12, 1999 (286 days).

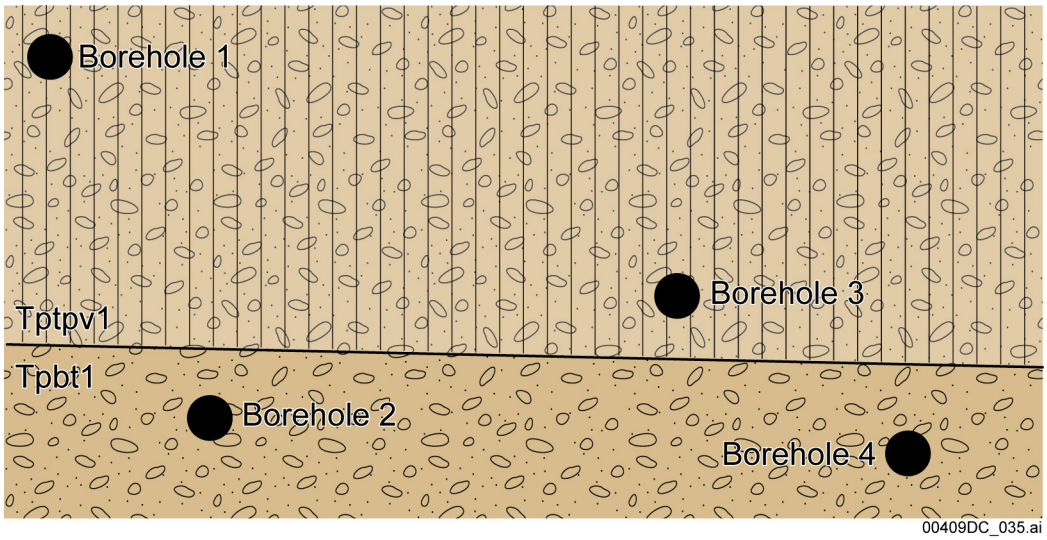

Source: BSC 2003d, Figure 6.13.1-3.

NOTE: Figure not drawn to scale.

Figure A-5. Schematic of Phase 1A Borehole Numbers and Relative Locations

Borehole injection was accomplished by pneumatically inflated borehole sealing and is illustrated in the upper part of Figure A-6. To allow visual inspection of the injection points under both standard and ultraviolet illumination, investigators developed a transparent packer system for the tracer-injection systems (BSC 2003d, Section 6.13.1.6).

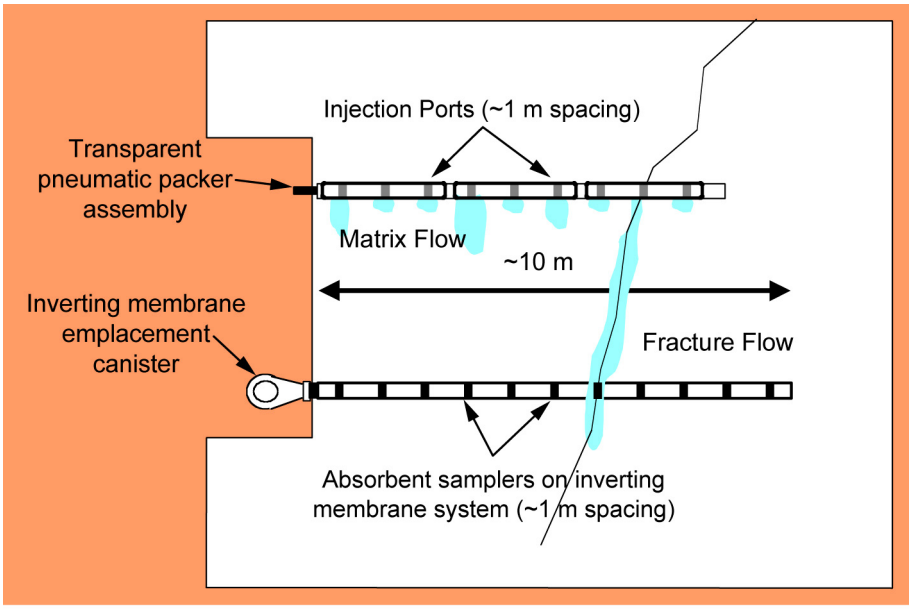

Source: BSC 2003d, Figure 6.13.1-2.

NOTE: Injection and collection boreholes are actually perpendicular in plan view. Absorbent sampler spacing is 0.25 to 0.50 m.

Figure A-6. Vertical Cross Section of Injection and Collection System Configuration

Following the injection period, a "mini-mineback" was done to expose the distribution of the tracer in the rock mass. Mineback of the Phase 1A test block began on January 15, 1999, and ended on March 3, 1999. The Phase 1A mineback consisted of four faces exposed at 50, 90, 115, and 140 cm from the adit wall. At each face, the stratigraphy was mapped and surveyed, and images of the fluorescein plume were taken under ultraviolet light. Figure A-7 (a through d) shows the fluorescein plume at each of the mineback faces.

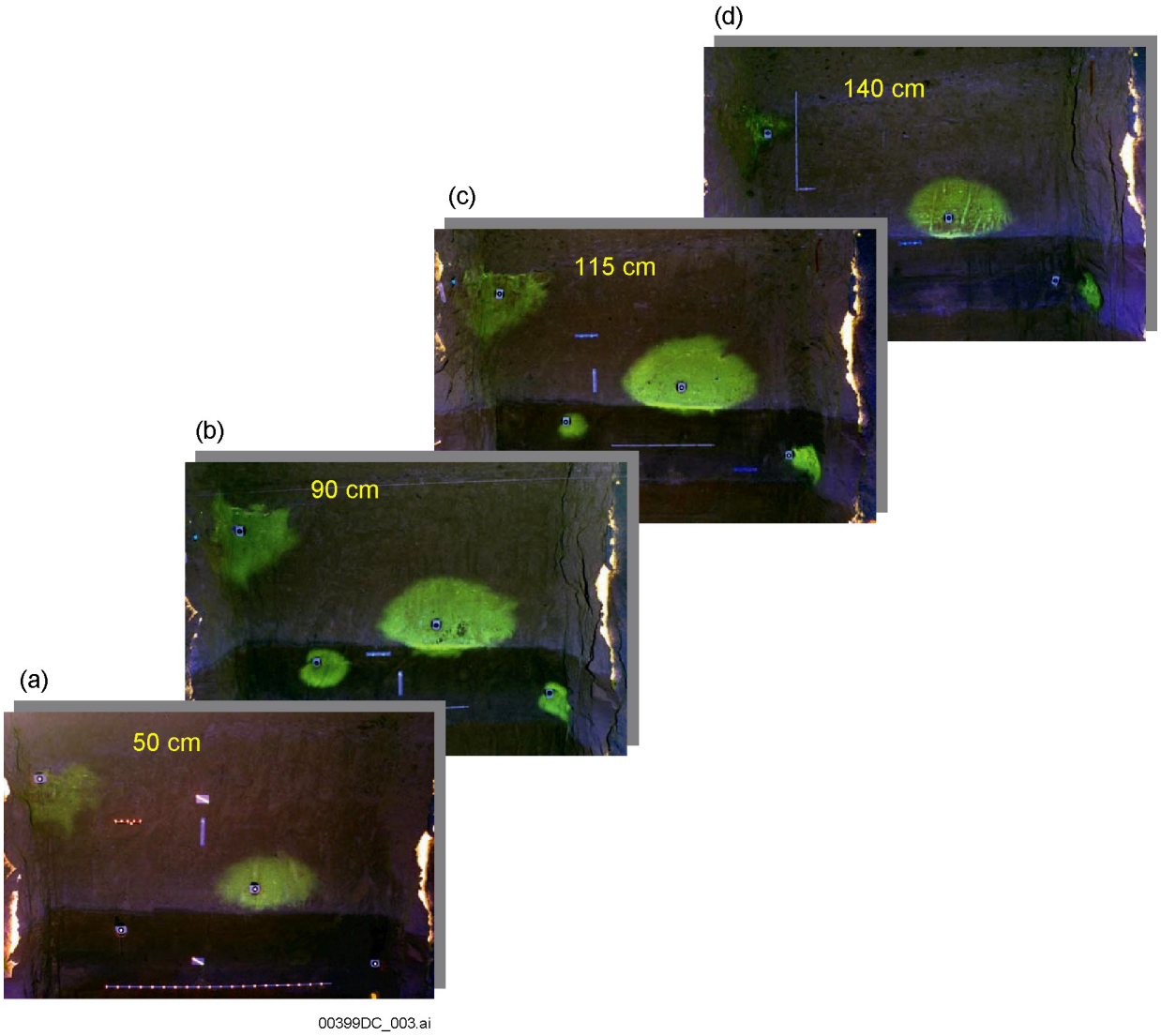

Source: BSC 2003d, Figure 6.13.2-1.

NOTE: The outlines of developing plumes mark the borehole positions identified in Figure A-5.

Figure A-7. Fluorescein Plume at Each of the Four Phase 1A Mineback Faces

Observations from the Phase 1A test demonstrate strong capillary-dominated flow for both the 1 and 10 mL/hr injection rates. The plumes are relatively uniformly distributed around the injection sites, though some borehole shielding effects (with tracer blocked or delayed from moving in the direction of the borehole) can be seen. Lithologic contacts, however, clearly influence the flow. At all of the mineback faces, the plumes are more oval than round. This reflects the ash layers just above boreholes 2 and 4 and just below borehole 3.

Although difficult to see from the image itself, Figure A-8 shows the location of a small fracture near the injection point in borehole 3.

In the upper right edge of the plume, there is a slight perturbation that may have resulted from the presence of the fracture. This indicates that, under the Phase 1A conditions, the fracture is acting as a permeability barrier rather than as a fast path.

There is a slight outburst of the lower part of the plume along the fracture within the Tac, which coincides with the contact of the Tptpv1 (ch1 (vit)) and the Tac. The very short travel along this portion of the fracture can be considered negligible, because the trace does not protrude outside the generally rugged outline of the plume. It may have been caused by the perturbation of the contact surface of the rock layers. Furthermore, preferential flow and transport along this structural discontinuity was not observed. This image demonstrates that fractures have a relatively minor effect on the flow in the Tac (Tptpv1 or ch1 (vit)) units.

Given that the testing was performed under a flow rate much larger than expected under ambient condition, the effects of fractures in the vitric layers can be considered negligible, and the flow can be reasonably approximated as a single-porosity matrix flow.

This testing result provides evidence from one experiment at one location. However, the dominance of matrix flow observed from the Phase 1A test does not lose generality for the CHn vitric units. Support for this assessment is provided by the relatively high matrix permeability and porosity of the CHn vitric unit. Matrix permeabilities for CHn are usually a few orders of magnitude higher than welded tuffs (Table A-1) (BSC 2003c, Tables 3 and 4). In addition, the nonwelded vitric layers within the CHn units have a low degree of fracturing (Table A-1). Under such conditions, the fractures embedded in a high-permeability matrix no longer function as fast paths for fluid flow (as do those in welded tuffs). Thus, it is very likely that the matrix flow forms the majority of the total flux in the CHn unit and that fracture flow is only a minor contributor.

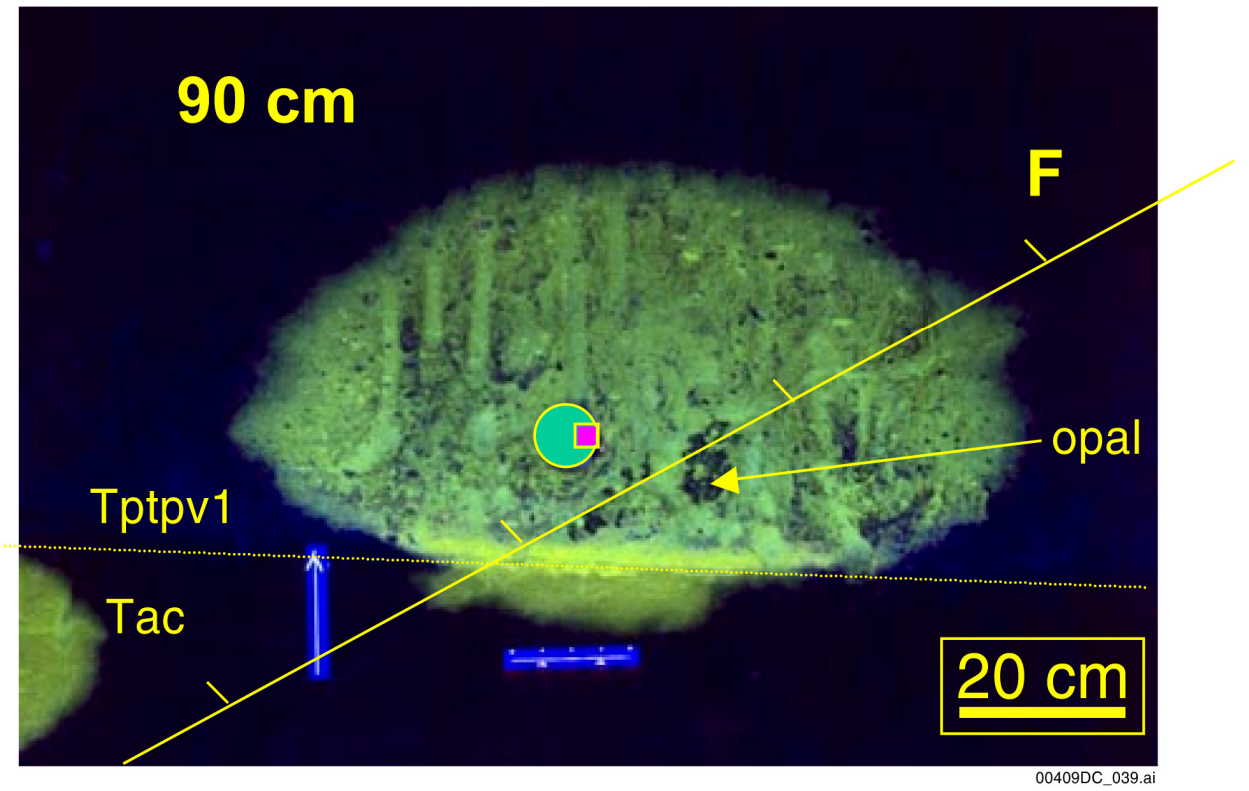

Source: BSC 2003d, Figure 6.13.2-2.

Figure A-8. Fluorescein Plume at 90-cm Mineback Face at Borehole 3

A.4.4 Field Test at the Exploratory Studies Facility Alcove 4 in the PTn Unit

As described in Section A.4.3, the effect of the fractures in the nonwelded vitric tuff layers at the CHn units can be considered negligible because of the relatively high matrix permeability (Table A-1). The insignificant role of fracture flow in the CHn vitric layers is corroborated by evidence from the ESF Alcove 4 experiment in the PTn unit, from which retarded flow and transport in a small fault have been observed.

Alcove 4 is located in the ESF north ramp within the nonwelded tuffs of the PTn unit, which has low fracture densities and relatively high matrix permeabilities and porosities (BSC 2003c, Tables 3 to 4, 11 to 13). Inside the PTn layers, Alcove 4 transects portions of the lower Pah Canyon Tuff (Tpp) and the upper pre-Pah Canyon bedded tuffs (Tpbt2) of the PTn (nomenclature of Buesch et al. 1996, p. 7). The test bed is located on the north face of the alcove, which is approximately 6 m wide and 5.3 m high (Figure A-9).

Exposed along the north face of Alcove 4 are the lower Tpp and upper Tpbt2 units D and C. Tpp is nonwelded and pumice-rich, exhibits a chalky-white color, and is apparently zeolitically altered. Tpbt2D is also nonwelded, possibly reworked, and has variably abundant (while zeolitically altered) pumice within a fine- to coarse-grained, medium-brown matrix. The contact between the lower Tpp and upper Tpbt2D is sharp in Alcove 4, marked by distinct color changes.

Below Tpbt2D, lying in the upper Tpbt2C, is a thin (0.20 to 0.30 m), light-pink to red argillically altered layer almost completely offset by a small, westward-dipping normal fault. The remaining Tpbt2C exposed along the north face below the argillic layer is massive and nonwelded, has very pale tan coloring, and contains abundant, coarse pumice and lithic fragments.

Cutting the north face of Alcove 4 is a normal fault with a small offset (0.25 m). As mapped along the crown at the end of the alcove, the fault has a strike of approximately 195° and a westward dip of 58°. The fault is open in the ceiling and is closed, with knife-edge thickness, near the invert on the north face. Intersecting the fault near the alcove crown along the north face is a high-angle fracture.

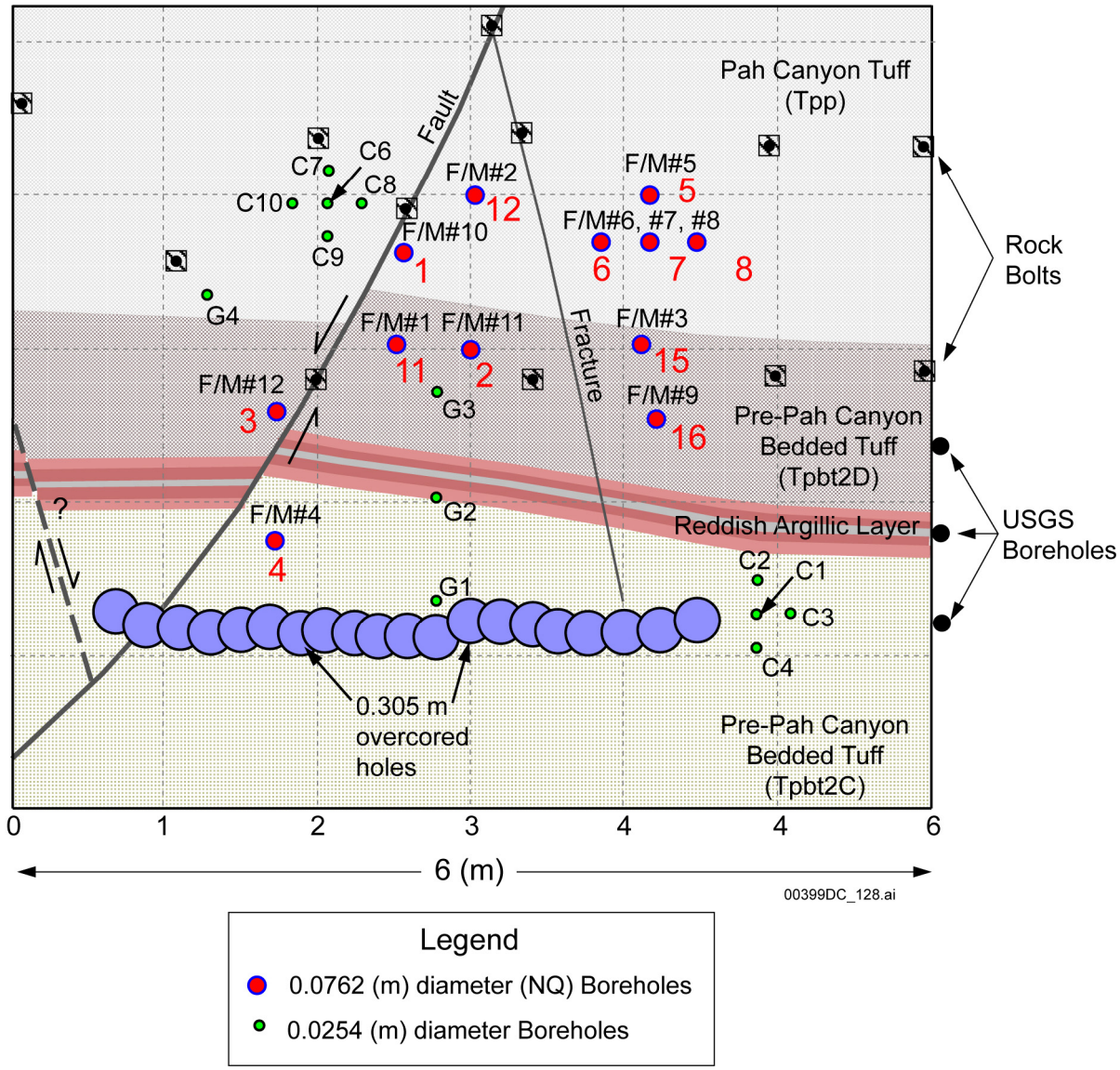

Source: BSC 2003d, Figure 6.7.1-1.

NOTE: Also included are the locations of boreholes and the slot. Boreholes labeled with red numbers were used in the field test of flow along the fault discussed in the text.

Figure A-9. Geologic Sketch and Schematic Illustration for the Test Bed in the North Face of Alcove 4 in the Exploratory Studies Facility

A total of twelve boreholes 6.0-m-long and 0.0762-m-wide were drilled into the alcove face, as illustrated in Figures A-9 (boreholes labeled with red) and A-10. Significantly, a number of boreholes (boreholes 1, 4, 11, and 12) were positioned to intersect the fault for the purpose of conducting flow tests within the fault. Borehole 2 was located to detect moisture that could migrate through the matrix below borehole 12. Borehole 12 was the injection borehole for the fault flow tests (BSC 2003d, Section 6.7.1.1). Liquid-release experiments were conducted at Alcove 4 and are described in detail in the document *In Situ Field Testing of Processes* (BSC 2003d, Section 6.7.1.1).

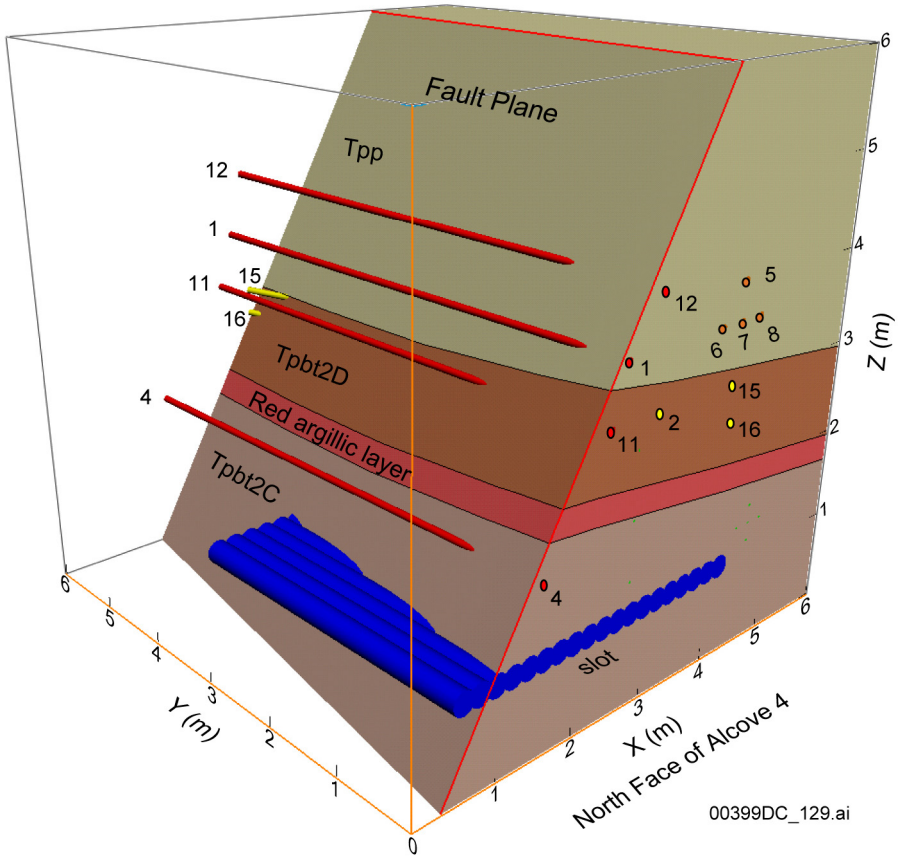

Source: BSC 2003d, Figure 6.7.1-2.

Figure A-10. Perspective Illustration of Three-Dimensional View of the Boreholes, Slot, and Lithologic Unit Contacts in the Alcove 4 Test Bed

In the liquid-release experiments, water was spiked with lithium bromide (BSC 2003d, Sections 6.5.2 and 6.7.1.3). The water was injected into the section of borehole 12 that intercepted the fault approximately 1.40 m from the collar. In this borehole, water was released over a 0.30-m interval. Here, the injection interval was centered at a distance 1.4 m from the borehole collar, determined from air-permeability measurements to be the location of the fault. A total of 193 L of water was released into the formation during seven events that extended over a period of two weeks, between October 21 and November 5, 1998. The time intervals between these tests (Tests 1 to 7) are approximately 1 day, with the exception of 4 days between Tests 2 and 3, and 7 days between Tests 5 and 6. Each event lasted between 4 and 7 hours, during which 20 to 43 L of water entered the injection zone. Each release event began with water filling the 1.37-L injection cavity in about 3 minutes, after which the liquid-release apparatus kept the injection zone filled by maintaining a constant-head boundary for the period of injection. After water was injected into the formation, the 1.37 L of water occupying the injection cavity was released to the formation under falling-head conditions.

The following examines the observed hydrologic responses to liquid releases in borehole 12 as detected by electrical resistivity probes and psychrometers. Details of the tests regarding the intake rates are included in the document *In Situ Field Testing of Processes* (BSC 2003d, Section 6.7.1.1).

The in-fault transport time was observed. When water was introduced into borehole 12, the time taken for the wetting front to travel 1.07 m along the fault to borehole 11 varied among the seven tests (Figure A-11). During the first release test, the wetting front advanced slowly as a result of significant matrix imbibition. Specifically, water was detected in the lower borehole about 300 minutes after the first release, while in the second test, the travel time was reduced to about 200 minutes. For the third test, this travel time was about 250 minutes; in the fourth test, water appeared in the fault in borehole 11 within about 150 minutes. The fastest travel time was observed for the fifth test, when the wetting front arrived within about 120 minutes in borehole 11. In the last two tests, the travel times were significantly slower, with increasing saturations observed 400 and 700 minutes after the initial release of water.

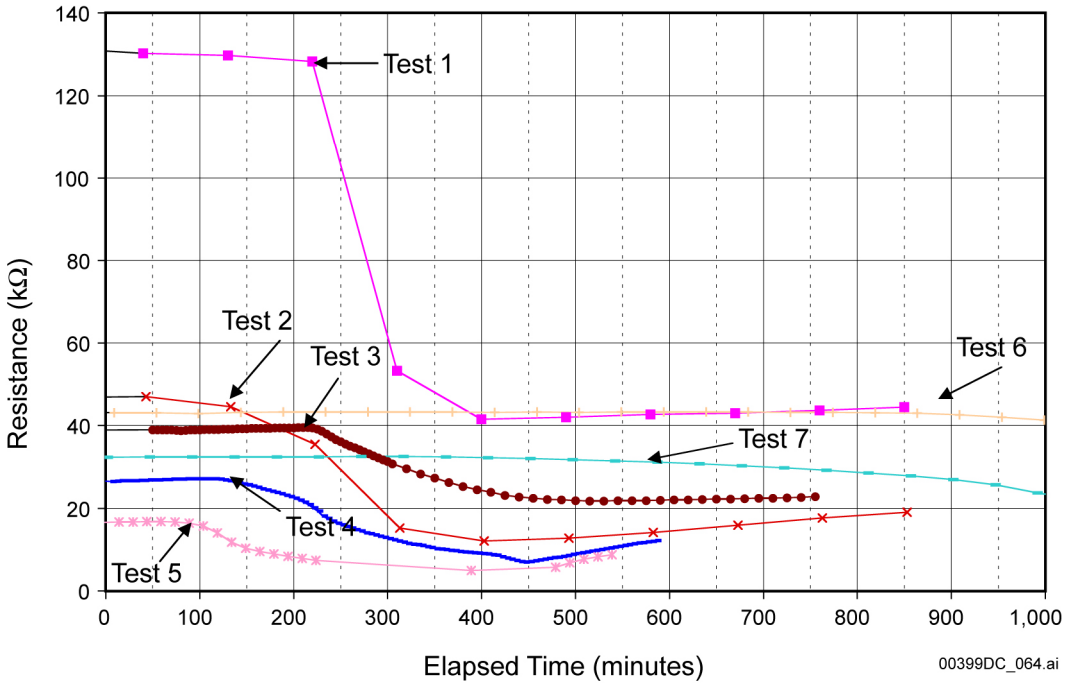

Source: BSC 2003d, Figure 6.7.2-2.

Figure A-11. Wetting Front Arrival in Borehole 11 Following Liquid Released into the Fault in Borehole 12

It was observed that the wetting front during the first release test advanced slowly as a result of significant matrix imbibition. Given that water release rates used in the tests were much larger than water percolation rates under ambient conditions, the fracture flow in the PTn porous matrix is considered significantly dampened and leading to the dominance of matrix flow. The dry, porous PTn matrix is capable of attenuating episodic percolation fluxes in localized areas (such as around faults) where fast flow would otherwise be expected to dominate (Salve et al. 2003, p. 282). Test results show that fracture flow in the nonwelded tuffs is significantly retarded because of the matrix imbibition. The observation of retarded fault flow at the PTn unit provides a corroborative line of evidence for fracture flow in the nonwelded units including the vitric CHn.

A.4.5 GEN 1.01 (Comment 26) Concerning the Multiple Interacting Continuum Model

The MINC model is more accurate than the dual permeability model in that it realistically reflects the transient fracture and matrix interaction. The model with MINC grid results in a later breakthrough time for a given concentration (BSC 2004, Figures 7 to 9, Section 7.2). This is because multiple interacting continua have higher spacing resolution in the matrix continuum, enabling the model to capture the transport of tracers (and radionuclides) from fracture into the matrix. However, the application of the MINC concept to the three-dimensional unsaturated zone site-scale model is overly burdensome for the incrementally greater accuracy because it necessitates replacement of the single matrix block in the current dual permeability system with several MINC subdomains. This increases the already large computation burden.

Considering all this, the present unsaturated zone flow model has adopted the dual-permeability approach for flow through both the fractures and the matrix (BSC 2003b, Section 6.1.2). Moreover, given that the dual permeability model yields earlier breakthrough times for a given concentration, the dual-permeability model can be considered more conservative than the MINC model.

A.4.6 Summary

The nonwelded vitric layers within the bottom TSw unit and the CHn units have a low degree of fracturing and high porosity. The matrix permeabilities of the CHn vitric units are relatively high, usually approximately a few orders higher than welded tuffs (BSC 2003c, Tables 3 and 4). The fractures associated with the matrix of such high permeability no longer function as fast paths for fluid flow as do those in welded tuffs. This forms the basis of modeling the nonwelded vitric layers within the CHn units as single porosity matrix. This conceptualization of dominance of matrix flow in the vitric layers is supported directly by the Busted Butte field test and corroboratively by the Alcove 4 test.

Busted Butte provides rare exposure of vitric layers of the CHn units. Field testing at the vitric layers shows that a tracer coming across a fracture advanced without any alteration of its plume shape. This observation demonstrates that flow in the CHn occurs in the matrix only.

The reduced role of fractures in nonwelded tuffs was also observed in the nonwelded tuffs in the PTn unit. In comparison with vitric layers in the CHn, the PTn unit has lower matrix permeability and smaller fracture spacing. Flow testing along a small fault under initial dry condition within the PTn unit at the ESF Alcove 4 had a slowly advancing wetting front as a result of significant matrix imbibition, following the first liquid release test. Delay of the wetting front under ambient conditions is expected to be even more significant. This is because water percolation rates under ambient conditions are much smaller than water release rates under the test condition. This liquid release test at the fault within the PTn unit provides corroborative evidence regarding the diminished role of fractures in the nonwelded vitric tuffs of the CHn units.

The unsaturated zone flow model adopted the dual-continuum approach for flows through both the fractures and matrix (BSC 2003b, Section 6.1.2), producing relatively conservative results, as opposed to those from the MINC model.

A.5 REFERENCES

BSC (Bechtel SAIC Company) 2001. *FY01 Supplemental Science and Performance Analyses, Volume 1: Scientific Bases and Analyses*. TDR-MGR-MD-000007 REV 00 ICN 01. Las Vegas, Nevada: Bechtel SAIC Company. ACC: MOL.20010801.0404; MOL.20010712.0062; MOL.20010815.0001.

BSC 2003a. *Radionuclide Transport Models Under Ambient Conditions*. MDL-NBS-HS-000008 REV 01. Las Vegas, Nevada: Bechtel SAIC Company. ACC: DOC.20031201.0002.

BSC 2003b. *UZ Flow Models and Submodels*. MDL-NBS-HS-000006 REV01. Las Vegas, Nevada: Bechtel SAIC Company. ACC: DOC.20030818.0002.

BSC 2003c. *Calibrated Properties Model*. MDL-NBS-HS 000003 REV 01. Las Vegas, Nevada: Bechtel SAIC Company. ACC: DOC.20030219.0001.

BSC 2003d. *In Situ Field Testing of Processes*. ANL-NBS-HS-000005 REV 02. Las Vegas, Nevada: Bechtel SAIC Company. ACC: DOC.20031208.0001.

BSC 2003e. *Development of Numerical Grids for UZ Flow and Transport Modelin*g. ANL-NBS-HS-000015 REV 01. Las Vegas, Nevada: Bechtel SAIC Company. ACC: DOC.20030404.0005.

BSC 2004. *Particle Tracking Model and Abstraction of Transport Processes*. MDL-NBS-HS-000020 REV 00. Las Vegas, Nevada: Bechtel SAIC Company. ACC: DOC.20040120.0001.

Buesch, D.C.; Spengler, R.W.; Moyer, T.C.; and Geslin, J.K. 1996. *Proposed Stratigraphic Nomenclature and Macroscopic Identification of Lithostratigraphic Units of the Paintbrush Group Exposed at Yucca Mountain, Nevada*. Open-File Report 94-469. Denver, Colorado: U.S. Geological Survey. ACC: MOL.19970205.0061.

Pruess, K. and Narasimhan, T.N. 1985. A Practical Method for Modeling Fluid and Heat Flow in Fractured Porous Media. *Society of Petroleum Engineers Journal, 25*, (1), 14-26. Dallas, Texas: Society of Petroleum Engineers. TIC: 221917.

Reamer, C.W. and Gil, A.V. 2001. Summary Highlights of NRC/DOE Technical Exchange and Management Meeting of Range on Thermal Operating Temperatures, September 18-19, 2001. Washington, D.C.: U.S. Nuclear Regulatory Commission. ACC: MOL.20020107.0162.

Reamer, C.W. and Williams, D.R. 2000. Summary of Highlights of NRC/DOE Technical Exchange and Management Meeting on Radionuclide Transport, December 5-7, 2000, Berkeley, California. Washington, D.C.: U.S. Nuclear Regulatory Commission. ACC: MOL.20010117.0063.

Salve, R.; Oldenburg, C.M.; and Wang, J.S.Y. 2003. Fault-Matrix Interactions in Nonwelded Tuff of the Paintbrush Group at Yucca Mountain. *Journal of Contaminant Hydrology, 62-63*, 269-286. New York, New York: Elsevier. TIC: 254205.

INTENTIONALLY LEFT BLANK

APPENDIX B

GEOCHEMICAL AND HYDROLOGIC DATA FOR FLOW BELOW THE REPOSITORY (RESPONSE TO RT 3.02, TSPAI 3.24, AND GEN 1.01 (COMMENT 106))

Note Regarding the Status of Supporting Technical Information

This document was prepared using the most current information available at the time of its development. This Technical Basis Document and its appendices providing Key Technical Issue Agreement responses that were prepared using preliminary or draft information reflect the status of the Yucca Mountain Project's scientific and design bases at the time of submittal. In some cases this involved the use of draft Analysis and Model Reports (AMRs) and other draft references whose contents may change with time. Information that evolves through subsequent revisions of the AMRs and other references will be reflected in the License Application (LA) as the approved analyses of record at the time of LA submittal. Consequently, the Project will not routinely update either this Technical Basis Document or its Key Technical Issue Agreement appendices to reflect changes in the supporting references prior to submittal of the LA.

APPENDIX B

GEOCHEMICAL AND HYDROLOGIC DATA FOR FLOW BELOW THE REPOSITORY (RESPONSE TO RT 3.02, TSPAI 3.24, AND GEN 1.01 (COMMENT 106))

This appendix provides a response for Key Technical Issue (KTI) agreement Radionuclide Transport (RT) 3.02, Total System Performance Assessment and Integration (TSPAI) 3.24, and general agreement (GEN) 1.01 (Comment 106). These agreements relate to providing geochemical and hydrologic data used for support of the flow field below the repository.

B.1 KEY TECHNICAL ISSUE AGREEMENTS

B.1.1 RT 3.02, TSPAI 3.24, and GEN 1.01 (Comment 106)

Agreement RT 3.02 was reached during the U.S. Nuclear Regulatory Commission (NRC)/U.S. Department of Energy (DOE) Technical Exchange and Management Meeting on Radionuclide Transport held December 5 to 7, 2000 (Reamer and Williams 2000), in Berkeley, California. RT subissue 3, radionuclide transport through fractured rock, was discussed at that meeting.

At that meeting, the NRC expressed the need for additional support for establishing the length of the flow path to which fracture transport conditions apply (Reamer and Williams 2000) and cautioned that when lacking a geostatistical analysis, estimation of flow length should err on the side of conservatism. The DOE responded that path lengths are generally the shortest between the repository and water table, with the exception where flow is diverted by perched water and that sensitivity analyses showed that the transport time is not significantly affected by the path length.

TSPAI 3.24 was reached during the NRC/DOE Technical Exchange and Management Meeting on Total System Performance Assessment and Integration held August 6 through 10, 2001, in Las Vegas, Nevada (Reamer and Gil 2001a). TSPAI subissue 3, model abstraction, was discussed at that meeting.

In the discussion of the model abstraction pertaining to the flow paths in the unsaturated zone, the NRC commented that there are insufficient water potential and geochemical data to support the flow fields predicted by the unsaturated zone site-scale model in the CHn, Prow Pass, and Bullfrog units below the repository (Cornell 2001). Of particular concern to the NRC staff was the estimated fraction of water that may travel significant distances through permeable nonwelded vitric tuff matrix versus the fraction that may be laterally diverted atop layers of low-permeability zeolitized or moderate to densely welded tuff to fast pathways to the water table (e.g., through faults). The focus of this concern is on areas where no perched water is predicted and unsaturated zones in the lower CHn, Prow Pass, and Bullfrog units below the perched water. In addition, the NRC staff requested a basis for the use of current hydraulic properties, rather than thermally perturbed properties; specifically, zeolitization of the nonwelded, unaltered Tptpv1, Tptb1, and upper Tac may be caused by the thermal pulse. The NRC staff also noted that statistics of flow percent in faults versus matrix and fractures that are relevant to the entire unsaturated zone model domain may not reflect flow regimes below the

repository footprint. In response, the DOE proposed to address the uncertainty in the CHn flow through sensitivity studies for radionuclide transport for a range of potential CHn flow conditions. In addition, the DOE proposed to update the unsaturated zone flow models and submodels to include the flow path and flow field for moisture tension and geochemical data.

Agreement GEN 1.01 was reached during the NRC/DOE Technical Exchange and Management Meeting on Range of Thermal Operating Temperatures, held September 18 to 19, 2001 (Reamer and Gil 2001b). At that meeting, the NRC provided additional comments, resulting in GEN 1.01 (Comment 106), which relates to TSPAI 3.24.

The wording of these agreements is as follows:

RT 3.02

> Provide the analysis of geochemical data used for support of the flow field below the repository. DOE will provide the analysis of geochemical data used for support of the fluid flow patterns in the AMR Unsaturated Zone Flow Models and Submodels, available to the NRC in FY 2002.

TSPAI 3.24[1]

> Provide the analysis of geochemical and hydrological data (water content, water potential, and temperature) used for support of the flow field below the repository, particularly in the Calico Hills, Prow Pass, and Bullfrog hydrostratigraphic layers. Demonstrate that potential bypassing of matrix flow pathways below the area of the proposed repository, as opposed to the entire site-scale model area, is adequately incorporated for performance assessment, or provide supporting analyses that the uncertainties are adequately included in the TSPA (UZ2.3.3).
>
> DOE will provide an analysis of available geochemical and hydrological data (water content, water potential, and temperature) used for support of the flow field below the repository, particularly in the Calico Hills, Prow Pass, and Bullfrog hydrostratigraphic layers. The analyses will demonstrate that potential bypassing of matrix flow pathways below the area of the proposed repository, as opposed to the entire site-scale model area, is adequately incorporated for performance assessment, or provide supporting analyses that the uncertainties are adequately included in the TSPA. These analyses will be documented in the Unsaturated Zone Flow Models and Submodels AMR (MDL-NBS-HS-000006), In-Situ Field Testing of Processes AMR (ANL-NBS-HS-000005), and Calibrated Properties Model AMR (MDL-NBS-HS-000003) expected to be available to NRC in FY 2003.

[1] UZ2.3.3 in this agreement refers to item 3.3 of NRC integrated subissue UZ2 (NRC 2002, Table 1.1-2). This item addresses NRC's concern that water potential and geochemical data to support flow fields are insufficient.

GEN 1.01 (Comment 106)

The DOE needs to provide additional technical bases for excluding uncertainties in infiltrating water compositions that are associated with the coupled THC model from TSPA analyses. The DOE has not adequately demonstrated that the initial water compositions used in sensitivity studies in the coupled THC models are appropriate and bounding (Chapters 3 and 6). What are the technical bases for selecting these particular water compositions selected for the analysis? Do they differ from one another in significant ways? Do they represent the full range of ground water compositions that have been collected and measured from Yucca Mountain and vicinity? How do variations in infiltrating water composition influence the In-Drift salts/evaporation models?

DOE Initial Response to GEN 1.01 (Comment 106)[2]

As stated on page 6-15, the Alcove-5 water compositions selected for most of the THC seepage modeling work were "the only available nearly full suites of analyses from a repository host unit" at the time the modeling work was initiated. In Section 6.3.1.5.3, additional simulations using UZ-14 perched water are presented. The UZ-14 perched-water composition is a good example of a reliable analysis significantly different from the Alcove-5 pore-water analyses. Additional work is planned for the next couple of years to collect additional pore-water samples from the TSw in the Exploratory Studies Facility, analyze the data, and use the data to improve the THC seepage model to better predict seepage chemistry consistent with TSPAI 3.24.

Sensitivity to starting water composition on evaporative chemical evolution is documented in Section 6.3.3.5.1.1 of SSPA Vol. 1. These studies take seven different known water compositions and evaporate them using the In-drift precipitates salts model. The results of these sensitivities indicate that for 7 waters there are three possible chemical divides that the brine generation follows. The first representing waters like J-13, perched water, water from the single heater test, and water from the drift scale test evolve to a sodium nitrate brine. The second set representative of the Topopah Spring pore water takes the brine towards calcium (or magnesium) chloride brine. The third set derived from the Rev 00 DST THC seepage abstraction results and associated grout modified waters that contain more sulfates than calcium. These three different brines would give different relative humidity thresholds for brine formation on the waste package and have different boiling point elevations for any brine associated with the waste package.

B.1.2 Related Key Technical Issue Agreements

KTI agreements RT 3.02, TSPAI 3.24, and GEN 1.01 (Comment 106) are related to RT 1.01. RT 1.01 addresses the justification of the approach for modeling flow through the CHnv units

[2] The specific section or page number referral cited below is from *FY01 Supplemental Science and Performance Analyses, Volume 1: Scientific Bases and Analyses* (BSC 2001a).

(i.e., dominant matrix flow). In comparison, RT 3.02, TSPAI 3.24, and GEN 1.01 (Comment 106) concern the general use of geochemical and hydrologic data in the calibration and validation of the unsaturated zone flow field for all hydrostratigraphic units below the repository. The response to agreement RT 1.01 is provided in Appendix A of this technical basis document.

B.2 RELEVANCE TO REPOSITORY PERFORMANCE

Flow and transport through the unsaturated zone plays an important part in the assessment of postclosure performance. Since fracture flow dominates radionuclide transport in most unsaturated hydrostratigraphic units (BSC 2003a, Section 6), the documentation of all geochemical and hydrologic data that are used to support the flow fields below the repository is important for confidence building in the TSPA-LA transport calculations.

B.3 RESPONSE

KTI agreements RT 3.02, TSPAI 3.24, and GEN 1.01 (Comment 106) pertain to the documentation and use of subsurface hydrologic, temperature, and geochemical data for support of the flow-field concept below the repository.

The unsaturated zone flow and transport models under discussion include the mountain-scale flow model (called the unsaturated zone flow model), temperature model, and geochemical models (chloride transport model, calcite model, and strontium isotope model) (BSC 2003b). All the models (except for the calcite model) were three-dimensional models. The unsaturated zone flow model investigates flow processes using hydrologic data (saturation, water potential, and perched water data). The TSPA-LA flow fields were generated from the unsaturated zone flow model, which uses the property set of the PTn with and without lateral flow diversion within the PTn (BSC 2003b, Sections 6.2.5, 6.6.2, 6.6.3). All other models support the unsaturated zone flow model through the investigation of ambient-thermal and geochemical processes using temperature and geochemical data.

No new data sets were used in the 2003 revision of the unsaturated zone flow model (BSC 2003b) at the repository horizon (the ESF and ECRB Cross-Drift). There were some new samplings in the ECRB Cross-Drift for pore-water chloride and other composition measurements; however, the new chloride data are considered to be redundant, because they cover locations that have the previously available chloride data.

The unsaturated zone flow model was supported by various data collected from boreholes, the Exploratory Studies Facility (ESF), and Enhanced Characterization of the Repository Block (ECRB) Cross-Drift before 2000 (KTI agreement RT 3.02 was established in a December 2000 meeting (Reamer and Williams 2000)). The field- and laboratory-measured data include hydrologic data (saturation, water potential, and perched water), pneumatic pressure data, temperature and geochemical data (chloride, calcite, and strontium). However, only the boreholes drilled below the repository horizon can provide data (except pneumatic pressure data) that directly support the flow and transport modeling below the repository. Most of the borehole data had been available and used in the initial version of *UZ Flow Models and Submodels* (CRWMS M&O 2000). Since then, the supporting database has not expanded noticeably. In the 2003 revision of *UZ Flow Models and Submodels* (BSC 2003b), no new data regarding

saturation, water potential, and perched water were available for the unsaturated zone flow model. A total of three more boreholes have available temperature measurements for the ambient thermal model, with removal of two previous boreholes (UE-25 NRG#5 and USW SD-7) and addition of five boreholes (USW H-4, USW H-5, UE-25 WT#18, UE-25 UZ#4, and UE-25 UZ#7a). The chloride transport model utilized chloride data from 10 more boreholes, compared to the initial one borehole (UE-25 UZ#16). Calcite data remain the same in the calcite model (UE-25 WT#24, USW SD-6, and USW G-2). A new strontium isotope model for two boreholes (USW SD-9 and UE-25 SD-12) and the ECRB Cross-Drift was added.

Responses to the KTI agreements are organized into six parts. Section B.3.1 briefly discusses the hydrologic properties of the welded and nonwelded tuffs as follows: (1) the conceptual model of layered representation of tuff hydrologic properties in the unsaturated zone flow model; (2) the subsurface hydrologic properties calibrated from a one-dimensional flow model; (3) the nonwelded vitric tuffs within the CHn units and its approximation as a single matrix porosity medium; and (4) the reasoning that hydrologic properties used in the unsaturated zone temperature model do not include thermally perturbed properties. Section B.3.2 discusses flow below the repository, including perched water, percolation rates, matrix, fractures, and fracture fluxes. Section B.3.3 deals with saturation and water potential hydrologic data. Section B.3.4 discusses the temperature data. Section B.3.5 presents the analyses of chloride, strontium and calcite geochemical data that were used to calibrate and verify the unsaturated zone flow model. Section B.3.6 contains the response to the comment regarding the compositions of infiltration water in the thermal-hydrologic-chemical seepage model (BSC 2003c). The model results of the unsaturated zone flow model are shown to be consistent with the various field-measured data below the repository. The technical basis for these responses is provided in Section B.4.

The first five parts of this section (Sections B.3.1 through B.3.5) pertain to the response to agreement TSPAI 3.24, with the response to agreement RT 3.02 provided in the fifth part (Section B.3.5). The sixth part (Section B.3.6) provides the response to GEN 1.01 (Comment 106).

B.3.1 Calibrated Properties of Tuffs below the Repository

The nonwelded and welded tuffs in the Yucca Mountain show varying degrees of fracture development. They are generally classified into separate identifiable hydrogeologic units according to their hydrologic properties (BSC 2003d; BSC 2003e). The hydrogeologic layers below the repository include the middle and lower parts of TSw, CHn (zeolitic or vitric), Prow Pass, and Bullfrog.

In the unsaturated zone flow model, the dual-permeability method (a continuum approach) is used for describing flow and transport: the fractured tuffs are modeled as fracture and matrix continua. Each matrix and fracture continuum has its own hydrologic properties (matrix permeabilities, matrix van Genuchten water potential relationship (α and m); fracture permeability, van Genuchten parameters α and m, and an active-fracture model parameter γ). The fracture and matrix hydrogeologic properties used for the three-dimensional mountain-scale unsaturated zone flow model were calibrated using one-dimensional inversion of field-measured saturation, water potential, and gas pressure data (BSC 2003d, Section 6.3). Fracture permeability and van Genuchten m are assigned data from laboratory and field measurements

and were not further calibrated because they are relatively insensitive to simulated matrix-saturation and water-potential distributions (BSC 2003d, Section 6.3.2, Table 4).

Matrix properties were calibrated with hydrologic data. The amount of hydrologic data available for model calibrations varies. Water-potential data used for the property calibration were collected from three boreholes. Continuous and rather evenly distributed saturation measurements were collected from as many as 13 boreholes from the ground surface to the bottom. Locations within and below the repository were represented as well as those above. The amount of water-potential data is much less than that of saturation (BSC 2003d, Section 6.3, Table 9). Water potential data from the borehole samples were measured in the laboratory. These measurements are very sensitive to alterations in moisture content, and, therefore, samples must be adequately preserved. Because of the experimental difficulty of obtaining uncompromised water potential measurements, fewer reliable water potential data are available for calibration.

Fracture permeabilities are calibrated by matching the pneumatic pressure data that correspond to a mountain-scale process. Pneumatic pressure data were collected from four boreholes (BSC 2003d, Table 7) at locations above the repository only. However, it makes sense that the pneumatic pressure measurements were made only at shallower depths, since the response of pneumatic pressures at locations below the repository is expected to be less sensitive and of less importance.

Calibration of fault properties was performed using data from a borehole (UE-25 UZ#7a) near the Ghost Dance Fault, located near the east boundary of the repository block. This fault is an important hydrogeologic feature since it is a potential flow path for receiving lateral flows along eastward-tilted layer interfaces (BSC 2003d, Section 6.3.4). Data (including saturation, water potential, and gas pressure data) were collected from the surface to the repository horizon. Locations below the repository have no data support.

The CHn vitric layers are modeled as a single-porosity matrix in the unsaturated zone flow model (BSC 2003b) from the consideration of the high permeable matrix. This is supported by observations of matrix-flow dominance shown in the Busted Butte field test of the nonwelded vitric layer and the ESF Alcove 4 test bed in the PTn layer, which has similar porous matrix properties as the CHn vitric layers (BSC 2003f, Sections 6.7 and 6.13).

Parameter uncertainties in calibrated parameter data (BSC 2003d, Section 6.4.1) come from sources such as model simplifications, scale effect, and infiltration-rate uncertainty. Infiltration rate contributes to parameter uncertainty because the fluxes in the unsaturated zone are largely determined by the upper boundary conditions. Using the three infiltration scenarios (present-day mean infiltration and infiltrations with lower and upper bounds) for parameter calibration captures this uncertainty (BSC 2003d, Section 6.4).

The unsaturated zone flow model utilizes properties from *Calibrated Properties Model* (BSC 2003d). Hydrologic data used in the one-dimensional inversion calibration are described in *Calibrated Properties Model* (BSC 2003d, Section 4.1.2). More discussion of calibrated properties for the KTI agreements is given Section B.4.1.

B.3.2 Flow Fields below the Repository

In the unsaturated zone flow model, flows in fractured tuffs are predominantly vertical flows, in response to gravity. However, below the repository horizon, such flow patterns are altered in the vitric zones within the CHn units in the central and southern portions of the model domain because of high matrix permeability and the eastward-tilted layering structure. The base-case flow fields at the water table show lateral flow of several hundreds of meters to the east in the area directly below the southern repository (BSC 2003b, Section 6.6.3).

In the northern part of the domain, the flow fields are less sensitive to the calibrated properties. Because of the impact of perched water and zeolitic units, flow is mainly focused into major faults.

Fracture flow is dominant both at the repository horizon and at the water table. In fact, fracture flow consists of more than 90% to 95% of the total percolation fluxes in the rock, fractures, and faults at the repository level, whereas it is about 70% to 80% at the water table. On the other hand, this percentage for fault flow alone increases from about 30% to 40% at the repository to about 60% at the water table, reflecting the conditions imposed by matrix-permeability reduction in the zeolitic zones in the CHn units, perched water formation, and lateral flow into the major faults.

In the general discussion of the flow fields, the water table was determined from the present-day measured data. The flow fields with a raised water table in future climates are addressed in Section B.4.2.

B.3.3 Hydrologic Data for the Unsaturated Zone Flow Model

The unsaturated zone flow model uses perched water, saturation, and water potential data measured from the field (BSC 2003b, Sections 6 and 7). Because the flow below the repository is studied as an integrated part in the unsaturated zone flow model, the relevant hydrologic property data at and below the repository are discussed together with those above the repository. Similarly, the same format is used in discussions of the temperature and geochemical data in the following sections.

Perched-water location data from seven boreholes were used in simulating the occurrences of perched water in the unsaturated zone flow model. Because the calibrated properties were derived based on one-dimensional inversion of field-measured data and are incapable of reproducing either perched-water formation or lateral flow, they are further adjusted in the unsaturated zone flow model to simulate the occurrence of perched water.

The saturation data used in the calibration of the unsaturated zone flow model come from seven boreholes (five of which were also used in *Calibrated Properties Model* (BSC 2003d)). Water potential data were from three boreholes (UE-25 SD-12 is also used in *Calibrated Properties Model* (BSC 2003d)). Overall, the water potential data for the TSw (and TCw) units are scarce or not available. The TSw units were characterized by water potential data locally distributed in the first few hundred meters from the entrance of the ECRB Cross-Drift. Generally, no data are available from the repository down to near the top of the CHn units.

Model results for perched water, saturation and water potential match well with the observed data (BSC 2003b, Section 6.6.3). The hydrologic data used in the calibration and validation are described in *UZ Flow Models and Submodels* (BSC 2003b, Section 4.1). More relevant discussion regarding the hydrologic data for the KTI agreements is provided in Section B.4.3.

B.3.4 Temperature Data for the Unsaturated Zone Flow Model

Model analyses of temperature data provide an independent examination of percolation fluxes simulated by the unsaturated zone flow model. The unsaturated zone temperature model uses temperature data measured from a total of nine surface-based deep boreholes (BSC 2003b, Sections 6.3 and 7.7). The borehole temperature data cover the depths below the repository as well as those above it. Model results compare well with the observed data of the boreholes.

The data used in the calibration and validation of the unsaturated zone model are described in *UZ Flow Models and Submodels* (BSC 2003b, Sections 4.1, 6.3, and 7.7; BSC 2001b). Section B.4.4 provides more relevant discussion regarding the KTI agreements.

B.3.5 Geochemical Data for the Unsaturated Zone Flow Model

Chloride and strontium concentrations in pore waters and calcite data were used for calibration and validation of the unsaturated zone flow model. The conceptual model for unsaturated zone chloride transport was based on the infiltration boundary, established using chloride fluxes, determined by the precipitation fluxes and the concentration in precipitation. The match of the simulated chloride concentrations to the field-measured pore-water concentration provides information regarding past infiltration. Similarly, in the simulation of strontium in the unsaturated zone, strontium input at the surface came from precipitation. Modeled strontium concentrations are compared to measured values to derive information related to infiltration. Data analyses of precipitated calcite in the unsaturated zone also provide information to constrain the infiltration flux. Downward water flows in the unsaturated zone interact with the geothermal gradient, causing the calcite to precipitate from percolating waters (BSC 2003b, Section 7.9.2).

Chloride concentrations were collected from various places, including 11 boreholes, the ECRB Cross-Drift, and the ESF. The ECRB Cross-Drift is relatively well sampled. However, chloride data from the ESF are restricted to three discrete locations. Moreover, the available chloride data are typically incomplete along a vertical profile through the unsaturated zone. Specifically, borehole chloride data for the TSw layers (as well as TCw layers above the repository) are usually missing. Chloride data are rare in the lower TSw units above CHn (i.e., chloride data correspond to the depth interval from the repository to the perched water). The limited chloride data in the TSw (and TCw) units results from TSw (and TCw) welded tuffs having a very low water content such that collecting enough rock mass to extract enough pore water for chemical analysis is experimentally difficult.

Strontium data are available from USW SD-9 and UE-25 SD-12 and the ECRB Cross-Drift. Calcite data are limited to UE-25 WT#24, USW SD-6, and USW G-2.

The model results for chloride, strontium, and calcite models also are in good agreement with the observed data. Chloride and strontium concentrations and calcite abundance data used in the

unsaturated zone geochemical models are described in *UZ Flow Models and Submodels* (BSC 2003b, Sections 6.5 and 7.10, respectively). Additional discussion of the geochemical data can be found in Section B.4.5.

B.3.6 Water Compositions in the Coupled Thermal-Hydrologic-Chemical Seepage Models

GEN 1.01 (Comment 106) relates to KTI agreement RT 3.02, regarding water compositions selected to represent infiltrating water related to the coupled thermal-hydrologic-chemical seepage models (BSC 2003c).

In the initial 2000 version of *Drift-Scale Coupled Processes (DST and THC Seepage) Models* (BSC 2003c, Section 6.2.2.1), the availability of infiltrating water data was limited to three pore-water samples collected from the highly fractured middle nonlithophysal zone (Tptpmn) geologic unit in Alcove 5 near the Drift Scale Test. Since then, a series of pore-water samples from repository host units have been collected and analyzed in the ECRB Cross-Drift and in boreholes USW SD-9 and USW NRG-7/7a (BSC 2003c, Section 6.2.2.1). In the 2003 revised version of the coupled thermal-hydrologic-chemical seepage models (BSC 2003c), the selection of water composition data included pore waters in the repository horizon, perched water, and saturated zone waters (J-13 well water). A total of five types of infiltrating waters were chosen with preference given to actual pore waters from unsaturated regions within or above the repository units and exclusion of the perched water and saturated zone water (BSC 2003c, Section 6.2.2.1). The choice of input water composition also takes into consideration the natural variability of pore-water compositions in the repository units. The selected five types of infiltrating waters are expected to show diverse brine developments under evaporation. Corrosive brine calcium chloride and other less corrosive brines are expected to develop in addition to sodium chloride brine.

However, since these new samples were mainly collected from the ECRB Cross-Drift, the spatial coverage of these data is too small to derive a probability of occurrence for any of these pore-water compositions.

Waters such as those from USW UZ-14 pore water and J-13 are excluded because they appear dramatically different from pore waters in the repository units, even though they are seemingly end-members of waters from Yucca Mountain and the vicinity. However, this end-member type of water with low pore water concentrations (with very low (Ca+Mg)/(Na+K) ratio) may exist in the repository horizon, as revealed in a recent finding of pore water with very low chloride concentrations. These low concentrations of chloride are similar to those of J-13 water and may have occurred in the ESF fracture or fault zones where bomb-pulse ^{36}Cl was found (Lu et al. 2003, Section 4.4). Under evaporation conditions, the water from such dilute concentrations is likely to develop into sodium chloride brine or other brines less deleterious than calcium chloride.

Notwithstanding the limitation in sample numbers and the question of their representativeness, the five infiltrating waters constitute a reasonable and appropriate selection of water compositions.

B.3.7 Summary of Response

In summary, a significant amount of several kinds of data, including hydrologic, temperature, and geochemical data, has been collected to characterize mountain-scale flow. Most of these data were collected from boreholes, with the ECRB Cross-Drift being a second source (for water-potential data and chloride and strontium-concentration data). A limited amount of data is from the ESF. In the unsaturated zone flow model and temperature and geochemical models, the model results are demonstrated to be consistent with both field-measured and laboratory data.

A large amount of saturation and temperature data has been collected from surface-based boreholes. Locations below the repository in these boreholes are generally well characterized by saturation and temperature data. Saturation data from surface-based boreholes for locations both above and below the repository horizon provide good spatial coverage from as many as 13 boreholes used in the one-dimensional property calibration and seven boreholes used in the unsaturated zone flow model (five of which were also used in the property calibration) (BSC 2003d). Temperature data were collected from as many as nine surface-based deep boreholes. The temperature boreholes are well represented in the model domain, and the data are rather evenly distributed above and below the repository.

Borehole water potential data have also been gathered. In the existing borehole water potential data from three boreholes, there are limited samples from locations immediately below the repository in the TSw units (from the repository to the top of the CHn). The water potential data for the TSw units were represented by field data locally distributed over a span of a few hundred meters in the ECRB Cross-Drift.

Fault properties were calibrated from inversion using saturation and water potential data from one borehole (UE-25 UZ#7a). The data were collected from the regions extending from the surface to the repository horizon. Data for calibration of fault properties below the repository are currently not available.

Geochemical data (chloride and strontium concentrations and calcite) are used in the unsaturated zone flow and transport model. The strontium data were collected from the ECRB Cross-Drift and two boreholes, whereas calcite data were collected from three surface-based boreholes.

Chloride data were used as natural tracers in the unsaturated zone transport model. Chloride data were collected from the ESF and ECRB Cross-Drift; 11 boreholes have pore-water chloride data. Locations in boreholes from the repository to the top of the CHn units have limited chloride data, because previous studies have had difficulty in obtaining enough pore water for chemical analysis, owing to the low water contents in the TSw (and TCw) nonwelded tuffs.

Regarding GEN 106 (Comment 106), the selection of the five types of infiltrating data is based on samples collected mainly from the ECRB Cross-Drift. Considering the limited amount of data available for characterizing the pore water, the selection represented a reasonable approximation. The water types are expected to develop corrosive calcium chloride and other less-corrosive brines on evaporation, in addition to sodium chloride. The probability of the occurrences of these five types of waters is unknown because the amount of available data is not large enough to derive the spatial variability of the water samples. The water types (W4 and

W6) may not represent end members pore waters typical of low concentrations. Very low water concentrations typical of the J-13 well water may have occurred in the repository horizon.

The information in this report is responsive to agreements RT 3.02 and TSPAI 3.24 and GEN 1.01 (Comment 106) made between the DOE and the NRC. The report contains the information that DOE considers necessary for NRC review for closure of these agreements.

B.4 BASIS FOR THE RESPONSE

This section provides the basis for the responses to KTI agreements RT 3.02 (Section B.4.5), TSPAI 3.24 (Sections B.4.1 to B.4.5), and GEN 1.01 (Comment 106) regarding the composition of infiltration waters in the thermal-hydrologic-chemical seepage model.

In simulating flow and transport within the fractured tuffs in the Yucca Mountain unsaturated zone, the dual-permeability modeling method (a continuum approach) is used. It considers global flow occurring not only between fractures, but also between matrix gridblocks, as well as the interflow between fractures and matrix. In this approach, each gridblock of the primary mesh is divided into two gridblocks, one for fracture and the other for matrix, and connected to each other. Correspondingly, the matrix and fracture continua have their own hydrologic properties. The relevant discussion of the advantage of using dual-permeability method in the unsaturated zone model can be found in *Calibrated Properties Model* (BSC 2003d, Section 6.1).

B.4.1 Hydrogeologic Layers and Hydrologic Properties

The volcanic welded or nonwelded tuffs at Yucca Mountain occur in layers and show variable degrees of fracturing. In the dual continuum approach of the unsaturated zone flow model, the fractured tuffs are described as both fracture and matrix continua, except for the CHn vitric units below the repository, which are treated as a single-porosity matrix only. This is because the CHn vitric units have relatively high matrix permeabilities and low fracture densities, resulting in the dominance of matrix flow.

B.4.1.1 Hydrogeologic Layers

Hydrologic properties of Yucca Mountain tuffs are different from layer to layer. But within one hydrogeologic layer the properties (referred to as layer average properties) are homogeneous, except where faulting or variable alteration (e.g., zeolitization) is present. The hydrogeologic layers at and below the repository are listed in Table B-1. Specifically, lying below the repository are the TSw hydrostratigraphic layers represented by tsw38 to tsw39, CHn represented by ch1 to ch6, Prow Pass represented by pp4 to pp1, and Crater Flat undifferentiated (Bullfrog) represented by bf3 to bf2 (BSC 2003b, Section 6.1). A typical geologic profile along a vertical east-west transect is illustrated in Figure B-1. The figure also shows the repository horizon from about 1,000 to 1,100 m in elevation, which is at the same level as the ESF and the ECRB Cross-Drift.

Table B-1. Selected Layers at and below the Repository Showing Geologic Framework Model 2000 Lithostratigraphy, Unsaturated Zone Model Layer, and Hydrogeologic Unit Correlation Used in the Unsaturated Zone Flow Model

Major Unit (Montazer and Wilson 1984)	Lithostratigraphic Nomenclature (BSC 2002)	Unsaturated Zone Model Grid Layer[a] (BSC 2003e)	Hydrogeologic Unit (Flint 1998)
Topopah Spring welded (TSw)	Tptrl, Tptf	tsw33	TUL
	Tptpul, RHHtop		
	Tptpmn	tsw34	TMN
	Tptpll	tsw35	TLL
	Tptpln	tsw36	TM2 (upper 2/3 of Tptpln)
		tsw37	TM1 (lower 1/3 of Tptpln)
	Tptpv3	tsw38	PV3
	Tptpv2	tsw39 (vit, zeo)	PV2
Calico Hills nonwelded (CHn)	Tptpv1	ch1 (vit, zeo)	BT1 or BT1*a* (altered)
	Tpbt1		
	Tac (Calico)	ch2 (vit, zeo)	CHV (vitric) Or CHZ (zeolitic)
		ch3 (vit, zeo)	
		ch4 (vit, zeo)	
		ch5 (vit, zeo)	
	Tacbt (Calicobt)	ch6 (vit, zeo)	BT
	Tcpuv (Prowuv)	pp4	PP4 (zeolitic)
	Tcpuc (Prowuc)	pp3	PP3 (devitrified)
	Tcpmd (Prowmd)	pp2	PP2 (devitrified)
	Tcplc (Prowlc)		
	Tcplv (Prowlv)	pp1	PP1 (zeolitic)
	Tcpbt (Prowbt)		
	Tcbuv (Bullfroguv)		
Crater Flat undifferentiated (CFu)	Tcbuc (Bullfroguc)	bf3	BF3 (welded)
	Tcbmd (Bullfrogmd)		
	Tcblc (Bullfroglc)		
	Tcblv (Bullfroglv)	bf2	BF2 (nonwelded)
	Tcbbt (Bullfrogbt)		
	Tctuv (Tramuv)		
	Tctuc (Tramuc)	tr3	Not Available
	Tctmd (Trammd)		
	Tctlc (Tramlc)		
	Tctlv (Tramlv)	tr2	Not Available
	Tctbt (Trambt) and below		

Source: BSC 2003b, Table 6.1-1 (modified).

NOTE: [a] Defined as a rock material type, represented by the code name, for gridblocks belonging to the rock unit.

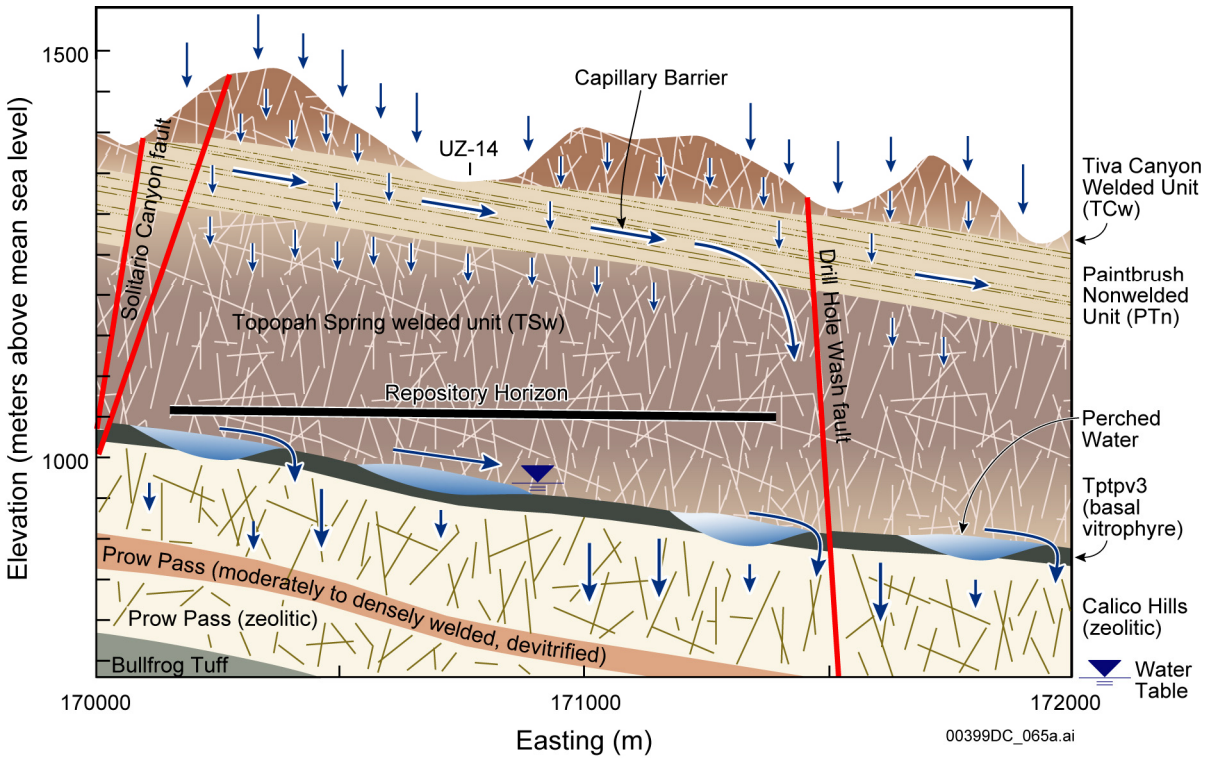

Source: BSC 2003b, Figure 6.2-1.

Figure B-1. Schematic Diagram Showing a Typical Geologic Profile along a Vertical East–West Transect and the Conceptualized Flow Processes and Effects of Capillary Barriers, Major Faults, and Perched-Water Zones within the Unsaturated Zone Flow Model Domain

B.4.1.2 Calibrated Hydrologic Properties and Uncertainties

The hydrologic properties of the layers were calibrated using one-dimensional inversion of saturation, water potential data, and gas pressure data (BSC 2003d, Section 6.3). The model report entitled *Calibrated Properties Model* (BSC 2003d) provides the basic input parameter sets of fractures and rock matrix for modeling efforts in *UZ Flow Model and Submodels* (BSC 2003b). In *Calibrated Properties Model* (BSC 2003d), the data used for one-dimensional calibration of drift-scale properties from each borehole are listed in Table B-2, and their locations are plotted in Figure B-2. In the drift-scale parameters, the matrix saturation used for the inversion corresponds to 13 surface-based boreholes, and water-potential data is from three boreholes (Table B-2 and Figure B-2). Pneumatic pressure data used for one-dimensional inversion come from four boreholes (BSC 2003d, Table 7), where the gas pressure data were generally taken at or above the repository horizon. Pressure data below the repository are not available. Generally speaking, saturation was sufficiently measured along the boreholes both above and below the repository (BSC 2003d). However, water potential data are scarce, especially for the TSw layers below the repository.

Table B-2. Data Used for One-Dimensional Calibration of Drift-Scale Properties from Each Borehole

Borehole	Matrix Liquid Saturation (core)	Matrix Liquid Water Potential (in situ)
USW NRG-6		✓
USW SD-6	✓	
USW SD-7	✓	
USW SD-9	✓	
UE-25 SD-12		✓
UE-25 UZ#4		✓
USW UZ-14	✓	
UE-25 UZ#16	✓	
USW UZ-N11	✓	
USW UZ-N31	✓	
USW UZ-N33	✓	
USW UZ-N37	✓	
USW UZ-N53	✓	
USW UZ-N57	✓	
USW UZ-N61	✓	
USW WT-24	✓	

Source: BSC 2003d, Table 9 (modified).

The scale-dependence of matrix permeability properties is assumed to be limited to a relatively small scale associated with the spacing between relatively large fractures (BSC 2003d, Section 6.3). However, drift-scale fracture permeabilities, determined from air-injection tests, cannot be applied to mountain-scale modeling because of the scale difference. Mountain-scale fracture permeabilities are calibrated with the pneumatic pressure data measured in surface borehole UE-25 SD-12 (BSC 2003d, Section 6.3.3).

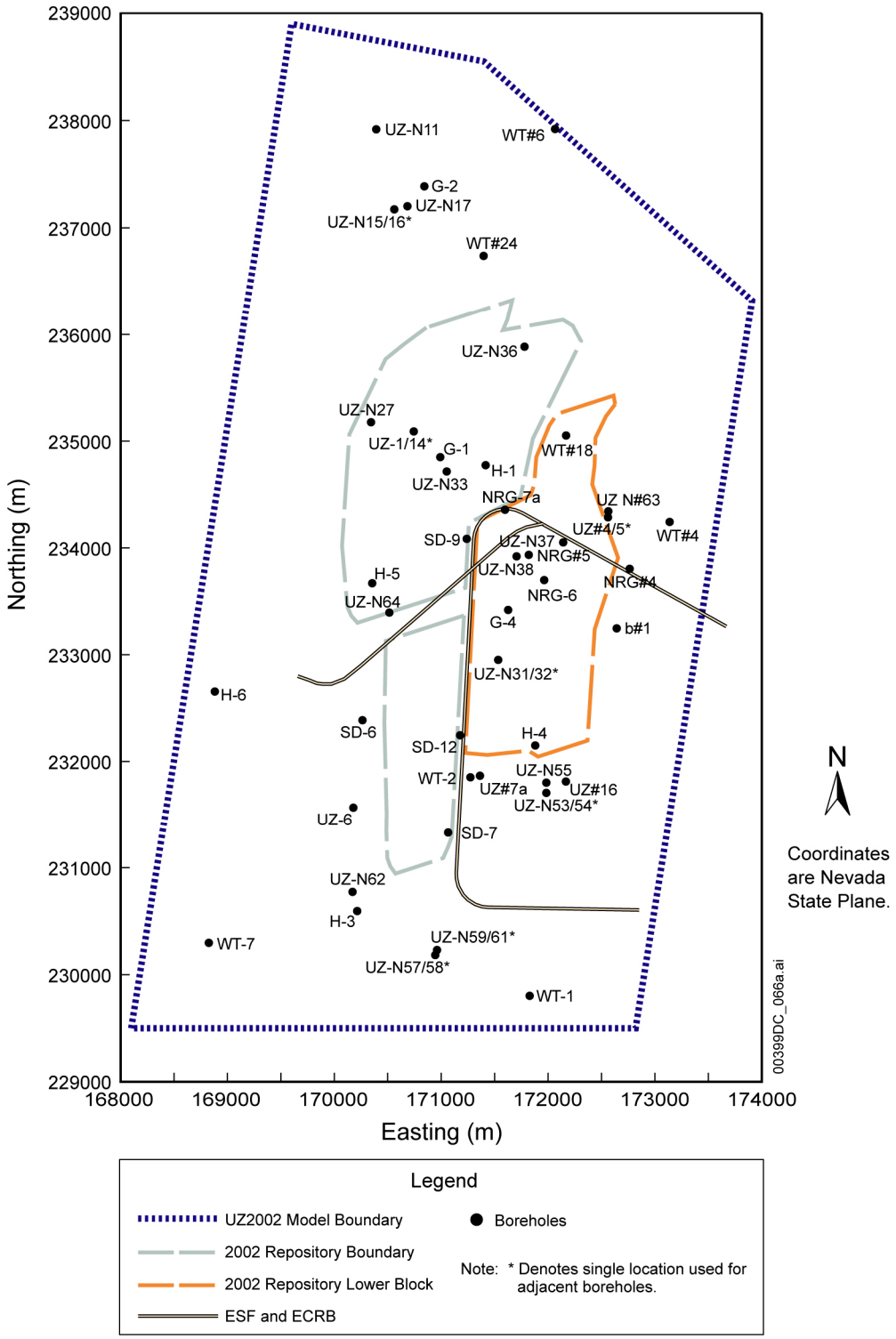

Source: BSC 2003e, Figure 1b.

Figure B-2. Locations of Boreholes in the Property Calibrations

Faults are modeled as vertical or near-vertical planes in the unsaturated zone flow model. Generally, high vertical permeability and low capillary forces are expected within the faults

(BSC 2003d, Section 6.3.4). The fault properties were generalized from the inversion of hydrologic data from borehole UE-25 UZ#7a, which cuts through the Ghost Dance Fault. Borehole UE-25 UZ#7a represents the most complete data set from within a fault zone. Saturation, water potential, and pneumatic data are available from the surface down into the repository horizon in the TSw units (BSC 2003d, Table 16, Figures 9 and 10). Data related to water flow in faults below the repository are not available.

The uncertainty in the calibration of hydrologic properties is addressed (BSC 2003d, Section 6.4.1). Uncertainty comes from simplification of the one-dimensional conceptual model. For example, one-dimensional models are used for calibrating drift-scale and mountain-scale property sets. Parameter uncertainty in the parameter calibration would result from model simplifications. As a result, lateral flow behavior in the unsaturated zone may not be captured by property sets determined from one-dimensional models. Infiltration-rate uncertainty also contributes to parameter uncertainty, because flow processes in the unsaturated zone are largely determined by upper boundary conditions. Using the three infiltration scenarios (present-day mean infiltration scenario as base case, along with infiltrations with lower bound and upper bound) for the parameter calibration documented in the calibrated properties captures this uncertainty. In addition, scale effects are a well-known source of parameter uncertainty. This is especially true for determination of the unsaturated zone model parameters. For example, matrix parameters are measured in the unsaturated zone at core scale on the order of several centimeters, whereas in the unsaturated zone flow and transport model, numerical gridblocks are on the order of a few meters to hundreds of meters.

B.4.1.3 Conceptualization of Matrix Flow in Calico Hills Nonwelded Vitric Units

The hydrogeologic layers are usually simulated as dual continua in the unsaturated zone flow model. Because the welded tuffs are characterized by low matrix permeability and considerable fracture development, liquid flow occurs predominantly in fractures, with the matrix mainly serving as liquid storage. However, in contrast, the nonwelded vitric layers in the CHn units below the repository have relatively high matrix permeabilities and low fracture densities, leading to predominant matrix flow.

The vitric portions of the CHn units and the lower part of the TSw units occur below the repository. The vitric layers occur in the tsw39, ch1, ch2, ch3, ch4, ch5, and ch6. They are located in the southwest portion of the model domain (BSC 2003e, Section 6.6.3). Vitric tuffs are subject to alteration to zeolite under suitable hydrologic conditions (i.e., closeness to water table). The vitric tuffs are considered to be complementary to the abundance of zeolite so that the vitric-zeolitic regions can be determined by the absence or presence of zeolite contents. However, there is insufficient zeolite X-ray diffraction data to effectively determine the vitric-zeolitic regions within the CHn units. The boundaries of vitric and zeolitic regions were selected using the results of saturated permeability data (BSC 2003e, Assumption 4), measured rock-property data for boreholes within the unsaturated zone model area (BSC 2003e, Assumption 5), and the location of faults with significant vertical offset (BSC 2003e, Assumption 6; Section 6.6.3).

These CHn vitric units are conceptualized and treated as a single-porosity matrix only in *Unsaturated Zone Flow Model* (BSC 2003b, Section 6.1.2). The effect of fractures in the flow model within the CHn vitric zones is considered negligible.

The conceptual model is supported by observation from the tracer tests in Busted Butte (BSC 2003f). The tests conducted at Busted Butte in the vitric layers of the upper CHn show that flow took place in the matrix but not in fractures, even though fractures are present. This observation was made under testing conditions with liquid-release rates much faster than ambient flow conditions (BSC 2003f, Section 6.13).

Corroborative evidence for matrix flow dominance is also found in the field testing at the ESF Alcove 4, which reveals that the PTn units have a significant dampening effect on fracture flow because of matrix imbibition of water flowing along the fracture (BSC 2003f, Section 6.7). The observations for ESF Alcove 4 and Busted Butte are comparable and underscored by the fact that both the CHn vitric units and the PTn have relatively high matrix permeability.

B.4.1.4 Current Hydraulic Properties and Thermally Perturbed Properties

The unsaturated zone flow model uses the hydraulic properties calibrated in *Calibrated Properties Model* (BSC 2003d), rather than thermally perturbed properties. (The mountain-scale thermal modeling is performed in *Mountain-Scale Coupled Processes (TH/THC/THM)* (BSC 2003g).) This is because on the mountain-scale domain, long-term analyses indicate the effects of thermal loading on flow and transport properties are small (BSC 2003g, Section 6.1.6).

During the first few years of the thermal-loading period, thermal effects may have a significant impact on thermal-hydrologic processes only at or near drifts. Many of the temperature-dependent properties, such as fluid density, viscosity, and specific enthalpy, are incorporated in the formulation of the thermal-hydrologic mountain-scale model (BSC 2003g, Section 6.1.6). However, thermal effects on rock properties (such as permeability, relative permeability, and relationship between capillary pressure and liquid saturation) are ignored because of the limitations of available field data and constitutive relations to describe these phenomena. Moreover, these effects are considered negligible when compared to the uncertainty of the rock properties existing in the collected data (BSC 2003g, Section 6.1.6).

B.4.2 Flow Fields below the Repository and Rising of Water Table

Flow fields are generated for the TSPA-LA calculations from the unsaturated zone flow model (BSC 2003b) using the property sets of the PTn with and without lateral flow diversion in the PTn. Accordingly, the base case flow model uses the property set of the PTn that would favor lateral flow diversion; the alternative model uses the property set of the PTn that would not likely cause flow diversion (BSC 2003b, Sections 6.2.5, 6.6.2, and 6.6.3) (Table B-3).

In the unsaturated zone flow model, infiltration is applied at the surface input boundary. Corresponding climate scenarios for infiltration considered in the unsaturated zone flow model include present-day (modern) and future monsoonal and glacial climates. Infiltration under each climate scenario is quantified through a mean, lower-, and upper-bound infiltration rate (Table B-3). The uncertainty in the infiltration rates as a boundary condition of the unsaturated zone flow model is thereby appropriately addressed. Infiltration under present-day climate and

mean infiltration scenarios is used in discussing the analyses of the observed data for the KTI agreements. Other climate scenarios are described here for sensitivity analysis and to address the issue of the water table rising (in future climates).

Table B-3. Present-Day, Monsoon, and Glacial Infiltration Scenarios in Unsaturated Zone Flow Model

Scenario Notations	Scenarios
preq_uA preq_uB	Modern upper
preq_mA preq_mB	Modern mean
preq_lA preq_lB	Modern low
monq_uA monq_uB	Monsoon upper
monq_mA monq_mB	Monsoon mean
monq_lA monq_lB	Monsoon low
Glaq_uA Glaq_uB	Glacial upper
Glaq_mA Glaq_mB	Glacial mean
Glaq_lA Glaq_lB	Glacial low

Source: BSC 2003b, Sections 6.2.5, 6.6.2, and 6.6.3.

NOTE: The uppercase A denotes the base-case model property set used by the corresponding flow model that would favor lateral flow diversion. The uppercase B denotes the alternative model, in which the property set of the PTn would not likely cause flow diversion. The lowercase letter l (before the uppercase A or B) stands for lower-bound infiltration, m for mean infiltration, and u for upper-bound infiltration scenario.

B.4.2.1 Flow Fields below the Repository

Flow at and below the repository can be illustrated through percolation fluxes, using present-day infiltration. Figures B-3 and B-4 show the percolation flux at the repository layer and at the water table for the present-day mean infiltration scenario of the base-case model.

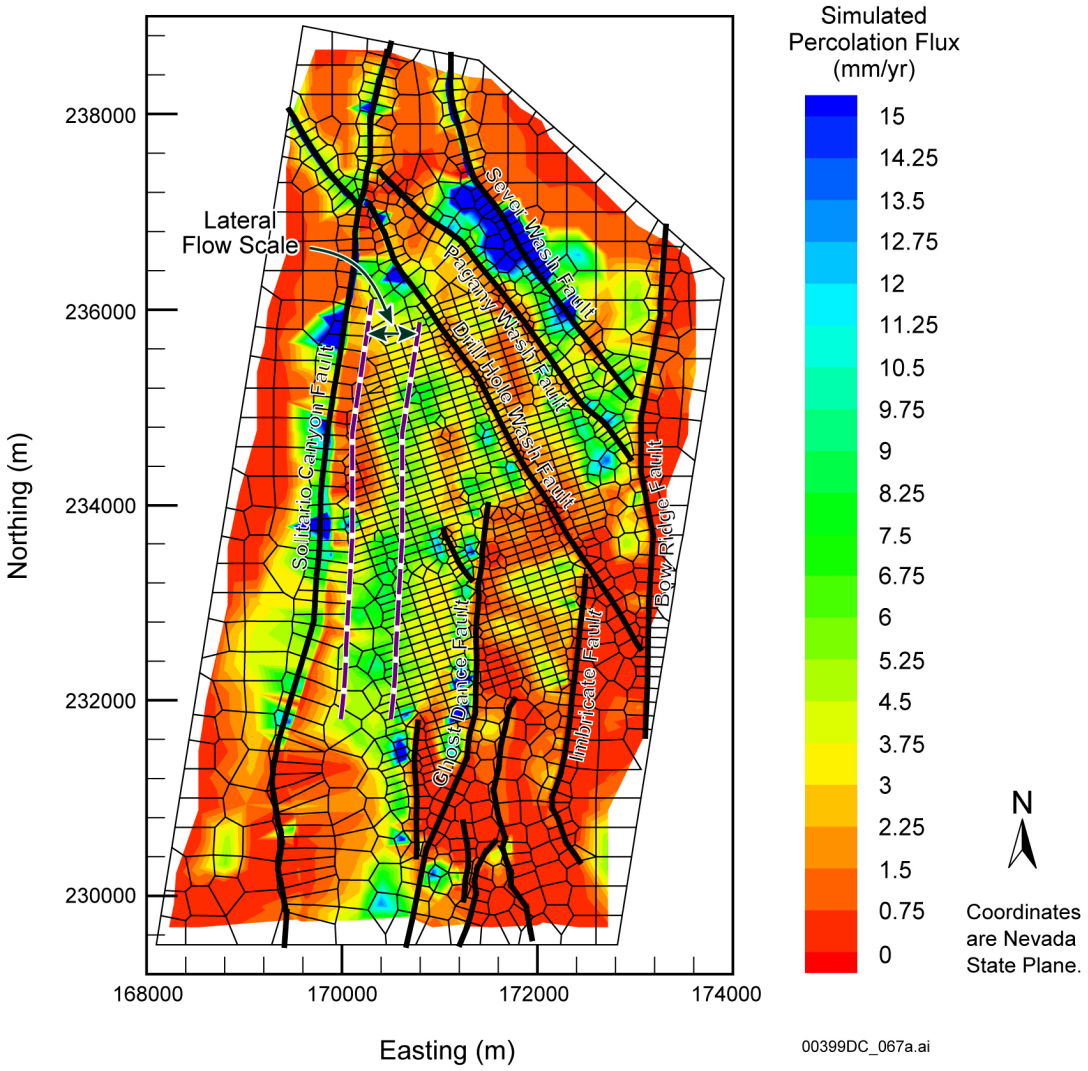

Source: BSC 2003b, Figure 6.6-1.

Figure B-3. Simulated Percolation Fluxes at the Repository Horizon under the Present-Day, Mean Infiltration Scenario Using the Results of Simulation preq_mA

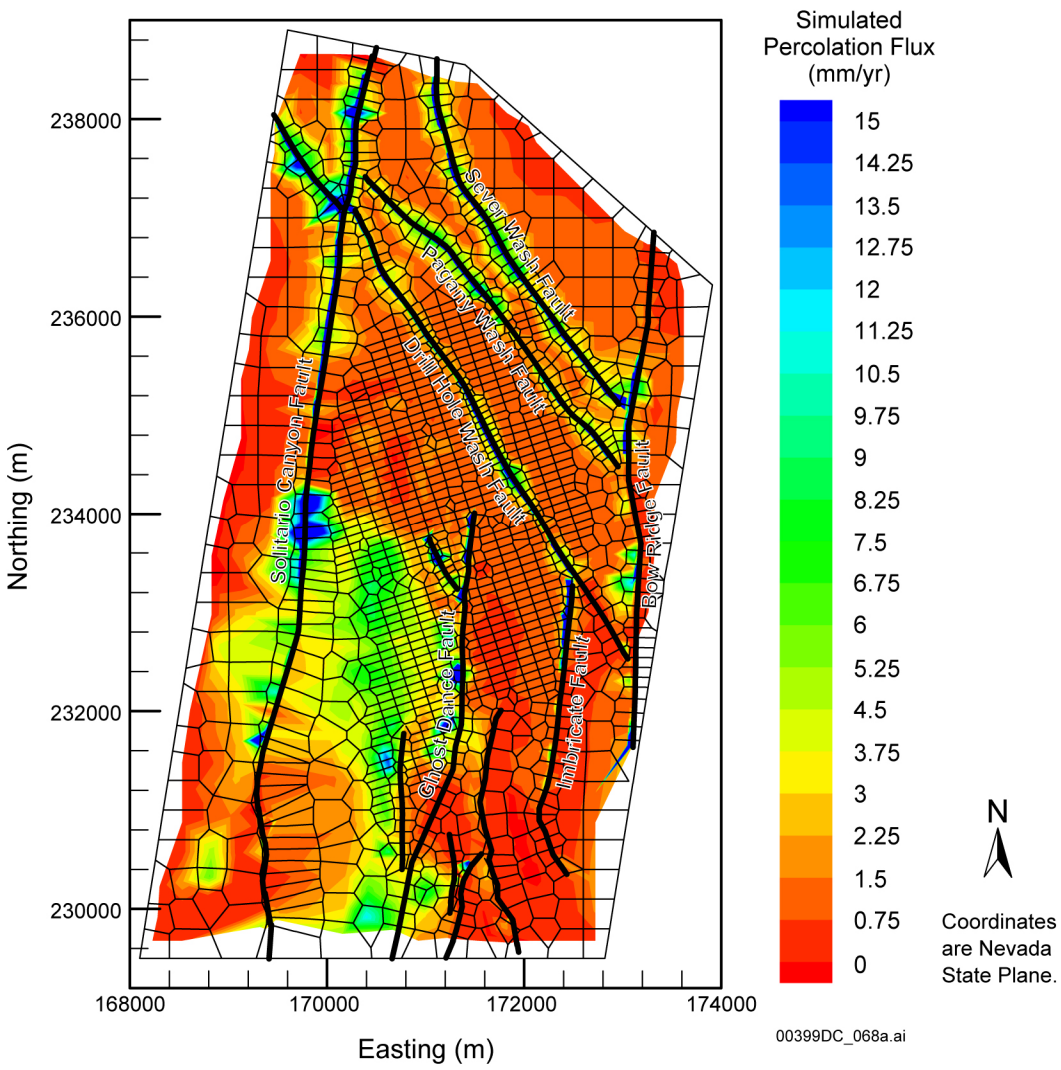

Source: BSC 2003b, Figure 6.6-6.

Figure B-4. Simulated Percolation Fluxes at the Water Table under the Present-Day, Mean Infiltration Scenario Using the Results of Simulating the Base Case Model preq_mA

By comparing the percolation fluxes at the repository with those at the water table for the base case (e.g., Figure B-3 with Figure B-4) and the alternative case (e.g., Figure B-5 at the water table) the following findings (BSC 2003b, Section 6.6.3) are evident:

- In the northern half of the domain, the base case flow fields are very similar to the alternative ones. Because of the impact of perched water and zeolitic units, flow is mainly focused into major faults.

- In the central and southern portions of the model domain, the base case flow fields at the water table show lateral flow of several hundreds of meters to the east in the area directly below the southern repository. This is the area where vitric zones are located within the CHn unit.

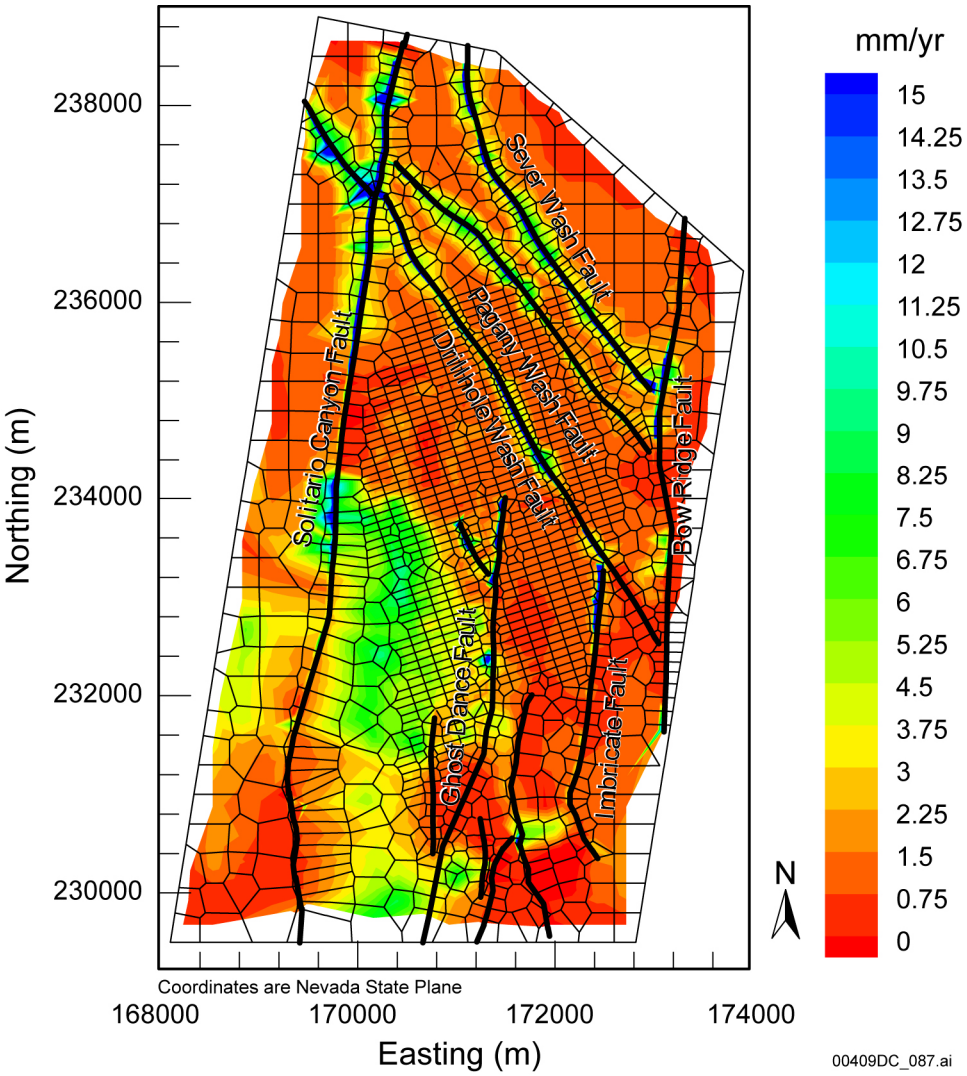

Source: BSC 2003b, Figure 6.6-7.

Figure B-5. Simulated Percolation Fluxes at the Water Table under the Present-Day, Mean Infiltration Scenario Using the Results of Simulating the Alternative Model preq_mB

B.4.2.2 Flow Paths to the Water Table

In addition to the flux distribution discussed above (Section B.4.2.1), flow below the repository is further investigated in terms of fluxes in the matrix, fractures, and faults (BSC 2003b, Section 6.6.3). Table B-4 lists percentages of fracture–matrix flow components and fault flow at the repository horizon and the water table within the model domain. The statistics are calculated from averaging an entire layer without considering spatial distributions of flow percentage. Fracture and matrix percentages taken together produce a sum total of 100%, while fault flow percentages represent total vertical flux through fault blocks. These statistics are calculated from vertical flow along each grid column for present-day base case flow. The statistics for other climate scenarios can be found in *UZ Flow Models and Submodels* (BSC 2003b, Section 6.6.3).

Table B-4. Comparison of the Water Flux through Matrix, Fractures, and Faults as a Percentage of the Total Flux at the Repository and at the Water Table for the Present-Day Base Case Flow Fields

Simulation Designation	Flux at Repository Horizon (%)			Flux at Water Table (%)		
	Fracture	Matrix	Fault	Fracture	Matrix	Fault
preq_lA	91.35	8.65	58.78	78.05	21.95	71.78
preq_mA	94.29	5.71	28.62	70.29	29.71	53.73
preq_uA	94.02	5.98	27.41	77.72	22.28	60.68

Source: BSC 2003b, Table 6.6-3 (modified).

NOTE: The uppercase letter A stands for the base-case model property set, the uppercase letter B for the alternative model, the lower-case letter l (before the uppercase A or B) for lower-bound infiltration, m for mean infiltration, and u for upper-bound infiltration scenario.

These statistics indicate that fracture flow is dominant both at the repository horizon and at the water table. At the repository level, fracture flow consists of 90% to 95% of the total percolation fluxes. Fracture flow at the water table takes 70% to 80% of the total flow. On the other hand, fault flow percentage increases from about 30% at the repository to about 50% to 60% at the water table, except for the present-day, lower-bound infiltration case.

B.4.2.3 Rising Water Table

In the unsaturated zone flow model, the flow fields were calculated using a fixed water table. These flow fields can also be used for a rising water table case in the future. A water-rise situation can be handled by simply moving the water table up to a new elevation.

A total of six unsaturated zone flow fields for future climates (monq_lA, monq_mA, monq_uA, glaq_lA, glaq_mA, and glaq_uA) (BSC 2003b, Sections 6.6.3 and 7.11) are converted to account for a higher future water table. The six new flow fields are extracted for a rising-water-table case (BSC 2004a) in the future by vertically transecting the six flow fields with the current water table at the new water table elevation of 850 m.

Truncated steady-state unsaturated zone flow fields are expected to represent actual flow fields well. Representation of the unsaturated zone flow fields with a higher water table in the absence of direct hydrologic data is justified through considering the fundamentals in model formulation (i.e., the mathematical model of the Richards equation, or more specifically, Darcy's law for description of unsaturated zone flow under a future high water table condition) (BSC 2004b, Sections 6.6.3 and 7.11).

The impact of a future increase in the water table is limited mainly to the lower part of the CHn units, below the repository horizon. The water table boundary is handled as a sink term in the unsaturated zone flow model. Near or at the future elevated water table, which is within the model domain of the unsaturated zone flow model, unsaturated zone flow is vertically dominant. The flow is determined primarily by the upstream or upper-layer conditions in the unsaturated zone flow model. According to Darcy's law, in particular, the vertical flow is decided by two factors: hydraulic conductivity and hydraulic gradient. Since the vertical hydraulic gradient is

dominated by a constant gravity term and the hydraulic conductivity is upstream-weighted in the model, the change in a downstream location is considered to have only a small effect on its upstream flow. Therefore, inserting a future water table boundary into the current unsaturated zone flow model will provide a good approximation for modeling the future flow fields with an elevated water table.

In addition, certain lateral flows may exist at or near a future water table, caused by intersecting perched-water low-permeability zones. These intersected perched water or low-permeability zones will have liquid saturation near 100%, as predicted by the unsaturated zone flow model, approximately under the same conditions needed for representing a future water table boundary. Therefore, truncated flow fields at a future, higher water table, using the current unsaturated zone flow fields, will provide a reasonable representation for unsaturated zone flow fields under future climates for both vertical and lateral flow components (BSC 2004b, Section 7.11).

B.4.3 Model Calibration against Hydrologic Data

The field data used in the three-dimensional unsaturated zone flow model calibration include matrix liquid saturation, matrix water-potential data, and perched-water elevations, as observed from boreholes (BSC 2003b, Section 6.2.1). Table B-5 shows the types of data from boreholes used in the calibration, and their locations are shown in Figure B-2. There is an abundance of borehole saturation data (from seven boreholes), sufficient to calibrate and validate the unsaturated zone flow model to support the flow modeling for the region below the repository in the unsaturated zone; however, there are insufficient data (from three boreholes) for water-potential measurement (Tables B-2 and B-5) (BSC 2003b, Table 6.2-1, Section 6.2.1). Moreover, the existing borehole water-potential data do not cover depths from the repository horizon to the top of CHn units. In the whole span of the repository level, the TSw units have the only available water-potential data collected locally for a few hundred meters from the entrance at the ECRB Cross-Drift.

Table B-5. Borehole Data Used for Three-Dimensional Flow Model Calibration

Borehole	Matrix Liquid Saturation (core)	Matrix Liquid Water Potential	Perched Water Elevation (masl)
USW NRG-7a	✓		✓
USW SD-6	✓	✓	
USW SD-7	✓		✓
USW SD-9	✓		✓
UE-25 SD-12	✓	✓	✓
USW UZ-14	✓		✓
UE-25 UZ#16	✓		
USW WT-24		✓	✓
USW G-2			✓

Source: BSC 2003b, Table 6.2-1 (modified).

B.4.3.1 Perched Water

Perched water has been encountered in a number of boreholes at Yucca Mountain, including USW UZ-14, USW SD-7, USW SD-9, UE-25 SD-12, USW NRG-7a, USW G-2, and USW WT-24 (BSC 2003b, Table 6.2-1, Section 6.2.2.2). These perched waters occur below the repository horizon and are found to be associated with low-permeability zeolites in the CHn or the densely welded basal vitrophyre (Tptpv3, Table B-1) of the TSw unit. Perched-water bodies in the vicinity of the ESF north ramp (near boreholes USW UZ-14, USW SD-9, USW NRG-7a, USW G-2, and UE-25 WT#24) are observed to occur above the base of the TSw, underlain by a zone of low-permeability zeolitized rock. The perched-water bodies in this northern area of the repository may be interconnected. However, the perched-water zones at boreholes USW SD-7 and UE-25 SD-12 are considered as local, isolated bodies.

A permeability-barrier water-perching model has been developed in the unsaturated zone flow model, in which perched waters were calibrated to match perched-water occurrences as observed at the site. Subsequently, the calibrated perched water was used to investigate the effects of flow-through and bypassing of perched bodies on tracer transport (BSC 2003b, Section 6.2).

Figure B-1 illustrates the conceptual model that characterizes potential lateral flow in the PTn units and the effects of faults and perched water on the unsaturated zone system. Perched water may occur where percolation flux exceeds the capacity of the geologic media to transmit vertical flux in the unsaturated zone. Possible mechanisms of water perching in the unsaturated zone may be permeability or capillary barrier effects at faults, or a combination of both.

In this water-perching conceptual model, both vertical and lateral water movements in the vicinity of the perched zones are considered to be controlled mainly by the fracture and matrix permeability distribution in these perched-water areas. The major aspects of the permeability-barrier conceptual model are: (1) no large-scale vertically connected potentially fluid-conducting fractures transect the underlying low-permeability units; (2) both vertical and horizontal permeabilities within and below the perched-water zone are small compared with permeabilities outside perching zones; and (3) sufficient percolation flux (greater than 1 mm/yr) exists locally. A permeability-barrier conceptual model for perched-water occurrence has been used in the unsaturated zone flow modeling studies since 1996 (Wu et al. 1999).

In the perched water model, rock properties are locally adjusted in several grid layers of the lower basal vitrophyre in the TSw units and upper zeolites in the CHn unit. The adjustment of the parameters for the modeling of perched water is detailed in *UZ Flow Models and Submodels* (BSC 2003b, Section 6.2.3). The unsaturated zone flow model reproduces the occurrences of perched water location well (Figures B-6 to B-8).

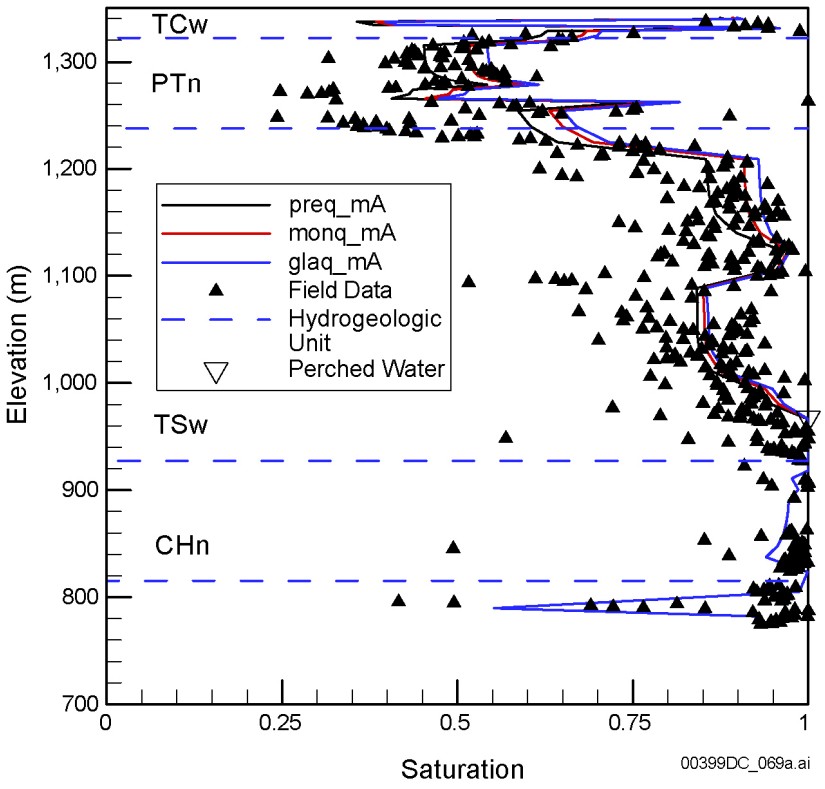

Source: BSC 2003b, Figure 6.2-2.

NOTE: The uppercase letter A stands for the base-case model property set; the lowercase letter m (before the uppercase letter A) stands for mean infiltration scenario.

Figure B-6. Comparison of Simulated and Observed Matrix Liquid Saturations and Perched-Water Elevations for Borehole USW UZ-14, Using the Results of the Simulations with Three Mean Infiltration Rates

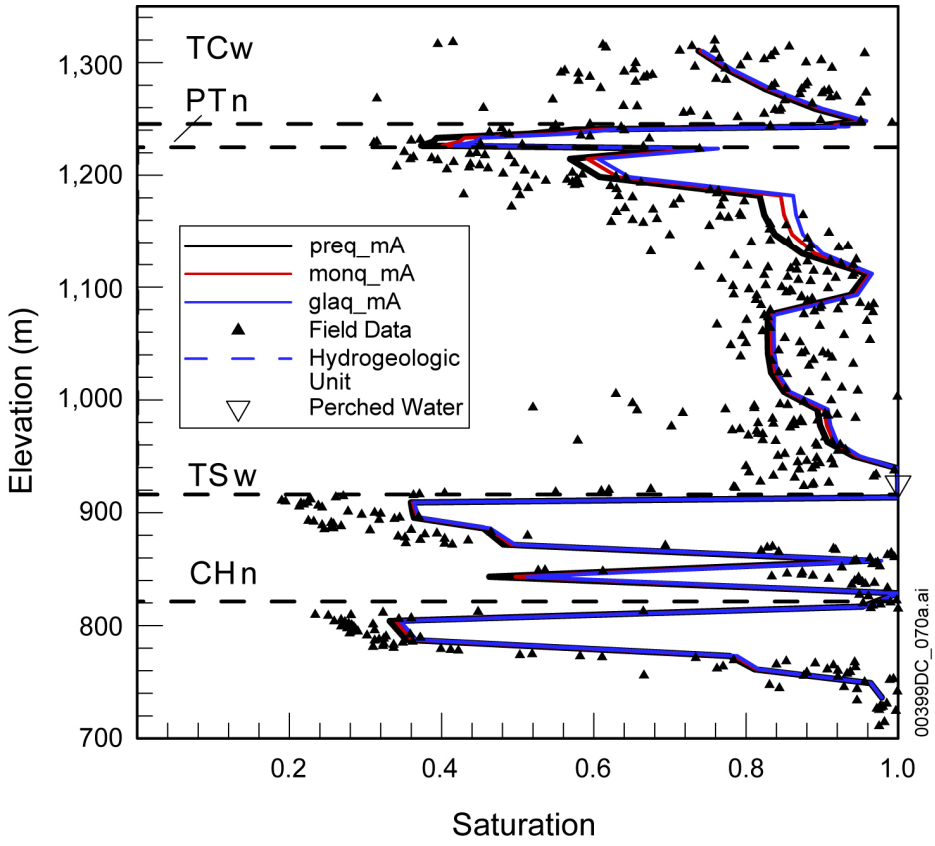

Source: BSC 2003b, Figure 6.2-3.

NOTE: The uppercase letter A stands for the base-case model property set; the lowercase letter m (before the uppercase letter A) stands for mean infiltration scenario.

Figure B-7. Comparison of Simulated and Observed Matrix Liquid Saturations and Perched-Water Elevations for Borehole UE-25 SD-12, Using the Results of the Simulations with Three Mean Infiltration Rates

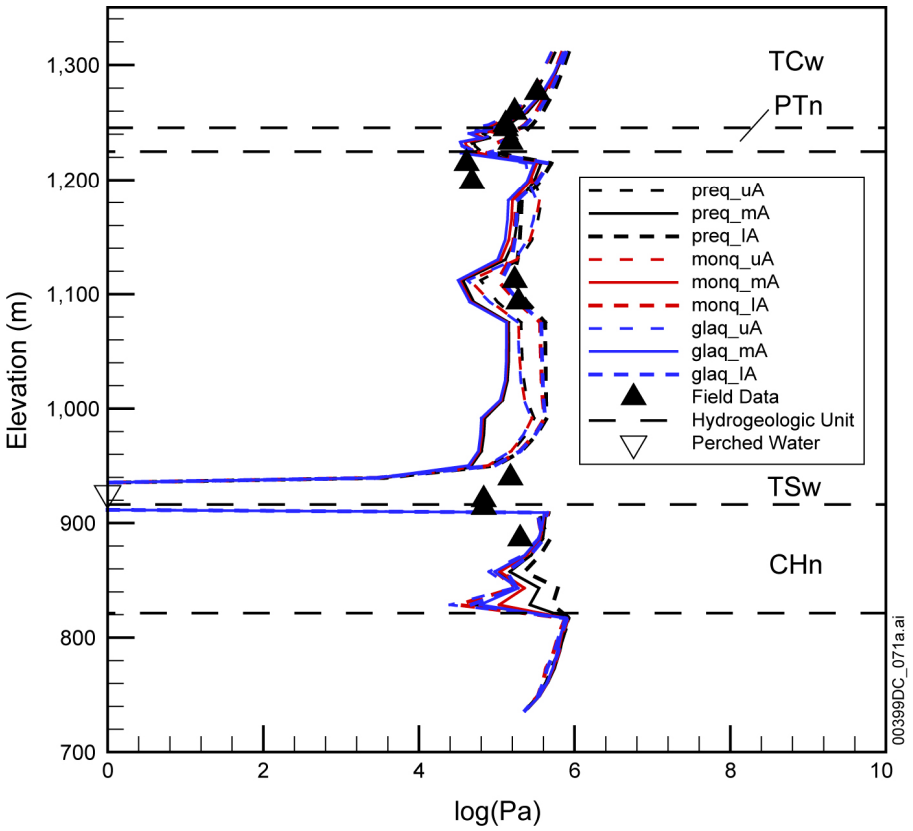

Source: BSC 2003b, Figure 6.2-4.

NOTE: The uppercase letter A stands for the base-case model property set; the lowercase letter l (before the uppercase A) stands for lower-bound infiltration, m for mean infiltration, and u for the upper bound-infiltration scenario.

Figure B-8. Comparison of Simulated and Averaged Observed Water Potentials and Perched-Water Elevations for Borehole UE-25 SD-12, Using the Results of the Simulations with Three Mean Infiltration Rates

B.4.3.2 Matrix Saturation and Water Potential Data

In the unsaturated zone flow model, simulations of the base case flow models are checked against observed saturation, water potential, and perched-water data. Model results show reasonable matches with the observed hydrologic data. Only a few of these comparisons are shown in the unsaturated zone flow model (BSC 2003b). Specifically, boreholes USW UZ-14 and UE-25 SD-12 are selected to show the match between observed and modeled vertical-saturation profiles and perched-water locations for simulations with perched-water occurrences (Figures B-6 to B-8).

B.4.4 Temperature Data

The analyses of temperature data provide another independent examination of percolation fluxes simulated by the unsaturated zone flow model. This is because the ambient temperature distribution within the unsaturated zone is related to percolation fluxes or infiltration rates (Bodvarsson et al. 2003). By matching borehole temperature measurements, the

thermal-hydrologic model helps to constrain infiltration rate ranges as well as fracture–matrix parameter values (BSC 2003b, Section 6.3.4).

Rather finely-sampled temperature profiles both above and below the repository (BSC 2003b, Table 6.3-1 and Section 7.7) were made for the three-dimensional thermal model. Specifically, qualified temperature measurements were made from the following nine boreholes:

- USW NRG-6
- USW NRG-7a
- UE-25 SD-12
- UE-25 UZ#5
- UE-25 UZ#7a
- UE-25 UZ#4
- USW H-5
- USW H-4
- UE-25 WT#18.

Boreholes UE-25 UZ#4 and UE-25 UZ#5 are so close to each other that they fall into the same grid column. Therefore, only UE-25 UZ#5 is used for calibrations. The locations of boreholes are spatially representative (Figure B-9) (BSC 2003b, Figure 6.3-1).

Figure B-10 (BSC 2003b, Figure 6.3-2) shows the final model calibrated results and measured temperature profiles in five temperature boreholes. The figure shows a good match between measured and simulated temperatures using the specified boundary conditions and the present-day, mean infiltration rate. Near the ground surface in the five boreholes, observed temperatures show significant seasonal variations. However, these seasonal changes in surface temperature have little impact on steady-state heat flow or temperature profiles in the deeper (more than 20 m) unsaturated zone.

In addition, the prediction of temperature is made at boreholes USW H-5, USW H-4, and UE-25 WT#18 (BSC 2003b, Section 7.7). These three boreholes penetrate the repository block and the entire unsaturated zone (see Figure B-9 for their locations) (BSC 2003b, Section 7.7). Comparisons of simulated and observed temperature profiles along these boreholes are shown in Figures B-11 to B-13, indicating a good match between the three-dimensional model prediction and observed data. Borehole USW H-5 is located close by the ECRB Cross-Drift, and Figures B-11 and B-12 show that the simulated temperatures differ from observed values by less than 1.5°C in all elevations. In borehole UE-25 WT#18 the simulated results again prove to be a reasonable match with field-measured data.

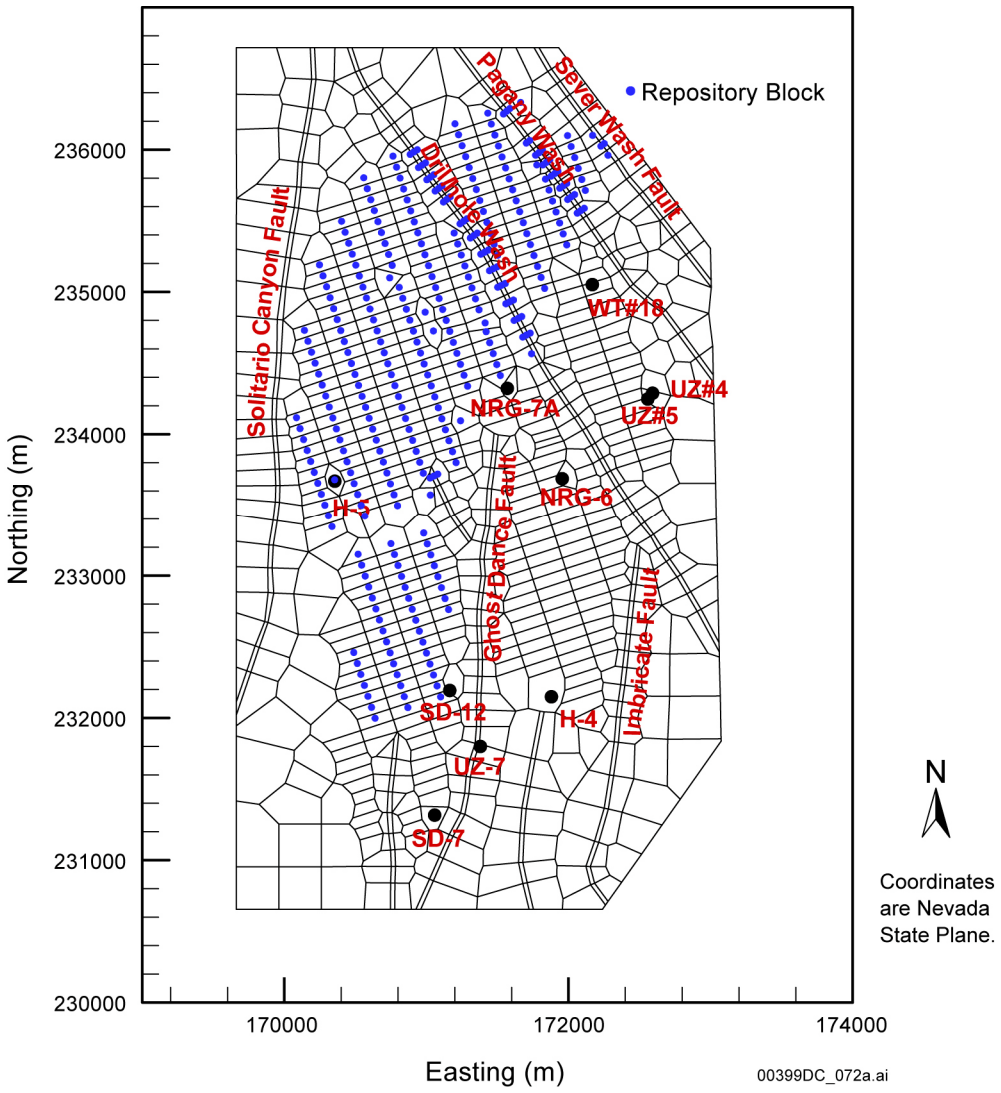

Source: BSC 2003b, Figure 6.3-1.

Figure B-9. Plan View of the Three-Dimensional Thermal Model Grid Showing the Model Domain, Faults Incorporated, Several Borehole Locations, and Thermal-Hydrologic Model Boundaries

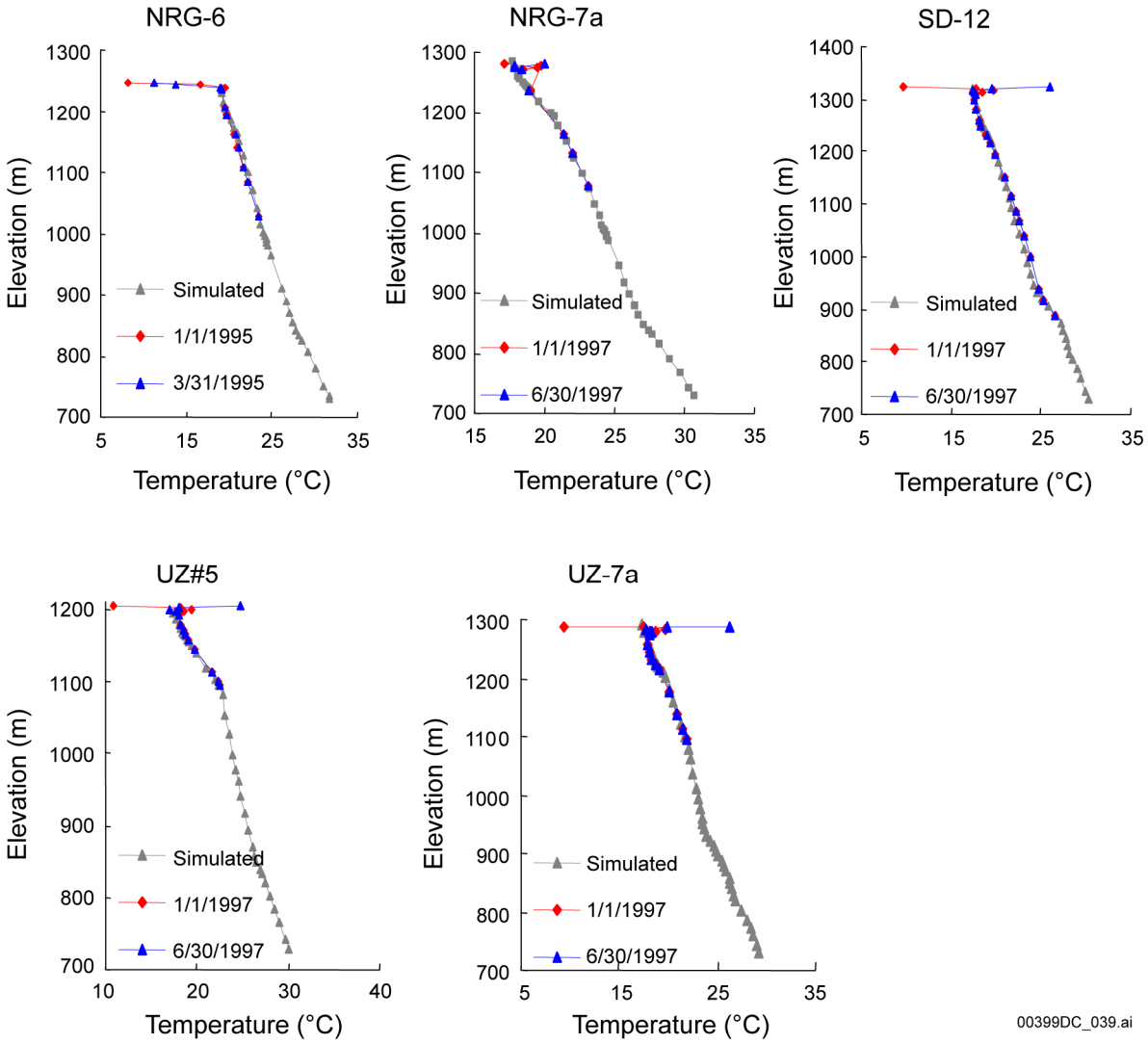

Source: BSC 2003b, Figure 6.3-2.

Figure B-10. Comparisons between Measured and Modeled Ambient Temperature Profiles for the Five Boreholes under the Present-Day Mean Infiltration Rate

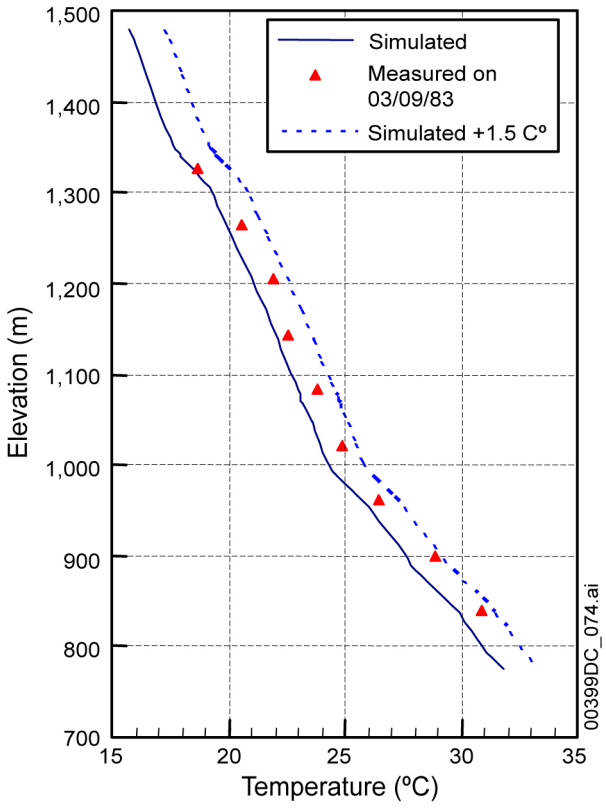

Source: BSC 2003b, Figure 7.7-1.

Figure B-11. Comparison of Simulated and Observed Temperature Profiles for Borehole USW H-5

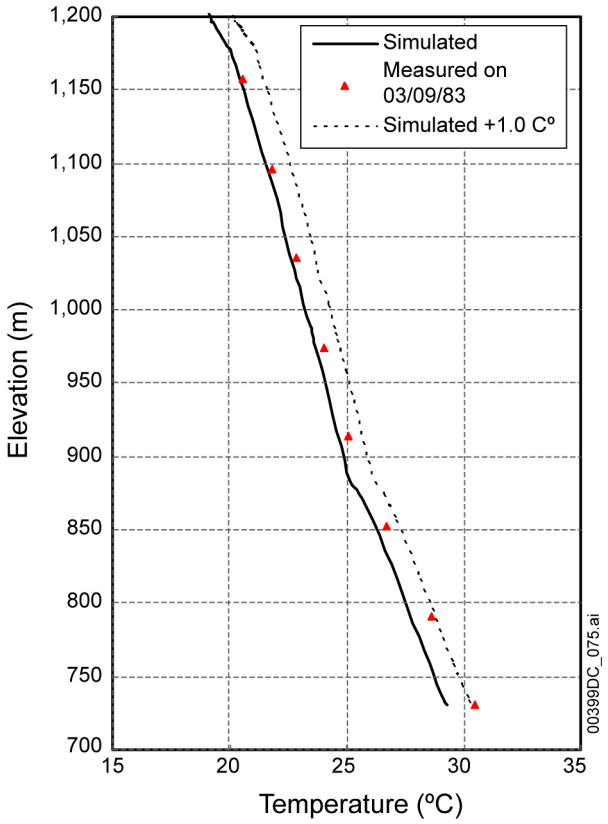

Source: BSC 2003b, Figure 7.7-2.

Figure B-12. Comparison of Simulated and Observed Temperature Profiles for Borehole USW H-4

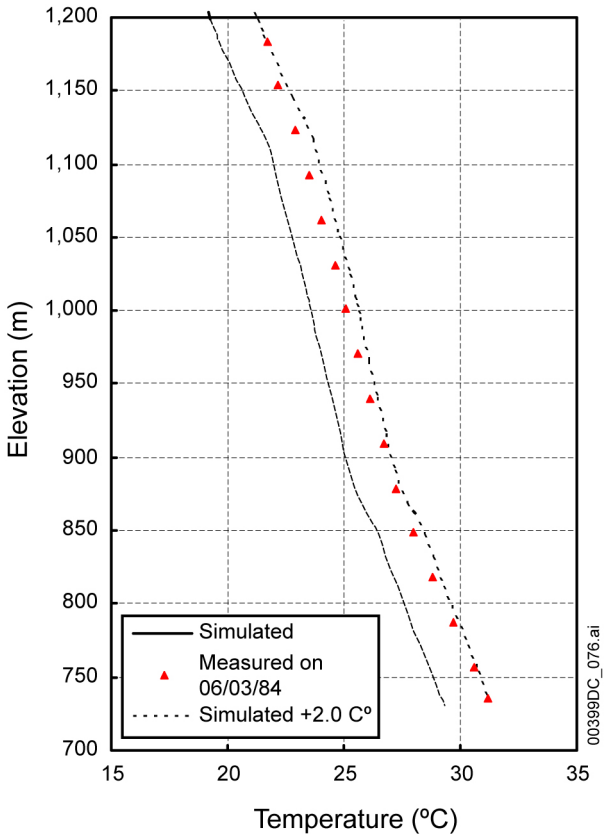

Source: BSC 2003b, Figure 7.7-3.

Figure B-13. Comparison of Simulated and Observed Temperature Profiles for Borehole UE-25 WT#18

B.4.5 Geochemical Data

Geochemical data, including chloride and strontium concentrations and calcite abundance data, were used in the calibration and validation of the unsaturated zone flow model. Available strontium concentration data are from boreholes USW SD-9 and UE-25 SD-12 and the ECRB Cross-Drift (BSC 2003b, Section 7.10). Calcite data are found in boreholes USW WT-24, USW SD-6, and USW G-2 (BSC 2003b, Section 7.9). Calcite abundance data for borehole USW SD-6 were not available at the time of unsaturated zone flow modeling; modeling of calcite deposition for USW SD-6 was not performed (BSC 2003b, Section 7.9.5.3).

The chloride data are relatively limited, especially within the TSw and TCw units. Chloride pore-water data were collected from the ESF, ECRB Cross-Drift, and 11 boreholes. However, these boreholes usually do not have data within the TSw layers. Therefore, these boreholes usually do not have data for locations around the repository level. In the ESF, chloride data are concentrated in three narrow locations, with the rest of the locations blank. The chloride pore-water data for TSw layers were mainly collected from the ECRB Cross-Drift and are considered locally distributed in terms of the span of the repository. Chloride data are generally limited for the CHn units.

B.4.5.1 Pore-Water Chloride Data

Chloride transport processes were also modeled in the unsaturated zone flow model analysis. The transport modeling of the conservative natural tracer chloride in the unsaturated zone is based on the conceptual model that the chloride flux as boundary input is determined from the precipitation flux and the chloride concentration in the precipitation (BSC 2003b, Section 6.5.1.2).

Chloride concentrations used in modeling were measured from pore waters extracted from field samples. These samples were collected from the ESF, the ECRB Cross-Drift, and a set of 11 surface-based boreholes. The boreholes are USW SD-6, USW SD-7, USW SD-9, UE-25 SD-12, USW NRG-6, USW NRG-7a, USW UZ-14, UE-25 UZ#16, UE-25 UZ#7a, USW WT-24, and USW G-2 (BSC 2003b, Table 6.5-1 Section 6.5) (see Figure B-2 for their locations).

Even with all the various sources for pore-water chloride data, limitations on this data exist. Generally, boreholes do not have pore-water data from the TSw and TCw units, and rarely have an evenly distributed or complete data profile. Early chloride data collected from the ECRB Cross-Drift were available for the 2001 unsaturated zone flow model (BSC 2001b). Another set of chloride (of another composition) data was recently collected from the ECRB Cross-Drift, which was not available at the time of the 2003 unsaturated zone flow model (BSC 2003b). However, these latest ECRB chloride data are considered to be somewhat redundant because they were from a repeated sampling over the region that had been covered by the previously available chloride data. The amount of the ESF chloride data is small and has limited spatial representation. The available data are restricted to three local segments (located 700 to 1,100, 3,600 to 3,700, and 6,600 to 7,500 m from the north portal entrance).

Generally, the 11 boreholes do not have data covering the TSw and TCw layers. Boreholes USW NRG-6 and UE-25 UZ#7a have no chloride below the repository at all. The limited data for the TSw and TCw welded tuff units historically result from the difficulty in obtaining enough pore waters for chemical analysis (owing to the low water content in the nonwelded tuffs).

For the CHn layers below the repository, chloride data were unevenly distributed, and most of those boreholes that have some chloride data in the CHn layers usually do not have any chloride data in other layers.

Figures B-14 and B–15 show the results of chloride modeling in boreholes USW NRG-6 and USW UZ-14 (BSC 2003b, Table 6.5.2, Section 6.5.1.2). These figures plot the chloride profiles of present day infiltration rates of mean infiltration with lower and upper bounds. The results demonstrate that the mean infiltration case has the closest match between the calculated concentrations and the field-measured chloride data. The upper-bound case shows a moderate match; the lower-bound case shows the least match.

A comparison between the base-case model and the alternative model results for borehole USW SD-9 is plotted in Figure B-16, and that for the ECRB Cross-Drift is given in Figure B-17 and Table B-6. In base case A, the unsaturated zone flow model uses the property set for the PTn that would favor lateral diversion of flow. In the alternative model B, the unsaturated zone flow

model uses a different property set for the PTn, one that does not favor large-scale lateral diversion (BSC 2003b, Table 6.5-2).

Table B-6. Comparison of Simulated Pore Water Chloride Concentrations with Measured Chloride Concentrations at the Enhanced Characterization of the Repository Block

RMS[a]	Lower-Bound Infiltration	Mean Infiltration	Upper-Bound Infiltration
Base Case Model (A)	120.0	18.0	24.5
Alternative Model (B)	340.8	183.6	31.4

Source: DTNs: LA0002JF12213U.002; LB0303CLINFL3D.001.

NOTE: [a]Root mean square of calculated concentrations with gridblock averaged measured concentrations. $\mathrm{RMS} = [\frac{1}{n-1}\sum_{i=1}^{n}(c-\bar{o})^2]^{1/2}$, where *c* is the simulated concentration and $\bar{O}$ is the gridblock-averaged measured concentration, *n* is the number of concentration data (gridblock averaged) in the calculation (*n* = 18).

Comparative studies of chloride distributions using the base case and alternative flow fields indicate generally that the base case flow field simulation results provide an overall better match with the observed chloride data. Statistics of the ECRB profile shows that the base-case models consistently yield closer matches than the alternative models for all the infiltration scenarios (Table B-6). The ECRB is considered to be influenced by the effect of the flow pattern in the PTn units, because the ECRB runs transverse to the mountain ridge and is located immediately below the PTn units. The main difference between the base-case and alternative flow fields is whether there is large- or small-scale lateral flow within the PTn units, while the base-case flow fields predict relatively large lateral diversion in general (BSC 2003b, Sections 6.2.5 and 6.6.3). Model calibration results with chloride data further reveal that large lateral diversion may exist in the PTn units. Therefore, pore-water chloride may provide key evidence for understanding the flow pattern in the PTn units, which has had a direct impact on chloride transport and distributions (BSC 2003b, Section 6.5.2.2).

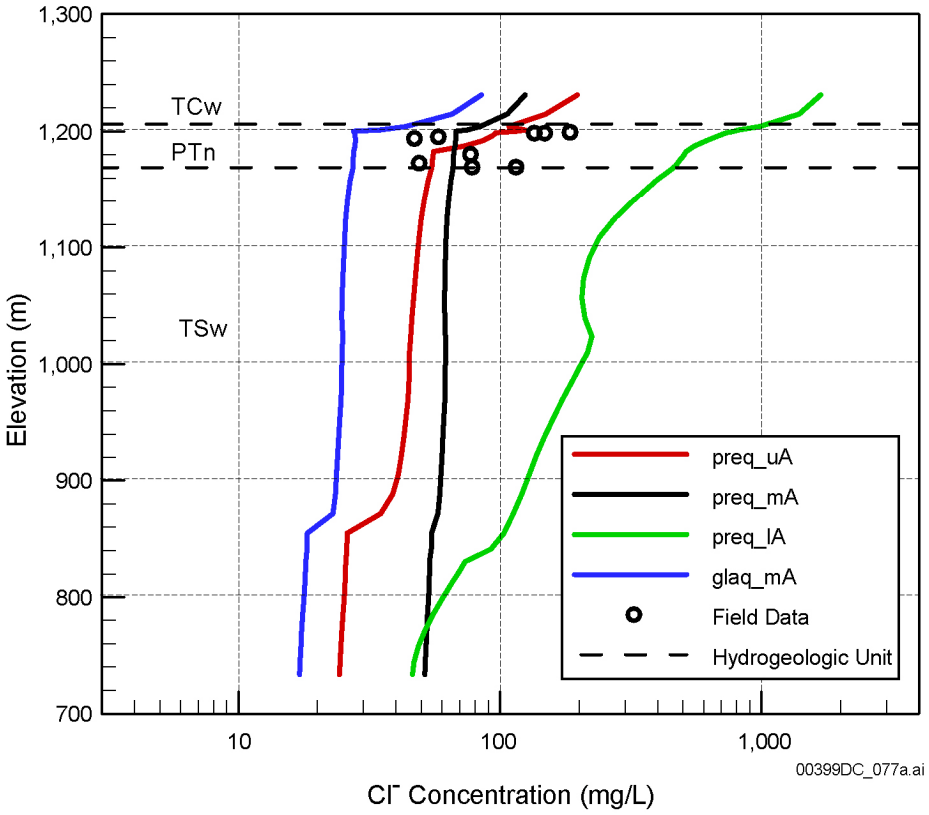

Source: BSC 2003b, Figure 6.5-1.

NOTE: The uppercase letter A stands for the base-case model property set, the lowercase letter l (before the uppercase A) for lower-bound infiltration, m for mean infiltration, and u for upper-bound infiltration scenario.

Figure B-14. Chloride Concentration Profiles at Borehole USW NRG-6 for Present Recharge with Mean, Upper, and Lower Bounds and Glacial Recharge

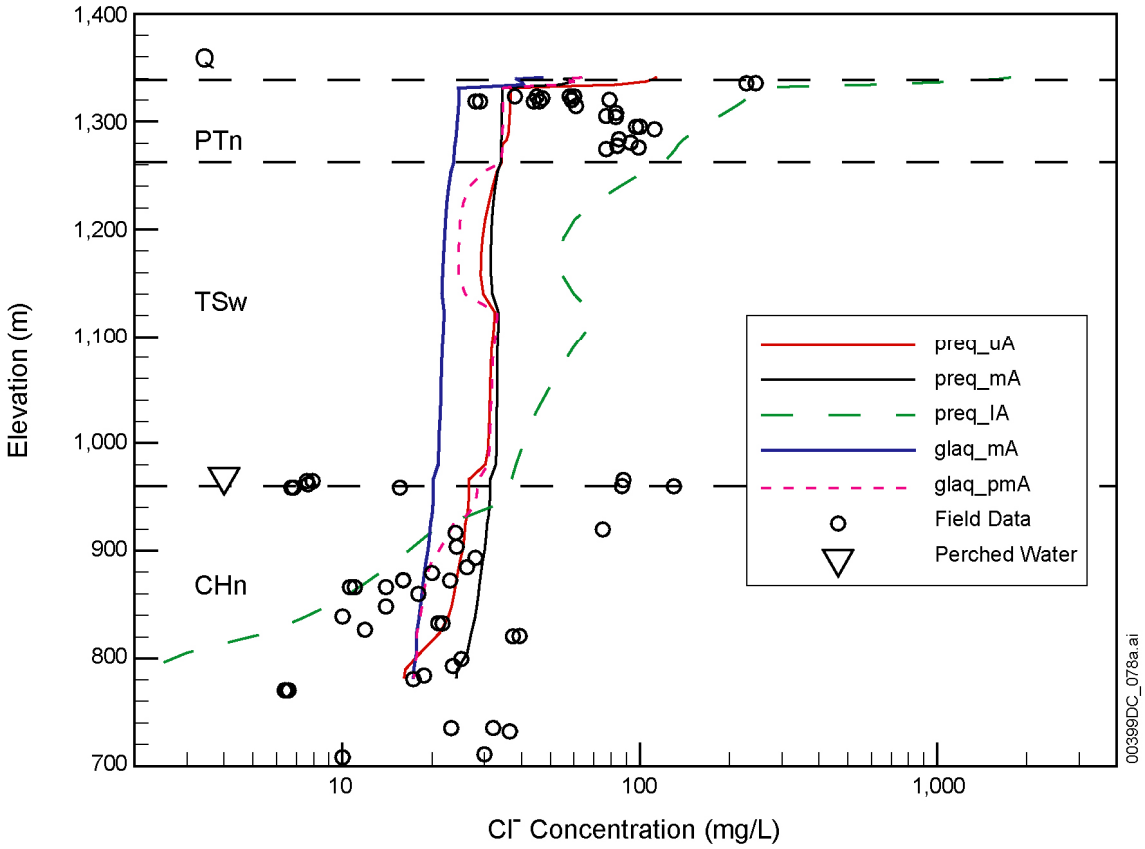

Source: BSC 2003b, Figure 6.5-2.

NOTE: The uppercase letter A stands for the base-case model property set, the lowercase letter l (before the uppercase A) for lower-bound infiltration, m for mean infiltration, and u for upper-bound infiltration scenario.

Figure B-15. Chloride Concentration Profiles at Borehole USW UZ-14 for Present Recharge with Mean, Upper, and Lower Bounds and Glacial Recharges

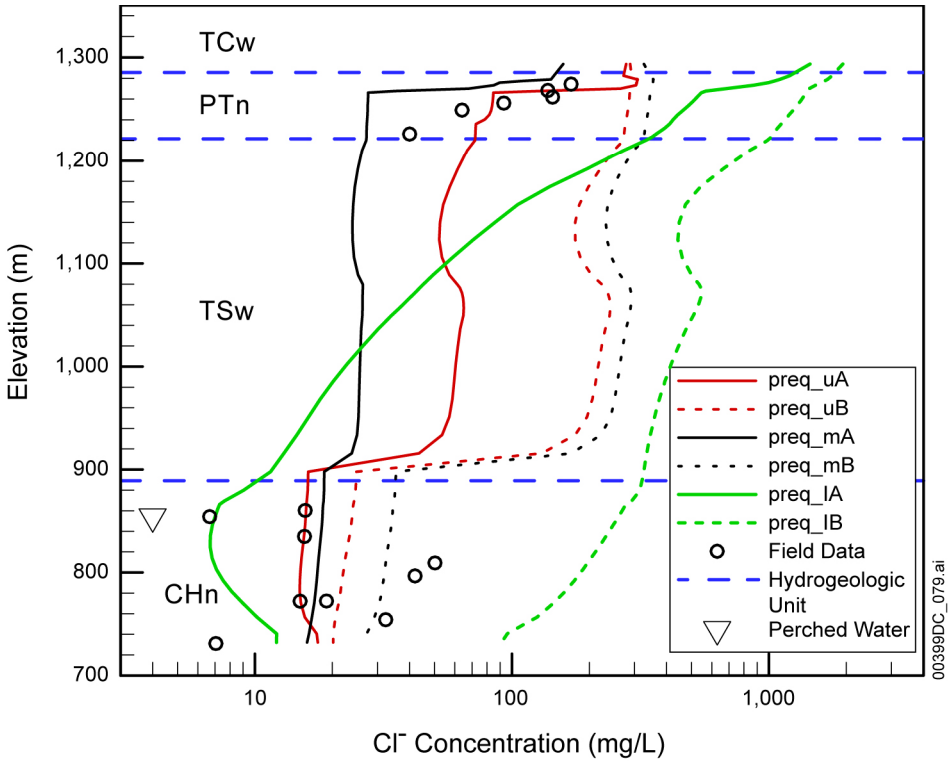

Source: BSC 2003b, Figure 6.5-3.

NOTE: The uppercase letter A stands for the base-case model property set, the uppercase letter B for the alternative model, the lowercase letter l (before the uppercase A or B) for lower-bound infiltration, m for mean infiltration, and u for upper-bound infiltration scenario.

Figure B-16. Chloride Concentration Profiles at Borehole USW SD-9 for Present Recharge with Mean, Upper, and Lower Bounds and Glacial Recharge

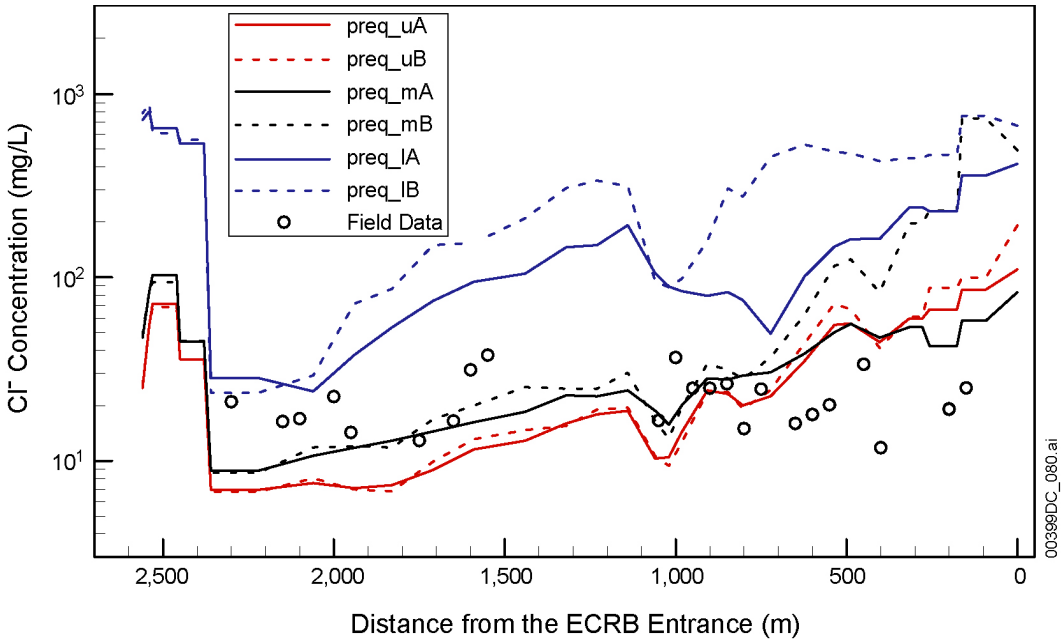

Source: BSC 2003b, Figure 6.5-4.

NOTE: The uppercase letter A stands for the base-case model property set, the uppercase letter B for the alternative model, the lowercase letter l (before the uppercase A or B) for lower-bound infiltration, m for mean infiltration, and u for upper-bound infiltration scenario.

Figure B-17. Chloride Concentration Profiles at the ECRB Cross-Drift for Present Recharge with Mean, Upper, and Lower Bounds

B.4.5.2 Strontium Concentrations

The modeling of strontium in the unsaturated zone assumes that the infiltration at the surface is the only source of strontium input (BSC 2003b, Section 7.10). Strontium data are measured values for pore salts extracted (by leaching) from surface-based boreholes USW SD-9 and UE-25 SD-12, as well as from perched waters and pore waters obtained by ultracentrifugation of core samples from the ECRB Cross-Drift (BSC 2003b, Section 7.10.3).

In Figure B-18, modeled strontium concentrations are compared to these measured values for boreholes USW SD-9 and UE-25 SD-12. Modeling results are shown to match the observed data well. Measured concentrations in the unsaturated zone above the perched water show a range of concentrations from about 0.1 to 2 mg/L, with perched-water concentrations (and pore-water concentrations at a similar depth) closer to 0.01 mg/L. This sharp reduction in strontium concentrations is greater than the equivalent drop in chloride concentrations in the perched-water bodies and is consistent with ion exchange in zeolitic rocks. The steady-state modeled concentrations above the perched water are very close to the mean values in boreholes USW SD-9 and UE-25 SD-12. Where perched-water samples were collected in USW SD-9, the model results capture the drop in concentration quite closely. In UE-25 SD-12, the measured and modeled concentrations below 900 m exhibit a reversal to higher concentrations. This reversal is consistent with lateral flow in the vitric units, rather than simple vertical flow through the zeolitic units that would result in consistently low concentrations below them.

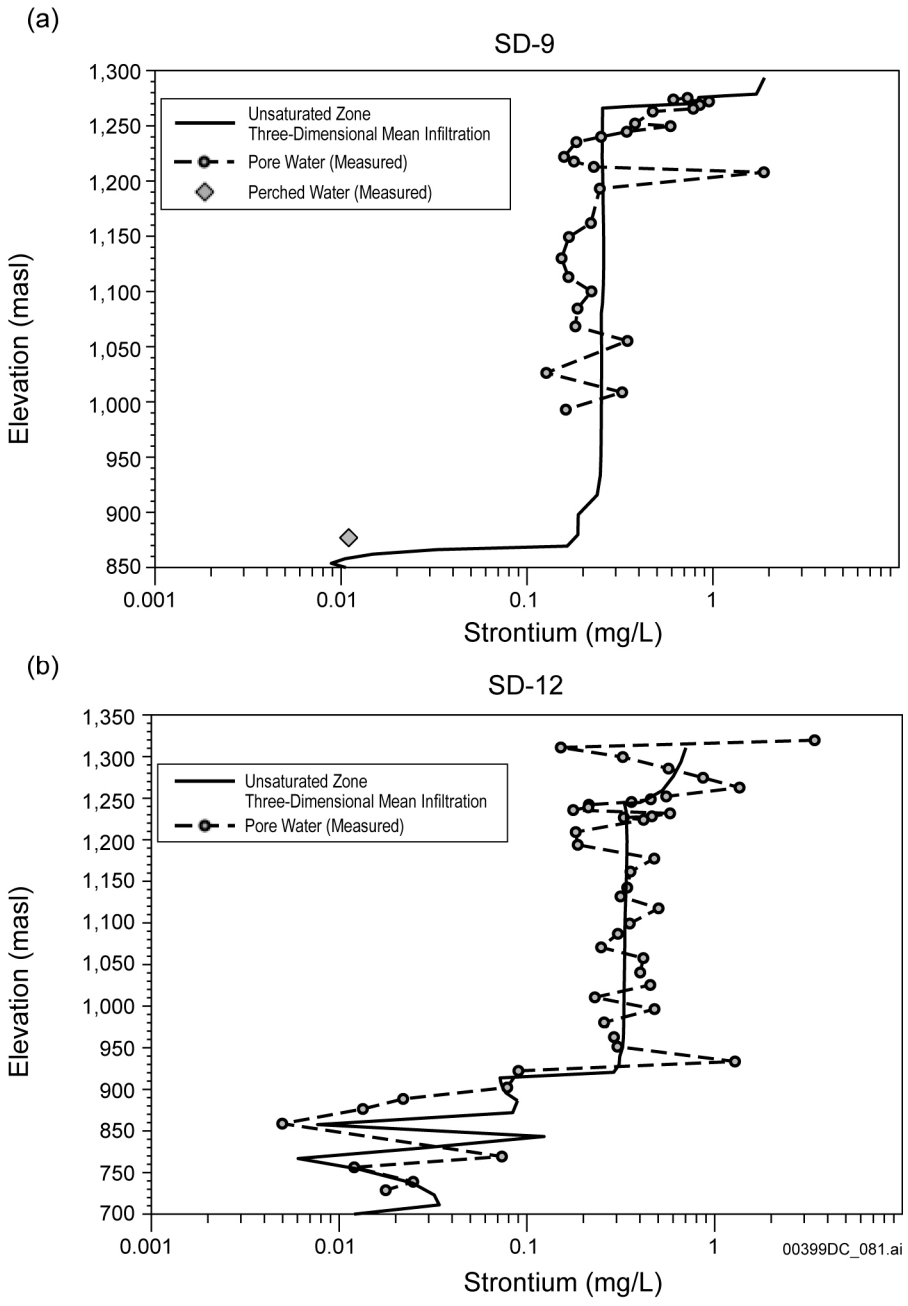

Source: BSC 2003b, Figure 7.10-1.

Figure B-18. Comparison of Measured and Modeled Strontium Concentrations as a Function of Elevation for the Surface-Based Boreholes (a) USW SD-9 and (b) UE-25 SD-12

B.4.5.3 Calcite Modeling

Analyses of precipitated calcite data in the unsaturated zone also provide information to constrain the infiltration flux. The calcium concentration and CO_2 partial pressure in percolating water are the major factors controlling the abundances of calcite and its stability. The primary driving force for calcite precipitation from percolating waters in the unsaturated zone is its

decreasing solubility with increasing temperature; calcite precipitates as water flows downward because of the geothermal gradient (BSC 2003b, Section 7.9.2).

One-dimensional modeling was performed for calcite deposition. Results were compared mainly with available measured calcite abundance from a deep borehole (UE-25 WT#24), with referencing to calcite data from USW SD-6 and USW G-2 (BSC 2003b, Section 7.9). Simulations were performed using three infiltration rates, a base case rate of 5.92 mm/yr (BSC 2003d), and bounding rates of 2 mm/yr and 20 mm/yr. Over a range of 2 to 20 mm/yr infiltration rates, the simulated calcite abundances generally fall within the range of calcite observed in the field (Figure B-19) (BSC 2003b, Section 7.9.5.1, Figure 7.9-3), which satisfies the validation criterion. The modeled calcite abundances generally increase with increasing infiltration rate (BSC 2003b, Section 7.9.6). Figure B-19 represents simulation results from a representative geochemical system that considers pH effect, CO_2 partial pressure, a broad assemblage of minerals (including all aluminosilicates and iron- and magnesium-bearing minerals), and aqueous species (BSC 2003b, Section 7.9.4.2, Table 7.9-2). The 20 mm/yr infiltration rate may be the upper bound for UE-25 WT#24 location, whereas the base case infiltration rate (5.92 mm/yr) used for the flow model gives the closest match to the data (BSC 2003b, Section 7.9.6). Modeling calcite deposition provides additional evidence for validation of the unsaturated zone flow model.

B.4.6 Compositions of Infiltration Waters in the Thermal-Hydrologic-Chemical Model

The amount of available data for infiltrating water has increased significantly since GEN 1.01 (Comment 106) was made. In the initial 2000 version of *Drift-Scale Coupled Processes (DST and THC Seepage) Models* (BSC 2003c, Section 6.2.2.1), the available data on infiltrating waters comprised three samples of one type of water (the HD-PERM samples), ultracentrifuged from core samples collected from the Tptpmn geologic unit in Alcove 5 near the Drift Scale Test. By the time of the 2003 revision of *Drift-Scale Coupled Processes (DST and THC Seepage) Models* (BSC 2003c), a series of pore-water samples had been collected (BSC 2003c, Section 6.2.2.1) from the following repository host units: the upper lithophysal zone (Tptpul), middle nonlithophysal zone (Tptpmn), and lower lithophysal zone (Tptpll). These samples were ultracentrifuged from core collected in the ECRB Cross-Drift and in boreholes USW UZ-14, USW SD-9, and USW NRG-7/7a (a total of 5 borehole pore-water samples from the TSw units). The compositions of these waters are shown on a Piper diagram in Figure B-20. For comparison, the figure also plots other water compositions, including perched water and pore water at similar depths (base of Tptpln) in borehole USW UZ-14, and groundwater from well J-13.

Possible choices of potential initial water compositions for the thermal-hydrologic-chemical seepage model span a wide range, with HD-PERM samples at one end (calcium-sulfate-chloride type) and groundwater from well J-13 at the other end (sodium-bicarbonate type) (Figure B-20).

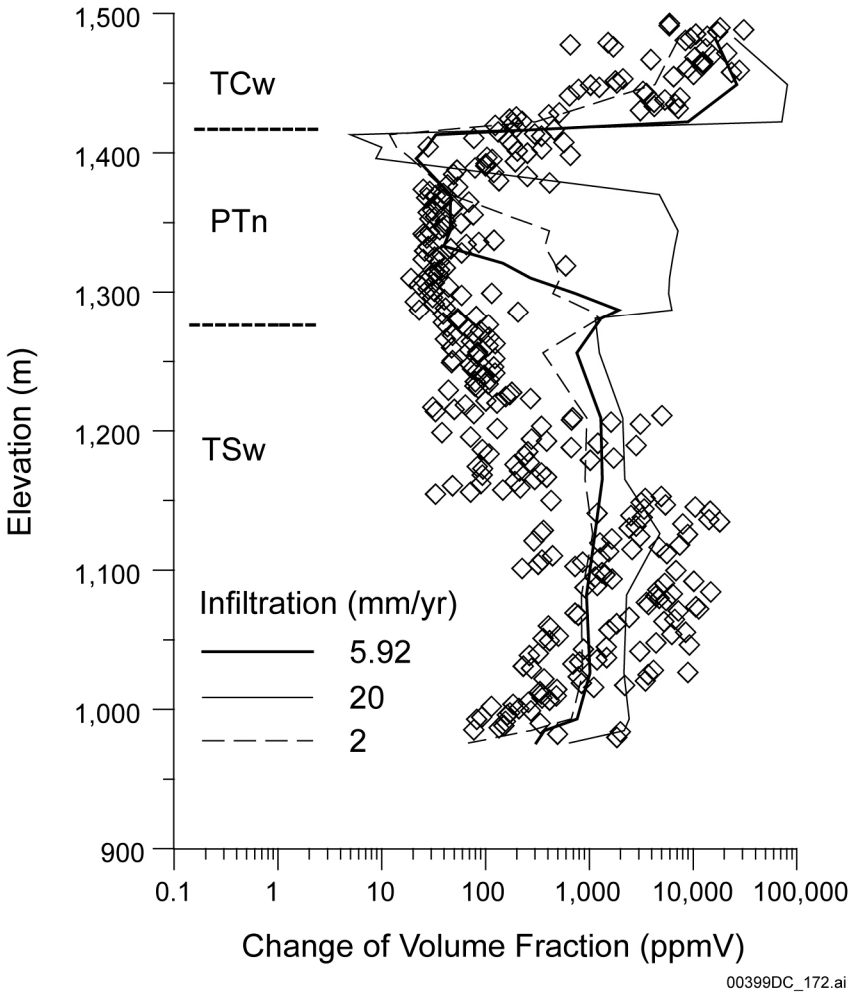

Source: BSC 2003b, Figure 7.9-3a.

Figure B-19. Simulated Total (Fracture plus Matrix) Calcite Abundances in Borehole USW WT-24 for Different Infiltration Rates after 10 Million Years

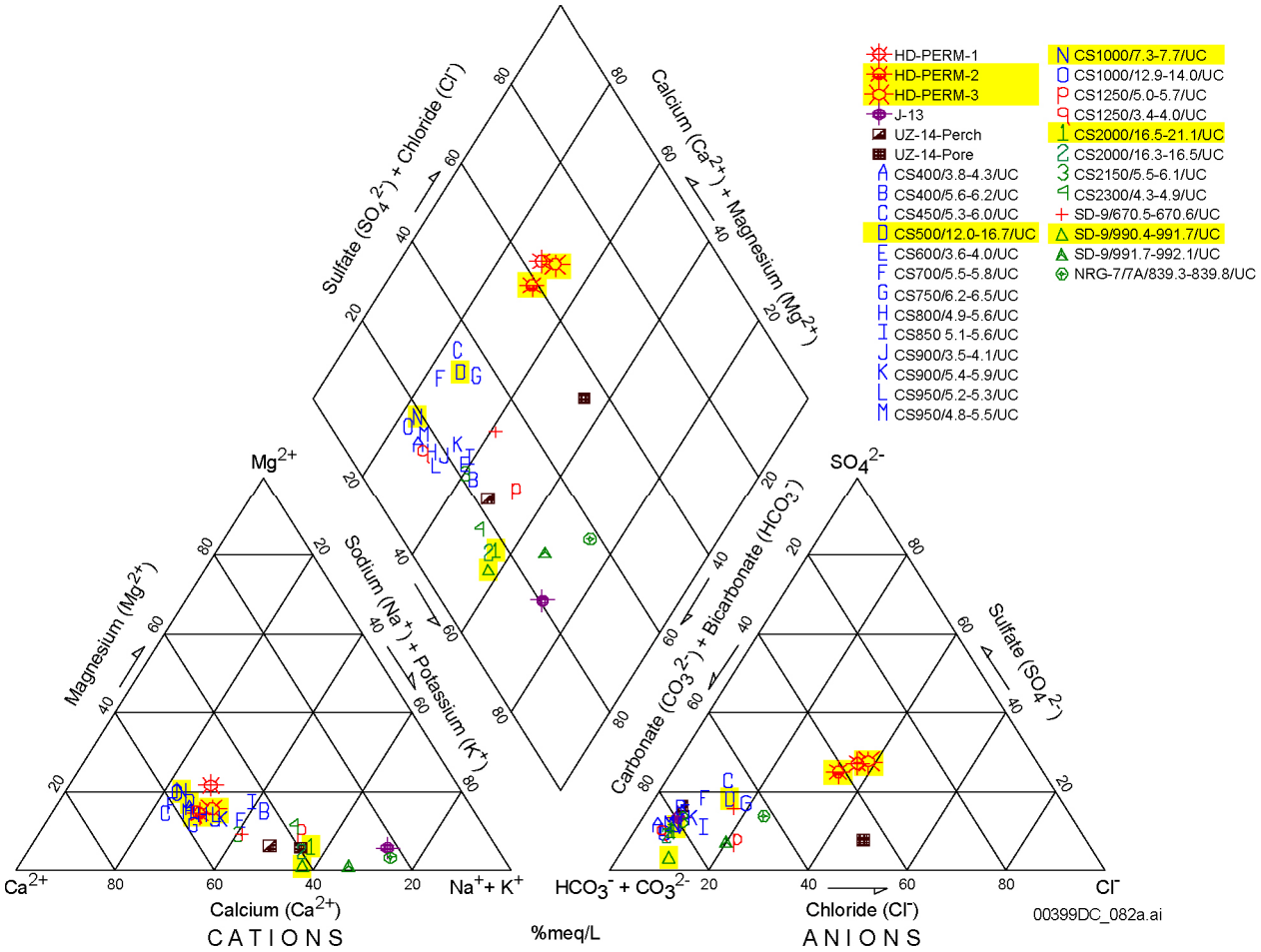

Source: BSC 2003c, Figure 6.2-4.

NOTE: Samples labeled HD-PERM are pore waters from the Tptpmn unit in Alcove 5 of the ESF. Samples IDs starting with CS represent pore waters from ECRB Cross-Drift and are listed in order of increasing distance (m) into the drift (down stratigraphy), with labels reflecting lithostratigraphic units as follows: Tptpul (capitals A-O), Tptpmn (lower case p-q), and Tptpll (numbers 1-4). Additional borehole interval information after each CS sample labeling is sample interval distances from borehole collar given in feet. CS is abbreviation for Construction Station, indicating distance along the ECRB Cross-Drift in meters. Sample IDs starting with USW SD-9 and USW NRG-7 represent pore waters from boreholes with the same names and show the sampling interval in feet from ground surface. The first USW SD-9 sample at 670 ft is from the base of the Tptpul, and the others are from the Tptpll. The USW NRG-7 sample is from the Tptpmn. Yellow-highlighted samples are those selected water types (W0 as ☼; W4 1; W5 N; W6 Δ; and W7 D; see following text).

Figure B-20. Piper Plot of Water Compositions from Repository Units

The following water compositions were selected, listed here with an assigned arbitrary identification (W0, W5, etc.), for the thermal-hydrologic-chemical seepage model:

W0: HD-PERM water, from the Tptpmn unit in Alcove 5.

W4: Sample CS-2000/16.5-21.1/UC, from the Tptpll lithostratigraphic unit in the ECRB Cross-Drift.

W5: Sample CS-1000/7.3-7.7/UC, from the base of the Tptpul lithostratigraphic unit in the ECRB Cross-Drift.

W6: Sample SD-9/990.4-991.7, from the Tptpll lithostratigraphic unit in borehole USW SD-9.

W7: Sample CS500/12.0-16.7, from the Tptpul lithostratigraphic unit in the ECRB Cross-Drift.

These five samples cover a significant portion of the spectrum of water types, and yet differ from one another in significant ways (Figure B-20). Water types W0, W4 (or W6), and W5 occupy the higher ends of sulfate/chloride, calcium/magnesium, and sodium/potassium, respectively. W0 (the HD-PERM samples) plot higher than other pore waters on the diamond-shaped area in Figure B-20, bounding the range of compositions in the calcium-sulfate-chloride field.

W4 and W6 exhibit the lowest (Ca+Mg)/(Na+K) ratio of the ECRB Cross-Drift samples. W4 also contains a higher fluoride concentration than the other samples and exhibits better charge balance than other samples of similar composition. W6 contains a higher nitrate concentration compared to most other samples and exhibits a better charge balance than W4. The W7 sample plots between Water W0 (the HD-PERM waters) and Water W5 on Figure B-20, further capturing the variability of water compositions in the upper part of the figure.

These five types of waters were chosen, with preference given to actual pore waters from unsaturated regions within or above the repository units and exclusion of waters from the perched water zone and saturated zone (BSC 2003c, Section 6.2.2.1). This is based on a number of considerations. The perched waters below the repository are generally much more dilute than unsaturated zone pore waters because isotopic compositions ($^{36}Cl/Cl$, $^{18}O/^{16}O$, D/H, ^{14}C) and chloride concentrations suggest that the perched waters have a large proportion of late Pleistocene-early Holocene water (Levy et al. 1997, p. 906; Sonnenthal and Bodvarsson 1999, pp. 107 and 108). The saturated zone water is also more dilute than pore waters, and neither saturated nor perched water reflect calculated CO_2 partial pressures consistent with CO_2 concentrations in gas measured in the unsaturated zone in repository units. The saturated zone and perched-water compositions are therefore deemed poor candidates as initial-input water compositions for the thermal-hydrologic-chemical seepage model.

The choice of input water composition also must take into account the natural variability of pore-water compositions in the repository units, as illustrated in Figure B-20. However, because these samples were mainly from the ECRB Cross-Drift, the spatial coverage of these data is too small to derive a probability of occurrence for any of these pore-water compositions.

The differences in the proportions (not absolute values) of cations and anions in analyzed waters have an important bearing on the types of residual brines that could develop upon evaporation and boiling due to thermal loading (BSC 2003h). Should these waters seep onto the surface of a hot waste package, knowledge of their end-brine composition is important to assess the likelihood and intensity of waste package corrosion (BSC 2004c). Therefore, the span of selected input water compositions could be used to check whether the selection has taken into account factors that influence the end-brine composition of these waters.

Evaporation can turn dilute groundwater into corrosive brine, and complete evaporation can result in the precipitation of hygroscopic salts (salts which have the ability to absorb water from the air). Among the concerns is the formation of potentially deleterious brines such as calcium (and magnesium) chloride rather than sodium chloride, or brines that are less hygroscopic. Factors such as composition plotting in the upper half of the diamond-shaped area of Figure B-20, together with low nitrate and sulfate concentrations relative to chloride, could be used to infer a higher likelihood of potentially deleterious brines developing.

As water evaporates from solution, dissolved solids concentrate until they become supersaturated with respect to a solid phase. If a solid phase is a binary salt and the normalities of the two reactants are not equal, the reactant having the lower normality will become depleted in solutions, while the reactant with higher normality will continue to concentrate. This mechanism is known as chemical divide. (Even if the normalities are close to each other, they will evolve quickly to differentiate themselves.)

Calcium chloride brines are more likely to form after calcite precipitation chemical divide if the total calcium concentration (in meq/L) exceeds the total aqueous carbonate concentration (in meq/L) in the initial water. Waters with such compositions would have a tendency to plot in the upper half of the diamond-shaped area in Figure B-20, although other waters may also plot in this area if their magnesium concentration were high relative to calcium. Other less hygroscopic salts are most likely formed from original waters if the nitrate and sulfate concentration in the original solution were elevated relative to chloride.

In summary, five types of infiltrating waters were chosen from the pore waters at or above the repository horizon. The samples were mainly from the ECRB Cross-Drift, and thus do not have sufficient spatial variation to warrant a probability analysis of their occurrences. J-13 water and UZ-14 pore water, although seemingly end-members of waters from the Yucca Mountain and the vicinity, were not included in the selections because their compositions contrasted with the pore waters in the repository horizon. However, this end-member type of water with very low chloride concentrations in the ESF pore waters likely has occurred in the ESF pore waters. A recent study showed that pore waters with low chloride concentrations were found in the ESF. These chloride concentrations were estimated to be as low as that of the J-13 well water (Lu et al. 2003, Section 4.4). The waters with very low chloride concentration were related to fracture or fault zones where bomb-pulse ^{36}Cl was found (Gascoyne 2003, p. 343). Overall, given the limitations in available data, the five infiltrating waters represent a reasonably approximate selection of water samples plotted in Figure B-20.

B.5 REFERENCES

B.5.1 Documents Cited

Bodvarsson, G.S.; Kwicklis, E.; Shan, C.; and Wu, Y.S. 2003. "Estimation of Percolation Flux from Borehole Temperature Data at Yucca Mountain, Nevada." *Journal of Contaminant Hydrology*, *62–63,* 3–22. New York, New York: Elsevier. TIC: 254205.

BSC (Bechtel SAIC Company) 2001a. *FY 01 Supplemental Science and Performance Analyses, Volume 1: Scientific Bases and Analyses*. TDR-MGR-MD-000007 REV 00 ICN 01. Las Vegas, Nevada: Bechtel SAIC Company. ACC: MOL.20010801.0404; MOL.20010712.0062; MOL.20010815.0001.

BSC 2001b. *UZ Flow Models and Submodels*. MDL-NBS-HS-000006 REV 00 ICN 01. Las Vegas, Nevada: Bechtel SAIC Company. ACC: MOL.20020417.0382.

BSC 2002. *Geologic Framework Model (GFM2000)*. MDL-NBS-GS-000002 REV 01. Las Vegas, Nevada: Bechtel SAIC Company. ACC: MOL.20020530.0078.

BSC 2003a. *Radionuclide Transport Models Under Ambient Conditions*. MDL-NBS-HS-000008 REV 01. Las Vegas, Nevada: Bechtel SAIC Company. ACC: DOC.20031201.0002.

BSC 2003b. *UZ Flow Models and Submodels*. MDL-NBS-HS-000006 REV 01. Las Vegas, Nevada: Bechtel SAIC Company. ACC: DOC.20030818.0002.

BSC 2003c. *Drift-Scale Coupled Processes (DST and THC Seepage) Models*. MDL-NBS-HS-000001 REV 02. Las Vegas, Nevada: Bechtel SAIC Company. ACC: DOC.20030804.0004.

BSC 2003d. *Calibrated Properties Model*. MDL-NBS-HS-000003 REV 01. Las Vegas, Nevada: Bechtel SAIC Company. ACC: DOC.20030219.0001.

BSC 2003e. *Development of Numerical Grids for UZ Flow and Transport Modeling*. ANL-NBS-HS-000015 REV 01. Las Vegas, Nevada: Bechtel SAIC Company. ACC: DOC.20030404.0005.

BSC 2003f. *In Situ Field Testing of Processes*. ANL-NBS-HS-000005 REV 02. Las Vegas, Nevada: Bechtel SAIC Company. ACC: DOC.20031208.0001.

BSC 2003g. *Mountain-Scale Coupled Processes (TH/THC/THM)*. MDL-NBS-HS-000007 REV 01. Las Vegas, Nevada: Bechtel SAIC Company. ACC: DOC.20031216.0003.

BSC 2003h. *In-Drift Precipitates/Salts Model*. ANL-EBS-MD-000045 REV 01 ICN 01B. Las Vegas, Nevada: Bechtel SAIC Company. ACC: DOC.20031028.0003.

BSC 2004a. *Particle Tracking Model and Abstraction of Transport Processes*. MDL-NBS-HS-000020 REV 00. Las Vegas, Nevada: Bechtel SAIC Company. ACC: DOC.20040120.0001.

BSC 2004b. *UZ Flow Models and Submodels*. MDL-NBS-HS-000006 REV 01 ICN 01A. Las Vegas, Nevada: Bechtel SAIC Company. ACC: MOL.20040126.0082.

BSC 2004c. *Engineered Barrier System: Physical and Chemical Environment Model*. ANL-EBS-MD-000033 REV 02. Las Vegas, Nevada: Bechtel SAIC Company. ACC: DOC.20040212.0004.

Cornell, V. 2001. *Analysis of Resolution Status Key Technical Issue: Total System Performance Assessment and Integration Subissue 3: Model Abstraction*. Slide presentation at U.S. Nuclear Regulatory Commission/U.S. Department of Energy Technical Exchange and Management Meeting on Total System Performance Assessment and Integration, August 6 through 10, 2001. ACC: MOL.20010921.0129.

CRWMS M&O (Civilian Radioactive Waste Management System Management and Operating Contractor) 2000. *UZ Flow Models and Submodels*. MDL-NBS-HS-000006 REV 00. Las Vegas, Nevada: CRWMS M&O. ACC: MOL.19990721.0527.

Flint, L.E. 1998. *Characterization of Hydrogeologic Units Using Matrix Properties, Yucca Mountain, Nevada*. Water-Resources Investigations Report 97-4243. Denver, Colorado: U.S. Geological Survey. ACC: MOL.19980429.0512.

Gascoyne, M. 2003. "Soluble Salts in the Yucca Mountain Tuff and their Significance." *Proceedings of the 10th International High-Level Radioactive Waste Management Conference (IHLRWM)*, March 30–April 2, 2003, Las Vegas, Nevada. 340–347. La Grange Park, Illinois: American Nuclear Society. TIC: 254202.

Levy, S.S.; Fabryka-Martin, J.T.; Dixon, P.R.; Liu, B.; Turin, H.J.; and Wolfsberg, A.V. 1997. "Chlorine-36 Investigations of Groundwater Infiltration in the Exploratory Studies Facility at Yucca Mountain, Nevada." *Scientific Basis for Nuclear Waste Management XX, Symposium held December 2-6, 1996, Boston, Massachusetts*. Gray, W.J. and Triay, I.R., eds. 465, 901–908. Pittsburgh, Pennsylvania: Materials Research Society. TIC: 238884.

Lu, G.; Sonnenthal, E.L.; and Bodvarsson, G.S. 2003. "Implications of Halide Leaching on 36Cl Studies at Yucca Mountain, Nevada." *Water Resources Research*, *39,* (12), 1361, 3-1 to 3-15. Washington, D.C.: American Geophysical Union. TIC: 255498.

Montazer, P. and Wilson, W.E. 1984. *Conceptual Hydrologic Model of Flow in the Unsaturated Zone, Yucca Mountain, Nevada*. Water-Resources Investigations Report 84-4345. Lakewood, Colorado: U.S. Geological Survey. ACC: NNA.19890327.0051.

NRC (U.S. Nuclear Regulatory Commission) 2002. *Integrated Issue Resolution Status Report*. NUREG-1762. Washington, D.C.: U.S. Nuclear Regulatory Commission, Office of Nuclear Material Safety and Safeguards. TIC: 253064.

Reamer, C.W. and Gil, A.V. 2001a. Summary Highlights of NRC/DOE Technical Exchange and Management Meeting on Total System Performance Assessment and Integration. Meeting held August 6–10, 2001, Las Vegas, Nevada. Washington, D.C.: U.S. Nuclear Regulatory Commission. ACC: MOL.20010921.0121.

Reamer, C.W. and Gil, A.V. 2001b. Summary Highlights of NRC/DOE Technical Exchange and Management Meeting of Range on Thermal Operating Temperatures, September 18-19, 2001. Washington, D.C.: U.S. Nuclear Regulatory Commission. ACC: MOL.20020107.0162.

Reamer, C.W. and Williams, D.R. 2000. Summary Highlights of NRC/DOE Technical Exchange and Management Meeting on Radionuclide Transport held December 5–7, 2000, Berkeley, California. Washington, D.C.: U.S. Nuclear Regulatory Commission. ACC: MOL.20010117.0063.

Sonnenthal, E.L. and Bodvarsson, G.S. 1999. "Constraints on the Hydrology of the Unsaturated Zone at Yucca Mountain, NV from Three-Dimensional Models of Chloride and Strontium Geochemistry." *Journal of Contaminant Hydrology*, *38,* (1–3), 107–156. New York, New York: Elsevier. TIC: 244160.

Wu, Y.S.; Ritcey, A.C.; and Bodvarsson, G.S. 1999. "A Modeling Study of Perched Water Phenomena in the Unsaturated Zone at Yucca Mountain." *Journal of Contaminant Hydrology*, *38,* (1–3), 157–184. New York, New York: Elsevier. TIC: 244160.

B.5.2 Data, Listed by Data Tracking Number

LA0002JF12213U.002. Chemistry Data for Porewater Extracted from ESF, Cross Drift and Busted Butte Drill Core. Submittal date: 02/15/2000.

LB0303CLINFL3D.001. Chloride Ion Distributions in UZ Flow-Fields. Submittal date: 03/28/2003.

APPENDIX C

DATA FOR CALIBRATION OF THE UNSATURATED ZONE FLOW MODEL (RESPONSE TO TEF 2.11 AND TSPAI 3.26)

Note Regarding the Status of Supporting Technical Information

This document was prepared using the most current information available at the time of its development. This Technical Basis Document and its appendices providing Key Technical Issue Agreement responses that were prepared using preliminary or draft information reflect the status of the Yucca Mountain Project's scientific and design bases at the time of submittal. In some cases this involved the use of draft Analysis and Model Reports (AMRs) and other draft references whose contents may change with time. Information that evolves through subsequent revisions of the AMRs and other references will be reflected in the License Application (LA) as the approved analyses of record at the time of LA submittal. Consequently, the Project will not routinely update either this Technical Basis Document or its Key Technical Issue Agreement appendices to reflect changes in the supporting references prior to submittal of the LA.

APPENDIX C

DATA FOR CALIBRATION OF THE UNSATURATED ZONE FLOW MODEL (RESPONSE TO TEF 2.11 AND TSPAI 3.26)

This appendix provides a response for Key Technical Issue (KTI) Agreement Thermal Effects on Flow (TEF) 2.11 and Total System Performance Assessment and Integration (TSPAI) 3.26. These agreements relate to providing updated properties for the calibration of the unsaturated zone flow model that incorporates all significant sources of uncertainties.

C.1 KEY TECHNICAL ISSUE AGREEMENTS

C.1.1 TEF 2.11 and TSPAI 3.26

Agreement TEF 2.11 was reached during the U.S. Nuclear Regulatory Commission (NRC)/U.S. Department of Energy (DOE) Technical Exchange and Management Meeting on Thermal Effects on Flow held January 8 to 9, 2001, in Pleasanton, California (Reamer and Williams 2001). The agreement resulted from the technical discussion of TEF subissue 2, thermal effects on temperature, humidity, saturation, and flux.

At that meeting, the NRC expressed concern that the data uncertainty in calibrated properties represented only uncertainty in the boundary flux condition (Reamer and Williams 2001). The multiscale thermal-hydrologic model (CRWMS M&O 2000) uses only the drift-scale property sets to calculate thermal-hydrologic variables. The NRC noted that it was not clear how this approach captures the variability and uncertainty seen in the predictions using other property sets or the uncertainty in comparison to actual test results (NRC 2002, p. 3.3.3-20). To address this uncertainty, the NRC suggested additional runs of the multiscale thermal-hydrologic model using important parameters at their 95% confidence (including parameters such as thermal conductivity, not determined in the *Calibrated Properties Model*) and binning these results into the abstraction along with results for the high, mean, and low boundary fluxes (Reamer and Williams 2001). In response, the DOE stated that it would address the following issues in this area: (1) uncertainty from spatially heterogeneous properties, which has been addressed in the DOE response to TEF 2.08; (2) uncertainty in measured data; (3) propagation of uncertainty in inverse modeling; and (4) upscaling.

TSPAI 3.26 was reached during the NRC/DOE Technical Exchange and Management Meeting on Total System Performance Assessment and Integration held August 6 to 10, 2001, in Las Vegas, Nevada (Reamer 2001). TSPAI subissue 3, model abstraction, was discussed at that meeting. In the discussion of the TSPA-LA model abstraction pertaining to the flow paths in the unsaturated zone, the NRC commented that the site-scale unsaturated zone flow model was not calibrated using the most recent in situ measurements of saturations and water potentials (Reamer 2001, p. MA-57). Specifically, the NRC was concerned that the saturation data used in the calibration were obtained from rock cores collected in situ but analyzed ex situ; therefore corresponding estimates of the water retention relationships underpredict saturations (NRC 2002, p. 3.3.6-13).

The NRC also noticed that preliminary results from the east–west Cross-Drift indicate that rock mass in the repository horizon is wetter and the moisture more uniformly distributed than

expected from earlier core analyses. Measurements of water potential taken from surface-based boreholes have gradually equilibrated to ambient conditions that are much wetter than data used to calibrate the unsaturated zone flow model. The NRC suggested that previous difficulties in matching saturations and water potentials might be alleviated by use of the ambient data in the calibration. The DOE stated that it is not clear what the effect would be on the calibrated data sets and predicted distributions of flow between fractures and the matrix.

The wording of these agreements is as follows:

TEF 2.11

> Provide the Calibrated Properties AMR, incorporating uncertainty from all significant sources. The DOE will provide an updated Calibrated Properties Model AMR (MDL-NBS-HS-000003) Rev 01 that incorporates uncertainty from significant sources to the NRC in FY02.

TSPAI 3.26[1]

> Calibrate the UZ flow model using the most recent data on saturations and water potentials, and clearly document the sources of calibration data and data collection methods (UZ2.3.5).
>
> DOE will calibrate the UZ flow model using the most recent data on saturations and water potentials, and document the sources of calibration data and data collection methods. The results will be documented in the *Calibrated Properties Model* AMR (MDL-NBS-HS-000003) expected to be available to NRC in FY 2003.

C.1.2 Related Key Technical Issue Agreements

Agreements TEF 2.11 and TSPAI 3.26 are related to TEF 2.08 in that they concern the remaining uncertainties in the calibrated properties sets developed from the calibration of the site-scale unsaturated zone flow model. As stated, TEF 2.08 is specifically concerned with the effect of heterogeneity.

C.2 RELEVANCE TO REPOSITORY PERFORMANCE

Agreements TEF 2.11 and TSPAI 3.26 are relevant to repository performance because the calibrated properties are used in the calibration of the unsaturated zone flow model, which provides the flow fields for the total system performance assessment for license application (TSPA-LA). The same property sets are also used in the calculations and abstractions of seepage, seepage chemistry, and in-drift hydrologic environment that provide direct feeds to the TSPA-LA.

[1]UZ2.3.5 in this agreement refers to item 2.3 of NRC integrated subissue UZ2 on flow paths in the unsaturated zone (NRC 2002, Table 1.1-2). This item addresses NRC's concern that the site-scale unsaturated zone flow model for TSPA is not calibrated using the most recent in situ measurements of saturation and water potential.

C.3 RESPONSE

C.3.1 Incorporation of Uncertainties from All Significant Sources in Model Calibration

C.3.1.1 Model Calibration Activities

Calibrated Properties Model (BSC 2003a) was revised to incorporate uncertainty from significant sources, in accordance with agreement TEF 2.11. The document was approved and reissued in February 2003 and is publicly available on the Office of Civilian Radioactive Waste Management web page (www.ocrwm.doe.gov). The report documents the calibrated properties model, which provides calibrated parameter sets for unsaturated zone flow and transport process models. The calibration was performed mainly using the one-dimensional inverse simulations because of the limitation of the current computational resources. The calibration was for both mountain and drift scales and for three infiltration maps. The report also documents the methodologies and data used for developing rock property sets. Uncertainties related to the calibrated rock hydraulic properties from the following sources are discussed in *Calibrated Properties Model*: (1) the conceptual model; (2) the infiltration rate; (3) scale effects; (4) measured data; and (5) uncertainty propagation through inversion (Section C.4.5.1 through C.4.5.3.)

Because the properties developed using one-dimensional simulation cannot be directly used for modeling lateral flow, further calibrations were performed for two- and three-dimensional mountain-scale modeling studies (BSC 2003b). These calibrations focus particularly on the PTn unit and potential perched-water layers (Section C.4.5.4).

C.3.1.2 Incorporation and Evaluation of Uncertainties

The determination of rock properties is subject to uncertainties. Uncertainties arising from uncertain infiltration rates have been addressed by developing different property sets corresponding to upper-bound, lower-bound, and mean infiltration rates. This document focuses on: (1) uncertainty from spatially heterogeneous properties; (2) uncertainties in measured data; (3) propagation of uncertainty in inverse modeling; and (4) upscaling effects (Reamer and Williams 2001). Uncertainties from theses sources have been evaluated, incorporated, and documented during data analyses (BSC 2003c) and calibration activities (BSC 2003a; BSC 2003b). This section briefly examines information on the incorporation and evaluation of uncertainties from these sources.

C.3.1.2.1 Uncertainty from Spatially Heterogeneous Properties

The effects of heterogeneity on thermal seepage were addressed in the response to KTI agreement TEF 2.08 (Appendix A of *Technical Basis Document No. 3: Water Seeping into Drifts*). This response stated that a drift-scale thermal-hydrologic process model was developed (the thermal-hydrologic seepage model) that incorporates all relevant thermal-hydrologic processes and accounts for small-scale heterogeneity in the drift vicinity. The thermal-hydrologic seepage model was applied to simulate thermally perturbed, channelized fluid flowing down to the drift and to calculate transient seepage rates during a period of elevated temperature. The numerical results of the thermal-hydrologic seepage model were compared to an improved semianalytical solution based on the Phillips solution (Phillips 1996), introduced as

an alternative conceptual model in *Drift-Scale Coupled Processes (DST and TH Seepage) Models* (BSC 2003d). This KTI agreement response focuses on the uncertainties arising mainly from mountain-scale (site-scale) heterogeneities.

Various efforts in the unsaturated zone model calibration have been made to incorporate the uncertainties arising from spatially heterogeneous properties. These efforts include:

1. Development of a dual-continuum model to capture the high conductivity of fractures (Pruess and Narasimhan 1985)

2. Spatial discretization that reflect the spatial extension of the faults and specific parameter sets assigned to the faulted rock units (BSC 2003e)

3. Capture of vertical heterogeneity by layer-based property sets (Section C.4.3 and C.4.5)

4. Assignment of assorted parameter sets for the zeolitic and vitrified rock units (BSC 2003c; BSC 2003a) to capture the geologic alterations (Section C.4.3 and C.4.5)

5. Evaluation of the heterogeneities within each model layer (Zhou et al. 2003), which concluded that heterogeneities within model layer have only a minor effect on site-scale flow processes (Section C.4.4).

C.3.1.2.2 Uncertainties in the Measured Data

Measured data used in the model calibration include property measurements (e.g. air permeability data) and acquired data (e.g., water saturation, water potential, pneumatic pressure).

Property Measurements–Measured data used to develop uncalibrated hydraulic properties include:

1. Detailed line survey fracture data collected from the ESF north and south ramps, main drift, and ECRB Cross-Drift, providing spatially varying frequency, length, and fracture dips and strikes, as well as boreholes providing fracture frequency for fracture properties development

2. Air-injection testing data (from vertical boreholes) used for fracture permeability estimates

3. Air-injection or gas tracer data from the Upper Tiva Canyon hydrologic unit, Bow Ridge Fault, Upper Paintbrush contact alcoves, the single heater test area, and the drift scale test area providing fracture permeability and porosity estimates

4. Data from liquid release-tests in the ESF niches that provide fracture van Genuchten α and porosity estimates

5. Measured properties from core samples (including effective porosity, bulk density, porosity, particle density, volumetric water content, saturation, water potential,

hydraulic conductivity, matrix van Genuchten α and *m* values, and residual saturation) and stratigraphic descriptions from borehole samples, which are used for developing matrix properties

The uncertainties in these measured data have been discussed (BSC 2003c). Uncertainties for most of these properties are reported using the corresponding standard deviations or standard errors (BSC 2003c, Tables 6 to 8). These uncertainties are incorporated in *Calibrated Properties Model* (BSC 2003a, Section C.4.3).

Acquired Data–Water saturation core data collected from several surface-based boreholes are used, and uncertainties in these data have been incorporated (BSC 2003a) by means of the following methods:

1. Evaluation of handling error caused by evaporation during the lab measurement and consideration of the evaluated handling error in the objective function of iTOUGH2 V5.0 (LBNL 2002) inverse models

2. Consideration of measure error in the objective function of iTOUGH2 V5.0 (LBNL 2002) inverse models

3. Performance of spatial averaging for comparison with model results from each gridblock with sizes from meters to tens of meters (measurement scales of the saturation are on the order of several centimeters) (Section C.4.1)

In situ measured water potential data are used in the one-dimensional inversions and model validations. The steady-state water potential values were carefully adopted from the observed water potential breakthrough from each instrumented station. The representativeness of these adopted values are justified in Section C.3.2 and detailed in Section C.4.2. Data from boreholes that do not intersect mapped faults are used to represent the rock mass of Yucca Mountain. Data measured in borehole USW UZ-7a, which intersects the Ghost Dance Fault, are used for the two-dimensional inversions and judged to be representative of the faulted rock of Yucca Mountain. In situ measured pneumatic pressure data were used in the one-dimensional inversion and model validation.

Section C.4.1 describes the use of water saturation data and the incorporation of uncertainties in the model calibration. Section C.4.2 describes the water potential data used in calibrating and determining steady-state values.

C.3.1.2.3 Uncertainty Propagation in the Inversion

Propagation of the uncertainties was addressed in *Calibrated Properties Model* (BSC 2003a). Uncertainty data for measurements are used as inputs into inversions. To handle the uncertainty from boundary conditions, different property sets were developed for distinct infiltration scenarios. The uncertainty in prior information was used for characterizing uncertainties for calibrated properties. Section C.4.5 describes the model calibration and the uncertainty propagation through calibration.

C.3.1.2.4 Uncertainties from Upscaling Effects

Scale effects are a well-known source of parameter uncertainty, and the scale-dependence of hydrologic parameters has been widely recognized in the scientific community (Neuman 1994). This is especially true for determining unsaturated zone model parameters, such as matrix permeability, where matrix parameters are measured in the unsaturated zone at core scale size of several centimeters. In the unsaturated zone flow and transport models, numerical gridblocks are on the order of a few meters to hundreds of meters. The upscaling effects for matrix properties were incorporated in two steps: (1) they were partially considered in developing uncalibrated matrix properties; and (2) scale-dependent properties were calibrated by inverse modeling at a large scale. The calibrated matrix permeability and matrix α values are on average higher than uncalibrated ones. This indicates that uncertainties resulting from scale effects have been incorporated in the inverse procedure. Scale-dependent behavior for fracture permeability is considered by developing parameter sets at two different scales: mountain scale and drift scale (Section C.4.5.2 and C.4.5.3). Upscaling of acquired data (such as water saturation) is discussed in Section C.4.1.

C.3.2 Use of the Recent Saturation and Water Potential Data to Calibrate Unsaturated Zone Flow Model

C.3.2.1 Water Saturation Data

For a number of reasons (summarized below), water saturation data collected from the drilling cores were selected and used for model calibration but not additional water saturation data collected from surface-based boreholes after the boreholes were drilled. Water saturation data from surface-based boreholes were used for one-dimensional unsaturated zone flow model calibration because these data represent the vertical water saturation profile covering most of the model layers. In addition, the data were suitable for comparison with simulation results obtained in the calibrations. Other saturation data were not used in the calibration for the following reasons:

1. Handling of the core caused excessive drying (Rousseau et al. 1999, p. 125).

2. Data measured on core from the ESF, ECRB Cross-Drift, alcoves, and niches represent only a single layer in the stratigraphic column, and multiple dimensional models are needed to match these data, which are computationally too intensive.

3. Geophysical saturation measurements contain larger uncertainties compared to direct measurements of saturation by oven dried core samples.

Handling error (caused by evaporation) for water saturation data was estimated before use and incorporated into the objective function (Equation C-28) of the inverse models along with measurement errors and standard error (Section C.4.1).

C.3.2.2 Water Potential Data

While no additional data for water saturation have become available, there are new data on water potential in Yucca Mountain. The available water potential data used for the model calibration

are continually collected from instrumented stations at different depth in several boreholes. Water potential data measured on cores are not used because drying during drilling and handling may have substantially changed the water potential. This change could not be recovered as was done for water saturation (BSC 2003a, Section 6.2.2). The data used in the calibrations were collected from boreholes USW NRG-6 and USW NRG-7a from November 1994 to March 31, 1998, from borehole UE-25 UZ#4 from June 1995 to March 31, 1998, and from borehole UE-25 SD-12 from November 1995 to March 31, 1998. The latest available data were collected December 18, 2001.

The more recent data collected on the following dates were not used in the model calibration as they were not available as qualified data at that time.

- April 1, 1998 to March 31, 2001, from borehole USW NRG-7a
- April 1998 to December 18, 2001, from UE-25 UZ#4
- April 1998 to December 1998, from UE-25 SD-12.

When the entire data set was analyzed, measured water potential was found to reach a quasi-steady-state within the first 20 months after the instrumentation. After that, measured water potential stabilized. The steady-state water potential data used for calibrating the unsaturated zone flow model were determined (BSC 2003a, Section 6.2.2) (see Section C.4.2). The determined steady-state water potential is consistent with newer data, although the newer data from two sensors show a slight wetter condition. The differences between the determined steady-state water potentials (used in the model calibration) and the newer measurements are within the range of the measurement error, plus or minus 0.2 MPa (Rousseau et al. 1999, p. 144). Some newer data shows unexpected behavior that was probably caused by the thermocouple psychrometers (TCP) sensor failure, such as a sensor (TCP 1688) in borehole UE-25 SD-12 (Section C.4.2). Consequently, the data from them are ignored.

In addition, water potential data measured from the ECRB Cross-Drift have been used for validation of three-dimensional unsaturated zone flow models (BSC 2003b).

The information in this report is responsive to agreements TEF 2.11 and TSPAI 3.26 made between the DOE and NRC. The report contains the information that DOE considers necessary for NRC review for closure of these agreements.

C.4 BASIS FOR THE RESPONSE

This section provides technical information supporting the responses given in Section C.3.

C.4.1 Water Saturation Data

The materials presented in this section come from *Calibrated Properties Model* (BSC 2003a, Section 6.2.2).

C.4.1.1 Measurements and Upscaling of Saturation Data from Core Samples

Drill cores were sampled in an interval of 0.3 m and core water saturation was measured by an oven drying method (BSC 2003a, Section 6.2.2). In the numerical grid mesh, each gridblock

covers meters to hundreds of meters. The arithmetic means of core measured water saturations that correspond to the intervals covered by each numerical grid element were calculated to compare the modeled water saturations with measured water saturations in the model calibration. Also, a standard deviation for core water saturation data corresponding to a gridblock was calculated and incorporated into the objective function of the iTOUGH2 inverse model (see Section C.4.1.2).

C.4.1.2 Weighting of the Measurements for iTOUGH2 Inverse Simulation

iTOUGH2 V5.0 (LBNL 2002) allows data to be weighted. The weight of each saturation data point is estimated from the number of measurements, the standard deviation of the measurements, and estimates of handling and measurement error. The total error, *TE*, which is equal to the inverse of the weight, is

$$TE = SE + ME + HE \qquad \text{(Eq. C-1)}$$

where *SE* is the standard error, *ME* is the measurement error, and *HE* is the handling error. Standard error, *SE*, is defined here as

$$SE = \frac{\sigma}{\sqrt{N}} \qquad \text{(Eq. C-2)}$$

where σ is the unbiased estimate of the standard deviation and *N* is the number of measurements. If there is no estimate of the standard deviation because *N* has a value of 1, σ and thus *SE* are set to 0.05 within the range of estimated *SE* values for *N* greater than 1. The total error, *TE*, was incorporated in the objective function (Equation C-28) of the inverse models.

C.4.1.3 Measurement Error

The measurement error for bulk properties is less than 0.5% (Flint 1998, p. 17). The *ME* for saturation is thus taken to be 0.005.

C.4.1.4 Estimate of the Handling Error Resulting from Evaporation

Core drying during handling is a potential source of error for saturation data (Flint 1998, pp. 18 to 19; Rousseau et al. 1999, pp. 129 to 131). The *HE* was therefore estimated for core drying effects. Saturation is not easily quantifiable because of the variable nature of the forces controlling drying. Drying during handling at the surface is related to saturation, water potential (and variation of water potential with saturation), and temperature of the core, as well as temperature, pressure, relative humidity, and the speed of the air around the core. Drying of the core during drilling is related to similar factors. Rather than correct the measured saturation data by an uncertain drying estimate, a contribution to the total uncertainty of the saturation data is made by estimating drying losses. This contribution is included as *HE* in Equation C-1.

A simplified model of core drying during handling is used to estimate its evaporation rate. A fully saturated core is approximated as a spherical rock with a surface that is always completely wet and that has the same area as the core; the operation time is only 5 minutes. A

solution for evaporation from a spherical drop of water in an air stream is given (Bird et al. 1960, p. 648) as

$$W = \eta \pi \delta^2 \frac{x_0 - x_\infty}{1 - x_\infty} \qquad \text{(Eq. C-3)}$$

where W is the evaporation rate, η is the mass-transfer coefficient of water vapor in air, δ is the diameter of a sphere with the same surface area as the core, x_0 is the water mole fraction in the air at the surface of the core, and x_∞ is the water mole fraction in air that is far away from the core. The mass-transfer coefficient of water vapor in air, η, is given (Bird et al. 1960, p. 649) as

$$\eta = \frac{cD}{\delta}\left[2 + 0.6\left(\frac{v\delta\rho}{\mu}\right)^{1/2}\left(\frac{\mu}{D\rho}\right)^{1/3}\right] \qquad \text{(Eq. C-4)}$$

where c is the total molar concentration of the air-water mixture, D is the effective binary diffusivity of water vapor in air, v is air speed, ρ is density of air, and μ is viscosity of air. Effective binary diffusivity, D (cm^2/s), for an air and water-vapor (components A and B) mixture is given (Bird et al. 1960, p. 505) as

$$D = \frac{3.64 \times 10^{-4}}{p}\left(\frac{T}{\sqrt{T_{cA}T_{cB}}}\right)^{2.334}\left(p_{cA}p_{cB}\right)^{1/3}\left(T_{cA}T_{cB}\right)^{5/12}\left(\frac{1}{M_A} + \frac{1}{M_B}\right)^{1/2} \qquad \text{(Eq. C-5)}$$

where p is pressure (atm), T is temperature (K), and p_c, T_c, and M are the critical pressure (atm), critical temperature (K), and molecular weight (g/g-mole), respectively, of components A and B.

The evaporation rate is estimated by setting the temperature of the core at 25°C and the temperature, pressure, relative humidity, and speed of the air that is far from the core at 30°C, 1 atm, 25%, and 3 km/h, respectively. These are all reasonable values for field conditions at Yucca Mountain. Neglecting the small effect of the water vapor in the air, the physical properties of air at 27.5°C (the average temperature) are $c = 4.05 \times 10^{-5}$ g-mole/cm^3, $\rho = 0.00118$ g/cm^3, and $\mu = 1.84 \times 10^{-4}$ g/cm/s (Roberson and Crowe 1990, p. A-22). The molecular weight, critical temperature, and critical pressure of air are 28.97 g/g-mole, 132 K, and 36.4 atm, respectively (Bird et al. 1960, p. 744). The molecular weight and critical temperature and pressure of water are 18.02 g/g-mole, 647.25 K, and 218.3 atm, respectively (Weast 1987, pp. B-94, F-66). The mole fraction of water vapor in air at the surface of the core, x_0, is 0.0313 (Weast 1987, p. D-190). Given a relative humidity of 25%, the mole fraction of water vapor in air that is far away from the core (i.e., assumed to be at an infinite distance, x_∞) is 0.0126 (Weast 1987, p. D-190). The core is approximately 7 cm in diameter and 10 cm long (Flint 1998, p. 11). Using these values, an evaporation rate of 2.69×10^{-4} g-mole/s is calculated based on Equations C-3 to C-5.

At this rate, the saturation of a fully saturated core sample with matrix porosity of 22.3% (a typical value for tuff matrix) (BSC 2003a, Table 3) will be reduced by 2.2% after 5 minutes, which is the given handling time (Flint 1998, p. 11). A completely dry core will have no

reduction in saturation. Using these two points, a linear dependence of saturation change on saturation yields the relation

$$\Delta S = 0.022S \qquad \text{(Eq. C-6)}$$

where S is the uncorrected saturation value and ΔS is saturation change resulting from handling, or *HE*. Although the actual relation between ΔS and S may be much more complex than Equation C-6, this equation is adequate for estimating *HE* in this instance.

Average porosity for the entire mountain is calculated as a layer-thickness weighted average of individual layer porosities. Water lost to drilling air is not considered because an approach to accurately estimate water loss is not available. However, the estimation of handling errors does not consider the effect of matrix capillary pressure, resulting in overestimated handling errors. This may partially compensate for the effects of water lost to drilling air.

C.4.2 Measurement of Water Potentials and Determination of the Steady-State Water Potential Values

The information in this section supports the response to KTI agreements TSPAI 3.26 and TEF 2.11. The materials presented here are from *Calibrated Properties Model* (BSC 2003a, Section 6.2.2).

Water potential is measured at instrumented boreholes with TCPs. These sensors, calibrated to an accuracy of 0.8 bars with a sensitivity of 0.05 bars (Rousseau et al. 1999, p. 144), give plus or minus 0.2 MPa as the 95% confidence interval (two standard deviations) for the in situ water potential measurements. One standard deviation, 0.1 MPa, is used as an estimate for the uncertainty. Because water potential is lognormally distributed, the standard error of log(water potential), $SE_{\log(\Psi)}$, is estimated as

$$SE_{\log(\Psi)} = \log(\Psi + 0.1) - \log(\Psi) \qquad \text{(Eq. C-7)}$$

where Ψ is the value of the water potential data point in MPa. The calculation of the standard error is performed. Water potential is reported to a precision greater than the accuracy because, in most cases, changes and differences between curves are more important than the absolute values of water potential. Measuring water potential in situ requires that the rock near the borehole and the granular fill of the borehole come into equilibrium with the surrounding rock. Prior to installation of the in situ sensors, these boreholes are open and the rock immediately around the borehole may have dried out (Rousseau et al. 1999, pp. 143 to 151). Thus, the in situ data vary with time for given locations and need to be evaluated to determine the equilibrium value of the data.

Data used were from boreholes USW NRG-6 and USW NRG-7a (November 1994 to March 1998), from borehole UE-25 UZ#4 (June 1995 to March 1998), and from borehole UE-25 SD-12 (November 1995 to March 1998). Measured water potential breakthrough for each instrument station was inspected to find the value that best represented the equilibrium value (steady-state) used as a direct input into *Calibrated Properties Model* (BSC 2003a, Section 6.2.2).

There are newer data in addition to the data used in *Calibrated Properties Model* (BSC 2003a, Section 6.2.2). They are collected from USW NRG-7a (April 1, 1998, to March 31, 2001), UE-25 UZ#4 (April 1, 1998, to December 18, 2001), and UE-25 SD-12 (April 1998 to December 1998). Among them, data collected from boreholes USW NRG-7a and UE-25 UZ#4 in the period from April 1999 to March 2001 are unqualified. The NRC expressed concern that the newer data could be more representative of water flow in the unsaturated zone. When the newer data were compared with the older data, it was found that the measured water potential reached a quasi-steady-state within the first 20 months after the instrumentation (Figures C-1 to C-4) and the most recently measured water potentials were stable. Newer data from two sensors in UE-25 SD-12 show a slightly wetter condition (TCP 1675 and TCP 1676 at 76.8 m deep and TCP 1682 at 65.2 m deep) (Figure C-4), but the difference between the adopted steady-state water potential value and the newer data is within the measurement error.

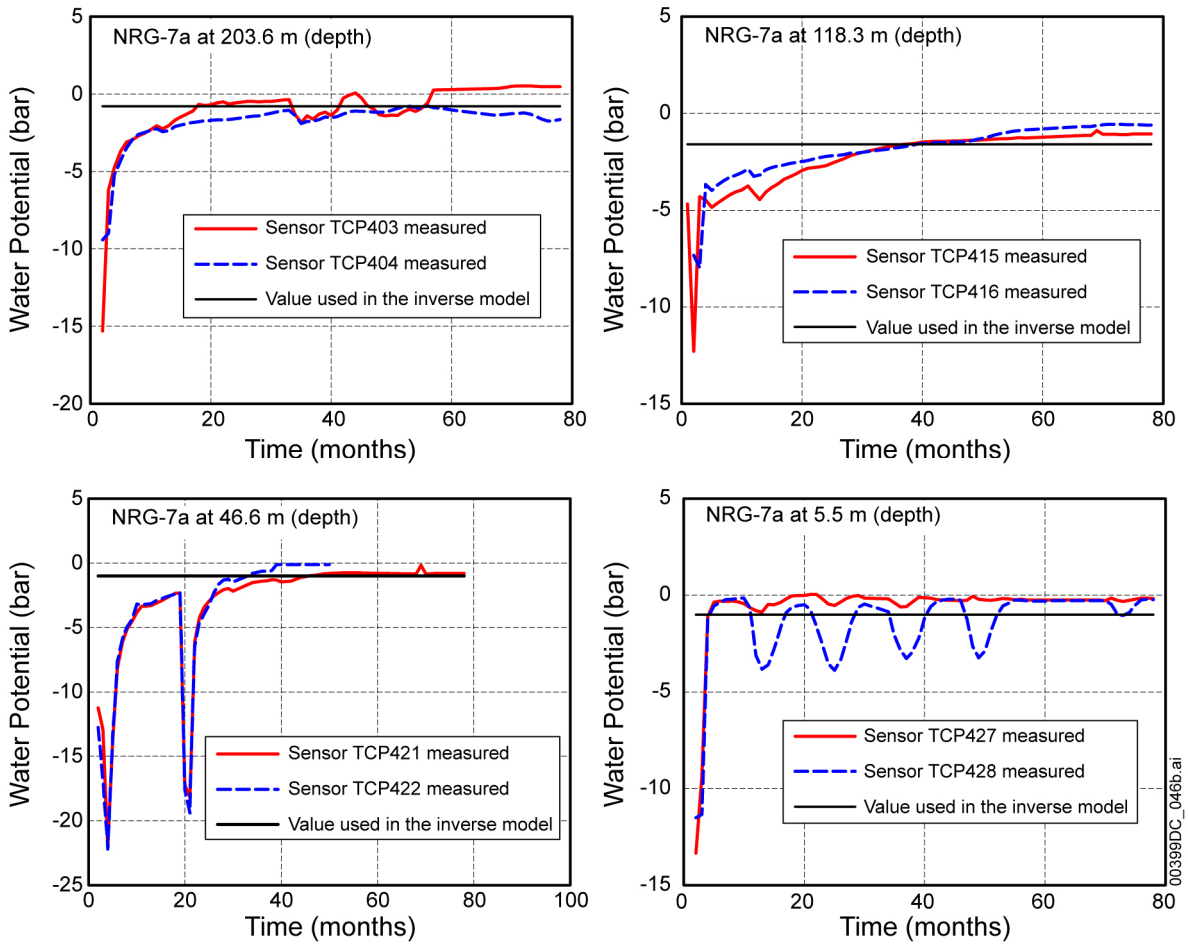

Source: DTN: LB0401H2OPOTEN.001.

NOTE: The used values were determined using the data collected before the end of March 1998 (month 42).

Figure C-1. Measured Water Potential (from Available Instruments Stations of Borehole USW NRG-7a) Breakthrough (Starting From October 1994, as Month 1) and the Determined Steady-State Value Used in the Inverse Model for Hydraulic Property Calibration

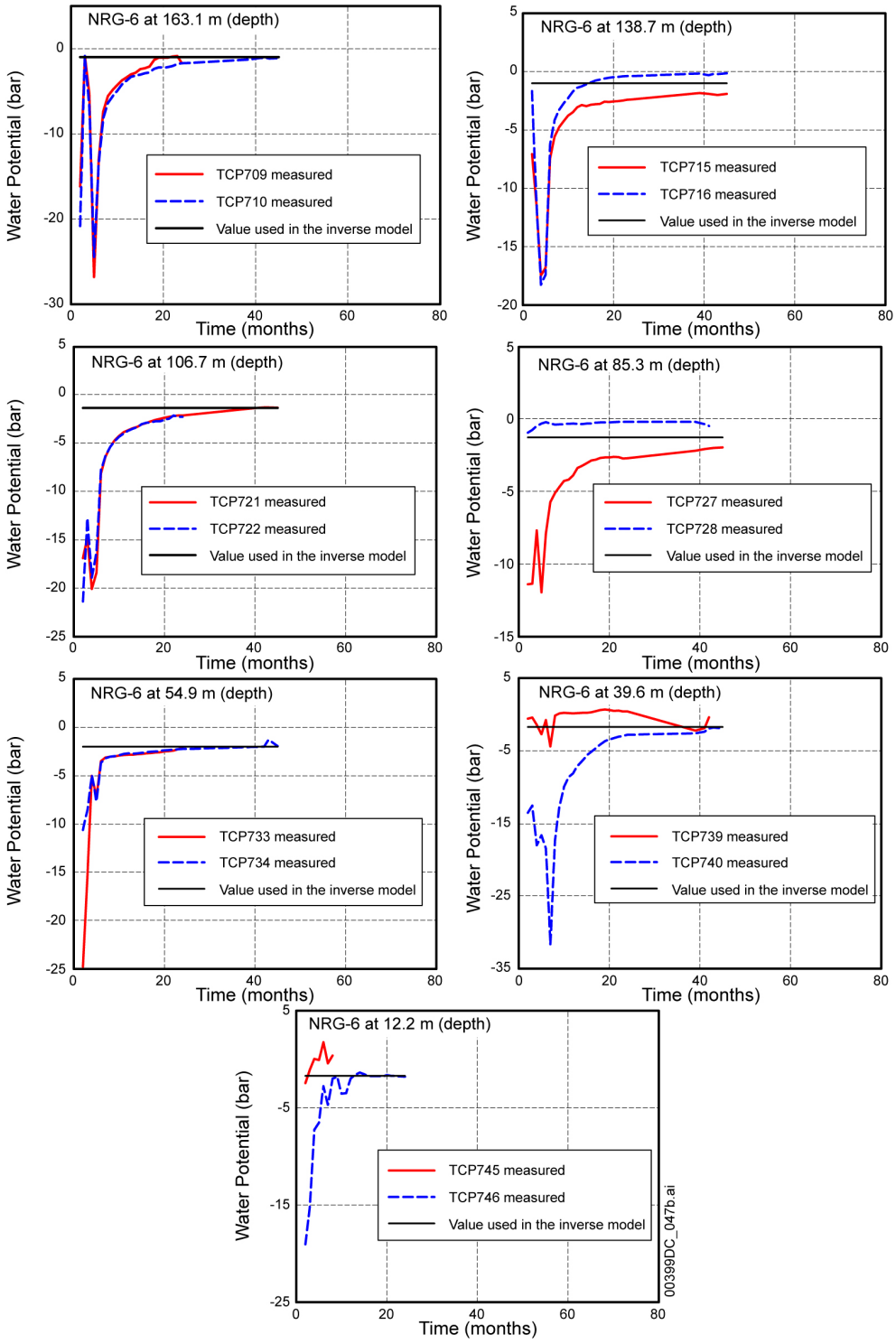

Source: DTN: LB0401H2OPOTEN.001.

NOTE: The used values were determined using the data collected before the end of March 1998 (month 42).

Figure C-2. Measured Water Potential (from Available Instruments Stations of Borehole USW NRG-6) Breakthrough (Starting From October 1994, as Month 1) and the Determined Steady-State Value Used in the Inverse Model for Hydraulic Property Calibration

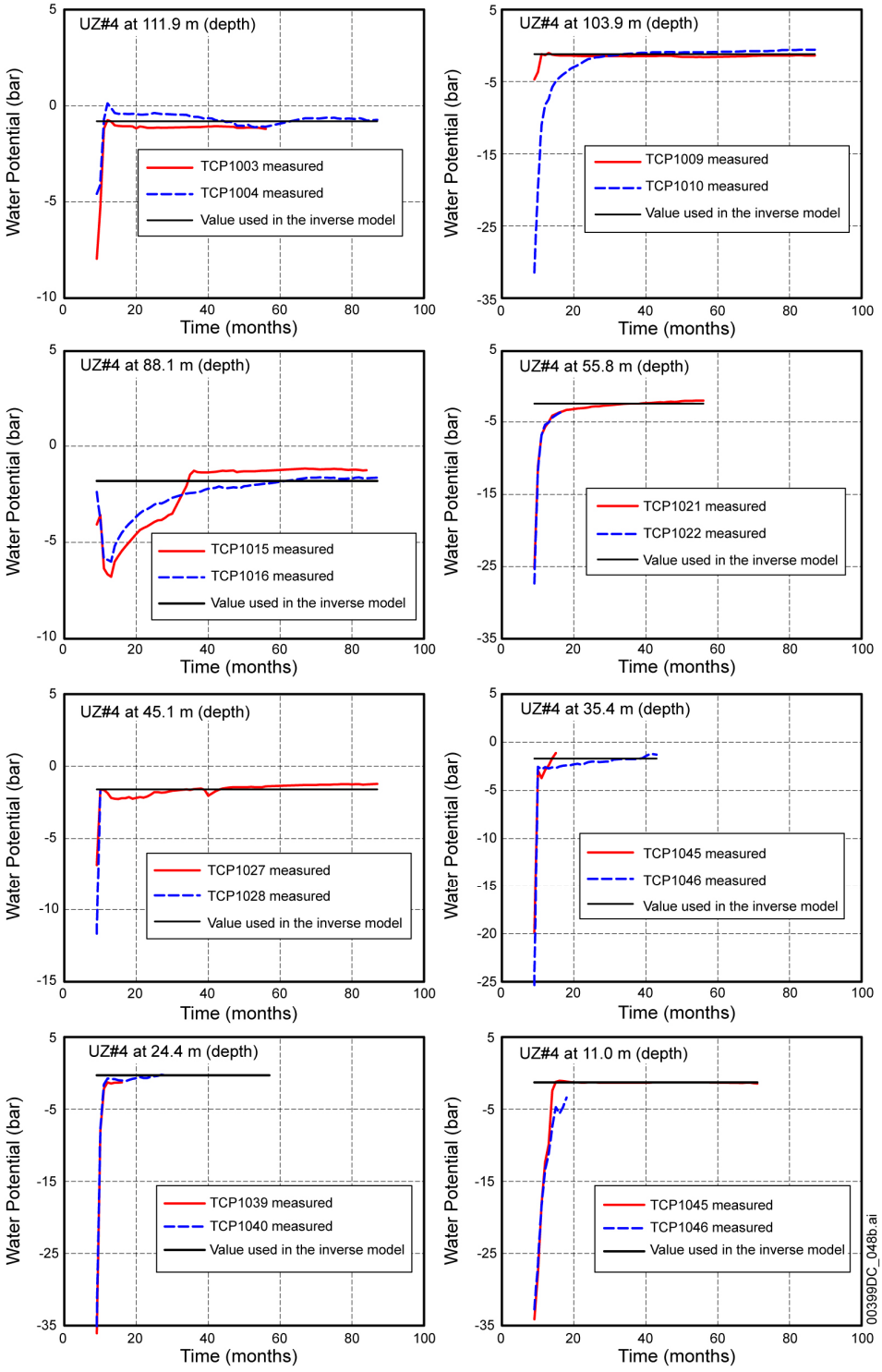

Source: DTN: LB0401H2OPOTEN.001.

NOTE: The used values were determined using the data collected before the end of March 1998 (month 42).

Figure C-3. Measured Water Potential (from Available Instruments Stations of Borehole UE-25 UZ#4) Breakthrough (Starting From October 1994, as Month 1) and the Determined Steady-State Value Used in the Inverse Model for Hydraulic Property Calibration

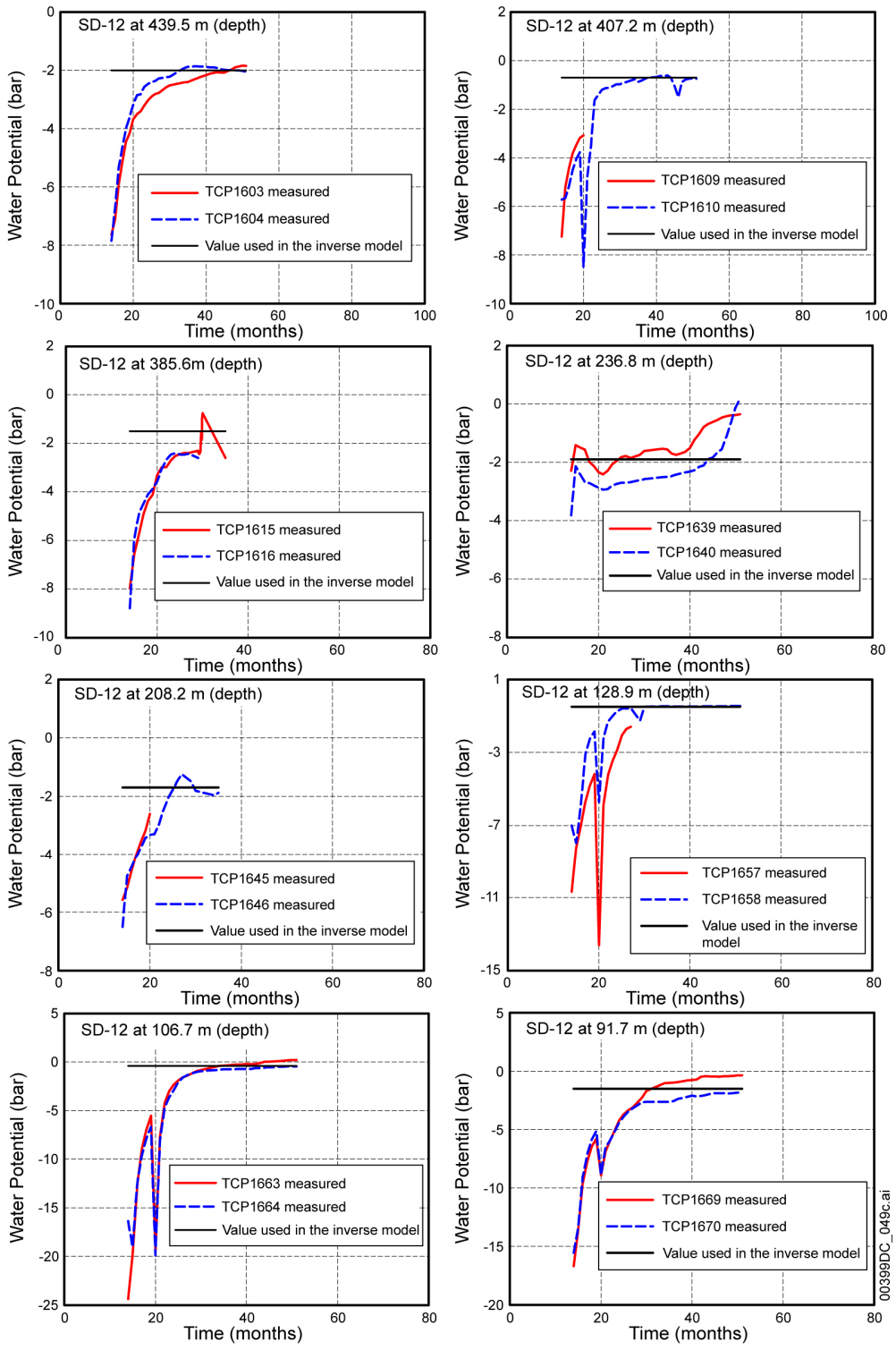

Source: DTN: LB0401H2OPOTEN.001.

NOTE: The used values were determined using the data collected before the end of March 1998 (month 42).

Figure C-4. Measured Water Potential (from Available Instruments Stations of Borehole UE-25 SD-12) Breakthrough (Starting From October 1994, as Month 1) and the Determined Steady-State Value Used in the Inverse Model for Hydraulic Property Calibration

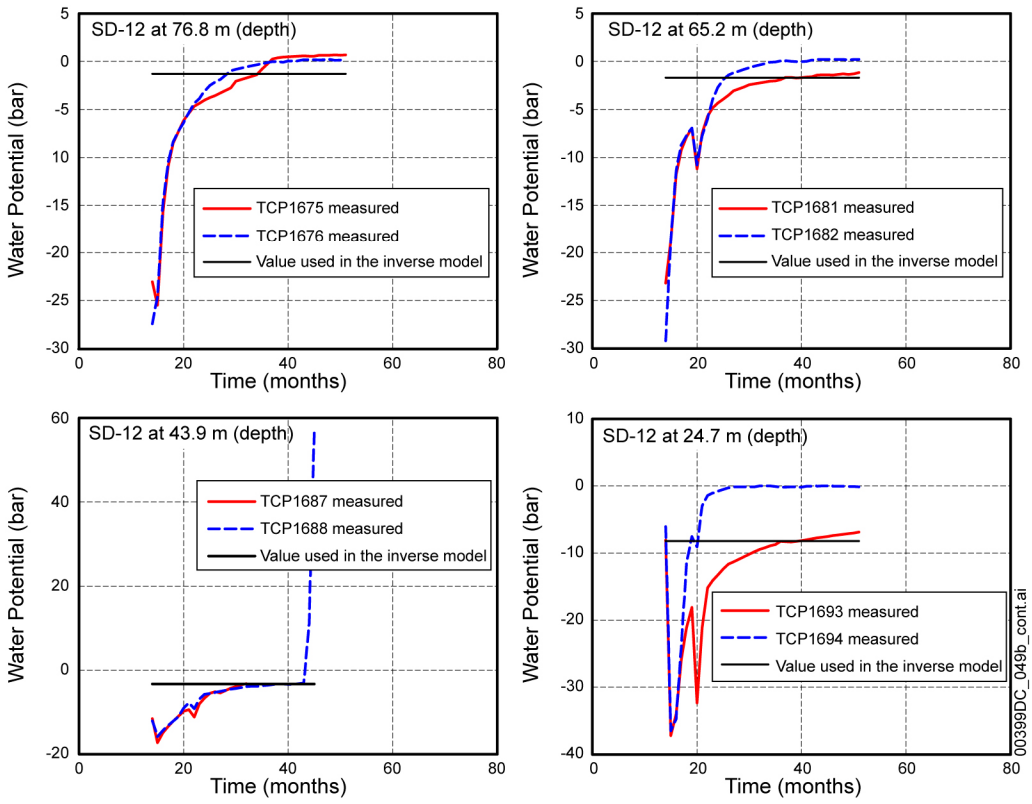

Source: DTN: LB0401H2OPOTEN.001.

NOTE: The used values were determined using the data collected before the end of March 1998 (month 42).

Figure C-4 (continued). Measured Water Potential (from Available Instruments Stations of Borehole USW SD-12) Breakthrough (Starting From October 1994, as Month 1) and the Determined Steady-State Value Used in the Inverse Model for Hydraulic Property Calibration

Some sensors failed and thus stopped measuring. Some measured data show unexpected behavior (such as data from Sensor TCP 1688 in borehole UE-25 SD-12, shown in Figure C-4), and these data were disregarded. The difference between the data from sensors at the same position (for example, TCP 1693 and TCP 1694 in borehole UE-25 SD-12, see Figure C-4) implies the measurement error. The difference between the adopted steady-state value and the newer data is within the range of the 95% confidence interval, plus or minus 0.2 MPa, except for data from sensor TCP 1688 and TCP 1694 in borehole UE-25 SD-12. The latest data from TCP 1688 show a drastic increase, illustrating a possible sensor failure. The difference between data from TCP 1693 and TCP 1694 (Figure C-4) indicates a large uncertainty in the measured water potential at this particular location.

In summary, the steady-state water potential values determined for model calibration using data collected before June 1998 is consistent with the newer data collected from July 1998 to March 2001. Exceptions exist for two sensor stations from which the measured water potential may reflect a wetter condition, but the magnitude of the water potential increment is within the range of the measurement error. Uncertainty in the water potential, 0.1 MPa, was incorporated into the model calibration.

C.4.3 Determination of the Initial Estimates and Incorporation of Hydraulic-Properties Uncertainty for Model Calibrations

The following section addresses the methodologies and data used to determine representative estimates of the fracture and matrix properties for the unsaturated zone model layers.. This information supports the response to KTI agreement TEF 2.11. Included are the methods used to determine uncalibrated fracture properties and matrix properties (BSC 2003c, Section 6.1-6.4).

C.4.3.1 Fracture Properties

Fracture properties include fracture frequency, fracture aperture, fracture porosity, fracture interface area, uncalibrated van Genuchten fracture α and m, and uncalibrated fracture permeability (BSC 2003c, Sections 6.1 to 6.4). The uncalibrated van Genuchten fracture α and m and uncalibrated fracture permeability were later calibrated (BSC 2003a; BSC 2003b). This section describes the determination of these three uncalibrated parameters and the uncertainties incorporated in them.

C.4.3.1.1 Fracture Permeability

The fracture permeabilities calculated for the unsaturated zone model layers are based on air permeabilities inferred from air-injection tests performed in vertical boreholes and in ESF alcoves. Permeabilities inferred from air-injection tests in boreholes are representative of fracture absolute permeabilities. These permeabilities were determined based on pneumatic-pressure data and are calculated using a modified version of the Hvorslev solution for steady-state elliptic flow (Hvorslev 1951, p. 30, Case 8; LeCain 1995, p. 10). The determined permeability values are combined to determine effective fracture permeabilities for the unsaturated zone model layers. The geometric means are considered to reflect upscaling of these fracture permeabilities for use as single values representative of each model layer.

For the Tiva Canyon welded hydrogeologic unit (TCw), fracture permeabilities were based on air-injection tests performed in vertical boreholes USW NRG-7a, USW NRG-6, UE-25 SD-12, and UE-25 UZ#16, as well as the Upper Tiva Canyon, Bow Ridge Fault, and Upper Paintbrush contact alcoves (Alcoves 1, 2, and 3). For the Paintbrush nonwelded hydrogeologic unit (PTn), the permeability data are from vertical borehole USW NRG-7a and Upper Paintbrush contact alcove (Alcove 3). For the Topopah Spring welded hydrogeologic unit (TSw), the permeability data are from vertical boreholes USW NRG-7a, USW NRG-6, UE-25 SD-12 and UE-25 UZ#16 as well as the single heater and drift scale test areas in Alcove 5. For the Calico Hills nonwelded hydrogeologic unit (CHn), permeability data are available only from a single sampled interval in the vertical borehole UE-25 UZ#16. No air-injection data are available for the Prow Pass (pp), Bullfrog (bf), and Tram (tr) units. For model layers where no data are available, analogs to other units are used based on those designated for matrix properties (Flint 1998, p. 46), the degree of zeolitic alteration, and the degree of welding. These fracture permeabilities are used as prior information and initial estimates for a separate report describing the calibrated properties model.

Table C-1 lists the geometric means of the fracture permeabilities for the unsaturated zone model layers. Lithostratigraphic units were assigned to the unsaturated zone model layers. The fracture permeabilities were treated as isotropic, and the data from vertical boreholes and the horizontal

and inclined boreholes in the ESF alcoves were combined. The scales of these measurements are similar.

Table C-1. Uncalibrated Fracture Permeabilities for the Unsaturated Zone Model Layers

Unsaturated Zone Model Layer	Fracture Permeability (m^2)				
	Basis[a]	k_G[b]	$\log(k_G)$	$\sigma_{\log(k_G)}$[c]	N[d]
tcw11	BRFA	3.0×10^{-11}	−10.52	-	2
tcw12	UTCA UPCA NRG-6 NRG-7a SD-12 UZ#16	5.3×10^{-12}	−11.28	0.78	80
tcw13	UPCA NRG-7a	4.5×10^{-12}	−11.35	1.15	3
ptn21	UPCA NRG-7a	3.2×10^{-12}	−11.49	0.88	12
ptn22	NRG-7a	3.0×10^{-13}	−12.52	0.20	4
ptn23	NRG-7a	3.0×10^{-13}	−12.52	0.20	4
ptn24	NRG-7a	3.0×10^{-12}	−11.52	-	1
ptn25	NRG-7a	1.7×10^{-13}	−12.78	0.10	7
ptn26	NRG-7a	2.2×10^{-13}	−12.66	-	1
tsw31	Average TSW	8.1×10^{-13}	−12.09	-	-
tsw32	NRG-6 NRG-7a SD-12 UZ#16	7.1×10^{-13}	−12.15	0.66	31
tsw33	NRG-6 NRG-7a SD-12 UZ#16	7.8×10^{-13}	−12.11	0.61	27
tsw34	SHT DST NRG-6 NRG-7a SD-12 UZ#16	3.3×10^{-13}	−12.48	0.47	180
alternate tsw34	SHT DST NRG-6 NRG-7a SD-12 UZ#16	1.5×10^{-13}	−12.81	0.75	180
tsw35	NRG-7a UZ#16	9.1×10^{-13}	−12.04	0.54	31

Table C-1. Uncalibrated Fracture Permeabilities for the Unsaturated Zone Model Layers (Continued)

Unsaturated Zone Model Layer	Fracture Permeability (m^2)					
tsw3[67]	SD-12 UZ#16	1.3×10^{-12}	−11.87	0.28	19
tsw38	Average TSw	8.1×10^{-13}	−12.09	-	-
tsw39	Average TSw	8.1×10^{-13}	−12.09	-	-
ch1Ze	ch2Ze	2.5×10^{-14}	−13.60	-	-
ch1VI	ptn26	2.2×10^{-13}	−12.66	-	-
ch[23456]VI	ptn26	2.2×10^{-13}	−12.66	-	-
ch[2345]Ze	UZ#16	2.5×10^{-14}	−13.60	-	1
ch6	ch2Ze	2.5×10^{-14}	−13.60	-	-
pp4	ch2Ze	2.5×10^{-14}	−13.60	-	-
pp3	ptn26	2.2×10^{-13}	−12.66	-	-
pp2	ptn26	2.2×10^{-13}	−12.66	-	-
pp1	ch2Ze	2.5×10^{-14}	−13.60	-	-
bf3	ptn26	2.2×10^{-13}	−12.66	-	-
bf2	ch2Ze	2.5×10^{-14}	−13.60	-	-
tr3	ptn26	2.2×10^{-13}	−12.66	-	-
tr2	ch2Ze	2.5×10^{-14}	−13.60	-	-

Source: BSC 2003c, Table 6.

NOTE: [a]Identifies the corresponding air-injection borehole(s) and/or alcove(s) or analog to another model layer(s). UTCA = Upper Tiva Canyon Alcove; BRFA = Bow Ridge Fault Alcove; UPCA = Upper Paintbrush Contact Alcove; SHT = Single Heater Test Area; DST = Drift Scale Test Area; and USW NRG-6, USW NRG-7a, UE-25 SD-12, and UE-25 UZ#16 are vertical boreholes. (This column is presented for information only and not from the cited DTN.)
[b]Geometric mean.
[c]Standard deviation.
[d]Number of sampled intervals.
"-" means that no data are available.

The mean fracture permeabilities range from 2.5×10^{-14} m^2 to 3.0×10^{-11} m^2. TCw has the highest fracture permeabilities. TSw fracture permeabilities are, in general, higher than those for PTn and CHn. Two fracture permeabilities are shown for the Topopah Spring middle nonlithophysal unit (tsw34), representing different approaches to weighting the available air-injection data. For tsw34, there were 143 sampled intervals in the Alcove 5 heater test areas, compared to 37 sampled intervals in the 4 vertical borehole injection tests. For the first case, the data from Alcove 5 were weighted with those from the vertical borehole tests ($k = 0.8\ k_{G,\text{vertical boreholes}} + 0.2\ k_{G,\text{Alcove 5}}$). In the alternate tsw34 case, each sampled interval is weighted equally.

The uncertainty and variability of fracture permeabilities for the unsaturated zone model layers are reflected by the standard deviations reported in Table C-1. These standard deviations would result in 95% confidence intervals covering three orders of magnitude, even for the units that have a large number of sampled intervals. The data indicate that fracture permeabilities are highly variable.

The permeabilities measured in the vertical boreholes and alcoves were combined to determine the fracture permeability for each unsaturated zone model layer. The packer lengths were approximately 4 m for vertical boreholes, 1 to 3 m for Alcoves 1, 2, and 3, and 5 to 12 m in the Single Heater Test and Drift Scale Test areas (Alcove 5). These data were all considered to be on the same relative scale and are representative of the fracture permeability on the scale of the unsaturated zone model after upscaling, using geometric means.

Additional air-permeability data on a scale of 1 ft intervals were also available from air-injection testing in ESF niches in the Topopah Spring middle nonlithophysal unit (tsw34). Air-injection data from the niche studies were not used for determining mean fracture permeabilities for the model layers since these data were on a smaller scale and may not be representative of larger-scale effective permeability. Figure C-5 compares the geometric means and range of data (mean plus or minus one standard deviation) for the model layer tsw34 corresponding to Tptpmn. The data shown for the niche studies are inferred from preexcavation air-injection testing. The ranges of the data overlap, but the geometric means for the measurements from the niche studies are generally lower than the other values. This difference is expected because the mean permeability decreases as the scale of the measurement decreases (Neuman 1994).

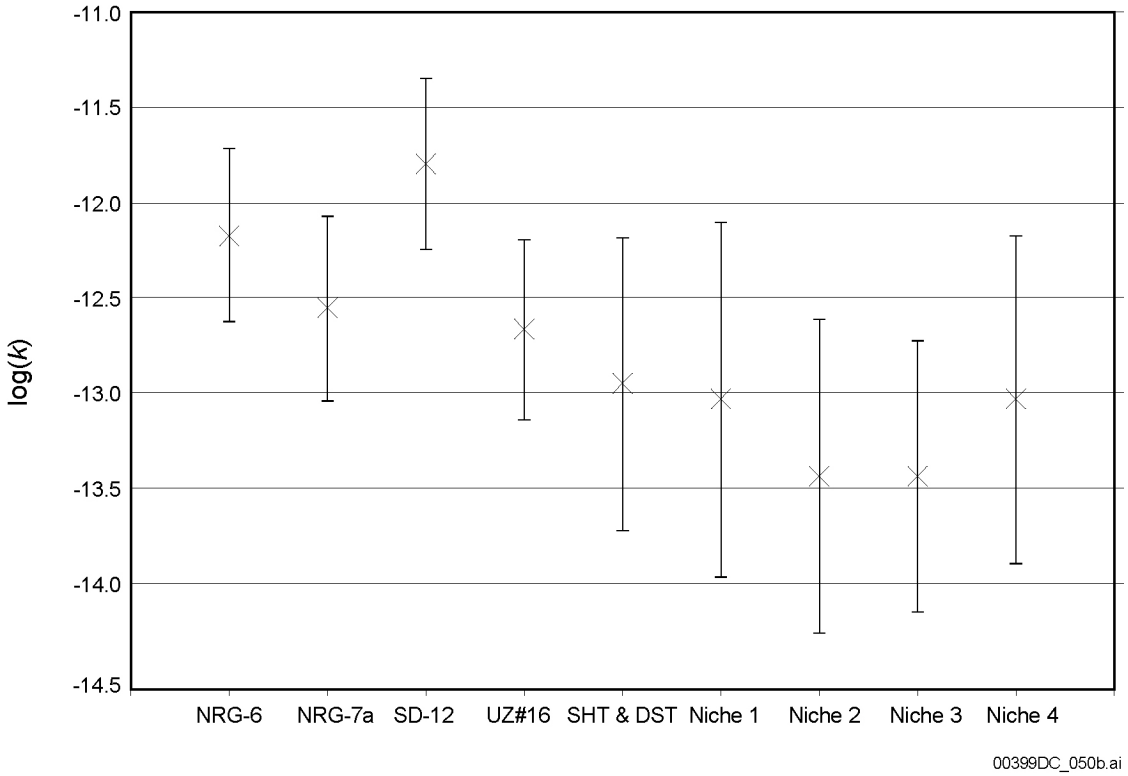

Source: BSC 2003c, Figure 2.

NOTE: Ranges for inferred permeabilities from air-injection data. X indicates the geometric means; SHT = Single Heater Test; DST = Drift Scale Test.

Figure C-5. Fracture Permeabilities for Topopah Spring Middle Nonlithophysal Unit

C.4.3.1.2 Fracture Frequency, Intensity, Fracture Interface Area, Aperture, and van Genuchten Parameters

Fracture frequency, interface area, and the van Genuchten *m* are determined from qualified fracture property data developed from field data. These include detailed line survey fracture data collected from the ESF north and south ramps, main drift, and ECRB Cross-Drift, (which provide spatially varying frequency, length, and fracture dips and strikes) and fracture frequency data collected from boreholes. For completeness, mathematical equations used for developing these properties are also described here.

For calculating fracture frequencies using the detailed line survey in the ESF and ECRB Cross-Drift, the mean fracture frequency is given by the inverse of the mean spacing. The mean spacing is calculated by:

$$\bar{s} = \frac{1}{nf - 1} \sum_{2}^{nf} \left(D_i - D_{i-1} \right) \qquad \text{(Eq. C-8)}$$

where D_i is the distance or station along the ESF where fracture i intersects the detailed line survey and nf is the number of fractures. This is the apparent spacing, not the normal distance between the center of fractures, and therefore a rough estimate of the true spacing. These values were not corrected for any possible orientation bias in the detailed line survey. The mean fracture frequency is given by the inverse of the mean apparent spacing:

$$\bar{f} = \frac{1}{\bar{s}} \qquad \text{(Eq. C-9)}$$

For calculating fracture frequency from borehole data, the data are processed to normalize for core recovery, corrected for bias in orientation, and scaled to represent larger length fracture. To correct for orientation bias from vertical borehole data, dip distributions are used as follows (modified from Lin et al. 1993, p. 24, Eq. 3-1):

$$f_{cb} = \frac{\sum_i f_{i,0-19° dip}}{\cos(10°)} + \frac{\sum_i f_{i,20-39° dip}}{\cos(30°)} + \frac{\sum_i f_{i,40-59° dip}}{\cos(50°)} + \frac{\sum_i f_{i,60-90° dip}}{\cos(75°)} \qquad \text{(Eq. C-10)}$$

where f_{cb} is the fracture frequency corrected for orientation bias and f_i is the fracture frequency corresponding to the range of dip distribution. Finally, these values are corrected to represent larger length fractures on the scale of those characterized in the ESF. A simple correction ratio is used based on comparisons of ESF data with corresponding vertical boreholes for that model layer:

$$\bar{f} = f_{corrected} = f_{cb} R$$
$$R = \left(\frac{f_{ESF}}{f_{borehole}} \right)_{average} \qquad \text{(Eq. C-11)}$$

Two correction factors *R* are calculated (one for welded units) using data for the Topopah Spring middle nonlithophysal hydrogeologic unit (tsw34) and one for nonwelded units using data for the Pah Canyon tuff in the Paintbrush hydrogeologic unit (ptn25). These units were selected because both ESF and borehole data are available and considered to be representative of the other units.

The fracture intensity is calculated by dividing the trace length of the fracture by the area surveyed. The area surveyed was 6 m (3 m above and below the traceline) times the length along the tunnel considered for that interval. The average fracture intensity I (m/m^2) is given by:

$$I = \frac{\sum_{i=1}^{nf} t_i}{\text{area}} = \frac{\sum_{i=1}^{nf} t_i}{(6\text{ m})(\text{interval length in meters})} \qquad \text{(Eq. C-12)}$$

where t_i is trace length in meters for fracture i. The fracture interface area is calculated by dividing the fracture area by the volume of the interval surveyed. The volume for the interval is estimated by multiplying the interval length surveyed by the square of the geometric mean of surveyed fracture trace length. The average fracture interface area per volume A_{fm} (m^2/m^3) is given by:

$$A_{fm} = \frac{\sum_{i=1}^{nf} \pi r_i^2}{\text{volume}} = \frac{\sum_{i=1}^{nf} \pi r_i^2}{(\text{interval length})(\text{geometric mean of trace lengths})^2} \qquad \text{(Eq. C-13)}$$

where r is the radius of fracture i, or one-half the trace length of fracture i. Fracture apertures are calculated by the cubic law with the fractures fully connected. The fracture aperture b is then given by (Bear et al. 1993, p. 15):

$$b = \left(\frac{12k}{\bar{f}}\right)^{1/3} \qquad \text{(Eq. C-14)}$$

where k is the fracture permeability. The fracture aperture determined in this way is an effective hydraulic aperture, not a physical aperture. The above equation is modified from Bear et al. (1993, p. 15, Equation 1.2.28). The k here refers to bulk fracture permeability rather than permeability in a fracture (Bear et al. 1993, p. 15).

Fitted parameters are required to utilize the van Genuchten equation relating the effective saturation S_e and capillary pressure P_c (van Genuchten 1980, pp. 892 to 895, Equations 2, 22, and 24):

$$P_c = \frac{1}{\alpha}\left(S_e^{-1/m} - 1\right)^{1/n} \qquad \text{(Eq. C-15a)}$$

where α, *m,* and $n = \frac{1}{1-m}$ are the van Genuchten parameters. The effective saturation is defined by

$$S_e = \frac{S - S_r}{S_s - S_r} \qquad \text{(Eq. C-15b)}$$

where S is total water saturation, S_s is satiated saturation, and S_r is residual saturation.

A simplified form of the Young-Laplace equation is assumed to directly calculate the van Genuchten fracture α (α_f) from b. The subscript f refers to fractures. The resulting relationship is:

$$\alpha_f = \frac{b}{2\tau_\sigma \cos\theta} \qquad \text{(Eq. C-16)}$$

where τ_σ is the surface tension of pure water at 20ºC (0.072 N/m) and θ is the contact angle. Essentially, Equation C-16 states that van Genuchten α can be estimated as an absolute value of the inverse of the air-entry value, which is often used in soil science literature (Wang and Narasimhan 1993, p. 374). The contact angle θ is set to zero (Wang and Narasimhan 1993, p. 329), since the rock is expected to be water wetting and no other specific data are available.

Fracture aperture and fracture van Genuchten alpha (α_f) are calculated from fracture frequency and fracture permeability estimates using Equations C-14 and C-16. The estimated mean apertures are approximately 100 to 400 μm, except for model layer tcw11, which has a relatively high fracture permeability, resulting in a higher estimated fracture aperture. The fracture van Genuchten alpha parameters (α_f) are on the order of 10^{-3} Pa^{-1}. There are large uncertainties in these values for the Calico Hills Formation and lower units because little or no fracture permeability and fracture frequency data are available.

The van Genuchten fracture m parameter (m_f) is determined by fitting Equation C-15a to the aperture-size distribution calculated from Equation C-14. An m_f value of 0.633 (determined based on this method) is used in this study. An alternative method to estimate m_f is not available.

The developed uncalibrated fracture properties and the uncertainty (represented by the standard deviation) are given in Table C-2.

Table C-2. Uncalibrated Fracture Properties for Unsaturated Zone Model Layers

Unsaturated Zone Model Layer	Permeability (m^2)				van Genuchten Parameter		
	k_G	$\log(k_G)$	$\sigma_{\log(k_G)}$	N	$\alpha(Pa^{-1})$	$\log(\alpha)$	m (-)
tcw11	3.0×10^{-11}	-10.52	-	2	5.0×10^{-3}	−2.30	0.633
tcw12	5.3×10^{-12}	-11.28	0.78	80	2.2×10^{-3}	−2.66	0.633
tcw13	4.5×10^{-12}	-11.35	1.15	3	1.9×10^{-3}	−2.73	0.633
ptn21	3.2×10^{-12}	-11.49	0.88	12	2.7×10^{-3}	−2.57	0.633
ptn22	3.0×10^{-13}	-12.52	0.20	4	1.4×10^{-3}	−2.86	0.633
ptn23	3.0×10^{-13}	-12.52	0.20	4	1.2×10^{-3}	−2.91	0.633
ptn24	3.0×10^{-12}	-11.52	-	1	3.0×10^{-3}	−2.53	0.633
ptn25	1.7×10^{-13}	-12.78	0.10	7	1.1×10^{-3}	−2.96	0.633
ptn26	2.2×10^{-13}	-12.66	-	1	9.6×10^{-4}	−3.02	0.633
tsw31	8.1×10^{-13}	-12.09	-	-	1.1×10^{-3}	−2.96	0.633
tsw32	7.1×10^{-13}	-12.15	0.66	31	1.4×10^{-3}	−2.86	0.633
tsw33	7.8×10^{-13}	-12.11	0.61	27	1.6×10^{-3}	−2.80	0.633
tsw34	3.3×10^{-13}	-12.48	0.47	180	6.7×10^{-4}	−3.18	0.633
alternate tsw34	1.5×10^{-13}	-12.81	0.75	180			
tsw35	9.1×10^{-13}	-12.04	0.54	31	1.0×10^{-3}	−2.99	0.633
tsw3[67]	1.3×10^{-12}	-11.87	0.28	19	1.1×10^{-3}	−2.96	0.633
tsw38	8.1×10^{-13}	-12.09	-	-	8.9×10^{-4}	−3.05	0.633
tsw39	8.1×10^{-13}	-12.09	-	-	1.5×10^{-3}	−2.82	0.633
ch1Ze	2.5×10^{-14}	-13.60	-	-	1.4×10^{-3}	−2.86	0.633
ch1Vl	2.2×10^{-13}	-12.66	-	-	2.1×10^{-3}	−2.69	0.633
ch[23456]Vl	2.2×10^{-13}	-12.66	-	-	1.9×10^{-3}	−2.73	0.633
ch[2345]Ze	2.5×10^{-14}	-13.60	-	1	8.9×10^{-4}	−3.05	0.633
ch6	2.5×10^{-14}	-13.60	-	-	1.4×10^{-3}	−2.86	0.633
pp4	2.5×10^{-14}	-13.60	-	-	8.9×10^{-4}	−3.05	0.633
pp3	2.2×10^{-13}	-12.66	-	-	1.6×10^{-3}	−2.78	0.633
pp2	2.2×10^{-13}	-12.66	-	-	1.6×10^{-3}	−2.78	0.633
pp1	2.5×10^{-14}	-13.60	-	-	8.9×10^{-4}	−3.05	0.633
bf3	2.2×10^{-13}	-12.66	-	-	1.6×10^{-3}	−2.78	0.633
bf2	2.5×10^{-14}	-13.60	-	-	8.9×10^{-4}	−3.05	0.633
tr3	2.2×10^{-13}	-12.66	-	-	1.6×10^{-3}	−2.78	0.633
tr2	2.5×10^{-14}	-13.60	-	-	8.9×10^{-4}	−3.05	0.633

Source: BSC 2003c, Table 7.

NOTE: k is permeability (geometric mean).
σ is standard deviation.
N is number of samples.
α and m are fitting parameters for the van Genuchten water potential relationship.
"-" means that no data are available.

C.4.3.2 Matrix Properties

Matrix properties include matrix permeability and van Genuchten (1980) parameters used to describe water retention and relative permeability relations. They were determined from laboratory measurements made on core samples. Sample collection and laboratory measurement methodologies, as well as estimates of core uncertainty, are described (Flint 1998, pp. 11 to 19; Rousseau et al. 1999, pp. 125 and 153). Core samples were grouped and analyzed according to the characterized hydrogeologic units (Flint 1998, pp. 19 to 46). The calculated matrix properties and the corresponding uncertainties are given in Table C-3.

C.4.3.2.1 Matrix Permeability

Matrix permeability was measured on core samples from eight boreholes. Measurements are available for layers from the CUC to the BF2 (Table C-3). Two different permeameters were used to measure permeability, with the detection limit of the first higher than the second. Most of the samples were tested using the first permeameter; the second was used to test some new samples and to retest some old samples tested using the first permeameter, including some with permeabilities too low to measure (nondetect results). When the same sample was tested with both permeameters, the permeability measured on the one with the lower detection limit was used because the one with the lower detection limit was expected to result in a more reliable measurement.

The measured data are presented in terms of saturated hydraulic conductivity (m/s), K, which is converted to permeability (m^2), k, by the following relationship

$$k = \frac{K\mu_w}{g\rho_w} \qquad \text{(Eq. C-17)}$$

where μ_w is the viscosity of water (0.001 N s/m^2), g is the acceleration of gravity (9.81 m/s^2), and ρ_w is the density of water (998 kg/m^3). These parameter values correspond to 20°C (a typical room temperature) at which hydraulic conductivity was measured (Lide 2002, p. 6-3).

Table C-3. Matrix Properties Developed from Core Data

Hydrogeologic Unit	ϕ	σ	*n*	SE	Upscaled *k* (m^2)	Upscaled log(*k*) (log(m^2))	$\sigma_{log(k)}$	*n*	nd	$SE_{log(k)}$	1/α(Pa)	log(1/α) (log(Pa))	$SE_{log(1/\alpha)}$	*m*	SE	S_r	η	SE
CCR & CUC	0.241	0.073	124	0.007	4.7×10^{-15}	-14.33	0.47	3	0	0.27	8.27×10^{4}	4.918	0.279	0.388	0.085	0.02	3.47	17.88
CUL & CW	0.088	0.032	694	0.001	6.4×10^{-20}	-19.20	2.74	15	25	0.43	5.46×10^{5}	5.737	0.178	0.280	0.045	0.20	12.29	19.35
CMW	0.200	0.055	96	0.006	1.8×10^{-16}	-15.74	2.38	5	1	0.97	2.50×10^{5}	5.398	0.188	0.259	0.042	0.31	6.08	0.00
CNW	0.387	0.069	104	0.007	4.0×10^{-14}	-13.40	2.05	10	0	0.65	2.03×10^{4}	4.308	0.199	0.245	0.032	0.24	-2.58	0.33
BT4	0.428	0.100	58	0.013	4.1×10^{-13}	-12.39	1.41	11	0	0.43	4.55×10^{3}	3.658	0.174	0.219	0.019	0.13	-0.26	1.17
TPY	0.233	0.057	39	0.009	1.3×10^{-15}	-14.90	0.64	2	0	0.46	7.63×10^{4}	4.883	0.379	0.247	0.064	0.07	3.46	16.73
BT3	0.413	0.082	73	0.010	1.3×10^{-13}	-12.87	1.09	11	1	0.31	8.90×10^{3}	3.950	0.088	0.182	0.008	0.14	-0.56	0.49
TPP	0.498	0.041	159	0.003	1.1×10^{-13}	-12.96	0.39	11	0	0.12	2.12×10^{4}	4.325	0.104	0.300	0.023	0.06	0.26	0.42
BT2	0.490	0.095	176	0.007	6.7×10^{-13}	-12.17	1.12	21	0	0.24	1.74×10^{4}	4.239	0.170	0.126	0.013	0.05	-2.64	0.67
TC	0.054	0.036	75	0.004	4.4×10^{-17}	-16.36	3.02	6	5	0.91	2.71×10^{5}	5.432	0.310	0.218	0.054	0.21	6.14	17.21
TR	0.157	0.030	449	0.001	3.2×10^{-16}	-15.50	0.94	46	1	0.14	9.43×10^{4}	4.974	0.116	0.290	0.025	0.07	5.00	17.49
TUL	0.155	0.030	438	0.001	2.8×10^{-17}	-16.56	1.61	37	12	0.23	1.75×10^{5}	5.244	0.111	0.283	0.024	0.12	7.06	17.98
TMN	0.111	0.020	277	0.001	4.5×10^{-19}	-18.34	0.97	74	35	0.09	1.40×10^{6}	6.147	0.108	0.317	0.042	0.19	10.90	19.28
TLL	0.131	0.031	502	0.001	3.7×10^{-17}	-16.44	1.65	51	24	0.19	6.01×10^{4}	4.779	0.521	0.216	0.061	0.12	6.27	17.23
TM2 & TM1	0.103	0.025	298	0.001	2.3×10^{-20}	-19.63	3.67	21	42	0.46	3.40×10^{6}	6.532	0.097	0.442	0.073	0.20	14.48	21.25
PV3	0.043	0.040	125	0.004	2.9×10^{-18}	-17.54	1.57	16	2	0.37	1.00×10^{6}	6.000	0.278	0.286	0.065	0.42	9.04	18.53
PV2a	0.275	0.096	13	0.027	a	a	a	a	a	a	2.17×10^{5}	5.336	0.156	0.059	0.007	0.36	5.03	15.63
PV2v	0.229	0.132	40	0.021	4.3×10^{-13}	-12.37	1.38	16	0	0.34	1.94×10^{4}	4.287	0.042	0.293	0.011	0.13	-0.19	0.23
BT1a	0.285	0.051	46	0.008	3.5×10^{-17}	-16.45	2.74	9	1	0.87	4.72×10^{6}	6.674	0.183	0.349	0.073	0.38	7.39	18.61
BT1v	0.331	0.091	76	0.010	2.1×10^{-13}	-12.67	1.11	35	0	0.19	1.35×10^{4}	4.131	0.049	0.240	0.008	0.06	-2.07	0.23
CHV	0.346	0.049	130	0.004	1.6×10^{-12}	-11.81	1.62	46	0	0.24	3.39×10^{3}	3.530	0.094	0.158	0.008	0.06	-3.80	0.23
CHZ	0.322	0.048	520	0.002	5.2×10^{-18}	-17.28	0.91	99	17	0.08	4.45×10^{5}	5.649	0.094	0.257	0.022	0.26	8.30	18.10
BTa	0.271	0.046	73	0.005	8.2×10^{-19}	-18.08	2.05	9	8	0.50	6.42×10^{6}	6.808	0.043	0.499	0.036	0.36	11.87	21.01
BTv	b	b	b	b	b	b	b	b	b	b	5.04×10^{4}	4.703	0.207	0.147	0.020	b	-0.87	14.77
PP4	0.321	0.047	52	0.006	1.5×10^{-16}	-15.81	2.74	6	2	0.97	5.00×10^{5}	5.699	0.401	0.474	0.224	0.29	7.13	19.55
PP3	0.318	0.032	168	0.002	6.4×10^{-15}	-14.20	0.75	51	0	0.11	1.32×10^{5}	5.120	0.084	0.407	0.031	0.08	3.37	18.01
PP2	0.221	0.058	127	0.005	5.4×10^{-17}	-16.27	1.18	34	3	0.19	6.22×10^{5}	5.794	0.147	0.309	0.041	0.10	6.69	18.09
PP1	0.297	0.043	280	0.003	8.1×10^{-17}	-16.09	1.52	27	1	0.29	1.13×10^{5}	5.052	0.234	0.272	0.036	0.30	6.05	17.63
BF3/TR3	0.175	0.104	126	0.009	1.1×10^{-15}	-14.95	1.64	7	1	0.58	8.94×10^{4}	4.951	0.931	0.193	0.117	0.11	3.11	16.20
BF2	0.234	0.049	40	0.008	c	c	c	c	c	c	8.46×10^{6}	6.927	0.032	0.617	0.070	0.21	8.86	21.17

Source: BSC 2003c, Table 8.

NOTES: (a) BT1a was used as an analogue for permeability because only one permeability data point is available for PV2a. (b) BT1v was used as an analogue for porosity, permeability and residual liquid saturation because only one sample is available for BTv. (c) PP1 was used as an analogue for permeability because only one measurable permeability data point is available for BF2.

ϕ is porosity; σ is standard deviation; *n* is number of samples; SE is standard error; *k* is permeability; η is the empirical constant defined in Equation C-23; nd is number of samples with nondetected permeability measurements; α and *m* are fitting parameters for the van Genuchten water potential relationship; S_r is residual liquid saturation.

Permeability is considered to be a log-normally distributed quantity (Gelhar 1993, p. 2). Therefore, the geometric mean was used to represent the average permeability of each model layer. The standard deviation of the log-transformed permeabilities, log(k), is used as the basis for uncertainty, which is detailed below. Where there are no nondetect measurements in the data set for a layer; the calculation of the average and standard deviation of the data is simple. When there are nondetect measurements present, they must be taken into account because they may represent important information about the extent of the lognormal distribution below the detection limit. They are taken into account as follows:

- All data points, including nondetects, are ranked and assigned a percentile.
- The data points are fit to a lognormal distribution based on their percentile ranking. The fitting parameters are k_g, the geometric mean of the permeability data, and $\sigma_{\log(k)}$, the standard deviation of the log transformed permeability data.

The geometric mean permeabilities calculated above represent the average behavior of the core-scale samples. For a given model layer, this averaged permeability can be very different from the effective matrix permeability used to represent large-scale water flow and solute transport due to the scale effects (Paleologos et al. 1996, Figure 4, p. 1337). While many upscaling methods are available, a method for highly heterogeneous porous media is described by the following expression (Paleologos et al. 1996, p. 1336)

$$k_e = k_g \exp\left[\sigma_{\ln(k)}^2\left(\frac{1}{2} - D\right)\right] \qquad \text{(Eq. C-18)}$$

where k_e is the effective permeability, k_g is the geometric mean of small (core) scale permeability, $\sigma_{\ln(k)}^2$ is the variance of the natural log-transformed permeability, and D is a function of spatial dimensions (e.g., two-dimensional and three-dimensional) and the correlation scale of ln(k). In general, the geometric mean permeability is not the same as the effective permeability. For a three-dimensional isotropic problem, D has a value of 1/3 when the characteristic size of a flow domain under consideration (e.g., a model layer) is much larger than the correlation length (Paleologos et al. 1996, p. 1336). For a site-scale model layer, these conditions are approximately satisfied. In this case, Equation C-18 can be rewritten as

$$\log(k_e) = \log(k_g) + 0.38\sigma_{\log(k)}^2 \qquad \text{(Eq. C-19)}$$

where $\sigma_{\log(k)}^2$ is the variance of the log transformed permeability.

In these layers, the amount of upscaling predicted by Equation C-18 is as large as 5 orders of magnitude. An upper limit of 1.5 orders-of-magnitude upscaling is imposed on layers CUL and CW, CMW, CNW, TC, TM2, and TM1, and BT1a and PP4. For all other layers, the amount of upscaling predicted by Equation C-18 is less than 1.5 orders of magnitude. Use of this limiting scheme is based mainly on the fact that Equation C-18 was developed for a porous medium (single continuum) and can only be considered as an approximation for a dual-continuum system. For example, the existence of fractures, which may act as a capillary barrier, can

increase liquid water flow tortuosity in the matrix and therefore reduce the effective permeability compared to the case without fractures. This situation is not considered in Equation C-18.

C.4.3.2.2 Matrix Porosity

Matrix porosity was also measured in core samples. Porosity was determined after drying samples in a 105°C oven for at least 48 hours to obtain a standard dry weight (Flint 1998, p. 17). Porosity is considered to be a normally distributed quantity, so the arithmetic mean of core measurements and standard deviation were used to characterize the porosity for a model layer. The matrix porosity was not calibrated.

C.4.3.2.3 Matrix van Genuchten Parameters

The relationships described by van Genuchten (1980, pp. 892 to 893) were used to characterize unsaturated flow in the Yucca Mountain matrix. Use of the water potential versus saturation relationship allows prediction of the relative permeability relationship. The predicted relative permeability is compared with permeability data where available.

The van Genuchten parameters are S_s (satiated saturation), S_r (residual saturation), α, and m. Satiated saturation is defined to be 1.0 (i.e., residual gas saturation is neglected). Residual saturation is calculated based on two porosity measurements, as described below. With satiated and residual saturation fixed, α and m are adjusted to fit water potential and saturation data.

Matrix Residual Saturation–Residual saturation was determined from relative humidity porosity and total porosity, which was measured after drying a core sample for 48 hours in a 60°C oven at 65% relative humidity. This process removes water that contributes to flow from the pores, leaving only bound water and water in the smallest pores (Flint 1998, pp. 17 to 18). Layer average values for relative humidity porosity are calculated in the same manner as total porosity. The layer average values of relative humidity porosity are subtracted from the layer average values of total porosity to provide an estimate of residual water content (i.e., the amount of water left in the pores and bound to the minerals after relative permeability or hydraulic conductivity has been reduced to zero). Residual saturation was calculated by dividing the residual water content by total porosity.

Matrix α and *m*–Water potential and saturation from a number of samples (at least one for each layer) were measured while a core sample was drying. These data were used to calculate the α and m parameters for each layer by fitting to Equation C-15. The best-fit parameters were obtained by minimizing the sum of the squared saturation residuals,

$$\sum_{i=1}^{n} r_i^2 = \sum_{i=1}^{n} \left(S_i - S(\Psi_i)\right)^2 \qquad \text{(Eq. C-20)}$$

where r_i is a saturation residual, n is the number of saturation and water potential data pairs for a layer, S_i is a saturation data point, and $S(\Psi_i)$ is the saturation predicted by the van Genuchten relationship for water potential, Ψ_i.

The uncertainty or standard error of α and *m* is given by the diagonal terms of the covariance matrix,

$$\boldsymbol{C} = s_0^{\,2}\left(\boldsymbol{J}^{\boldsymbol{T}}\boldsymbol{J}\right)^{-1} \qquad \text{(Eq. C-21)}$$

where *C* is the covariance matrix, s_0^2 is the error variance, and *J* is the Jacobian matrix. Standard error, *SE*, can be related to the standard deviation, σ, which has been given for other properties by Equation C-2.

C.4.3.2.4 Matrix Relative Permeability

According to van Genuchten (1980, p. 893), relative permeability (k_r) can be related to effective water saturation (S_e) as

$$k_r = S_e^{1/2}\left[1-\left(1-S_e^{1/m}\right)\right]^{2m} \qquad \text{(Eq. C-22)}$$

However, recent studies indicate that a more general expression for relative permeability is (Schaap and Leij 2000, pp. 843 to 844):

$$k_r = S_e^{\eta}\left[1-\left(1-S_e^{1/m}\right)\right]^{2m} \qquad \text{(Eq. C-23)}$$

where η is an empirical constant. Many studies show that η is not 0.5 as assumed by van Genuchten (1980), but varies over a very large range (Schaap and Leij 2000, pp. 843 to 844). This is consistent with the matrix relative permeability data collected from the unsaturated zone.

To determine an η estimate for an unsaturated zone model layer, the following equation was used to fit the unsaturated conductivity (*K*) data collected within the model layer:

$$\frac{K(S_e)}{K(S_0)} = \frac{S_e^{\eta}\left[1-\left(1-S_e^{1/m}\right)\right]^{2m}}{S_0^{\eta}\left[1-\left(1-S_0^{1/m}\right)\right]^{2m}} \qquad \text{(Eq. C-24)}$$

$K(S_0)$ is the conductivity at a saturation S_0, which is selected to be close to one. Equation C-24 is derived by writing Equation C-23 for a general value of S_e and for S_e=S_0. The fitted η values are reported in Table C-3 for different model layers. They range from −3.80 to 14.48, which are consistent with those values cited by Schaap and Leij (2000, p. 844). Directly fitted η values are available only for hydrogeologic units CMW, CNW, BT4, BT3, TPP, BT2, PV2v, BT1v, and CHV, where unsaturated hydraulic conductivity data are collected (Table C-3). For other units, the following empirical relation is used to estimate the η values:

$$\eta = Am - B\log(k) + C \qquad \text{(Eq. C-25)}$$

and the corresponding standard errors are estimated by

$$SE_\eta = SE_A m - SE_B \log(k) + SE_C \qquad \text{(Eq. C-26)}$$

where k is absolute permeability and A (8.14), B (1.99), and C (−28.24) are empirical parameters determined by fitting Equation C-25 to η values for hydrogeologic units CMW, CNW, BT4, BT3, TPP, BT2, PV2v, BT1v, and CHV, where unsaturated hydraulic conductivity data are collected. SE_A, SE_B, and SE_C are the standard errors for A, B, and C, respectively, and determined from the curve fitting. Values calculated from Equations C-25 and C-26 are reported in Table C-3. A comparison between the currently obtained results based on Equation C-23 and the van Genuchten relative permeability-saturation relation, Equation C-22, can be easily made with

$$\frac{k_r(S_e)}{k_{r,VG}(S_e)} = S_e^{\eta-0.5} \qquad \text{(Eq. C-27)}$$

where subscript VG refers to relative permeability obtained from the van Genuchten relation, Equation C-22. Equation C-27 is derived from Equations C-22 and C-23. Since estimated η values were very different from 0.5 for many model layers (Table C-3), relative permeabilities predicted with the van Genuchten relation (Equation C-22) have considerable errors, especially for low saturations. The errors become insignificant for saturations close to one, which is the case for welded units under the ambient conditions. A large degree of uncertainty in estimated η values exists because of data limitations. Therefore, the van Genuchten relation is still used in modeling studies.

C.4.4 Treatment of Spatial Heterogeneity

This section provides additional information supporting the response to the discussion of uncertainty arising from spatial heterogeneity in KTI agreement TEF 2.11.

Heterogeneities exist at different scales within both fracture and matrix continua in the Yucca Mountain unsaturated zone. Treatment of subsurface heterogeneity is important for modeling flow and transport processes. A geology-based deterministic approach, in which an entire model layer is assigned uniform properties, is used mainly for representing subsurface heterogeneity at site-scale.

The key justification for this approach is that the overall behavior of site-scale flow and transport processes is determined mainly by relatively large-scale heterogeneities associated with the geologic stratification of the mountain. Stratification and faulting, which places units with highly different properties against each other, are the heterogeneities within the unsaturated zone. Within the same geologic unit, hydrologic properties are relatively uniformly distributed because of the intrastrata homogenization induced by tuff depositional environments.

The validity of this approach in dealing with subsurface heterogeneity was demonstrated using a two-dimensional vertical cross-section in the east-west direction through borehole USW UZ-14 to investigate the effect of multiscale heterogeneity on unsaturated flow and transport within the unsaturated zone (Zhou et al. 2003). Specifically, random fields of three selected properties: matrix permeability k_M, matrix van Genuchten parameter α_M, and fracture permeability k_F were generated and used (Zhou et al. 2003, Figure 13). For comparison, different sets of rock property distributions were employed in three cases. In these cases, mean rock properties for a given

geologic layer are the same. In Case A, the layered approach mentioned above was used. In Case B, stochastically generated k_f variability was considered within each geologic layer. In Case C, variabilities of all the selected rock properties were included, with the variabilities determined from the measured hydrologic properties. Thus, Case A only considers large-scale heterogeneity, while Cases B and C include small-scale heterogeneity within a geologic unit.

Figure C-6 shows comparisons of vertical water fluxes within the matrix and fractures along the repository zone for the three cases. Although relatively large differences exist for the matrix water flux, distributions of fracture water fluxes are very similar for these three cases. Because the matrix flux corresponds to only a small percentage of total water flux, the three cases essentially provide similar water flow fields at the site scale. Simulated results for tracer transport from the repository to the water table were compared, and it was again found that the results are similar for the three cases (Zhou et al. 2003). In summary, it has been clearly demonstrated that heterogeneities within each geologic unit have only a minor effect on the site-scale flow processes (Zhou et al. 2003).

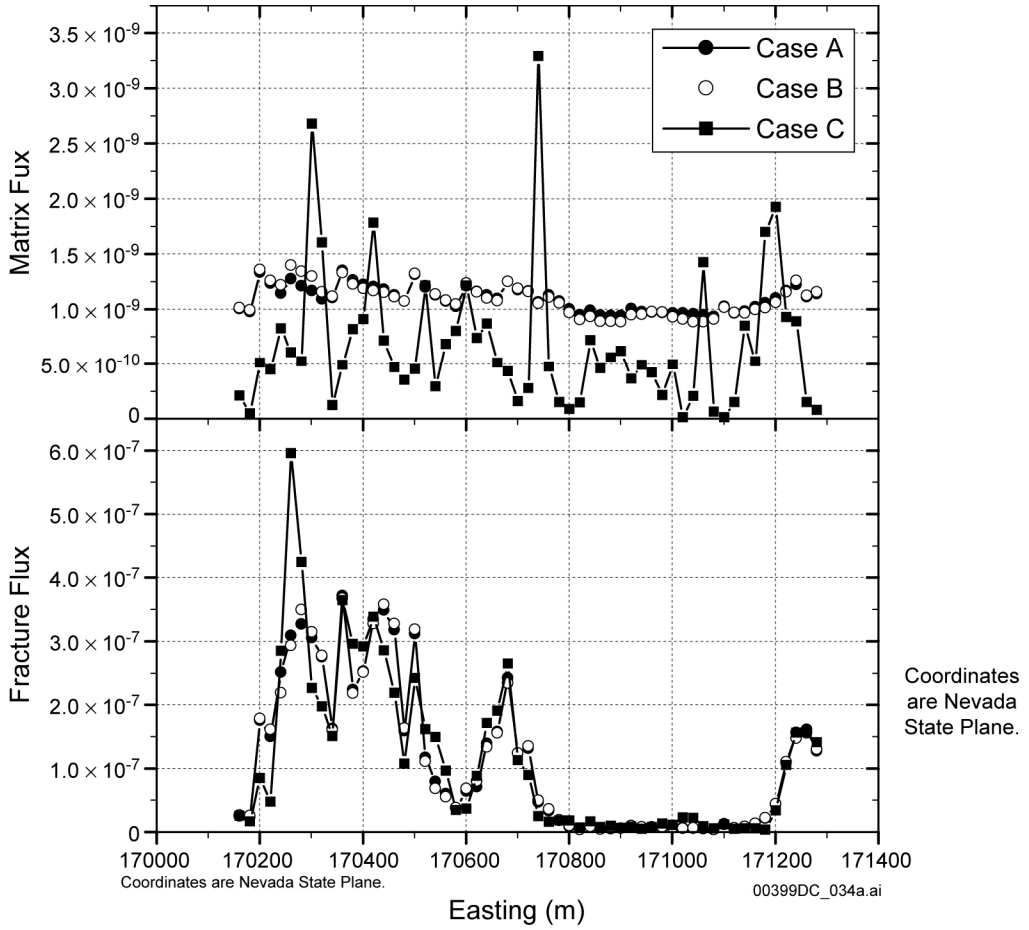

Source: Zhou et al. 2003, Figure 16.

NOTE: The unit of the water flux is kg/m^2/s rather than m/s as mentioned in Figure 16 of Zhou et al. (2003). Case A: Heterogeneity was captured using layer-wise homogeneous properties. Case B: Fracture permeability (K_F) within each geologic layer was stochastically generated. Case C: Variabilities of all the selected rock properties (K_F, K_M, and α_M) were included, with the variabilities determined from the measured hydrologic properties.

Figure C-6. Comparison of Simulated Matrix and Fracture Flux (kg/m^2/s) at the Repository Horizon in Cases A, B, and C

C.4.5 Model Calibration

This section provides information regarding model calibration in response to KTI agreement TEF 2.11.

C.4.5.1 General Calibration Approach

Model calibration involves using numerical models for the unsaturated zone to predict unsaturated zone conditions and then compare them to field observations (such as saturation data and gas pressure data). Model parameters are calibrated so that the difference between model predictions and observed data is minimized. Inversion is an iterative process in which predictions from a numerical model are compared to data. The numerical model parameters are calibrated to improve the match between the model prediction and the data.

Data that are inverted to provide the calibrated properties include saturation in the rock matrix, water potential in the rock matrix, and pneumatic pressure in the fractures. Hydrologic property estimates from laboratory and field measurements, which provide initial uncalibrated estimates for model parameters, are also included as data in the inversion (Section C.4.3). These data, which are referred to as prior information, are just as important to the inversion as data regarding the state of the system (e.g., saturation). The combination of the two types of information allows the inversion to match the data as closely as possible while simultaneously estimating model parameters that are reasonable according to the prior information. Two kinds of parameter sets, drift scale and mountain scale, are determined from these calibration activities.

The software iTOUGH2 V5.0 (LBNL 2002) is used to carry out the automatic portion of the inversion process. This software allows the consideration of both data and prior information, and allows them to be weighted (Finsterle 1998; Finsterle 1999), Section C.4.1.2) according to the uncertainty of the estimated value. The software attempts to minimize the sum of the squared, weighted residuals (called the objective function):

$$F = \sum_i \frac{(z_i * - z_i)^2}{U_i^2} \qquad \text{(Eq. C-28)}$$

where z_i* and z_i are measurement i and the corresponding simulation result, respectively. U_i is the uncertainty of measurement z_i*.

iTOUGH2 V5.0 iteratively updates the selected model parameters until the objective function reaches minimum (Finsterle 1998; Finsterle 1999). Averaged matrix saturation values for the corresponding numerical gridblocks are used in inversions (Section C.4.1.1).

The inversion using iTOUGH2 V5.0 (LBNL 2002) is performed with one-dimensional forward models because the available water potential and saturation data were collected from surface-based vertical boreholes and only provide vertical profiles of water potential and saturation, and because the inverse model using three-dimensional forward simulations (with a quarter million gridblocks) is robust and constrained by the current computational resources. From the surface to the repository, lateral flow is not expected to be significant because perched water has not been found there. Below the repository, in the Calico Hills nonwelded unit and the Crater Flat undifferentiated unit (CFu), areas of perched water exist where lateral flow may be significant. Properties needed to produce perched water and varying degrees of lateral flow are then addressed using a manual (trial-and-error) calibration approach (BSC 2003b, Section 6.2).

C.4.5.2 Calibration of Drift-Scale Parameters

Calibration Procedure–One-dimensional inversion of the matrix-saturation and water potential data is carried out for drift-scale parameters. The EOS9 module (Richards equation) of iTOUGH2 V5.0 (LBNL 2002) is used for the inversion. The one-dimensional submodels correspond to 16 surface-based boreholes from which saturation and water potential have been measured. Table C-4 shows the types of data used from each borehole. Steady-state water flow is simulated simultaneously in all columns. Layer-averaged effective parameters are estimated.

Three calibrated parameter sets are produced, one for each present-day infiltration case. The base-case infiltration scenario gives the expected, spatially varying infiltration rates over Yucca Mountain. Parameters calibrated using this scenario are the base-case parameter set. The upper- and lower-bound infiltration scenarios give bounds to the uncertainty of the base-case infiltration scenario. Parameters calibrated using the bounding scenarios are also provided. This yields the parameter sets that consider underestimation and overestimation of the present-day infiltration by the base-case scenario.

Table C-4. Data Used for One-Dimensional Calibration of Drift-Scale Properties from Each Borehole

Borehole	Matrix Liquid Saturation (core)	Matrix Liquid Water Potential (in situ)
USW NRG-6		√
USW SD-6	√	
USW SD-7	√	
USW SD-9	√	
UE-25 SD-12		√
UE-25 UZ#16		√
USW UZ-1	√	
UE-25 UZ#16	√	
USW UZ-N11	√	
USW UZ-N31	√	
USW UZ-N33	√	
USW UZ-N37	√	
USW UZ-N53	√	
USW UZ-N57	√	
USW UZ-N61	√	
USW WT-2	√	

Source: BSC 2003a, Table 9.

Choice of Parameters for Calibration–Model parameters to be estimated are matrix permeability k, matrix van Genuchten parameter α (van Genuchten 1980, pp. 892 to 893), fracture van Genuchten parameters α and m, and active-fracture-model parameter γ (Liu et al. 1998). Other parameters are not changed in the calibration. These parameters are calibrated for model layers, although in some cases a common parameter value is estimated for groups of layers.

Properties for the zeolitic portion of CHn, the unit where perched water is observed, are not calibrated here. Fracture permeability and van Genuchten m are not calibrated in this stage because they are expected to be relatively insensitive to simulated matrix-saturation and water-potential distributions. Bandurraga and Bodvarsson (1999, Section 5) provide a detailed discussion of sensitivities of rock properties to the relevant simulation results. Nevertheless, reduction in the number of calibrated properties is necessary because of the limited data points available for inversions. A total of 78 rock parameters are estimated. This set was chosen for calibration because it is relatively small and could represent ambient conditions in the unsaturated zone.

Residual and satiated saturation are parameters that do not influence the calibration to ambient data as strongly as the van Genuchten parameter α. This is because ambient saturation and water potential data are generally not at the extremes of the relationships where these bounding values play a stronger role. Like matrix porosity, matrix residual saturation is another property that is simple to measure with low error, so it makes more sense to calibrate the parameters that are not well constrained.

The matrix van Genuchten parameter *m*, which is essentially a pore-size distribution index, is well constrained by the desaturation data, whereas the same data may give an estimate of the van Genuchten α that is biased toward the drainage condition. In this study, matrix van Genuchten *m* parameters are not calibrated, which reduces the number of parameters in the calibration.

Other hydrologic parameters not calibrated are fracture and matrix porosity, residual saturation, and satiated saturation. Liquid flow simulations, because they are in steady state, are insensitive to porosity variations, so porosity could not be calibrated by inversion of saturation and water potential data. Further, matrix porosity is a well-constrained property because the techniques used to measure porosity are simple and the measurement error is low.

Because no data exists for model layers tr3 and tr2, they are assigned the same properties as model layers bf3 and bf2, respectively. This assignment is based on the common depositional profile of the Tram and Bullfrog tuffs. Because the Bullfrog tuff represents a very small portion of the unsaturated zone within the unsaturated zone model boundaries (it is present above the water table only immediately next to the Solitario Canyon Fault and in the extreme northern portion of the unsaturated zone) (BSC 2003e, Section 6), the impact of this approximation is not significant.

Common values of k_M, α_M, and α_F, are used for the vitric Tac (material types ch2v, ch3v, chv, and ch5v) and for the zeolitic Tac (material types ch2z, ch3z, chz, and ch5z), respectively. The common value refers to a property value shared by several model layers. These layers do not represent actual geologic or hydrogeologic divisions but are employed to better characterize which portions of the Tac are vitric or zeolitic (BSC 2003e, Section 6).

The lower nonlithophysal layer of the TSw (Tptpln) is subdivided into two layers based on matrix property development (Flint 1998, pp. 27 to 29). This division does not exist for the fracture properties (see Table C-5), so common values of fracture properties are used for material types tsw36 and tsw37.

Table C-5. Calibrated Parameters from One-Dimensional Inversion of Saturation and Water Potential Data for the Base-Case Infiltration Scenario

Model Layer	k_M (m^2)	α_M (1/Pa)	m_M	k_F (m^2)	α_F (1/Pa)	m_F	γ
tcw11	3.74×10^{-15}	1.01×10^{-5}	0.388	3.0×10^{-11}	5.27×10^{-3}	0.633	0.587
tcw12	5.52×10^{-20}	3.11×10^{-6}	0.280	5.3×10^{-12}	1.57×10^{-3}	0.633	0.587
tcw13	5.65×10^{-17}	3.26×10^{-6}	0.259	4.5×10^{-12}	1.24×10^{-3}	0.633	0.587
ptn21	4.60×10^{-15}	1.62×10^{-4}	0.245	3.2×10^{-12}	8.70×10^{-4}	0.633	0.232
ptn22	4.43×10^{-12}	1.46×10^{-4}	0.219	3.0×10^{-13}	1.57×10^{-3}	0.633	0.232
ptn23	9.20×10^{-15}	2.47×10^{-5}	0.247	3.0×10^{-13}	5.18×10^{-3}	0.633	0.232
ptn2	2.35×10^{-12}	7.90×10^{-4}	0.182	3.0×10^{-12}	1.86×10^{-3}	0.633	0.232
ptn25	2.15×10^{-13}	1.04×10^{-4}	0.300	1.7×10^{-13}	1.33×10^{-3}	0.633	0.232
ptn26	1.00×10^{-11}	9.83×10^{-4}	0.126	2.2×10^{-13}	1.34×10^{-3}	0.633	0.232
tsw31	2.95×10^{-17}	8.70×10^{-5}	0.218	8.1×10^{-13}	1.60×10^{-5}	0.633	0.129
tsw32	2.23×10^{-16}	1.14×10^{-5}	0.290	7.1×10^{-13}	1.00×10^{-4}	0.633	0.600
tsw33	6.57×10^{-18}	6.17×10^{-6}	0.283	7.8×10^{-13}	1.59×10^{-3}	0.633	0.600
tsw3	1.77×10^{-19}	8.45×10^{-6}	0.317	3.3×10^{-13}	1.04×10^{-4}	0.633	0.569
tsw35	4.48×10^{-18}	1.08×10^{-5}	0.216	9.1×10^{-13}	1.02×10^{-4}	0.633	0.569
tsw36	2.00×10^{-19}	8.32×10^{-6}	0.442	1.3×10^{-12}	7.44×10^{-4}	0.633	0.569
tsw37	2.00×10^{-19}	8.32×10^{-6}	0.442	1.3×10^{-12}	7.44×10^{-4}	0.633	0.569
tsw38	2.00×10^{-18}	6.23×10^{-6}	0.286	8.1×10^{-13}	2.12×10^{-3}	0.633	0.569
tswz (zeolitic portion of tsw39)	3.50×10^{-17}	4.61×10^{-6}	0.059	8.1×10^{-13}	1.5×10^{-3}	0.633	0.370 [b]
tswv (vitric portion of tsw39)	1.49×10^{-13}	4.86×10^{-5}	0.293	[a]	[a]	[a]	[a]
ch1z	3.50×10^{-17}	2.12×10^{-7}	0.349	2.5×10^{-14}	1.4×10^{-3}	0.633	0.370 [b]
ch1v	6.65×10^{-13}	8.73×10^{-5}	0.240	[a]	[a]	[a]	[a]
ch2v	2.97×10^{-11}	2.59×10^{-4}	0.158	[a]	[a]	[a]	[a]
ch3v	2.97×10^{-11}	2.59×10^{-4}	0.158	[a]	[a]	[a]	[a]
chv	2.97×10^{-11}	2.59×10^{-4}	0.158	[a]	[a]	[a]	[a]
ch5v	2.97×10^{-11}	2.59×10^{-4}	0.158	[a]	[a]	[a]	[a]
ch6v	2.35×10^{-13}	1.57×10^{-5}	0.147	[a]	[a]	[a]	[a]
ch2z	5.20×10^{-18}	2.25×10^{-6}	0.257	2.5×10^{-14}	8.9×10^{-4}	0.633	0.370 [b]
ch3z	5.20×10^{-18}	2.25×10^{-6}	0.257	2.5×10^{-14}	8.9×10^{-4}	0.633	0.370 [b]
chz	5.20×10^{-18}	2.25×10^{-6}	0.257	2.5×10^{-14}	8.9×10^{-4}	0.633	0.370 [b]
ch5z	5.20×10^{-18}	2.25×10^{-6}	0.257	2.5×10^{-14}	8.9×10^{-4}	0.633	0.370 [b]
ch6z	8.20×10^{-18}	1.56×10^{-7}	0.499	2.5×10^{-14}	1.4×10^{-3}	0.633	0.370 [b]
pp	8.77×10^{-17}	4.49×10^{-7}	0.474	2.5×10^{-14}	1.83×10^{-3}	0.633	0.370
pp3	7.14×10^{-14}	8.83×10^{-6}	0.407	2.2×10^{-13}	2.47×10^{-3}	0.633	0.199
pp2	1.68×10^{-15}	2.39×10^{-6}	0.309	2.2×10^{-13}	3.17×10^{-3}	0.633	0.199
pp1	2.35×10^{-15}	9.19×10^{-7}	0.272	2.5×10^{-14}	1.83×10^{-3}	0.633	0.370 [b]
bf3	4.34×10^{-13}	1.26×10^{-5}	0.193	2.2×10^{-13}	2.93×10^{-3}	0.633	0.199
bf2	8.10×10^{-17}	1.18×10^{-7}	0.617	2.5×10^{-14}	8.9×10^{-4}	0.633	0.370 [b]

Source: BSC 2003a, Table 11.

NOTE: [a]Calibrated properties conceptual model does not include fractures in these model layers.

[b]The gamma parameter was not calibrated for those layers. The value from pp is assigned to these layers.

The fracturing characteristics of Yucca Mountain rocks are considered to be primarily dependent on the degree of welding and alteration. The welded rocks have higher fracture frequencies than nonwelded rocks. Because of the general division between the fracture characteristics of welded and nonwelded rocks, model layers are grouped together, based on welding, to estimate common values of the active fracture parameter. Alteration is believed to possibly influence the active fracture parameter, so it is also used as a criterion for grouping layers. Common values of gamma are estimated for the TCw, PTn, some layers of the TSw, zeolitic portions of the TSw, CHn and CFu, and devitrified or welded portions of the CHn and CFu. Table C-6 shows the material types included in each of these groups. The value of gamma is estimated individually for tsw31 because matrix-to-fracture flow is expected to be high in this layer as a result of the transition from matrix-dominated flow in the PTn to fracture-dominated flow in the TSw. No prior information exists for the active fracture parameter γ. Initial estimates for gamma are taken as 0.25 for all layers, as shown in Table C-6.

Table C-6. Initial Estimates of the Active Fracture Parameter, Gamma, for Saturation and Water Potential Data Inversion

Material Type (group)	γ
tcw11, tcw12, tcw13	0.25
ptn21, ptn22, ptn23, ptn2, ptn25, ptn26	0.25
tsw31	0.25
tsw32 and tsw33	0.25
tsw3, tsw35, tsw36, tsw37, tsw38, tsw39	0.25
ch1z, ch2z, ch3z, chz, ch5z, ch6, pp, pp1, bf2 and tswz (zeolitic portion of tsw39)	0.25
pp3, pp2, bf3	0.25

Source: BSC 2003a, Table 10.

Prior information (Section C.4.3) is used for initial guesses of inversions, except for the upper infiltration case. For that case, numerical convergence is difficult to obtain, and, therefore, the calibrated drift-scale property set for the base-case infiltration scenario is used for an initial guess. Fracture permeabilities for pp and pp3 are adjusted.

Calibration Results–The one-dimensional calibrated drift-scale parameter set for the base-case (mean) infiltration scenario is presented in Table C-5. Matches to the saturation data achieved with this parameter set for USW SD-9 are shown in Figure C-7. Figure C-8 shows matches to the water potential data for UE-25 SD-12.

The one-dimensional calibrated parameter set for the upper-bound infiltration scenario is presented in Table C-7. Matches to the saturation data achieved with this parameter set for USW SD-9 are shown in Figure C-9. A comparison between data and simulation results for the zeolitic portion of CHn is not shown because saturation data from that location are not used for calibration. Figure C-10 shows matches to the water potential data for UE-25 SD-12.

The one-dimensional calibrated parameter set for the lower-bound infiltration scenario is presented in Table C-8. Matches to the saturation data achieved with this parameter set for

USW SD-9 are shown in Figure C-11. A comparison between data and simulation results for the zeolitic portion of CHn is not shown because saturation data from that location are not used for calibration. Figure C-12 shows matches to the water potential data for UE-25 SD-12.

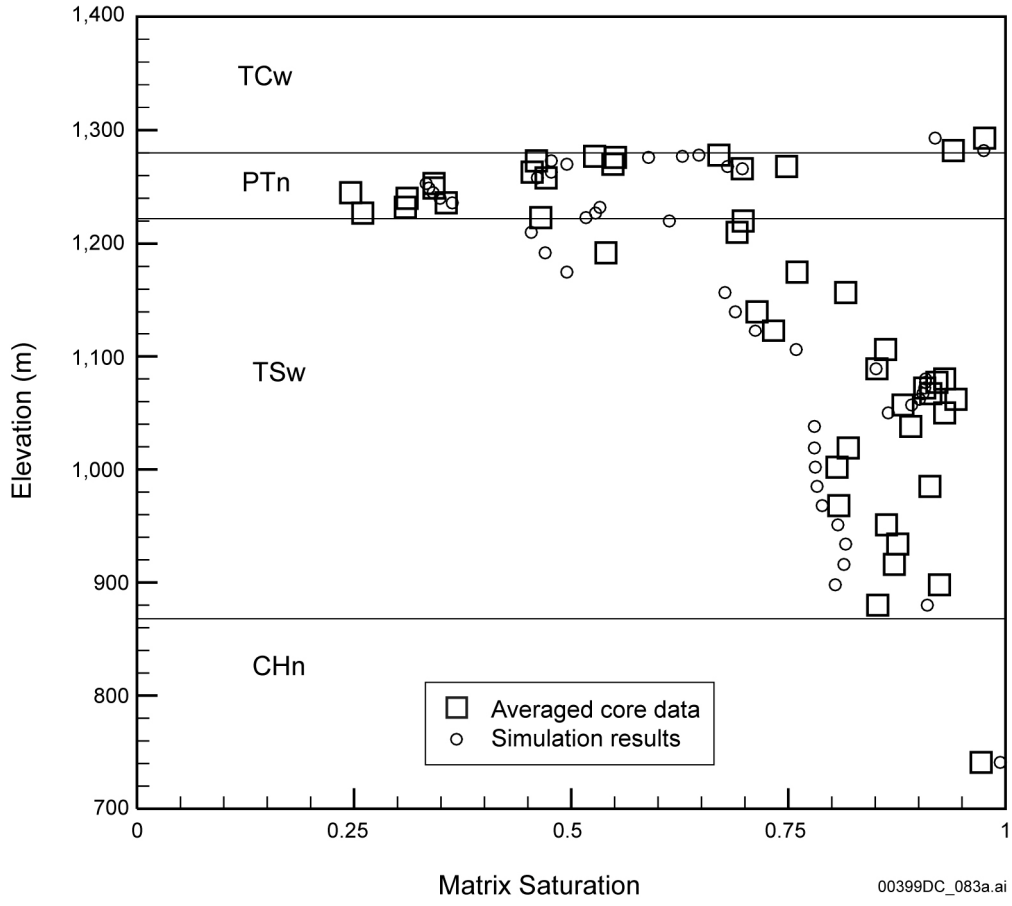

Source: BSC 2003a, Figure 2.

Figure C-7. Saturation Matches at USW SD-9 for a One-Dimensional, Drift-Scale, Calibrated Parameter Set for the Base-Case Infiltration Scenario

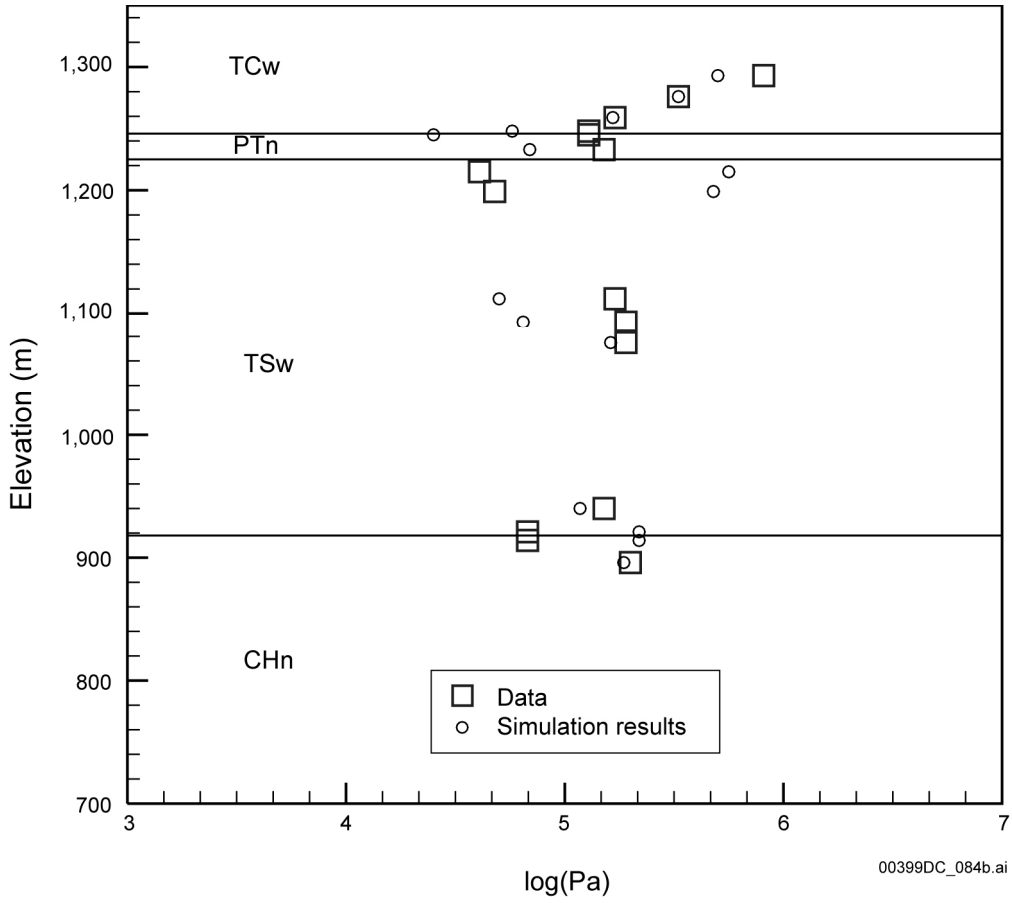

Source: BSC 2003a, Figure 3.

Figure C-8. Water Potential Matches at UE-25 SD-12 for a One-Dimensional, Drift-Scale, Calibrated Parameter Set for the Base-Case Infiltration Scenario

Table C-7. Calibrated Parameters from One-Dimensional Inversion of Saturation and Water Potential Data for the Upper-Bound Infiltration Scenario

Model Layer	k_M (m^2)	α_M (1/Pa)	m_M	k_F (m^2)	α_F (1/Pa)	m_F	γ
tcw11	3.90×10^{-15}	1.23×10^{-5}	0.388	3.0×10^{-11}	5.01×10^{-3}	0.633	0.500
tcw12	1.16×10^{-19}	3.39×10^{-6}	0.280	5.3×10^{-12}	2.19×10^{-3}	0.633	0.500
tcw13	4.41×10^{-16}	3.25×10^{-6}	0.259	4.5×10^{-12}	1.86×10^{-3}	0.633	0.500
ptn21	2.14×10^{-14}	1.56×10^{-4}	0.245	3.2×10^{-12}	2.69×10^{-3}	0.633	0.100
ptn22	1.29×10^{-11}	1.33×10^{-4}	0.219	3.0×10^{-13}	1.38×10^{-3}	0.633	0.100
ptn23	4.07×10^{-14}	2.39×10^{-5}	0.247	3.0×10^{-13}	1.23×10^{-3}	0.633	0.100
ptn2	4.27×10^{-12}	5.62×10^{-4}	0.182	3.0×10^{-12}	2.95×10^{-3}	0.633	0.100
ptn25	1.01×10^{-12}	9.48×10^{-5}	0.300	1.7×10^{-13}	1.10×10^{-3}	0.633	0.100
ptn26	1.00×10^{-11}	5.23×10^{-4}	0.126	2.2×10^{-13}	9.55×10^{-4}	0.633	0.100
tsw31	1.77×10^{-17}	4.85×10^{-5}	0.218	8.1×10^{-13}	1.58×10^{-5}	0.633	0.100
tsw32	2.13×10^{-16}	1.96×10^{-5}	0.290	7.1×10^{-13}	1.00×10^{-4}	0.633	0.561
tsw33	2.39×10^{-17}	5.22×10^{-6}	0.283	7.8×10^{-13}	1.58×10^{-3}	0.633	0.561
tsw3	2.96×10^{-19}	1.65×10^{-6}	0.317	3.3×10^{-13}	1.00×10^{-4}	0.633	0.570
tsw35	8.55×10^{-18}	5.03×10^{-6}	0.216	9.1×10^{-13}	5.78×10^{-4}	0.633	0.570
tsw36	7.41×10^{-19}	1.08×10^{-6}	0.442	1.3×10^{-12}	1.10×10^{-3}	0.633	0.570
tsw37	7.41×10^{-19}	1.08×10^{-6}	0.442	1.3×10^{-12}	1.10×10^{-3}	0.633	0.570
tsw38	7.40×10^{-18}	5.58×10^{-6}	0.286	8.1×10^{-13}	8.91×10^{-4}	0.633	0.570
tswz (zeolitic portion of tsw39)	3.50×10^{-17}	4.61×10^{-6}	0.059	8.1×10^{-13}	1.50×10^{-3}	0.633	0.500[b]
tswv (vitric portion of tsw39)	2.24×10^{-13}	4.86×10^{-5}	0.293	[a]	[a]	[a]	[a]
ch1z	3.50×10^{-17}	2.12×10^{-7}	0.349	2.5×10^{-14}	1.40×10^{-3}	0.633	0.500[b]
ch1v	1.39×10^{-12}	8.82×10^{-5}	0.240	[a]	[a]	[a]	[a]
ch2v	4.90×10^{-11}	2.73×10^{-4}	0.158	[a]	[a]	[a]	[a]
ch3v	4.90×10^{-11}	2.73×10^{-4}	0.158	[a]	[a]	[a]	[a]
chv	4.90×10^{-11}	2.73×10^{-4}	0.158	[a]	[a]	[a]	[a]
ch5v	4.90×10^{-11}	2.73×10^{-4}	0.158	[a]	[a]	[a]	[a]
ch6v	2.72×10^{-13}	1.67×10^{-5}	0.147	[a]	[a]	[a]	[a]
ch2z	5.20×10^{-18}	2.25×10^{-6}	0.257	2.5×10^{-14}	8.9×10^{-4}	0.633	0.500[b]
ch3z	5.20×10^{-18}	2.25×10^{-6}	0.257	2.5×10^{-14}	8.9×10^{-4}	0.633	0.500[b]
chz	5.20×10^{-18}	2.25×10^{-6}	0.257	2.5×10^{-14}	8.9×10^{-4}	0.633	0.500[b]
ch5z	5.20×10^{-18}	2.25×10^{-6}	0.257	2.5×10^{-14}	8.9×10^{-4}	0.633	0.500[b]
ch6z	8.2×10^{-19}	1.56×10^{-7}	0.499	2.5×10^{-14}	1.4×10^{-3}	0.633	0.500[b]
pp	1.02×10^{-15}	4.57×10^{-7}	0.474	2.5×10^{-12}	8.91×10^{-4}	0.633	0.500
pp3	1.26×10^{-13}	9.50×10^{-6}	0.407	2.2×10^{-12}	1.66×10^{-3}	0.633	0.500
pp2	1.70×10^{-15}	2.25×10^{-6}	0.309	2.2×10^{-13}	1.66×10^{-3}	0.633	0.500
pp1	2.57×10^{-15}	8.77×10^{-7}	0.272	2.5×10^{-14}	8.91×10^{-4}	0.633	0.500[b]
bf3	3.55×10^{-14}	3.48×10^{-5}	0.193	2.2×10^{-13}	1.66×10^{-3}	0.633	0.500
bf2	8.1×10^{-17}	1.18×10^{-7}	0.617	2.5×10^{-14}	8.9×10^{-4}	0.633	0.500[b]

Source: BSC 2003a, Table 12.

NOTE: [a] The calibrated properties conceptual model does not include fractures in these model layers.

[b] The gamma was not calibrated for these layers. The value from pp is assigned to these layers.

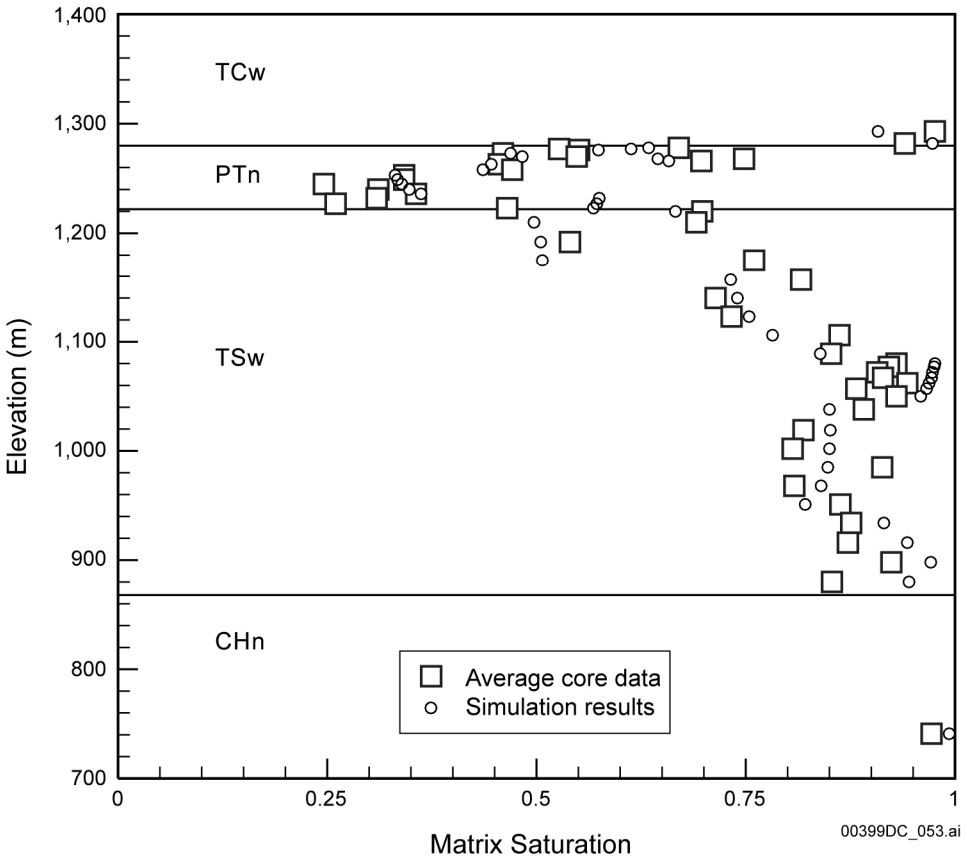

Source: BSC 2003a, Figure 4.

Figure C-9. Saturation Matches at USW SD-9 for a One-Dimensional, Drift-Scale, Calibrated Parameter Set for the Upper-Bound Infiltration Scenario

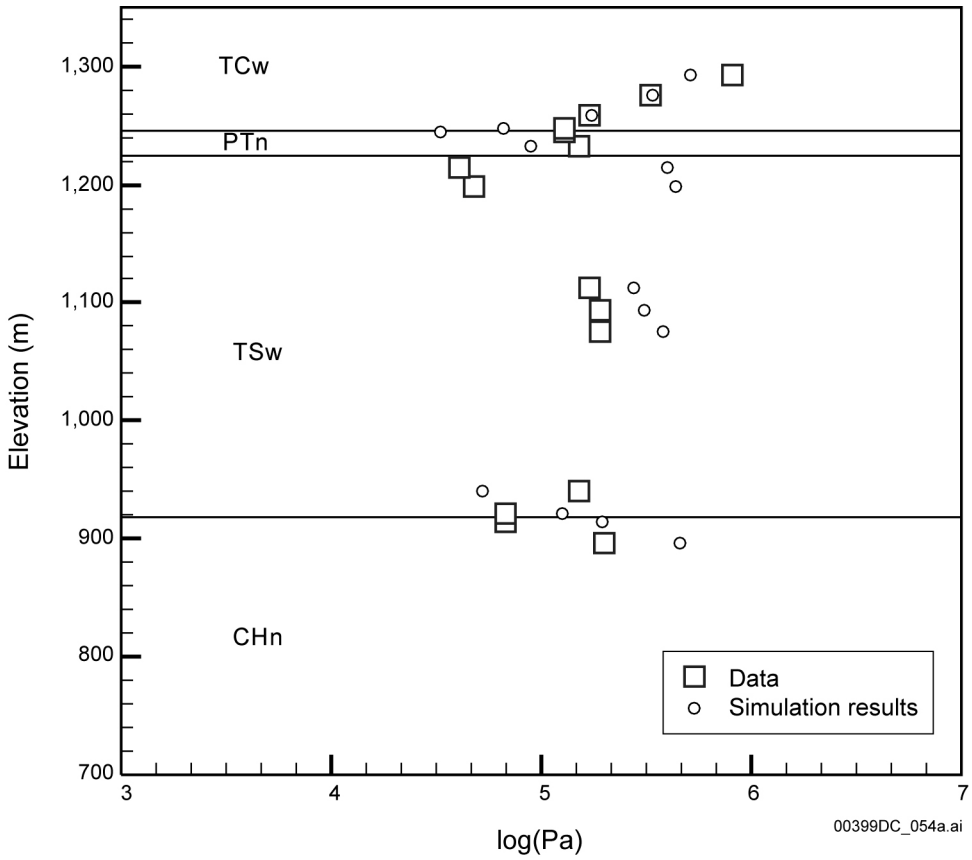

Source: BSC 2003a, Figure 5.

Figure C-10. Water Potential Matches at UE-25 SD-12 for a One-Dimensional, Drift-Scale, Calibrated Parameter Set for the Upper-Bound Infiltration Scenario

Table C-8. Calibrated Parameters from One-Dimensional Inversion of Saturation and Water Potential Data for the Lower-Bound Infiltration Scenario

Model Layer	k_M (m^2)	α_M (1/Pa)	m_M	k_F (m^2)	α_F (1/Pa)	m_F	γ
tcw11	3.44×10^{-15}	1.16×10^{-5}	0.388	3.0×10^{-11}	4.68×10^{-3}	0.633	0.483
tcw12	3.00×10^{-20}	2.67×10^{-6}	0.280	5.3×10^{-12}	3.20×10^{-3}	0.633	0.483
tcw13	3.96×10^{-17}	1.64×10^{-6}	0.259	4.5×10^{-12}	2.13×10^{-3}	0.633	0.483
ptn21	5.55×10^{-15}	6.38×10^{-5}	0.245	3.2×10^{-12}	2.93×10^{-3}	0.633	0.065
ptn22	8.40×10^{-12}	1.67×10^{-4}	0.219	3.0×10^{-13}	6.76×10^{-4}	0.633	0.065
ptn23	1.92×10^{-14}	4.51×10^{-5}	0.247	3.0×10^{-13}	3.96×10^{-3}	0.633	0.065
ptn2	6.66×10^{-13}	2.52×10^{-3}	0.182	3.0×10^{-12}	2.51×10^{-3}	0.633	0.065
ptn25	1.96×10^{-14}	1.24×10^{-4}	0.300	1.7×10^{-13}	1.53×10^{-3}	0.633	0.065
ptn26	1.00×10^{-11}	1.63×10^{-3}	0.126	2.2×10^{-13}	1.52×10^{-3}	0.633	0.065
tsw31	1.42×10^{-17}	8.02×10^{-5}	0.218	8.1×10^{-13}	1.58×10^{-5}	0.633	0.037
tsw32	3.96×10^{-16}	9.46×10^{-6}	0.290	7.1×10^{-13}	1.31×10^{-4}	0.633	0.528
tsw33	1.60×10^{-18}	4.25×10^{-6}	0.283	7.8×10^{-13}	1.94×10^{-3}	0.633	0.528
tsw3	1.38×10^{-19}	1.19×10^{-6}	0.317	3.3×10^{-13}	6.55×10^{-4}	0.633	0.476
tsw35	2.33×10^{-18}	1.97×10^{-6}	0.216	9.1×10^{-13}	1.35×10^{-3}	0.633	0.476
tsw36	5.58×10^{-19}	4.22×10^{-7}	0.442	1.3×10^{-12}	1.31×10^{-3}	0.633	0.476
tsw37	5.58×10^{-19}	4.22×10^{-7}	0.442	1.3×10^{-12}	1.31×10^{-3}	0.633	0.476
tsw38	2.93×10^{-18}	1.43×10^{-6}	0.286	8.1×10^{-13}	1.75×10^{-3}	0.633	0.476
tswz (zeolitic portion of tsw39)	3.50×10^{-17}	4.61×10^{-6}	0.059	8.1×10^{-13}	1.5×10^{-3}	0.633	0.276 [b]
tswv (vitric portion of tsw39)	3.15×10^{-13}	1.86×10^{-5}	0.293	[a]	[a]	[a]	[a]
ch1z	3.50×10^{-17}	2.12×10^{-7}	0.349	2.5×10^{-14}	1.4×10^{-3}	0.633	0.276 [b]
ch1v	3.15×10^{-14}	4.50×10^{-5}	0.240	[a]	[a]	[a]	[a]
ch2v	1.13×10^{-11}	1.22×10^{-4}	0.158	[a]	[a]	[a]	[a]
ch3v	1.13×10^{-11}	1.22×10^{-4}	0.158	[a]	[a]	[a]	[a]
chv	1.13×10^{-11}	1.22×10^{-4}	0.158	[a]	[a]	[a]	[a]
ch5v	1.13×10^{-11}	1.22×10^{-4}	0.158	[a]	[a]	[a]	[a]
ch6v	2.54×10^{-13}	9.05×10^{-6}	0.147	[a]	[a]	[a]	[a]
ch2z	5.2×10^{-18}	2.25×10^{-6}	0.257	2.5×10^{-14}	8.9×10^{-4}	0.633	0.276 [b]
ch3z	5.2×10^{-18}	2.25×10^{-6}	0.257	2.5×10^{-14}	8.9×10^{-4}	0.633	0.276 [b]
chz	5.2×10^{-18}	2.25×10^{-6}	0.257	2.5×10^{-14}	8.9×10^{-4}	0.633	0.276 [b]
ch5z	5.2×10^{-18}	2.25×10^{-6}	0.257	2.5×10^{-14}	8.9×10^{-4}	0.633	0.276 [b]
ch6z	8.2×10^{-19}	1.56×10^{-7}	0.499	2.5×10^{-14}	1.4×10^{-3}	0.633	0.276 [b]
pp	2.98×10^{-16}	2.88×10^{-7}	0.474	2.5×10^{-14}	1.88×10^{-3}	0.633	0.276
pp3	5.37×10^{-14}	7.97×10^{-6}	0.407	2.2×10^{-13}	1.32×10^{-3}	0.633	0.248
pp2	4.24×10^{-16}	2.41×10^{-6}	0.309	2.2×10^{-13}	2.80×10^{-3}	0.633	0.248
pp1	7.02×10^{-16}	1.36×10^{-6}	0.272	2.5×10^{-14}	6.39×10^{-4}	0.633	0.276 [b]
bf3	2.97×10^{-14}	1.32×10^{-5}	0.193	2.2×10^{-13}	1.91×10^{-3}	0.633	0.248
bf2	8.1×10^{-17}	1.18×10^{-7}	0.617	2.5×10^{-14}	8.9×10^{-4}	0.633	0.276 [b]

Source: BSC 2003a, Table 13.

NOTE: [a] Calibrated properties conceptual model does not include fractures in these model layers.

[b] The gamma parameter was not calibrated for these layers. The value from pp is assigned to these layers.

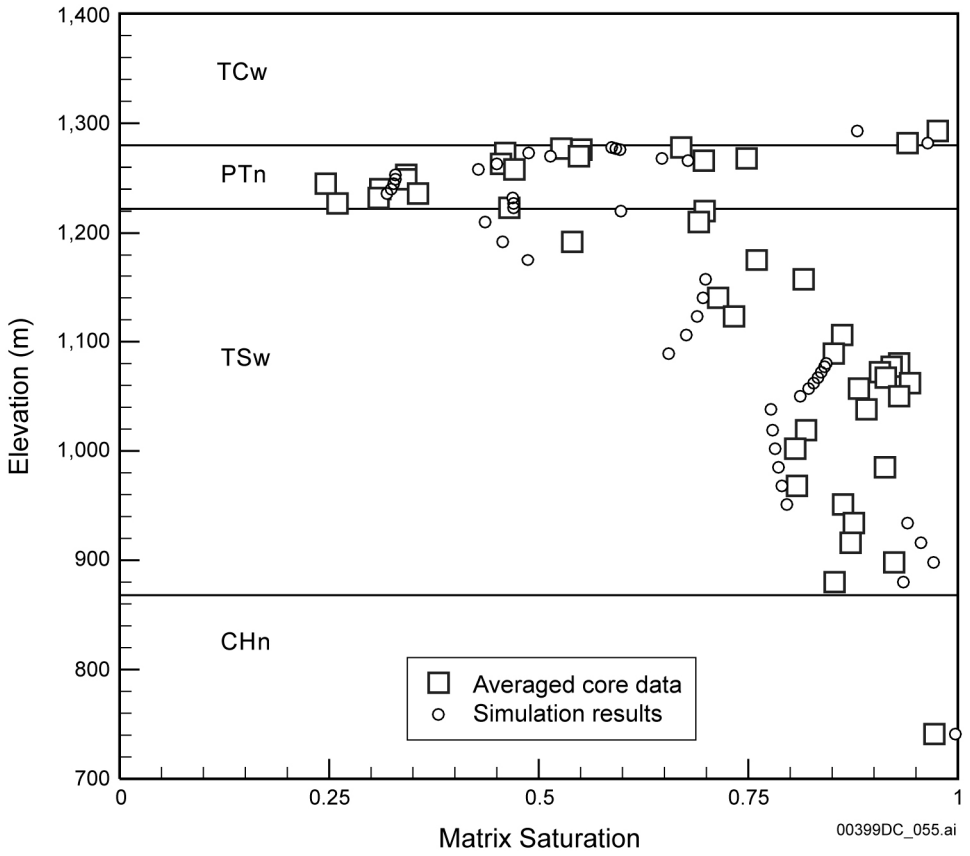

Source: BSC 2003a, Figure 6.

Figure C-11. Saturation Matches at USW SD-9 for a One-Dimensional, Drift-Scale, Calibrated Parameter Set for the Lower-Bound Infiltration Scenario

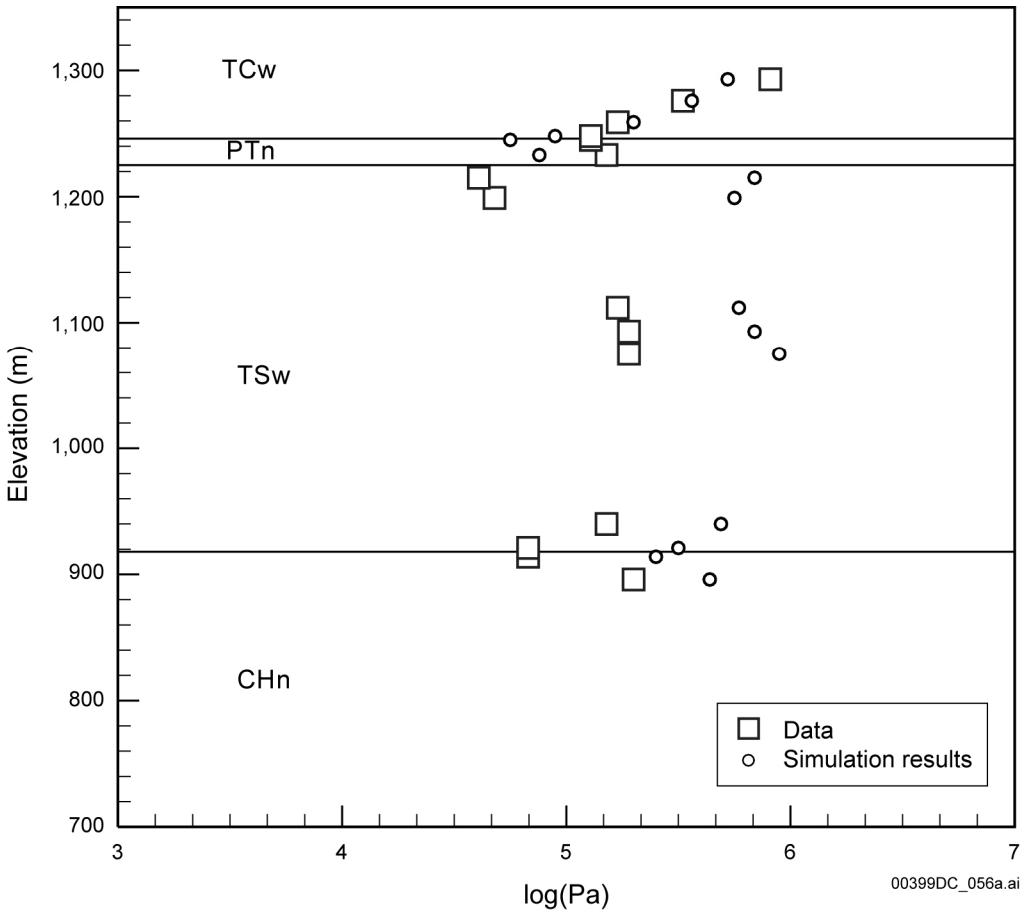

Source: BSC 2003a, Figure 7.

Figure C-12. Water Potential Matches at UE-25 SD-12 for a One-Dimensional, Drift-Scale, Calibrated Parameter Set for the Lower-Bound Infiltration Scenario

C.4.5.3 Calibration of Mountain-Scale Parameters

Scale Dependence of Fracture Permeability–It is well documented that large-scale effective permeabilities are generally larger than smaller-scale ones (Neuman 1994). An intuitive explanation for this scale-dependent behavior is that on a large observation there is a higher opportunity to encounter connected permeable flow paths that considerably increase values of the observed permeability. Because of the scale difference, drift-scale fracture permeabilities, determined from air-injection tests, cannot be directly applied to mountain-scale modeling. Therefore, development of mountain-scale properties is needed. In addition to matching matrix-saturation and water potential data, the determination of mountain-scale parameters also involves matching pneumatic pressure data measured in surface boreholes. In the drift-scale parameter sets, fracture permeabilities correspond to those determined from air-injection tests. The pneumatic pressure data result from mountain-scale gas-flow processes, while air-injection tests correspond to scales on an order of several meters or less.

Unlike the connected fracture networks and soils, studies on the scale-dependent behavior of matrix properties in unsaturated fractured rocks are limited. However, it is reasonable to believe that the scale-dependent behavior of the matrix is different from fracture networks. For example,

relatively large fractures can act as capillary barriers for flow between matrix blocks separated by these fractures, even when the matrix is essentially saturated (water potential is close to the air-entry value). This might limit the matrix scale-dependent behavior to a relatively small scale associated with the spacing between relatively large fractures. Although it is expected that estimated large-scale matrix permeabilities should be larger than those measured on a core scale, no evidence exists to indicate that matrix properties should be very different on both the site and drift scales, which are much larger than the scale characterized by the fracture spacing. This point is also supported by the inversion results for the drift-scale properties. For example, the estimated drift-scale matrix permeabilities are generally much closer to prior information than estimated site-scale fracture permeabilities.

Based on these premises, only fracture permeabilities for the mountain-scale property sets are recalibrated whereas other properties remain the same as those in the corresponding drift-scale properties. The calibration includes three steps.

1. Fracture permeabilities are calibrated by matching the pneumatic pressure data.

2. The matches to matrix-saturation and water potential data are checked using parameter sets that include calibrated fracture permeabilities.

3. If the matches are not maintained, a new calibration using matrix-saturation and water potential data would be needed for fracture permeabilities.

These steps may need to be repeated until parameter sets match both pneumatic pressure data and matrix-saturation or water potential data. As evident from the steps, this calibration is an iterative process.

Calibration Procedure Using Pneumatic Pressure Data—The EOS3 module of iTOUGH2 V5.0 (LBNL 2002) is used for transient pneumatic simulations. Both the gas and liquid phases are considered in the flow calculations. The pneumatic inversion is carried out in two steps. Firstly, the fracture permeabilities for layers tcw11 through ptn26 are calibrated. Secondly, the permeabilities for layers tsw31 through 37 are calibrated as a group by multiplying the prior information for all seven layers by the same factor.

The calibrated fracture permeabilities resulting from inversion of pneumatic data are expected to be higher than the prior information owing to the scale dependency of fracture permeabilities described above. Therefore, the initial estimates for the fracture permeabilities are $10^{-10.5}$ m^2 for tcw11, tcw12, and tcw13, and $10^{-11.5}$ m^2 for ptn21 through ptn26. These estimates are higher than the corresponding prior information. The permeabilities of layers tsw31 through 37 are set to the values previously calibrated using the pneumatic data.

The lack of significant attenuation in the TSw unit is considered an important feature shown by the gas pressure data. The calibrated fracture permeabilities for the model layers in the TSw unit need to be consistent with this feature. Therefore, fracture permeabilities in the TSw need to be determined in such a way that the simulated and observed gas pressure signals at the upper and lower sensor locations in the TSw have similar degrees of attenuation for borehole UE-25 SD-12. Borehole UE-25 SD-12 is chosen for this analysis because the distance between the two TSw sensors within this borehole is the largest among all the relevant boreholes. The degree of

attenuation of the barometric signal through the TSw in UE-25 SD-12, or the relative difference between the signals at the two sensor locations, was determined by using standard functions of Excel 97 SR-1 to evaluate:

$$F = \frac{1}{N}\left\{\sum_{i=1}^{N}\left[\left(P_u(t_i) - P_u(t_1)\right) - \left(P_b(t_i) - P_b(t_1)\right)\right]^2\right\}^{1/2} \qquad \text{(Eq. C-29)}$$

where N is the total number of calibration time points, P is the gas pressure, and subscripts u and b refer to the sensors in the upper and lower (bottom) portions of the TSw within borehole UE-25 SD-12. Obviously, if the gas signals from the two sensors are identical, F should be equal to zero. For the UE-25 SD-12 gas-signal data, the F value is 2.01×10^{-3} (kPa). In this study, fracture permeabilities need to be determined that will predict F values similar to the value calculated from the data, such that the simulated and observed gas pressure signals have similar degrees of attenuation.

Since the gas pressure data from the TSw are relatively limited compared to TCw and PTn units and the insignificant attenuation and time lag between the uppermost and lowermost sensors are used for calibration, the fracture permeabilities for different model layers in this unit could not be independently estimated in a reliable manner. The attenuation and time lag are determined by the overall hydraulic properties between the two sensors rather than by properties in a single model layer. Therefore, the ratios of the permeabilities of layers tsw31 through tsw37 are held constant and the prior information permeability values are multiplied by a single factor, d. For a given infiltration map, a number of values, log(d), between 1 and 2 with an interval of 0.1 are tested to determine the d resulting in an F value closest to the F value corresponding to the data. To calculate an F value for a d factor, modelers used the outputs from the TCw and PTn fracture permeability calibrations to run the forward simulation using iTOUGH2 V5.0 (LBNL 2002) for generating gas pressures used in Equation C-29. In a forward simulation, all the rock properties are the same as those determined from the corresponding TCw and PTn fracture permeability calibration, except that fracture permeabilities for model layers tsw31 to tsw37 are determined using the d factor and prior information.

The determined log(d) values based on the above procedure for the three infiltration maps as follows: base case, 2.0; upper bound, 1.9; lower bound, 1.8 (BSC 2003a, Table 14). The log(d) values range from 1.8 to 2.0, indicating that the fracture permeabilities for the relevant model layers are increased by about 2 orders of magnitude compared to the prior information. This results from the scale effects, as previously discussed.

Table C-9 provides mountain-scale fracture permeabilities calibrated with pneumatic pressure data for three infiltration scenarios.

Table C-9. Calibrated Mountain-Scale Fracture Permeabilities

Model Layer[a]	Base Case	Upper Bound	Lower Bound
tcw11	4.24×10^{-11}	3.16×10^{-12}	3.16×10^{-12}
tcw12	9.53×10^{-11}	1.00×10^{-10}	9.73×10^{-11}
tcw13	1.32×10^{-11}	9.67×10^{-13}	9.47×10^{-13}
ptn21	2.11×10^{-11}	1.00×10^{-11}	1.00×10^{-11}
ptn22	9.41×10^{-12}	3.85×10^{-13}	1.00×10^{-11}
ptn23	5.35×10^{-13}	9.04×10^{-14}	1.16×10^{-13}
ptn2	1.00×10^{-11}	3.16×10^{-13}	1.00×10^{-11}
ptn25	1.24×10^{-12}	1.59×10^{-14}	4.37×10^{-13}
ptn26	3.17×10^{-13}	9.23×10^{-14}	8.29×10^{-14}
tsw31	8.13×10^{-11}	6.46×10^{-11}	5.13×10^{-11}
tsw32	7.08×10^{-11}	5.62×10^{-11}	4.47×10^{-11}
tsw33	7.76×10^{-11}	6.17×10^{-11}	4.90×10^{-11}
tsw3	3.31×10^{-11}	2.63×10^{-11}	2.09×10^{-11}
tsw35	9.12×10^{-11}	7.24×10^{-11}	5.75×10^{-11}
tsw36	1.35×10^{-10}	1.07×10^{-10}	8.51×10^{-11}
tsw37	1.35×10^{-10}	1.07×10^{-10}	8.51×10^{-11}

Source: BSC 2003a, Table 15.

NOTE: [a] In the numerical grids used in inversions, the name of (fracture) model layer is the same as the corresponding model layer name in the table except that the th character is "F".

Saturation and Water Potential Check–Matches to the saturation and water potential data were checked and found to be satisfactory because, for a given infiltration scenario, the objective-function values are almost identical for both the mountain-scale property set and the corresponding drift-scale property set. Therefore, no further adjustment is needed. This also further confirms the previous assertion that under ambient conditions, simulated matrix water potential and saturation distributions are insensitive to fracture permeability values.

Figure C-13 shows pneumatic pressure matches at UE-25 SD-12 for a one-dimensional, mountain-scale, calibrated parameter set for the base-case infiltration scenario. Similar matches are obtained for other boreholes and for two other infiltration scenarios. In Figure C-13, both simulated and observed pressure curves for a given geologic layer (Tptrn and Tpbt2) are shifted an identical distance along the vertical axis to better display the matches.

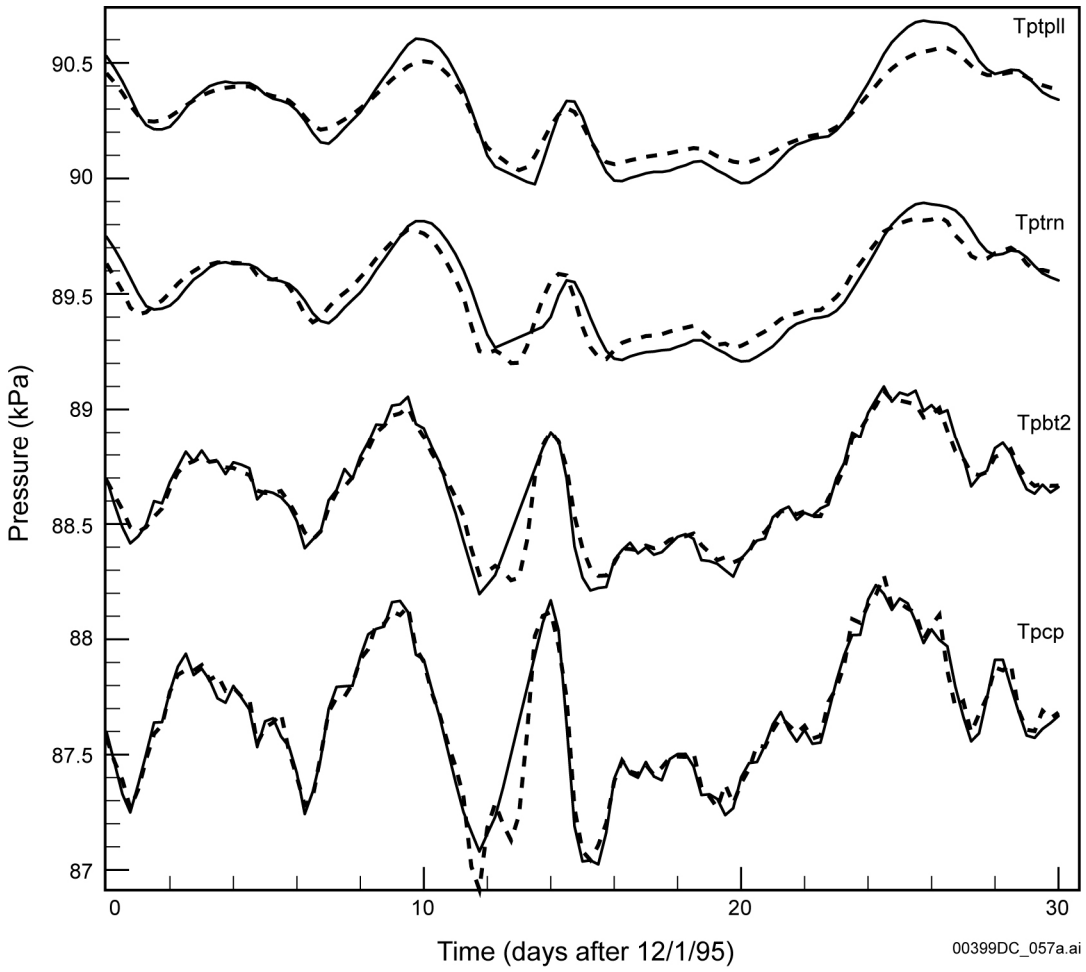

Source: BSC 2003a, Figure 8.

NOTE: Solid lines correspond to the interpolated raw data and dashed lines correspond to simulated results.

Figure C-13. Pneumatic Pressure Matches at UE-25 SD-12 for the One-Dimensional, Mountain-Scale, Calibrated Parameter Set for the Base-Case Infiltration Scenario

C.4.5.4 Three-Dimensional Calibration

One major limitation of the one-dimensional models is that they cannot capture important three-dimensional flow behavior, such as lateral flow, because of capillary barrier effects in the PTn and the effects of perched water. To resolve this issue, three-dimensional models are used for limited trial-and-error calibrations and verification of simulation results against many different data sets, including those used for one- and two-dimensional calibrations (BSC 2003b). Automatic calibrations have been used for one- and two-dimensional cases. Additional data sets used at this stage for model calibration include pneumatic pressure data and perched-water-elevation data from several surface-based boreholes. Property adjustments were made to calibrate the three-dimensional unsaturated zone flow model against the data mentioned above. Figures C-14 and C-15 show some of the calibration results. More details can be found in *UZ Flow Models and Submodels* (BSC 2003b, Figures 6.2-2, 6.2-3, 6.2-4, and 6.4-2).

The three-dimensional unsaturated zone flow model with the calibrated properties were extensively verified using measured water potential data from the ECRB Cross-Drift (Figure C-16), in situ test data from Alcove 8-Niche 3 (Figure C-17), ^{14}C aging data (Figure C-18), and calcite coating data (Figure C-19). Verification is not a part of a model calibration that involves adjustment of parameter values. The simulation results from model verification (ECRB-predicted water potentials, simulated seepage rates from Alcove 8–Niche 3 tests, simulated ^{14}C ages of USW UZ-1 pore waters and calcite abundance of USW WT-24 core samples) are within the ranges of measured data, as shown in Figures C-16 through C-19.

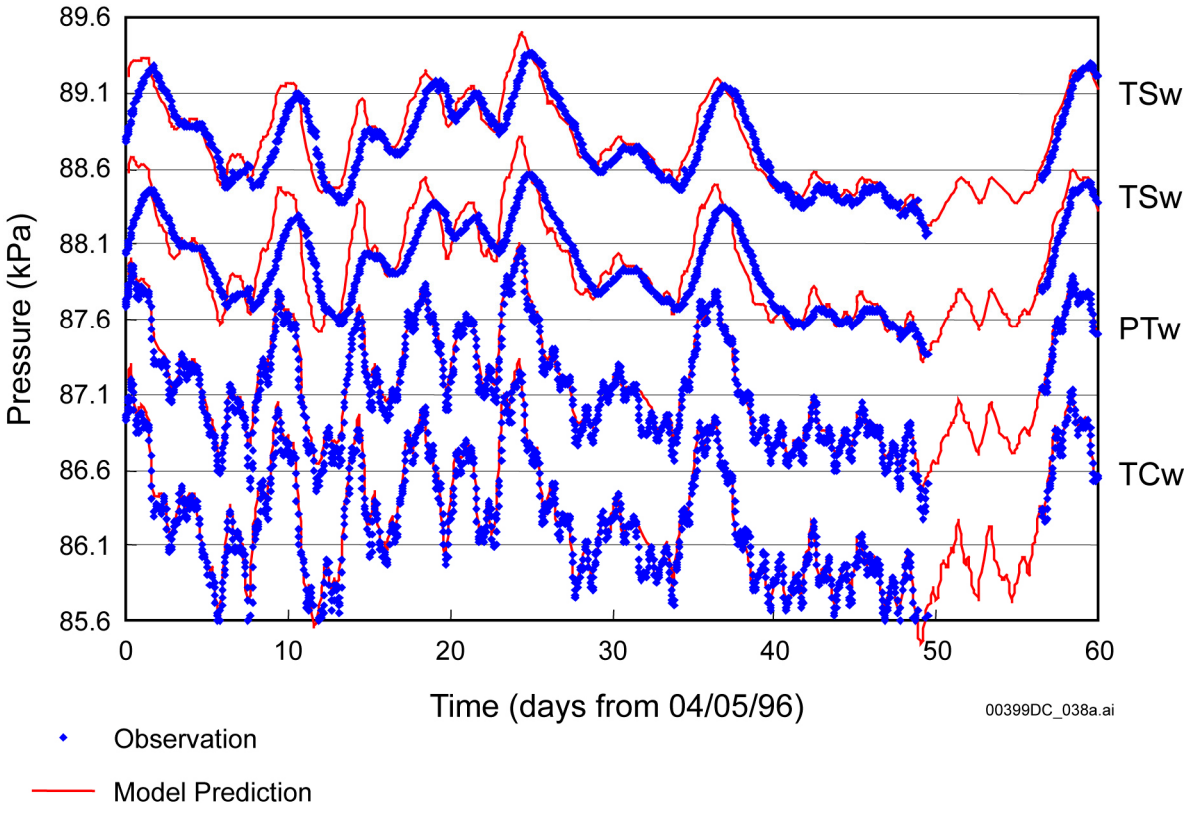

Source: BSC 2003b, Figure 6.4-1.

Figure C-14. Comparison of Simulated and Observed Gas Pressure at Borehole USW SD-7 in a 60-Day Period (Three-Dimensional Model Calibration Results)

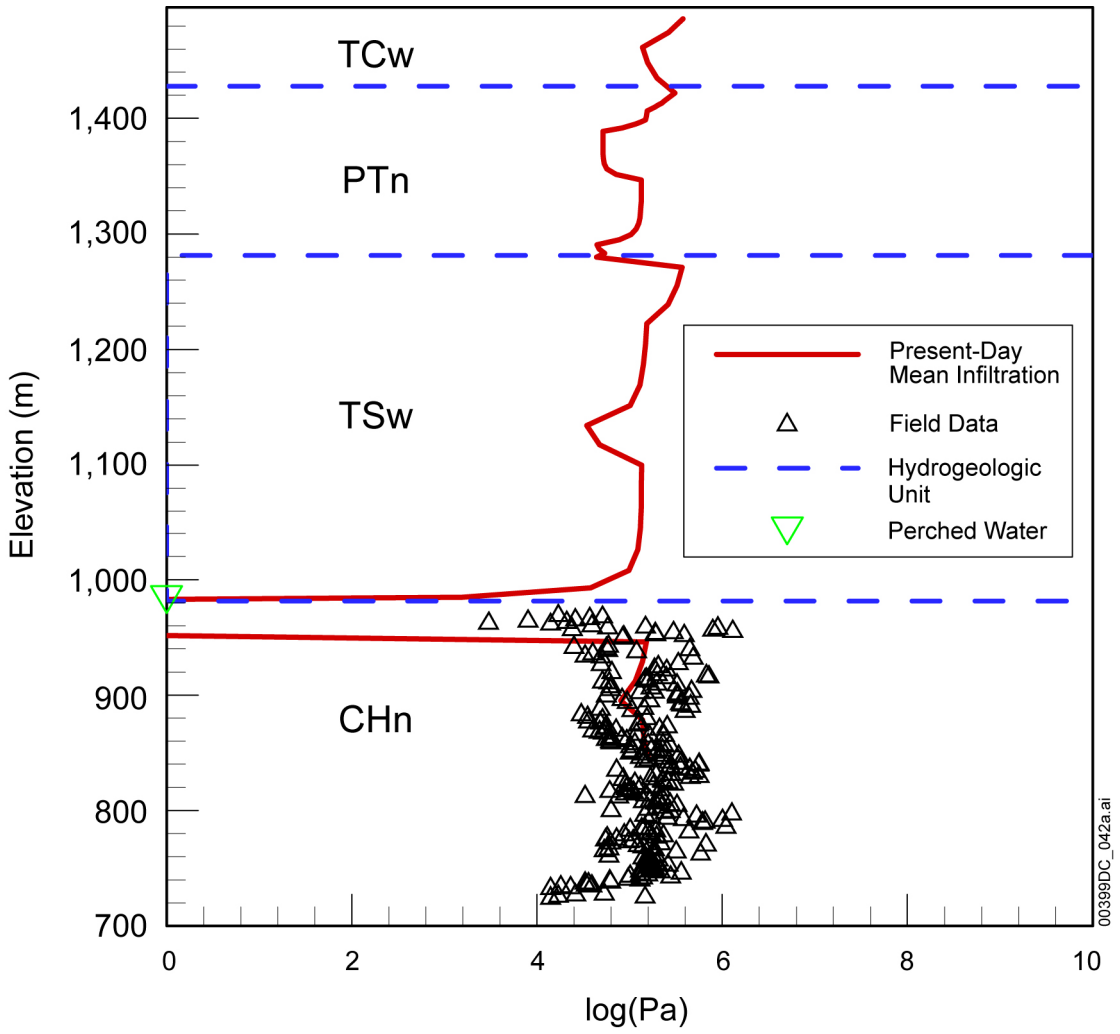

Source: BSC 2003b, Figure 7.3-1.

Figure C-15. Comparison of Predicted and Measured Matrix Water Potentials and Perched-Water Elevations at Borehole UE-25 WT#24 Using the Present-Day Mean Infiltration Rate (Three-Dimensional Model Calibration Results)

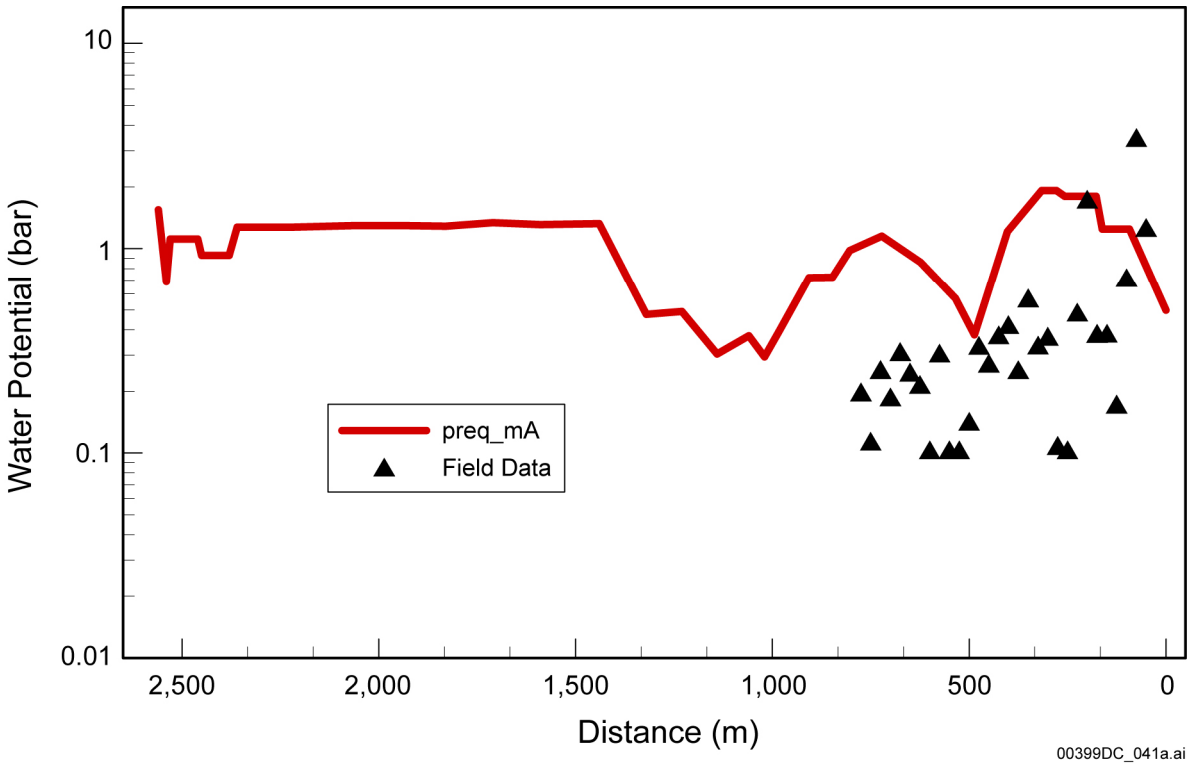

Source: BSC 2003b, Figure 7.2-1.

Figure C-16. Comparison of Predicted and Measured Water Potential along the Enhanced Characterization of the Repository Block Using the Present-Day, Mean Infiltration Rates (Three-Dimensional Model Verification Results)

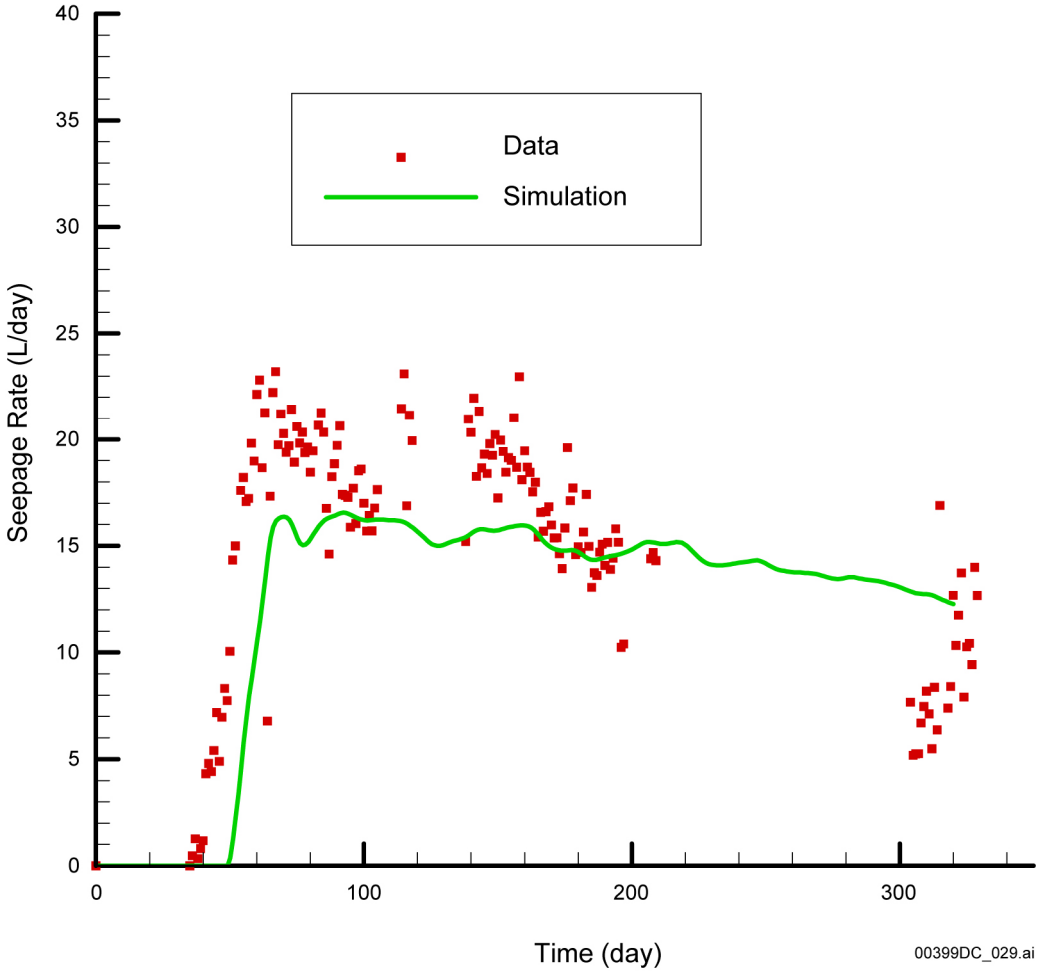

Source: BSC 2003b, Figure 7.6-8.

Figure C-17. Comparison between Simulated Seepage Rates as a Function of Time and Field Observations Collected from Alcove 8–Niche 3 Tests (Three-Dimensional Model Verification Results)

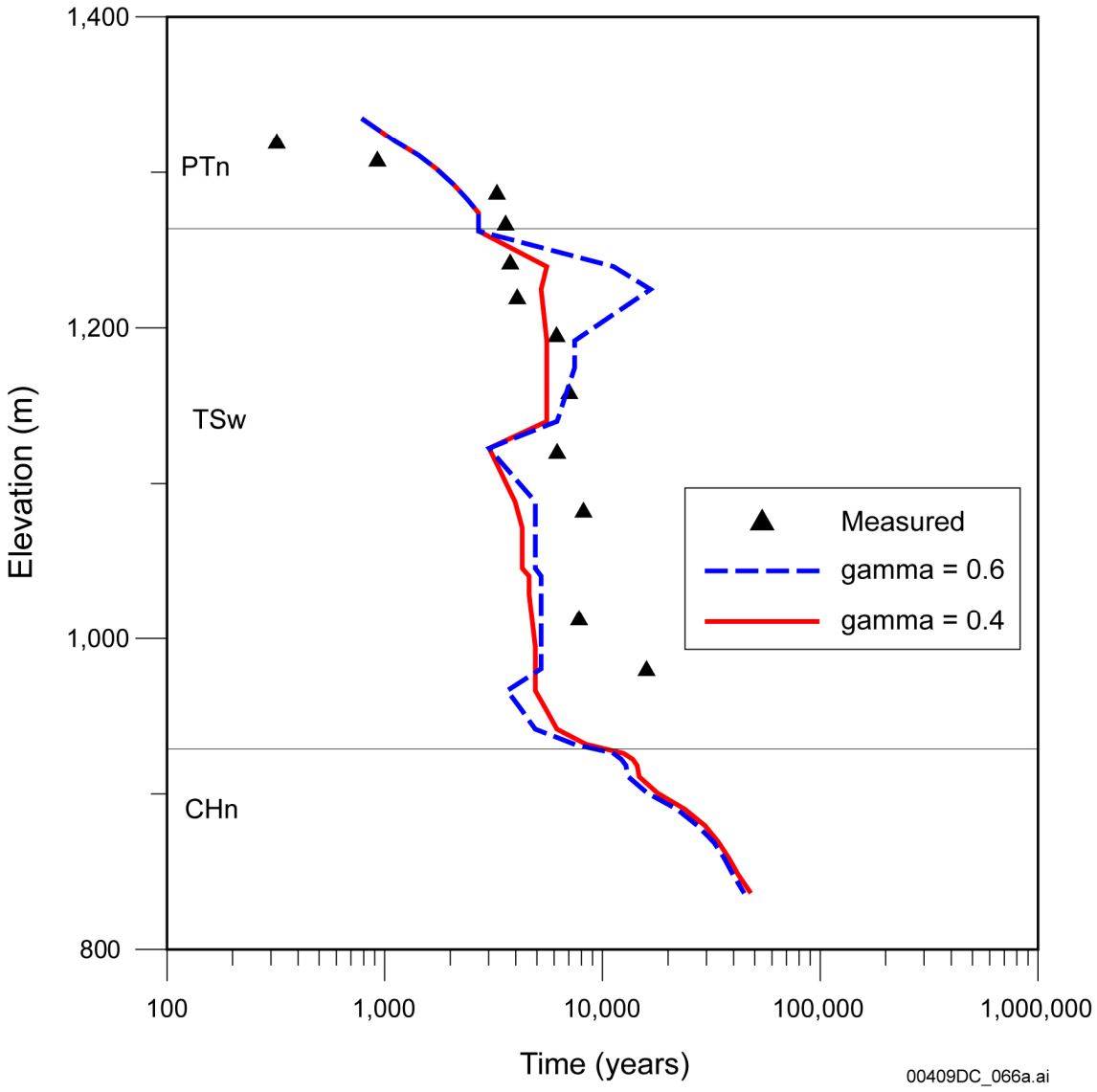

Source: BSC 2003b, Figure 7.5-1.

Figure C-18. Comparison between Simulated and Observed Water Residence Ages in the Matrix for Borehole USW UZ-1 (Three-Dimensional Model Verification Results)

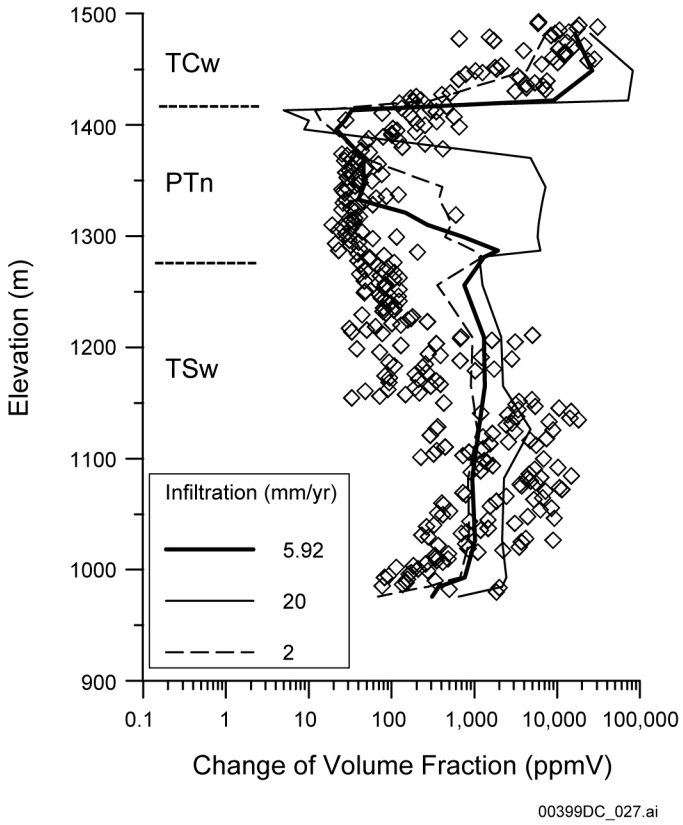

Source: BSC 2003b, Figure 7.9-3.

Figure C-19. Comparison between Measured and Simulated Total (Fracture plus Matrix) Calcite Abundances in the UE-25 WT#24 Column for Different Infiltration Rates (Three-Dimensional Model Verification Results)

C.4.6 Uncertainty in the Calibrated Parameter

Model calibration is subject to uncertainty. A major source of parameter uncertainty is the conceptual model. Infiltration rate uncertainty also contributes to parameter uncertainty because flow processes in the unsaturated zone are largely determined by top boundary conditions. To capture this uncertainty, three infiltration scenarios (including present-day mean, upper-bound, and lower-bound infiltration maps) are used for the parameter calibration. In addition, scale effects are a well-known source of parameter uncertainty. This is especially true for determining unsaturated zone model parameters. For example, matrix parameters are measured in the unsaturated zone at core scale on the order of several centimeters, whereas in the unsaturated zone flow model, numerical gridblocks are on the order of a few meters to hundreds of meters. Scale-dependence of hydrologic parameters is widely recognized in the scientific community (Neuman 1994). Although upscaling is partially considered in developing uncalibrated matrix properties, the calibrated matrix permeabilities are, on average, higher than uncalibrated ones for the three infiltration scenarios. This increase is consistent with reported findings (Neuman 1994) and implies that the scale effects were captured by the model calibration. Fracture permeability values calibrated against pneumatic pressure data are also about 2 orders of magnitude higher than averaged permeability values measured from air injection tests with injection intervals of

several meters. Furthermore, calibrated properties are not unique because of data limitations, meaning different property sets may match the data equally well.

Considering the difficulties in accurately quantifying parameter uncertainty, parameter uncertainties (standard deviations) for the uncalibrated parameter sets are used for the calibrated parameter sets because these uncertainties are determined from measurements (BSC 2003b, Section 6.4). The parameter uncertainty of the uncalibrated property sets is largely a result of small-scale spatial variability. Because the degree of spatial variability decreases with scale (subgrid scale or high frequency spatial variability is removed at a large scale), this treatment is likely to provide the upper limits of uncertainty on calibrated parameters for the given conceptual model and infiltration rates.

C.4.6.1 Parameter Residuals

This section uses parameter residuals to examine the scale effects considered in the inversion and the appropriations of the calibrated property sets as compared with the property measurements. The residual of parameter x for each layer is defined as uncalibrated log x minus calibrated log x, where x has a value of k_M or α_M. Uncalibrated properties are not directly measured, but are estimated values for the scales used in the unsaturated zone model due to the difference between measurement scale and modeling scale. As a result, residuals cannot be used to evaluate the uncertainty as to the true parameter value, although they may be used to bound this uncertainty (discussed below).

Table C-10 shows the average absolute residual for calibrated matrix properties for three infiltration scenarios. The absolute value of the residual is always positive, and, therefore the average absolute residual is greater than the average residual (Table C-11). The average standard deviation of log(k_M) for uncalibrated matrix property sets is 1.61. Permeability could be approximately related to α (Wang and Narasimhan 1993) by

$$k \propto \alpha^2 \qquad \text{(Eq. C-30)}$$

This yields

$$\sigma_{\log(\alpha)} = \frac{1}{2}\sigma_{\log(k)} \qquad \text{(Eq. C-31)}$$

where σ refers to standard deviation. Based on Equation C-31, log(α) can be expressed as log(k)/2 plus a constant (for a given model layer), resulting in Equation C-31. For each model layer, a standard deviation for log(α_M) can be estimated from the corresponding standard deviation of log(k_M) based on Equations C-30 and C-31. Average standard deviation (calculated manually) for log(α_M) for the uncalibrated matrix property set is 0.81. The absolute residual values (Table C-10) for the matrix properties are smaller than the corresponding average standard deviations. The residual values for log (α_F) are also given in Table C-10. They are close to or smaller than the average standard deviation of log(α_F) (0.30) determined from uncalibrated fracture property sets using Equation C-31. All these support the appropriateness of the calibrated property sets documented in this report, which results from the use of uncalibrated rock properties as initial guesses and prior information in most inversions.

Table C-10. Average Absolute Residual for Calibrated Matrix Properties for Three Infiltration Scenarios

	Absolute Residual for log(k_M)	Absolute Residual for log(α_M)	Absolute Residual for log(α_F)
Base case	0.75	0.44	0.41
Upper-bound	0.81	0.38	0.19
Lower-bound	0.74	0.43	0.28

Source: BSC 2003a, Table 19.

NOTE: The absolute residual refers to an absolute difference between uncalibrated matrix property and the corresponding calibrated property.

Table C-11. Average Residual for Calibrated Matrix Properties for Three Infiltration Scenarios

	Residual for log(k_M)	Residual for log(α_M)
Base case	-0.37	-0.25
Upper bound	-0.65	-0.17
Lower bound	-0.17	-0.06

Source: BSC 2003a, Table 18.

NOTE: The residual refers to an uncalibrated matrix property minus the corresponding calibrated property.

C.4.6.2 Quantification of Parameter Uncertainty

Quantifiable uncertainties are difficult to establish for the estimated parameter sets. In principle, these uncertainties could be evaluated either by Monte Carlo simulation or by linear error analysis, both of which are capabilities of iTOUGH2 V5.0 (LBNL 2002). Because of the large numbers of parameters and the high nonlinearity of the unsaturated flow process, the linear error analysis is not reliable (Finsterle 1999). The linear uncertainty analysis quantifies the parameter uncertainty by linearization (based on its first-order Taylor series expansion). This method is a powerful tool only for problems that have sufficiently small parameter uncertainties (e.g., a small number of parameters and a large number of data points for model calibration) or are linear (Finsterle 1999, Section 2.8.7). However, the problem under consideration is characterized by a large number of parameters (on the same order of data point number for drift-scale parameter calibrations) and high nonlinearity.

The criteria for the linear uncertainty analysis to apply are not met for the problem under consideration. The sensitivity matrix evaluated at the solution and the resulting covariance matrix provides insight into the correlation structure of the estimated parameters, revealing strong interdependencies. This information is used to support the qualitative statements regarding estimation uncertainty. It also indicates that probabilistic statements about the confidence region around the best-estimate parameter set cannot be based on a linear uncertainty analysis, which assumes linearity and normality within that region (as previously discussed). Such statements would have no defensible basis. Evaluating the correct shape and extent of the confidence region would require mapping the objective function in the n-dimensional parameter space and determining the hypersurface corresponding to the appropriate confidence level. Such an approach is outlined (for two parameters only) (Finsterle and Pruess 1995). Alternatively, Monte Carlo-type/Latin Hypercube Sampling (LHS) methods (such as the bootstrap method)

would be required. However, the large number of parameters makes uncertainty analysis by Monte Carlo simulation prohibitively time consuming, and LHS was not available in iTOUGH2 V5.0 (LBNL 2002) at the time when the work was done. Based on these considerations, the uncertainty information from prior information is believed to be more reliable (and practical) for determining uncertainties for the calibrated property sets.

Table C-12 gives the parameter uncertainties for the calibrated parameters. They are applied to both drift-scale and mountain-scale property sets because both scales are larger than those on which uncalibrated parameters were measured. Uncertainties for $\log(k_M)$, and $\log(k_F)$ are taken directly from uncalibrated properties and uncertainties (BSC 2003a, Tables 3 and 4). When a $\log(k_F)$ uncertainty is not available for a model layer, the largest value among the uncertainties (standard deviations) in all the layers for which uncertainty values are available is used. Uncertainties for $\log(\alpha_M)$ and $\log(\alpha_F)$ are approximated from uncertainty values of the corresponding permeability, based on Equation C-31. Uncertainties of the active-fracture-model parameter gamma are provided in *Analyses Of Hydrological Properties Data* (BSC 2003c) and *UZ Flow Model And Submodels* (BSC 2004). No information is available for quantifying uncertainties for m_F that are not calibrated parameters.

Table C-12. Uncertainties of Calibrated Parameters

Model layer	Matrix Property		Fracture Property	
	$\log(k_M)$	$\log(\alpha_M)$	$\log(k_F)$	$\log(\alpha_F)$
tcw11	0.47	0.24	1.15	0.58
tcw12	2.74	1.37	0.78	0.39
tcw13	2.38	1.19	1.15	0.58
ptn21	2.05	1.03	0.88	0.44
ptn22	1.41	0.71	0.20	0.10
ptn23	0.64	0.32	0.20	0.10
ptn24	1.09	0.55	1.15	0.58
ptn25	0.39	0.20	0.10	0.05
ptn26	1.12	0.56	1.15	0.58
tsw31	3.02	1.51	1.15	0.58
tsw32	0.94	0.47	0.66	0.33
tsw33	1.61	0.81	0.61	0.31
tsw34	0.97	0.49	0.47	0.24
tsw35	1.65	0.83	0.75	0.38
tsw36	3.67	1.84	0.54	0.27
tsw37	3.67	1.84	0.28	0.14
tsw38	1.57	0.79	1.15	0.58
tswz (zeolitic portion of tsw39)	2.74	1.37	1.15	0.58
tswv (vitric portion of tsw39)	1.38	0.69	[a]	[a]
ch1z	2.74	1.37	1.15	0.58
ch1v	1.11	0.56	[a]	[a]

Table C-12. Uncertainties of Calibrated Parameters (Continued)

Model layer	Matrix Property		Fracture Property	
	$\log(k_M)$	$\log(\alpha_M)$	$\log(k_F)$	$\log(\alpha_F)$
ch2v	1.62	0.81	[a]	[a]
ch3v	1.62	0.81	[a]	[a]
chv4	1.62	0.81	[a]	[a]
ch5v	1.62	0.81	[a]	[a]
ch6v	1.11	0.56	[a]	[a]
ch2z	0.91	0.46	1.15	0.58
ch3z	0.91	0.46	1.15	0.58
ch4z	0.91	0.46	1.15	0.58
ch5z	0.91	0.6	1.15	0.58
ch6z	2.05	1.03	1.15	0.58
pp4	2.74	1.37	1.15	0.58
pp3	0.75	0.38	1.15	0.58
pp2	1.18	0.59	1.15	0.58
pp1	1.52	0.76	1.15	0.58
bf3	1.64	0.82	1.15	0.58
bf2	1.52	0.76	1.15	0.58
tcwf	[b]	[b]	1.15	0.58
ptnf	[b]	[b]	1.15	0.58
tswf	[b]	[b]	1.15	0.58
chnf	[b]	[b]	1.15	0.58

Source: BSC 2003a, Table 20.

NOTE: [a] The calibrated properties conceptual model does not include fractures in these model layers.

[b] Fault property set does not include matrix properties.

Table C-12 also shows estimated uncertainties for calibrated fault properties. Because fault properties are calibrated with limited data points, the parameter uncertainties are expected to be relatively large. For each parameter type, the largest parameter uncertainty within the corresponding hydrogeologic unit for the nonfault property set is used as the corresponding fault parameter uncertainty.

Finally, the propagation of uncertainty in model calibration is addressed in this study. Uncertainty data for measurements are used as inputs into inversions. Uncertainty in boundary conditions is reflected by developing property sets for different infiltration scenarios. Uncertainty in prior information has been used for characterizing uncertainties for calibrated properties.

C.5 REFERENCES

C.5.1 Documents Cited

Bandurraga, T.M. and Bodvarsson, G.S. 1999. "Calibrating Hydrogeologic Parameters for the 3-D Site-Scale Unsaturated Zone Model of Yucca Mountain, Nevada." *Journal of Contaminant Hydrology, 38*, (1-3), 25-46. New York, New York: Elsevier. TIC: 244160.

Bear, J.; Tsang, C.F.; and de Marsily, G., eds. 1993. *Flow and Contaminant Transport in Fractured Rock*. San Diego, California: Academic Press. TIC: 235461.

Bird, R.B.; Stewart, W.E.; and Lightfoot, E.N. 1960. *Transport Phenomena*. New York, New York: John Wiley & Sons. TIC: 208957.

BSC (Bechtel SAIC Company) 2003a. *Calibrated Properties Model*. MDL-NBS-HS-000003 REV 01. Las Vegas, Nevada: Bechtel SAIC Company. ACC: DOC.20030219.0001.

BSC 2003b. *UZ Flow Models and Submodels*. MDL-NBS-HS-000006 REV 01. Las Vegas, Nevada: Bechtel SAIC Company. ACC: DOC.20030818.0002.

BSC 2003c. *Analysis of Hydrologic Properties Data*. MDL-NBS-HS-00001 REV 00. Las Vegas, Nevada: Bechtel SAIC Company. ACC: DOC.20030404.0004.

BSC 2003d. *Drift-Scale Coupled Processes (DST and TH Seepage) Models*. MDL-NBS-HS-000015 REV 00C. Las Vegas, Nevada: Bechtel SAIC Company. ACC: MOL.20030910.0160.

BSC 2003e. *Development of Numerical Grids for UZ Flow and Transport Modeling*. ANL-NBS-HS-000015 REV 01. Las Vegas, Nevada: Bechtel SAIC Company. ACC: DOC.20030404.0005.

BSC 2004. *UZ Flow Models and Submodels*. MDL-NBS-HS-000006 REV 01. Las Vegas, Nevada: Bechtel SAIC Company. ACC: DOC.20030818.0002; DOC.20040211.0008.

CRWMS M&O (Civilian Radioactive Waste Management System Management and Operating Contractor) 2000. *Multiscale Thermohydrologic Model*. ANL-EBS-MD-000049 REV 00. Las Vegas, Nevada: CRWMS M&O. ACC: MOL.20000609.0267.

Finsterle, S. 1998. *ITOUGH2 V3.2 Verification and Validation Report*. LBNL-42002. Berkeley, California: Lawrence Berkeley National Laboratory. ACC: MOL.19981008.0014.

Finsterle, S. 1999. *ITOUGH2 User's Guide*. LBNL-40040. Berkeley, California: Lawrence Berkeley National Laboratory. TIC: 243018.

Finsterle, S. and Pruess, K. 1995. "Solving the Estimation-Identification Problem in Two-Phase Flow Modeling." *Water Resources Research, 31,* (4), 913-924. Washington, D.C.: American Geophysical Union. TIC: 252318.

Flint, L.E. 1998. *Characterization of Hydrogeologic Units Using Matrix Properties, Yucca Mountain, Nevada*. Water-Resources Investigations Report 97-4243. Denver, Colorado: U.S. Geological Survey. ACC: MOL.19980429.0512.

Gelhar, L.W. 1993. *Stochastic Subsurface Hydrology*. Englewood Cliffs, New Jersey: Prentice-Hall. TIC: 240652.

Hvorslev, M.J. 1951. *Time Lag and Soil Permeability in Ground-Water Observations*. AEWES Bulletin 36. Vicksburg, Mississippi: U.S. Army Corps of Engineers, Waterways Experiment Station. TIC: 238956.

LBNL (Lawrence Berkeley National Laboratory) 2002. *Software Code: iTOUGH2*. V5.0. SUN UltraSparc., DEC ALPHA, LINUX. 10003-5.0-00.

LeCain, G.D. 1995. *Pneumatic Testing in 45-Degree-Inclined Boreholes in Ash-Flow Tuff Near Superior, Arizona*. Water-Resources Investigations Report 95-4073. Denver, Colorado: U.S. Geological Survey. ACC: MOL.19960715.0083.

Lide, D.R., ed. 2002. *CRC Handbook of Chemistry and Physics*. 83rd Edition. Boca Raton, Florida: CRC Press. TIC: 253582.

Lin, M.; Hardy, M.P.; and Bauer, S.J. 1993. *Fracture Analysis and Rock Quality Designation Estimation for the Yucca Mountain Site Characterization Project*. SAND92-09. Albuquerque, New Mexico: Sandia National Laboratories. ACC: NNA.1992120.0012.

Liu, H.H.; Doughty, C.; and Bodvarsson, G.S. 1998. "An Active Fracture Model for Unsaturated Flow and Transport in Fractured Rocks." *Water Resources Research, 3*, (10), 2633-266. Washington, D.C.: American Geophysical Union. TIC: 243012.

Neuman, S.P. 1994. "Generalized Scaling of Permeabilities: Validation and Effect of Support Scale." *Geophysical Research Letters, 21*, (5), 39-352. Washington, D.C.: American Geophysical Union. TIC: 240142.

NRC (U.S. Nuclear Regulatory Commission) 2002. *Integrated Issue Resolution Status Report*. NUREG-1762. Washington, D.C.: U.S. Nuclear Regulatory Commission, Office of Nuclear Material Safety and Safeguards. TIC: 253064.

Paleologos, E.K.; Neuman, S.P.; and Tartakovsky, D. 1996. "Effective Hydraulic Conductivity of Bounded, Strongly Heterogeneous Porous Media." *Water Resources Research, 32*, (5), 1333-131. Washington, D.C.: American Geophysical Union. TIC: 245760.

Phillips, O.M. 1996. "Infiltration of a Liquid Finger Down a Fracture into Superheated Rock." *Water Resources Research, 32*, (6), 1665-1670. Washington, D.C.: American Geophysical Union. TIC: 239025.

Pruess, K. and Narasimhan, T.N. 1985. "A Practical Method for Modeling Fluid and Heat Flow in Fractured Porous Media." *Society of Petroleum Engineers Journal, 25*, (1), 1-26. Dallas, Texas: Society of Petroleum Engineers. TIC: 221917.

Reamer, C.W. 2001. "U.S. Nuclear Regulatory Commission/U.S. Department of Energy Technical Exchange and Management Meeting on Total System Performance Assessment and Integration (August 6 through 10, 2001)." Letter from C.W. Reamer (NRC) to S. Brocoum (DOE/YMSCO), August 23, 2001, with enclosure. ACC: MOL.20011029.0281.

Reamer, C.W. and Williams, D.R. 2001. *Summary Highlights of NRC/DOE Technical Exchange and Management Meeting on Thermal Effects on Flow*. Meeting held January 8-9, 2001, Pleasanton, California. Washington, D.C.: U.S. Nuclear Regulatory Commission. ACC: MOL.20010202.0095 through MOL.20010202.0108.

Roberson, J.A. and Crowe, C.T. 1990. *Engineering Fluid Mechanics.* 4th Edition. Boston, Massachusetts: Houghton Mifflin. TIC: 247390.

Rousseau, J.P.; Kwicklis, E.M.; and Gillies, D.C., eds. 1999. Hydrogeology of the Unsaturated Zone, North Ramp Area of the Exploratory *Studies Facility, Yucca Mountain, Nevada*. Water-Resources Investigations Report 98-050. Denver, Colorado: U.S. Geological Survey. ACC: MOL.1999019.0335.

Schaap, M.G. and Leij, F.J. 2000. "Improved Prediction of Unsaturated Hydraulic Conductivity with the Mualem-van Genuchten Model." *Soil Science Society of America Journal, 64,* (3), 843–851. Madison, Wisconsin: Soil Science Society of America. TIC: 253607.

van Genuchten, M.T. 1980. "A Closed-Form Equation for Predicting the Hydraulic Conductivity of Unsaturated Soils." *Soil Science Society of America Journal,* (5), 892-898. Madison, Wisconsin: Soil Science Society of America. TIC: 217327.

Wang, J.S.Y. and Narasimhan, T.N. 1993. "Unsaturated Flow in Fractured Porous Media." Chapter 7 of *Flow and Contaminant Transport in Fractured Rock*. Bear, J.; Tsang, C-F.; and de Marsily, G., eds. San Diego, California: Academic Press. TIC: 235461.

Weast, R.C., ed. 1987. *CRC Handbook of Chemistry and Physics: 1987-1988*. 68th Edition. Pages A-1, F-72, F-185 only. Boca Raton, Florida: CRC Press. TIC: 245444.

Zhou, Q.; Liu, H-H.; Bodvarsson, G.S.; and Oldenburg, C.M. 2003. "Flow and Transport in Unsaturated Fractured Rock: Effects of Multiscale Heterogeneity of Hydrogeologic Properties." *Journal of Contaminant Hydrology, 60*, (DIRS 1-2), 1-30. New York, New York: Elsevier. TIC: 253978.

C.5.2 Data, Listed by Data Tracking Number

LB0401H2OPOTEN.001. Unsaturated Zone Water Potential Data from NRG-6, NGR#7-A, UZ#4, SD-12 (Oct. 1994–Dec. 2001). Submittal date: 01/23/2004.

APPENDIX D

UNCERTAINTY OF HYDROLOGIC PROPERTIES FOR FUTURE CLIMATE CONDITIONS (RESPONSE TO TSPAI 3.22 AIN-1)

Note Regarding the Status of Supporting Technical Information

This document was prepared using the most current information available at the time of its development. This Technical Basis Document and its appendices providing Key Technical Issue Agreement responses that were prepared using preliminary or draft information reflect the status of the Yucca Mountain Project's scientific and design bases at the time of submittal. In some cases this involved the use of draft Analysis and Model Reports (AMRs) and other draft references whose contents may change with time. Information that evolves through subsequent revisions of the AMRs and other references will be reflected in the License Application (LA) as the approved analyses of record at the time of LA submittal. Consequently, the Project will not routinely update either this Technical Basis Document or its Key Technical Issue Agreement appendices to reflect changes in the supporting references prior to submittal of the LA.

APPENDIX D

UNCERTAINTY OF HYDROLOGIC PROPERTIES FOR FUTURE CLIMATE CONDITIONS (RESPONSE TO TSPAI 3.22 AIN-1)

This appendix provides a response to Key Technical Issue (KTI) agreement Total System Performance Assessment and Integration (TSPAI) 3.22 AIN-1. This agreement relates to the technical basis for the representation of unsaturated zone flow under future climate conditions.

D.1 KEY TECHNICAL ISSUE AGREEMENT

D.1.1 TSPAI 3.22 AIN-1

Agreement TSPAI 3.22 was reached during the U.S. Nuclear Regulatory Commission (NRC)/U.S. Department of Energy (DOE) Technical Exchange and Management Meeting on Total System Performance Assessment and Integration held August 6 to 10, 2001, in Las Vegas, Nevada (Reamer 2001). TSPAI subissues 1, 2, 3, and 4 were discussed at that meeting.

Agreement TSPAI 3.22 was initially addressed using a risk-informed approach in the DOE letter report of August 29, 2002 (Ziegler 2002). After reviewing this report, the NRC requested additional information from the DOE to complete KTI agreement TSPAI 3.22 (Schlueter 2003).

The wording of the agreement is as follows:

TSPAI 3.22[1]

> Provide an assessment or discussion of the uncertainty involved with using a hydrological property set obtained by calibrating a model on current climate conditions and using that model to forecast flow for future climate conditions (UZ2.3.1). DOE will provide an assessment or discussion of the uncertainty involved with using a hydrological property set obtained by calibrating a model on current climate conditions and using that model to forecast flow for future climate conditions. This assessment will be documented in the UZ Flow Models and Submodels AMR (MDL-NBS-HS-000006) expected to be available to NRC in FY 2003.

Wording of the additional information needed is as follows:

TSPAI 3.22 AIN-1

> Satisfactory information to address the technical topic of the agreement would be sufficient to complete Agreement TSPAI.3.22. DOE had proposed to compare modeling predictions with actual test results from field tests (such as Alcove 8-Niche 3) conducted at higher flow rates that are expected to encompass flow

[1] UZ2.3.1 in this agreement refers to item 2.3 of NRC integrated subissue UZ2 on flow paths in the unsaturated zone (NRC 2002, Table 1.1-2). This item addresses NRC's concern that the effect of lateral surface or near-surface flow on net infiltration may be underestimated.

behavior representative of future climates. Alternatively, sensitivity analyses which adequately address NRC's concerns with DOE's approach to resolving agreements via risk arguments would be sufficient to complete the agreement.

D.1.2 Related Key Technical Issue Agreements

KTI agreement TSPAI 3.22 is related to agreements TSPAI 3.26 and Thermal Effects on Flow (TEF) 2.11 in that these agreements are also concerned with unsaturated zone flow model calibration. TSPAI 3.26 and TEF 2.11 are addressed in other appendices.

D.2 RELEVANCE TO REPOSITORY PERFORMANCE

This KTI agreement is related to the calibration of models used to determine flow fields in the unsaturated zone for different climates corresponding to different infiltration rates. Specifically, it addresses the uncertainties that arise from calibration of unsaturated zone models when calibration data are limited to current climate conditions. This will affect the unsaturated zone barrier performance calculations by determining uncertainties in input values.

D.3 RESPONSE

Agreement TSPAI 3.22 requests an assessment or discussion of the uncertainty involved with using a hydrologic property set obtained by calibrating a model on present-day climate conditions and using that model to forecast flow for future climate conditions. TSPAI 3.22 AIN-1 requests additional information for response to agreement TSPAI 3.22. The NRC proposed that the DOE respond to this AIN by either providing satisfactory technical information to address the technical topic of the agreement or by performing sensitivity analyses that adequately address the NRC's concerns with the DOE's approach to resolving agreements via risk arguments. The method chosen to address this AIN was to provide technical information.

The unsaturated zone flow models are used to generate flow fields for predicting the amount of flux in the unsaturated zone under various climate conditions. These models use hydrologic properties calibrated on current climate conditions. The predicted flow fields are determined based on the infiltration projected to occur in the future. (The infiltration rates are higher in the future.) Calibrated rock properties based on current climate may cause uncertainties in the prediction of unsaturated zone flow fields for future climate conditions.

As background information, the uncertainties of hydrologic properties obtained by calibrating a model on current climate conditions are discussed (see Section D.4.1). Model analyses of field infiltration tests at Alcove 8–Niche 3 and Alcove 1 are presented in Section D.4.2. These tests were conducted at high infiltration rates that are expected to encompass flow behavior representative of future climates. These models demonstrate flow model performance under higher infiltration conditions by comparing field-measured data to model-predicted results. A comparison of rock-property data obtained using model calibrations for high infiltration rates and present-day infiltration is provided in Section D.4.3. The comparison indicates that the properties obtained under high infiltration rates are consistent with those obtained under the current climate conditions. Therefore, it is appropriate to use models based on rock properties calibrated under the current climate to predict flow fields under future climate conditions.

The information in this report is responsive to agreement TSPAI 3.22 made between the DOE and NRC and is responsive to AIN request TSPAI 3.22 AIN-1. This report contains the information that DOE considers necessary for NRC review for closure of this agreement.

D.4 BASIS FOR THE RESPONSE

This response demonstrates the consistency of rock-property sets obtained by model calibrations at different infiltration rate ranges. This is done by comparing calibrated rock property data from the drift-scale model under present-day climate conditions to the corresponding property data from models representing field infiltration tests. The consistency of two sets of rock property is defined as the difference between log values of the corresponding parameters and assuring that it is smaller than the standard deviation of that calibrated parameter distribution under the current climate condition. The field tests discussed below include the fault test and large plot test at Alcove 8–Niche 3 (BSC 2003a), and the infiltration test at Alcove 1 (Liu et al. 2003). These tests with high infiltration rates are expected to represent flow behavior under future climates. In addition, the uncertainties of models calibrated on current climate conditions to predict future flow fields will be addressed through theoretical discussion and analysis of data uncertainties.

D.4.1 Rock Property Calibration on Current Climate Conditions

This appendix first describes the rock-property calibration based on the current climate conditions. Because hydrologic parameters are scale-dependent, drift-scale parameters and mountain-scale parameters are used for models at different scales. In the following discussion, emphasis is placed on the calibration of drift-scale model parameters because the field tests took place at scales corresponding to the drift scale. Uncertainties of the calibrated hydrologic parameters are also discussed. Calibration results will be used for evaluating the consistency of rock-property sets calibrated on different infiltration conditions (BSC 2003b).

It is well documented that large-scale effective permeabilities are generally larger than smaller-scale ones (Neuman 1994). An intuitive explanation for this scale-dependent behavior is that a larger observation scale, in an average sense, corresponds to a larger opportunity to encounter more permeable zones or paths when observations are made, which considerably increases values of the observed permeability. Although it is expected that estimated large-scale matrix permeabilities should also be larger than those measured on a core scale, no evidence exists to indicate that matrix properties should be very different on both the mountain and drift scales. Only fracture permeabilities for the mountain-scale property sets may demonstrate large differences from drift-scale data, whereas other properties are the same as or close to those in the corresponding drift-scale properties. Even though fracture permeabilities at drift-scale and mountain-scale may be different, we can find that the effects of changes in infiltration on the parameter for both scales are similar by comparing the calibration results (BSC 2003b, Tables 11-13 and 15). Only the calibration of drift-scale model parameters will be discussed.

D.4.1.1 Calibration of Drift-Scale Parameters

One-dimensional inversion of the matrix-saturation and water-potential data is carried out for determining drift-scale parameters. The one-dimensional submodels correspond to surface-based boreholes from which saturation and water potential have been measured. In the calibration

procedure, steady-state water flow is simulated simultaneously in all columns. Layer-averaged effective parameters are estimated (i.e., the same set of parameter values is used for each geologic layer in all columns, or each geological layer is considered to be homogeneous) (BSC 2003c, Table 6.1-1).

Three calibrated parameter sets are produced, one for each present-day infiltration case (lower-bound, mean, and upper-bound) (BSC 2003c, Section 6.1.4). Uncalibrated rock-property data (BSC 2003b, Tables 3 and 4) are used as the initial guesses. Uncalibrated rock-property data here are defined as the layer averaged properties determined from field measurement data. The infiltration scenarios are key inputs to the unsaturated zone model because flow and transport are dependent on the amount of water infiltrating into the mountain. The base-case infiltration scenario gives the expected spatially varying infiltration rates over Yucca Mountain, and parameters calibrated using this scenario are the base-case parameter set. The upper- and lower-bound infiltration scenarios give bounds to the uncertainty of the base-case infiltration scenario. Parameters calibrated using the bounding scenarios are also provided; this gives the parameter sets that consider underestimation and overestimation of the present-day infiltration by the base-case scenario.

Model parameters to be estimated are matrix k_M, matrix van Genuchten parameter α_M (van Genuchten 1980, pp. 892 to 893), fracture van Genuchten parameters α_F, and an active-fracture-model parameter γ (Liu et al. 1998). Parameters are calibrated for model layers, though in some cases a common parameter value is estimated for groups of layers. Other parameters, such as fracture permeability (k_F) and van Genuchten m parameters for fracture (m_F) and matrix (m_M), are not changed in the calibration. These parameters may be insensitive to model performance or can be well constrained. A detailed discussion of sensitivities of rock properties to the relevant simulation results is provided by Bandurraga and Bodvarsson (1999, Section 5).

The one-dimensional calibrated drift-scale parameter sets for the base-case (mean), upper-bound, and lower-bound infiltration scenarios are presented in Tables D-1, D-2, and D-3, respectively. By comparing the calibration results in Tables D-1, D-2, and D-3, it can be seen that the calibrated parameters do not vary much between different infiltration scenarios. Matches to the saturation data achieved with the parameter set for borehole USW SD-9 for the mean infiltration case are shown in Figure D-1. A comparison between data and simulation results for the zeolitic portion of CHn is not shown because saturation data from that location are not used for calibration. Figure D-2 shows matches to the water potential data for borehole UE-25 SD-12 for the same case (BSC 2003b).

Table D-1. Calibrated Parameters from One-Dimensional Inversion of Saturation and Water Potential Data for the Base-Case Infiltration Scenario

Model Layer	k_M (m^2)	α_M (1/Pa)	m_M	k_F (m^2)	α_F (1/Pa)	m_F	γ
tcw11	3.74×10^{-15}	1.01×10^{-5}	0.388	3.0×10^{-11}	5.27×10^{-3}	0.633	0.587
tcw12	5.52×10^{-20}	3.11×10^{-6}	0.280	5.3×10^{-12}	1.57×10^{-3}	0.633	0.587
tcw13	5.65×10^{-17}	3.26×10^{-6}	0.259	4.5×10^{-12}	1.24×10^{-3}	0.633	0.587
ptn21	4.60×10^{-15}	1.62×10^{-4}	0.245	3.2×10^{-12}	8.70×10^{-4}	0.633	0.232
ptn22	4.43×10^{-12}	1.46×10^{-4}	0.219	3.0×10^{-13}	1.57×10^{-3}	0.633	0.232
ptn23	9.20×10^{-15}	2.47×10^{-5}	0.247	3.0×10^{-13}	5.18×10^{-3}	0.633	0.232
ptn24	2.35×10^{-12}	7.90×10^{-4}	0.182	3.0×10^{-12}	1.86×10^{-3}	0.633	0.232
ptn25	2.15×10^{-13}	1.04×10^{-4}	0.300	1.7×10^{-13}	1.33×10^{-3}	0.633	0.232
ptn26	1.00×10^{-11}	9.83×10^{-4}	0.126	2.2×10^{-13}	1.34×10^{-3}	0.633	0.232
tsw31	2.95×10^{-17}	8.70×10^{-5}	0.218	8.1×10^{-13}	1.60×10^{-5}	0.633	0.129
tsw32	2.23×10^{-16}	1.14×10^{-5}	0.290	7.1×10^{-13}	1.00×10^{-4}	0.633	0.600
tsw33	6.57×10^{-18}	6.17×10^{-6}	0.283	7.8×10^{-13}	1.59×10^{-3}	0.633	0.600
tsw34	1.77×10^{-19}	8.45×10^{-6}	0.317	3.3×10^{-13}	1.04×10^{-4}	0.633	0.569
tsw35	4.48×10^{-18}	1.08×10^{-5}	0.216	9.1×10^{-13}	1.02×10^{-4}	0.633	0.569
tsw36	2.00×10^{-19}	8.32×10^{-6}	0.442	1.3×10^{-12}	7.44×10^{-4}	0.633	0.569
tsw37	2.00×10^{-19}	8.32×10^{-6}	0.442	1.3×10^{-12}	7.44×10^{-4}	0.633	0.569
tsw38	2.00×10^{-18}	6.23×10^{-6}	0.286	8.1×10^{-13}	2.12×10^{-3}	0.633	0.569
tswz (zeolitic portion of tsw39)	3.5×10^{-17}	4.61×10^{-6}	0.059	8.1×10^{-13}	1.5×10^{-3}	0.633	0.370 [b]
tswv (vitric portion of tsw39)	1.49×10^{-13}	4.86×10^{-5}	0.293	[a]	[a]	[a]	[a]
ch1z	3.5×10^{-17}	2.12×10^{-7}	0.349	2.5×10^{-14}	1.4×10^{-3}	0.633	0.370 [b]
ch1v	6.65×10^{-13}	8.73×10^{-5}	0.240	[a]	[a]	[a]	[a]
ch2v	2.97×10^{-11}	2.59×10^{-4}	0.158	[a]	[a]	[a]	[a]
ch3v	2.97×10^{-11}	2.59×10^{-4}	0.158	[a]	[a]	[a]	[a]
ch4v	2.97×10^{-11}	2.59×10^{-4}	0.158	[a]	[a]	[a]	[a]
ch5v	2.97×10^{-11}	2.59×10^{-4}	0.158	[a]	[a]	[a]	[a]
ch6v	2.35×10^{-13}	1.57×10^{-5}	0.147	[a]	[a]	[a]	[a]
ch2z	5.2×10^{-18}	2.25×10^{-6}	0.257	2.5×10^{-14}	8.9×10^{-4}	0.633	0.370 [b]
ch3z	5.2×10^{-18}	2.25×10^{-6}	0.257	2.5×10^{-14}	8.9×10^{-4}	0.633	0.370 [b]
ch4z	5.2×10^{-18}	2.25×10^{-6}	0.257	2.5×10^{-14}	8.9×10^{-4}	0.633	0.370 [b]
ch5z	5.2×10^{-18}	2.25×10^{-6}	0.257	2.5×10^{-14}	8.9×10^{-4}	0.633	0.370 [b]
ch6z	8.2×10^{-19}	1.56×10^{-7}	0.499	2.5×10^{-14}	1.4×10^{-3}	0.633	0.370 [b]
pp4	8.77×10^{-17}	4.49×10^{-7}	0.474	2.5×10^{-14}	1.83×10^{-3}	0.633	0.370
pp3	7.14×10^{-14}	8.83×10^{-6}	0.407	2.2×10^{-13}	2.47×10^{-3}	0.633	0.199
pp2	1.68×10^{-15}	2.39×10^{-6}	0.309	2.2×10^{-13}	3.17×10^{-3}	0.633	0.199

Table D-1. Calibrated Parameters from One-Dimensional Inversion of Saturation and Water Potential Data for the Base-Case Infiltration Scenario (Continued)

Model Layer	k_M (m^2)	α_M (1/Pa)	m_M	k_F (m^2)	α_F (1/Pa)	m_F	γ
pp1	2.35×10^{-15}	9.19×10^{-7}	0.272	2.5×10^{-14}	1.83×10^{-3}	0.633	0.370 [b]
bf3	4.34×10^{-13}	1.26×10^{-5}	0.193	2.2×10^{-13}	2.93×10^{-3}	0.633	0.199
bf2	8.1×10^{-17}	1.18×10^{-7}	0.617	2.5×10^{-14}	8.9×10^{-4}	0.633	0.370 [b]

Source: BSC 2003b, Table 11.

NOTE: [a] = The calibrated properties conceptual model does not include fractures in these layers.
[b] = The γ parameter was not calibrated for those layers. The value from pp4 is assigned to these layers.

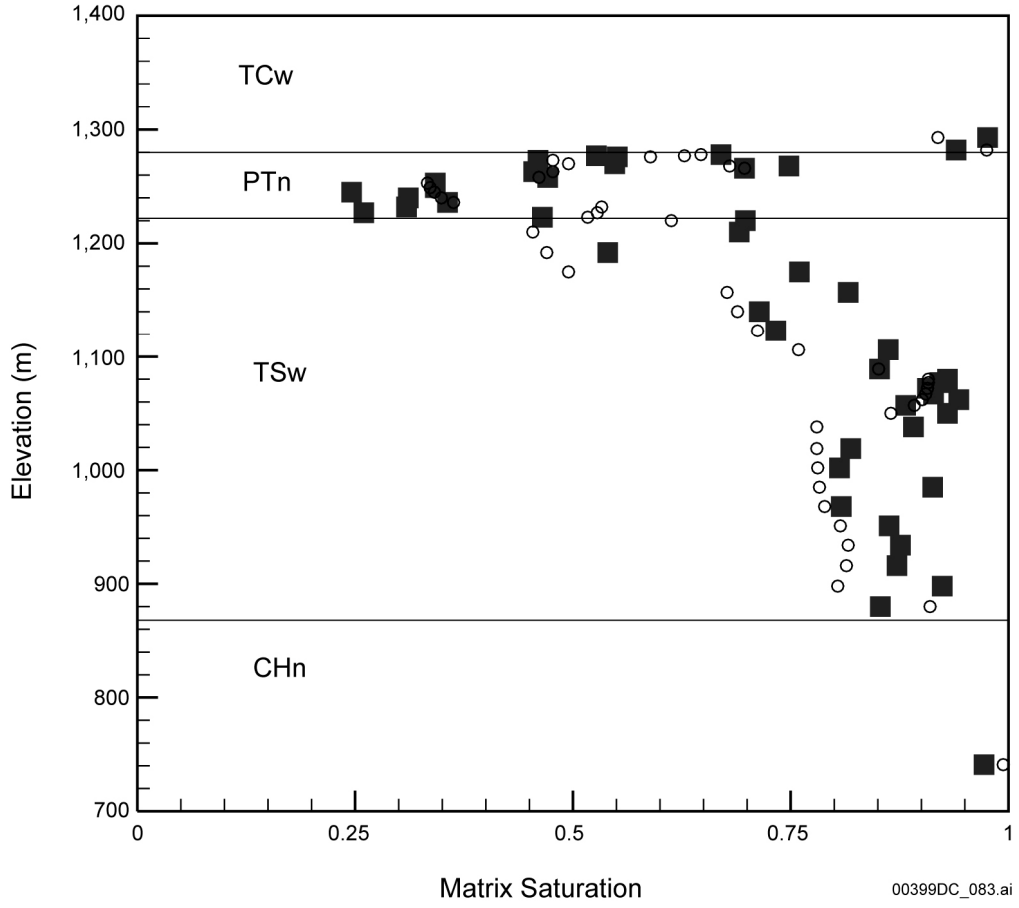

Source: BSC 2003b, Figure 2.

NOTE: Filled squares correspond to averaged core data and circles correspond to simulation results.

Figure D-1. Measured and Simulated Saturation Comparison at USW SD-9 for a One-Dimensional, Drift-Scale, Calibrated Parameter Set for the Base-Case Infiltration Scenario

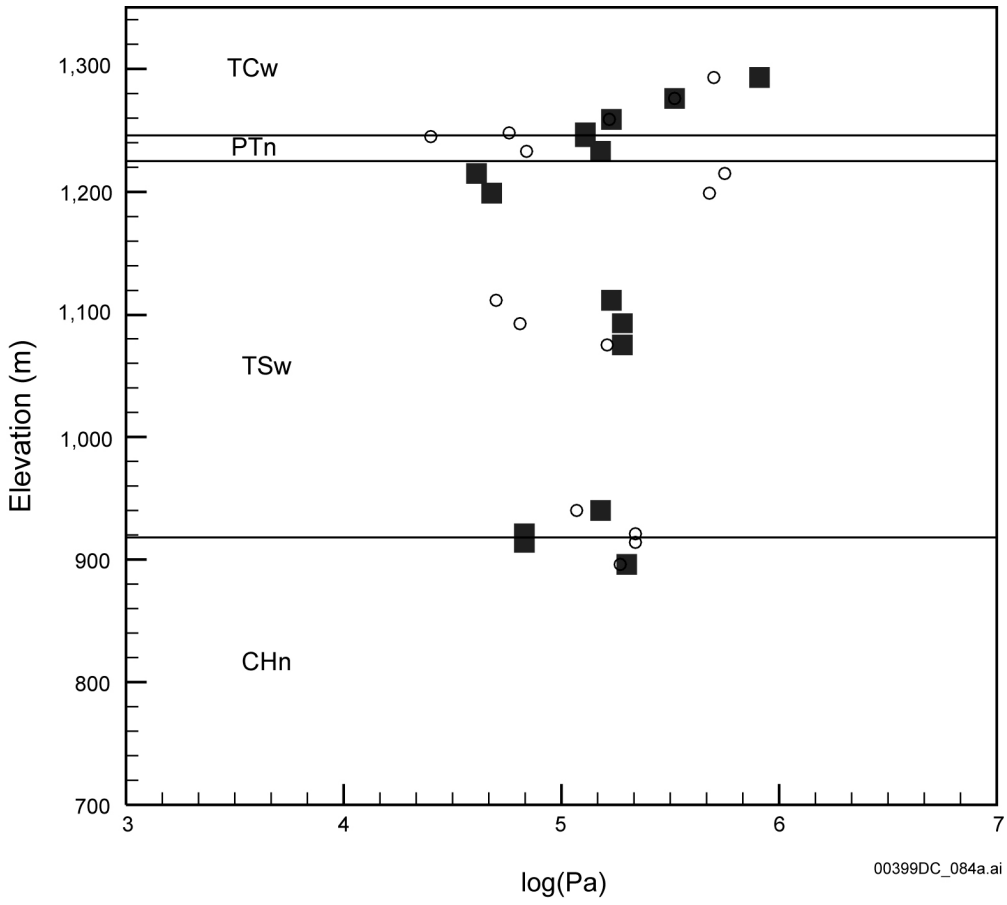

Source: BSC 2003b, Figure 3.

NOTE: Filled squares correspond to data and circles correspond to simulation results.

Figure D-2. Measured and Simulated Water Potential Comparison at UE-25 SD-12 for a One-Dimensional, Drift-Scale, Calibrated Parameter Set for the Base-Case Infiltration Scenario

Table D-2. Calibrated Parameters from One-Dimensional Inversion of Saturation and Water Potential Data for the Upper-Bound Infiltration Scenario

Model Layer	k_M (m^2)	α_M (1/Pa)	m_M	k_F (m^2)	α_F (1/Pa)	m_F	γ
tcw11	3.90×10^{-15}	1.23×10^{-5}	0.388	3.0×10^{-11}	5.01×10^{-3}	0.633	0.500
tcw12	1.16×10^{-19}	3.39×10^{-6}	0.280	5.3×10^{-12}	2.19×10^{-3}	0.633	0.500
tcw13	4.41×10^{-16}	3.25×10^{-6}	0.259	4.5×10^{-12}	1.86×10^{-3}	0.633	0.500
ptn21	2.14×10^{-14}	1.56×10^{-4}	0.245	3.2×10^{-12}	2.69×10^{-3}	0.633	0.100
ptn22	1.29×10^{-11}	1.33×10^{-4}	0.219	3.0×10^{-13}	1.38×10^{-3}	0.633	0.100
ptn23	4.07×10^{-14}	2.39×10^{-5}	0.247	3.0×10^{-13}	1.23×10^{-3}	0.633	0.100
ptn24	4.27×10^{-12}	5.62×10^{-4}	0.182	3.0×10^{-12}	2.95×10^{-3}	0.633	0.100
ptn25	1.01×10^{-12}	9.48×10^{-5}	0.300	1.7×10^{-13}	1.10×10^{-3}	0.633	0.100
ptn26	1.00×10^{-11}	5.23×10^{-4}	0.126	2.2×10^{-13}	9.55×10^{-4}	0.633	0.100
tsw31	1.77×10^{-17}	4.85×10^{-5}	0.218	8.1×10^{-13}	1.58×10^{-5}	0.633	0.100
tsw32	2.13×10^{-16}	1.96×10^{-5}	0.290	7.1×10^{-13}	1.00×10^{-4}	0.633	0.561
tsw33	2.39×10^{-17}	5.22×10^{-6}	0.283	7.8×10^{-13}	1.58×10^{-3}	0.633	0.561
tsw34	2.96×10^{-19}	1.65×10^{-6}	0.317	3.3×10^{-13}	1.00×10^{-4}	0.633	0.570
tsw35	8.55×10^{-18}	5.03×10^{-6}	0.216	9.1×10^{-13}	5.78×10^{-4}	0.633	0.570
tsw36	7.41×10^{-19}	1.08×10^{-6}	0.442	1.3×10^{-12}	1.10×10^{-3}	0.633	0.570
tsw37	7.41×10^{-19}	1.08×10^{-6}	0.442	1.3×10^{-12}	1.10×10^{-3}	0.633	0.570
tsw38	7.40×10^{-18}	5.58×10^{-6}	0.286	8.1×10^{-13}	8.91×10^{-4}	0.633	0.570
tswz (zeolitic portion of tsw39)	3.5×10^{-17}	4.61×10^{-6}	0.059	8.1×10^{-13}	1.5×10^{-3}	0.633	0.500[b]
tswv (vitric portion of tsw39)	2.24×10^{-13}	4.86×10^{-5}	0.293	[a]	[a]	[a]	[a]
ch1z	3.5×10^{-17}	2.12×10^{-7}	0.349	2.5×10^{-14}	1.4×10^{-3}	0.633	0.500 [b]
ch1v	1.39×10^{-12}	8.82×10^{-5}	0.240	[a]	[a]	[a]	[a]
ch2v	4.90×10^{-11}	2.73×10^{-4}	0.158	[a]	[a]	[a]	[a]
ch3v	4.90×10^{-11}	2.73×10^{-4}	0.158	[a]	[a]	[a]	[a]
ch4v	4.90×10^{-11}	2.73×10^{-4}	0.158	[a]	[a]	[a]	[a]
ch5v	4.90×10^{-11}	2.73×10^{-4}	0.158	[a]	[a]	[a]	[a]
ch6v	2.72×10^{-13}	1.67×10^{-5}	0.147	[a]	[a]	[a]	[a]
ch2z	5.2×10^{-18}	2.25×10^{-6}	0.257	2.5×10^{-14}	8.9×10^{-4}	0.633	0.500 [b]
ch3z	5.2×10^{-18}	2.25×10^{-6}	0.257	2.5×10^{-14}	8.9×10^{-4}	0.633	0.500 [b]
ch4z	5.2×10^{-18}	2.25×10^{-6}	0.257	2.5×10^{-14}	8.9×10^{-4}	0.633	0.500 [b]
ch5z	5.2×10^{-18}	2.25×10^{-6}	0.257	2.5×10^{-14}	8.9×10^{-4}	0.633	0.500 [b]
ch6z	8.2×10^{-19}	1.56×10^{-7}	0.499	2.5×10^{-14}	1.4×10^{-3}	0.633	0.500 [b]
pp4	1.02×10^{-15}	4.57×10^{-7}	0.474	2.5×10^{-12}	8.91×10^{-4}	0.633	0.500
pp3	1.26×10^{-13}	9.50×10^{-6}	0.407	2.2×10^{-12}	1.66×10^{-3}	0.633	0.500
pp2	1.70×10^{-15}	2.25×10^{-6}	0.309	2.2×10^{-13}	1.66×10^{-3}	0.633	0.500

Table D-2. Calibrated Parameters from One-Dimensional Inversion of Saturation and Water Potential Data for the Upper-Bound Infiltration Scenario (Continued)

Model Layer	k_M (m^2)	α_M (1/Pa)	m_M	k_F (m^2)	α_F (1/Pa)	m_F	γ
pp1	2.57×10^{-15}	8.77×10^{-7}	0.272	2.5×10^{-14}	8.91×10^{-4}	0.633	0.500 [b]
bf3	3.55×10^{-14}	3.48×10^{-5}	0.193	2.2×10^{-13}	1.66×10^{-3}	0.633	0.500
bf2	8.1×10^{-17}	1.18×10^{-7}	0.617	2.5×10^{-14}	8.9×10^{-4}	0.633	0.500 [b]

Source: BSC 2003b, Table 12.

NOTE: [a] = The calibrated properties conceptual model does not include fractures in these layers.
[b] = The γ was not calibrated for these layers. The value from pp4 is assigned to these layers.

Table D-3. Calibrated Parameters from One-Dimensional Inversion of Saturation and Water Potential Data for the Lower-Bound Infiltration Scenario

Model Layer	k_M (m^2)	α_M (1/Pa)	m_M	k_F (m^2)	α_F (1/Pa)	m_F	γ
tcw11	3.44×10^{-15}	1.16×10^{-5}	0.388	3.0×10^{-11}	4.68×10^{-3}	0.633	0.483
tcw12	3.00×10^{-20}	2.67×10^{-6}	0.280	5.3×10^{-12}	3.20×10^{-3}	0.633	0.483
tcw13	3.96×10^{-17}	1.64×10^{-6}	0.259	4.5×10^{-12}	2.13×10^{-3}	0.633	0.483
ptn21	5.55×10^{-15}	6.38×10^{-5}	0.245	3.2×10^{-12}	2.93×10^{-3}	0.633	0.065
ptn22	8.40×10^{-12}	1.67×10^{-4}	0.219	3.0×10^{-13}	6.76×10^{-4}	0.633	0.065
ptn23	1.92×10^{-14}	4.51×10^{-5}	0.247	3.0×10^{-13}	3.96×10^{-3}	0.633	0.065
ptn24	6.66×10^{-13}	2.52×10^{-3}	0.182	3.0×10^{-12}	2.51×10^{-3}	0.633	0.065
ptn25	1.96×10^{-14}	1.24×10^{-4}	0.300	1.7×10^{-13}	1.53×10^{-3}	0.633	0.065
ptn26	1.00×10^{-11}	1.63×10^{-3}	0.126	2.2×10^{-13}	1.52×10^{-3}	0.633	0.065
tsw31	1.42×10^{-17}	8.02×10^{-5}	0.218	8.1×10^{-13}	1.58×10^{-5}	0.633	0.037
tsw32	3.96×10^{-16}	9.46×10^{-6}	0.290	7.1×10^{-13}	1.31×10^{-4}	0.633	0.528
tsw33	1.60×10^{-18}	4.25×10^{-6}	0.283	7.8×10^{-13}	1.94×10^{-3}	0.633	0.528
tsw34	1.38×10^{-19}	1.19×10^{-6}	0.317	3.3×10^{-13}	6.55×10^{-4}	0.633	0.476
tsw35	2.33×10^{-18}	1.97×10^{-6}	0.216	9.1×10^{-13}	1.35×10^{-3}	0.633	0.476
tsw36	5.58×10^{-19}	4.22×10^{-7}	0.442	1.3×10^{-12}	1.31×10^{-3}	0.633	0.476
tsw37	5.58×10^{-19}	4.22×10^{-7}	0.442	1.3×10^{-12}	1.31×10^{-3}	0.633	0.476
tsw38	2.93×10^{-18}	1.43×10^{-6}	0.286	8.1×10^{-13}	1.75×10^{-3}	0.633	0.476
tswz (zeolitic portion of tsw39)	3.5×10^{-17}	4.61×10^{-6}	0.059	8.1×10^{-13}	1.5×10^{-3}	0.633	0.276 [b]
tswv (vitric portion of tsw39)	3.15×10^{-13}	1.86×10^{-5}	0.293	[a]	[a]	[a]	[a]
ch1z	3.5×10^{-17}	2.12×10^{-7}	0.349	2.5×10^{-14}	1.4×10^{-3}	0.633	0.276 [b]
ch1v	3.15×10^{-14}	4.50×10^{-5}	0.240	[a]	[a]	[a]	[a]
ch2v	1.13×10^{-11}	1.22×10^{-4}	0.158	[a]	[a]	[a]	[a]
ch3v	1.13×10^{-11}	1.22×10^{-4}	0.158	[a]	[a]	[a]	[a]
ch4v	1.13×10^{-11}	1.22×10^{-4}	0.158	[a]	[a]	[a]	[a]
ch5v	1.13×10^{-11}	1.22×10^{-4}	0.158	[a]	[a]	[a]	[a]
ch6v	2.54×10^{-13}	9.05×10^{-6}	0.147	[a]	[a]	[a]	[a]

Table D-3. Calibrated Parameters from One-Dimensional Inversion of Saturation and Water Potential Data for the Lower-Bound Infiltration Scenario (Continued)

Model Layer	k_M (m^2)	α_M (1/Pa)	m_M	k_F (m^2)	α_F (1/Pa)	m_F	γ
ch2z	5.2×10^{-18}	2.25×10^{-6}	0.257	2.5×10^{-14}	8.9×10^{-4}	0.633	0.276 [b]
ch3z	5.2×10^{-18}	2.25×10^{-6}	0.257	2.5×10^{-14}	8.9×10^{-4}	0.633	0.276 [b]
ch4z	5.2×10^{-18}	2.25×10^{-6}	0.257	2.5×10^{-14}	8.9×10^{-4}	0.633	0.276 [b]
ch5z	5.2×10^{-18}	2.25×10^{-6}	0.257	2.5×10^{-14}	8.9×10^{-4}	0.633	0.276 [b]
ch6z	8.2×10^{-19}	1.56×10^{-7}	0.499	2.5×10^{-14}	1.4×10^{-3}	0.633	0.276 [b]
pp4	2.98×10^{-16}	2.88×10^{-7}	0.474	2.5×10^{-14}	1.88×10^{-3}	0.633	0.276
pp3	5.37×10^{-14}	7.97×10^{-6}	0.407	2.2×10^{-13}	1.32×10^{-3}	0.633	0.248
pp2	4.24×10^{-16}	2.41×10^{-6}	0.309	2.2×10^{-13}	2.80×10^{-3}	0.633	0.248
pp1	7.02×10^{-16}	1.36×10^{-6}	0.272	2.5×10^{-14}	6.39×10^{-4}	0.633	0.276 [b]
bf3	2.97×10^{-14}	1.32×10^{-5}	0.193	2.2×10^{-13}	1.91×10^{-3}	0.633	0.248
bf2	8.1×10^{-17}	1.18×10^{-7}	0.617	2.5×10^{-14}	8.9×10^{-4}	0.633	0.276 [b]

Source: BSC 2003b, Table 13.

NOTE: [a] = The calibrated properties conceptual model does not include fractures in these layers (Section 5).
[b] = The γ-parameter was not calibrated for these layers. The value from pp4 is assigned to these layers.

D.4.1.2 Calibration of Fault Parameters

The fault property set for the unsaturated zone is obtained by calibrating a two-dimensional model. Two-dimensional flow (vertical and east–west) is used to describe the flow patterns around borehole USW UZ-7a and for fault-property calibration. Data from USW UZ-7a are the most comprehensive with respect to faults. Saturation, water potential, and pneumatic pressure data are available within the Ghost Dance fault zone from the surface to the upper layers of the TSw. Because the data on faults are so limited, they are separated into four layers to reduce the number of parameters used to characterize the fault zones. The layers are the TCw, PTn, TSw, and CHn/CFu (Calico Hills nonwelded/Crater Flat Undifferentiated). Data for inversion are available for only the first three layers, so only the parameters of these layers are calibrated. Minimization of the inversion function is the only criterion used for a successful calibration.

Fault properties to be calibrated are fracture properties, whereas matrix properties within fault zones are the same as those in nonfault zones (DTN: LB02081DKMGKID.001). Fracture permeabilities are fixed during the saturation and water potential inversion and are the only parameters calibrated to the pneumatic data. Parameters to be calibrated against matrix-saturation and water potential data are fracture α and active-fracture-model parameter γ. The fault parameters calibrated for the base-case infiltration scenario are checked to determine whether they are satisfactory for the other two infiltration scenarios. The objective function values for the two infiltration scenarios, determined with forward runs of iTOUGH2 V5.0 (LBNL 2002), are even smaller than that for the base-case infiltration scenario. Therefore, a single calibrated fault parameter set is applied to all three infiltration scenarios. The calibrated fault parameter set is presented in Table D-4.

Table D-4. Calibrated Fault Parameters from Two-Dimensional Inversions of Saturation, Water Potential, and Pneumatic Data

Model Layer	k_F (m^2)	α_F (1/Pa)	m_F	γ
Tcwf	9.77×10^{-10}	3.89×10^{-3}	0.633	0.40
Ptnf	1.00×10^{-10}	2.80×10^{-3}	0.633	0.11
Tswf	2.51×10^{-11}	3.16×10^{-4}	0.633	0.30
Chnf	3.70×10^{-13}	2.30×10^{-3}	0.633	0.30

Source: BSC 2003b, Table 17.

NOTE: Tcwf, Ptnf, Tswf, and Chnf represent faults at the four layers TCw, PTn, TSw and CHn, respectively.

D.4.1.3 Uncertainties of Hydrologic Property Data

This section discusses sources and quantification of uncertainties for the calibrated parameters. The uncertainty information provided in this section will be used later to assess the uncertainty of using calibrated models (on current climate conditions) to forecast flow conditions under future climates.

D.4.1.3.1 Sources of Parameter Uncertainty

A major source of parameter uncertainty is the conceptual model (e.g. different continuum approaches). Parameter calibration is based on the conceptual model for unsaturated zone flow and transport (CRWMS M&O 2000). Model simplifications will also contribute to parameter uncertainty. For example, one-dimensional models are used for calibrating drift-scale property sets. As a result, lateral flow behavior in the unsaturated zone may not be captured by property sets determined from one-dimensional models.

Infiltration-rate uncertainty also contributes to parameter uncertainty because flow processes in the unsaturated zone are largely determined by top boundary conditions. Using the three infiltration scenarios for the parameter calibration documented in this study captures this uncertainty (BSC 2003b). Other sources of certainty may include field measurement uncertainty (e.g., the uncertainty in the measurement data of saturation, water potential, and pneumatic pressure). The measurement uncertainty is propagated to parameter uncertainty in the calibration procedure. Compared to other uncertainty sources, measurement uncertainty contributes little to the parameter uncertainty because measurement data can be constrained in a small range.

In addition, scale effects are a well-known source of parameter uncertainty. This is especially true for determination of the unsaturated zone model parameters. For example, matrix parameters are measured in the unsaturated zone at core scale on the order of several centimeters, whereas in the unsaturated zone flow and transport model, numerical gridblocks are on the order of a few meters to hundreds of meters. The scale-dependence of hydrologic parameters has been widely recognized in the scientific community (Neuman 1994). Although upscaling is partially considered in developing uncalibrated matrix properties, the calibrated matrix permeabilities are on average higher than uncalibrated ones for the three infiltration scenarios (Table D-5). The general increase in permeability with scale is consistent with reported findings (Neuman 1994).

Consequently, the calibrated matrix α values are on average also higher than uncalibrated ones. A higher permeability is generally expected to correspond to a higher van Genuchten α. For example, fracture α values are significantly higher than matrix values. The residuals for each layer (uncalibrated log x minus calibrated log x, where $x = k_M$ or α_M) were averaged to calculate the values shown in Table D-5. Because of the difference between measurement scale and modeling scale, uncalibrated properties are not directly measured, but are estimated values by averaging the measurements from the layer for the scales used in the unsaturated zone model. As a result, residuals cannot be used to evaluate the uncertainty as to the true parameter value, although they may be used to bound this uncertainty (as will be discussed below).

Table D-5. Average Residual for Calibrated Matrix Properties for Three Infiltration Scenarios

	Residual for log(k_M)	**Residual for log(α_M)**
Base-case	-0.37	-0.25
Upper bound	-0.65	-0.17
Lower bound	-0.17	-0.06

Source: BSC 2003b, Table 18.

NOTE: The residual refers to an uncalibrated matrix property minus the corresponding calibrated property.

Calibrated properties are nonunique because of data limitation. For example, in drift-scale parameter calibration, 78 parameters are calibrated to about 300 data points. This is, therefore, a poorly constrained problem. Further complicating the calibrating process, many of the parameters are cross-correlated; that is, variations in two or more parameters may have the same effect on predicted system response. Because the problem is poorly constrained, there is no well-defined global minimum in the objective function. Rather, there are likely to be many equivalent local minima. With respect to moisture and water potential data, any of these minima provide an equally good parameter set. To address this issue, uncalibrated parameters are used as initial guesses and prior information in most inversions.

Table D-6 shows the average absolute residual, which refers to an absolute difference between uncalibrated property and its corresponding calibrated property, for calibrated matrix properties for three infiltration scenarios. The absolute value of the residual is always positive, and the average absolute residual is, therefore, greater than the average residual, as shown in Table D-5. The average standard deviation of log(k_M) for uncalibrated matrix property sets is 1.61. Average standard deviation (calculated by hand) for log(α_M) for the uncalibrated matrix property set is 0.81. The residual values for log(α_F) are also given in Table D-6. They are close to or smaller than the average standard deviation of log(α_F), which is 0.30, determined from uncalibrated fracture property sets (BSC 2003b, Table 4).

Table D-6. Average Absolute Residual for Calibrated Matrix Properties for Three Infiltration Scenarios

	Average Absolute Residual for log(k_M)	Average Absolute Residual for log(α_M)	Average Absolute Residual for log(α_F)
Base case	0.75	0.44	0.41
Upper bound	0.81	0.38	0.19
Lower bound	0.74	0.43	0.28

Source: BSC 2003b, Table 19.

NOTE: The absolute residual refers to an absolute difference between uncalibrated matrix property and the corresponding calibrated property.

D.4.1.3.2 Quantification of Parameter Uncertainty

Quantifiable uncertainties are difficult to establish for the estimated parameter sets. In principle, these uncertainties could be evaluated either by Monte Carlo simulation or by linear error analysis, both of which are capabilities of iTOUGH2 V5.0 (LBNL 2002). Because of the large numbers of parameters and the high nonlinearity of the unsaturated flow process, the linear error analysis is not reliable (Finsterle 1999). Alternatively, Monte Carlo-type methods (such as the bootstrap method) would be required. However, the large number of parameters make uncertainty analysis by Monte Carlo simulation prohibitively time consuming. Based on these considerations, the uncertainty information from prior information is believed to be more reliable (and practical) for determining uncertainties for the calibrated property sets.

In this study, parameter uncertainties (standard deviations) for the uncalibrated parameter sets are directly used for the calibrated parameter sets because these uncertainties are determined from measurements. The parameter uncertainty of the uncalibrated property sets is largely a result of small-scale spatial variability. Because the degree of spatial variability decreases with scale (spatial variability is averaged at a large scale), it is likely to provide upper limits of uncertainty on calibrated parameters for the given conceptual model and infiltration rates (BSC 2003b).

Table D-7 gives the uncertainties of the parameters k_M, α_M, k_F, and α_F (BSC 2003b, Table 20). When a log(k_F) uncertainty is not available in these two tables (BSC 2003b) for a model layer, the largest value among the uncertainties (standard deviations) in all the layers for which uncertainty values are available is used. Uncertainties for log(α_M) and log(α_F) are approximated from uncertainty values of the corresponding permeability. Uncertainties of the active-fracture-model parameter γ are difficult to obtain here and have not been calculated because prior information for γ is not available. Further discussions of the uncertainties of γ are provided in other model reports describing analyses of hydrologic properties data and unsaturated zone flow model and submodels (BSC 2002, Sections 1.10.4 and I-1-1). No information is available for quantifying uncertainties for m_F that are not calibrated parameters. Neither γ nor m_F is very sensitive to flow model performance, nor can they be constrained in a small range (see BSC 2003c, Section 6.81). Therefore, uncertainty of these two parameters may have limited influence on model results.

Table D-7 also shows estimated uncertainties for calibrated fault properties. Because fault properties are calibrated with limited data points, the parameter uncertainties are expected to be relatively large. For each parameter type, the largest parameter uncertainty within the corresponding hydrogeologic unit for the nonfault property set is used as the corresponding fault parameter uncertainty. The fault property set does not include matrix parameters. Use of large uncertainty for a parameter may lead to relatively large uncertainty of model results and provide conservative ranges of simulation results. This treatment should not have adverse effects on risk estimation for the repository.

Table D-7. Uncertainties of Calibrated Parameters

Model Layer	Matrix Property		Fracture Property	
	$\log(k_M)$	$\log(\alpha_M)$	$\log(k_F)$	$\log(\alpha_F)$
tcw11	0.47	0.24	1.15	0.58
tcw12	2.74	1.37	0.78	0.39
tcw13	2.38	1.19	1.15	0.58
ptn21	2.05	1.03	0.88	0.44
ptn22	1.41	0.71	0.20	0.10
ptn23	0.64	0.32	0.20	0.10
ptn24	1.09	0.55	1.15	0.58
ptn25	0.39	0.20	0.10	0.05
ptn26	1.12	0.56	1.15	0.58
tsw31	3.02	1.51	1.15	0.58
tsw32	0.94	0.47	0.66	0.33
tsw33	1.61	0.81	0.61	0.31
tsw34	0.97	0.49	0.47	0.24
tsw35	1.65	0.83	0.75	0.38
tsw36	3.67	1.84	0.54	0.27
tsw37	3.67	1.84	0.28	0.14
tsw38	1.57	0.79	1.15	0.58
tswz (zeolitic portion of tsw39)	2.74	1.37	1.15	0.58
tswv (vitric portion of tsw39)	1.38	0.69	[a]	[a]
ch1z	2.74	1.37	1.15	0.58
ch1v	1.11	0.56	[a]	[a]
ch2v	1.62	0.81	[a]	[a]
ch3v	1.62	0.81	[a]	[a]
ch4v	1.62	0.81	[a]	[a]
ch5v	1.62	0.81	[a]	[a]
ch6v	1.11	0.56	[a]	[a]
ch2z	0.91	0.46	1.15	0.58
ch3z	0.91	0.46	1.15	0.58
ch4z	0.91	0.46	1.15	0.58
ch5z	0.91	0.46	1.15	0.58
ch6z	2.05	1.03	1.15	0.58
pp4	2.74	1.37	1.15	0.58
pp3	0.75	0.38	1.15	0.58
pp2	1.18	0.59	1.15	0.58
pp1	1.52	0.76	1.15	0.58

Table D-7. Uncertainties of Calibrated Parameters (Continued)

Model Layer	Matrix Property		Fracture Property	
	log(k_M)	log(α_M)	log(k_F)	log(α_F)
bf3	1.64	0.82	1.15	0.58
bf2	1.52	0.76	1.15	0.58
Tcwf	[b]	[b]	1.15	0.58
Ptnf	[b]	[b]	1.15	0.58
Tswf	[b]	[b]	1.15	0.58
Chnf	[b]	[b]	1.15	0.58

Source: BSC 2003b, Table 20.

NOTE: [a] =The calibrated properties conceptual model does not include fractures in these layers.
[b] = Fault property set does not include matrix properties.

The propagation of uncertainty in model calibration is addressed in this study. The uncertainty data for measurements are used as inputs into inversions. The uncertainty in boundary conditions is reflected by developing property sets for different infiltration scenarios. The uncertainty in prior information has been used for characterizing uncertainties for calibrated properties.

D.4.2 Rock-Property Calibration on Higher Infiltration Conditions

The field tests at Alcove 8–Niche 3 and Alcove 1 conducted at high infiltration rates are expected to encompass flow behavior representative of future climates. The numerical models developed for these tests are calibrated based on the high infiltration rates. The calibrated rock properties for these models are compared to rock properties from the calibrated drift-scale model (BSC 2003b). If these two data sets are consistent, one can conclude that the models calibrated based on the current climate conditions can be used for forecasting flow in future climate condition.

The information in this section is based on *In Situ Field Testing of Processes* (BSC 2003a) for the Alcove 8–Niche 3 tests and *Modeling Flow and Transport in Unsaturated Fractured Rock: An Evaluation of the Continuum Approach* (Liu et al. 2003) for the Alcove 1 test.

D.4.2.1 Alcove 8–Niche 3 Tests

Two types of tests were conducted at the site. One is a fault test and the other is a large-plot test. Alcove 8 has been excavated for liquid releases through a fault (fault tests) and a network of fractures (large-plot tests). Niche 3 (also referred to as Niche 3107) serves as the site for monitoring wetting-front migration of seepage originating from water applied to either the fault or large plot in Alcove 8 and for the collection and subsequent analysis of tracer concentrations of the seeping water.

Figure D-3 (top) shows the location of the test site within the ESF main drift and the ECRB Cross-Drift. Figure D-3 (bottom) shows a three-dimensional representation of the test area, including several slanted (near-vertical) boreholes. Alcove 8 is located within the upper

lithophysal zone of the TSw (Tplpul). Niche 3 is located in the middle nonlithophysal zone of the TSw (Tptpmn).

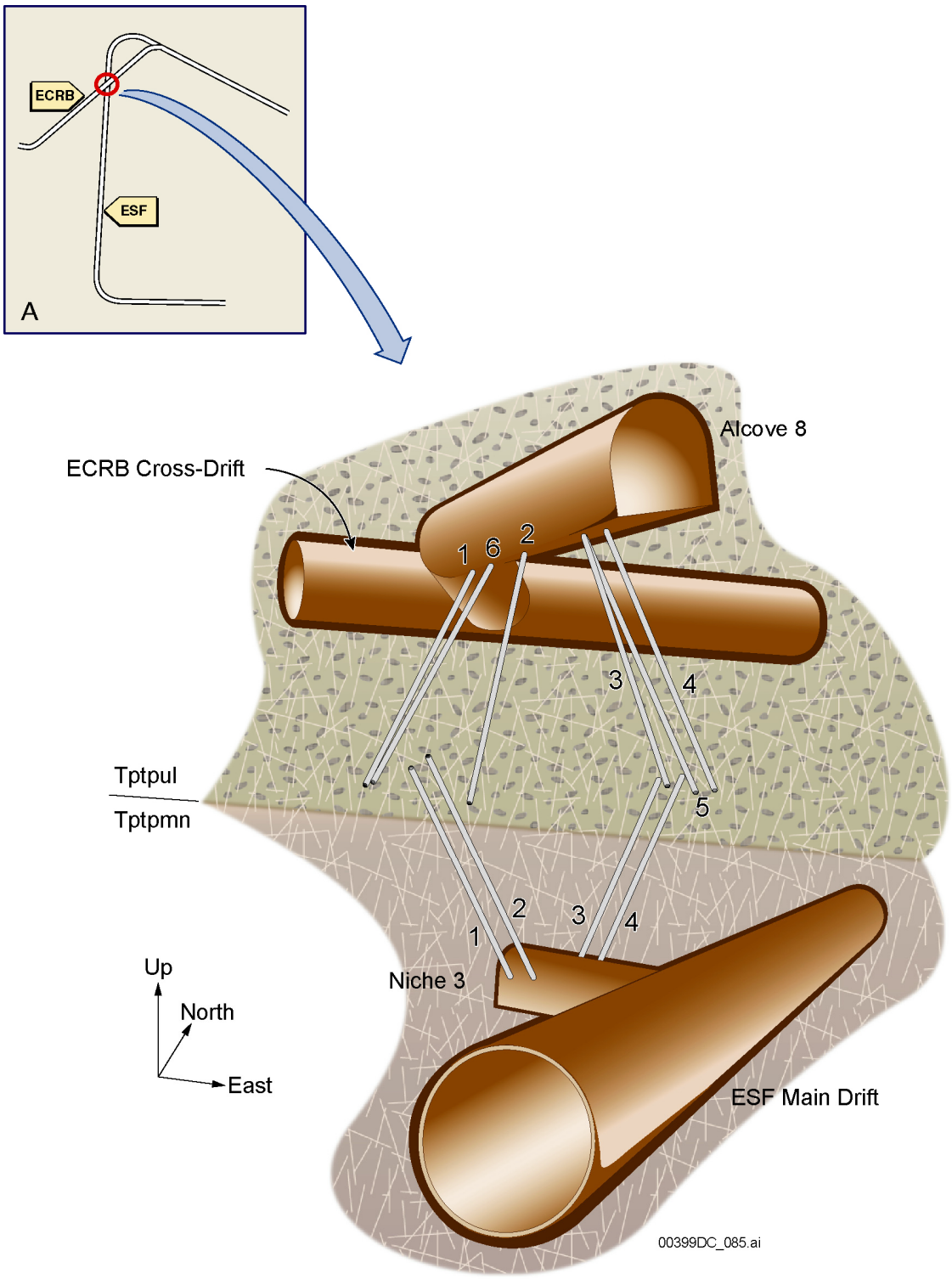

Source: BSC 2003a, Figure 6.12.1-2.

Figure D-3. Illustration of the Test Bed for the Alcove 8–Niche 3 Tests

A distinctive feature of the test bed in Alcove 8 is a near-vertical fault that cuts across the floor (Figure D-4). It is open on the ceiling of Niche 3 and appears to be closed along the floor of the alcove. To facilitate ponded releases of water, a trench about 5 cm wide and about 5 cm deep was etched along this fault for the fault tests.

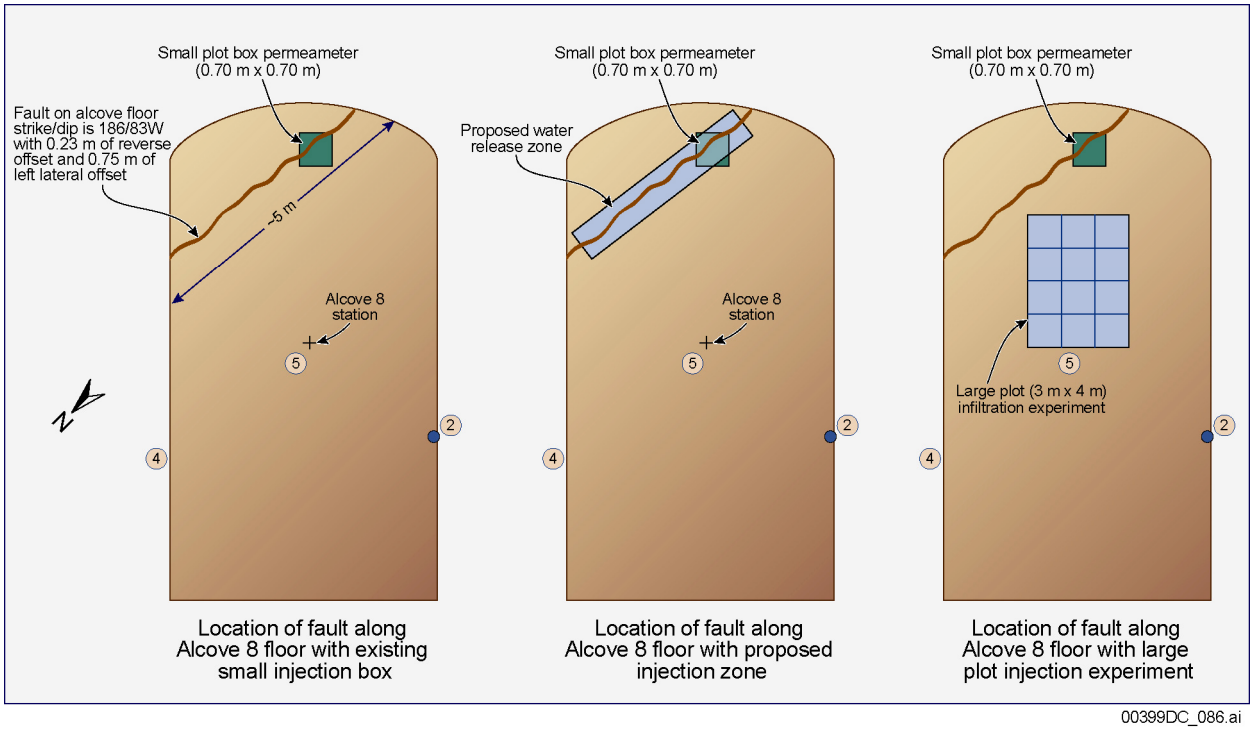

Source: BSC 2001, Figure 6.12.1-3.

Figure D-4. Illustration of the Infiltration Zones along the Floor of Alcove 8

Niche 3 is approximately 4 m wide and extends to about 14 m from the centerline in the ESF main drift. The distance from the ceiling to the floor of the niche gradually drops from 3.25 m at the opening to 2.5 m towards the midpoint of the niche.

Both fault tests and large-plot tests were planned to include two phases involving water release with and without tracers. Phase I corresponds to an experimental condition characterized by positive water pressure head (2 cm) at the infiltration plots. In this case, the fault or fracture network is saturated (at least near the infiltration plots). Phase II corresponds to an experimental condition characterized by much smaller infiltration rates (or more negative water pressure heads) than phase I. The planned phase II fault tests were not performed due to time constraints and conflicting experimental test schedules. Results of phase II testing (large-plot) are not yet available and, subsequently, are not used in the calibration.

Water was applied at infiltration plots in Alcove 8. For the fault tests, initially the application area was over a small section of the fault. This was increased from 30 cm to 1.0 m and then to 5.15 m. Water was first released from the smallest injection zone, which is a cylinder 30 cm in diameter. During the second release, the cylinder zone was replaced with a box that measured 70 cm × 70 cm. For the third set of water releases (along 5.15 m), the fault was divided into four

sections with each section serving as a separate release point. In each of these applications, water along the release zone was ponded to a head of about 0.02 m.

The large-plot tests involve the release of water (without and with tracers) under both ponded and nonponded conditions in a 3 × 4 m plot. The infiltration zone was divided into 12 sections each 1 × 1 m (Figure D-5). Observations from this phase of testing include the seepage rates measured at Niche 3. Infiltration was initiated in the large-plot on the floor of Alcove 8 by maintaining an approximately 2 cm head of ponded water (for phase I). The amount of water necessary to maintain the 2 cm of ponding was recorded and thus the infiltration rates (liters/day) over time were also known for all plots (1-12 in Figure D-5) (BSC 2003a, Section 6.12).

D.4.2.2 Model Analysis of the Fault Test at Alcove 8–Niche 3

Model Development–A numerical model was developed to simulate the fault test. Simulation results are compared to the relevant field observations. This model is calibrated to the higher infiltration rates used in the field test.

A three-dimensional numerical grid is constructed for simulating the fault test (Figure D-6). The fault is represented as a vertical fracture, and surrounding fractured rock is approximated as a dual-continuum system (consisting of overlapped, interacting fracture and matrix continua). Global water flow and solute transport are allowed to occur in both continua. Figure D-6 shows a cross section of the grid within the fault. The thickness of the grid in the direction perpendicular to fault walls is 3 m along each side of the fault. The fracture frequency used for generating the dual-continuum grid is 1.03 for tsw33 (determined from the fracture map at the alcove floor) and 1.72 for tsw34 (determined from the fracture map at the ceiling of the niche) (BSC 2003c, Section 7.6).

As shown in Figure D-6, within a cross section of the grid along the fault the grid spacing is 10 cm just above the ceiling of the niche, enabling the seepage process to be accurately simulated. The grid spacings in the direction perpendicular to the fault are 0.024 m, 0.168 m, 0.456 m, 0.756 m and 1.44 m. The smallest spacing is adjacent to the fault so that water imbibition and tracer diffusion into the fractured rock from the fault can be accurately captured. Cross sections parallel to the fault walls have identical grid meshes (Figure D-6) for different distances from the fault. The niche is represented by an opening at the bottom of the grid (Figure D-6), with the geometry of the opening determined from the survey data of the niche near the fault. This is an approximation of the geometry of the test site; a three-dimensional geometry of the niche with an underground tunnel connected to the niche is difficult to incorporate into the model. However, since our main concern is flow and transport processes within the fault, this geometric representation should be adequate.

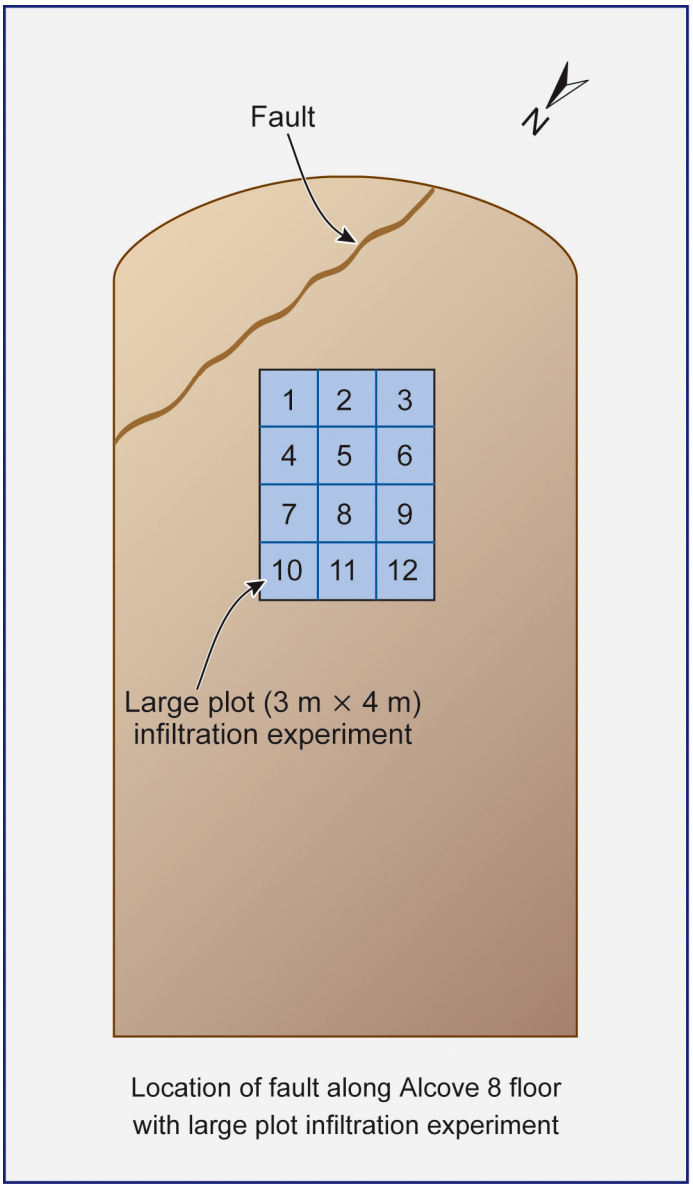

Source: BSC 2003a, Figure 6.12.4-1.

NOTE: Plot numbers are added here.

Figure D-5. Illustration of the Infiltration Zones along the Floor of Alcove 8 Large-Plot Test with the Numbers Identifying the 12 Infiltration Subplots

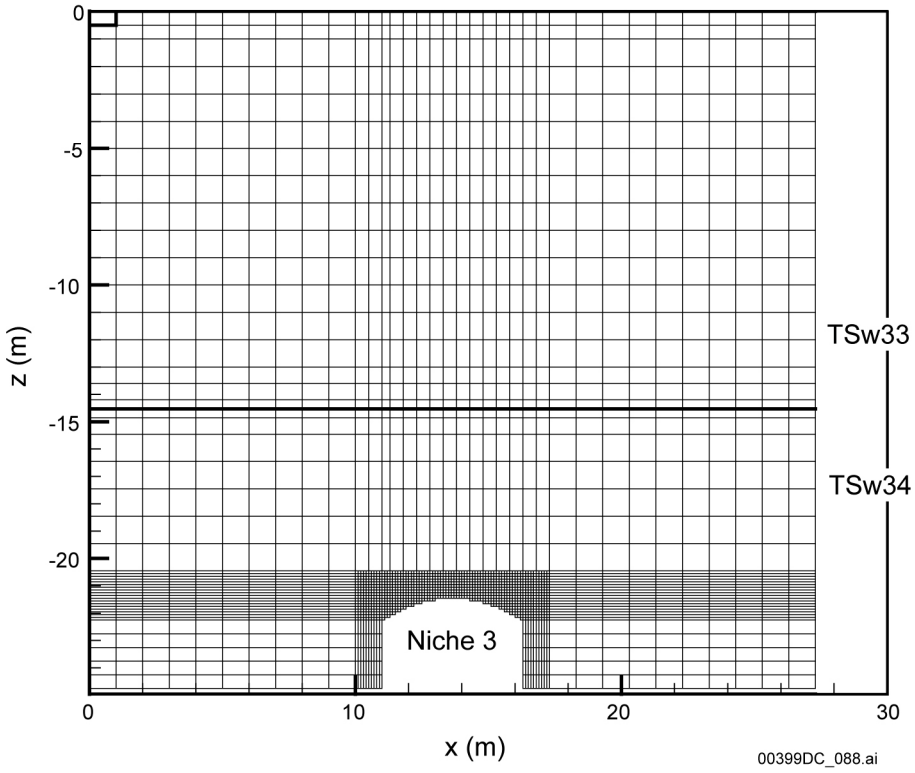

Source: BSC 2003c, Figure 7.6-5.

Figure D-6. Cross-Sectional Illustration (Along Fault) of the Three-Dimensional Numerical Grid Used for Modeling Studies of Alcove 8–Niche 3

Time-dependent inflow rates are imposed on the model top boundary, corresponding to the infiltration plot (Figure D-7) at the alcove floor. Figure D-7 shows the total infiltration rate as a function of time. For simplicity, the model considers the uniformly distributed infiltration rate along the infiltration plot to be consistent with the uniform property distribution in the unsaturated zone model.

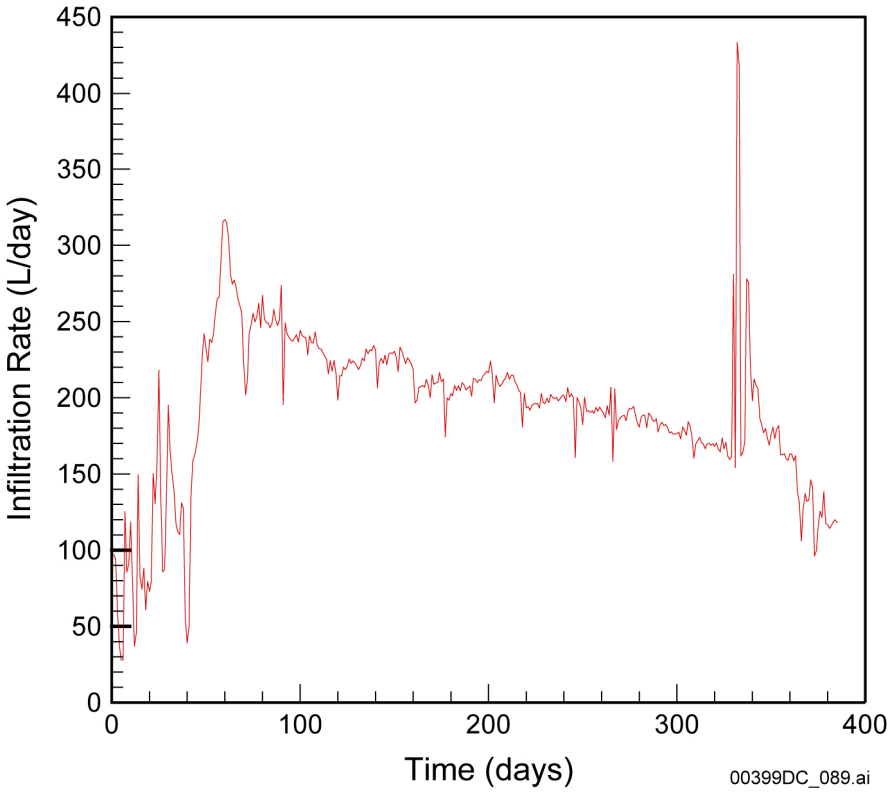

Source: BSC 2003c, Figure 7.6-1.

Figure D-7. Infiltration Rate along Fault in Alcove 8 as a Function of Time

The side boundary corresponds to zero-flow conditions (in the direction perpendicular to the boundaries of the simulation domain). The niche wall boundary is modeled by a zero capillary-pressure condition, representing capillary barrier effects (Birkholzer et al. 1999). The bottom boundary was assigned a constant matrix saturation of 0.85, which is consistent with field observations under ambient conditions (Flint 1998, p. 44, Table 7). Also based on field observations, matrix saturations are initially assigned to be 0.72 for tsw33 and 0.85 for tsw34 (Flint 1998, p. 44). Other initial conditions for the rock mass within the model domain are that both the fractures and the fault are solute-free and have a small water saturation (1.05×10^{-2}).

Model Calibration Based on Higher Infiltration–The numerical model was calibrated against the seepage and water-travel-velocity data to obtain the calibrated rock properties and the corresponding water flow field.

Both fracture and matrix properties were assumed to be homogeneous within each geologic subunit (tsw33 and tsw34). Fault properties were assumed to be the same for both units. This is based mainly on the following three considerations:

1. Consideration of heterogeneity within each subunit would introduce a large number of rock properties that need to be determined by more data than was available from the test site.

2. These treatments have been used by the site-scale model of the Yucca Mountain unsaturated zone. This simple representation of subsurface heterogeneity can be used to model the fault test.

3. It is implied that flow and transport in the unsaturated zone are mainly determined by large-scale heterogeneity, characterized by property differences between different geologic units rather than by property variability within a geologic unit (Zhou et al. 2003).

Rock hydraulic properties needed as inputs into the model include fracture and matrix permeabilities, fracture and matrix porosities, fault aperture and permeabilities, van Genuchten (1980) parameters (for matrix, fractures, and the fault), and the parameter of the active fracture model, γ, for fractures (BSC 2003c, Table 7.6-1). Because fracture van Genuchten parameters for tsw33 and tsw34 are similar, a simple average of these parameters was used as the corresponding parameters for the fault. The averaged k/ϕ (where k is fracture permeability and ϕ is the corresponding fracture porosity) was calculated as fault permeability. Because there is no matrix in the fault in our model (or $\phi = 1$), the weighted k/ϕ (rather than weighted k) is employed for estimating fault permeability. The aperture of the fault was estimated as the average of fracture apertures of the two subunits. The active fracture model was developed for fracture networks rather than for a single fracture. Consequently, the active fracture model does not apply to the fault here. To reduce the number of variables in model calibration (or inverse modeling), parameters expected to significantly affect simulated water transport time and seepage rate were varied in the calibration, while other parameters were kept unchanged. The varied parameters were fracture and fault permeabilities, fracture porosity, fault aperture, and fracture and fault van Genuchten α values.

Figure D-8 shows a comparison between seepage-rate data and the simulation result from a model calibration (run 1) without considering the water-travel-velocity data. In this calibration run, fracture porosity and fault aperture were not varied. A fairly good match to the observed seepage data was obtained (Figure D-8); however, water travel velocity is significantly overestimated (Figure D-9). Water travel velocities were calculated from water arrival times at locations about 1 m above the middle of the opening in Figure D-6. The transport time was defined as the time when fault or fracture saturation was increased from the initial value of 1.05×10^{-2} to 1.06×10^{-2}. This comparison implies that seepage rate as a function of time may be mainly controlled by rock properties near seepage locations (Liu et al. 2002, Section 3.3). Also, water travel velocities are determined by rock properties from the infiltration plot to the locations where water travel velocities are monitored. Table D-8 gives the calibrated properties obtained from run 1.

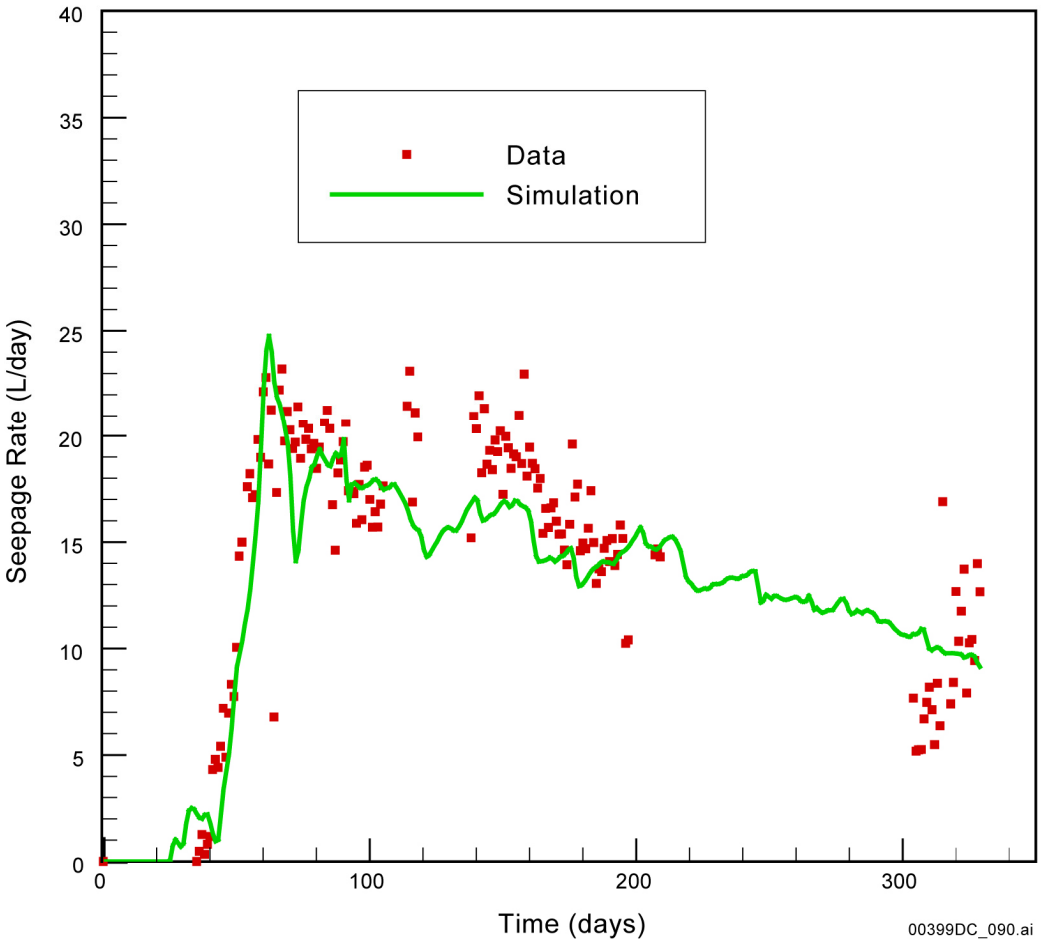

Source: BSC 2003c, Figure 7.6-6.

Figure D-8. A Comparison between Simulated Seepage Rates as a Function of Time (Run 1) and Field Observations

Table D-8. Rock Properties Calibrated from Seepage Rate Data (Run 1)

Rock Property	Fault	tsw33	tsw34
Fracture Permeability (m2)	6.67×10^{-11}	8.93×10^{-13}	3.16×10^{-14}
Fracture van Genuchten α (Pa-1)	1.15×10^{-3}	1.67×10^{-3}	4.59×10^{-4}

Source: BSC 2003c, Table 7.6-2.

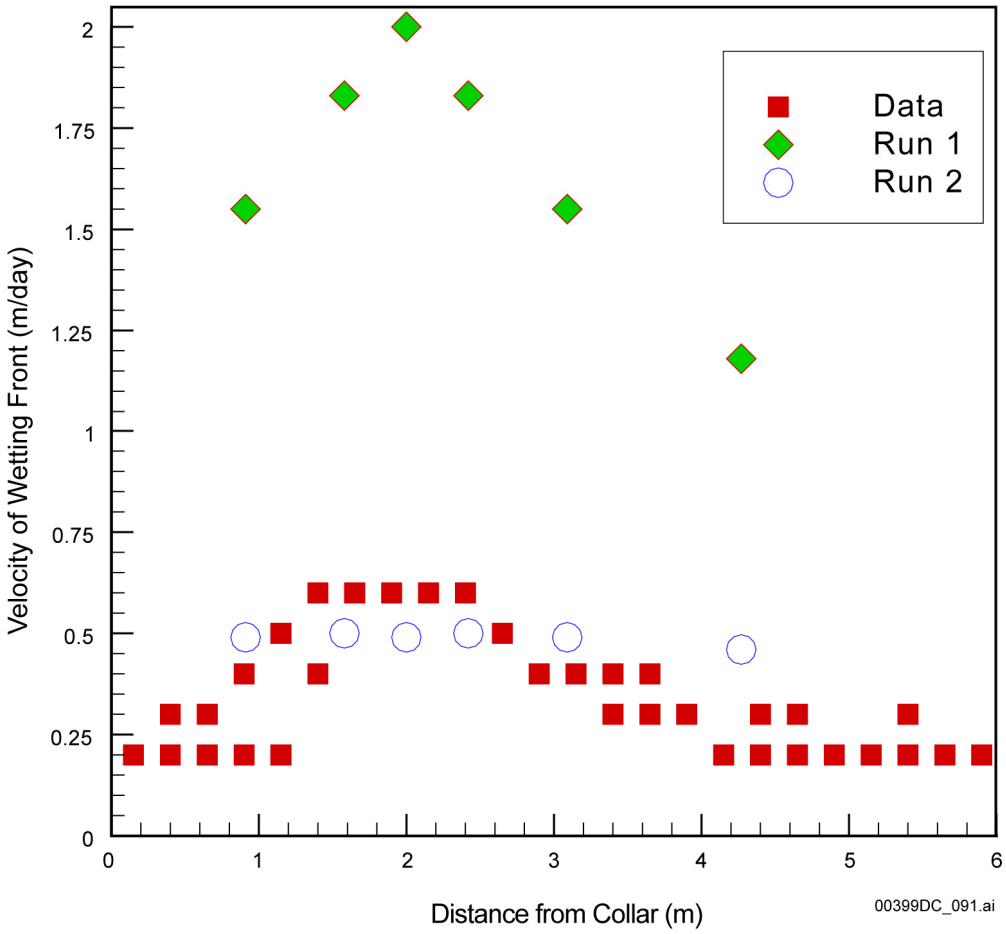

Source: BSC 2003c, Figure 7.6-7.

Figure D-9. A Comparison among Calculated Water Travel Velocities from Two Calibration Runs and the Velocity Data Observed from the Fault Test

The overestimation of the water travel velocities may result from the following: (1) some cavities in tsw33 are connected to fractures and could contribute to increasing the storage in the fracture continuum; (2) in reality, the fault is a zone rather than a single fracture. The effective aperture from this zone may be much larger than the assumed aperture value for the fault. Neither of these factors was considered in run 1 (first calibration). Taking these factors into consideration, the new calibration (run 2) allowed both fault aperture and fracture porosity in tsw33 to be varied. The resultant values are 3 cm for fault aperture and 0.066 for fracture porosity of tsw33 (Table D-9). While the actual width of the fault zone is unknown, the estimated equivalent fault aperture (3 cm) is considered to be acceptable. The estimated fracture porosity is consistent with those estimated from water release tests performed in the same geologic unit (BSC 2003a).

Table D-9. Rock Properties Calibrated from Both Seepage Rate and Water Travel Velocity Data (Run 2)

Rock Property	Fault	tsw33	tsw34
Fracture Permeability (m2)	1.12×10^{-10}	1.23×10^{-12}	5.01×10^{-13}
Fracture Porosity		0.066	
Fracture aperture (m)	0.03		
Fracture van Genuchten α (Pa-1)	1.24×10^{-3}	2.19×10^{-3}	1.09×10^{-3}

Source: BSC 2003c, Table 7.6-3.

Figure D-9 shows a comparison between calculated water travel velocities from two calibration runs and the velocity data observed from the fault test. The simulated water travel velocities from run 2 are much closer to the observed data than those from run 1 (especially near the fault). However, the water travel velocities away from the fault are still overestimated. One possible explanation is that matrix imbibition from fractures above the niche were underestimated because the dual-continuum approach considerably underestimates the pressure gradient near a fracture matrix interface during transient flow conditions (Pruess and Narasimhan 1985). While this problem could be resolved with the multiple interacting continua model (Pruess and Narasimhan 1985), the computational intensity of the inverse model problem under consideration would be significantly increased. A model calibration involves a great number of forward simulation runs. Considering that (1) the transient flow effects would be considerably reduced later in the test, and (2) the focus is on flow and transport within and near faults, simulated flow field and calibrated rock properties from run 2 were used for simulating tracer transport at the test site. Figure D-10 also shows a comparison between simulated seepage rates as a function of time (run 2) and field observations. The match is still reasonable.

D.4.2.3 Model Analysis of the Large Plot Test at Alcove 8–Niche 3

Model Development–A numerical model was developed to simulate and better understand results from the large-plot tests (phase I). The seepage and infiltration-rate data were used to calibrate the model to obtain the site-specific rock properties. A three-dimensional numerical grid was constructed for modeling the large-plot tests (Figure D-11). The top of the grid corresponds to the floor of Alcove 8, where infiltration occurred. The 12 infiltration plots and the projected outline boundary of Niche 3 ceiling (under which seepage trays were installed) are also shown on the top of the grid in Figure D-11. Small grid sizes were used above the niche ceiling and near the interface between model layers tsw33 and tsw34, to capture diverted water flow around the niche and rock property transition at the interface between model layers. The dips of the contact between tsw33 and tsw34 are ignored because flow in fractures is expected to occur mainly in the vertical direction. For simplicity, the niche ceiling was approximated as a flat surface. To capture the transient flow and transport behavior, the multiple interacting continua (MINC) model (Pruess and Narasimhan 1985) was used, a model that can handle steep pressure and concentration gradients. In the numerical grid shown in Figure D-11, each gridblock includes a fracture element and five matrix elements.

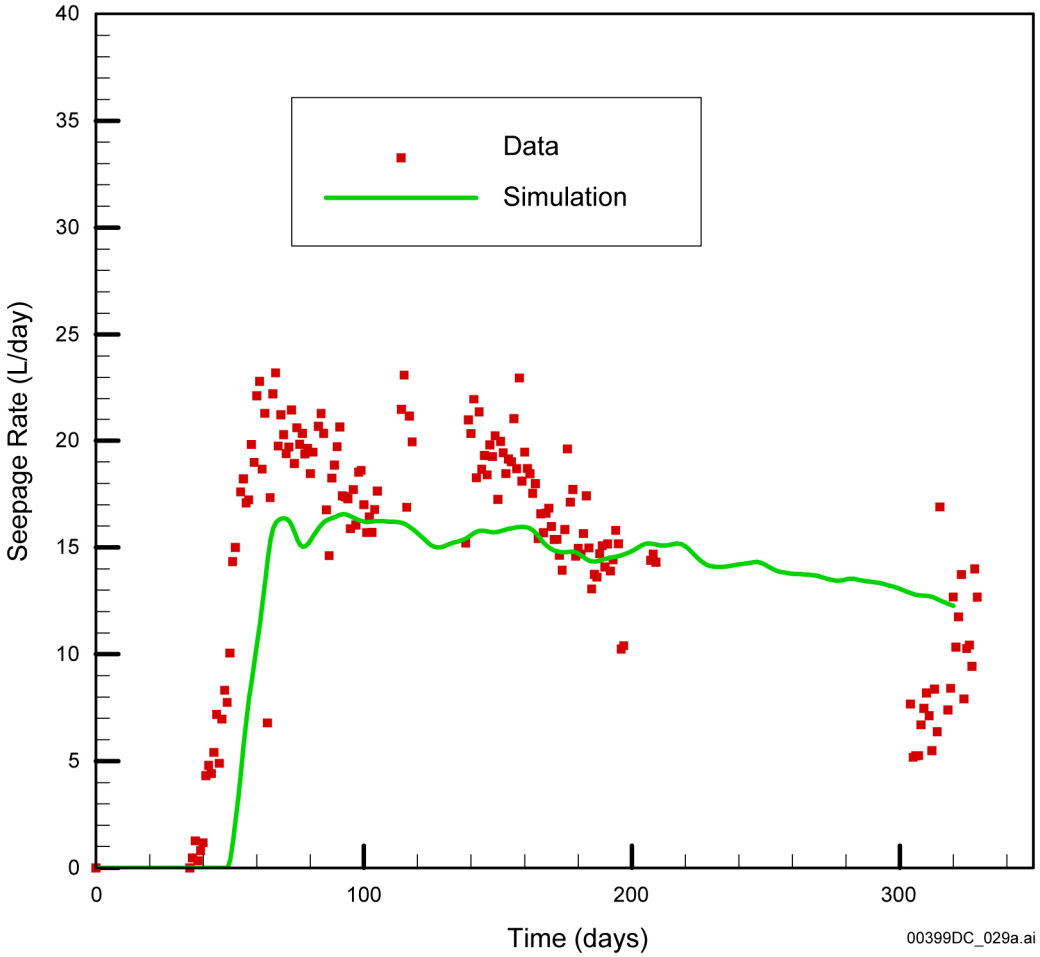

Source: BSC 2003c, Figure 7.6-8.

Figure D-10. A Comparison between Simulated Seepage Rates as a Function of Time (Run 2) and Field Observations

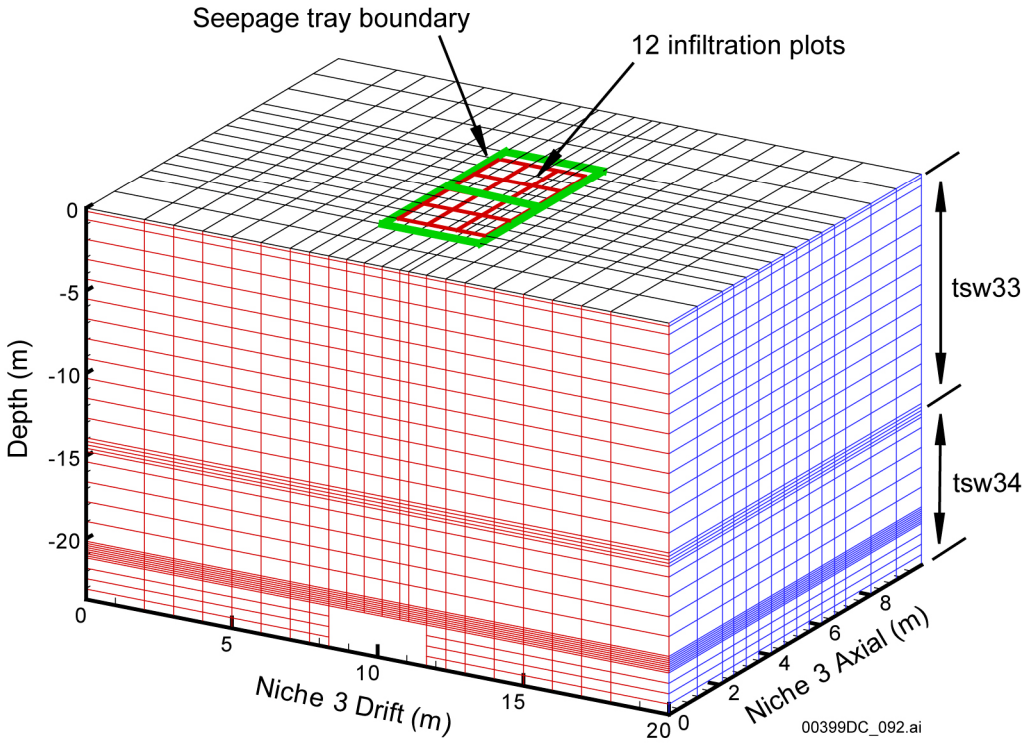

Source: DTN: LB0312A8N3MDLG.001.

Figure D-11. Three-Dimensional Numerical Grids for the Large-Plot Tests

To handle the spatial variabilities observed from both the infiltration rates in Alcove 8 and seepage rates in Niche 3, heterogeneous distributions of fracture properties within a given model layer were considered in the three-dimensional model. Within a model layer, fractured rock is divided into a number of vertical columns within zones below the infiltration plots (for tsw33) or above the ceiling of Niche 3 (for tsw34). Therefore, there are two sets of vertical columns that are located in tsw33 and tsw34, respectively. Each column in the upper layer (tsw33) corresponds to an infiltration plot, and each column in the lower layer (tsw34) corresponds to one seepage tray. The rest of the rock was considered to have homogeneous property distributions within each model layer. The homogeneous property distributions were also generally used for each column.

Considerable temporal variability in the infiltration rate occurred during the large-plot tests, although a constant water-pressure head (2 cm) was applied at the infiltration plot. This may result from in-filled materials within the fractures just below the infiltration plots. In other words, the effective permeability of fractures just below the plot changed with time, although fracture properties may not change for zones away from the infiltration plots. Given these considerations, infiltration rates (that are both spatially and temporally variable, based on Figure D-12) at Alcove 8, rather than the pressure head, were used as the boundary condition at the large infiltration plot. The side boundary corresponds to zero-flow conditions (in the direction perpendicular to the simulation domain). The niche wall boundary was again modeled by a zero-capillary-pressure condition, representing capillary barrier effects. The bottom boundary corresponds to free drainage conditions. Under ambient conditions, matrix saturation is 0.72 for tsw33 and 0.85 for tsw34 (Flint 1998, p. 44, Table 7). Because of the disturbance of

nearby fault tests, the actual matrix saturations are expected to be higher than these values. In the model, a value of 1.0 averaged with the saturation value reported by Flint (1998, p. 44, Table 7) was used as the initial matrix saturation value for each model layer. Because of this approximation, a larger degree of uncertainty is expected to exist for initial conditions assigned in the model. Other initial conditions for the rock mass within the model domain are that the rock is solute-free and has a small water saturation (1.05×10^{-2}) in fractures.

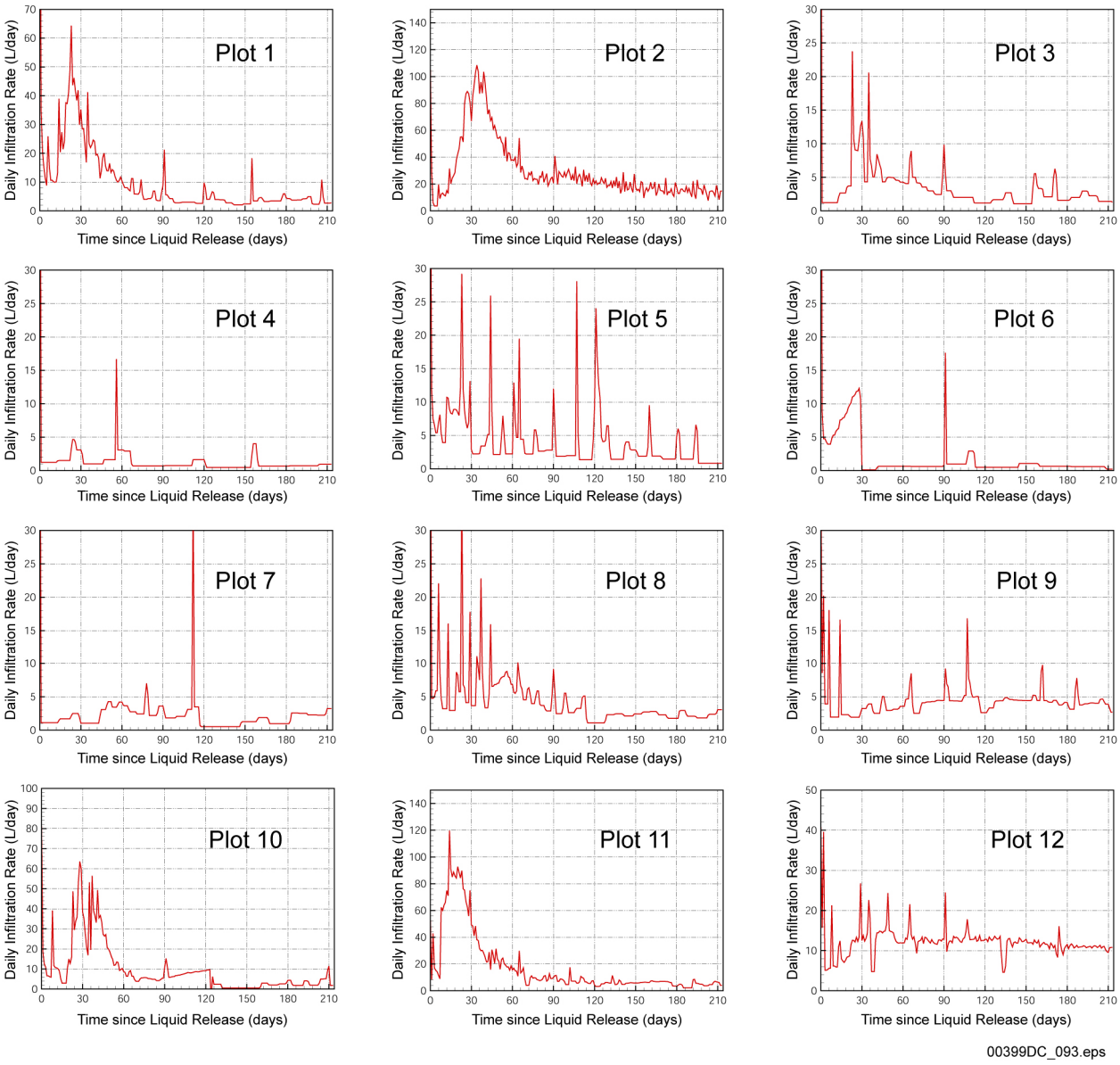

Source: DTNs: GS031008312242.007 from 8/20/02 to 11/19/02; GS030608312242.005 from 11/19/02 to 3/21/03.

NOTE: Plot numbers correspond to those in Figure D-5.

Figure D-12. Infiltration Rates for Each Plot in the Large-Plots Test in Alcove 8 from 9/16/02 to 3/16/03

Calibration Based on Higher Infiltration–Model calibration is carried out to determine site-specific rock properties. The observed spatial distribution of seepage rate on the ceiling of Niche 3 was explicitly considered. In addition to the observed total seepage rate as a function of time, the seepage rates from individual intersections between the niche ceiling and the vertical columns in tsw34 were matched in the model calibration procedure.

To reduce the total number of rock parameters to be calibrated, the most sensitive parameters to the infiltration rate and measured seepage rate are considered in the calibration. In this case, fracture permeability and fracture van Genuchten parameter α are the most important rock properties for water redistribution. The other parameters are assumed to be homogeneous within each hydrogeologic unit. For TSw34, there are seepage rate data for over 215 days to be used as calibration data and two unknowns for each rock column. However, for TSw33, the infiltration rate is sensitive to the saturated hydraulic conductivity beneath an infiltration subplot but not sensitive to the van Genuchten parameter α in the rock column. For simplicity, van Genuchten parameter α in the TSw33 unit is assumed to be uniform for all of the columns.

Model calibration adjusts rock properties such that modeling results match field observations. For model layer tsw33, calibrated rock properties are fracture permeabilities and van Genuchten alphas for vertical columns (corresponding to individual infiltration plots) and for the rest of the rock mass. An initial guess of fracture permeability for a column was determined by the largest infiltration rate (for time t greater than 1 day) at the infiltration plot under water pressure head of 2 cm. The largest infiltration rate (per unit area) is considered to be the saturated hydraulic conductivity for the column. A scale factor was used to calibrate all these fracture permeability values for the columns in tsw33, such that calibrated fracture permeability for a vertical column is equal to its initial guess, multiplied by the calibrated scale factor. In this way, the effects of observed spatial variability of infiltration rate were approximately captured by the model calibration. (A vertical column in tsw33 has a uniform property distribution.)

For model layer tsw34, calibrated rock properties are again fracture permeabilities and van Genuchten alphas for vertical columns (corresponding to seepage trays) and for the rest of rock mass. While most vertical columns have uniform distributions in this model layer, Columns 1, 6, 11, and 12 were further divided into two parts: upper and lower. These two parts have different rock properties for each of the columns mentioned above, in order to consider rock-damage effects on rock properties near the niche ceiling. The lower parts correspond to rock between the niche ceiling and 0.4 m above the ceiling. Fracture porosity calibrated from the fault tests and matrix properties used in fault-test modeling studies are used here. These properties were not varied during model calibration.

Matches between the simulated and observed seepage rates associated with different vertical columns are shown in Figure D-13. Fairly good matches were obtained except for a few columns (e.g., Columns 1, 4, and 7). Figure D-14 shows a comparison between simulated and observed total seepage rate as a function of time. In general, matches shown in the two figures are reasonable. Table D-10 lists calibrated rock properties.

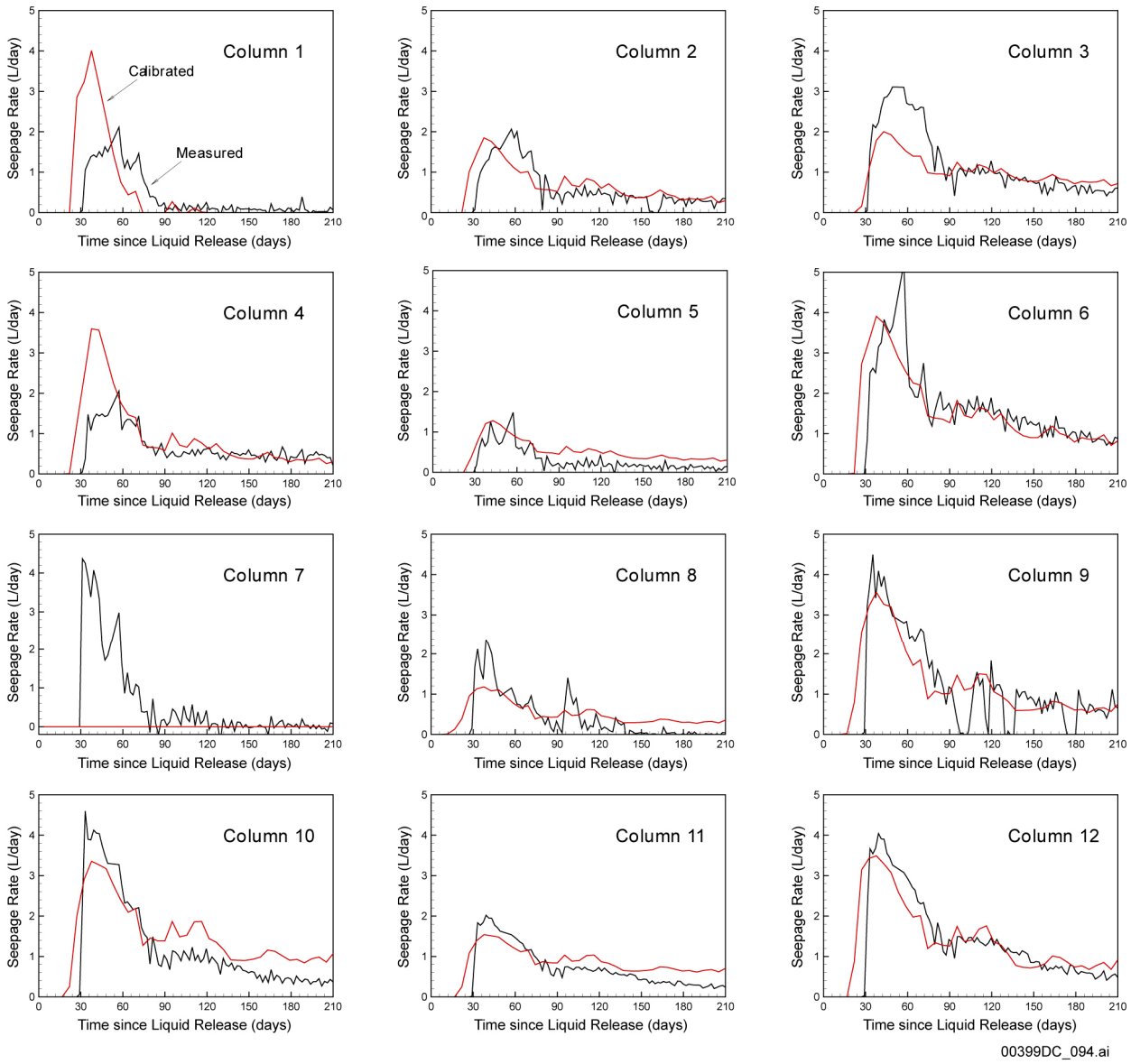

Source: Observed data: DTN: LB0306A8N3LIQR.001 from 9/18/02 to 10/16/02; DTN: LB0308A8N3SEEP.001 from 10/16/02 to 4/2/03; Model results: DTN: LB0312A8N3MDLG.001.

Figure D-13. Matches between the Simulated and Observed Seepage Rates Associated with Different Vertical Columns.

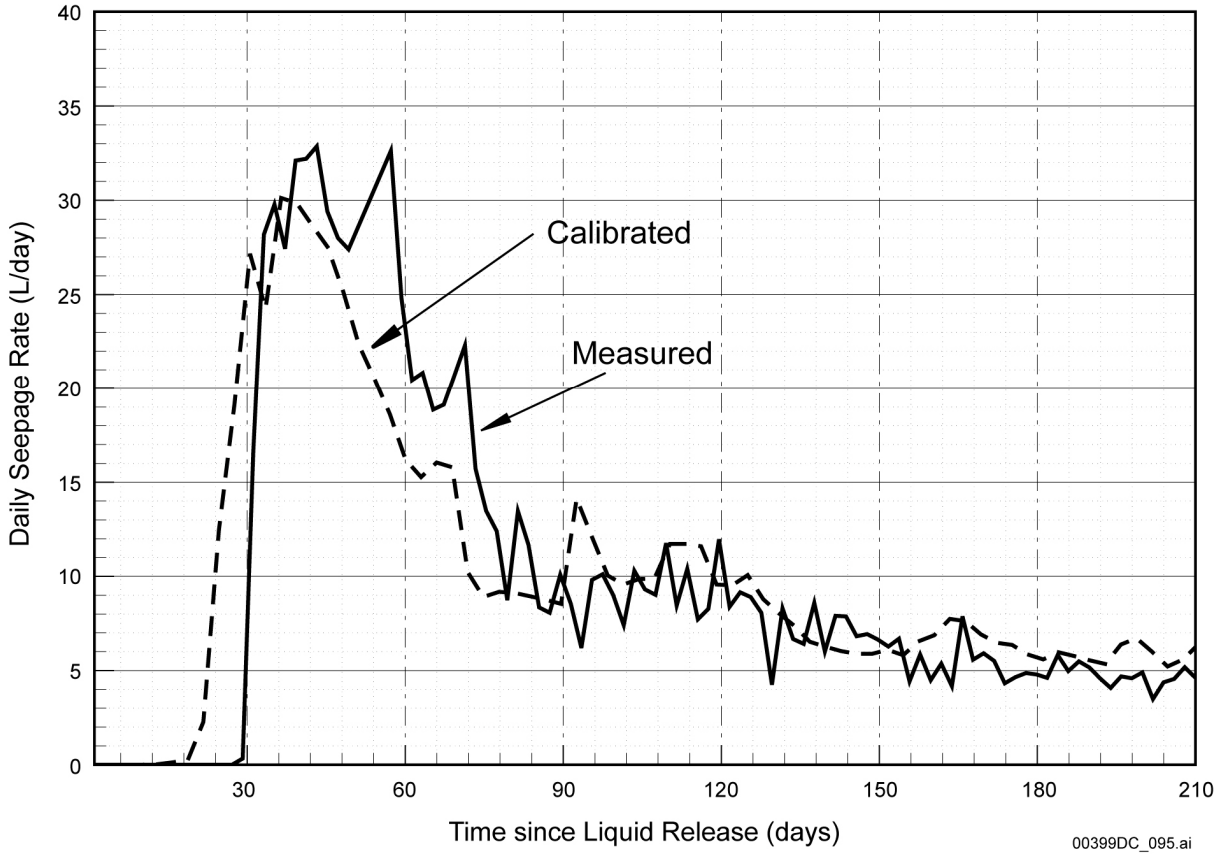

Source: Observed data: DTN: LB0306A8N3LIQR.001 from 9/18/02 to 10/16/02; DTN: LB0308A8N3SEEP.001 from 10/16/02 to 4/2/03; Model results: DTN: LB0312A8N3MDLG.001.

Figure D-14. A Comparison between Simulated and Observed Total Seepage Rate as a Function of Time

Table D-10. Calibrated Rock Properties

Model Layer		Permeability	van Genuchten α	van Genuchten *m*	Porosity
tsw33	Column 1	0.9926×10^{-13}	0.2453×10^{-3}	0.608[a]	0.066[a]
	Column 2	0.1685×10^{-12}			
	Column 3	0.2959×10^{-13}			
	Column 4	0.3146×10^{-13}			
	Column 5	0.5569×10^{-13}			
	Column 6	0.1845×10^{-13}			
	Column 7	0.1314×10^{-13}			
	Column 8	0.6757×10^{-13}			
	Column 9	0.2470×10^{-13}			
	Column 10	0.9786×10^{-13}			
	Column 11	0.1864×10^{-12}			
	Column 12	0.3332×10^{-13}			
	Rest rock mass	0.1190×10^{-11}	0.4787×10^{-3}		
tsw34	Column 1 (upper)	0.225×10^{-11}	0.5677×10^{-3}	0.608[a]	0.010[a]
	Column 2	0.704×10^{-12}	0.1480×10^{-2}		
	Column 3	0.448×10^{-14}	0.1152×10^{-2}		
	Column 4	0.171×10^{-13}	0.3857×10^{-2}		
	Column 5	0.304×10^{-14}	0.8647×10^{-3}		
	Column 6 (upper)	0.149×10^{-13}	0.2932×10^{-3}		
	Column 7	0.434×10^{-11}	0.1891×10^{-2}		
	Column 8	0.614×10^{-13}	0.3208×10^{-2}		
	Column 9	0.104×10^{-13}	0.5316×10^{-2}		
	Column 10	0.616×10^{-14}	0.9825×10^{-3}		
	Column 11 (upper)	0.189×10^{-14}	0.3107×10^{-3}		
	Column 12 (upper)	0.143×10^{-13}	0.2424×10^{-3}		
	Rest rock mass	0.495×10^{-12}	0.7399×10^{-3}		
	Column 1 (lower)	0.5012×10^{-12a}	0.1275×10^{-2}		
	Column 6 (lower)	0.5012×10^{-12a}	0.2052×10^{-2}		
	Column 11 (lower)	$0.5012 \times 10^{-12\ a}$	0.2360×10^{-2}		
	Column 12 (lower)	$0.5012 \times 10^{-12\ a}$	0.1721×10^{-2}		

Source: DTN: LB0312A8N3MDLG.001.

NOTE: [a]These properties are not varied during model calibration.

D.4.2.4 Infiltration Test at Alcove 1 and Model Analysis

The infiltration test site is located in Alcove 1 near the North Portal of the ESF. Alcove 1, about 30 m below the ground surface, was constructed for collecting seepage water originating from an infiltration plot located at the ground surface. During the infiltration test, water was applied at the ground surface directly above the end of the alcove. The infiltration test started on March 9, 1998 (time t = 0), and was conducted in two phases (Liu et al. 2003). Alcove 1 data used in the infiltration test are documented in *In Situ Field Testing of Processes* (BSC 2003a).

Infiltration rates in phase I exhibited a greater degree of temporal variability than those in phase II. During the late stage of phase II, bromide was introduced into the infiltrating water as a tracer. Seepage into the alcove was collected as a function of time, with tracer concentrations obtained by analyzing the seepage water (Liu et al. 2003).

A numerical model was developed to simulate the test using the modeling software TOUGH2 (LBNL 2002). A cylindrical grid was constructed for the model using a dual-continuum approach. Both fracture and matrix were treated as homogeneous continua. The grid extended 45 m in the vertical and 30 m in the radial direction (the diameter was 60 m). The ground surface was approximated as horizontal. The model domain was considered to be large enough, in comparison with size of the alcove and infiltration application area, such that side boundaries had an insignificant effect on flow and transport near the alcove. On the basis of the site data, a square opening representing the alcove was created in the grid 30 to 35.5 m below the ground surface. The grid was regular with 10 cm grid spacing around the alcove and 1 m grid spacing away from the alcove.

The temporally variable inflow rates are imposed on the top boundary, representing the infiltration condition (Figure D-15). The side boundary corresponds to a zero-flow condition in the radial direction. The alcove wall boundary is modeled by a zero-capillary-pressure condition, representing a relative humidity of 100% in the alcove (Birkholzer et al. 1999). The bottom boundary was assigned a constant matrix saturation of 0.61, which is consistent with field observations under ambient conditions (Flint 1998).

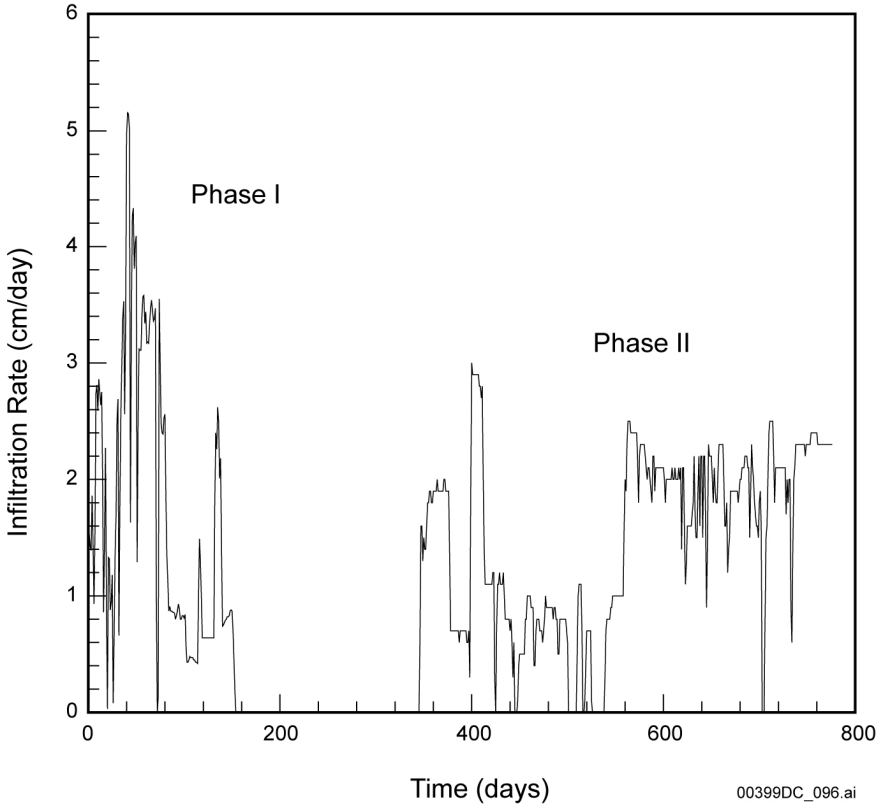

Source: Liu et al. 2003, Figure 1.

Figure D-15. Infiltration Rates Used for the Alcove 1 Infiltration Test

The model was calibrated to the seepage data measured at Alcove 1 during the infiltration test. Calibration results are presented in Table D-11 (Liu et. al. 2003).

Table D-11. Hydrologic Properties for the Fracture and Matrix Continua

Property	Fracture	Matrix
Porosity	Initial Guess: 0.01 First Calibration: 0.028 Second Calibration: 0.03	0.164[a]
Vertical permeability (m^2)	Initial Guess: 2.29×10^{-11} First Calibration: 2.90×10^{-11} Second Calibration: 3.08×10^{-11}	Initial Guess: 1.2×10^{-15} First Calibration: 3.64×10^{-16} Second Calibration: 1.01×10^{-15}
Horizontal permeability (m^2)	Initial Guess: 2.29×10^{-11} First Calibration: 3.14×10^{-11} Second Calibration: 2.99×10^{-11}	Initial Guess: 1.2×10^{-15} First Calibration: 9.35×10^{-16} Second Calibration: 3.42×10^{-16}
α (1/Pa)	Initial Guess: 2.37×10^{-3} First Calibration: 2.07×10^{-3} Second Calibration: 2.34×10^{-3}	Initial Guess: 7.12×10^{-6} First Calibration: 1.84×10^{-5} Second Calibration: 1.90×10^{-5}
m	0.633[a]	0.346[a]
Fracture spacing (m)	0.377[a]	
Residual saturation	0.01[a]	0.06[a]
γ	Initial Guess: 0.15 First Calibration: 0.28 Second Calibration: 0.21	

Source: Liu et al. 2003, Table 1.

NOTE: [a] These properties are fixed during model calibrations.

D.4.3 Comparison of Hydrologic Property Data Calibrated under Different Infiltration Conditions

Model analyses of the field tests corresponding to high infiltration conditions were discussed in previous sections. Several sets of hydrologic property data are obtained from these analyses. The models with high infiltration rates are expected to encompass flow behavior representative of future climates. Rock property sets obtained for high infiltration rates are consistent with those from the calibrated drift-scale model under present-day climate conditions. This indicates that extrapolation of a model calibrated to present-day climate conditions to predict unsaturated flow under future climate conditions is appropriate.

Table D-12 gives average infiltration rates for current and future climate conditions, estimated infiltration rates for fault test and large plot tests at Alcove 8–Niche 3, and the test at Alcove 1. Infiltration rates for the tests are approximately estimated from infiltration plots (Figures D-7, D-12, and D-15) of these tests. The infiltration rates in millimeters per year are calculated by reading infiltration rates in liters per day from infiltration plots and transforming to millimeters per year based on the information of applied area of infiltration water. As shown in the table, the infiltration rates for field tests are all much higher than those for future climate conditions. For example, the highest peak infiltration for the tests is 43,800 mm/yr, which is about 1,500 times the average infiltration rate for the upper bound of the glacial transition period. The highest average infiltration rate (employed in Plot 2 of the Alcove 8 test) is 7,300 mm/yr. This rate is about 250 times the average infiltration rate for the upper bound of the glacial transition period. The use of these tests to represent future climate conditions is conservative.

Table D-12. Infiltration Rate Information

Climate Conditions or Testing Schemes	Peak Infiltration Rate		Average Infiltration Rate	
	L/day	mm/yr	L/day	mm/yr
Present-day mean				4.43
Present-day upper bound				10.74
Present-day lower bound				1.25
Monsoon mean				11.83
Monsoon upper bound				19.23
Monsoon lower bound				4.43
Glacial transition mean				17.02
Glacial transition upper bound				31.69
Glacial transition lower bound				2.35
Fault test at Alcove 8–Niche 3	400	4,000	180	1,800
Plot 1, Large plot test at Alcove 8	65	23,735	6	2,190
Plot 2, Large plot test at Alcove 8	105	38,325	20	7,300
Plot 3, Large plot test at Alcove 8	24	8,700	3	1,095
Plot 4, Large plot test at Alcove 8	16	5,800	1	365
Plot 5, Large plot test at Alcove 8	29	10,585	3	1,095
Plot 6, Large plot test at Alcove 8	17	6,205	0.5	183
Plot 7, Large plot test at Alcove 8	30	10,905	2	730
Plot 8, Large plot test at Alcove 8	30	10,950	4	1,460
Plot 9, Large plot test at Alcove 8	18	6,570	4	1,460
Plot 10, Large plot test at Alcove 8	62	22,630	5	1,825
Plot 11, Large plot test at Alcove 8	120	43,800	8	2,920
Plot 12, Large plot test at Alcove 8	40	14,600	11	4,015
Infiltration test at Alcove 1		18,250		2,190

Source: Average infiltration rates for current and future climates are from *UZ Flow Models and Submodels* (BSC 2003c). Infiltration rates for the tests are estimated from the infiltration plots of the tests, Figures D-7, D-12, and D-15.

D.4.3.1 Comparison for Alcove 8–Niche 3 Test

Table D-13 shows a comparison of calibrated fracture permeability for the unit tsw33, tsw34, and the fault from different infiltration conditions. The three present-day infiltration scenarios give identical fracture permeability for the tsw33 and tsw34 unit. Calibrated results on higher infiltration for tsw33 have a maximum value of 1.23×10^{-12} m^2 and minimum value of 1.314×10^{-14} m^2, with an average of 2.11×10^{-13} m^2. Calibrated results for tsw34 has a maximum value of 4.34×10^{-12} m^2 and minimum value of 1.89×10^{-15} m^2 with an average of 5.69×10^{-13} m^2. Differences between calibration results for tests may be caused by local heterogeneity within geologic units. The corresponding calibrated results from current climate conditions are in the range of the higher infiltration calibration results and close to their average values. As discussed in Section D.4.1.3.2, the parameter uncertainties (standard deviations) for the uncalibrated parameter sets can be directly used for the calibrated parameter sets. From Table D-7, one sees that the standard deviation (uncertainty) for $\log(K_f)$ is 0.61 for tsw33 and 0.47 for tsw34. The differences between averaged $\log(K_f)$ for the tests and results of calibrated drift-scale models are 0.57 and 0.24 for tsw33 and tsw34, respectively. Both are smaller than

their standard deviations. Therefore, calibrated fracture permeabilities for tsw33 and tsw34 from different climate conditions can be considered consistent. The results from drift-scale model calibration are the average value of entire layers at the Yucca Mountain site, and the results from the calibration of infiltration tests represent the value at the specific test location.

Calibrated fault permeability for the TSw unit on present-day mean infiltration and the corresponding results of the two runs of fault test at Alcove 8 are in the same order of magnitude. The average of the two runs is 8.94×10^{-11} m^2. The log(K_f) difference between average value for fault test and calibration result of drift-scale model is 0.55, which is again smaller than the uncertainty (standard deviation) of that unit (1.15, see Table D-7).

Table D-13. Comparison of Calibrated Fracture Permeabilities

Data Sources	Fault (m^2)	tsw33 (m^2)	tsw34 (m^2)
Calibrated on fault test (run 1)	6.67×10^{-11}	8.93×10^{-13}	3.16×10^{-14}
Calibrated on fault test (run 2)	1.12×10^{-10}	1.23×10^{-12}	5.01×10^{-13}
Calibrated on large plot test, plot 1		9.926×10^{-14}	2.25×10^{-12}
Calibrated on large plot test, plot 2		1.685×10^{-13}	7.04×10^{-13}
Calibrated on large plot test, plot 3		2.959×10^{-14}	4.48×10^{-15}
Calibrated on large plot test, plot 4		3.146×10^{-14}	1.71×10^{-14}
Calibrated on large plot test, plot 5		5.569×10^{-14}	3.04×10^{-15}
Calibrated on large plot test, plot 6		1.845×10^{-14}	1.49×10^{-14}
Calibrated on large plot test, plot 7		1.314×10^{-14}	4.34×10^{-12}
Calibrated on large plot test, plot 8		6.757×10^{-14}	6.14×10^{-14}
Calibrated on large plot test, plot 9		2.470×10^{-14}	1.04×10^{-14}
Calibrated on large plot test, plot 10		9.786×10^{-14}	6.16×10^{-15}
Calibrated on large plot test, plot 11		1.864×10^{-13}	1.89×10^{-15}
Calibrated on large plot test, plot 12		3.332×10^{-14}	1.43×10^{-14}
Calibrated on present-day mean infiltration	2.51×10^{-11}	7.8×10^{-13}	3.3×10^{-13}
Calibrated on present-day lower-bound infiltration		7.8×10^{-13}	3.3×10^{-13}
Calibrated on present-day upper-bound infiltration		7.8×10^{-13}	3.3×10^{-13}

Source: Tables D-1, D-2, D-3, D-4, D-8, D-9, and D-10.

The values for the calibrated fracture van Genuchten parameter α from different infiltration conditions are listed in Table D-14. The calibration results from fault tests are close to the results from the calibrated property set on current climate conditions. The results from large plot tests show little deviation from the results of current climates. The log(α_f) differences between average values for large plot test and drift-scale calibrated properties for both units are larger than their corresponding uncertainties provided in Table D-7. This could be caused by the local heterogeneity of the unit; however, they are still in the same order of magnitude. The calibrated results on higher infiltration for tsw33 have a maximum value of 2.19×10^{-3} Pa^{-1} and minimum value of 2.45×10^{-4} Pa^{-1}, with an average of 4.86×10^{-4} Pa^{-1}. Those results for tsw34 have a maximum value of 5.32×10^{-3} Pa^{-1} and minimum value of 2.42×10^{-4} Pa^{-1}, with an average of 1.55×10^{-3} Pa^{-1}. The corresponding calibrated results from current climate conditions are in the range of the higher infiltration calibration results.

Table D-14. Comparison of Calibrated Fracture van Genuchten Parameters α

Data Sources	Fault (Pa^{-1})	tsw33 (Pa^{-1})	tsw34 (Pa^{-1})
Calibrated on fault test (run 1)	1.15×10^{-3}	1.67×10^{-3}	4.59×10^{-4}
Calibrated on fault test (run 2)	1.24×10^{-3}	2.19×10^{-3}	1.09×10^{-3}
Calibrated on large plot test, plot 1		$2.453\ 10^{-4}$	$5.677\ 10^{-4}$
Calibrated on large plot test, plot 2		$2.453\ 10^{-4}$	$1.480\ 10^{-3}$
Calibrated on large plot test, plot 3		$2.453\ 10^{-4}$	$1.152\ 10^{-3}$
Calibrated on large plot test, plot 4		$2.453\ 10^{-4}$	$3.857\ 10^{-3}$
Calibrated on large plot test, plot 5		$2.453\ 10^{-4}$	$8.647\ 10^{-4}$
Calibrated on large plot test, plot 6		$2.453\ 10^{-4}$	$2.932\ 10^{-4}$
Calibrated on large plot test, plot 7		$2.453\ 10^{-4}$	$1.891\ 10^{-3}$
Calibrated on large plot test, plot 8		$2.453\ 10^{-4}$	$3.208\ 10^{-3}$
Calibrated on large plot test, plot 9		$2.453\ 10^{-4}$	$5.316\ 10^{-3}$
Calibrated on large plot test, plot 10		$2.453\ 10^{-4}$	$9.825\ 10^{-4}$
Calibrated on large plot test, plot 11		$2.453\ 10^{-4}$	$3.107\ 10^{-4}$
Calibrated on large plot test, plot 12		$2.453\ 10^{-4}$	$2.424\ 10^{-4}$
Calibrated on present-day mean infiltration	3.16×10^{-4}	1.59×10^{-3}	1.04×10^{-4}
Calibrated on present-day lower-bound infiltration		1.94×10^{-3}	6.55×10^{-4}
Calibrated on present-day upper-bound infiltration		1.58×10^{-3}	1.00×10^{-4}

Source: Tables D-1, D-2, D-3, D-4, D-8, D-9, and D-10.

An examination of Tables D-12, D-13, and D-14 reveals that the calibrated results do not show clear evidence of dependence on the infiltration rates.

D.4.3.2 Comparison for Alcove 1 Test

Table D-15 presents the comparison of calibrated rock properties for the tcw11 unit in which the Alcove 1 infiltration test was conducted. The table shows fracture permeability is almost identical from calibration on higher infiltration and current climate conditions. Other parameters all have quite close values. The differences in log value for matrix permeability, fracture α, and matrix α are 0.57, 0.35, and 0.27, respectively. They are all close to or smaller than their corresponding standard deviations (0.47, 0.58, and 0.24).

Table D-15. Comparison of Calibrated Rock-Property Data for tcw11

Data Sources	Fracture Permeability (m^2)	Matrix Permeability (m^2)	Fracture α (Pa^{-1})	Matrix α (Pa^{-1})
Calibrated on infiltration test at Alcove 1	2.99×10^{-11} (horizontal) 3.08×10^{-11} (vertical)	3.42×10^{-16} (horizontal) 1.01×10^{-15} (vertical)	2.34×10^{-3}	1.90×10^{-5}
Calibrated on present-day mean infiltration	3.0×10^{-11}	3.74×10^{-15}	5.27×10^{-3}	1.01×10^{-5}
Calibrated on present-day lower-bound infiltration	3.0×10^{-11}	3.44×10^{-15}	4.68×10^{-3}	1.16×10^{-5}
Calibrated on present-day upper-bound infiltration	3.0×10^{-11}	3.90×10^{-15}	5.01×10^{-3}	1.23×10^{-5}

Source: Tables D-1, D-2, D-3, and D-11.

D.4.4 A Final Remark on Uncertainty

The uncertainty involved in using a hydrologic property set obtained by calibrating a model on current climate conditions and using that model to forecast flow for future climate conditions results mainly from the uncertainties of the hydrologic property set. The major sources of calibrated parameter uncertainty may include the numerical model uncertainty, infiltration rate uncertainty, scale effects, and field measurement uncertainty. These uncertainties can be propagated to the model for forecasting flow and transport in future climate condition.

Theoretically speaking, the actual hydrologic parameters are not infiltration-rate dependent. They should be the same under different climate conditions. It is reasonable to consider that the rock properties at the unsaturated zone should be the same under current and future climate conditions. Although the future climate is wetter, it is not substantially wetter than the modern climate, and the future infiltration rate is much lower than the infiltration rates used in Alcove 8–Niche 3 tests and Alcove 1 test.

However, uncertainties still remain. These uncertainties could be caused by many sources, as discussed in Section D.4.1.3.1.

The consistency between property sets calibrated under different infiltration indicates that it is appropriate to use calibrated rock properties on present-day climate conditions in the model for predicting future flow and transport condition, based on information provided in previous sections.

D.5 REFERENCES

D.5.1 Documents Cited

Bandurraga, T.M. and Bodvarsson, G.S. 1999. "Calibrating Hydrogeologic Parameters for the 3-D Site-Scale Unsaturated Zone Model of Yucca Mountain, Nevada." *Journal of Contaminant Hydrology, 38*, (1–3), 25–46. New York, New York: Elsevier. TIC: 244160.

Birkholzer, J.; Li, G.; Tsang, C-F.; and Tsang, Y. 1999. "Modeling Studies and Analysis of Seepage into Drifts at Yucca Mountain." *Journal of Contaminant Hydrology, 38*, (1–3), 349–384. New York, New York: Elsevier. TIC: 244160.

BSC (Bechtel SAIC Company) 2001. *In Situ Field Testing of Processes*. ANL-NBS-HS-000005 REV 01. Las Vegas, Nevada: Bechtel SAIC Company. ACC: MOL.20020108.0351.

BSC 2002. *Technical Work Plan for: Performance Assessment Unsaturated Zone*. TWP-NBS-HS-000003 REV 02. Las Vegas, Nevada: Bechtel SAIC Company. ACC: MOL.20030102.0108.

BSC 2003a. *In Situ Field Testing of Processes.* ANL-NBS-HS-000005 REV 02. Las Vegas, Nevada: Bechtel SAIC Company. ACC: DOC.20031208.0001.

BSC 2003b. *Calibrated Properties Model*. MDL-NBS-HS-000003 REV 01. Las Vegas, Nevada: Bechtel SAIC Company. ACC: DOC.20030219.0001.

BSC 2003c. *UZ Flow Models and Submodels*. MDL-NBS-HS-000006 REV 01. Las Vegas, Nevada: Bechtel SAIC Company. ACC: DOC.20030818.0002.

CRWMS M&O (Civilian Radioactive Waste Management System Management and Operating Contractor) 2000. *Conceptual and Numerical Models for UZ Flow and Transport*. MDL-NBS-HS-000005 REV 00. Las Vegas, Nevada: CRWMS M&O. ACC: MOL.19990721.0526.

Finsterle, S. 1999. *ITOUGH2 User's Guide*. LBNL-40040. Berkeley, California: Lawrence Berkeley National Laboratory. TIC: 243018.

Flint, L.E. 1998. *Characterization of Hydrogeologic Units Using Matrix Properties, Yucca Mountain, Nevada*. Water-Resources Investigations Report 97-4243. Denver, Colorado: U.S. Geological Survey. ACC: MOL.19980429.0512.

LBNL (Lawrence Berkeley National Laboratory) 2002. *Software Code: iTOUGH2*. V5.0. SUN UltraSparc., DEC ALPHA, LINUX. 10003-5.0-00.

Liu, H.H.; Bodvarsson, G.S.; and Finsterle, S. 2002. "A Note on Unsaturated Flow in Two-Dimensional Fracture Networks." *Water Resources Research, 38*, (9), 15-1 to 15-9. Washington, D.C.: American Geophysical Union. TIC: 253307.

Liu, H.H.; Doughty, C.; and Bodvarsson, G.S. 1998. "An Active Fracture Model for Unsaturated Flow and Transport in Fractured Rocks." *Water Resources Research, 34*, (10), 2633–2646. Washington, D.C.: American Geophysical Union. TIC: 243012.

Liu, H.H.; Haukwa, C.B.; Ahlers, C.F.; Bodvarsson, G.S.; Flint, A.L.; and Guertal, W.B. 2003. "Modeling Flow and Transport in Unsaturated Fractured Rock: An Evaluation of the Continuum Approach." *Journal of Contaminant Hydrology, 62–63*, 173–188. New York, New York: Elsevier. TIC: 254205.

Neuman, S.P. 1994. "Generalized Scaling of Permeabilities: Validation and Effect of Support Scale." *Geophysical Research Letters, 21*, (5), 349–352. Washington, D.C.: American Geophysical Union. TIC: 240142.

NRC (U.S. Nuclear Regulatory Commission) 2002. *Integrated Issue Resolution Status Report.* NUREG-1762. Washington, D.C.: U.S. Nuclear Regulatory Commission, Office of Nuclear Material Safety and Safeguards. TIC: 253064.

Pruess, K. and Narasimhan, T.N. 1985. "A Practical Method for Modeling Fluid and Heat Flow in Fractured Porous Media." *Society of Petroleum Engineers Journal, 25*, (1), 14–26. Dallas, Texas: Society of Petroleum Engineers. TIC: 221917.

Reamer, C.W. 2001. "U.S. Nuclear Regulatory Commission/U.S. Department of Energy Technical Exchange and Management Meeting on Total System Performance Assessment and Integration (August 6 through 10, 2001)." Letter from C.W. Reamer (NRC) to S. Brocoum (DOE/YMSCO), August 23, 2001, with enclosure. ACC: MOL.20011029.0281.

Schlueter, J.R. 2003. "The U.S. Nuclear Regulatory Commission Review of the U.S. Department of Energy Documents Pertaining to Agreement Unsaturated and Saturated Flow under Isothermal Conditions (USFIC).3.02 (Status: Additional Information Needs) and Agreement Total System Performance Assessment and Integration (TSPAI).3.22 (Status: Additional Information Needs)." Letter from J.R. Schlueter (NRC) to J.D. Ziegler, (DOE), February 26, 2003, 030436305, with attachment. ACC: MOL.20030424.0627.

van Genuchten, M.T. 1980. "A Closed-Form Equation for Predicting the Hydraulic Conductivity of Unsaturated Soils." *Soil Science Society of America Journal, 44*, (5), 892–898. Madison, Wisconsin: Soil Science Society of America. TIC: 217327.

Zhou, Q.; Liu, H-H.; Bodvarsson, G.S.; and Oldenburg, C.M. 2003. "Flow and Transport in Unsaturated Fractured Rock: Effects of Multiscale Heterogeneity of Hydrogeologic Properties." *Journal of Contaminant Hydrology, 60*, (1–2), 1–30. New York, New York: Elsevier. TIC: 253978.

Ziegler, J.D. 2002. "Transmittal of Report Addressing Key Technical Issue (KTI) Agreement Item Total System Performance Assessment and Integration (TSPAI) 3.22." Letter from J.D. Ziegler (DOE) to J.R. Schlueter (NRC), August 29, 2002, with enclosure. ACC: MOL.20021022.0273.

D.5.2 Data, Listed by Data Tracking Number

GS030608312242.005. Surface Infiltration in a Large Plot in Alcove 8 Using Permeameters from November 19, 2002 to March 24, 2003. Submittal date: 06/24/2003.

GS031008312242.007. Surface Infiltration in a Large Plot in Alcove 8 Using Permeameters from August 20, 2002 to November 19, 2002. Submittal date: 10/31/2003.

LB02081DKMGRID.001. 2002 UZ 1-D and 2-D Calibration Grids. Submittal date: 08/26/2002.

LB0306A8N3LIQR.001. Fault Infiltration Test from Alcoves to Niche3 (9/18/2002 10/16/2002). Submittal date: 06/19/2003.

LB0308A8N3SEEP.001. Niche 3 Seepage (10/16/2002-04/02/2003). Submittal date: 08/29/2003.

LB0312A8N3MDLG.001. Pre-Test Prediction Results for Alcove8/Niche 3: Simulations. Submittal date: 12/17/2003.

APPENDIX E

EVALUATION OF UNCERTAINTY IN THERMAL-HYDROLOGIC MODELS (RESPONSE TO TEF 2.12)

Note Regarding the Status of Supporting Technical Information

This document was prepared using the most current information available at the time of its development. This Technical Basis Document and its appendices providing Key Technical Issue Agreement responses that were prepared using preliminary or draft information reflect the status of the Yucca Mountain Project's scientific and design bases at the time of submittal. In some cases this involved the use of draft Analysis and Model Reports (AMRs) and other draft references whose contents may change with time. Information that evolves through subsequent revisions of the AMRs and other references will be reflected in the License Application (LA) as the approved analyses of record at the time of LA submittal. Consequently, the Project will not routinely update either this Technical Basis Document or its Key Technical Issue Agreement appendices to reflect changes in the supporting references prior to submittal of the LA.

APPENDIX E

EVALUATION OF UNCERTAINTY IN THERMAL-HYDROLOGIC MODELS (RESPONSE TO TEF 2.12)

This appendix provides a response for Key Technical Issue (KTI) agreement Thermal Effects on Flow (TEF) 2.12. This agreement relates to providing an evaluation of uncertainty in the thermal-hydrologic models.

E.1 KEY TECHNICAL ISSUE AGREEMENT

E.1.1 TEF 2.12

Agreement TEF 2.12 was reached during the U.S. Nuclear Regulatory Commission (NRC)/U.S. Department of Energy (DOE) Technical Exchange and Management Meeting on Thermal Effects on Flow held January 8 to 9, 2001, in Pleasanton, California (Reamer and Williams 2001). The agreement resulted from the technical discussion of subissue 2, thermal effects on temperature, humidity, saturation, and flux.

At the meeting, the DOE indicated that there was uncertainty in the conceptual thermal-hydrologic models, and stated that this uncertainty was being evaluated using alternative conceptual models such as discrete fracture models, which would be discussed in the Unsaturated Zone Flow and Transport PMR, Rev 00 ICN 02 (Reamer and Williams 2001, p. 8).

Furthermore, the NRC noted that the DOE multiscale thermal-hydrologic model (CRWMS M&O 2000a) used only the drift scale property sets to calculate thermal-hydrologic variables. The NRC was not clear how this captured the variability and uncertainty seen in predictions using other property sets or the uncertainty in comparisons to actual test results (NRC 2002, p. 3.3.6-22). The NRC also noted that, since all thermal tests have been conducted in the tsw34 model-layer, the predicted variability would be greater if the thermal-hydrologic model analyses were performed for the remaining geologic units.

The wording of the agreement is as follows:

TEF 2.12[1]

> Provide the Unsaturated Zone Flow and Transport PMR, Rev. 00, ICN 02, documenting the resolution of issues on page 5 of the OI 8 presentation. The DOE will provide the *Unsaturated Zone Flow and Transport PMR* (TDR-NBS-HS-000002) Rev 00 ICN 02 to the NRC in February 2001. It should be noted, however, that not all of the items listed on page 5 of the DOE's Open Item 8 presentation at this meeting are included in that revision. The DOE will include all the items listed on page 5 of the DOE's Open Item 8 presentation in Revision 02 of the Unsaturated Zone Flow and Transport PMR, scheduled to be available in FY 02.

[1] The DOE Open Item 8 presentation refers to *Thermal Effects on Flow Subissue 2, Open Item 8: Model Uncertainty* (Bodvarsson 2001).

Page 5 of DOE Open Item 8 presentation includes the following:

1. To close this Open Item, DOE needs to evaluate model uncertainty as seen in the results from various alternative conceptual models such as equivalent continuum model, dual permeability model and active fracture model and propagate this uncertainty through the thermal-hydrologic model abstraction

2. Basis for Resolution

   - DOE has considered model uncertainty, including:
   - Types of model uncertainty
   - Flow conceptualization under ambient conditions
   - Flow conceptualization under thermal conditions
   - Fracture flow under ambient and thermal conditions
   - Fracture–matrix interaction model evolution
   - Discrete fracture description
   - Reducing model uncertainty.

This provides the response to TEF 2.12.

E.1.2 Related Key Technical Issue Agreements

Several of the KTI agreements relate to uncertainty with regard to modeling thermal effects on flow.

Agreement TEF 2.12 is related to agreements TEF 2.13 in that TEF 2.13 also involves model uncertainty, although it specifically addresses uncertainties in the continuum representation of fractures and van Genuchten parameterization for flow in fractures. The response to agreement TEF 2.13 is provided in Appendix F.

Agreement TEF 2.12 is related to TEF 2.11 and Total System Performance and Integration (TSPAI) 3.26 that address parameter uncertainty. The NRC discussions of TEF 2.11 also raise concern of the use of drift-scale properties in the multiscale thermal-hydrologic model and gave specific recommendations regarding additional runs. The responses to TEF 2.11 and TSPAI 3.26 are provided in Appendix C.

Agreement TEF 2.12 relates to TEF 2.10. TEF 2.10 concerns the variability and uncertainty in the results of the thermal effects on flow simulations in the abstraction of thermodynamic variables to other models. TEF 2.10 will be addressed in Appendix I of *Technical Basis Document No. 3: Water Seeping into Drifts*.

E.2 RELEVANCE TO REPOSITORY PERFORMANCE

TEF 2.12 is related to the conceptual uncertainty in the thermal-hydrologic models for evaluating mountain-scale and drift-scale thermal conditions at the repository. To support the total system performance assessment for the license application (TSPA-LA), the thermal seepage model and thermal seepage abstraction model are used to evaluate rates of seepage into the emplacement

drifts during the thermal period, and the mountain-scale coupled processes models provide justification that the thermal-hydrologic, thermal-hydrologic-chemical, and thermal-hydrologic-mechanical effects do not need to be explicitly incorporated into the TSPA-LA. Appropriate treatment of the conceptual uncertainty in these models is therefore important to the evaluation of the performance of both the unsaturated zone natural barrier and the engineered barriers.

E.3 RESPONSE

This KTI agreement response addresses model uncertainty and its propagation through thermal-hydrologic model abstraction. In order to address this, model uncertainty in the various process models that treat thermal effects on flow must be considered. These models are:

- *Mountain-Scale Coupled Processes (TH/THC/THM)* (BSC 2003a)–This model provides the framework to test conceptual hypotheses for analyzing mountain-scale hydrologic-chemical-mechanical changes and predict flow behavior in response to heat release. The thermal-hydrologic model captures mountain-scale three-dimensional flow effects, including lateral diversion at the interface of the PTn and TSw hydrogeologic units, and mountain-scale flow patterns. The mountain-scale thermal-hydrologic-chemical model evaluates thermal-hydrologic effects on water and gas chemistry, mineral dissolution and precipitation, and the resulting impact to unsaturated zone hydrologic properties, flow and transport. The thermal-hydrologic-mechanical model addresses changes in permeability due to mechanical and thermal disturbances in stratigraphic units above and below the repository host rock. The mountain-scale thermal-hydrologic-mechanical model focuses on evaluating the changes in three-dimensional unsaturated zone flow fields arising out of thermal stress and rock deformation during and after the thermal periods. The model results are used as the basis for neglecting the site-scale thermal-hydrologic-chemical and thermal-hydrologic-mechanical effects in the TSPA-LA, and for evaluating the effect of drift ventilation on the flow fields.

- *Drift-Scale Coupled Processes (DST and TH Seepage) Models* (BSC 2003b)–The Drift Scale Test is developed and calibrated using the Drift Scale Test data and the thermal-hydrologic seepage model is used for thermal-hydrologic seepage predictions. The drift-scale thermal-hydrologic output is abstracted in *Abstraction of Drift Seepage* (BSC 2003c), which develops an appropriate abstraction methodology for drift seepage, determines the uncertainty and spatial variability of seepage-relevant parameters, provides lookup tables for seepage into either nondegraded or collapsed drifts as a function of these parameters, and evaluates and discusses the impact of additional factors affecting seepage, such as thermal-hydrologic-mechanical and thermal-hydrologic-chemical processes, rock bolts, and igneous events.

The thermal-hydrologic models are fed by other unsaturated zone models for site-scale flow-fields (BSC 2003d), drift-scale flow parameters (BSC 2003e), and lithologic properties (BSC 2003f; BSC 2003g). The seepage calibration model provides the conceptual basis for modeling ambient seepage processes (BSC 2003e, Section 6.3). It also provides estimates of seepage-relevant capillary-strength parameters through calibration of the model against seepage data obtained from in situ liquid-release tests.

The *Multiscale Thermohydrologic Model* (BSC 2003h) evaluates the impact of thermal loading on the in-drift thermal-hydrologic conditions, including temperature, relative humidity and water flow between the rock and drift invert, and provides these conditions to the model of the engineered barrier system. The model provides the duration of boiling and percolation flux at the PTn–TSw, which can be selected by the TSPA-LA for input to the seepage abstraction, and the invert saturation and rock-invert flux to the engineered barrier system radionuclide transport abstraction, which is used in the TSPA-LA. At the time this KTI agreement was made, the multiscale thermohydrologic model was the only model used for drift-scale thermal predictions, and therefore, it was the subject of the discussion in Section E.1.1. Subsequently, the thermal-hydrologic seepage model was developed and is now used for thermal-hydrologic seepage predictions in the TSPA-LA. Therefore, the multiscale thermohydrologic model is not a part of this response.

The aspects of model uncertainty listed in the Open Item 8 presentation (Bodvarsson 2001) and in Section E.1.1 are summarized in the following subsections, with detailed discussions in Section 4 where noted. The NRC concerns noted in the third paragraph of Section E.1.1, regarding evaluation of variability and uncertainty based on tests that were performed in only one geologic unit, are addressed in Sections E.3.7 and E.4.6, which discuss activities to reduce model uncertainty. The last part of Section 3 summarizes the approach to evaluating model uncertainty and propagating it through to thermal-hydrologic abstraction, with detailed discussion in Section E.4.7.

Since the time of the agreement, *Unsaturated Zone Flow and Transport Model Process Model Report* (CRWMS M&O 2000b) has been cancelled, and no further revision is currently planned. However, resolution of the issues pertaining to this KTI are documented in the model reports and analyses described in this response.

The information in this report is responsive to agreement TEF 2.12 made between the DOE and the NRC. The report contains the information that the DOE considers necessary for the NRC to review for closure of this agreement.

E.3.1 Types of Model Uncertainty

The types of model uncertainty considered in the unsaturated zone flow and thermal-hydrologic models are property, parameter, and conceptual model uncertainty. Property and parameter uncertainty is treated in Appendix C of this technical basis document and in Appendix A of *Technical Basis Document No. 3: Water Seeping into Drifts*. While the main focus of this response is model uncertainty, percolation flux distributions, thermal conductivity, and drift-scale capillary strength and permeability distributions are integral to model uncertainty, and are discussed in Section E.4.1.1.

Conceptual model uncertainty refers to the uncertainty in the conceptual models for flow through the hydrogeologic units under ambient and thermal conditions, discussed in the following three subsections and in Section E.4.1.2. Conceptual model uncertainty also includes uncertainty in the representation of fracture and matrix flow and fracture–matrix interaction in the numerical model, which is discussed in Section 4.2.2, Section E.3.5 (fracture–matrix interaction model evolution), and Sections E.3.6 and E.4.5 (discrete fracture description).

E.3.2 Flow Conceptualization under Ambient Conditions

The conceptual model for site-scale flow is described in Section 3.1. An alternative conceptual model for lateral flow through the PTn has been developed and flow fields were simulated to account for major uncertainties in the conceptual model. Section 5.4 notes the uncertainty of focused flow paths in the unsaturated zone, such as the lack of knowledge regarding the detailed spatial distribution of focused flow paths and magnitude of water flux within these flow paths. This is partially accounted for by the use of flow focusing factors in the seepage abstraction (see Section E.4.2). The uncertainty in the effects of perched water on flow fields is not considered in the mountain-scale thermal-hydrologic model because perched water mainly occurs at locations below the repository horizon where boiling conditions are not attained. Flow conceptualization under ambient conditions is further discussed in Section E.4.2.

E.3.3 Flow Conceptualization under Thermal Conditions

Flow conceptualization at the mountain scale is discussed in Sections 3.2.6 and E.4.3. Results of the *Mountain-Scale Coupled Processes (TH/THC/THM) Model* (BSC 2003a) show that (1) the extent of thermal-hydrologic effects on flow away from the repository level depends upon the ventilation scenario; (2) mineral precipitation and dissolution will not significantly affect the hydrologic properties; and (3) thermal-hydrologic-mechanical-induced changes in mountain-scale hydrologic properties have no significant impact on the vertical percolation flux through the repository horizon. Because thermal-hydrologic-chemical effects would tend to increase flow diversion around the drift, neglecting them in the site-scale flow fields used in the TSPA-LA is a reasonable approach. The background for these conclusions is given in Section E.4.3.

The estimates of the input thermal-hydrologic-mechanical properties are deemed sufficient for bounding the possible impact of the thermal-hydrologic-mechanical processes on permeability and percolation flux at the mountain scale (Section 4.4).

Hysteresis in the constitutive relationships for relative permeability and capillary pressure due to drying and rewetting during and following the thermal period is not considered in the thermal-hydrologic models. Hysteresis effects are expected to be small relative to the uncertainty in the capillary pressure and relative permeability relationships (Section E.4.3).

E.3.4 Fracture Flow under Ambient and Thermal Conditions

Uncertainties that arise from representing fracture flow using the continuum approach are evaluated and reduced by comparing model results with field data (Section E.4.6.1) and with simulations using an alternative conceptual model, the discrete fracture model (Sections E.3.5 and E.4.5). The active fracture model is used to account for the reduction in the number of flowing fractures and the fracture–matrix surface area due to fingering flow. The van Genuchten constitutive relationships are applied to multiphase flow in fractures. The application of these models for ambient conditions, and resulting uncertainties, are discussed in Appendix F.

The active fracture model is not modified for thermal conditions to account for different fluid behavior in fractures and the effect of liquid fingering on mass and heat transfer. The thermal-hydrologic seepage model evaluates the alternative conceptual model of episodic finger

flow, which can overcome the capillary and vaporization barriers at the drift wall (Section E.4.6.2).

Several other alternative conceptual models have been suggested as important for fracture flow under thermal conditions (Section E.4.4). Within the condensation zone, fractures at all scales are important because vapor flow is likely to occur through all fractures, in contrast to fingering liquid flow through a fraction of fractures, as described by the active fracture model. Small fractures have not been included in the models but constitute the greatest number of fractures in the Tptpll (Section E.4.6.2). However, the thermal-hydrologic seepage model uses properties derived from air permeability and seepage measurements that implicitly include the effects of the small fractures.

E.3.5 Fracture–Matrix Interaction Model Evolution

Numerical models have evolved to improve the representation of unsaturated zone flow at Yucca Mountain. The first equivalent continuum models that used only one continuum to represent both matrix and fractures were succeeded by the dual continuum models, which treat fractures and matrix as two separate, yet interacting, continua capable of accounting for nonequilibrium flow conditions between fractures and matrix (Section 4.1.1, Figure 4-1). While the continuum approach is a practically reasonable approach for dealing with a large-scale, average unsaturated zone flow process, its usefulness for capturing effects of highly localized (or focused) subgrid-scale flow paths has been questioned (Section 4.5). Discrete fracture-network models of simple geometries are useful for concept evaluation or model-based process studies and were used to show the importance of fracture–matrix interaction (Buscheck and Nitao 1991). However, they are difficult to apply to the complex and large-scale domain of the unsaturated zone of Yucca Mountain (see Section 4.1.1).

The active fracture model improves the dual permeability representation by accounting for liquid flow fingering and the related reduction in fracture–matrix interface area (Section 4.1.3). It has been theoretically shown to be consistent with fractal flow patterns often observed in unsaturated systems. Numerical models based on the active fracture model have also been found to be able to reasonably represent field observations. However, because data and approaches to directly validate the active fracture model are still lacking, TSPA modeling uses a range of active fracture model parameters from three infiltration scenarios to account for uncertainty in the active fracture model. This is discussed in Appendix C of *Technical Basis Document No. 10: Unsaturated Zone Transport*.

E.3.6 Discrete Fracture Description

The discrete fracture model cannot be realistically tested against the site-scale dual permeability flow models because the fracture geometry and property distributions required by the discrete fracture model are unattainable at the mountain scale. However, a comparison of the two approaches has been performed for drift-scale seepage and is described in Appendix D of *Technical Basis Document No. 3: Water Seeping into Drifts*. This comparison demonstrated that the results obtained with either model are consistent, provided that each model is calibrated against seepage-rate data. While the continuum models do not predict the strength of individual

seeps or specific drip locations, the approach is appropriate for predicting average seepage into waste emplacement drifts in a probabilistic framework (Section E.4.5).

E.3.7 Evaluating and Reducing Model Uncertainty

The conceptual model for the flow and thermal-hydrologic models and relevant parameters are evaluated by comparing model predictions with ambient hydrologic and geochemical data, the comparison of alternative conceptual models, and through sensitivity studies (Section E.4.6). Field tests under ambient and heated conditions provide data for evaluating conceptual model uncertainty (Section E.4.6.1). The injection tests at Niche 2 (Section E.1.1) have been superseded by subsequent testing that has produced higher-quality data and have not been used for calibration. Therefore, Niche 2 tests are not discussed in this response.

Field tests under heated conditions create the types of flow processes that will be encountered due to heat release during the decay of radioactive wastes. Measurements from these tests are compared with drift-scale models to reduce uncertainty in the model representation of thermal effects on flow. The Drift Scale Test thermal-hydrologic model compares model predictions to measured data from the thermal Drift Scale Test. The confirmation of the conceptual representation at the drift scale is then used to reduce uncertainty in the mountain-scale thermal-hydrologic model that uses the same conceptual model (Section E.4.6.3). Confidence in the mountain-scale thermal-hydrologic model is improved through corroboration with alternative mathematical models, publication of the model approaches, and testing in refereed professional journals. These activities provide improved confidence in the underlying conceptual models in a qualitative sense, and conservative assumptions are employed (Section E.4.6.3).

An issue of concern is that thermal field tests have been performed in the middle nonlithophysal (Tptpmn) unit and not in the lower lithophysal unit (Tptpll), where the majority of the emplacement drifts will be located. Thermal-hydrologic seepage model sensitivity studies (BSC 2003b, Section 6.2), using properties for both the Tptpll and Tptpmn, showed that the range of thermal-hydrologic conditions expected from the variability of properties is smaller than the range in thermal-hydrologic conditions produced from the variations in thermal loads and percolation rates that were used (Section E.4.6.2).

E.3.8 Model Uncertainty Quantification and Propagation

Model uncertainty and its propagation to the TSPA-LA are addressed in several ways. The uncertainty in the ambient flow fields is propagated from the unsaturated zone flow model to the thermal-hydrologic models through the generation of three infiltration scenarios for the three climate stages and the two PTn conceptual models. Further discussion of the propagation of uncertainty in flow fields among the various models used in the TSPA-LA can be found in Appendix G. The mountain-scale coupled processes model screens the thermal-hydrologic, thermal-hydrologic-chemical, and thermal-hydrologic-mechanical effects on site-scale flow, which can be used as a basis for justifying model simplification in the TSPA-LA. Uncertainty in this model is handled by applying conservative assumptions.

The ambient and heater field tests provide data to compare with the conceptual representation of the numerical models, as described in the previous section.

A systematic process of quantifying model uncertainty and propagating it through to thermal-hydrologic abstraction was performed for the ambient and thermal drift seepage models, and is the subject of Appendix I of *Technical Basis Document No. 3: Water Seeping into Drifts*. Selected aspects of this process are presented in Section E.4.7.

E.4 BASIS FOR THE RESPONSE

E.4.1 Types of Model Uncertainty

E.4.1.1 Property and Parameter Uncertainty

While the main focus of this response is model uncertainty, percolation flux distributions, thermal conductivity, and drift-scale capillary strength and permeability distributions are integral to model uncertainty, and are therefore discussed in this section.

Percolation Flux–The thermal-hydrologic models use the site-scale unsaturated zone flow fields (BSC 2003d) for spatial distribution of percolation flux under ambient conditions, as described in Section 4.5 and listed in Table 4-1. The site-scale model incorporates the entire Yucca Mountain unsaturated zone and the conceptual model described in Section E.4.1.2. The model accounts for the main stratigraphic units using layer-averaged rock properties and represents the major faults. Relevant rock properties of each hydrogeologic unit (for fractures, matrix, and fault zones) have been calibrated against saturation data, water-potential data, pneumatic-pressure data, perched-water data, temperature data, and geochemical data (BSC 2003g, Section 6.2; BSC 2003d, Sections 6.2 through 6.5). The calibrated model is validated by comparing model results with additional data that have not been used for calibration (BSC 2003d, Section 7).

Model predictions are conducted for three different climate stages that are expected to occur during the 20,000-year period considered in the TSPA-LA (USGS 2001a). The first climate stage is a continuation of the current modern-day climate conditions from present day to 600 years into the future (present-day climate). The second climate stage begins at 600 years from present day and is characterized as a monsoon climate with wetter summers than the modern climate. The third climate stage begins at approximately 2,000 years from present day and is characterized as a glacial transition climate with, on average, higher infiltration. The glacial transition climate is predicted to last the remainder of the 20,000-year period.

Uncertainty in climate predictions is accounted for by defining three alternative climate scenarios, referred to as the mean, upper-bound, and lower-bound scenarios (USGS 2001a), within each climate state. The probability of occurrence of each climate scenario is provided (BSC 2003i). This can be used in the TSPA-LA to assign the appropriate weight to the considered site-scale flow field but is not used in the process models. Based on the precipitation rates and temperature predicted for the future climates, distributions of net infiltration have been simulated (USGS 2001b).

The infiltration distributions, available for the three climate stages and the associated mean, upper-bound, and lower-bound scenarios, are used as direct inputs at the upper boundary of the unsaturated zone flow model (BSC 2003d, Section 6.1.3). Steady-state simulation runs are conducted with this model for each climate stage and climate scenario, resulting in a total of nine three-dimensional flow fields that give the spatial distribution of percolation flux (BSC 2003d,

Section 6.1.4). The TSPA-LA uses the steady-state flow fields as being representative over the entire time of the respective climate stage. Therefore, stepwise changes in percolation flux occur at 600 years (transition from present-day to monsoon climate) and at 2,000 years (transition from monsoon to glacial transition climate). Consequently, the values of percolation flux also have a stepwise change at 600 years and at 2,000 years, corresponding to climate changes. The times required for the flow conditions in the unsaturated zone to adjust to the stepwise changes in net infiltration are short compared to the duration of the different climatic stages. Therefore, the steady-state conditions are representative over most of the TSPA-LA time, except for short duration following the stepwise changes at 600 and 2,000 years when the flow field equilibrates. Since climate changes lead to an increase in average percolation, the steady-state representation leads to an overestimation of seepage rates during these equilibration periods.

Seepage abstraction uses the percolation flux distributions across the PTn–TSw boundary to provide input to the seepage lookup table. These fluxes incorporate the important effects of flow dampening and lateral flow diversion in the PTn and are fairly representative of the fluxes at the repository horizon. The effect of flow focusing is estimated with a submodel that has the bottom of the PTn as its upper boundary (BSC 2003c, Section 6.6.4.2).

Thermal Conductivity–The mountain-scale thermal-hydrologic model uses wet and dry thermal conductivity values (BSC 2002a) without a sensitivity or uncertainty analysis (BSC 2003a, Section 6.1.6). For thermal-hydrologic seepage, sensitivity studies show that spatial variability and uncertainty in thermal conductivity can affect the thermal-hydrologic conditions in the rock (BSC 2003b, Section 6.2.4.3).

The Capillary Strength Parameter and Permeability Distributions–The distributions of the capillary strength parameter ($1/\alpha$) and permeability are key for the drift-scale ambient and thermal seepage models (BSC 2003c, Section 6.6). Calibrated $1/\alpha$ values are available from ten test intervals in four different niche or drift locations (BSC 2003c, Section 6.6). The four locations provide broad spatial coverage of the Tptpmn, one of the primary repository units. However, the tests performed in the second main unit, the Tptll, provided limited spatial coverage. Because seepage models derive and apply $1/\alpha$ as an effective process parameter that accounts for a number of additional factors affecting seepage, uncertainty is reduced by having adequate spatial coverage of calibration data from both main repository host rock units. Some of the factors that are accounted for by the effective $1/\alpha$ (drift wall roughness, film flow along the drift surface, drop formation and detachment, artifacts of finite discretization) are largely independent of intermediate- and large-scale rock type variation. Other factors depend on fracture characteristics that are not significantly different for the two main repository host rock units. For example, the possible existence of individual fractures cutting into the opening is mainly governed by the fracture frequency (which is measured for both units) such that an analysis of statistical measures could be conducted without distinguishing between geologic units.

The seepage calibration model (BSC 2003e) and the predictive models for seepage (the seepage model for performance assessment (BSC 2003j) and the thermal-hydrologic seepage model (BSC 2003b)) apply a stochastic continuum conceptualization for fracture permeability in the drift vicinity. The small-scale variability of the continuum permeability (with a resolution of about 1 ft) is implicitly accounted for in these models using lognormal probability distributions

based on air-injection measurements that were performed on the same scale. While the standard deviation of these small-scale permeability distributions, σ_S, can be treated as a constant for abstraction (BSC 2003c, Section 6.4.2), their mean values, μ_S, may vary significantly over the repository rock units. For the TSPA-LA, distributions covering the intermediate-scale variability and the uncertainty of these mean values of small-scale permeability need to be developed. The statistical parameters describing the distribution of intermediate-scale variability are the mean permeability μ and the standard deviation σ (BSC 2003c, Section 6.6.2).

A systematic evaluation of parameter spatial variability and uncertainty for ambient and thermal seepage (drift-scale) was performed in the seepage abstraction (BSC 2003c, Section 7) in terms of measurement, conceptual model and estimation uncertainties. Probability distributions were passed on to the TSPA-LA (Section E.4.7).

E.4.1.2 Conceptual Model Uncertainty

Conceptual model uncertainty includes the uncertainty in the conceptual models for flow through the hydrogeologic units under ambient and thermal conditions (Sections E.4.2 through E.4.4) as well as the uncertainty in the representation of fracture and matrix flow and fracture–matrix interaction in the numerical models (Sections 3.2.1 and 4.1). Conceptual model uncertainty is treated by consideration of alternative conceptual models for flow under ambient and thermal conditions (Section E.4.6.2) and evaluation of a given model's ability to represent field data (Section E.4.6.1).

The site-scale representations of flow through the unsaturated zone, including the unsaturated zone flow model (BSC 2003d) and the mountain-scale thermal-hydrologic model (BSC 2003a) implement the following concepts and approaches: (1) the continuum approach for fracture networks; (2) the dual-permeability model to represent the different flow behavior in fractures and matrix; (3) the active fracture model to account for the reduction in the number of flowing fractures and the fracture–matrix surface area due to fingering (see Section 4.1.3); and (4) the van Genuchten (1980) constitutive relationships for multiphase flow in fractures and the matrix. Uncertainties owing to these representations are addressed at the end of Section 4.5. A comparison with flow simulations through two-dimensional fracture networks shows that the van Genuchten relationships are valid for predicting relative permeability in fractures at low water saturations but underestimate relative permeability through fractures at higher saturations (Liu and Bodvarsson 2001). This implies that the van Genuchten relationships may be valid for modeling water flow in the Yucca Mountain unsaturated zone under the ambient conditions that generally involve very low fracture saturations but may underestimate fracture relative permeability at the higher fracture saturations that are predicted for thermal conditions. The uncertainties arising from the use of the active fracture model and the application of van Genuchten's constitutive relationships for fractures are discussed in Appendix F.

E.4.2 Flow Conceptualization under Ambient Conditions

Flow conceptualization under ambient conditions is the basis for the unsaturated zone flow and ambient seepage models, which feed the thermal-hydrologic models. Therefore, ambient flow conceptualization needs to be considered within the context of thermal-hydrologic model uncertainty.

The conceptual model for site-scale flow is described in Section 3.1 and illustrated in Figures E-1 and 3-4.

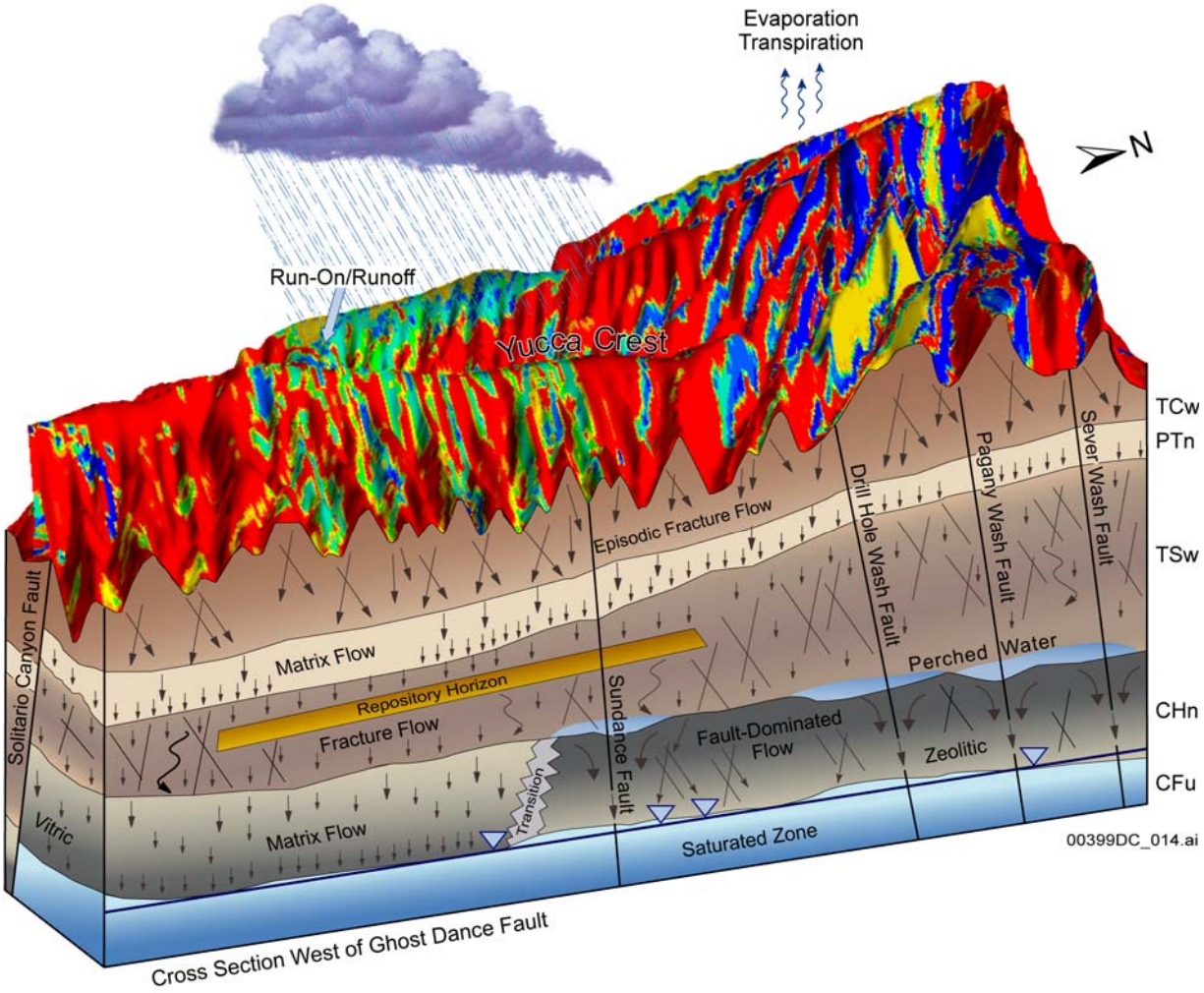

Figure E-1. Overall Water Flow Behavior in the Unsaturated Zone, Including the Relative Importance of Fracture and Matrix Flow Components in the Different Hydrogeologic Units

The main assumptions of the conceptual model can be summarized as follows:

- Percolation processes below the PTn unit are approximately at steady state under ambient conditions.
- Fracture liquid water flow is dominant in the welded units and matrix flow is dominant in nonwelded units.
- Only a small portion of fractures actively conducts liquid water in the unsaturated zone.
- Isolated, transient, and fast flow paths may exist but carry only a small amount of water.
- Fracture–matrix interaction in the welded units is limited.

- The existence of perched water bodies introduces three-dimensional lateral flow within the unsaturated zone.

- Below the repository, flow occurs predominantly in the matrix within the vitric CHn and the major faults are considered to serve as focused flow paths resulting from lateral flow.

In general, percolation flux through the first fractured bedrock unit below alluvial deposits, the Tiva Canyon welded tuff unit, is governed by the imposed distribution of net infiltration. Flow in this unit occurs mostly in the fractures before entering the underlying PTn. With its high matrix porosity and low fracture frequency characteristics and the existence of tilted layers of nonwelded vitric and bedded tuff, the PTn can divert a fraction of the percolating water to intercepting faults and fault zones (Wu et al. 2002; BSC 2003d, Section 6.2.2). The diversion capacity of the PTn unit is very important for the spatial distribution of percolation fluxes in the TSw. However, the characterization of groundwater flow within the PTn is critically dependent on detailed knowledge of the rock properties and the heterogeneity within the PTn unit. *UZ Flow Models and Submodels* (BSC 2003d, Section 6.6) provides two flow fields that represent two different conceptualizations of flow through the PTn. The base-case flow fields allow for lateral flow through the PTn and the alternative flow fields yield considerably less lateral diversion relative to the base case.

The PTn unit has been shown to effectively dampen spatial and temporal variations in percolation flux (Wu et al. 2000, pp. 30 to 32 and pp. 39 to 41), although this assessment has been questioned and is evaluated in Appendix I.

Owing to the potential for lateral flow diversion and dampening of percolation flux variations, the percolation distribution below the PTn unit is considerably different from the distribution of net infiltration, both spatially and temporally. This difference is substantiated by geochemical data obtained at Yucca Mountain (BSC 2003d, Section 6.5). The geologic unit below the PTn is the TSw, a thick, densely fractured unit that hosts the repository. Results from the unsaturated zone flow model indicate that the flux in the TSw is mainly vertical without significant lateral diversion; as a result, the flux distribution at the repository horizon should be similar to that at the PTn–TSw interface (BSC 2003d).

While the average fluxes over the repository area are not affected by the different PTn flow conceptualization (e.g., significant or minimal lateral flow diversion), the maximum flux values are considerably smaller compared to the base-case scenario (BSC 2003c). In simulations with the alternative flow fields, less water is diverted toward fault zones. A Monte Carlo analysis of flux distributions shows that seepage rates are hardly affected by this alternative conceptual model, and it is therefore not considered in the TSPA-LA simulations (BSC 2003c, Section 6.8.2).

The role of perched water bodies (see Section 3.2.5) on three-dimensional lateral flow is another source of uncertainty. The lateral flow may divert the water to fast-flowing faults as shown in Figure 3-8. The conceptual model is supported by various field observations including hydrogeologic and geochemical data from the unsaturated zone. However, data relating to geologic structure, distribution of perched water bodies, and rock hydrologic properties below the repository are inadequate to verify certain conceptual aspects of the flow pattern below the

repository. These aspects include the spatial distribution of focused flow paths, the magnitude of water flux within these flow paths, and the role of major faults (Sections 4.5 and 5.4).

In the framework of seepage abstraction, flow focusing denotes the potential concentration of downward flow in the unsaturated zone onto a particular drift segment (BSC 2003c, Section 6.6). This flow concentration would increase the local percolation flux in some locations, which would then increase the amount of seepage in those locations while at the same time reducing the seepage potential for other drift segments. The potential for flow focusing stems from the scale difference between the unsaturated zone flow model (which provides the three-dimensional distribution of percolation fluxes in the unsaturated zone) and the drift-scale seepage models (which use these percolation fluxes as inflow at the top model boundary). While the site-scale model accounts for variability in net infiltration and explicitly models the different stratigraphic units and faults, it cannot represent the intermediate-scale heterogeneity within geologic units because of the layer-averaged rock properties and the relatively coarse gridding (on the order of about 100 m). Drift-scale seepage models, on the other hand, have a lateral model extent on the order of a few drift diameters; the model domain typically includes the vicinity of one particular drift segment. Consequently, seepage abstraction needs to describe the variability of the percolation flux on the spatial resolution of a few drift diameters. Because the percolation flux distributions provided by the site-scale model do not explicitly describe this spatial detail, they need to be adjusted by multiplication with appropriately distributed flow focusing factors (BSC 2003c, Section 6.6.4.2). The uncertainty in the distribution of the flow focusing factors is accounted for by bounding their values for the TSPA-LA.

At the drift, flow tends to be diverted around the opening because of capillarity. This condition, known as the capillary barrier, arises when coarse-grained soils are overlain by fine-grained soils (Ross 1990; Oldenburg and Pruess 1993). The stronger negative capillary pressure developed in the fine-grained material prevents water from entering the larger pores of the underlying coarse-grained material (Birkholzer et al. 1999). If a drift is conceptualized as very coarse-grained with essentially zero capillarity, seepage into the drift can only occur if the capillary pressure in the rock close to the drift walls becomes zero (i.e., the fractured rock becomes locally saturated). The rock can become locally saturated by disturbance to the flow field, which is caused by the presence of the drift opening (Philip et al. 1989) and more importantly by spatial heterogeneity that promotes channelized flow and local ponding (Birkholzer et al. 1999). The most important parameters that control seepage at ambient temperatures are the amount of percolation flux above the drifts, the local heterogeneity of the fracture flow field, and the capillary strength of the fractures close to the wall (Birkholzer et al. 1999; BSC 2003j, Section 6.3).

E.4.3 Flow Conceptualization under Thermal Conditions

The flow conceptualization under thermal conditions is discussed in Section 3.2.6 and the results of mountain-scale thermal-hydrologic simulations are summarized in Section 4.4. Thermal-hydrologic processes occur at different physical scales, as shown in Figure E-2. During the early part of the heating period, important thermal-hydrologic processes are expected to occur near the emplacement drifts. At this scale, variability in heat output from individual waste packages and different times of waste emplacement may give rise to variability in the extent of dryout, rewetting, and water flux along drifts and at different drift locations. The emplacement

of heat-generating wastes in the repository is likely to alter large-scale flow processes. Heat-driven features at this scale potentially include the development of large-scale, gas phase, buoyant convection cells and thermally altered liquid phase flow fields, both above and below the repository.

The flow conceptualization is summarized as follows:

- Temperature increases will cause pore water to boil and vaporize.
- Most of the generated vapor will move into the fractures and away from the drifts.
- Vapor will condense when it encounters cooler rock, increasing fracture saturation locally.
- A portion of the condensate imbibes into the matrix.
- A portion of the condensate remains in the fractures and may flow back toward the boiling zone and drain by gravity (Figure 3-9).
- Where heat pipe conditions (vapor–liquid counterflow with phase change) form, temperatures remain at the nominal boiling point.
- The flow field will return to steady-state when the heat output decreases and the dryout zones near the drifts are completely resaturated.

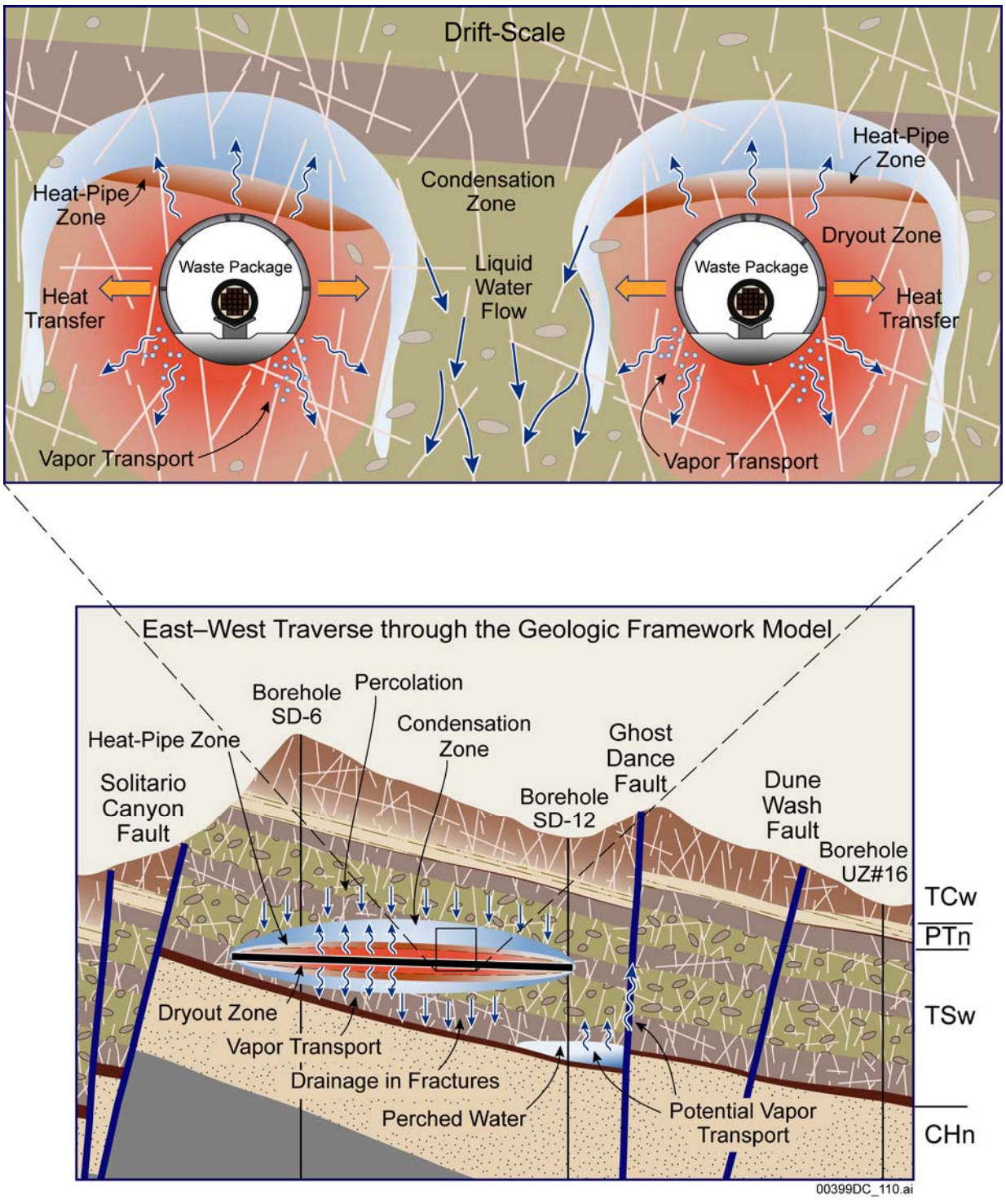

Source: BSC 2003b, Figure 6.1-1; CRWMS M&O 2000b, Figure 3.3-8.

Figure E-2. Thermal-Hydrologic Processes at the Drift Scale and the Mountain Scale

Alternative modes of thermal operation (with and without ventilation) are considered in the mountain-scale thermal-hydrologic model (BSC 2003a) and are reviewed in Section E.4.6.2. The mountain-scale thermal-hydrologic model predicts that repository heating will have, in general, only a limited impact on far-field flow fields with ventilation. Without ventilation, on the other hand, thermally impacted flux zones above the repository grow to as thick as 100 m (BSC 2003a, Section 8.1). While neglecting thermal-hydrologic effects at the mountain scale may introduce uncertainties into the TSPA-LA (Section 5.4), *Abstraction of Drift Seepage* (BSC 2003c, Section 6.4.3.3) showed that thermal seepage is less than ambient seepage; therefore, the neglect will most likely be conservative for the TSPA-LA.

Within the repository footprint, perched water is typically 100 m to 150 m below the repository horizon (Wu et al. 1999). Because the dominant heat-transfer mechanism at these locations is heat conduction and boiling conditions are not attained, the effect of repository thermal load on perched-water bodies is ignored in the mountain-scale thermal-hydrologic model (BSC 2003a).

Results of the site-scale thermal-hydrologic-chemical model (BSC 2003a, Section 6.4) indicate that mineral precipitation and dissolution will not significantly affect the hydrologic properties and percolation flux compared to the effects caused by thermal-hydrologic processes alone. The thermal-hydrologic-chemical processes are summarized in Section 3.2.6. The dissolution of minerals at one point in the fracture network and their redeposition at another could lead to the formation of a precipitate cap over the repository (Figure 3-9). In the precipitate cap, the porosity and permeability of fractures and portions of the matrix near the fractures may be reduced. When thermal perturbation decreases, the cap may begin to dissolve into ambient, downward-percolating water. However, because dissolution occurs at a much slower rate than precipitation, the cap may remain relatively unchanged after thermal perturbation. As a consequence, the porosity and permeability reductions due to the precipitation cap will influence the flow field both during and after the thermal period.

The predicted percolation flux at the repository horizon by the thermal-hydrologic and thermal-hydrologic-chemical mountain-scale models is compared in Figure 4-19. The percolation flux for both models is almost the same, with the only difference occurring at 600 years. At this time, the thermal-hydrologic-chemical model predicts greater flux between the drifts than the thermal-hydrologic model, indicating that the precipitate cap causes an increase in flow diversion around the drifts. Since neglecting thermal-hydrologic-chemical effects is therefore a conservative assumption, thermal-hydrologic-chemical effects are not incorporated in the TSPA-LA.

With regard to thermal-hydrologic-mechanical effects (where potential changes in hydrologic properties are based upon conservative estimates of input thermal-hydrologic-mechanical properties), thermal-hydrologic-mechanical–induced changes in mountain-scale hydrologic properties are shown to have no significant impact on the vertical percolation flux through the repository horizon (see Figure 4-19). The estimates of the coupled thermal-hydrologic-mechanical material properties include a thermal expansion coefficient that leads to the maximum possible thermal stress and a stress-versus-permeability function that leads to maximum-possible permeability change. The mechanical rock-mass properties used for the mountain-scale thermal-hydrologic-mechanical model are from the *Drift-Scale THM Model* (BSC 2003k, Section 4.1.1.1), used in conjunction with a scale dependency for applying these

properties at the mountain scale (BSC 2003a, Section 6.5.8). The estimates of the input thermal-hydrologic-mechanical properties are deemed sufficient for bounding the possible impact of the thermal-hydrologic-mechanical processes on permeability and percolation flux at the mountain scale (see Section 4.4).

Hysteresis effects will accompany drying (drainage) and rewetting (imbibition) processes during and following the thermal pulse. This leads to different curves of relative permeability and capillary pressures for describing drainage and imbibing processes, respectively. In the thermal-hydrologic models, hysteresis effects are ignored because they are expected to be small compared to the uncertainty inherent to the development of the capillary pressure and relative permeability relationships (BSC 2003a, Section 6.1.6).

As noted in Section 4.4, thermal loading at the repository has a significant impact on percolation fluxes near repository drifts for times less than 1,000 years. Thermal seepage refers to seepage during the time that the flow around drifts is perturbed from heating. This effect is particularly important for above-boiling temperature conditions where a large, hot, dryout region develops in the vicinity of a drift. This hot dryout zone (the vaporization barrier) provides an additional barrier preventing seepage since percolating water can be entirely vaporized prior to reaching the drift wall. Owing to the vaporization barrier, thermal seepage is unlikely as long as boiling conditions exist.

On the other hand, condensed water forms a zone of elevated water saturation above the rock dryout zone. Water from this zone may be mobilized to flow rapidly down toward the drift, possibly promoting seepage. The combined effect of thermal-hydrologic perturbation, vaporization barrier, and capillary barrier formation is investigated with a series of sensitivity studies using the thermal-hydrologic-seepage model (BSC 2003b), described in Section E.4.6.2.

E.4.4 Fracture Flow under Ambient and Thermal Conditions

Under ambient conditions, fracture flow dominates in the welded units. The selection of the approach to numerical representation of fraction flow is reviewed in Section 4.1.1. Due to the large number of fractures, flow can be represented by the continuum approach. Its evaluation compared to the discrete fracture model is discussed in Section E.4.5. The active fracture model is employed to account for the fact that unsaturated flow may be restricted to a limited number of (active) fractures and that flow within a fracture is likely to be channelized (Liu et al. 1998, p. 2636) (see Section 4.1.3). Both effects may effectively reduce fracture–matrix interaction and thus have to be considered in thermal-hydrologic simulations where strong vapor and condensate transfer is expected between the fractures and the matrix. The van Genuchten (1980) constitutive relationships developed for two-phase flow in porous media are applied to multiphase flow in fractures. Both the active fracture model and the use of van Genuchten relationships give rise to uncertainties, which are discussed in Appendix F.

The active-fracture model is not employed in the ambient seepage models (the seepage calibration model and the seepage model for performance assessment) because: (1) flow channeling within fractures is already accounted for through explicit modeling of small-scale heterogeneity; (2) the correction of the fracture–matrix interface area (the main effect captured by the active fracture model) is not significant for ambient seepage; and (3) the potential impact

of active-fracture model effects on seepage is automatically reflected in the calibrated capillary-strength parameter (BSC 2003c, Section 6.4.3.1).

In contrast to the ambient seepage models, where only the fracture continuum is represented for ambient conditions, the contribution of the rock matrix cannot be neglected in thermal-hydrologic simulations. The fractured rock is therefore treated as a dual-permeability domain, accounting for the fractures and the rock matrix as two separate, overlapping continua (Doughty 1999).

Under thermal conditions, vaporized pore water is transported through the fractures. Some portion of the condensate also will remain in the fractures, become mobile, and may flow back toward the boiling zone. The stronger the vapor flux away from the drifts and the reflux toward the drifts, the more obvious the heat pipe conditions (vapor–liquid counterflow with phase change) with its characteristic signature in the temperature field. Where heat pipe conditions exist, the temperature will remain at the nominal boiling point. During the thermal period, a substantial amount of gravity-driven condensate is expected to drain between waste emplacement drifts (Figure 3-9). Eventually, the heat output will decrease and become small enough so as not to affect the liquid flow field, and the flow field will return to steady state. The thermal-hydrologic seepage model evaluates the alternative conceptual model of episodic finger flow that can overcome the capillary and vaporization barriers at the drift wall during the thermal period. This evaluation is discussed in Section E.4.6.2.

In simulating the flow of vaporized pore water through fractures, it may not be appropriate to limit the number of fractures and the fracture–matrix interfacial area, as done by the active fracture model. It was suggested that all the fractures at all scales in the near-drift environment are important within the condensation zone (Hinds et al. 2003). In contrast to the fingering flow of liquid, vapor flow is likely to occur through all fractures. Using all fractures in drift-scale thermal-hydrologic models was not considered as an alternative conceptual model to the use of the active-fracture model. Small fractures (less than 1 m long) constitute the greatest number of fractures in the Tptpll and could significantly affect thermal seepage (Hinds et al. 2003). Small fractures have been mapped in 12 areas in the Enhanced Characterization of Repository Block Cross-Drift (DTN: GS040108314224.001). Although the small fracture data have not been explicitly used in the flow models, the thermal-hydrologic seepage model uses air permeability and seepage measurements that implicitly incorporate the effects of the small fractures (BSC 2003b, Section 4.1.1).

As discussed in Section 4.2.2, unsaturated zone flow models under thermally perturbed conditions use the van Genuchten relationships. Liu and Bodvarsson (2001) reported that van Genuchten relationships underestimate fracture-relative permeability for a range of relatively high water saturations and argued that an improved relationship model may be needed for fractures under thermally disturbed conditions (see Section 4.5). This issue is addressed in Appendix F.

E.4.5 Discrete Fracture Description

The dual-continuum conceptualization provides an appropriate representation of the unsaturated zone processes within the unsaturated zone at Yucca Mountain (Doughty 1999). It is much less

demanding in computational effort or data requirements than the discrete-fracture modeling approach. A comparison of the two approaches is described in Appendix D of *Technical Basis Document No. 3: Water Seeping into Drifts*. This analysis demonstrated that the results obtained with either model are consistent, provided that each model is calibrated against seepage data (see Section D.4.2.2 of *Technical Basis Document No. 3: Water Seeping into Drifts*). While the seepage models do not predict the strength of individual seeps or specific drip locations, the continuum approach is appropriate for predicting average seepage into waste emplacement drifts in a probabilistic framework, specifically:

- A continuum model and a discrete fracture network model (Finsterle 2000; BSC 2003e) yield consistent predictions of seepage threshold and seepage rates if calibrated against data from liquid-release tests (see Section D.4.2.2 of *Technical Basis Document No. 3: Water Seeping into Drifts*).

- A two-dimensional discrete fracture network model (Liu et al. 2002; BSC 2003e) resulted in insignificant flow diversion (i.e., no capillary barrier effect exists for discrete, two-dimensional systems that neglect in-plane flow diversion) (see Section D.4.2.3 of *Technical Basis Document No. 3: Water Seeping into Drifts*).

- Alternative conceptual models (such as a discrete fracture network model) require detailed, currently unavailable characterization data. More importantly, these alternative models are based on additional model assumptions that are difficult to justify and require a calibration step similar to that needed for the continuum approach (see Section D.4.2.4 of *Technical Basis Document No. 3: Water Seeping into Drifts*).

Use of the discrete fracture or weeps-type model (Cacas et al. 1990; Dverstorp and Andersson 1989) as an alternative is limited by: (1) large uncertainties in the distribution of fractures within the mountain; (2) the need for many (unvalidated) submodels that relate the geometric information from fracture-network maps to hydrologic flow parameters; and (3) an extensive computational burden to simulate the behavior of the discrete fracture system. On the other hand, the dual-continuum approach, although computationally the most efficient, may not capture important nonequilibrium fracture–matrix thermal-hydrologic processes under thermal loading conditions (BSC 2003a, Section 6.1.2). While the continuum approach is a practically reasonable approach for dealing with a large-scale, average unsaturated zone flow process (which is generally supported by the previous studies) (see Section 4.2.2), its ability to quantify the effects of highly localized (or focused), subgrid-scale flow paths has been questioned (see Section 4.5).

E.4.6 Evaluating and Reducing Model Uncertainty

Model uncertainty is evaluated and reduced through the comparison of model predictions with ambient hydrologic and geochemical data (Section 3.1), the comparison of alternative conceptual models, and through sensitivity studies. This section reviews some of the model testing that was performed with data from ambient and thermal field tests showing specific tests for the unsaturated zone flow model and the drift-scale thermal models (Drift Scale Test, thermal-hydrologic, and thermal-hydrologic seepage). Sensitivity studies and alternative conceptual models are then summarized for the drift-scale thermal models, including the

evaluation of the impact of property differences among the two major host rock units on thermal seepage, followed by the mountain-scale thermal-hydrologic model. Finally, the approach to reducing uncertainty for the mountain-scale thermal-hydrologic model is described.

E.4.6.1 Model Comparison with Field Test Data

E.4.6.1.1 Ambient Tests

Ambient field testing is described in *In Situ Field Testing of Processes* (BSC 2003l).

Seepage Tests–Seepage tests are described in Appendices B and C of *Technical Basis Document No. 3: Water Seeping into Drifts*. A brief summary is also provided in Section 4.3. Multiple liquid-release tests were performed in the niches of the Exploratory Studies Facility and along the Enhanced Characterization of the Repository Block Cross-Drift to observe, document, and quantify any water migrating to and seeping into the underground openings. The tests were performed by sealing a short section of the borehole above the opening using an inflatable packer system and then releasing water at a specified rate into the test interval. Any water that migrated from the borehole to the ceiling and dripped into the opening was captured and measured.

Qualitative observations during the tests helped provide an understanding and corroboration of flow diversion and seepage concepts. The effectiveness of the capillary barrier and the presence of a seepage threshold can be directly observed from liquid-release tests conducted at different rates, which show that seepage ceases at a nonzero injection rate (referred to as a seepage threshold).

Moreover, a quantitative analysis of the seepage-rate data provided calibrated values of seepage-relevant formation parameters. Spatial variability in the estimated capillary-strength parameter $1/\alpha$ is relatively large compared to the estimation uncertainty at a given location. The main contribution to the estimation uncertainty is small-scale heterogeneity that can only be described stochastically. Random fluctuations in seepage rate data lead to insignificant uncertainty in the parameter estimates.

Alcove 8–Niche 3 Test–The liquid release tests performed in Alcove 8–Niche 3 are mentioned in Section 2.4.4, with a schematic of the test location in Figure 2-12. The verification of the unsaturated zone flow model with these data is described in *UZ Flow Models and Submodels* (BSC 2003d, Section 7).

A numerical model was developed for the test site to compare the simulation results with the field observations. The model accounted for the flow of liquid water into the fault that intersected the floor of the alcove and then into fractured networks connected to the fault. Matrix imbibition occurring at the interfaces between fractures and the matrix and between the fault and the matrix was modeled. The capillary barrier effect to divert a portion of water around the niche opening was also accounted for. Tracer transport time was determined by fracture porosity, fault aperture, and the matrix imbibition process.

Figure E-3 shows a comparison between seepage-rate data and the simulation result from a model calibration (run 1) without considering the water-transport-velocity data. In this calibration run, fracture porosity and fault aperture were not varied. A fairly good match to the

observed seepage data was obtained (see Figure E-3); however, water transport velocity is significantly overestimated (see Figure E-4). These results imply that seepage rate as a function of time may be mainly controlled by rock properties near seepage locations, owing to the capillary barrier effect (Liu et al. 2002, Section 3.3), and those rock properties are correctly represented in the model. On the other hand, water transport velocities are determined by rock properties farther away from the niche wall (BSC 2003d, Section 7), which implies that the overestimation of velocities is a result of incorrect representation of the fracture and fault geometry and properties farther away from the niche wall.

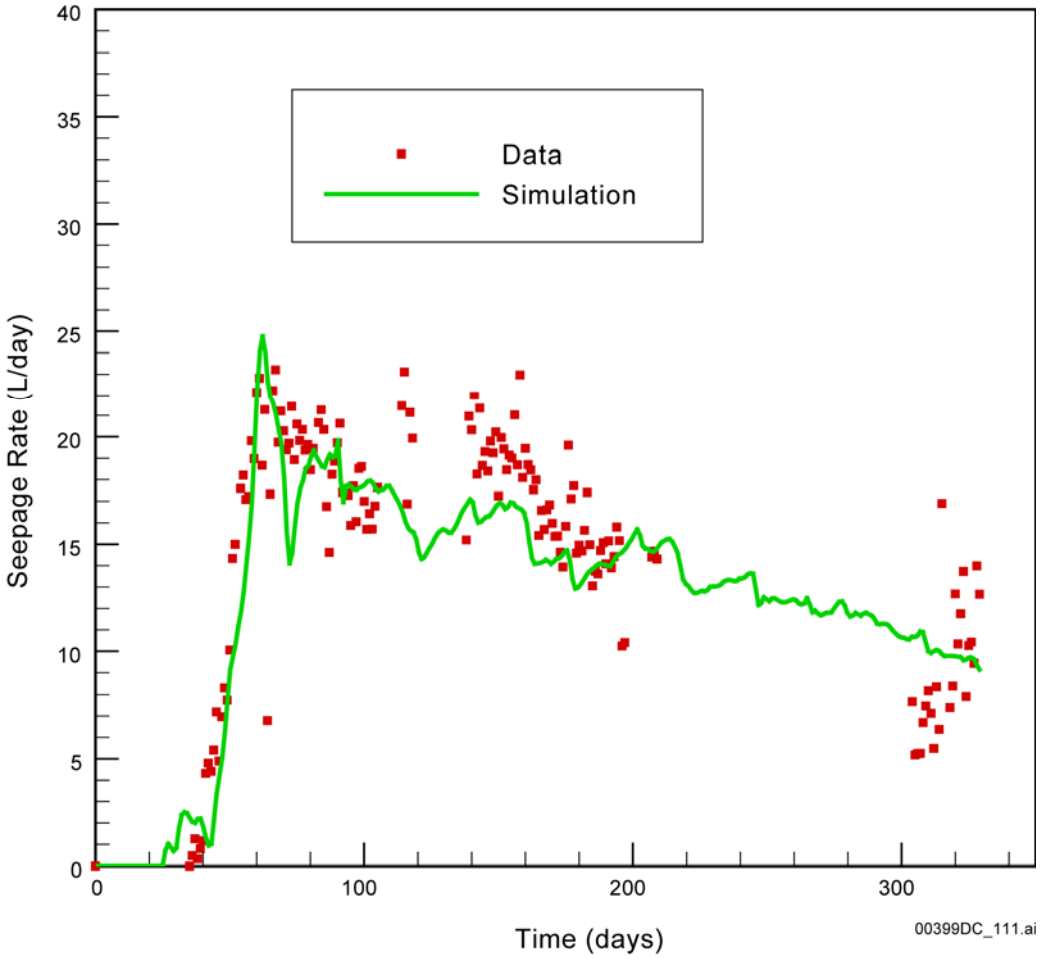

Source: BSC 2003d, Figure 7.6-6.

Figure E-3. A Comparison between Simulated Seepage Rates as a Function of Time (Run 1) and Field Observations

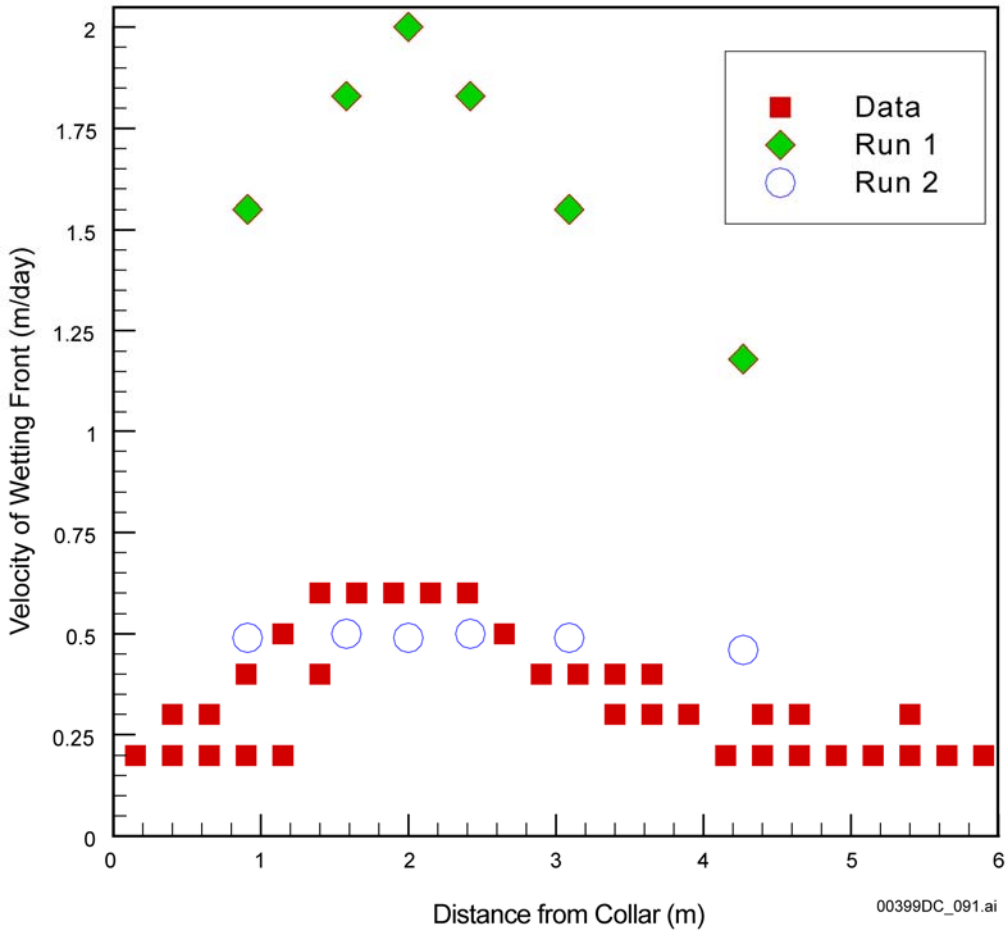

Source: BSC 2003d, Figure 7.6-7.

Figure E-4. A Comparison among Calculated Water Travel Velocities from Two Calibration Runs and the Velocity Data Observed from the Fault Test

A second calibration (run 2) accounted for the effect of rock properties away from the niche wall by allowing both fault aperture and fracture porosity to be varied. The values that produced the best fit to the data are physically realistic and consistent with other field measurements in the same unit (BSC 2003d).

E.4.6.1.2 Heater Tests

Three heater tests have been conducted at Yucca Mountain: the Single Heater Test, the Drift Scale Test, and the Large Block Test. All three are located in the middle nonlithophysal unit, Tptpmn (tsw34).

Of these three tests, the Drift Scale Test is the best suited for validation against measured data because its geometric setup and scale are similar to the proposed design of waste emplacement drifts. The Single Heater and Large Block Tests are of a smaller scale and have geometry different from that of waste emplacement drifts. The coupled thermal-hydrologic processes observed in the Single Heater and Large Block Tests have been successfully simulated with conceptual approaches similar to the one described later in this section for *Drift-Scale Coupled*

Processes (DST and TH Seepage) Models (BSC 2003b). Modeling of the Single Heater Test (BSC 2001a; Tsang and Birkholzer 1999) and the Large Block Test (Lin et al. 2001; Mukhopadhyay and Tsang 2002) has been documented.

The Drift Scale Test is the largest (and longest) in situ heater test of its kind. The heating phase of the Drift Scale Test lasted for slightly more than four years with a large volume of rock heated to temperatures close to and above boiling. The test is described in Section 2.4.3 and shown schematically in Figure 2-11, with a plan view in Figure E-5. At the center of the Drift Scale Test is the heated drift, which is 47.5 m long and 5.0 m wide. The heated drift has nine waste-package-sized heat sources. Emanating from either side of the heated drift are 50 horizontal boreholes (25 on each side) containing wing heaters that provide additional heating to simulate (in an accelerated fashion) the influence of heating from neighboring emplacement drifts. The hot side of the heated drift is separated from the cold side with a thermally insulated bulkhead.

The thermal load from these two kinds of heat sources (simulated waste packages and wing heaters) is designed to induce thermal-hydrologic coupled processes, such as vaporization, vapor transport, drying, and condensation, for the duration of the test. These same processes will also occur in the repository but will continue to operate for centuries after emplacement. Data from the Drift Scale Test provide a representation of the likely thermal-hydrologic, thermal-hydrologic-mechanical, and thermal-hydrologic-chemical processes that will be encountered in the near field of the emplacement drifts.

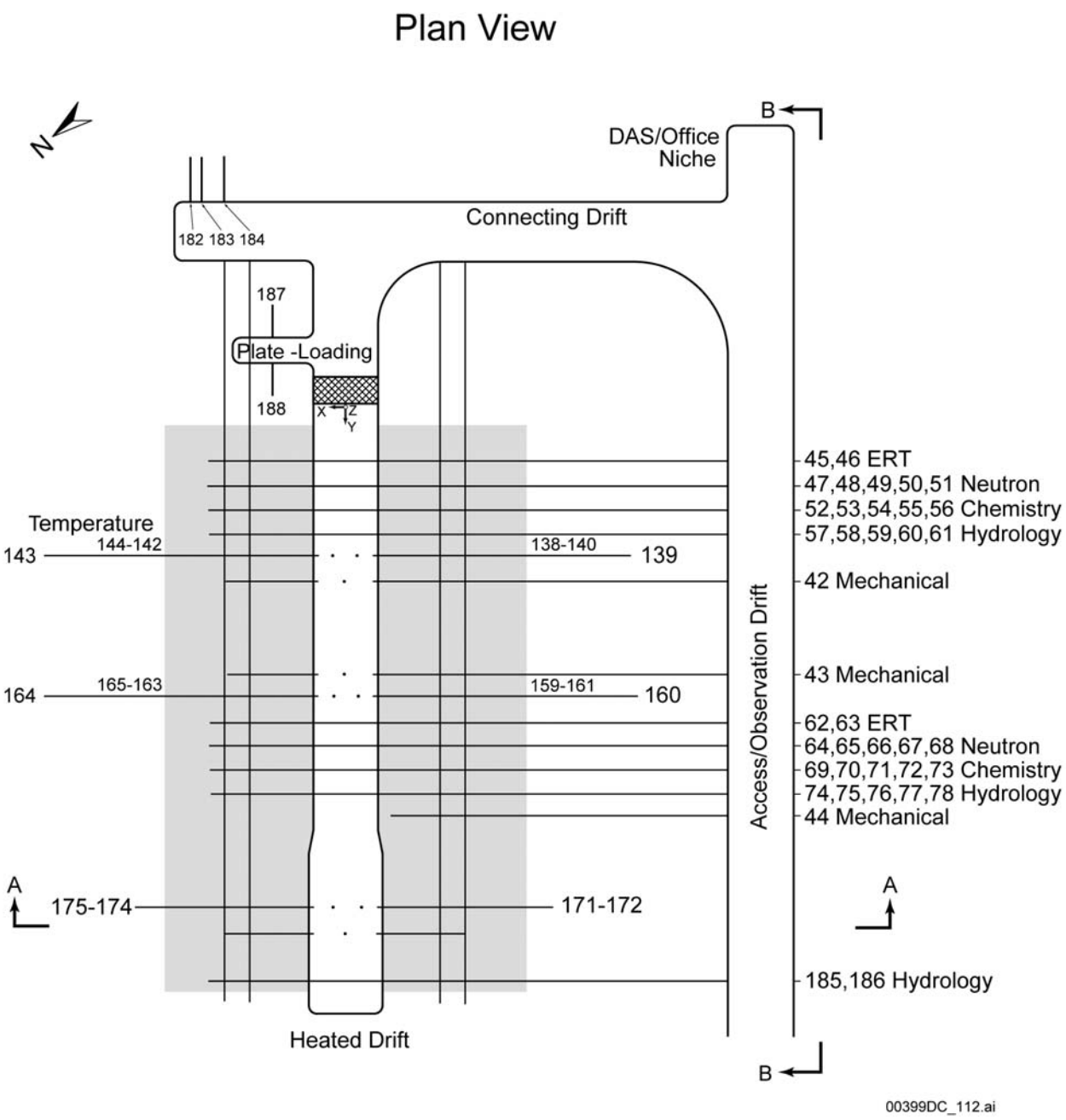

Source: BSC 2003b, Figure 7.2.1-1.

Figure E-5. Plan View of the Drift Scale Test Area

Confidence in the mountain-scale thermal-hydrologic, thermal-hydrologic-chemical, and thermal-hydrologic-mechanical models relies on the validation of the corresponding drift-scale models because no direct experimental measurements exist at the mountain scale (BSC 2002b, Section I.3.1). The same processes occurring at the mountain scale have been modeled at smaller spatial and time scales (BSC 2003b). Through a detailed comparison of measured and simulated thermal-hydrologic, thermal-hydrologic-mechanical, and thermal-hydrologic-chemical drift-scale data, it was concluded that the physical processes were adequately represented by the

model (BSC 2003b, Section 8.2). This builds confidence in the mountain-scale coupled-processes models since the underlying flow and heat-transfer processes are similar both on the drift-scale and on the mountain-scale. However, the thermal tests (including the Drift Scale Test) provide only limited data for calibration and validation of the numerical models. The small spatial and temporal scales limit validation of the mountain-scale models. The validation is also limited by the uncertainties arising from parameter estimates in a geologically complex system and the upscaling of drift-scale results to the mountain scale. Uncertainty in the mountain-scale coupled-processes models is reduced by the conceptual and mathematical validity of the models, by means of their application to other thermal-hydrologic applications and publication of results in the open scientific literature (Section E.4.6.3).

E.4.6.1.3 Drift Scale Test Thermal-Hydrologic and Thermal-Hydrologic Seepage Models

The Drift Scale Test thermal-hydrologic model is the numerical model used to compare model predictions to measured data from the Drift Scale Test. By the agreement of model predictions with measurements, confidence is gained that similar models deploying these same processes and incorporating the repository conditions and time scales can help to address questions important to repository performance. The Drift Scale Test thermal-hydrologic model is at the same scale (drift scale) and uses the same conceptual model as the thermal-hydrologic seepage model. Therefore, if the Drift Scale Test thermal-hydrologic model is validated by comparison with data, the predictive thermal-hydrologic seepage model can also be considered validated with respect to thermal-hydrologic behavior of the fractured rock in the vicinity of emplacement drifts (Birkholzer and Tsang 2000).

Measurements of temperature, gas pressure, and water saturation from the first six months of heating were used to discriminate between alternative modeling concepts applied in pretest simulations. It became apparent, for example, that the dual-permeability method describes fracture–matrix interaction much better than the effective-continuum model (BSC 2003b, Section 7.3.1).

In the assessment of the Drift Scale Test model results, heat pipe signals have been analyzed for all boreholes equipped with temperature sensors. On average, the extent and location of these thermal-hydrologic coupling signals is well represented in the temperature profiles though the measured data show more spatial variability. In short, there is good qualitative agreement between measured and simulated temperatures, even in the subtle signals that indicate thermal-hydrologic coupling.

The model validation included quantitative evaluation of continuously measured temperature data with a detailed analysis of subtle temperature signals indicative of thermal-hydrologic coupling as well as qualitative evaluation of periodic measurements that monitored moisture redistribution processes using geophysical methods, air-injection data, and withdrawal of liquid water in packed-off boreholes.

In comparing the matrix saturation predicted by the Drift Scale Test thermal-hydrologic model against measured ground penetrating radar tomography data, the goal is to demonstrate that the Drift Scale Test thermal-hydrologic model captures the essential elements of the coupled

thermal-hydrologic processes expected to occur in the rock matrix. Because of the qualitative nature of measured geophysical data, the comparison between measured and simulated matrix saturation is also qualitative. However, matching the patterns and time evolution of simulated and measured dryout and the condensation zone does provide effective validation for the model's representation of the dominant thermal-hydrologic processes.

Both the air-permeability results and the analysis of water collection data provide confidence in the model's capability to accurately represent the coupled thermal-hydrologic processes. Though the predicted fracture saturation from the Drift Scale Test thermal-hydrologic model is not always consistent with the pattern of measured air permeability changes, the differences can be explained by thermal-hydrologic-mechanical effects that are not incorporated in the model. Assuming that the general location of seepage into boreholes should coincide with regions of elevated fracture saturation, the water collection data is used to analyze whether the simulated trends in fracture saturation are accurate. The calculated fracture saturation evolution compares favorably with water collection in several hydrology boreholes (BSC 2003b, Section 7.4.3.3).

The thermal load in the Drift Scale Test gives rise to vigorous boiling and subsequent water condensation with rock temperature exceeding 200°C. With such intense thermal-hydrologic processes occurring, the Drift Scale Test data provide the base for an excellent model validation with respect to the near-field thermal-hydrologic conditions in the rock mass, as described by temperature and saturation changes. With respect to the vaporization barrier, however, the Drift Scale Test data are not sufficient for validation. No seepage of liquid water was observed in the heated drift of the Drift Scale Test. The vaporization barrier generated by the heater output appears to be effective in the Drift Scale Test because of the intense thermal load. However, heat load designed for the repository is less intense (thus giving rise to maximum temperatures lower than in the Drift Scale Test) and will be applied over much longer time frames.

In addition to the more intense thermal loading in the Drift Scale Test, vapor losses through the bulkhead of the heated drift (BSC 2003b, Section 7.3.4) imply that the Drift Scale Test results should not be used as direct evidence for no seepage. The issue of heat and mass losses through the bulkhead was discussed and evaluated in several thermal workshops. It was concluded that the objectives of the Drift Scale Test (acquiring a more in-depth understanding of the coupled thermal-hydrologic processes and validating the conceptual models in comparison with data) were being met despite these heat and mass losses. However, it was also understood that the measurements in the Drift Scale Test should not be directly used to evaluate the potential of seepage into drifts during the thermal period because the potential of seepage in the Drift Scale Test might be reduced as a result of the vapor losses. The Drift Scale Test results therefore provide demonstration of the potential performance of the repository under a hot thermal operating mode but offer no seepage data (observed seepage rates and seepage fractions) that can be used for thermal-seepage validation purposes.

As a result of these limitations, validation of the seepage part of the thermal-hydrologic seepage model is indirect, based on a separate assessment of the two relevant barriers. Validation of the coupled thermal-hydrologic processes (using the Drift Scale Test data and data from other in situ tests) provides confidence regarding the predicted effectiveness of the vaporization barrier, while validation of the ambient-seepage conceptual model (using liquid-release data) provides confidence regarding the predicted effectiveness of the capillary barrier. (The conceptual

framework for the capillary barrier treatment in the thermal-hydrologic seepage model can already be considered validated because the conceptual model is identical to the one validated and successfully applied in the seepage calibration model (BSC 2003c, Section 6.4.3.2). However, some uncertainty remains since no direct test data on thermal seepage at extreme flux conditions are available.

To gain additional confidence, an alternative conceptual model was introduced in *Drift-Scale Coupled Processes (DST and TH Seepage) Models* (BSC 2003b, Section 6.3) that accounts for episodic fingering flow through the vaporization barrier. The alternative model is described in Section E.4.6.2. The alternative conceptualization of unsaturated fracture flow confirms the assessment of the vaporization barrier from the thermal-hydrologic seepage model.

Since there is no thermal test in the lower lithophysal unit at Yucca Mountain, validation of the thermal-hydrologic seepage model does not include direct comparison with measured data from the Tptpll. The agreement of the model predictions and data from the Tptpmn provides confidence that the thermal-hydrologic effects of heating are well captured by the model. This means that application to the Tptpll unit is appropriate because essentially the same thermal-hydrologic processes need to be described.

E.4.6.2 Sensitivity Studies and Evaluation of Alternative Conceptual Models

E.4.6.2.1 The Drift Scale Test Thermal-Hydrologic and Thermal-Hydrologic Seepage Models: Sensitivity Studies

The sensitivity analyses performed with the thermal-hydrologic seepage model comprise a variety of simulation cases in order to cover the potential variability of seepage-affecting factors and to evaluate related sensitivities (BSC 2003b, Section 6.2). These cases include the following:

- Two repository host rock units
- Four different thermal operating modes
- Various infiltration scenarios including the effect of climate changes and flow focusing
- Variation of drift-scale rock properties
- Homogeneous versus heterogeneous host rock properties
- Variation of drift wall boundary conditions
- A dual-permeability model with and without the active fracture model
- Transient thermal representation versus steady-state ambient representation.

The different simulation cases studied with the thermal-hydrologic seepage model show considerable variability with respect to the thermal-hydrologic conditions in the rock. Despite this variability, there were several important observations with respect to thermal seepage that are common to all cases (BSC 2003b, Sections 6.2.4 and 8.1):

- Thermal seepage was never observed in simulation runs where the respective ambient seepage was zero.

- Thermal seepage never occurred during the period of above-boiling temperatures in the rock close to the emplacement drifts.

- In simulation cases where ambient seepage was obtained, thermal seepage was initiated at several hundred to a few thousand years after the rock temperature has returned to below boiling.

- Thermal-seepage rates were always smaller than the respective ambient reference values. The ambient seepage values provide an asymptotic upper limit for thermal seepage.

While these conclusions hold for all simulation cases, considerable variability exists among simulation runs with respect to the thermal-seepage initiation time, the evolution of seepage with time, and the long-term rate of thermal seepage. From the quantitative and qualitative results presented in *Drift-Scale Coupled Processes (DST and TH Seepage) Models* (BSC 2003b, Sections 6.2.2.2.4, 6.2.3.2.3, 6.2.4.2, and 6.2.4.3), the key parameters affecting thermal seepage can be categorized as follows: (1) parameters mainly affecting the thermal-hydrologic conditions; (2) parameters mainly affecting the capillary barrier behavior; and (3) parameters that impact both the thermal-hydrologic conditions and the capillary barrier behavior.

Thermal load and conductivity, for example, belong to the first category. Varying these parameters results in considerable differences in the duration of the boiling period and the predicted maximum temperature in the rock. These conditions are important for the initiation time and the evolution of thermal seepage but do not change the ambient seepage rate (which defines the asymptotic upper limit for thermal seepage at later stages). Results showing the sensitivity of thermal seepage to the thermal load are given in Figures E-6 and E-7 for flow-focusing factors of 10 and 20, respectively.

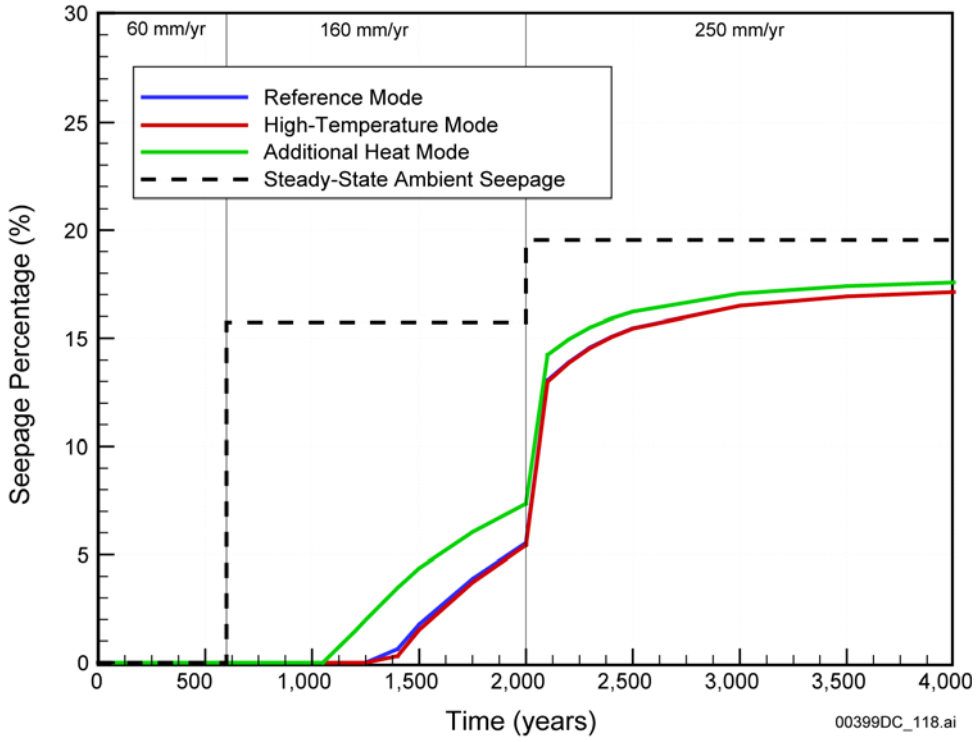

Source: BSC 2003b, Figure 6.2.4.2-3.

NOTE: The simulation cases are MN-HET-03, MN-HET-05, and MN-HET-06, as defined in *Drift-Scale Coupled Processes (DST and TH Seepage) Models* (BSC 2003b, Table 6.2.1.6-1).

Figure E-6. Seepage Percentage for Tptpmn Submodel with Different Heat Loads and Flow Focusing Factor 10, Showing Results from Thermal Run and from Long-Term Ambient Runs

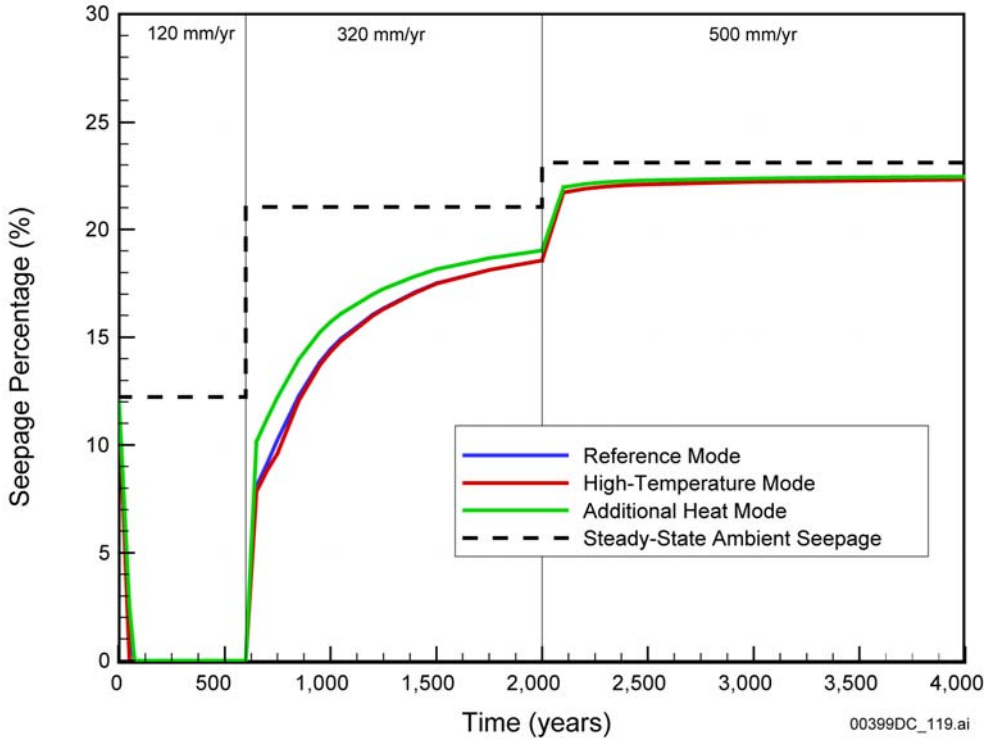

Source: BSC 2003b, Figure 6.2.4.2-4.

NOTE: The simulation cases are MN-HET-04, MN-HET-07, and MN-HET-08, as defined in *Drift-Scale Coupled Processes (DST and TH Seepage) Models* (BSC 2003b, Table 6.2.1.6-1).

Figure E-7. Seepage Percentage for Tptpmn Submodel with Different Heat Loads and Flow Focusing Factor 20, Showing Results from Thermal Run and from Long-term Ambient Runs

Fracture capillary strength belongs to the second category. This parameter has minor impact on the thermal-hydrologic behavior in the fractured rock (BSC 2003b, Section 6.2.2.1.4) but significantly affects the asymptotic upper limit for thermal seepage at later stages. As a result of the different seepage threshold saturation, the initiation time and evolution of thermal seepage can also be affected. This is shown in a comparison of results for a small capillary-strength parameter $1/\alpha$ value of 400 Pa in Figure E-8, with the respective simulation case using a $1/\alpha$ value of 589 Pa in Figure E-9.

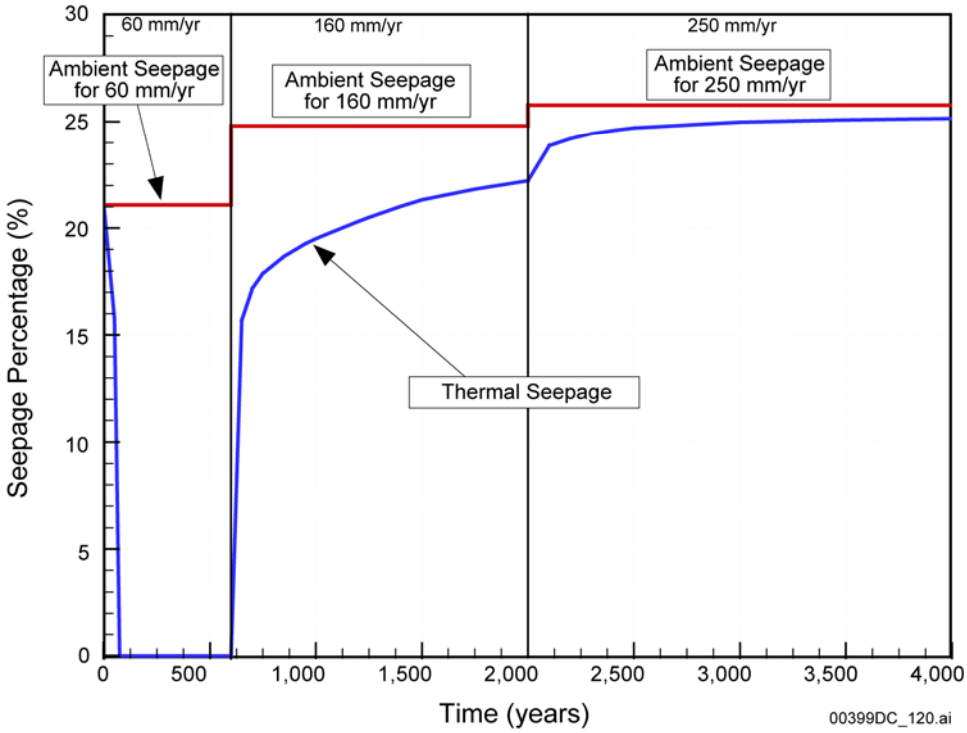

Source: BSC 2003b, Figure 6.2.4.2-5.

NOTE: The simulation case is MN-HET-09, as defined in *Drift-Scale Coupled Processes (DST and TH Seepage) Models* (BSC 2003b, Table 6.2.1.6-1).

Figure E-8. Seepage Percentage for Tptpmn Submodel with a Fracture Capillary-Strength Parameter $1/\alpha$ value of 400 Pa, and Flow-Focusing Factor of 10, Showing Results from Thermal Run and from Long-Term Ambient Runs

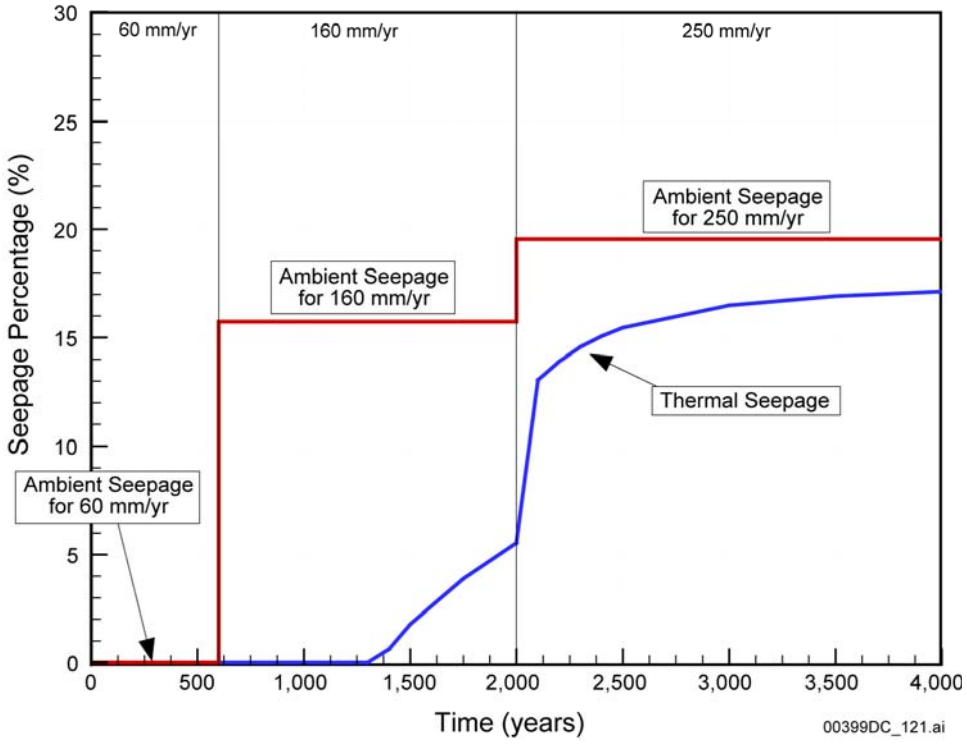

Source: BSC 2003b, Figure 6.2.2.2-7b.

NOTE: The simulation case is MN-HET-03, as defined in *Drift-Scale Coupled Processes (DST and TH Seepage) Models* (BSC 2003b, Table 6.2.1.6-1).

Figure E-9. Thermal-Hydrologic Conditions for Tptpmn Submodel with a Fracture Capillary-Strength Parameter $1/\alpha$ value of 589 Pa and Flow Focusing Factor 10, Showing Seepage Percentage for Thermal Run and Long-Term Ambient Runs

The third category comprises parameters that are important for ambient seepage and also affect the intensity of thermal-hydrologic coupling. Large percolation fluxes, for example, are typically related to large ambient seepage rates (BSC 2003b, Section 6.4.1.2). At the same time, increased percolation flux gives rise to a reduction of temperature and a shorter duration of the boiling period. Thus, for large percolation fluxes, thermal seepage may start earlier and approach larger asymptotic values at later stages of heating. Example results illustrating the impact of percolation flux changes can be seen by comparing Figures E-6 and E-7 for flow focusing factors of 10 and 20, respectively.

Changes in fracture permeability can also affect both the vaporization and the capillary barrier but are expected to have counteracting effects on these barriers. Large permeabilities are generally beneficial for the performance of the capillary barrier because they allow for more flow diversion around the drifts. The vaporization barrier, on the other hand, may be less effective because large permeabilities may cause strong heat-pipe processes that would result in considerably lower rock temperatures.

It is possible that the initially circular-shaped open emplacement drifts will degrade with time as a result of thermal stress, seismic ground motion, and time-dependent degradation of rock strength (BSC 2003c, Section 6.3.1). Depending on the type of rock, the stress conditions, and

the time-dependent rock mechanical properties, damage to the drifts may be rather small, with local rockfall at the ceiling of otherwise intact drift openings, or, in extreme cases, may result in partial or complete drift collapse, with rubble rock material filling the enlarged drifts. These changes affect the potential for drift seepage.

Complete drift collapse may lead to significantly different seepage behavior (BSC 2003c, Section 6.4.2.2). However, even though the collapsed drifts are filled with rubble material, capillary barrier effects still give rise to considerable flow diversion at the interface between the solid rock and the rubble-filled drift opening. This is because of the large scattered voids between the fragmented rock particles (particle sizes on the order of centimeters and decimeters, suggesting that the capillary strength parameter in the rubble-filled drift is very small, most likely close to the zero capillarity of an air-filled opening. Also, a small gap can be expected between the solid rock at the ceiling and the collapsed rubble material as a result of consolidation. Therefore, capillary-driven flow diversion remains an important mechanism reducing seepage in collapsed drifts.

Systematic seepage simulations for the collapsed drift case were conducted for the full set of parameter combinations, with capillary strength values ranging from 100 Pa to 1,000 Pa, mean permeability values ranging from −14 to −10 (in $\log_{10}$), and percolation flux values ranging from 1 mm/yr to 1,000 mm/yr. There is a considerable increase in seepage percentage relative to the nondegraded drift scenarios, caused by the larger size of the collapsed drift (reducing the effectiveness of flow diversion around the drift) and by the nonzero capillary strength in the drift (reducing the effectiveness of the capillary barrier). Nevertheless, the simulation results demonstrate that most of the percolation flux is still diverted around the collapsed drift for most of the considered parameter range. The simulations also show that the related seepage rates for the collapsed drift scenario are much larger than for nondegraded drifts. The increase in seepage rates occurs because the footprint of the drifts has doubled in size, thereby doubling the amount of percolation flux arriving at the collapsed drift.

Thermal-Hydrologic Seepage Submodels to Evaluate Effects of Tptpll and Tptpmn Properties–The Tptpmn and Tptpll submodels were developed to address the fact that the validation of the thermal-hydrologic seepage model (BSC 2003b) does not include direct comparison with measured data from the Tptpll. While application of the validated model to the Tptpll unit is appropriate since similar thermal-hydrologic processes need to be described, some uncertainty remains about the rock properties in this unit and the influence of lithophysal cavities.

Simulations of seepage into the two different host rocks with different thermal and hydrologic properties were compared. The first one, the Tptpmn submodel, considers a drift located in the Topopah Spring Tuff middle nonlithophysal unit (Tptpmn unit). The second one, the Tptpll submodel, considers a drift located in the Topopah Spring Tuff lower lithophysal unit (Tptpll unit).

The rock properties assigned to the various stratigraphic units in the thermal-hydrologic seepage model have been mainly derived from site-scale calibration runs (most hydrologic properties) and supplemental data analyses (thermal properties). Since these properties are different for the

Tptpmn and the Tptpll host rock units, some effect of parameter variation is already accounted for by analyzing the Tptpmn and the Tptpll submodels.

The rock properties that have the strongest impact on the thermal-hydrologic conditions in the fractured tuff are the thermal properties, most importantly the bulk thermal conductivity (important for conductive heat transport) and the fracture permeability (important for moisture redistribution). In the thermal-hydrologic seepage model, the bulk thermal conductivity varies by about 10% between the Tptpmn and the Tptpll, while fracture permeability varies by about one-half order of magnitude (BSC 2003b, Table 4.1-2). These parameter ranges are smaller than the estimated variability of these properties over the repository area. By comparison, the standard deviation describing the variability of bulk thermal conductivity was reported on the order of 0.25 W/m/K in the Tptpmn and the Tptpll units (BSC 2002a, Table 7-10) while the standard deviation of mean permeability is 0.34 and 0.47 (in log10) for the two units, respectively (BSC 2003b, Section 6.7.1.1).

Effects of variation of these parameters beyond the range explicitly accounted for by the thermal seepage simulation were qualitatively discussed in Section 6.2.4.3 of *Drift-Scale Coupled Processes (DST and TH Seepage) Models* (BSC 2003b), based on sensitivity analyses reported in *FY01 Supplemental Science and Performance Analyses, Volume 1: Scientific Bases and Analyses* (BSC 2001b, Sections 5.3.1.4.7 and 5.3.1.4.8). These analyses demonstrate that the potential variability in thermal conductivity and fracture permeability is expected to result in considerable variability in the thermal-hydrologic conditions. However, it was concluded that the validity of the simple abstraction method for thermal seepage should not be affected. This assessment was based on the fact that the range of thermal-hydrologic conditions expected from the variability of these properties is smaller than the range of thermal-hydrologic conditions explicitly addressed in the modeling analysis by varying the thermal load and using vastly different percolation rates.

The Impact of Different Conceptual Models for Fracture–Matrix Interaction–Simulations of the thermal-hydrologic processes measured in the Drift Scale Test using the dual-permeability method were compared with and without the active fracture model (BSC 2003c, Section 7). The comparison of measured data and model results did not clearly discriminate between them because both conceptual models produced good agreement between measured and simulated thermal-hydrologic behavior for the Drift Scale Test (BSC 2003b, Section 7.4.4). The impact of using the active fracture model for seepage evaluation was tested in scoping simulations. One simulation case was conducted using a dual-permeability method without employing the active fracture model. The seepage rates are comparable to but smaller than the active fracture model results, indicating that the active fracture model is the more conservative conceptual model with respect to seepage. The higher seepage rates with the active fracture model occur because of the flow channeling effect that results from the segregation into active and nonactive portions of the fracture network. In the thermal-hydrologic seepage model, the active fracture model is mainly applied because fracture–matrix interaction is important for the transient thermal-hydrologic processes. Also, the model is intended to be consistent with other models for unsaturated flow and transport at Yucca Mountain.

Comparison of Steady State and Transient Flow Simulations–Transient seepage rates were explicitly calculated by the thermal-hydrologic seepage model to directly quantify the potential

for seepage during the thermally perturbed time. These transient seepage rates were compared with results from ambient steady-state simulations to provide reference values for evaluating the vaporization barrier. In this manner, seepage results considering the combined effectiveness of the vaporization and the capillary barrier are compared with seepage results considering only the capillary barrier contribution. Even without heating the repository, the capillary barrier at the drift wall is predicted to be fully effective during the first 600 years after waste emplacement. This provides additional confidence, as two barriers prevent seepage simultaneously and independently, and also suggests that incorporating the effect of vaporization into seepage abstraction may be less important than expected. This is because the period when vaporization processes are most effective always coincides with the period of present-day climate, where percolation flux is comparably small and ambient seepage is much less likely than during the monsoon and the glacial transition climate.

E.4.6.2.2 Thermal-Hydrologic Seepage Model Alternative Conceptual Model for the Vaporization Barrier

During the time of above-boiling temperature conditions, a large, hot dryout region develops in the vicinity of the drift. The dryout region provides an additional barrier to the capillary barrier, preventing seepage since percolating water can be entirely vaporized prior to reaching the drift wall. The thermal-hydrologic seepage model predictions regarding the effectiveness of the vaporization barrier were tested by comparison with an alternative conceptual model of water flow in the superheated rock environment (BSC 2003b, Section 6.3). In this alternative model, the thermally perturbed downward flux from the condensation zone toward the superheated rock zone is conceptualized to form episodic preferential-flow events (finger flow), shown in Figure E-10.

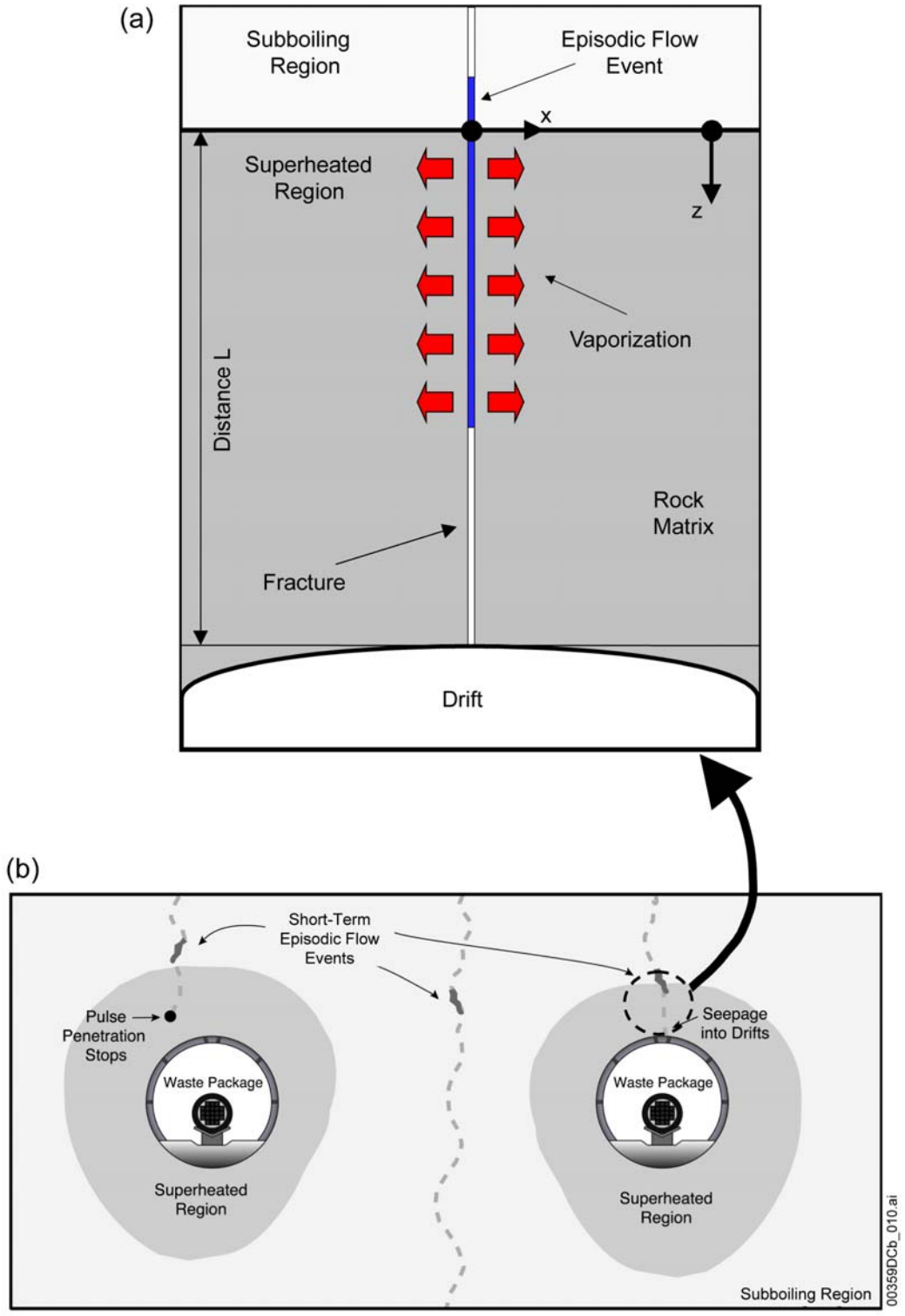

Source: BSC 2003b, Figure 6.3-1.

NOTE: For simplicity, the drip shield above waste packages is not shown.

Figure E-10. (a) Conceptual Model for Finger Flow in a Vertical Fracture above a Drift with Heat Conduction from the Adjacent Rock and (b) Episodic Finger Flow in Unsaturated Fractured Rock in the Vicinity of Waste Emplacement Drifts

The effectiveness of the vaporization barrier was tested for the extreme conditions where downward flux in small fingers is fast and large in magnitude compared to average flow. A semianalytical solution (Birkholzer 2002) was employed to simulate the complex flow processes of episodic finger flow in a superheated fracture. With this solution, the maximum penetration distance into the superheated rock was determined for specific episodic flow events and thermal conditions, and the amount of water arriving at the drift crown was calculated. It was shown that finger flow is not likely to penetrate through the superheated rock during the first several centuries of heating when rock temperature is high and boiling conditions exist in a sufficiently large region above the drifts. These are the conditions when the largest thermal perturbation occurs (i.e., when the potential for episodic finger flow is highest). Only later, when the boiling zone is small and the impact of vaporization is limited, may channelized water arrive at the drift crown (BSC 2003b, Section 6.3).

The fact that water can reach the drift during the period of above-boiling temperatures makes the alternative conceptual model distinct from the thermal-hydrologic seepage model. However, the strong thermal perturbation observed at early heating stages has already diminished during this time, and the net result of water arrival at the drift—considering the combined impact of water buildup in the condensation zone and vaporization in the superheated zone—is similar to ambient percolation. Seepage of water into the drift is not expected from this limited water arrival because the flow should be effectively diverted around the drift by the capillary barrier capability of the cavity (BSC 2003b, Section 6.3). These findings were consistent over a wide range of finger flow characteristics studied in a sensitivity analysis covering the potential uncertainty in finger flow patterns. Thus, the alternative conceptual model results clearly supports the main findings of the thermal-hydrologic seepage model, adding confidence in the model and reducing the conceptual model uncertainty.

E.4.6.2.3 Mountain-Scale Thermal-Hydrologic Ventilation Sensitivity Study

During the preclosure period, a ventilation scenario of 86.3% heat removal for the first 50 years after emplacement is considered the base case of thermal load. A no-ventilation case is also investigated for comparison and sensitivity analysis. In both cases, the thermal load is applied to the entire drift length (continuous or smeared heat source) for each repository block (BSC 2003a).

Early on (less than or equal to 100 years after waste emplacement), ventilation for 50 years with 86.3% heat removal has a significant impact on overall thermal-hydrologic behavior at the repository and the immediate surrounding areas. With ventilation, it takes 50 and 80 years for boiling to occur (as predicted by the two-dimensional and three-dimensional models, respectively). As predicted by the base-case model, however, boiling develops within the northern, main repository block only and does not occur in the smaller southern repository block. The highest temperature at the repository is predicted to be 100°C after 100 years for the ventilation case and to reach more than 130°C after 10 years for the no-ventilation scenario. In the case of no ventilation, both models estimate that boiling will occur at the repository in one to two years. However, both two-dimensional and three-dimensional base-case models predict that during this early period, thermal-hydrologic changes are limited to the near field of the emplacement drifts. Far away (greater than 100 m) from drifts, conditions at these earlier times remain ambient.

The impact of 50-year ventilation becomes less significant for longer times (greater than or equal to 1,000 years after waste emplacement). For example, the termination times for boiling are nearly the same with or without ventilation operations. The two-dimensional model predicts that the boiling period will end at 2,000 years for both ventilation scenarios while the three-dimensional model estimates the boiling will terminate at 1,000 years with or without ventilation. For the base-case ventilation scenario, two-dimensional simulated peak temperatures near drifts are 190°C at 60 years whereas the three-dimensional model predicts a peak temperature of 100°C occurring at 100 years. In addition, the three-dimensional thermal-hydrologic models predict that either localized boiling zones will develop near the drifts or no large-scale boiling will occur with ventilation operations.

The two-dimensional model predicts consistently higher temperatures at and near the repository under the same infiltration and thermal-loading conditions (particularly for the first couple centuries) as those used by the three-dimensional model. This is primarily because the two-dimensional model does not account for heat transfer or thermal energy loss into the third dimension, which is equivalent to introducing more heat into the two-dimensional cross section than would the corresponding slice of the three-dimensional model under the same modeling conditions. Secondly, the three-dimensional model contains coarser gridblocks and larger-scale volume averages at and near repository drifts. These large gridblocks will average out peak temperature values, leading to lower predictions of elevated temperatures in the three-dimensional thermal-hydrologic model. The peak temperatures predicted by the three-dimensional thermal-hydrologic model are also somewhat lower than those predicted by the multiscale thermal-hydrologic model (BSC 2003h).

E.4.6.3 Other Activities to Reduce Uncertainty in the Mountain-Scale Thermal-Hydrologic Model

Validation of the Physical Processes–Fluid flow and heat transfer in a fractured geologic medium are the main focus of the mountain-scale thermal-hydrologic model. Such fluid-flow and heat-transfer processes consist of some or all of the following physical processes:

- Heat conduction
- Convective heat transfer
- Flow of liquid water and air or water vapor
- Vaporization and condensation
- Drainage through fractures and imbibition into matrix
- Capillary effects.

These processes have been routinely modeled and numerically simulated in the geothermal and petroleum reservoir engineering disciplines. Such numerical models of geothermal and petroleum systems have also been validated against a wealth of field-scale tests and production data.

These processes have been modeled at a smaller scale (in space and time) (BSC 2003b). The Drift Scale Test data gave an adequate representation of the likely thermal-hydrologic, thermal-hydrologic-mechanical, and thermal-hydrologic-chemical processes to be encountered in the near field of the emplacement drifts. Through a detailed comparison of measured and

simulated thermal-hydrologic, thermal-hydrologic-mechanical, and thermal-hydrologic-chemical data, it was concluded that the physical processes were adequately represented by the model (BSC 2003b). This builds confidence into the mountain-scale coupled-processes models since the underlying flow and heat-transfer processes are similar both in the drift-scale and in the mountain-scale. However, the thermal tests (including the Drift Scale Test) provide only limited data for calibration and validation of the numerical models. The small spatial and temporal scales limit validation of the mountain-scale models. The validation is also limited by the uncertainties arising from parameter estimates in a geologically complex system and the upscaling of drift-scale results to the unsaturated zone mountain-scale model (BSC 2003a, Section 7.1.1). Confidence in the mountain-scale thermal-hydrologic model is improved through corroboration with alternative mathematical models, publication of the model approaches, and testing in refereed professional journals, as described below. These activities provide improved confidence in the underlying conceptual models in a qualitative sense and when conservative assumptions are employed.

Validation of the Numerical Modeling Approach–In the absence of direct data to validate the mountain-scale coupled-processes models, validations of the modeling approach must rely mainly on the conceptual and mathematical validity of models. The analyses conducted in *Mountain-Scale Coupled Processes (TH/THC/THM)* (BSC 2003a) provide the mountain-scale response to thermal loading under the proposed thermal-loading conditions. The numerical models are used to determine the effect of thermal loading on mountain-scale liquid and gas flux, temperature, and moisture distribution in the unsaturated zone. In these models, the relevant thermal-hydrologic conditions at the repository are explicitly represented over the applicable time and space scale. Contemporary practice in modeling fluid-flow and heat-transfer processes has been incorporated in the mountain-scale thermal-hydrologic model approach. The formulation of the simulation code TOUGH2 V1.6 (LBNL 2003) allows numerical modeling of such processes. The following provides evidence of successful application of TOUGH2 in modeling two-phase flow and heat transfer in an unsaturated geologic medium.

The TOUGH2 family of codes has also been used in numerical models of the natural state of geothermal systems (Bodvarsson et al. 1984a; 1986; 1988; Hanano 1992; Ingebritsen and Sorey 1988; O'Sullivan et al. 1990) and in the predictions of their performance under exploitation (Bodvarsson et al. 1984b; 1987a; 1987b; 1990; 1993; Garg and Pritchett 1990; Hunt et al. 1990; Lam et al. 1988; Menzies et al. 1991). Mathematical models of the two-phase flow in such systems are identical to numerical modeling of thermal-hydrologic response to thermal loading described in this report. Major differences exist mainly in equations correlating flow and saturation and the existence of preferential flow paths in unsaturated zone flow for heterogeneous media (e.g., fingering and flow channeling). The other major difference is in the time scale of modeled behavior. For example, evolution of the natural state of geothermal systems is typically modeled over a period of a few hundred to several hundred thousand years. The exploitation prediction is over a period of 30 to 50 years, the economic life of such systems based on measured field response. On the other hand, modeling of the mountain-scale thermal-hydrologic response requires numerical prediction for tens of thousands of years in a system for which limited field data exist. In many ways, however, the process for setting up the conceptual model, building the numerical grid, specifying boundary conditions, developing the natural state, and conducting numerical model predictions is the same and is documented in the cited references as well as in *Mountain-Scale Coupled Processes (TH/THC/THM)* (BSC 2003a).

Versions of TOUGH2 (Pruess et al. 1999) have been used in a number of numerical models for evaluating the thermal-hydrologic effects of thermal loading at Yucca Mountain (Pruess and Tsang 1994; Buscheck et al. 1994; Haukwa et al. 1999; Haukwa et al. 2003). Model conceptualizations have focused mainly on large-scale average behavior or on local simplified domains of two-dimensional representations. Both the effective-continuum and dual-permeability methods have been used in previous applications of TOUGH2 in modeling two-phase flow and heat transfer through fractured rock. The mountain-scale thermal-hydrologic model considers only the dual-permeability approach for handling fracture–matrix interaction.

Various versions of the TOUGH2 code have also been used in sensitivity studies on thermal-hydrologic conditions near an infinite linear string of waste packages (Pruess and Wang 1984). Fluid and heat flow (including phase change effects) were modeled in a one-dimensional cylindrical geometry, and it was found that strong two-phase vapor-liquid counter flow (heat pipe) occurred in some cases (Pruess and Wang 1984). Repository-scale simulations with an emphasis on thermally driven natural convection were conducted (Tsang and Pruess 1987). Details of temperature, saturation, and gas-phase composition in the hydrothermally disturbed zone were considered (Nitao 1988). This was modeled using a 3-km diameter, disk-shaped repository to examine the thermal-hydrologic responses. Pruess et al. (1990a; 1990b) used TOUGH2 to perform a comprehensive modeling study of the simultaneous transport of heat, liquid water, vapor, and air in a partially saturated fractured porous rock (Pruess et al. 1990a; Pruess et al. 1990b). A two-dimensional idealized model was used, which included an explicit consideration of fracture effects. This model included most of the physical effects that are important in multiphase fluid and heat flow in fractured media. It demonstrated the capability of modeling multiphase, nonisothermal water and airflow with phase changes in a fractured medium.

These modeling efforts demonstrate the capability of TOUGH2 to model thermal-hydrologic processes on a mountain scale in addition to the validity of process models and the assumptions used. Mass, momentum, and energy are inherently conserved in the mathematical formulation or numerical modeling results with the TOUGH2 family of codes, which adds further confidence to the numerical models.

Confidence Building through Publication–For corroboration, the mountain-scale impact of thermal loading at Yucca Mountain has also been published in open scientific literature (Haukwa et al. 1999; Haukwa et al. 2003). These journal publications have undergone independent technical review and public scientific scrutiny. The underlying physical processes and model validation with measured data have also undergone independent technical review in the open literature (Birkholzer and Tsang 2000; Mukhopadhyay and Tsang 2003), although these papers are concerned mainly with processes at a smaller time and space scale. Additionally, the basic formulations of physical processes implemented in the mountain-scale thermal-hydrologic models, as represented by two-phase flow equations (Pruess et al. 1999, pp. 144 to 145), the van Genuchten-Mualem model (Luckner et al. 1989, pp. 2191 to 2192), and the active fracture model (Liu et al. 1998) for representation of preferential flow paths through selected fractures are all in the open literature, have gone through proper technical review, and have withstood scrutiny of the scientific community since their dates of publication.

E.4.7 Quantification and Propagation of Model Uncertainty in the Thermal-Hydrologic Models

Model uncertainty and its propagation to TSPA are addressed in several ways. The uncertainty in the ambient flow fields is propagated from the unsaturated zone flow model to the thermal-hydrologic models through the generation of three infiltration scenarios for the three climate stages and the two PTn conceptual models. Further discussion of the propagation of uncertainty in flow fields among the various models used in TSPA can be found in Appendix G. The mountain-scale coupled processes model screens the thermal-hydrologic, thermal-hydrologic-chemical and thermal-hydrologic-mechanical effects on site-scale flow, which can be used as a basis for justifying model simplification in TSPA. Uncertainty in this model is handled by applying conservative assumptions, as discussed in Section E.4.3.

The ambient and heater field tests provide data to compare with the conceptual representation of the numerical models, as described in the preceding section.

A systematic process of quantifying model uncertainty and propagating it through to thermal-hydrologic abstraction was performed for the ambient and thermal drift seepage models and is the subject of Appendix I of *Technical Basis Document No. 3: Water Seeping into Drifts*. Selected aspects of this process are presented in this section, taken from *Abstraction of Drift Seepage* (BSC 2003c).

All sources of uncertainty related to seepage-relevant parameters and seepage simulation results have been characterized in and propagated through the seepage abstraction for the TSPA-LA. Uncertainty in the key parameters for ambient seepage has been explicitly represented through appropriate probability distributions (BSC 2003c, Section 6.6). The probabilities assigned to these key parameters distinguish between spatial variability (aleatory uncertainty) and uncertainty (epistemic uncertainty) using separate distributions. Spatial variability distributions for the capillary strength parameter and the local permeability have been derived by detailed statistical analysis of the sparsely distributed data (BSC 2003c, Sections 6.6.1 and 6.6.2). Spatial variability distributions for the local percolation flux are provided from site-scale simulations with the unsaturated zone flow model (BSC 2003c, Section 6.6.3). These fluxes are then adjusted to account for intermediate-scale heterogeneity using a spatial distribution of flow focusing factors. Uncertainty has been characterized by evaluation of all potential sources for uncertainty (i.e., uncertainty in the measurements, conceptual model, estimation process, and spatial variability).

Information on uncertainty provided in upstream analyses or modeling has been included in this evaluation. Uncertainty inherent in the capillary strength parameter and the local permeability is described by triangular probability distributions (see *Abstraction of Drift Seepage* (BSC 2003c, Sections 6.6.1 and 6.6.2)). Alternative methods have been employed to derive statistical parameters describing the probability distributions for the capillary-strength parameter. It is recommended that TSPA conduct a sensitivity analysis and choose the most conservative method with respect to the overall seepage. Uncertainty in the percolation flux distributions is incorporated using three different flow scenarios (BSC 2003c, Section 6.6.4). In addition, an alternative unsaturated zone flow scenario has been evaluated in *Abstraction of Drift Seepage* (BSC 2003c, Section 6.8.2) but can be neglected in TSPA because of its limited impact.

Uncertainty in the abstracted thermal seepage results is a result of uncertainty in the ambient seepage estimates used as the quantitative basis of the abstraction and uncertainty in the evolution of thermal seepage compared to the ambient seepage estimates. The first contribution to thermal seepage uncertainty is automatically included in the thermal abstraction because the abstracted ambient seepage rates explicitly account for the conceptual model uncertainty and the uncertainty in seepage-relevant parameters (BSC 2003c, Section 6.5.1.3). The second contribution to thermal seepage uncertainty needs further discussion.

Conceptual model uncertainty related to the thermal-hydrologic seepage model has been addressed in *Drift-Scale Coupled Processes (DST and TH Seepage) Models* (BSC 2003b, Sections 7 and 8.2) by careful validation of the coupled thermal-hydrologic processes in comparison with in situ heater tests (summarized in Section E.4.6.1). This validation provides confidence regarding the thermally induced flux processes and the predicted effectiveness of the vaporization barrier. In addition, validation of the ambient seepage conceptual model (in comparison with liquid-release tests) provides confidence in the predicted effectiveness of the capillary barrier. Results of an alternative conceptual model, considering the potential penetration of episodic preferential flow into the superheated zone above emplacement drifts (see Section E.4.6.2), corroborate the main findings of the thermal-seepage process model. Based on this discussion, the conceptual model uncertainty of the thermal-hydrologic seepage model is expected to be small. Some conceptual model uncertainty, however, remains because the in situ heater tests used for model validation were operated at natural percolation, which is comparably small, and were conducted only in the Tptpmn unit. Thus, the tests do not provide seepage data for extreme percolation conditions and cannot account for the potential effect of lithophysal cavities on the thermal-hydrologic conditions (BSC 2003c, Section 6.4.3.2). Discussions of the two abstraction models that account for conceptual model uncertainty follow.

Abstraction Model 1–This conservative abstraction model does not incorporate the vaporization barrier formed as a result of heating. The abstraction merely requires that no enhanced seepage occurs during the thermal period compared to ambient seepage estimates. Enhanced seepage could only occur when strong condensate reflux coincides with late heating periods, when vaporization is not effective. However, model results clearly demonstrate that this potential can be neglected in the abstraction since the thermal perturbation is strongest early in the heating period when vaporization is most intense (BSC 2003c, Section 6.4.3.3). The model validation, corroborated by the alternative conceptual model, provides sufficient confidence to support this conservative abstraction model without explicit consideration of conceptual model uncertainty.

Abstraction Model 2–This abstraction model assumes that no thermal seepage occurs during the period of above-boiling temperatures in the drift vicinity. Here, the remaining uncertainty related to the predictive effectiveness of the vaporization barrier needs to be accounted for in the abstraction. This is done by using a threshold temperature higher than the nominal boiling temperature to define the duration of the boiling period for abstraction. As explained, the 100°C isotherm of the fracture continuum is the recommended threshold temperature. This ensures that the boiling isotherm is at some distance from the drift (and there is a small dryout zone around the wall) when the zero seepage is switched back to ambient seepage in the abstraction. Additional confidence is provided because the abstraction model does not incorporate the delayed seepage initiation caused by the time-dependent saturation buildup at the drift. Thus,

abstraction model 2, despite assuming no seepage for rock temperature above 100°C, still gives conservative seepage estimates compared to the predicted thermal seepage results.

Another source of uncertainty in the thermal-seepage modeling results is uncertainty in the relevant input parameters to the model. The selected sensitivity cases analyzed in *Drift-Scale Coupled Processes (DST and TH Seepage) Models* (BSC 2003b, Section 6.2) provide enough confidence that the recommended abstraction procedures are valid over the required range of conditions and values used in TSPA. In other words, the general conclusions about the qualitative magnitude and evolution of thermal seepage (i.e., no seepage during boiling and thermal seepage bounded by ambient seepage estimates) remain consistent for all parameter combinations of capillary strength, permeability, percolation flux, thermal load, and thermal conductivity studied in the TSPA calculations. They also remain consistent for the three different realizations analyzed in *Drift-Scale Coupled Processes (DST and TH Seepage) Models* (BSC 2003b, Section 6.2). Consequently, there is no estimation uncertainty regarding these conclusions.

Based on this assessment, abstraction model 1 can be immediately implemented into TSPA because the abstraction is independent of the thermal processes. Abstraction model 2, on the other hand, requires detailed knowledge about the duration of the boiling period in the vicinity of emplacement drifts. In this case, the spatial variability and uncertainty of additional parameters relevant for the thermal conditions in the repository must be described (e.g., thermal load and thermal conductivity), and more thermal simulation cases have to be analyzed for various combinations and stochastic realizations of these additional parameters. The latter tasks were not included in *Abstraction of Drift Seepage* (BSC 2003c).

Another contribution to uncertainty in the TSPA seepage calculations stems from the simulation results of drift-scale models that describe seepage-relevant processes. Drift-scale models are introduced in *Abstraction of Drift Seepage* (BSC 2003c, Section 6.4) and includes a detailed assessment of the respective model validation and corroboration with alternative conceptual models. As discussed in *Abstraction of Drift Seepage* (BSC 2003c, Section 6.5), the treatment of uncertainty in simulation results is based on this assessment and considers the respective use of the model in the abstraction. The estimation uncertainty of the seepage model for performance assessment simulation results, used directly in the TSPA-LA as a quantitative measure of seepage, is explicitly incorporated in the seepage abstraction by uniform uncertainty distributions (BSC 2003c, Section 6.5.1.4). Other drift-scale models provide quantitative and qualitative information used to adjust the seepage model for performance assessment seepage results for additional factors (thermal-hydrologic-mechanical and thermal-hydrologic-chemical parameter alterations, drift degradation, rock bolts, and thermal seepage). These adjustments are generally based on simplifications of the more complex process model results. To incorporate uncertainty, these simplifications are chosen to be conservative. This means that the simplified abstractions tend to overestimate the seepage compared to the predicted process model results. Thermal-hydrologic-chemical parameter alterations, for example, were found to decrease the potential of seepage because of a precipitation umbrella forming a few meters above drifts. This process, however, is neglected in the abstraction because of considerable uncertainties in modeling the coupled thermal-hydrologic-chemical processes (BSC 2003c, Section 6.5.1.4).

E.5 REFERENCES

E.5.1 Documents Cited

Birkholzer, J.T. 2002. *TH_PULSE: Program for Calculating Infiltration of Episodic Liquid Fingers in Superheated Rock Fractures, Theory, User's Manual, and Sample Applications*. LBNL/PUB-3277. Berkeley, California: Lawrence Berkeley National Laboratory. TIC: 253581.

Birkholzer, J.T.; Li, G.; Tsang, C-F.; and Tsang, Y. 1999. "Modeling Studies and Analysis of Seepage into Drifts at Yucca Mountain." *Journal of Contaminant Hydrology, 38*, (1-3), 349-384. New York, New York: Elsevier. TIC: 244160.

Birkholzer, J.T. and Tsang, Y.W. 2000. "Modeling the Thermal-Hydrologic Processes in a Large-Scale Underground Heater Test in Partially Saturated Fractured Tuff." *Water Resources Research, 36,* (6), 1431-1447. Washington, D.C.: American Geophysical Union. TIC: 248278.

Bodvarsson, G.S. 2001. *Thermal Effects on Flow, Subissue 2, Open Item 8: Model Uncertainty*. Presentation to the DOE/NRC Technical Exchange on Key Technical Issue and Subissues Related to Thermal Effects on Flow, January 8-9, 2001, Pleasanton, California. Las Vegas, Nevada: Yucca Mountain Site Characterization Office. ACC: MOL.20010202.0105.

Bodvarsson, G.S.; Bjornsson, S.; Gunnarsson, A.; Gunnlaugsson, E.; Sigurdsson, O.; Stefansson, V.; and Steingrimsson, B. 1988. "A Summary of Modeling Studies of the Nesjavellir Geothermal Field, Iceland." *Proceedings, Thirteenth Workshop, Geothermal Reservoir Engineering, January 19-21, 1988, Stanford, California.* Workshop Report SGP-TR-113. Pages 83-91. Stanford, California: Stanford University. TIC: 246824.

Bodvarsson, G.S.; Gislason, G.; Gunnlaugsson, E.; Sigurdsson, O.; Stefansson, V.; and Steingrimsson, B. 1993. "Accuracy of Reservoir Predictions for the Nesjavellir Geothermal Field, Iceland." *Proceedings, Eighteenth Workshop, Geothermal Reservoir Engineering, Stanford, California, January 26-28, 1993*. Ramey, H.J., Jr.; Horne, R.N.; Kruger, P.; Miller, F.G.; Brigham, W.E.; and Cook, J.W., eds. Workshop Report SGP-TR-145. Pages 273-278. Stanford, California: Stanford University. TIC: 246821.

Bodvarsson, G.S.; Pruess, K.; Haukwa, C.; and Ojiambo, S.B. 1990. "Evaluation of Reservoir Model Predictions for Olkaria East Geothermal Field, Kenya." *Geothermics, 19,* (5), 399-414. New York, New York: Pergamon Press. TIC: 246739.

Bodvarsson, G.S.; Pruess, K.; and Lippmann, M.J. 1986. "Modeling of Geothermal Systems." *Journal of Petroleum Technology,* 1007-1021. Richardson, Texas: Society of Petroleum Engineers. TIC: 246733.

Bodvarsson, G.S.; Pruess, K.; Stefansson, V.; Bjornsson, S.; and Ojiambo, S.B. 1987a. "East Olkaria Geothermal Field, Kenya, 1. History Match with Production and Pressure Decline Data." *Journal of Geophysical Research, 92,* (B1), 521-539. Washington, D.C.: American Geophysical Union. TIC: 236629.

Bodvarsson, G.S.; Pruess, K.; Stefansson, V.; Bjornsson, S.; and Ojiambo, S.B. 1987b. "East Olkaria Geothermal Field, Kenya, 2. Predictions of Well Performance and Reservoir Depletion." *Journal of Geophysical Research, 92,* (B1), 541-554. Washington, D.C.: American Geophysical Union. TIC: 246738.

Bodvarsson, G.S.; Pruess, K.; Stefansson, V.; and Eliasson, E.T. 1984a. "The Krafla Geothermal Field, Iceland, 2. The Natural State of the System." *Water Resources Research, 20,* (11), 1531-1544. Washington, D.C.: American Geophysical Union. TIC: 246734.

Bodvarsson, G.S.; Pruess, K.; Stefansson, V.; and Eliasson, E.T. 1984b. "The Krafla Geothermal Field, Iceland: 3. The Generating Capacity of the Field." *Water Resources Research, 20,* (11), 1545-1559. Washington, D.C.: American Geophysical Union. TIC: 246737.

BSC (Bechtel SAIC Company) 2001a. *Thermal Tests Thermal-Hydrological Analyses/Model Report*. ANL-NBS-TH-000001 REV 00 ICN 02. Las Vegas, Nevada: Bechtel SAIC Company. ACC: MOL.20011116.0025.

BSC 2001b. *FY 01 Supplemental Science and Performance Analyses, Volume 1: Scientific Bases and Analyses*. TDR-MGR-MD-000007 REV 00 ICN 01. Las Vegas, Nevada: Bechtel SAIC Company. ACC: MOL.20010801.0404; MOL.20010712.0062; MOL.20010815.0001.

BSC 2002a. *Thermal Conductivity of the Potential Repository Horizon Model Report.* MDL-NBS-GS-000005 REV 00. Las Vegas, Nevada: Bechtel SAIC Company. ACC: MOL.20020923.0167.

BSC 2002b. *Technical Work Plan for: Performance Assessment Unsaturated Zone.* TWP-NBS-HS-000003 REV 02. Las Vegas, Nevada: Bechtel SAIC Company. ACC: MOL.20030102.0108.

BSC 2003a. *Mountain-Scale Coupled Processes (TH/THC/THM).* MDL-NBS-HS-000007 REV 01. Las Vegas, Nevada: Bechtel SAIC Company. ACC: DOC.20031216.0003.

BSC 2003b. *Drift-Scale Coupled Processes (DST and TH Seepage) Models*. MDL-NBS-HS-000015 REV 00C. Las Vegas, Nevada: Bechtel SAIC Company. ACC: MOL.20030910.0160.

BSC 2003c. *Abstraction of Drift Seepage.* MDL-NBS-HS-000019 REV 00 ICN 01. Las Vegas, Nevada: Bechtel SAIC Company. ACC: DOC.20031112.0002.

BSC 2003d. *UZ Flow Models and Submodels*. MDL-NBS-HS-000006 REV 01. Las Vegas, Nevada: Bechtel SAIC Company. ACC: DOC.20030818.0002.

BSC 2003e. *Seepage Calibration Model and Seepage Testing Data*. MDL-NBS-HS-000004 REV 02. Las Vegas, Nevada: Bechtel SAIC Company. ACC: DOC.20030408.0004.

BSC 2003f. *Analysis of Hydrologic Properties Data*. MDL-NBS-HS-000014 REV 00. Las Vegas, Nevada: Bechtel SAIC Company. ACC: DOC.20030404.0004.

BSC 2003g. *Calibrated Properties Model*. MDL-NBS-HS-000003 REV 01. Las Vegas, Nevada: Bechtel SAIC Company. ACC: DOC.20030219.0001.

BSC 2003h. *Multiscale Thermohydrologic Model.* ANL-EBS-MD-000049 REV 01. Las Vegas, Nevada: Bechtel SAIC Company. ACC: DOC.20040301.0004.

BSC 2003i. *Analysis of Infiltration Uncertainty*. ANL-NBS-HS-000027 REV 01. Las Vegas, Nevada: Bechtel SAIC Company. ACC: DOC.20031030.0003.

BSC 2003j. *Seepage Model For PA Including Drift Collapse*. MDL-NBS-HS-000002 REV 02. Las Vegas, Nevada: Bechtel SAIC Company. ACC: DOC.20030709.0001.

BSC 2003k. *Drift Scale THM Model.* MDL-NBS-HS-000017 REV 00 ICN 01. Las Vegas, Nevada: Bechtel SAIC Company. ACC: DOC.20031014.0009.

BSC 2003l. *In Situ Field Testing of Processes.* ANL-NBS-HS-000005 REV 02. Las Vegas, Nevada: Bechtel SAIC Company. ACC: DOC.20031208.0001.

Buscheck, T.A. and Nitao, J.J. 1991. *Nonequilibrium Fracture-Matrix Flow During Episodic Infiltration Events in Yucca Mountain*. Livermore, California: Lawrence Livermore National Laboratory. ACC: NNA.19920131.0220.

Buscheck, T.A.; Nitao, J.J.; and Saterlie, S.F. 1994. "Evaluation of Thermo-Hydrological Performance in Support of the Thermal Loading Systems Study." *High Level Radioactive Waste Management, Proceedings of the Fifth Annual International Conference, Las Vegas, Nevada, May 22-26, 1994. 2*, 592-610. La Grange Park, Illinois: American Nuclear Society. TIC: 210984.

Cacas, M.C.; Ledoux, E.; De Marsily, G.; Tillie, B.; Barbreau, A.; Durand, E.; Feuga, B.; and Peaudecerf, P. 1990. "Modeling Fracture Flow with a Stochastic Discrete Fracture Network: Calibration and Validation 1. The Flow Model." *Water Resources Research, 26,* (3), 479–489. Washington, D.C.: American Geophysical Union. TIC: 222351.

CRWMS M&O (Civilian Radioactive Waste Management System Management and Operating Contractor) 2000a. *Multiscale Thermohydrologic Model.* ANL-EBS-MD-000049 REV 00. Las Vegas, Nevada: CRWMS M&O. ACC: MOL.20000609.0267.

CRWMS M&O 2000b. *Unsaturated Zone Flow and Transport Model Process Model Report.* TDR-NBS-HS-000002 REV 00 ICN 02. Las Vegas, Nevada: CRWMS M&O. ACC: MOL.20000831.0280.

Doughty, C. 1999. "Investigation of Conceptual and Numerical Approaches for Evaluating Moisture, Gas, Chemical, and Heat Transport in Fractured Unsaturated Rock." *Journal of Contaminant Hydrology, 38,* (1-3), 69-106. New York, New York: Elsevier. TIC: 244160.

Dverstorp, B. and Andersson, J. 1989. "Application of the Discrete Fracture Network Concept with Field Data: Possibilities of Model Calibration and Validation." *Water Resources Research, 25,* (3), 540–550. Washington, D.C.: American Geophysical Union. TIC: 254736.

Finsterle, S. 2000. "Using the Continuum Approach to Model Unsaturated Flow in Fractured Rock." *Water Resources Research, 36*, (8), 2055-2066. Washington, D.C.: American Geophysical Union. TIC: 248769.

Garg, S.K. and Pritchett, J.W. 1990. "Cold Water Injection Into Single- and Two-Phase Geothermal Reservoir." *Water Resources Research, 26,* (2), 331-338. Washington, D.C.: American Geophysical Union. TIC: 247136.

Hanano, M. 1992. "Reservoir Engineering Studies of the Matsukawa Geothermal Field, Japan." *Geothermal Resources Council Transactions, 16,* 643-650. Davis, California: Geothermal Resources Council. TIC: 247116.

Haukwa, C.B.; Wu, Y-S.; and Bodvarsson, G.S. 1999. "Thermal Loading Studies Using the Yucca Mountain Unsaturated Zone Model." *Journal of Contaminant Hydrology, 38,* (1-3), 217-255. New York, New York: Elsevier. TIC: 244160.

Haukwa, C.B.; Wu, Y-S.; and Bodvarsson, G.S. 2003. "Modeling Thermal-Hydrological Response of the Unsaturated Zone at Yucca Mountain, Nevada, to Thermal Load at a Potential Repository." *Journal of Contaminant Hydrology, 62-63,* 529-552. New York, New York: Elsevier. TIC: 254205.

Hinds, J.J., Bodvarsson, G.S., and Nieder-Westerman, G. 2003. "Conceptual Evaluation of the Potential Role of Fractures in Unsaturated Processes at Yucca Mountain." *Journal of Contaminant Hydrology, 62-63,* 111-132. New York, New York: Elsevier TIC: 254205.

Hunt, T.M.; Allis, R.G.; Blakeley, M.R.; and O'Sullivan, M.J. 1990. "Testing Reservoir Simulation Models for the Broadlands Geothermal Field Using Precision Gravity Data." *1990 International Symposium on Geothermal Energy, Transactions, Geothermal Resources Council, 1990 Annual Meeting, 20-24 August, 1990, Kailua-Kona, Hawaii.* Volume 14, Part II. Pages 1287-1294. Davis, California: Geothermal Resources Council. TIC: 246942.

Ingebritsen, S.E. and Sorey, M.L. 1988. "Vapor-Dominated Zones Within Hydrothermal Systems: Evolution and Natural State." *Journal of Geophysical Research, 93,* (B11), 13635-13655. Washington, D.C.: American Geophysical Union. TIC: 247149.

Lam, S.T.; Hunsbedt, A.; Kruger, P.; and Pruess, K. 1988. "Analysis of the Stanford Geothermal Reservoir Model Experiments Using the LBL Reservoir Simulator." *Geothermics, 17,* (4), 595-605. Oxford, United Kingdom: Elsevier. TIC: 247098.

LBNL (Lawrence Berkeley National Laboratory) 2003. *Software Code: TOUGH2.* V1.6. PC/MS-DOS under Windows 98, Sun UltraSparc OS 5.5.1, DEC-Alpha OSF1 V4.0. 10007-1.6-01.

Lin, W.; Blair, S.C.; Wilder, D.; Carlson, S.; Wagoner, J.; DeLoach, L.; Danko, G.; Ramirez, A.L.; and Lee, K. 2001. *Large Block Test Final Report.* UCRL-ID-132246, Rev. 2. Livermore, California: Lawrence Livermore National Laboratory. TIC: 252918.

Liu, H.H. and Bodvarsson, G.S. 2001. "Constitutive Relations for Unsaturated Flow in a Fracture Network." *Journal of Hydrology, 252*, (1-4), 116-125. New York, New York: Elsevier. TIC: 253269.

Liu, H.H.; Bodvarsson, G.S.; and Finsterle, S. 2002. "A Note on Unsaturated Flow in Two-Dimensional Fracture Networks." *Water Resources Research, 38*, (9), 15-1 to 15-9. Washington, D.C.: American Geophysical Union. TIC: 253307.

Liu, H.H.; Doughty, C.; and Bodvarsson, G.S. 1998. "An Active Fracture Model for Unsaturated Flow and Transport in Fractured Rocks." *Water Resources Research, 34,* (10), 2633-2646. Washington, D.C.: American Geophysical Union. TIC: 243012.

Luckner, L.; van Genuchten, M.T.; and Nielsen, D.R. 1989. "A Consistent Set of Parametric Models for the Two-Phase Flow of Immiscible Fluids in the Subsurface." *Water Resources Research, 25,* (10), 2187-2193. Washington, D.C.: American Geophysical Union. TIC: 224845.

Menzies, A.J.; Granados, E.E.; Sanyal, S.K.; Merida-I, L.; and Caicedo-A, A. 1991. "Numerical Modeling of the Initial State and Matching of Well Test Data from the Zunil Geothermal Field, Guatemala." *Proceedings, Sixteenth Workshop, Geothermal Reservoir Engineering, January 23-25, 1991, Stanford, California.* Workshop Report SGP-TR-134. Pages 193-201. Stanford, California: Stanford University. TIC: 246832.

Mukhopadhyay, S. and Tsang, Y.W. 2002. "Understanding the Anomalous Temperature Data from the Large Block Test at Yucca Mountain, Nevada." *Water Resources Research, 38,* (10), 28-1 through 28-12. Washington, D.C.: American Geophysical Union. TIC: 253867.

Mukhopadhyay, S. and Tsang, Y.W. 2003. "Uncertainties in Coupled Thermal-Hydrological Processes Associated with the Drift Scale Test at Yucca Mountain, Nevada." *Journal of Contaminant Hydrology, 62-63,* 595-612. New York, New York: Elsevier. TIC: 254205.

Nitao, J.J. 1988. *Numerical Modeling of the Thermal and Hydrological Environment Around a Nuclear Waste Package Using the Equivalent Continuum Approximation: Horizontal Emplacement.* UCID-21444. Livermore, California: Lawrence Livermore National Laboratory. ACC: NNA.19890317.0021.

NRC (U.S. Nuclear Regulatory Commission) 2002. *Integrated Issue Resolution Status Report*. NUREG-1762. Washington, D.C.: U.S. Nuclear Regulatory Commission, Office of Nuclear Material Safety and Safeguards. TIC: 253064.

Oldenburg, C.M. and Pruess, K. 1993. "On Numerical Modeling of Capillary Barriers." *Water Resources Research, 29*, (4), 1045-1056. Washington, D.C.: American Geophysical Union. TIC: 238834.

O'Sullivan, M.J.; Barnett, B.G.; and Razali, M.Y. 1990. "Numerical Simulation of the Kamojang Geothermal Field, Indonesia." *1990 International Symposium on Geothermal Energy, Transactions, Geothermal Resources Council, 1990 Annual Meeting, 20-24 August, 1990, Kailua-Kona, Hawaii.* Volume 14, Part II. Pages 1317-1324. Davis, California: Geothermal Resources Council. TIC: 246942.

Philip, J.R.; Knight, J.H.; and Waechter, R.T. 1989. "Unsaturated Seepage and Subterranean Holes: Conspectus, and Exclusion Problem for Circular Cylindrical Cavities." *Water Resources Research, 25*, (1), 16-28. Washington, D.C.: American Geophysical Union. TIC: 239117.

Pruess, K.; Oldenburg, C.; and Moridis, G. 1999. *TOUGH2 User's Guide, Version 2.0.* LBNL-43134. Berkeley, California: Lawrence Berkeley National Laboratory. TIC: 253038.

Pruess, K. and Tsang, Y. 1994. *Thermal Modeling for a Potential High-Level Nuclear Waste Repository at Yucca Mountain, Nevada.* LBL-35381. Berkeley, California: Lawrence Berkeley National Laboratory. ACC: NNA.19940427.0248.

Pruess, K. and Wang, J.S.Y. 1984. "TOUGH - A Numerical Model for Nonisothermal Unsaturated Flow to Study Waste Canister Heating Effects." *Scientific Basis for Nuclear Waste Management VII, Symposium held November 14-17, 1983, Boston, Massachusetts.* McVay, G.L., ed. *26*, 1031-1038. New York, New York: Elsevier. TIC: 204393.

Pruess, K.; Wang, J.S.Y.; and Tsang, Y.W. 1990a. "On Thermohydrologic Conditions Near High-Level Nuclear Wastes Emplaced in Partially Saturated Fractured Tuff, 1. Simulation Studies with Explicit Consideration of Fracture Effects." *Water Resources Research, 26,* (6), 1235-1248. Washington, D.C.: American Geophysical Union. TIC: 221923.

Pruess, K.; Wang, J.S.Y.; and Tsang, Y.W. 1990b. "On Thermohydrologic Conditions Near High-Level Nuclear Wastes Emplaced in Partially Saturated Fractured Tuff, 2. Effective Continuum Approximation." *Water Resources Research, 26,* (6), 1249-1261. Washington, D.C.: American Geophysical Union. TIC: 224854.

Reamer, C.W. and Williams, D.R. 2001. Summary Highlights of NRC/DOE Technical Exchange and Management Meeting on Thermal Effects on Flow. Meeting held January 8-9, 2001, Pleasanton, California. Washington, D.C.: U.S. Nuclear Regulatory Commission. ACC: MOL.20010202.0095 through MOL.20010202.0108.

Ross, B. 1990. "The Diversion Capacity of Capillary Barriers." *Water Resources Research, 26*, (10), 2625-2629. Washington, D.C.: American Geophysical Union. TIC: 225235.

Tsang, Y.W. and Birkholzer, J.T. 1999. "Predictions and Observations of the Thermal-Hydrological Conditions in the Single Heater Test." *Journal of Contaminant Hydrology, 38,* (1-3), 385-425. New York, New York: Elsevier. TIC: 244160.

Tsang, Y.W. and Pruess, K. 1987. "A Study of Thermally Induced Convection near a High-Level Nuclear Waste Repository in Partially Saturated Fractured Tuff." *Water Resources Research, 23,* (10), 1958-1966. Washington, D.C.: American Geophysical Union. TIC: 240715.

USGS (U.S. Geological Survey) 2001a. *Analysis of Infiltration Uncertainty*. ANL-NBS-GS-000008 REV 00. Denver, Colorado: U.S. Geological Survey ACC: MOL.20011107.0004.

USGS 2001b. *Simulation of Net Infiltration for Modern and Potential Future Climates*. ANL-NBS-HS-000032 REV 00 ICN 02. Denver, Colorado: U.S. Geological Survey. ACC: MOL.20011119.0334.

van Genuchten, M.T. 1980. "A Closed-Form Equation for Predicting the Hydraulic Conductivity of Unsaturated Soils." *Soil Science Society of America Journal, 44,* (5), 892-898. Madison, Wisconsin: Soil Science Society of America. TIC: 217327.

Wu, Y.S.; Ritcey, A.C.; and Bodvarsson, G.S. 1999. "A Modeling Study of Perched Water Phenomena in the Unsaturated Zone at Yucca Mountain." *Journal of Contaminant Hydrology, 38,* (1-3), 157-184. New York, New York: Elsevier. TIC: 244160.

Wu, Y-S.; Zhang, W.; Pan, L.; Hinds, J.; and Bodvarsson, G.S. 2000. *Capillary Barriers in Unsaturated Fractured Rocks of Yucca Mountain, Nevada*. LBNL-46876. Berkeley, California: Lawrence Berkeley National Laboratory. TIC: 249912.

Wu, Y-S.; Zhang, W.; Pan, L.; Hinds, J.; and Bodvarsson, G.S. 2002. "Modeling Capillary Barriers in Unsaturated Fractured Rock." *Water Resources Research, 38,* (11), 35-1 through 35-12. Washington, D.C.: American Geophysical Union. TIC: 253854.

E.5.2 Data, Listed by Data Tracking Number

GS040108314224.001. Detailed Line Survey Data for Horizontal and Vertical Traverses, ECRB. Submittal date: 02/27/2004.

APPENDIX F

UNCERTAINTY IN CONTINUUM MODELS AND VAN GENUCHTEN RELATIONS (RESPONSE TO TEF 2.13 AIN-1)

Note Regarding the Status of Supporting Technical Information

This document was prepared using the most current information available at the time of its development. This Technical Basis Document and its appendices providing Key Technical Issue Agreement responses that were prepared using preliminary or draft information reflect the status of the Yucca Mountain Project's scientific and design bases at the time of submittal. In some cases this involved the use of draft Analysis and Model Reports (AMRs) and other draft references whose contents may change with time. Information that evolves through subsequent revisions of the AMRs and other references will be reflected in the License Application (LA) as the approved analyses of record at the time of LA submittal. Consequently, the Project will not routinely update either this Technical Basis Document or its Key Technical Issue Agreement appendices to reflect changes in the supporting references prior to submittal of the LA.

APPENDIX F

UNCERTAINTY IN CONTINUUM MODELS AND VAN GENUCHTEN RELATIONS (RESPONSE TO TEF 2.13 AIN-1)

This appendix provides a response for Key Technical Issue (KTI) agreement Thermal Effects on Flow (TEF) 2.13 additional information needed (AIN)-1. This agreement relates to providing additional information on the conceptual and numerical models for unsaturated zone flow and transport: specifically, the uncertainty in continuum models versus discrete fracture models and in the van Genuchten relations.

F.1 KEY TECHNICAL ISSUE AGREEMENT

F.1.1 TEF 2.13 AIN-1

Agreement TEF 2.13 was reached during the U.S. Nuclear Regulatory Commission (NRC)/U.S. Department of Energy (DOE) Technical Exchange and Management Meeting on Thermal Effects on Flow held January 8 to 9, 2001, in Pleasanton, California (Reamer and Williams 2001). The agreement resulted from the technical discussion of subissue 2: thermal effects on temperature, humidity, saturation, and flux.

The wording of this agreement is as follows:

TEF 2.13

> Provide the Conceptual and Numerical Models for Unsaturated Zone Flow and Transport AMR, Rev. 01 and the Analysis of Hydrologic Properties Data AMR, Rev. 01. The DOE will provide updates to the Conceptual and Numerical Models for UZ Flow and Transport (MDL-NBS-HS-000005) Rev 01 and the Analysis of Hydrologic Properties Data (ANL-NBS-HS-000002) Rev 01 AMRs to the NRC. Scheduled availability is FY 2002.

The DOE submitted an initial response to TEF 2.13 using a risk-informed approach (Ziegler 2003). The response was based on sensitivity studies that showed the information to be developed in addressing this KTI agreement would not be significant in determining compliance with individual and groundwater protection standards. After its review of the initial DOE response, the NRC requested additional information from the DOE to complete TEF 2.13 (Schlueter 2003).

Wording of the AIN is as follows:

TEF 2.13 AIN-1

> DOE may choose to complete Agreement TEF 2.13 by either providing: (1) additional technical information as discussed in Section 4.1 of the attachment including a technical basis demonstrating that: (i) preferential flow in fractures is not masked by the volume-averaging of coarse grid cell in continuum models; (ii) appropriate heterogeneity representing fractures are appropriate for

unsaturated flow in fractures; and (iii) the van Genuchten relations and parameters are appropriate for unsaturated flow in fractures; and (iv) the model uncertainty noted above have been addressed in all appropriate hydrologic and thermal-hydrologic process and abstraction models; or (2) additional risk information as discussed in Section 4.3 of the attachment. With regards to the latter option, the disposition of Agreement TEF 2.13 can be determined after DOE adequately address NRC's concerns with its approach to resolving agreements via risk arguments and sensitivity analyses as discussed in the January 27, 2003, risk letter.

F.1.2 Related Key Technical Issue Agreements

Agreement TEF 2.13 is related to Unsaturated and Saturated Flow under Isothermal Conditions (USFIC) 4.06, USFIC 4.01, and TEF 2.12. While TEF 2.13 is related to the use of the continuum approach and van Genuchten relations in coupled process models, USFIC 4.06 is concerned with providing justification of the continuum models for seepage calculations. USFIC 4.01 includes providing test data from the Alcove 8–Niche 3 tests for the justification of these models. TEF 2.12 involves model uncertainty. Responses to USFIC 4.01, 4.06, and TEF 2.12 are provided in Appendices C, D, and E of *Technical Basis Document No. 3: Water Seeping into Drifts*.

F.2 RELEVANCE TO REPOSITORY PERFORMANCE

Agreement TEF 2.13 is relevant to repository performance because the continuum model approach and van Genuchten relations are used in coupled process models for evaluating thermal effects, including those quantifying seepage and seepage chemistry under thermally perturbed conditions. The relevant models are the unsaturated zone flow model, the seepage calibration model, the seepage model for performance assessment, the thermal-hydrologic seepage model, and the seepage abstraction model. Outputs from these models provide feeds of seepage rate, seepage chemistry, and in-drift environment parameters to the total system performance assessment for license application (TSPA-LA).

F.3 RESPONSE

This appendix provides a technical basis demonstrating that: (1) the preferential flow in fractures is not masked by the volume averaging of coarse grid cells in continuum models; (2) appropriate heterogeneity representing fractures has been incorporated into the models; (3) the van Genuchten relations and parameters are appropriate for unsaturated flow in fractures; and (4) the model uncertainty noted above has been addressed in all appropriate hydrologic and thermal-hydrologic process and abstraction models.

Justification for the treatment of preferential flow in fractures has been documented (BSC 2003a; Liu et al. 1998). The justification for use of the continuum approach for dealing with preferential flow in fractures is as follows:

1. A traditional continuum approach assumes uniformly distributed flow patterns at a subgrid scale. Therefore, such an approach cannot be used for representing gravity-driven fingering flow and transport in fracture networks resulting from subsurface heterogeneities and nonlinearities involved in unsaturated flow. To incorporate this flow behavior into the large-scale continuum models, the site-scale unsaturated zone models uses the active fracture model. Details are discussed in Section F.4.1.1.

2. An alternative conceptual model was developed to support the finding of the continuum-approach-based thermal-hydrologic seepage model. The alternative model (for episodic finger flow) along fractures is applied to investigate the potential impact of episodic finger flow on thermal seepage. Consistent results were obtained from the continuum-approach-based model and the alternative model that is not based on the continuum approach. Details are discussed in Section F.4.1.2.

3. The comparison between continuum and discrete fracture models is provided to support the usefulness of the continuum approach for modeling flow and fractures in the unsaturated zone of Yucca Mountain. Details are discussed in Section F.4.1.3.

The second part of the response to TEF 2.13 (see Section F.4.2) presents the justification that the appropriate heterogeneity representing fractures has been incorporated into the models at different scales.

1. The treatment of site scale heterogeneity demonstrates that heterogeneities within each geologic unit have only a minor effect on the site-scale flow processes. This is documented by Zhou et al. (2003) and is summarized in Section F.4.2.1.

2. The treatment of drift scale heterogeneity was examined by liquid release testing. Uncertainty on small-scale heterogeneity was estimated by a stochastic continuum approach. Detail about drift scale heterogeneity is documented in *Seepage Calibration Model and Seepage Testing Data* (BSC 2003b) and is summarized in Section F.4.2.2.

The third part of the response to TEF 2.13 (see Section F.4.3) presents the justification for (and limitations of) using van Genuchten relations for modeling unsaturated flow in fractures. This justification is based on a study by Liu and Bodvarsson (2001).

The fourth part of the response to TEF 2.13 (see Section F.4.4) addresses NRC concerns with the treatment of uncertainties (related to fingering flow in fractures and effects of the heterogeneities) in relevant hydrologic and thermal-hydrologic process models and abstraction models. In all models, van Genuchten relations have been used to model flow in the fracture continuum, although it has not been fully evaluated.

The information in this report is responsive to agreement TEF 2.13 made between the DOE and NRC and is responsive to AIN request TEF 2.13 AIN-1. The report contains the information that the DOE considers necessary for NRC review for closure of this agreement.

F.4 BASIS FOR THE RESPONSE

F.4.1 Justification for the Use of the Continuum Approach to Deal with Preferential Flow in Fractures

Because of subsurface heterogeneity and nonlinearity involved in unsaturated flow in fractured rock, fingering flow occurs at both the fracture network scale and the single fracture scale. The NRC is concerned with the usefulness of the continuum approach in dealing with the fingering flow. A variety of approaches have been developed for modeling preferential flow in the unsaturated zone, many of them combining "fast" and "slow" flow components (Hendrickx and Flury 2001). Although complex models have been used to simulate preferential flow, in Yucca Mountain (1) large-scale fingering flow at the fracture network scale can be captured by the active fracture model (Section F.4.1.1); (2) fingering flow associated with thermal reflux is captured by an alternative model that provides results consistent with a continuum-approach-based model (Section F.4.1.2); and (3) discrete fracture model results are consistent with results obtained with the continuum model (Section F.4.1.3).

F.4.1.1 The Active Fracture Model

Liu et al. (1998) suggested that in unsaturated fractured rock, fingering flow occurs at both a single-fracture scale and a connected fracture network scale. This concept is supported in a study by Kwicklis and Healy (1993, pp. 4097 to 4099), who used numerical simulations to investigate liquid water flow in a simple, unsaturated, fracture network. They found that a large portion of the connected fracture network played no role in conducting flow when the fractures do not have uniform apertures. The study shows that fingering flow at a network scale has an important effect on large-scale flow and transport, and significantly contributes to the reduction of fracture–matrix interaction.

The active fracture concept is based on the reasoning that because of fingering flow, only portions of fractures in a connected, unsaturated fracture network contribute to liquid water flow, while others are simply bypassed. The portions of the connected fractures that actively conduct water are called active fractures. Liu et al. (1998) hypothesized that the number of active fractures in the Yucca Mountain unsaturated zone is small compared with the number of connected fractures, and that, therefore, active fractures, rather than total connected fractures, should be used in numerical models. They further hypothesized that the number of active fractures within a gridblock is large, such that a continuum approach is still valid for describing fracture flow. These hypotheses are consistent with the consideration that flowing fractures in the unsaturated zone are many and highly dispersed. Note that continuum approach may be questioned when the active fracture spacing is on the same order of gridblock size.

To use the active fracture concept to model flow and transport in fractures, Liu et al. (1998) treat active fractures as part of a homogeneous fracture continuum for a given gridblock. The active fracture model presumes gravity-dominated, nonequilibrium, preferential liquid water flow in

fractures, which is expected to be similar to fingering flow in unsaturated porous media. A liquid finger can bypass a large portion of a porous medium, which does not necessarily correspond to large pores. It is also consistent with the numerical study results of Kwicklis and Healy (1993, pp. 4097 to 4099), showing that distribution of liquid water in a connected fracture network is not necessarily determined by fracture apertures. Liu et al. (1998) relate the number of active fractures to water saturation by a parameter γ (which indicates the activity of connected fractures). This makes it possible to treat all the ramifications of the active fracture hypothesis (modified fracture capillarity, relative permeability, and fracture–matrix interaction reduction) in an integrated manner, as described by Liu et al. (1998).

The active fracture model is used in the unsaturated zone flow model. In the site-scale unsaturated zone model, γ is obtained through inverse modeling. The active fracture model uses a combination of the volume-averaged method and a simple filter to deal with fracture flow and transport. Inactive fractures are filtered out in modeling fracture–matrix interaction, flow, and transport in the fracture continuum. The use of this filtering method within a continuum approach could add the capability to capture dispersed fingering flow at a subgrid scale. (A major limitation of traditional continuum approaches was considered to be their inability to represent subgrid-scale fingering flow (Glass et al. 1996, p. 7).)

Sensitivity analyses were performed to investigate the effects of connected-fracture activity on flow and transport in the Yucca Mountain unsaturated zone (Liu et al. 1998; BSC 2004a). The impacts of uncertainty in the active fracture parameter (γ) on the simulated flow and transport were evaluated by sensitivity analyses of flow and transport simulation results and were validated for the abstraction model. Two three-dimensional flow simulations, using reduced values of active fracture parameter γ for TSw units and all units below the repository (including the units where the repository is located), respectively, were performed to carry out the analyses and validation. By comparing liquid saturation, water potential, and the percolation flux obtained by these two simulations with those obtained by simulations using unmodified (calibrated) γ values, it was found that the changes in liquid saturation, water potential, and percolation flux are rather small. In general, the flow fields are not very sensitive to the active fracture parameter γ. On the other hand, tracer transport times were found to be sensitive to the value (BSC 2003c, Section 6.8). The implementation of the active fracture matrix in the abstraction model was shown to reproduce the qualitative features of the breakthrough curves documented in the process model reports, adding confidence to the unsaturated zone model (BSC 2004a, Section 7.3.3).

Sensitivity analyses indicate that calibrated γ value (about 0.6) for the hydrostratigraphic units underneath the repository horizon provided conservative estimates of transport times through the unsaturated zone (BSC 2003c, Section 6.8.2) when the tracers were released directly into the repository fractures. However, this value of γ leads to an optimistic breakthrough estimate if the tracers are released into the matrix of the repository gridblocks (BSC 2003d, Section 6.3.3). The simulation results of water pore velocity in connected fractures have been provided by Liu et al. (1998, Figure 12). For a γ value of 0.8, the resultant fracture pore velocity is about 10^{-4} m/s (in the TSw unit), or 3,153.6 m/yr. This velocity corresponds to very fast flow paths. Therefore, the fingering fast flow behavior can be captured by using different γ values in the active fracture model.

F.4.1.2 Alternative Model for Preferential Flow in Fractures during the Thermal Period

As mentioned in Section F.1, the NRC is concerned that unsaturated zone flow models may not adequately represent preferential flow along a fracture. Specifically, it is concerned that fingering flow may be inadequately represented by the volume-averaging approaches in continuum models for reflux during the thermal period, as well as potential breaching of the dryout zone by transient or steady-state finger or rivulets of water along a fracture (Schlueter 2003). This issue is addressed in Section F.4.1.2.1. The arguments used here are documented in *Drift-Scale Coupled Process (DST and TH) Seepage) Models* (BSC 2003a, Section 6.2).

F.4.1.2.1 Alternative Conceptual Model

Unsaturated fracture flow may occur in fast-flowing preferential pathways (thin fingers) that drain downward intermittently. Water buildup in the condensation zone above waste emplacement drifts can provide a potential source of such downward finger flow, carrying water at flow rates much larger than the average percolation under ambient conditions. Such high-flux conditions may promote the potential of seepage during the thermal period at Yucca Mountain because finger flow may penetrate far into the superheated rock zone (i.e., rock temperature above the boiling point of water) around waste emplacement drifts.

The alternative conceptual model (also referred to as the thermal-hydrologic model for episodic finger flow) is applied to investigate the potential impact of episodic finger flow on thermal seepage. The thermal-hydrologic model for episodic finger flow analyzes the fate of episodic preferential flow events that originate somewhere in the condensation zone above the repository and percolate downward toward the emplacement drifts. Figure F-1 shows an illustration of episodic fingers flowing through fractures and penetrating into the superheated rock in the vicinity of waste emplacement drifts. As flow arrives at the superheated rock region around drifts, water begins to boil off. Depending on the magnitude and duration of each flow event and on the temperature and pressure conditions in the fractured rock, the water may vaporize above the drift crown, or it may penetrate far into the superheated region and reach the drift.

The alternative model is an improved version of the model developed in *Infiltration of a Liquid Finger Down a Fracture into Superheated Rock* (Phillips 1996). The Phillips model was modified because it yielded an unrealistic solution at early times. The alternative conceptualization is highly simplified and, therefore, conservative, particularly because it is not clear if such finger-flow behavior is characteristic for Yucca Mountain, and the solution assumes fracture geometries that are not realistic (vertical continuous fracture connecting high-saturation condensation zone with drifts).

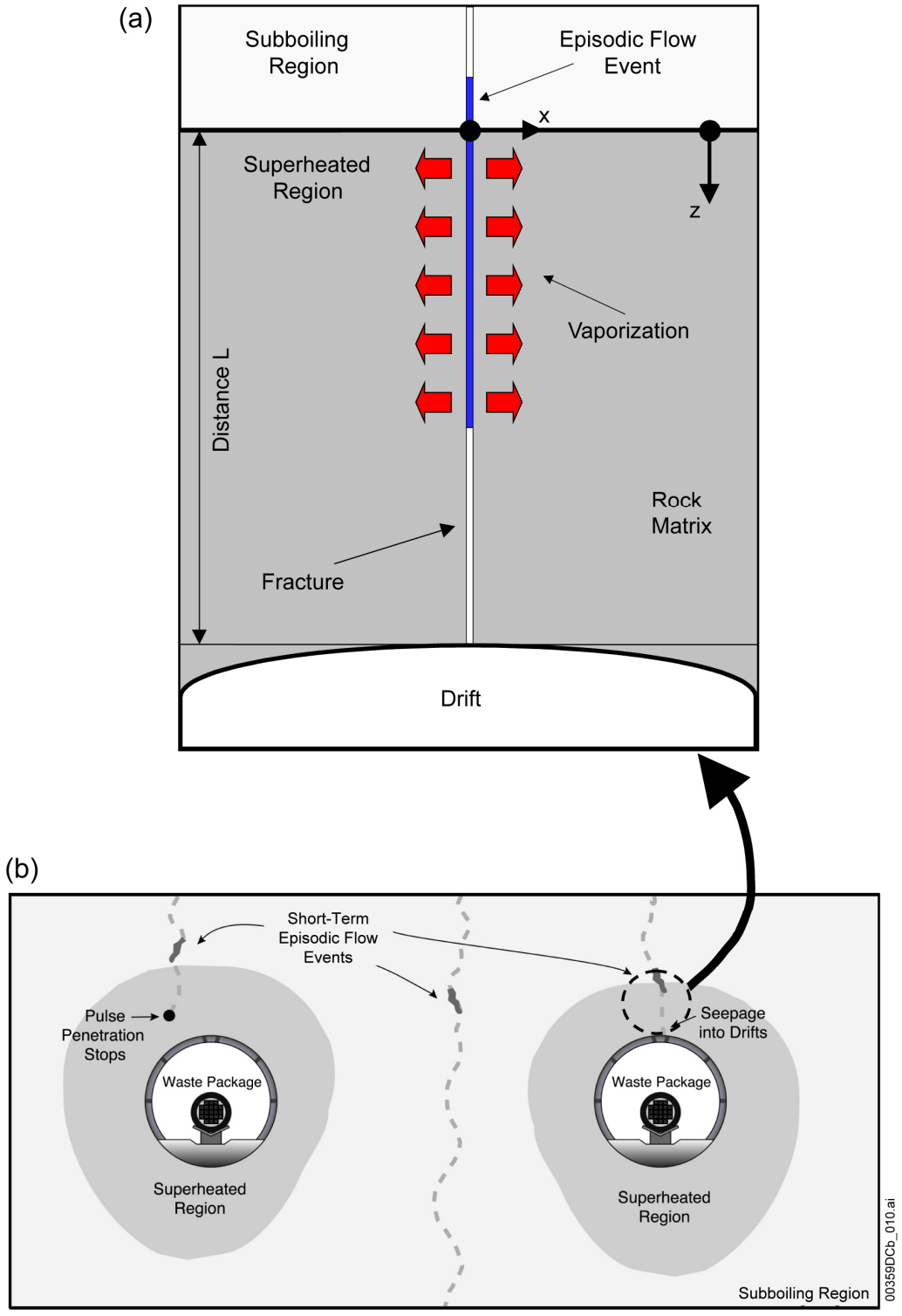

Source: BSC 2003a, Figure 6.3-1.

NOTE: The drip shield above waste packages is not shown here for simplicity.

Figure F-1. Illustration of Conceptual Model for Finger Flow in a Vertical Fracture above a Drift with Heat Conduction from the Adjacent Rock (a) and Episodic Finger Flow in Unsaturated Fractured Rock in the Vicinity of Waste Emplacement Drifts (b)

F.4.1.2.2 Modeling Procedure

The first step in applying the thermal-hydrologic model for episodic finger flow is to derive estimates for the possible characteristics of episodic finger flow at Yucca Mountain. Experimental data from a comprehensive laboratory study by Su et al. (1999) are used for that purpose, and a simplified finger-flow model for downward drainage is developed. Details on the experimental approach are given in *Drift-Scale Coupled Processes (DST and TH) Seepage* (BSC 2003a, pp. 138 to 142). The second step consists of simulating the fate of such episodic finger-flow events when the flow penetrates into the superheated rock region above waste emplacement drifts using the semianalytical solution of Birkholzer (2002; BSC 2003a). The semianalytical solution of Birkholzer (2002; BSC 2003a) is used to determine the maximum penetration distance of episodic fingers subject to vigorous vaporization from the hot rock. In case the flow from these events penetrates through the entire superheated zone above drifts, the solution also gives the total amount of water arriving at the drift crown. The solution is implemented at several discrete times after waste emplacement to cover the range of rock temperature conditions and extent of superheated zone around drifts. Details on the semianalytical solutions are given in *Drift-Scale Coupled Processes (DST and TH) Seepage Models* (BSC 2003a, pp. 142 to 144). The third step consists of evaluating the results; namely, the relative percentage of water arriving at the drift crown at different times after emplacement, in relation to the perturbed flow situation above the drifts at these times (i.e., the elevated downward flux from the condensation zone toward the drift).

The long-term evolution of thermal-hydrologic conditions in the rock is accounted for by applying the thermal-hydrologic model for episodic finger flow at 11 selected times after waste emplacement, covering the time period during which repository temperatures remain above boiling (about 1,000 years). The simulation result of the thermal-hydrologic model for episodic finger flow demonstrated that finger flow is not able to penetrate through the superheated rock during the first several hundred years of heating, when rock temperature is high and boiling conditions exist in a sufficiently large region above the drifts. Only later, when the boiling zone is small and the impact of vaporization is limited, can finger flow arrive at the drift crown. Details about the application of the alternative conceptual model and results can be found in *Drift-Scale Coupled Processes (DST and TH) Seepage Models* (BSC 2003a, pp. 144 to 159).

F.4.1.2.3 Comparison between the Alternative Conceptual Model and Thermal-Hydrologic Seepage Model

The alternative conceptual model was used to corroborate the results and conclusions of the thermal-hydrologic seepage model. The thermal-hydrologic seepage model (the base-case model) is based on the continuum approach, incorporates all relevant thermal-hydrologic processes, and accounts for small-scale heterogeneity in the drift vicinity. The thermal-hydrologic seepage model was applied to explicitly simulate thermally perturbed channelized fluid flow down to the drift and to directly calculate transient seepage rates during the period of elevated temperature. However, it is not clear whether process models using a continuum representation are able to capture such small-scale fingering flow processes, even though small-scale heterogeneity in fracture permeability has been incorporated. Therefore, the alternative conceptual model was applied to investigate the potential impact of episodic finger flow on thermal seepage.

The thermal-hydrologic model for episodic finger flow used a conceptualization of unsaturated fracture flow that is very conservative with respect to the potential for thermal seepage. The assumed finger-flow events are fast and intense compared to the average flow conditions generally considered in process models like the thermal-hydrologic seepage model, and vaporization effects are limited as a result of the small cross-sectional area between the draining water and the hot rock. These conditions, along with a simplified one-dimensional finger-flow model representing continuous vertical fractures, create an adverse environment for the vaporization barrier above heated waste emplacement drifts.

As an example, Figure F-2 shows the results of a thermal seepage simulation for the Topopah Spring Tuff lower lithophysal unit (Tptpll unit), where the majority of the emplacement drifts will be located. This simulation assumes a flow-focusing factor of 10 (BSC 2003a, Section 6.2.3) and a fracture capillarity-strength parameter equal to those used to evaluate seepage in the Tptpmn unit.

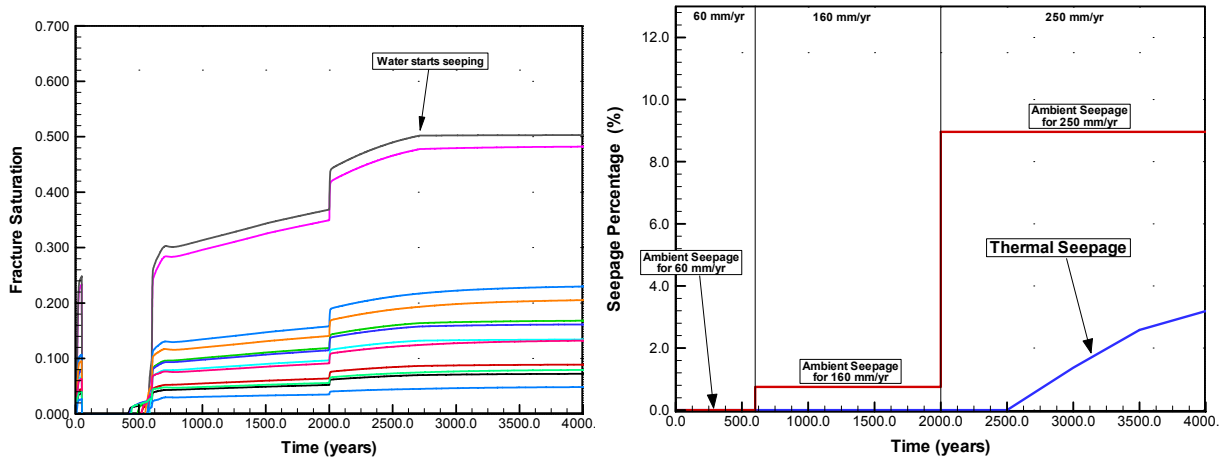

(a) (b)

Source: BSC 2003a, Figure 6.2.3.2-2.

NOTE: (a) Fracture saturation is shown for all rock discretization elements along the drift periphery from the crown to the springline. (b) Seepage rate in percent is shown for thermal run and long-term ambient runs.

Figure F-2. Thermal-Hydrologic Conditions for Tptpll Submodel with Flow-Focusing Factor of 10, Simulation Case LL-HET-02, Realization 1

In general, no water arrives at the drift during the boiling period. As rock temperature decreases and the first stepwise change in infiltration occurs at 600 years, the saturation values build up strongly, while significant variability in saturation becomes evident. However, no saturation values reach the seepage threshold saturation of 0.5, and the seepage percentage is zero at all times. For the infiltration scenario with a flow-focusing factor of 10, saturation buildup is faster and more pronounced. Eventually, between 2,500 and 3,000 years after emplacement, fracture saturation in one gridblock at the wall reaches the threshold value, so that water starts seeping into the drift (Figure F-2). The thermal seepage rate is small compared to the respective long-term ambient seepage rates. At the end of the simulation period, the thermal seepage is at about 3.19%, compared to the long-term ambient value of the glacial transition period of 8.96%.

For the conceptual model, Figure F-3 illustrates the maximum penetration distance of the flow event and the percentage of water arriving at the drift for the 12 selected time steps. In the Tptpll, the vaporization barrier is fully effective for the first 600 years after emplacement because the superheated rock zone is large enough to avoid full penetration. Compared with the Tptpmn, water arrival at the drift crown starts later, and the amount of water is smaller, for the Tptpll conditions. This is also reflected in Figure F-4, where the combined effects of flux perturbation and vaporization are considered. Though this perturbation is more significant than in the Tptpmn (with a maximum downward percolation of about 97 mm/yr at 75 years, giving a flux-elevation factor of 16.1), the resulting potential for water arrival at the drift crown is very small, and seepage is not to be expected.

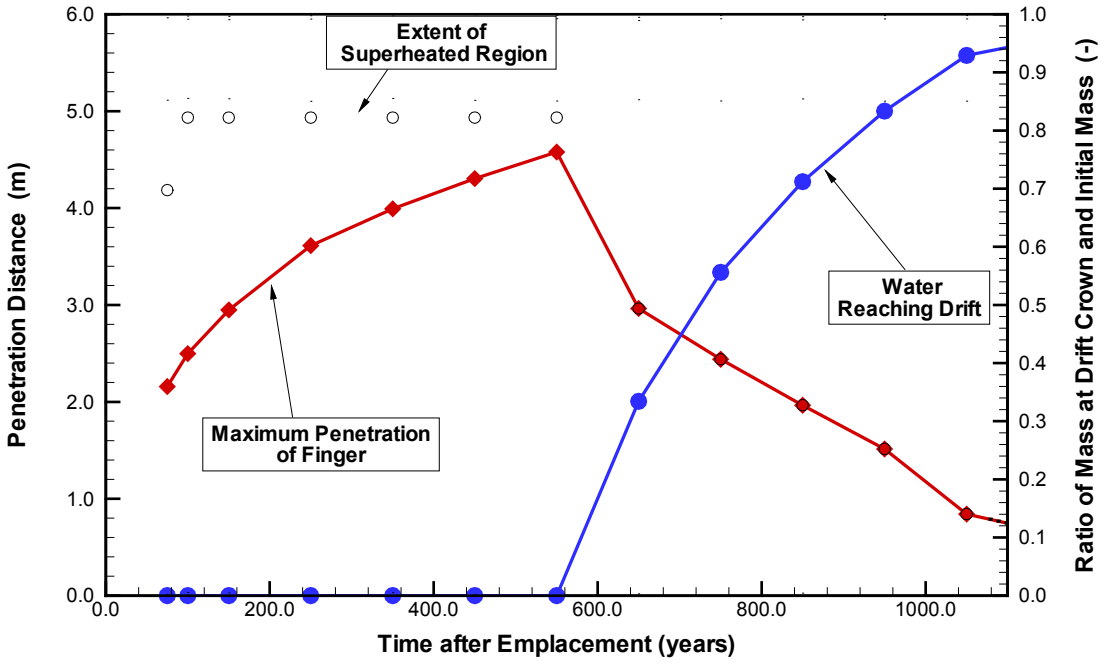

Source: BSC 2003a, Figure 6.3.3-2.

NOTE: Finger width is 1 mm.

Figure F-3. Maximum Penetration and Percentage of Water Mass Arriving at Drift Crown for Case 1 (Tptpll Unit) at 12 Different Time Steps after Waste Emplacement

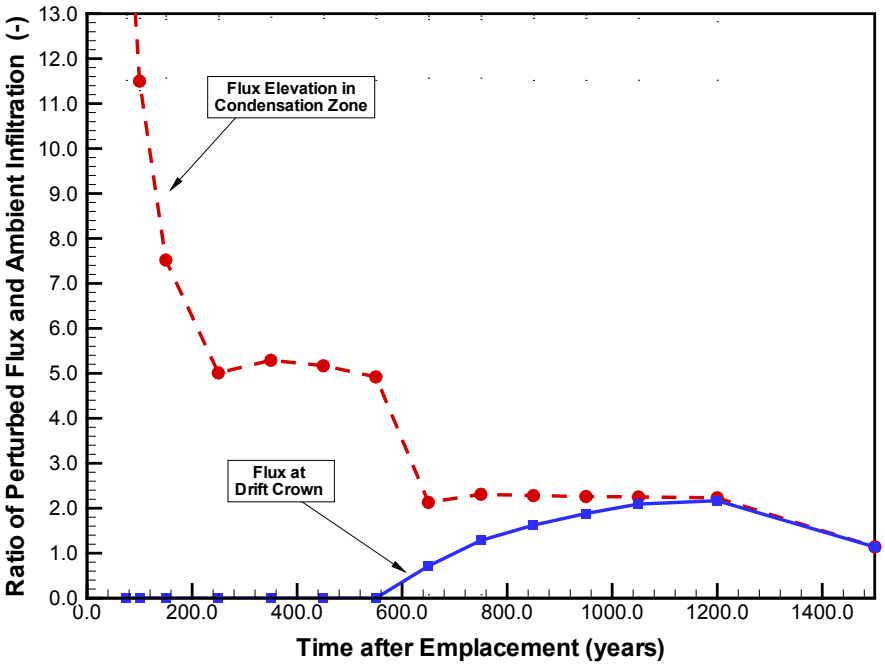

Source: BSC 2003a, Figure 6.3.3-3.

NOTE: The red line shows flux ratio in the condensation zone as simulated by the thermal-hydrologic seepage model. The blue line shows the flux ratio of water at the drift crown, including the effect of vaporization. Finger width is 1 mm.

Figure F-4. Ratio of Thermally Perturbed Vertical Flux and Ambient Percolation for Case 1 (Tptpll Unit) at 14 Different Time Steps after Waste Emplacement

Although the alternative conceptual model is not based on the continuum representation of unsaturated fracture flow, it was demonstrated that results of the alternative conceptual model are fairly consistent with the process-model results obtained with the thermal-hydrologic seepage model. The simulation results of the thermal-hydrologic model for finger flow and the base case model indicated that finger flow is not able to penetrate through the superheated rock during the first several hundred years of heating, and finger flow will arrive at the drift crown at a much later time (BSC 2003a). Thus, the alternative conceptual model results clearly support the main findings of the thermal-hydrologic seepage model, adding confidence in model results and reducing conceptual model uncertainty.

F.4.1.3 Comparison between Continuum and Discrete Fracture Network Models

The NRC is concerned with the usefulness of the continuum approach for modeling flow and fractures in the Yucca Mountain unsaturated zone (Schlueter 2003). Section F.4.1.3.1 presents comparisons between continuum and discrete fracture network models (Finsterle 2000). The comparison of seepage study was performed in drift-scale. The continuum approach is expected to be more valid at larger scale (e.g., site-scale unsaturated zone model). In addition, Appendix D of *Technical Basis Document No. 3: Water Seeping into Drifts* provides discussion of continuum approach for seepage.

Discrete fracture network models are considered to be conceptually and visually appealing alternatives to continuum approaches. This model involves the stochastic generation of fracture networks whose geometry is statistically similar to that seen on fracture trace maps or borehole logs. In addition to the geometric information, fracture hydraulic properties must be determined by calibration or derived from aperture-distribution data before flow and transport simulations can be performed. This key process and some of its pitfalls have been described in detail by Cacas et al. (1990) and Dverstorp and Andersson (1989). Moreover, when considering unsaturated flow through fracture networks, various assumptions must be made regarding phase occupancy of fracture segments, accessibility of certain portions of the fracture network, entrapment of wetting and nonwetting phases, and flow along and across fracture intersections. Flow channeling within a fracture plane—already significant in fully saturated media—becomes increasingly complex under unsaturated flow conditions. All these aspects must be conceptualized and implemented in a defensible discrete fracture network model if such an approach is chosen.

The discreteness of unsaturated fracture flow and seepage phenomena suggests the use of a discrete fracture network model for seepage studies at Yucca Mountain. The continuum approach was chosen because it was considered appropriate for the purpose of seepage prediction into waste emplacement drifts. The following sections summarize studies comparing the two approaches, demonstrating that the results obtained with one model are consistent with the other, provided that each model is calibrated against seepage data (see Section F.4.1.3.1).

F.4.1.3.1 Seepage Predictions with Discrete Fracture Network and Continuum Model

Finsterle (2000) compared seepage predictions calculated with a fracture-continuum model to those obtained with a discrete fracture network model. The models were calibrated against one another (the discrete model providing the synthetic data) to account for the calibration step involved in the development of the continuum model. The study involved the following steps:

1. A model with a complex network of discrete features was developed (see Figure F-5a). The purpose of the model was to produce discrete flow behavior and localized seepage events (see Figure F-5b). Unsaturated flow simulations performed with this discrete fracture network model are considered to represent the response of a fractured system.

2. Air-injection tests, liquid-release experiments, and seepage under natural flow conditions were simulated using the discrete fracture network model to generate synthetic characterization, calibration, and confirmation data, respectively.

3. A simplified heterogeneous fracture continuum model was developed, based on the available synthetic air-permeability data (see Figure F-6).

4. Effective parameters were determined by calibrating the fracture-continuum model against the synthetic liquid-release test data.

5. Responses from additional liquid-release tests were predicted with the continuum model and compared to results obtained with the discrete fracture network model.

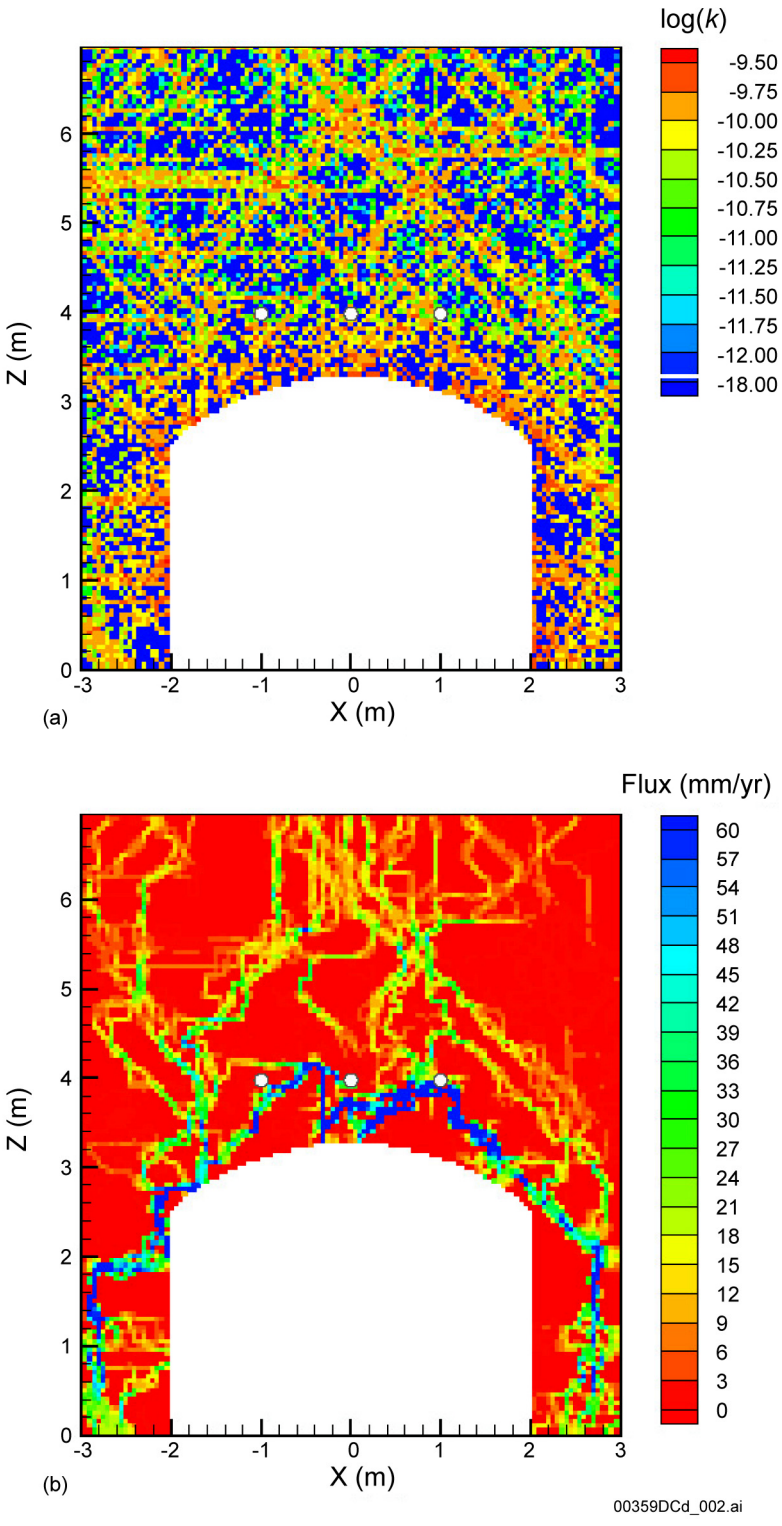

Source: Finsterle 2000, Plate 1.

NOTE: (a) High-resolution permeability field; (b) Discrete flow path and discrete seepage behavior.

Figure F-5. Two-Dimensional Discrete Fracture Network Model

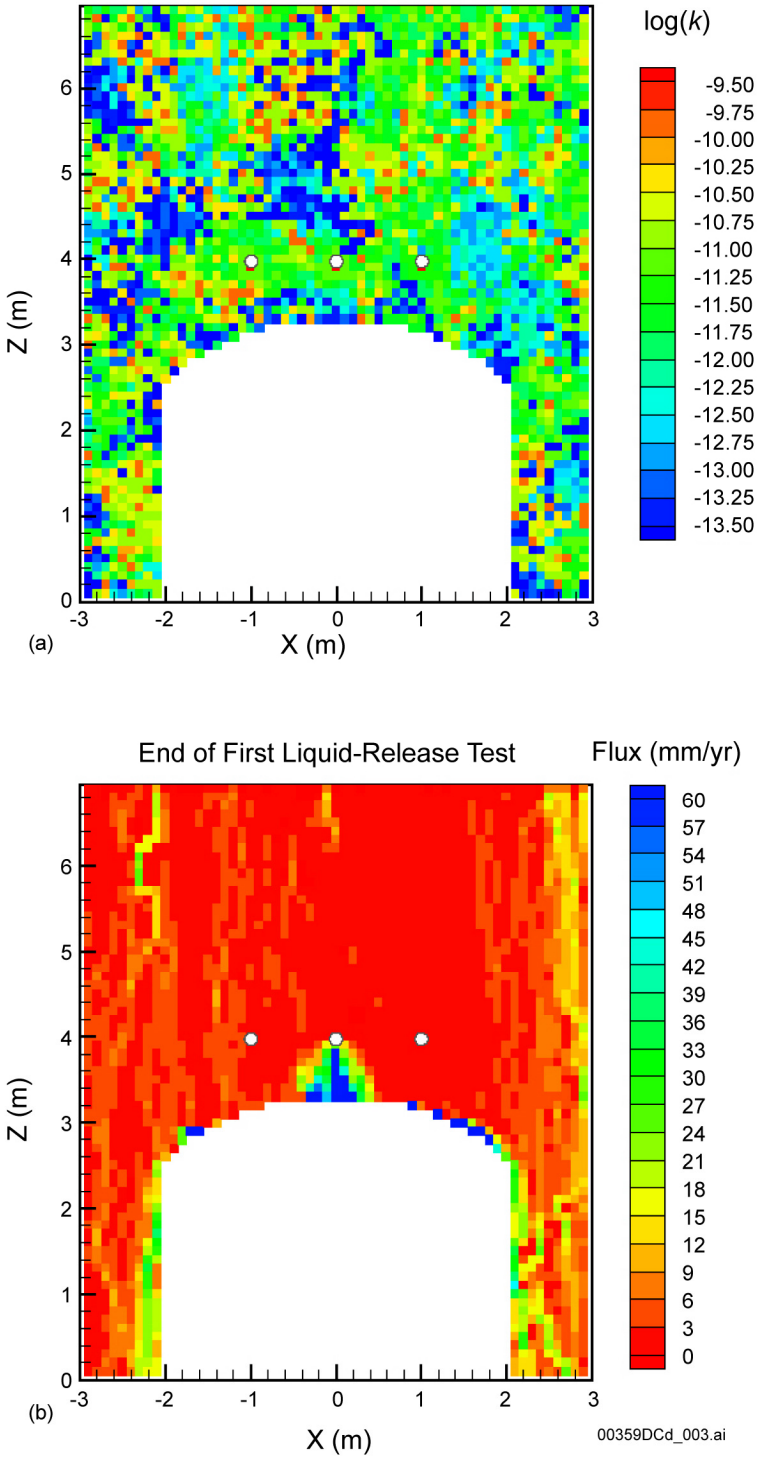

Source: Finsterle 2000, Plate 2.

NOTE: (a) Permeability field; (b) Flow field at end of simulated liquid-release test.

Figure F-6. Two-Dimensional Fracture Continuum

6. The critical performance test for the continuum model is the examination of its ability to predict unobservable quantities (e.g., the seepage threshold and seepage rates under low percolation conditions). The fracture continuum model predictions were thus compared to the calculated response from the discrete system.

The main purpose of the modeling study was to gain confidence in the appropriateness of the continuum model to simulate and predict seepage into underground openings excavated from fractured rock. However, the study inherently contains a comparison between the two modeling approaches. The synthetically generated data could be replaced with actual seepage-rate data from liquid-release tests to which both models are calibrated. Subsequently, both models are used to estimate the seepage threshold under natural percolation conditions. Both models yield consistent results (see Figure F-7).

The comparison between the two models uses the extreme assumption that all fractures are perfectly parallel to the drift axis. Even under these extreme conditions, where in-plane flow diversion is prevented, the calibrated continuum model yields reasonable seepage predictions for conditions that are different from those used during calibration.

F.4.1.3.2 Summary

Continuum and discrete modeling approaches yield similar results for seepage problems at the waste emplacement drift. The use of the continuum approach is supported by the study of Finsterle (2000), who demonstrated that the continuum approach can capture flow behavior generated from a discrete feature model. The parsimony of the continuum model, its computational efficiency, and its support by available field data are considered advantages that warrant use of it for seepage studies at Yucca Mountain. Most importantly, the continuum model is validated against field data in the middle nonlithophysal zone and lower lithophysal zone and is well integrated into the comprehensive data analysis and modeling approach for studying the performance of the unsaturated zone at Yucca Mountain. The fact that there is no perched water in the fractured welded tuffs implies that fractures in these units are very well connected. This supports the use the continuum approach.

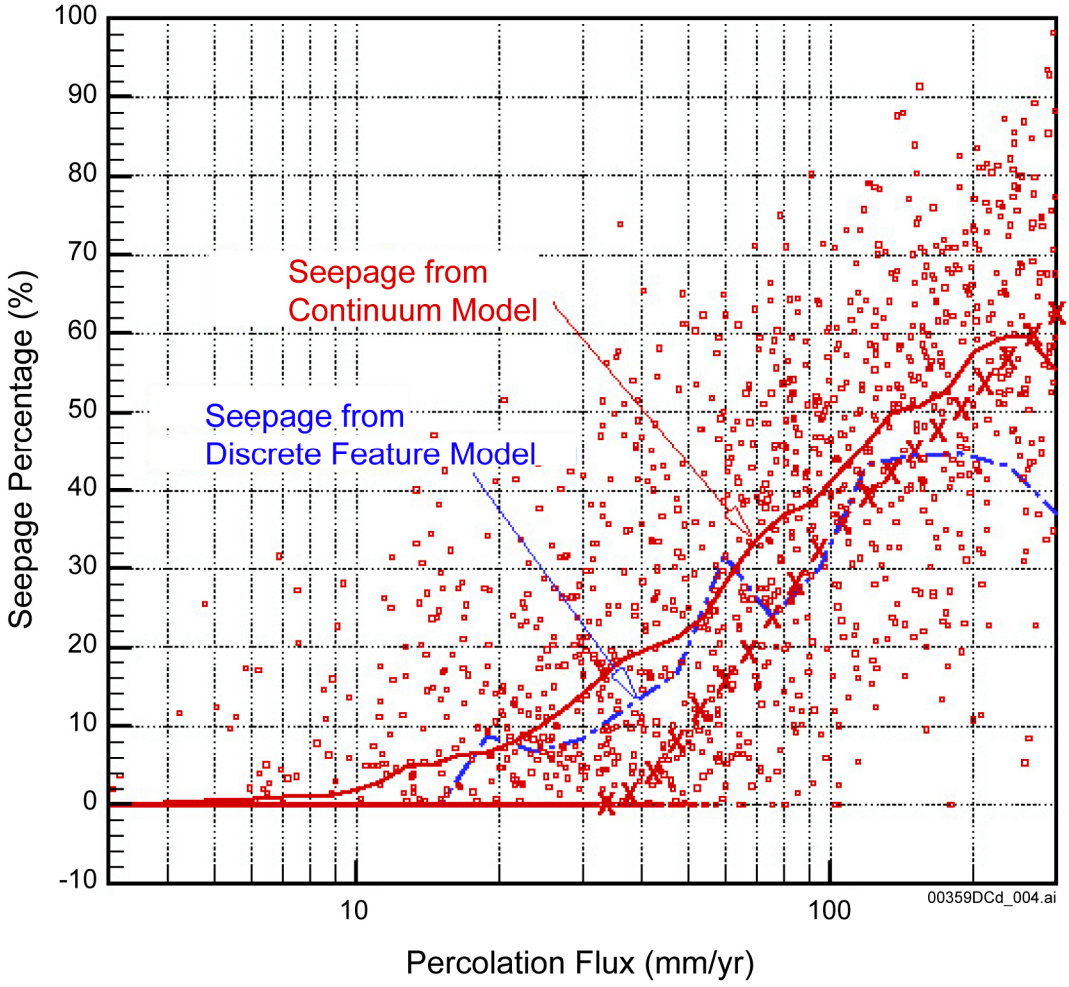

Source: Finsterle 2000, Figure 3.

NOTE: Prediction of seepage percentage with fracture continuum model shown with solid line; results from Monte Carlo simulations shown with dots; seepage data provided by the discrete fracture network model shown with the dash-dotted line. The Xs represent the prediction based on the realization of the permeability field that was used to calibrate the model.

Figure F-7. Prediction of Seepage Percentage with Fracture Continuum Model, Including Results from Monte Carlo Simulations, and Comparison to Seepage Data Provided by the Discrete Fracture Network Model

F.4.2 Justification that the Appropriate Heterogeneity Representing Fractures Has Been Incorporated into the Models

Heterogeneities exist at different scales within both the fracture and matrix continua in the Yucca Mountain unsaturated zone. Treatment of subsurface heterogeneity at different scales is important for modeling flow and transport processes. In the following sections, detailed explanations of treatment of heterogeneities at site scale and drift scale are presented. Details about treatment of site-scale heterogeneity in unsaturated zone flow models are documented in *UZ Flow Models and Submodels* (BSC 2003c). The treatment of drift-scale heterogeneity is documented in *Seepage Calibration Model and Seepage Testing Data* (BSC 2003b).

F.4.2.1 Treatment of Heterogeneity at Site Scale

A geology-based deterministic approach, in which an entire model layer is assigned uniform properties, is used mainly for representing subsurface heterogeneity and modeling site-scale flow and transport in the Yucca Mountain unsaturated zone.

The key justification for the above approach is that the overall behavior of site-scale flow and transport processes is determined mainly by relatively large-scale heterogeneities associated with the geologic stratification of the mountain. Stratification and faulting, which places units with highly different properties against each other, are the heterogeneities within the unsaturated zone. Within the same geologic unit, hydrologic properties are relatively uniformly distributed because of the intrastrata homogenization induced by tuff depositional environments. This justification is also consistent with the field observation that matrix saturation distribution is relatively uniform within a given geologic unit (CRWMS M&O 2000, Section 6.4.3).

Zhou et al. (2003) demonstrated the validity of this approach in dealing with subsurface heterogeneity. They used a two-dimensional vertical cross section in the east-west direction through borehole USW UZ-14 to investigate the effect of multiscale heterogeneity on unsaturated flow and transport within the unsaturated zone. Specifically, they generated and used random fields of three selected properties: matrix permeability, k_m; matrix van Genuchten parameter, α_m; and fracture permeability, k_f (Zhou et al. 2003, Figure 13). For comparison, they employed different sets of rock property distributions in three cases. In these cases, mean rock properties for a given geologic layer are the same. In Case A, the layered approach mentioned above was used. In Case B, stochastically generated k_f variability was considered within a geologic layer. In Case C, variabilities of all the selected rock properties were included, with the variabilities determined from the measured hydrologic properties. Thus, Case A only considers large-scale heterogeneity, while Cases B and C include small-scale heterogeneity within a geologic unit.

Figure F-8 shows comparisons of vertical water fluxes within the matrix and fractures along the repository zone for three cases. Although relatively large differences exist for the water flux in the matrix, distributions of water fluxes in fractures are very similar for these three cases. Because the matrix flux corresponds to only a small percentage of total water flux, the three cases essentially provide similar water flow fields at the site scale. Zhou et al. (2003, Figure 17) also compared simulated results for tracer transport from the repository to the water table, again finding that results were similar for the three cases.

In summary, the study of Zhou et al. (2003) clearly demonstrates that heterogeneities within each geologic unit have only a minor effect on the site-scale flow processes.

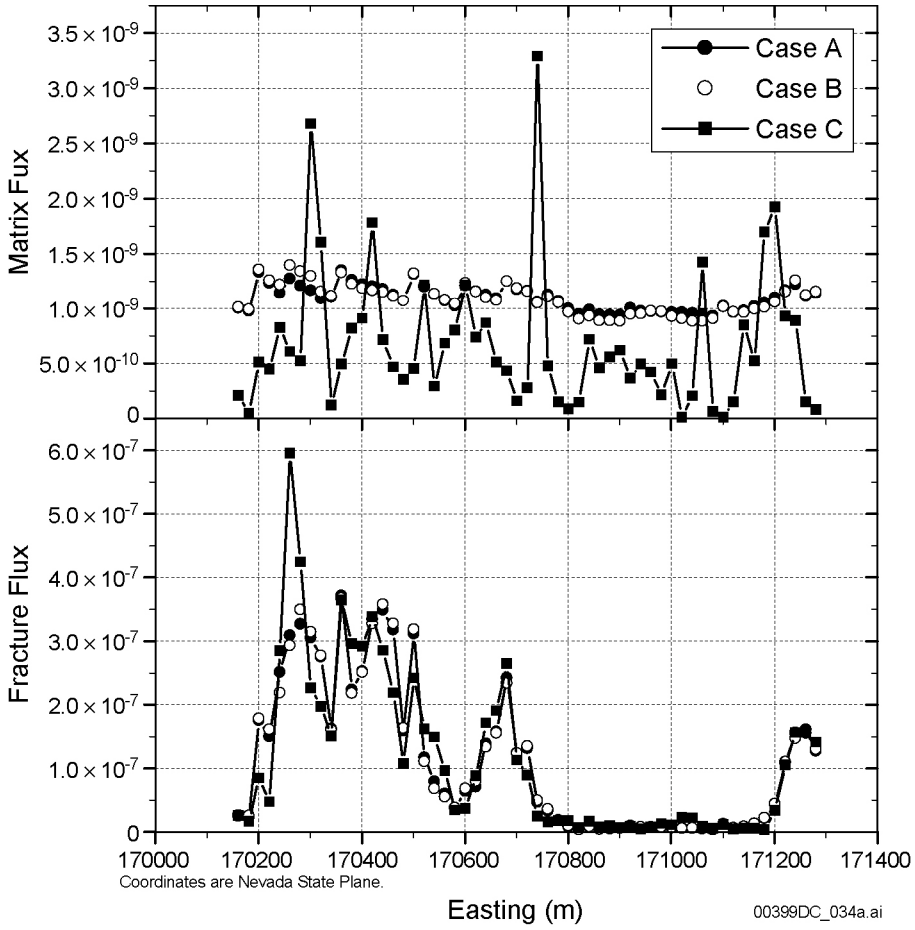

Source: Zhou et al. 2003, Figure 16.

Figure F-8. Comparison of Simulated Matrix and Fracture Flux at the Repository Horizon in Cases A, B, and C

F.4.2.2 Drift-Scale Heterogeneity, Model Calibration, and Validation

Small-scale heterogeneities within each geologic layer may be important for seepage processes at the drift scale. At the drift scale, heterogeneity was examined using liquid-release tests at various sites along the Exploratory Studies Facility and the Enhanced Characterization of the Repository Block (ECRB) and were incorporated into the seepage calibration model (BSC 2003b).

Models of niches and the ECRB Cross-Drift (summarily referred to as the seepage calibration model) are calibrated against late-time seepage-rate data from numerous liquid-release tests conducted in several boreholes in both the middle nonlithophysal zone and the lower lithophysal zone. Early-time seepage data are discarded because they are affected by storage effects and the properties of a few fractures connecting the injection interval with the opening. These fractures are not necessarily representative of the fracture network that is activated in flow diversion around the entire opening under steady-state conditions. Late-time data are more representative of near-steady conditions and are less influenced by storage effects. Moreover, the relatively large amount of released water at late time has likely encountered a larger portion of the capillary

barrier. Consequently, the late-time seepage data better reflect average conditions on the scale of interest.

Measured seepage-rate data from 22 liquid-release tests performed in boreholes above Niches 3 (also referred to as Niche 3107), 4 (also referred to as Niche 4788), and 5 (also referred to as Niche 1620), and along the ECRB Cross-Drift were used to calibrate the seepage calibration model and to estimate the seepage-relevant, model-related van Genuchten capillary-strength parameter $1/\alpha$. The remainder of the seepage-rate data was used to validate the seepage calibration model (i.e., to determine whether it is appropriate and adequate for its intended use). The choice of the tests used for calibration and validation is discussed in *Seepage Calibration Model and Seepage Testing Data* (BSC 2003b, Section 6.6.3.2).

Examples of calibrated liquid-release tests conducted along the ECRB Cross-Drift and in Niche 5 are shown in Figure F-9. For the tests conducted along the ECRB (Figure F-10a, F-10b, and F-10c), a significant component of the fluctuations in both the simulated and observed seepage rates are a result of variations in the relative humidity and, thus, evaporation potential in the ventilated drift; the effect is appropriately captured by the model. No such fluctuations are observed in the Niche 5 test, where relative humidity was approximately constant at 85%.

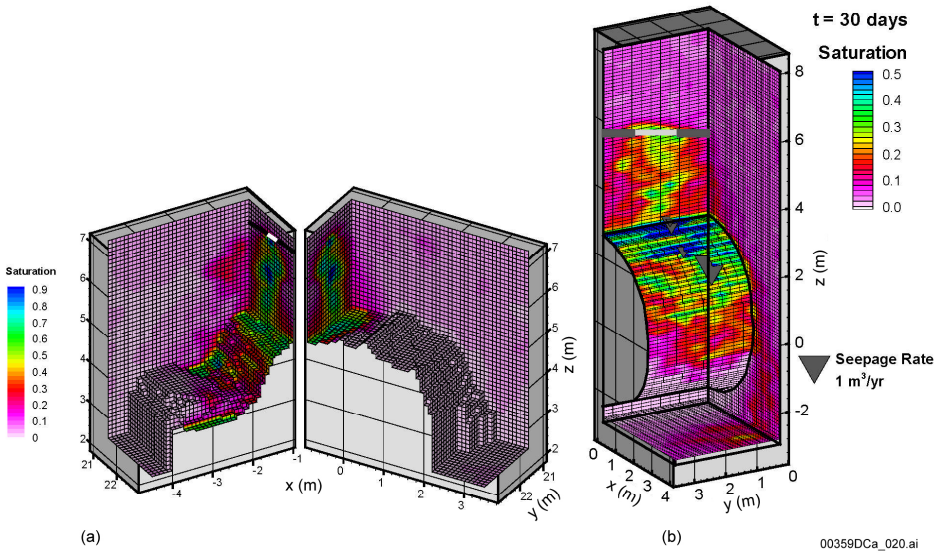

Source: BSC 2003b, Figures 26a and 21d.

Figure F-9. Saturation Distributions at the End of a Liquid-Release Test Conducted in (a) Niche 5 and (b) the Enhanced Characterization of the Repository Block, as Simulated with the Calibrated Seepage Process Model

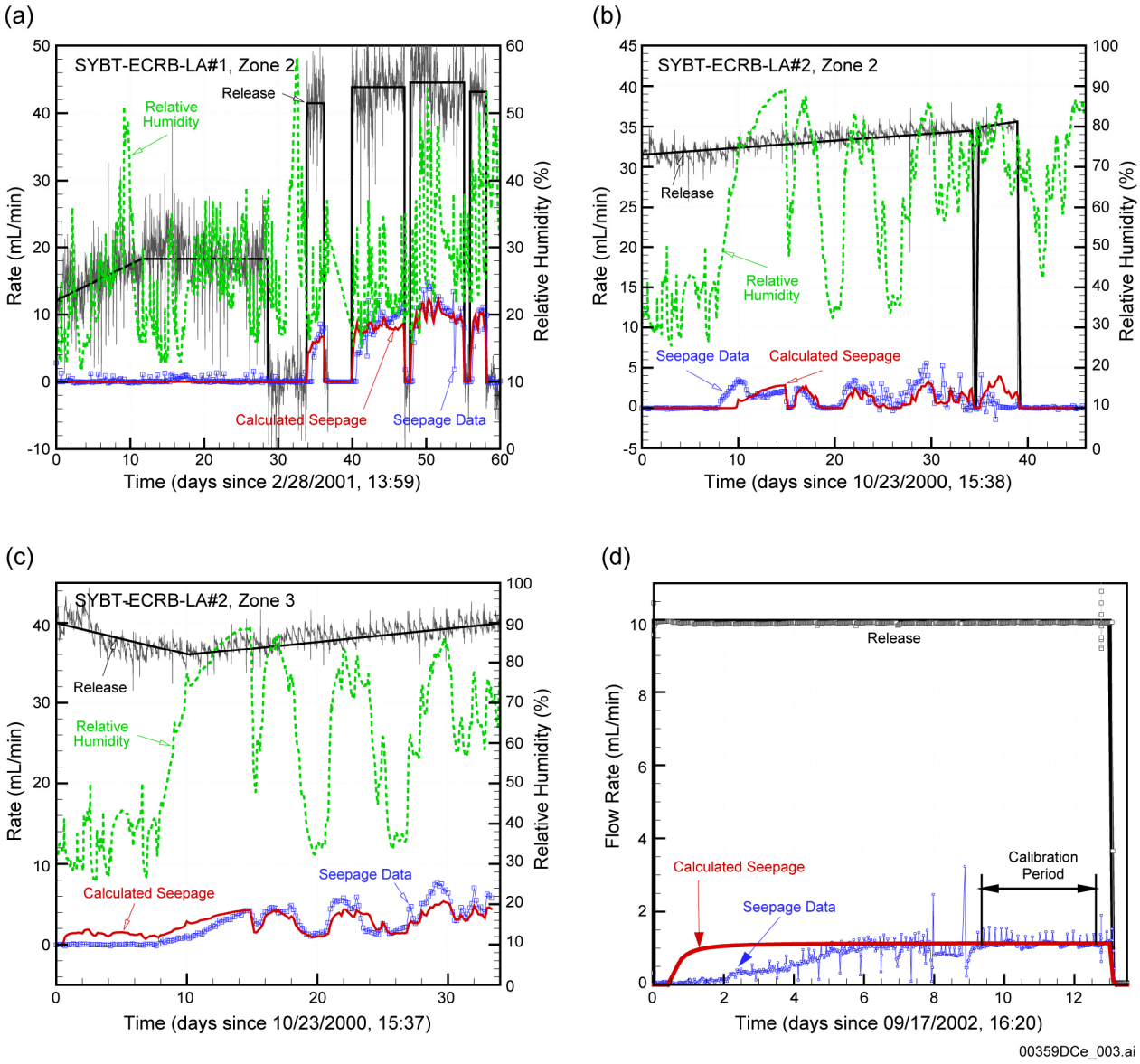

Source: BSC 2003b, Figures 19, 22, 23, and 25.

NOTE: The gray line represents the measured release rate, which is approximated in the model by the black line. Blue symbols represent measured seepage-rate data; the red line is calculated with the calibrated models. The green line represents the relative humidity used to prescribe the evaporation boundary condition. Relative humidity in Niche 5 was constant at approximately 85%.

Figure F-10. Calibration of Seepage Rate Data from Liquid Release Tests in Zone 2 of Boreholes (a) SYBT-ECRB-LA#1 and (b) SYBT-ECRB-LA#2; (c) Zone 3 of Borehole SYBT-ECRB-LA#2; and (d) Borehole 4 in Niche 5

Figure F-11 shows examples of validation runs, in which seepage rates for liquid-release tests conducted in Niche 3 were predicted with the calibrated model using a single parameter set and compared to measured data that had not been used for model calibration. Linear error propagation analysis yielded the uncertainty of the model prediction as a result of uncertainty in the input parameters. The data fall within the range of predicted seepage rates. Based on the acceptance criteria outlined in *Seepage Calibration Model and Seepage Testing Data* (BSC 2003b, Section 7.2), seven of the eight test predictions are considered acceptable.

The capillary-strength parameter for each tested borehole interval was determined by calibrating the model against multiple tests using different liquid-release rates. Some of these release rates induced a local percolation flux that was above the seepage threshold (i.e., water dripped into the opening and yielded seepage-rate data valuable for calibration). However, tests were also performed below the seepage threshold. Moreover, the model was validated against tests conducted above and below the seepage threshold. The system was probed and the model was validated for the critical range of percolation rates about the seepage threshold. Seepage predictions for natural percolation fluxes that are even less than the low fluxes (below the seepage threshold) induced during the low-rate tests will yield the correct result, namely, zero seepage. A high-infiltration climate or strong flow focusing can cause the natural local percolation flux to exceed the seepage threshold.

F.4.2.3 Summary of Experimentally Observed Heterogeneity

Experimental data and models based on this data have demonstrated heterogeneity existing at different scales in Yucca Mountain. At the site scale, hydrologic properties within each geologic unit are assumed to be homogeneous, which has been shown to be reasonable for that scale. For example, the study of Zhou et al. (2003) clearly demonstrates that heterogeneities within each geologic unit have only a minor effect on the site-scale flow processes. However, small-scale heterogeneity also exists and has the potential to affect drift-scale water flow processes. Specifically, seepage properties have been demonstrated to be spatially variable using liquid-release tests at various sites along the Exploratory Studies Facility and the ECRB Cross-Drift. The spatial variability in the estimated van Genuchten capillary-strength parameter $1/\alpha$, which is an important parameter for determining the seepage threshold, is relatively large compared to estimated uncertainty at a given location. The main contribution of experimentally observed heterogeneity to estimating modeling uncertainty is that the small-scale heterogeneity can be described stochastically. However, it has also been shown that this small-scale uncertainty from seepage-rate data does not lead to significant uncertainty in model parameter estimates. Therefore, the capillary strength parameters determined using seepage data collected at the relatively high-rate liquid-release tests provide a solid basis for seepage predictions under low and high natural percolation fluxes at that scale.

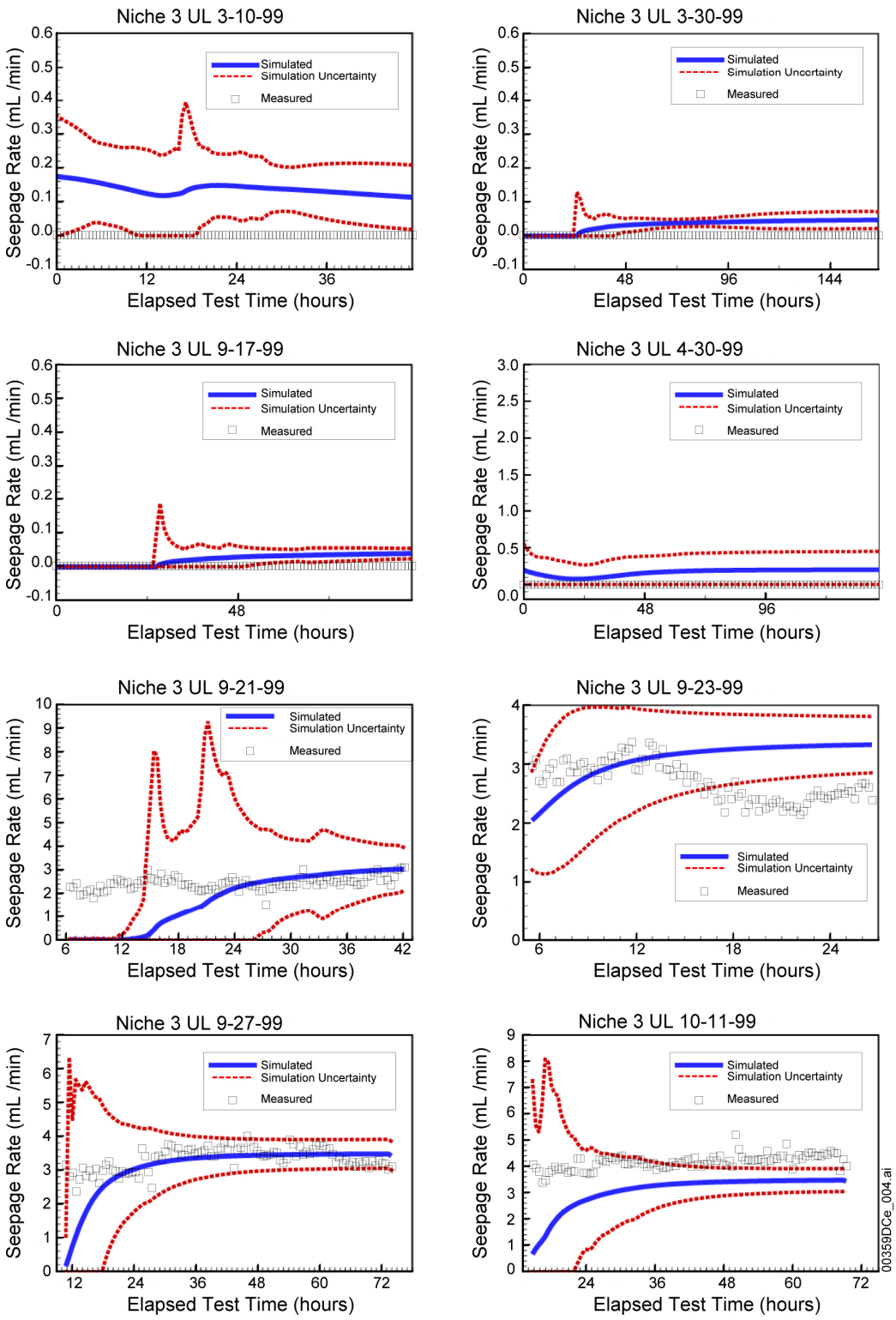

Source: BSC 2003b, Figure 43.

NOTE: Linear uncertainty propagation analysis was used to calculate the uncertainty band of the model predictions.

Figure F-11. Validation of Seepage Model and Tptpmn Seepage-Relevant Parameters Using Data from Niche 3

F.4.3 Evaluation of van Genuchten Relations for Modeling Unsaturated Flow in Fractures

The NRC is concerned with the appropriateness of using van Genuchten relations for modeling unsaturated flow in fractures (Section F.4.4.1). This section presents an evaluation of these relations based on a study by Liu and Bodvarsson (2001).

F.4.3.1 van Genuchten Relations

Key parameters for an unsaturated zone flow model based on the continuum approach include constitutive relations (relations between capillary pressure, saturation, and relative permeability). Accuracy of modeling results is largely determined by the accuracy of these constitutive relations. Several well-known parametric models, including the van Genuchten relations, have been developed for unsaturated soils and successfully used in describing flow processes in unstructured porous media. Based on a conceptual idea that in the continuum approach, the role of individual fractures in fractured media is considered to be similar to that of individual pores in porous media, the van Genuchten relations have often been borrowed in modeling unsaturated flow in the fracture continuum. The van Genuchten (1980) relations are given by

$$S_e = [1 + |\alpha P_c|^n]^{-m} \quad \text{(Eq. F-1)}$$

$$k_r = \sqrt{S_e}[1 - (1 - S_e^{1/m})^m]^2 \quad \text{(Eq. F-2)}$$

where P_c is the capillary pressure; k_r is the relative permeability; α, n, and m are empirical fitting parameters with m equal to $1 - 1/n$; and S_e is the effective saturation given by

$$S_e = \frac{S - S_r}{S_s - S_r} \quad \text{(Eq. F-3)}$$

where S is the water saturation, S_r is the residual saturation, and S_s is the satiated saturation. The parameter m is an index of pore size distribution.

F.4.3.2 Effective Constitutive Relations for Fracture Networks

While van Genuchten (1980) relations have been widely used in porous media, their usefulness for fractures has not been fully established. To evaluate these relations, Liu and Bodvarsson (2001) performed numerical experiments for two-dimensional fracture networks. Although a fracture network is three-dimensional in reality, the two-dimensional model is expected to capture the essential part of actual water flow behavior in fractures. Figure F-12 shows one of the fracture networks generated from fracture data collected in the unsaturated zone of Yucca Mountain.

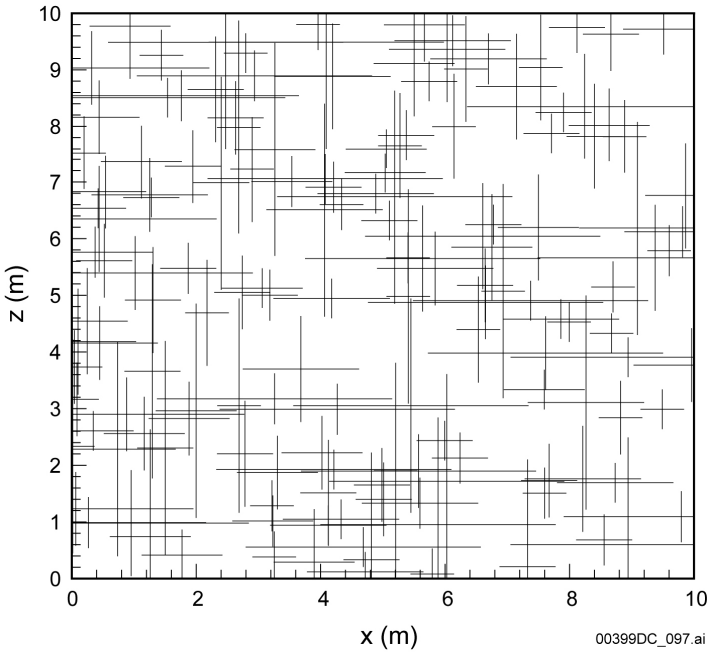

Source: Liu and Bodvarsson 2001, Figure 1b.

Figure F-12. A Computationally Generated Fracture Network

The effective constitutive relations for fractures were determined by numerical simulations of steady-state unsaturated flow in two-dimensional fracture networks using TOUGH2 (Pruess 1991). The rock matrix is treated as being impermeable for purposes of focusing the fracture continuum. Liu and Bodvarsson (2001) imposed the same capillary pressures at the top and bottom boundaries of a fracture network and nonflow conditions at the side boundaries. The capillary pressures at the top and bottom boundaries were considered to be effective capillary pressures of the fracture network although pressure variability exists in a fracture network. Because the effective capillary pressure gradient is zero in the vertical direction (resulting from the same pressure values used as the top and bottom boundary conditions), the average vertical flux should (according to Darcy's law) be the same as the hydraulic conductivity of the corresponding fracture network. The network is considered to be a fracture continuum within the context of the dual continuum approach. For a number of different uniform capillary pressures at the boundaries, the corresponding values of volumetric saturation and hydraulic conductivity (or relative permeability) can be obtained for a fracture network, resulting in the desired constitutive relations. This computational procedure is similar to laboratory procedures to determine constitutive relations for porous media. The relative permeability is determined as the ratio of the unsaturated conductivity to the saturated conductivity (Liu and Bodvarsson 2001).

F.4.3.3 Evaluation of van Genuchten Relations

Some evaluation results of Liu and Bodvarsson (2001) are given in Figures F-13 and F-14. These figures also show the results for Brooks–Corey (Brooks and Corey 1964) relations, which can be expressed by

$$S_e = \left| P_c / P_d \right|^{-\lambda} \quad \text{(Eq. F-4)}$$

$$k_r = S_e^{(3+\frac{2}{\lambda})} \quad \text{(Eq. F-5)}$$

where P_d is known as the air entry pressure and λ is a dimensionless index of pore size distribution. If P_d is approximated by $1/\alpha$, the Brooks–Corey's capillary pressure-saturation relation is equivalent to that of the van Genuchten model with (van Genuchten 1980; Wang and Narasimhan 1993)

$$\lambda = n - 1 \quad \text{(Eq. F-6)}$$

This relation allows use of the van Genuchten parameter n to estimate relative permeability using the Brooks-Corey model that has been used in this study to minimize the number of property parameters.

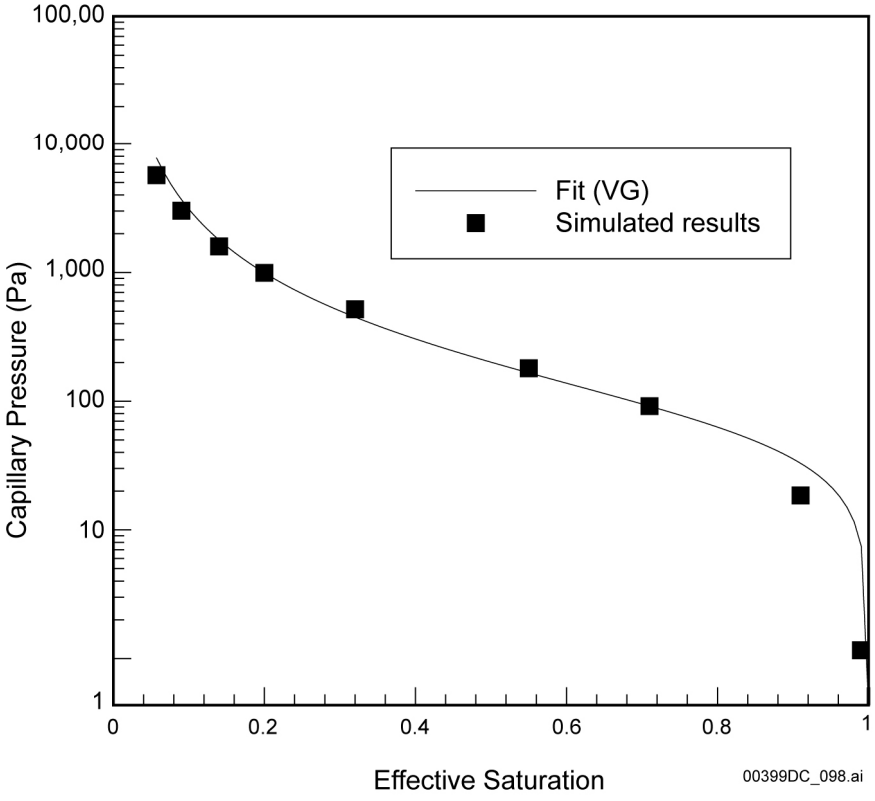

Source: Liu and Bodvarsson 2001, Figure 2a.

NOTE: VG = van Genuchten model.

Figure F-13. Fit of the van Genuchten Model to the Simulated Capillary Pressure–Effective Saturation Relations

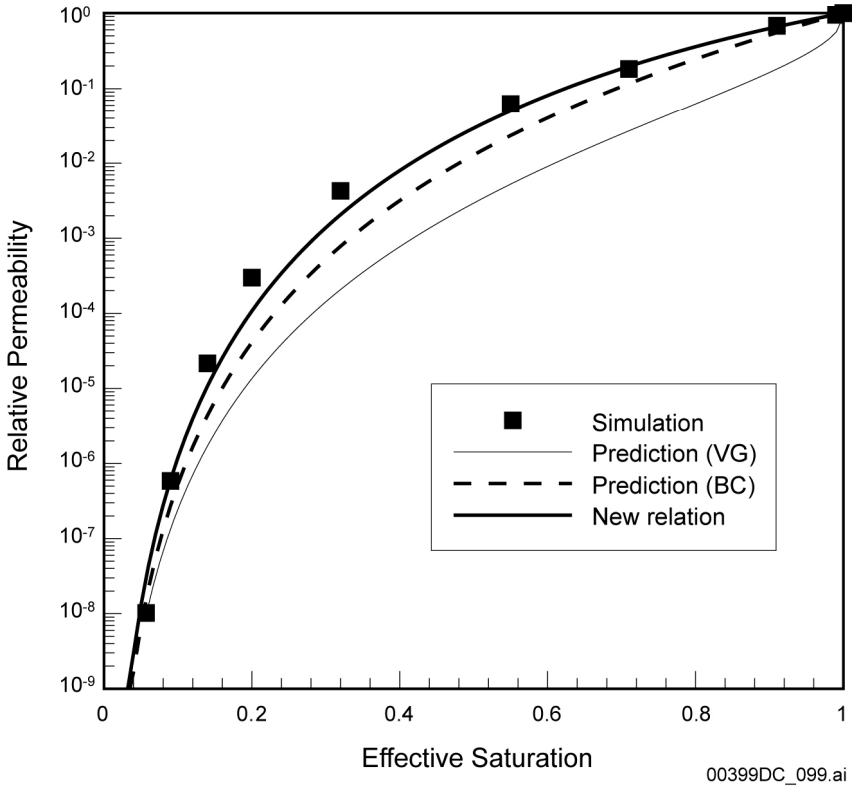

Source: Liu and Bodvarsson 2001, Figure 3a.

NOTE: VG = van Genuchten model; BC = Brooks-Corey model; New relation plot shows results from Equation F-10 when using van Genuchten *m* parameter values determined from Figure F-13.

Figure F-14. Comparison between Simulated Relative Permeability–Effective Saturation Relations, the Curves Predicted Using the van Genuchten Model, the Brooks–Corey Model, and the New Relation Having Derived van Genuchten *m* Parameter Values

Figure F-13 shows fairly good fits between the van Genuchten (1980) capillary pressure–effective saturation relation and the simulated retention curves, except for high saturations for a fracture network. Figure F-14 shows comparisons between the simulated relative permeability–effective saturation relations and curves predicted using the van Genuchten model and the Brooks–Corey model, with the *m* values obtained from curve fitting in Figure F-13. The predicted relative permeability values are consistently smaller than the simulated ones for a given saturation, while the Brooks–Corey model gives better results than the van Genuchten model. This may result from the following: first, the Brooks–Corey's (Brooks and Corey 1964) relative permeability–saturation relation was derived from Burdine's model, in which pores are represented with a group of parallel capillary tubes with different radii, whereas the van Genuchten relation is based on the more complicated pore-geometry model of Mualem (1976). Burdine's model representing pores with a group of parallel capillary tubes may be more consistent with the unsaturated flow in a fracture network characterized by a number of major flow paths in the vertical direction (Kwicklis and Healy 1993). Second, because of the difference between fracture network geometry and pore space geometry, tortuosities of flow paths in a fracture network are considerably different from those in a porous medium. Because pore sizes in a porous medium are generally much smaller than fracture apertures, unsaturated flow in a fracture network is mainly gravity-driven (Liu et al. 1998), especially for a large

fracture water saturation and, consequently, the capillary force is generally much stronger in a porous media. The latter is expected to result in more tortuous flow paths around solid particles (or pores) in a porous medium. The following expression for tortuosity factor τ was assumed in deriving Equation F-5 (Brooks and Corey 1964).

$$\tau = S_e^{\,2} \qquad \text{(Eq. F-7)}$$

If τ is assumed to be its maximum value of 1, Equation F-5 will become

$$k_r = S_e^{\,(1+\frac{2}{\lambda})} \qquad \text{(Eq. F-8)}$$

Both the Brooks-Corey and van Genuchten models reasonably predict the simulated relative permeability–saturation relations for small water saturations (e.g., less than 0.10 in Figure F-14). This may be because capillary force becomes important at low saturations, resulting in similar unsaturated flow behavior in both a porous media and a fracture network. These two models are thus approximately valid for modeling water flow in the Yucca Mountain unsaturated zone under ambient conditions, which generally involve very low fracture saturations as a result of low infiltration rates in that region. However, under disturbed conditions, the thermal-hydrologic response of the unsaturated rocks to the decay heat of nuclear wastes can give rise to relatively high fracture saturations around the repository. The van Genuchten and Brooks-Corey models may lead to considerable error in modeling flow processes under these conditions. A detailed discussion on flow processes under disturbed conditions in the Yucca Mountain unsaturated zone can be found in Tsang and Birkholzer (1999).

To improve the accuracy of the Brooks-Corey model in predicting the relative permeability-effective saturation relation for a fracture network, Liu and Bodvarsson (2001) modify the tortuosity expression (Equation F-7) for the Brooks–Corey model to

$$\tau = S_e^{\,2(1-S_e^{\,3/4})} \qquad \text{(Eq. F-9)}$$

Compared with Equation F-7, the above equation gives tortuosity factor values that are closer to 1 for large saturations and essentially the same as those calculated from Equation F-7 for low saturations. Although Equation F-9, like the expressions for tortuosity factor used in both the Brooks-Corey and the van Genuchten models, is empirical, it is consistent with the previous discussion. Following Brooks and Corey (1964) and using Equation F-9 leads to

$$k_r = S_e^{\,(3-2S_e^{\,3/4}+2/\lambda)} = S_e^{\,(3-2S_e^{\,3/4}+\frac{2}{n-1})} \qquad \text{(Eq. F-10)}$$

Improved matches between the simulated relative permeability–saturation relations and those calculated with Equation F-10 are shown in Figure F-14. Therefore, the new simulated constitutive relations can be represented by a combination of van Genuchten's capillary pressure–effective saturation relation and the modified Brooks–Corey's relative permeability-effective saturation relation.

Liu and Bodvarsson (2001) imply that van Genuchten relations may be valid for modeling water flow in the Yucca Mountain unsaturated zone under the ambient conditions that generally involve very low fracture saturations resulting from low infiltration rates in that region. However, under disturbed conditions, the thermal-hydrologic response of the unsaturated rocks to the decay heat of nuclear wastes can give rise to relatively high fracture saturations around the repository. Under these conditions, use of the van Genuchten and Brooks–Corey models may lead to considerable uncertainties in modeling flow processes. The van Genuchten model has been used to develop all Yucca Mountain flow and transport models, although it has not been fully evaluated.

F.4.4 Treatment of Model Uncertainties

The NRC is concerned about whether model uncertainties (related to fingering flow in fractures, effects of the heterogeneities, and the use of van Genuchten relations) have been addressed in the relevant hydrologic and thermal-hydrologic process models (Section F.4.1) and abstraction models. The relevant models are the site-scale unsaturated zone flow model, drift-scale models, and multiscale thermal-hydrologic model.

The site-scale unsaturated zone flow model (BSC 2004b) was developed for generating three-dimensional flow fields for the unsaturated zone that are used by the TSPA-LA. The unsaturated zone model also provides inputs into drift-scale models. A geology-based deterministic approach, in which an entire model layer is assigned uniform properties, is used, mainly for representing subsurface heterogeneity and modeling flow and transport in the site-scale unsaturated zone model (Section F.4.2). The study of Zhou et al. (2003) demonstrates that small-scale heterogeneities in a fractured zone within each geologic unit have only a minor effect on site-scale flow processes. Fingering flow in fractures is handled by the active fracture model, which can model a large range of fast (fingering) flow behavior (Section F.4.1.1). Efforts have been made to quantify and reduce uncertainties associated with model parameters and output results for the site-scale unsaturated zone flow model. A total of six sets of model input parameters are developed (i.e., three base cases and three alternatives) that cover the effect of uncertainties in lower-bound, mean, and upper-bound infiltration rates. Uncertainties with present-day and future climates are investigated using three scenarios (i.e., present day, monsoon, and glacial transition climates) that combine for nine different net infiltration scenarios. In addition, sensitivity and uncertainty with the active fracture model parameter, γ, is evaluated for its impact on flow and transport modeling results. The sensitivity analysis shows that γ has little effect on simulated percolation fluxes, but a large impact on tracer transport. The γ value used in the unsaturated zone model produces more conservative transport results.

Drift-scale models include the seepage calibration model (BSC 2003b), the seepage model for performance assessment (BSC 2003e), and the thermal-hydrologic seepage model (BSC 2003a). The seepage calibration model provides the conceptual basis for modeling ambient seepage processes and estimates of the seepage-relevant rock parameters through model calibration. The seepage model for performance assessment conducts ambient seepage fluxes into waste emplacement drifts. The thermal-hydrologic seepage model is employed to evaluate the coupled thermal-hydrologic processes and their impact on seepage processes near waste emplacement drifts during the heating phase of the repository. These models provide the bases for seepage abstraction for the TSPA-LA (BSC 2003f, Section 6.4). In all these drift-scale models,

continuum approaches have been used. Heterogeneities are explicitly considered in these models based on the stochastic continuum approach (BSC 2003f, Section 6.4). Fingering flow associated with small-scale heterogeneity is explicitly modeled (Section F.4.1.2). An alternative model (i.e., not based on the continuum approach) for fingering flow associated with thermal reflux in a single fracture is also developed, and its results are compared with those from the continuum-approach-based thermal-hydrologic seepage model. The models show consistent results for thermal seepage (Section F.4.2). Therefore, the uncertainties associated with heterogeneity and the use of the continuum approach have been incorporated in the drift-scale models.

The multiscale thermal-hydrologic model is used to describe the thermal-hydrologic evolution of the near-field environment and engineered barrier system throughout the repository (BSC 2003g, Section 1). Approaches for dealing with heterogeneity and fingering flow in this model are similar to the site-scale unsaturated zone flow model. The multiscale thermal-hydrologic model differs from the drift-scale thermal-hydrologic seepage model in the way it treats flow focusing at the drift scale. Flow focusing denotes the potential concentration of flow from the large scale, as simulated with the unsaturated zone flow model, to the drift scale, as simulated by the thermal-hydrologic seepage model. Sensitivity studies using the multiscale thermal-hydrologic model consider a similar range of flow focusing to that used in the drift-scale thermal-hydrologic seepage model, and uncertainty in host-rock thermal conductivity was performed to investigate the effects of these factors on the repository (BSC 2003g, Sections 6.3.3 and 8.2). The results indicate that the range of behavior for peak waste-package temperature and duration of boiling captured with the lower-bound, mean, and upper-bound flux scenarios covers roughly 75% of the maximum range when the effects of flow focusing and thermal conductivity uncertainty are included.

The seepage abstraction model was developed to evaluate the future amount and distribution of seepage into the waste emplacement drifts at Yucca Mountain (BSC 2003h). The model is based on seepage prediction from detailed process models (seepage calibration model, seepage model for performance assessment, thermal-hydrological seepage model, unsaturated zone flow model, thermal-hydrologic mechanical and thermal-hydrologic chemical model) and additional inputs from scientific analyses. The process models and scientific analyses are required to define appropriate probability distribution for the TSPA-LA (BSC 2003h, Section 6.6). The treatments of uncertainties of seepage relevant properties have been characterized by evaluation of all potential sources of uncertainty (i.e., uncertainty in the measurements, the conceptual model, the estimation process and the spatial variability) (BSC 2003h, Section 6.6). In addition, sources of uncertainties in seepage affected by thermal, mechanical, and chemical effects, changes in the drift shape due to drift degradation, and from the presence of bolts used for ground support are evaluated (BSC 2003h, Section 6.5). In summary, the abstraction is based on seepage predictions from detailed process models that have been validated in previous analyses to ensure appropriate representation of the physical process and relevant parameters.

In all the models discussed in this section, van Genuchten (1980) relations have been used for modeling flow and transport in fractures. As indicated in Section F.4.3, van Genuchten relations may be valid for modeling water flow in the Yucca Mountain unsaturated zone under the ambient conditions and may lead to considerable uncertainties in modeling flow processes under thermally disturbed conditions (Liu and Bodvarsson 2001).

In summary, uncertainties related to fingering flow in fractures and effects of the heterogeneities, relations have been addressed in the relevant hydrologic and thermal-hydrologic processes and abstraction models in Yucca Mountain. In all models, van Genuchten relations have been used to model flow in the fracture continuum, although it has not been fully evaluated.

F.5 REFERENCES

Birkholzer, J.T. 2002. *TH_PULSE: Program for Calculating Infiltration of Episodic Liquid Fingers in Superheated Rock Fractures, Theory, User's Manual, and Sample Applications*. LBNL/PUB-3277. Berkeley, California: Lawrence Berkeley National Laboratory. TIC: 253581.

Brooks, R.H. and Corey, A.T. 1964. *Hydraulic Properties of Porous Media*. Hydrology Paper No. 3. Fort Collins, Colorado: Colorado State University. TIC: 217453.

BSC (Bechtel SAIC Company) 2003a. *Drift-Scale Coupled Processes (DST and TH Seepage) Models*. MDL-NBS-HS-000015 REV 00C. Las Vegas, Nevada: Bechtel SAIC Company. ACC: MOL.20030910.0160.

BSC 2003b. *Seepage Calibration Model and Seepage Testing Data*. MDL-NBS-HS-000004 REV 02. Las Vegas, Nevada: Bechtel SAIC Company. ACC: DOC.20030408.0004.

BSC 2003c. *UZ Flow Models and Submodels*. MDL-NBS-HS-000006 REV 01. Las Vegas, Nevada: Bechtel SAIC Company. ACC: DOC.20030818.0002.

BSC 2003d. *Drift-Scale Radionuclide Transport.* MDL-NBS-HS-000016 REV 00. Las Vegas, Nevada: Bechtel SAIC Company. ACC: DOC.20030902.0009.

BSC 2003e. *Seepage Model For PA Including Drift Collapse*. MDL-NBS-HS-000002 REV 02. Las Vegas, Nevada: Bechtel SAIC Company. ACC: DOC.20030709.0001.

BSC 2003f. *Abstraction of Drift Seepage*. MDL-NBS-HS-000019 REV 00. Las Vegas, Nevada: Bechtel SAIC Company. ACC: DOC.20030826.001

BSC 2003g. *Multiscale Thermohydrologic Model.* ANL-EBS-MD-000049 REV 01. Las Vegas, Nevada: Bechtel SAIC Company. ACC: DOC.20040301.0004.

BSC 2003h. *Abstraction of Drift Seepage*. MDL-NBS-HS-000019 REV 00 ICN 01. Las Vegas, Nevada: Bechtel SAIC Company. ACC: DOC.20031112.0002.

BSC 2004a. *Particle Tracking Model and Abstraction of Transport Processes.* MDL-NBS-HS-000020 REV 00. Las Vegas, Nevada: Bechtel SAIC Company. ACC: DOC.20040120.0001.

BSC 2004b. *UZ Flow Models and Submodels*. MDL-NBS-HS-000006 REV 01. Las Vegas, Nevada: Bechtel SAIC Company. ACC: DOC.20030818.0002; DOC.20040211.0008.

Cacas, M.C.; Ledoux, E.; De Marsily, G.; Tillie, B.; Barbreau, A.; Durand, E.; Feuga, B.; and Peaudecerf, P. 1990. "Modeling Fracture Flow with a Stochastic Discrete Fracture Network: Calibration and Validation. 1. The Flow Model." *Water Resources Research, 26,* (3), 479–489. Washington, D.C.: American Geophysical Union. TIC: 222351.

CRWMS M&O (Civilian Radioactive Waste Management System Management and Operating Contractor) 2000. *Conceptual and Numerical Models for UZ Flow and Transport*. MDL-NBS-HS-000005 REV 00. Las Vegas, Nevada: CRWMS M&O. ACC: MOL.19990721.0526.

Dverstorp, B. and Andersson, J. 1989. "Application of the Discrete Fracture Network Concept with Field Data: Possibilities of Model Calibration and Validation." *Water Resources Research, 25,* (3), 540–550. Washington, D.C.: American Geophysical Union. TIC: 254736.

Finsterle, S. 2000. "Using the Continuum Approach to Model Unsaturated Flow in Fractured Rock." *Water Resources Research, 36*, (8), 2055–2066. Washington, D.C.: American Geophysical Union. TIC: 248769.

Glass, R.J.; Nicholl, M.J.; and Tidwell, V.C. 1996. *Challenging and Improving Conceptual Models for Isothermal Flow in Unsaturated, Fractured Rock Through Exploration of Small-Scale Processes*. SAND95-1824. Albuquerque, New Mexico: Sandia National Laboratories. ACC: MOL.19970520.0082.

Hendrickx, J.M.H. and Flury, M. 2001. "Uniform and Preferential Flow Mechanisms in the Vadose Zone." Chapter 5 of *Conceptual Models of Flow and Transport in the Fractured Vadose Zone.* Washington, D.C.: National Academy Press. TIC: 252777.

Kwicklis, E.M. and Healy, R.W. 1993. "Numerical Investigation of Steady Liquid Water Flow in a Variably Saturated Fracture Network." *Water Resources Research, 29,* (12), 4091–4102. Washington, D.C.: American Geophysical Union. TIC: 226993.

Liu, H.H. and Bodvarsson, G.S. 2001. "Constitutive Relations for Unsaturated Flow in a Fracture Network." *Journal of Hydrology, 252,* (1–4), 116–125. New York, New York: Elsevier. TIC: 253269.

Liu, H.H.; Doughty, C.; and Bodvarsson, G.S. 1998. "An Active Fracture Model for Unsaturated Flow and Transport in Fractured Rocks." *Water Resources Research, 34*, (10), 2633–2646. Washington, D.C.: American Geophysical Union. TIC: 243012.

Mualem, Y. 1976. "A New Model for Predicting the Hydraulic Conductivity of Unsaturated Porous Media." *Water Resources Research, 12,* (3), 513–522. Washington, D.C.: American Geophysical Union. TIC: 217339.

Phillips, O.M. 1996. "Infiltration of a Liquid Finger Down a Fracture into Superheated Rock." *Water Resources Research, 32*, (6), 1665–1670. Washington, D.C.: American Geophysical Union. TIC: 239025.

Pruess, K. 1991. "TOUGH2—A General-Purpose Numerical Simulator for Multiphase Fluid and Heat Flow." LBL-29400. Berkeley, California: Lawrence Berkeley National Laboratory. ACC: NNA.19940202.0088; TIC: 213489.

Reamer, C.W. and Williams, D.R. 2001. Summary Highlights of NRC/DOE Technical Exchange and Management Meeting on Thermal Effects on Flow. Meeting held January 8-9, 2001, Pleasanton, California. Washington, D.C.: U.S. Nuclear Regulatory Commission. ACC: MOL.20010202.0095 through MOL.20010202.0108.

Schlueter, J. 2003. "Review of Documents Pertaining to Agreement Thermal Effects on Flow (TEF) 2.13 (Status: Need Additional Information)". Letter from J. Schlueter (NRC) to J.D. Ziegler (DOE), May 16, 2003, with enclosure. ACC: MOL.20030702.0256.

Su, G.W.; Geller, J.T.; Pruess, K.; and Wen, F. 1999. "Experimental Studies of Water Seepage and Intermittent Flow in Unsaturated, Rough-Walled Fractures." *Water Resources Research, 35*, (4), 1019–1037. Washington, D.C.: American Geophysical Union. TIC: 245798.

Tsang, Y.W. and Birkholzer, J.T. 1999. "Predictions and Observations of the Thermal-Hydrological Conditions in the Single Heater Test." *Journal of Contaminant Hydrology*, *38*, (1–3), 385–425. New York, New York: Elsevier. TIC: 244160.

van Genuchten, M.T. 1980. "A Closed-Form Equation for Predicting the Hydraulic Conductivity of Unsaturated Soils." *Soil Science Society of America Journal, 44*, (5), 892–898. Madison, Wisconsin: Soil Science Society of America. TIC: 217327.

Wang J.S.Y. and Narasimhan T.N. 1993. "Unsaturated Flow in Fractured Porous Media." Chapter 7 of *Flow and Contaminant Transport in Fractured Rocks*. Bear, J.; Tsang, C.F.; and de Marsily, G., eds. New York, New York: Academic Press. TIC: 235461.

Zhou, Q.; Liu, H-H.; Bodvarsson, G.S.; and Oldenburg, C.M. 2003. "Flow and Transport in Unsaturated Fractured Rock: Effects of Multiscale Heterogeneity of Hydrogeologic Properties." *Journal of Contaminant Hydrology, 60*, (1–2), 1–30. New York, New York: Elsevier. TIC: 253978.

Ziegler, J.D. 2003. "Transmittal of Report Addressing Key Technical Issue (KTI) Agreement Items Total System Performance Assessment and Integration (TSPAI) 3.18, 3.21, and 3.23 and Thermal Effects on Flow (TEF) 2.13." Letter from J.D. Ziegler (DOE) to J.R. Schlueter (NRC), January 21, 2003, with enclosure, "KTI Letter Report Response to TSPAI 3.18, 3.21, and 3.23, and TEF 2.13." Correspondence Log #0122035753. ACC: ENG.20030210.0004.

INTENTIONALLY LEFT BLANK

APPENDIX G

INTEGRATION OF WATER FLOW RATES AMONG VARIOUS UNSATURATED ZONE AND NEAR-FIELD FLOW MODELS SUPPORTING THE TOTAL SYSTEM PERFORMANCE ASSESSMENT FOR THE LICENSE APPLICATION (RESPONSE TO TSPAI 3.27)

Note Regarding the Status of Supporting Technical Information

This document was prepared using the most current information available at the time of its development. This Technical Basis Document and its appendices providing Key Technical Issue Agreement responses that were prepared using preliminary or draft information reflect the status of the Yucca Mountain Project's scientific and design bases at the time of submittal. In some cases this involved the use of draft Analysis and Model Reports (AMRs) and other draft references whose contents may change with time. Information that evolves through subsequent revisions of the AMRs and other references will be reflected in the License Application (LA) as the approved analyses of record at the time of LA submittal. Consequently, the Project will not routinely update either this Technical Basis Document or its Key Technical Issue Agreement appendices to reflect changes in the supporting references prior to submittal of the LA.

APPENDIX G

INTEGRATION OF WATER FLOW RATES AMONG VARIOUS UNSATURATED ZONE AND NEAR-FIELD FLOW MODELS SUPPORTING THE TOTAL SYSTEM PERFORMANCE ASSESSMENT FOR THE LICENSE APPLICATION (RESPONSE TO TSPAI 3.27)

This appendix provides a response to Key Technical Issue (KTI) agreement Total System Performance Assessment and Integration (TSPAI) 3.27. This agreement relates to the integration of water flow rates used in various unsaturated zone, near-field, and in-drift flow models.

G.1 KEY TECHNICAL ISSUE AGREEMENT

G.1.1 TSPAI 3.27

Agreement TSPAI 3.27 was reached during the U.S. Nuclear Regulatory Commission (NRC)/U.S. Department of Energy (DOE) Technical Exchange and Management Meeting on Total System Performance Assessment and Integration held August 6 to 10, 2001, in Las Vegas, Nevada (Reamer 2001). TSPAI KTI subissues 1, 2, 3, and 4 were discussed at that meeting. No submittal related to this KTI agreement has been made to the NRC.

Wording of the agreement is as follows:

TSPAI 3.27[1]

> Provide an overview of water flow rates used in the UZ model above and below the repository, in the MSTHM, in the seepage abstraction, and in the in-drift flow path models, to ensure appropriate integration between the various models (UZ2.TT.3). DOE will provide an overview of water flow rates used in the UZ model above and below the repository, in the Multi-Scale Thermohydrologic Model (MSTHM), in the seepage abstraction, and in the in drift flow path models, to ensure appropriate integration between the various models. This will be documented in the TSPA for any potential license application expected to be available to NRC in FY 2003.

G.1.2 Related Key Technical Issue Agreements

This agreement is related to KTI agreement TSPAI 3.11 in that both agreements are concerned with integration between various unsaturated zone flow models, including the multiscale thermal-hydrologic model and the seepage models. The focus of TSPAI 3.11 is on seepage into drifts, while TSPAI 3.27 provides an overview of water flow rates. Response to TSPAI 3.11 will be provided in *Technical Basis Document No. 3: Water Seeping into Drifts*.

[1] Refers to Integrated Subissue "Flow Paths in the Unsaturated Zone" with regard to what water mass flux balance is used above, at, and below the repository horizon.

G.2 RELEVANCE TO REPOSITORY PERFORMANCE

The issues covered by this agreement are directly related to the performance of the unsaturated zone barrier. It covers each of the models used in analyzing flow rates and the integration between these models, so the potential impact is on assessment of the entire barrier performance.

G.3 RESPONSE

Water flow models are used to describe flow, and coupled thermal and chemical processes that affect flow, for the total system performance assessment for the license application (TSPA-LA). These models are integrated, but may be categorized based on spatial domain: mountain-scale unsaturated zone flow, drift-scale unsaturated zone flow, and in-drift flow.

The mountain-scale flow model and the associated infiltration model are integrated with the drift-scale unsaturated zone flow models and unsaturated zone transport models that compute drift seepage, seepage water chemistry, and radionuclide transport. The infiltration model provides the flux boundary condition at the ground surface for the mountain-scale unsaturated zone flow model. However, there is no direct feed from the infiltration model to the TSPA-LA. The unsaturated zone flow model is used to provide the flux boundary condition for the multiscale thermal-hydrologic model and the seepage abstraction model; this boundary condition is taken at the PTn–TSw interface to account for lateral diversion in the PTn on the flux distribution at the repository (see major hydrogeologic units in Table 2-1). Large-scale lateral diversion is not observed in the unsaturated zone flow model between the PTn–TSw interface and the repository.

Drift-scale flow models address drift seepage and seepage water chemistry. The underlying process models for drift seepage (seepage model for performance assessment and drift-scale thermal-hydrologic seepage model) that support the seepage abstraction model are exercised to be implemented as a response function for drift seepage in the TSPA-LA. Thus, the range of flow boundary conditions investigated with these models is derived from the range of expected flow rates, based on the results of the infiltration model and unsaturated zone flow model. Ultimately, the drift seepage rates are tied to the boundary condition imposed by the unsaturated zone flow model at the PTn–TSw interface on the seepage abstraction model. The drift-scale thermal-hydrologic-chemical model computes the evolution of water and gas chemistry in the rock to support the evaluation of water and gas compositions that enter waste emplacement drifts. This model uses an average flux from the infiltration model as a boundary condition for water flux into the top of the model.

The in-drift flow model, which is part of the engineered barrier system radionuclide transport abstraction model, uses the seepage abstraction flux through the crown of the drift and the flux from the rock to the drift invert as computed from the multiscale thermal-hydrologic model. The flux between the host rock and the invert flux from the multiscale thermal-hydrologic model is confined to the smaller intragranular pore spaces of the crushed tuff.

Material balance is maintained between the infiltration, unsaturated zone flow, and unsaturated zone radionuclide transport models. Material balance between the unsaturated zone flow, multiscale thermal-hydrologic, and seepage abstraction models is captured in an average sense,

based on spatial averaging over regions used to discretize the repository in the TSPA-LA model. However, differences in the treatment of flow focusing between the seepage abstraction and multiscale thermal-hydrologic models exist at the drift scale. Material balance between the sources of water entering the drift and the in-drift flow model is maintained. The material balance between the flux out of the drift and the flux in the unsaturated zone flow model is not captured due to the change in spatial scales between the models. At any given location, the flow out of the drift is only a minor component of the total flow in the unsaturated zone flow model because of the size of the mountain-scale flow model grid relative to the drift. The representation of flux for the drift-scale thermal-hydrologic-chemical model is captured in a bounding manner but does not include the spatial flux variability as represented in the other drift-scale flow models. Finally, some differences in conceptual models, model implementation, and treatment of uncertainty exist between the various flow models. These differences are explained in the next section in terms of the different objectives and sensitivities of the various models.

The information in this report is responsive to agreement TSPAI 3.27 made between the DOE and NRC. This report contains the information that DOE considers necessary for NRC review for closure of this agreement.

G.4 BASIS FOR THE RESPONSE

Summary of Unsaturated Zone and In-Drift Water Flow Models Affecting TSPA-LA–Water flow is modeled in several components of the TSPA-LA, as shown in Figures G-1 and G-2. Flow models used in the TSPA-LA are represented in blue, while other components are in green.

The component models are:

- **Infiltration Model**–Provides the spatially distributed magnitude of water flux entering the unsaturated zone. This is used as the water flux boundary condition at the ground surface for the unsaturated zone flow model and as boundary conditions at the ground surface for flux in the drift-scale thermal-hydrologic seepage and drift-scale thermal-hydrologic-chemical models (see Section G.4.1).

- **Unsaturated Zone Flow Model**–Provides the three-dimensional water flux and velocities from the surface to the water table under natural thermal conditions. The unsaturated zone flow model outputs are used as boundary conditions for the multiscale thermal-hydrologic model and the drift seepage abstraction model, and they define the velocity fields for the unsaturated zone radionuclide transport abstraction model (see Section G.4.2).

- **Multiscale Thermal-Hydrologic Model**–Provides the thermal-dynamic environment in the drift and water flow between the rock and drift invert using a thermal-hydrologic flow model that accounts for the effects of waste heat from the repository (see Section G.4.3).

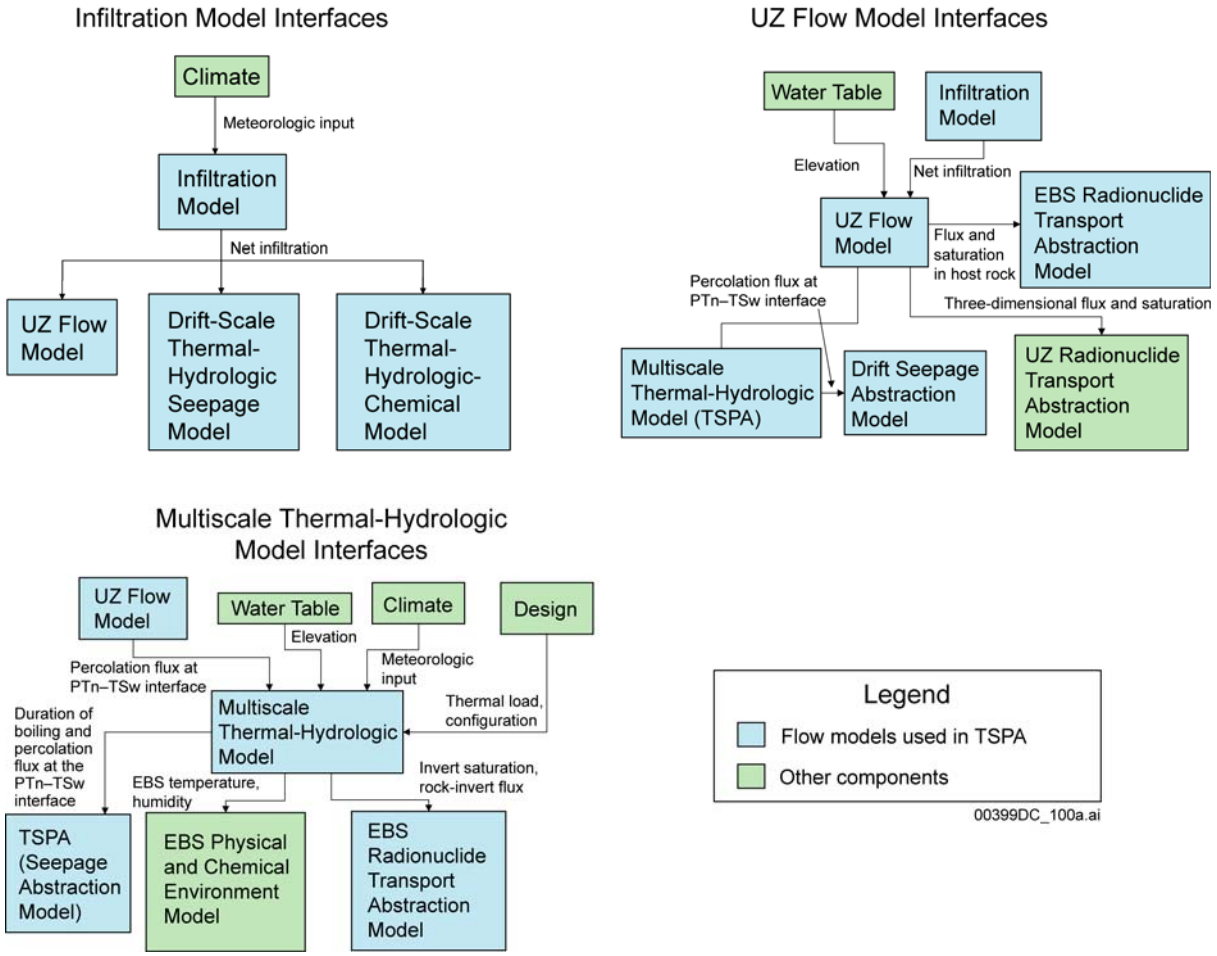

NOTE: PTn and TSw are geologic layers seen in Figure 2-3. UZ = unsaturated zone; TSPA = total system performance assessment; EBS = engineered barrier system.

Figure G-1. Interface Diagrams for Total System Performance Assessment Flow Models: Infiltration Model, Unsaturated Flow Model, and Multiscale Thermal-Hydrologic Model

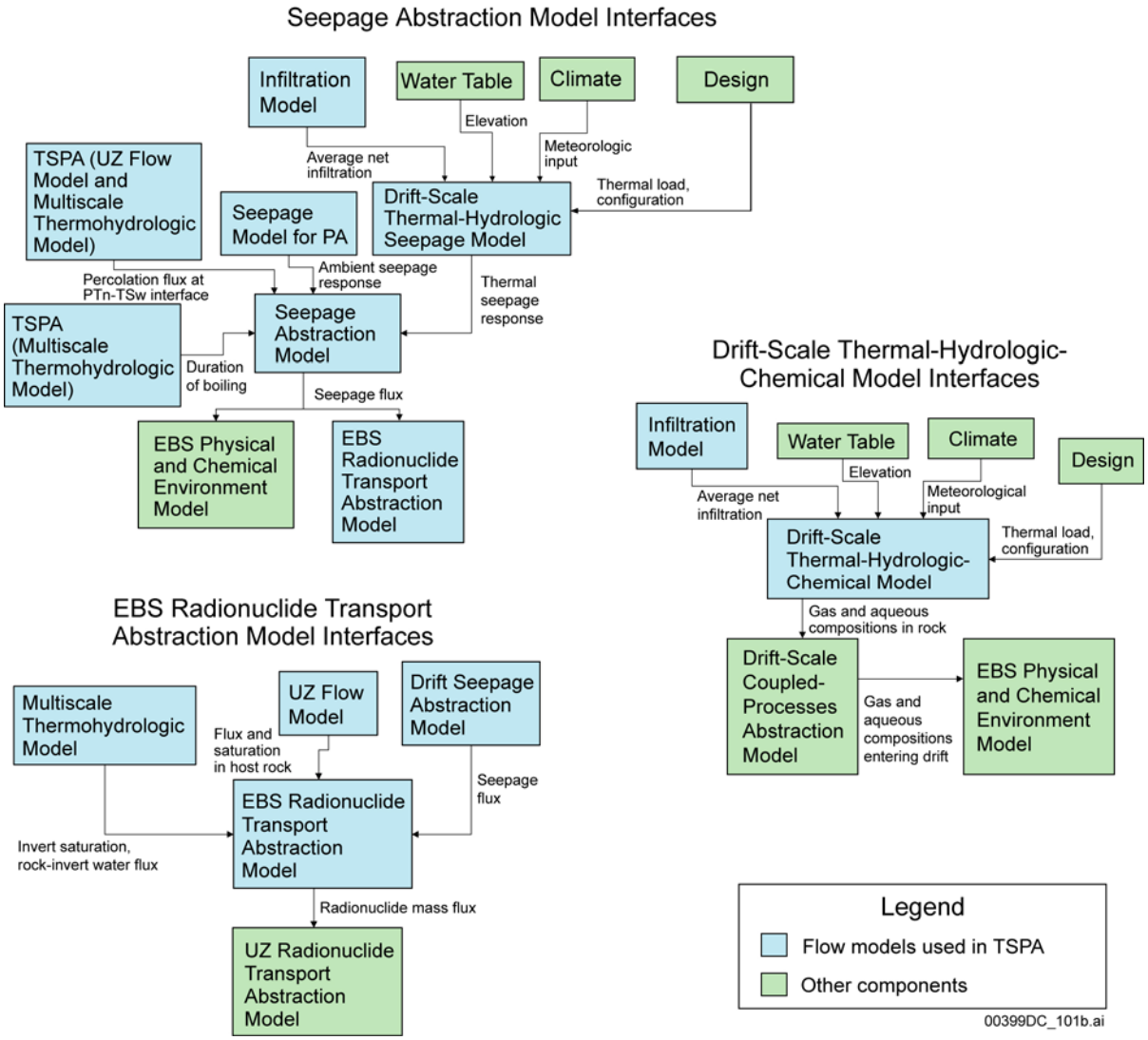

NOTE: PTn and TSw are geologic layers seen in Figure 2-3. UZ = unsaturated zone; TSPA = total system performance assessment; EBS = engineered barrier system; PA = performance assessment.

Figure G-2. Interface Diagrams for Total System Performance Assessment Flow Models: Seepage Abstraction Model, Engineered Barrier System Radionuclide Transport Abstraction Model, and Drift-Scale Thermal-Hydrologic-Chemical Model

- **Seepage Abstraction Model and Supporting Process Models**–Provides the seepage flux into the crown of waste emplacement drifts. This is determined using the seepage model for performance assessment, an ambient temperature drift seepage process model, and the drift-scale thermal-hydrologic seepage model, all of which are represented in the TSPA-LA through the drift seepage abstraction model. The drift seepage flux is used as a boundary condition for the engineered barrier system radionuclide transport abstraction model (see Section G.4.4).

- **Drift-Scale Thermal-Hydrologic-Chemical Model**–Provides the composition of aqueous and gas phases that may enter waste emplacement drifts. This is determined

using the drift-scale thermal-hydrologic-chemical model. The results are further processed in the drift-scale coupled processes abstraction model, which provides the compositions of water and gas entering the waste emplacement drift to the engineered barrier system physical and chemical environment model (see Section G.4.5).

- **Engineered Barrier System Radionuclide Transport Abstraction Model**–Provides the water velocities used to compute radionuclide transport in the engineered barrier system. This is determined through analyses of the flow of water through and around the drip shield, through and around the waste package; the evaporative flux from the invert; and the flow into the invert and from the invert into the unsaturated zone rock (see Section G.4.6).

The remainder of this appendix presents specific details for each water flow model with regards to the conceptual background, model implementation, treatment of uncertainty, and interfaces between models for water flow.

G.4.1 Infiltration Model

Conceptual Background–The hydrologic cycle is used to identify, define, and separate the various field-scale components and processes controlling net infiltration. The starting point of the hydrologic cycle is precipitation, which for the current (modern) climate at Yucca Mountain occurs primarily as rain but may also occur as snow. Precipitation can accumulate on the ground surface, infiltrate the soil or exposed bedrock surfaces, contribute to runoff, or accumulate as snow. The contribution of precipitation to runoff generation depends on precipitation intensity relative to soil and exposed bedrock hydraulic conductivity and also on the available storage capacity of soil and shallow bedrock with thin or no soil cover. Water accumulated in the snow pack can sublimate into the atmosphere or become snowmelt, which can then infiltrate, evaporate, or contribute to runoff. Rain or snowmelt that becomes runoff accumulates in surface depressions and basins or contributes to surface water flow, which is routed to downstream locations as run-on. Run-on contributes to either infiltration or accumulated surface-water run-on at downstream locations. Infiltrated water percolates through the root zone as either saturated or unsaturated ground water and is subject to evapotranspiration. Water percolating through the root zone is available as potential net infiltration, but the actual net-infiltration rate is limited by the bulk (or field-scale) saturated hydraulic conductivity of the bedrock or soil underlying the root zone. In the conceptual model, the bulk saturated hydraulic conductivity represents a weighted averaging of the field-scale matrix and fracture saturated hydraulic conductivity. Estimates of saturated hydraulic conductivity were calculated using these measured values of fracture conductivity for the percentage of area covered by the fracture per square meter of rock, given the fracture density and aperture size available for water to flow through. This was added to the saturated hydraulic conductivity of the rock matrix. Weighted averages of bulk saturated hydraulic conductivity of bedrock, on the basis of percentages of matrix and fractures, were calculated by lithostratigraphic unit (USGS 2001a, Attachment IV, Part 2). When infiltration from rain, snowmelt, or surface-water run-on occurs at a rate greater than the bulk saturated hydraulic conductivity of a subsurface layer, water will begin to fill the available storage capacity of the overlying soil. When the total storage capacity is exceeded, runoff is generated. While runoff can occur while the subsurface is still unsaturated due to precipitation exceeding the saturated hydraulic conductivity of the soil, this is on a small scale,

and irrelevant to modeling of 30 × 30 m gridblocks. In the Yucca Mountain area, the hydrologic cycle can be limited to atmospheric, surface, and shallow subsurface processes because contributions from groundwater discharge and the deep unsaturated zone are insignificant relative to the other components of the cycle. There is no perennial stream flow at the site.

Net infiltration is defined as water that has percolated from the land surface to below the root zone. The root zone is defined as the zone from the ground surface to some variable depth in soil or bedrock from which infiltrated water is readily removed on an annual or seasonal basis by evapotranspiration. The depth of the root zone can be estimated from field studies but cannot be defined precisely. In addition, the depth of the root zone depends on variable climate and surface conditions controlling vegetation and other factors affecting evapotranspiration, thus being transient and spatially variable. Infiltration is the movement of water across the air–soil or air–bedrock interface, and percolation is defined as the downward movement of water within the unsaturated zone.

Model Implementation–The distributed-parameter water-balance model developed as the FORTRAN program INFIL V2.0 (USGS 2001b) follows the conceptual model of infiltration and is represented using a storage volume approach for modeling the root zone. The total root-zone water storage capacity is calculated using the 30 × 30 m area of each grid cell multiplied by the depth of the root zone (including soil and bedrock layers). Infiltration into the root zone and net infiltration through the root zone is calculated independently for all grid cells and corresponding root-zone storage volumes. Because all grid cells have equal areas, the root-zone water storage terms are calculated as one-dimensional vertical storage depths, which can easily be converted to volumes based on grid cell areas. The components of the root-zone water balance are determined for each layer, using the water content of each layer. For water contents less than or equal to the water content at field capacity, infiltration is set to zero, and water loss caused by evapotranspiration from that layer is modeled as an empirical function of relative saturation (with relative saturation based on porosity and the residual water content) and potential evapotranspiration (Flint and Childs 1991). For water contents greater than the water content at field capacity, water losses caused by both infiltration and evapotranspiration from the layer are calculated. Infiltration into the underlying layer is set equal to the bulk saturated hydraulic conductivity of that layer (in millimeters per day). If the available water for net infiltration (calculated based on the amount of water remaining after evapotranspiration losses have been calculated) is less than the maximum infiltration amount determined using saturated hydraulic conductivity, water loss to infiltration is set equal to the amount of available water in the layer. For the lowermost root-zone layer in thick (6 m or greater) soils, the daily water loss to infiltration is used to determine net infiltration. For upland areas with shallow soils, where the root zone is modeled as having a lowermost layer in bedrock, the amount of water available to evapotranspiration losses is calculated using the fracture porosity and the thickness of the bedrock layer. Once the water content of the bedrock layer has reached the limit defined by the fracture porosity, if water continues to infiltrate or percolate into the bedrock layer, net infiltration is calculated based on either the saturated hydraulic conductivity of the bedrock layer or the amount of available water (whichever determines the lower net infiltration amount).

Division of the net infiltration model domain into a set of smaller isolated watershed model domains was needed to decrease simulation run times for INFIL V2.0 (USGS 2001b). This was achieved by allowing the simulation to be distributed over multiple computer processors. The

isolated watershed domains allow for a more efficient analysis of the impact of watershed characteristics on simulation results. Additionally, the smaller, closed modeling systems enable a more efficient mass-balance checking because each model domain is a single watershed with only one outflow location. The main watersheds included in the composite watershed model area are Yucca Wash, Drill Hole Wash, Dune Wash, Solitario Canyon #1, and Plug Hill, as shown in Figure G-3 (USGS 2001a, Figure 6-12). Additional drainages included in the composite model to provide a buffer zone along the western edge of the unsaturated zone model are Jet Ridge #1, Jet Ridge #2, Jet Ridge #3, Solitario Canyon #2, and Solitario Canyon #4. The watershed model domains were restricted to the western side of the Fortymile Wash channel because the Yucca Mountain digital elevation model (DTN: GS000308311221.006) captures only a small part of the lower Fortymile Wash drainage and complete watersheds cannot be defined for most sections of the digital elevation model east of Fortymile Wash. With the exception of Yucca Wash and Jet Ridge #1, all watersheds are fully defined by the digital elevation model. For Yucca Wash, northern sections of the watershed are missing because the digital elevation model does not extend far enough north (the northern perimeter of the watershed is defined by the digital elevation model boundary). The missing area is small relative to the total watershed area, and the only potential impact occurs in the Yucca Wash channel along the northeastern perimeter of the unsaturated zone flow model area. For Jet Ridge #1, the lowermost segment of the eastern perimeter is defined by the digital elevation model boundary. These default watershed boundaries defined by the domain of the digital elevation model are treated as no-flow boundaries. The missing eastern section of Jet Ridge #1 is an insignificant area that does not affect results obtained for the unsaturated zone flow model area.

On a daily basis, precipitation, snowmelt, and surface water run-on are added (as water depth) to the top layer of the root-zone profile at each grid cell. The surface water run-on depth is calculated as runoff generated and routed from upstream grid cells. If the amount of precipitation, snowmelt, and run-on added to the top layer exceeds the maximum daily amount calculated using the saturated hydraulic conductivity of the soil, then runoff (set equal to the amount of excess water) occurs at that grid cell location and is routed to the downstream grid cell. Surface water flow depths are routed as part of an instantaneous flow-routing algorithm representing a daily water balance. All overland flow is routed as a time-independent flow depth for each grid cell within a 24-hour time step (the physics of overland flow are not considered in this type of model). Daily surface water flow volumes are calculated using grid cell areas and converted to standard stream discharge units (cubic feet per second) for comparison with measured stream flow records.

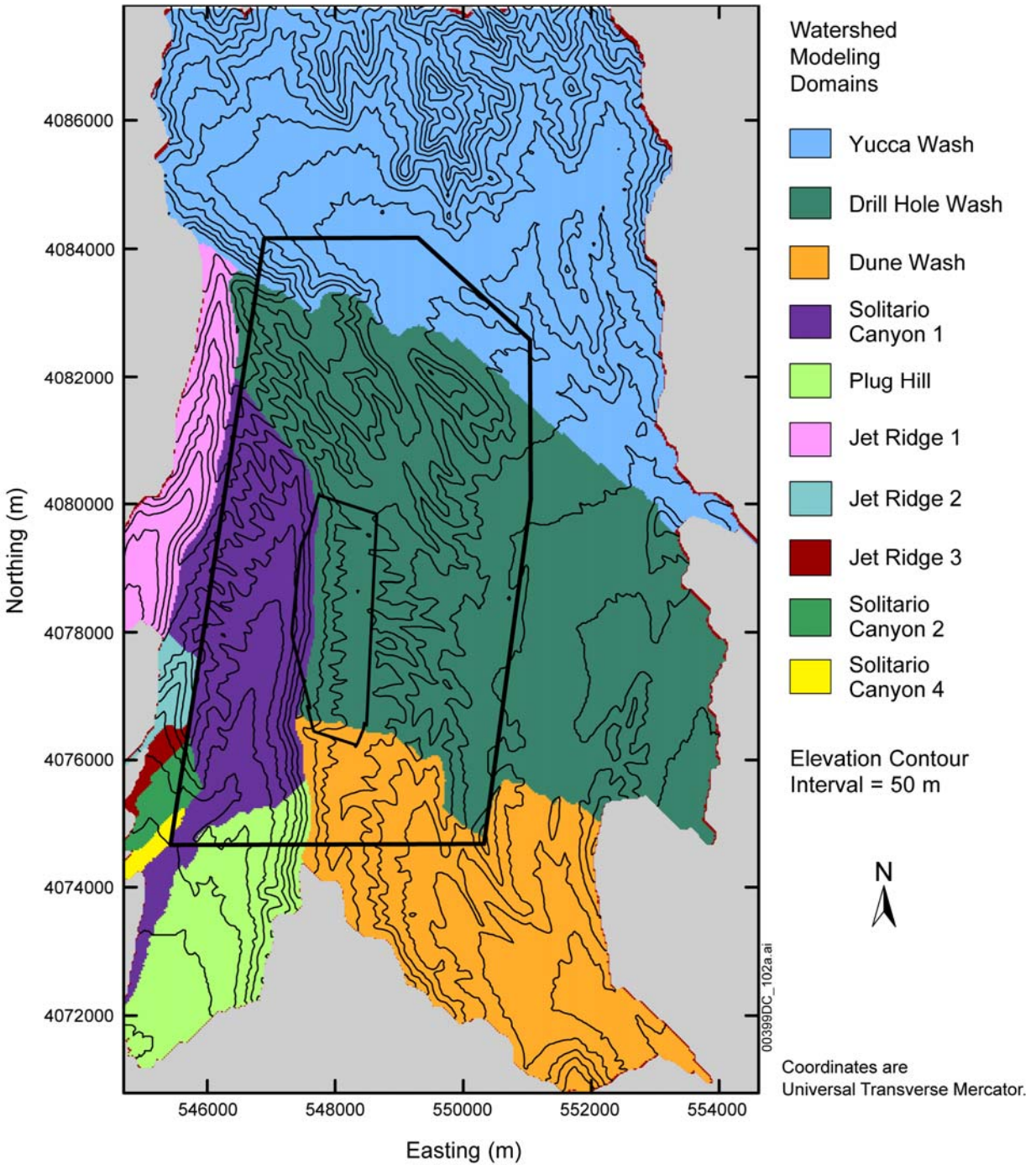

Source: USGS 2001a, Figure 6-12.

NOTE: The elevation contour interval is 50 m.

Figure G-3. Location of 10 Watershed Model Domains Included in the Composite Watershed Model Area Overlying the Area of the Unsaturated Zone Flow Model

For locations where the lowermost root-zone layer is in bedrock, net infiltration is numerically equal to the bulk saturated hydraulic conductivity of the underlying bedrock (in millimeters per day) for the period of time where the water content of the lowermost root-zone layer exceeds the

field capacity of that layer. Net infiltration is simulated as the bulk saturated hydraulic conductivity of the underlying bedrock when the water content of the bedrock root-zone layer equals the fracture porosity of that layer. This condition is maintained only as long as the field capacity of the bottom soil layer (the soil layer above the bedrock layer) is exceeded. Thus, for upland areas with shallow soils, net infiltration is simulated as an episodic process requiring saturated conditions at the soil–bedrock interface and throughout the effective flow path of the bedrock layer included in the root zone.

For locations with thick (greater than 6 m) soil, net infiltration does not require saturated conditions at the bottom of the root zone but does require that the water content of the bottom soil layer exceed the field capacity of the layer. For upland areas, it is assumed that water ponded at the soil–bedrock interface and saturating the effective flow path through the bedrock root-zone layer percolates below the root zone as net infiltration on a daily basis under a unit gradient. In all cases, water losses caused by evapotranspiration are simulated for all root-zone layers having water content greater than residual prior to the calculation of net infiltration. During winter, when potential evapotranspiration is at a minimum, ponded or saturated conditions at the soil–bedrock interface and throughout the effective flow path of the bedrock root-zone layer may exist for several days. Thus, the total net infiltration is calculated as approximately the saturated hydraulic conductivity, multiplied by the number of days net infiltration occurred. For days when the amount of water available for net infiltration is less than the limit set by the saturated hydraulic conductivity of the bedrock (this condition applies only to the last day of an extended net infiltration event), net infiltration equals the amount of water available to net infiltration in the lowermost root-zone layer.

The daily water-balance model is applied over a continuous multiyear period and is driven by the continuous daily climate input provided for the total simulation period. The daily net infiltration rates calculated for each grid cell location are used to calculate an average annual net infiltration rate for each grid cell based on the total simulation period. The average annual net infiltration rate is calculated in units of length per time (millimeters per year) and can be directly applied as a specified flux upper boundary condition for the unsaturated zone flow model.

Climate change is treated using three distinct climate types identified from paleoclimate evidence over the last 400,000 years. The paleoclimate data shows a broad pattern of four glacial–interglacial climate cycles over this time period (USGS 2001c, Figure 8). Furthermore, evidence suggests that a longer period cycle on the order of 400,000 years is expected (USGS 2001c, Section 6.5.2). Therefore, the climate forecast for the next 10,000 years is based on the climate patterns discerned from the paleoclimate data from roughly 400,000 years ago. The first climate stage is a continuation of the current modern climate conditions from present day to approximately 600 years into the future. The second climate stage begins at approximately 600 years from present day and is characterized as a monsoon climate, with wetter summers relative to the modern climate. The third climate stage begins at approximately 2,000 years from present day and is characterized as a glacial transition climate with cooler air temperatures and (on average) higher annual precipitation relative to modern climate. The duration of the glacial transition climate is estimated to be 10,000 years, extending 2,000 years beyond the required 10,000-year estimation period.

Treatment of Uncertainty–The modern, monsoon, and glacial–transition climate stages are each represented with a drier lower-bound, a wetter upper-bound, and an intermediate mean climate scenario (DTN: GS000208311221.002). The lower- and upper-bound scenarios are developed to account for uncertainty and variability in the characteristics of precipitation and air temperature for each estimated future climate stage. The mean climate scenario is developed to represent average conditions within each stage. To develop a total of nine separate climate scenarios (three for each climate stage), separate INFIL V2.0 simulation results are averaged or sampled (USGS 2001a, Section 6.9). Separate simulation results are obtained for each of the 10 watershed modeling domains into a single result for the composite watershed model domain. Each individual simulation is defined by a unique combination of daily climate input and root-zone model coefficients (the coefficients are used to represent different vegetation characteristics). Characteristics of precipitation and air temperature for the estimated drier lower-bound and wetter upper-bound monsoon and glacial–transition climate scenarios are defined (USGS 2001c). To define the mean net-infiltration values for the monsoon and glacial transition scenarios, the lower- and upper-bound net infiltration estimates for each climate stage are averaged for each model grid cell. This implies that the distribution of net infiltration between the lower- and upper-bound scenarios for the monsoon and glacial–transition climate stages is symmetric (e.g., normal or uniform).

To develop the daily climate input for INFIL V2.0 that is considered representative of the characteristics of the estimated upper-bound monsoon, lower-bound glacial–transition, and upper-bound glacial–transition future climate scenario, available daily climate records at modern analogue sites were used. Selection of the representative analog sites is defined (USGS 2001c) and based on a comparison of predicted versus measured mean annual precipitation, mean annual temperature, and the seasonal distribution of mean annual precipitation and mean annual temperature. For each climate scenario, at least two analog sites were identified. Individual simulations were performed for each analog site, and the multiple simulations were averaged for all model grid cells to obtain a single net infiltration estimate for each climate scenario.

Results include the identification of a set of appropriate current climate analog sites for representing the estimated future climate stages in terms of mean annual precipitation, mean annual temperature, and seasonal distributions of mean annual precipitation and mean annual temperature (USGS 2001c). To incorporate uncertainty as variability in precipitation and, to a lesser degree, air temperature characteristics in the three estimated climate stages and corresponding estimates of net infiltration, results define a lower- and upper-bound climate scenario within each climate stage (USGS 2001c). To reduce uncertainty in the selection of a single "best" analog site, the lower- and upper-bound climate scenarios are represented using a set of two or three analog sites (USGS 2001c). Net infiltration is simulated using the climate input developed from the records at each analog site, and the results are averaged to obtain an estimate of net infiltration for a given climate scenario.

Assumptions and uncertainties regarding the estimated monsoon and glacial–transition potential future climate scenarios, including the timing and duration of each estimated future climate stage, are documented (USGS 2001c). For model application using the developed daily climate input for each climate scenario, assumptions in defining the root-zone model coefficients are required. In developing the net infiltration estimates for each climate scenario using a simple averaging of multiple simulation results, it is assumed that the length of the various simulation

periods are adequate for characterizing a given climate scenario. To develop an estimate of net infiltration for the mean climate scenario within the monsoon and glacial–transition climate stages, a uniform distribution of net infiltration rates is assumed between the upper- and lower-bound estimates at each model grid cell. Net infiltration estimates for the mean modern climate net infiltration scenario were obtained by averaging simulations performed specifically for the mean modern climate and thus are not necessarily equivalent to the arithmetic mean of the estimates for the upper- and lower-bound modern climate scenarios.

The results of the lower-bound, mean, and upper-bound infiltration scenarios are sampled in the TSPA-LA to represent infiltration uncertainty. A separate analysis of infiltration uncertainty for the glacial transition climate was performed to provide an estimate of infiltration uncertainty based on the uncertainty of the input parameters (BSC 2003a). Multiple simulations were conducted for input parameters randomly sampled, using a variant of the Monte Carlo method called Latin Hypercube Sampling. The output of the analysis is a probability distribution for the average infiltration. Climate analog infiltration rates were then fit to this probability distribution to establish the appropriate sampling frequencies in the TSPA-LA for the lower-, mean, and upper-climate analog infiltration scenarios. Although only strictly applicable to the glacial transition climate, these sampling frequencies are also used as an approximation for modern and monsoon climates. Eighty percent of the 10,000-year regulatory period is predicted to be under the glacial transition climate.

Interfaces and Integration with Other Models–The primary output of the infiltration model is the set of nine infiltration maps (three infiltration scenarios in each of the three climates) (DTN: GS000308311221.005). The primary interfaces with the infiltration model are subsurface flow models that have a boundary at the ground surface.

The infiltration model output provides the boundary condition at the ground surface for the water entering the unsaturated zone. This is a major control on overall hydrologic and thermal-hydrologic conditions within the unsaturated zone at Yucca Mountain. Net infiltration is the ultimate source of percolation through the unsaturated zone. Water percolating downward through the unsaturated zone will be the principal means by which radionuclides may be transported from the repository to the water table. The unsaturated zone flow model uses net infiltration rates as surface water recharge boundary conditions. The unsaturated zone flow model is concerned primarily with steady-state flow under each infiltration scenario, while future climates are expected to act sequentially. The climate states anticipated over the 10,000-year regulatory period are modern, monsoon, and then glacial transition climates. The transition from modern to monsoon climate is predicted to occur at 600 years after present, and the transition from monsoon to glacial transition climate is predicted to occur at 2,000 years after present.

The infiltration rates applied at the top of the drift-scale thermal-hydrologic seepage model and the drift-scale thermal-hydrologic-chemical model are adopted from the mean infiltration scenario that includes modern, monsoon, and glacial transition climates (USGS 2001a, Sections 6.9 and 6.11). The specific infiltration values (6, 16, and 25 mm/yr for the modern, monsoon, and glacial transition periods, respectively) represent repository-wide averages. These values have been calculated as the arithmetic average of the 31 repository locations considered in the multiscale thermal-hydrologic model (BSC 2001a, Section 6.3.1).

In terms of the ways in which hydrologic processes are represented, the infiltration model is different from other unsaturated zone models that calculate flow in porous media and fractured rock. The fundamental difference is that the other mathematical models of water flow in geologic media use the standard extension of Darcy's law for unsaturated conditions, employing relative permeability and capillary pressure concepts. This modeling approach allows for a continuum of flow responses that are a function of the hydrologic conditions throughout the model domain. In contrast, flow through the multilayered soil and fractured rock in the infiltration model is computed using a cascading, piston-flow method. The flow rate is zero if water saturation drops to a threshold value known as the field capacity. If the saturation exceeds the field capacity, the water volume in that layer in excess of the field capacity is added to the water content of the underlying layer. If this flux exceeds the saturated hydraulic conductivity of the underlying layer, the percolation rate between the two layers is set to this limiting value.

Furthermore, the flow is treated as an equivalent continuum with a single bulk hydraulic conductivity rather than as a dual continuum in the unsaturated zone flow model. In connection with the differences in hydrologic modeling methods, the infiltration model uses fracture properties for bedrock that are distinct from those used in the unsaturated zone flow model. The bulk saturated hydraulic conductivity represents a combination of the saturated hydraulic conductivity of the matrix (Flint 1998) and the saturated hydraulic conductivity of fracture-fill material (DTN: GS950708312211.003) based on the fracture density of the particular rock type. The saturated hydraulic conductivity of the fracture fill material was measured in the laboratory and averaged 43.2 mm/day (DTN: GS950708312211.003; USGS 2001a, Attachment IV). Permeabilities of filled fractures were used because surface observations indicated that many near-surface fractures are filled with calcium carbonate and siliceous materials. In addition, the use of filled fractures helps compensate for use of a saturated conductivity, when, in reality, water will infiltrate under a range of saturation conditions that would average to an effective conductivity that is less than the saturated conductivity. Estimates of saturated hydraulic conductivity were calculated using these values of fracture conductivity for the percentage of area covered by the fracture per square meter of rock, given the fracture density and size of aperture available through which water can flow. This was added to the saturated hydraulic conductivity of the rock matrix, and weighted averages of bulk bedrock saturated hydraulic conductivity were calculated on the basis of percentages of matrix and fractures by lithostratigraphic unit. The bulk saturated hydraulic conductivities range from a minimum of less than 10 mm/yr for densely welded tuffs with low matrix hydraulic conductivity and relatively small fracture densities, to a maximum of more than 100,000 mm/yr for alluvium and colluvium. The typical bedrock underlying soil within the repository footprint is the TCw, and fracture bulk hydraulic conductivity in this unit in the calibrated property set for the unsaturated zone flow model ranges from about 3×10^5 mm/yr to 3×10^7 mm/yr.

G.4.2 Unsaturated Zone Flow Model

Conceptual Background–The physical processes associated with flow and transport in porous media are governed by the fundamental conservation laws (i.e., conservation of mass, momentum, and energy), which govern the behavior of fluid flow through fractured porous media. The macroscopic continuum approach has been most commonly used in practical applications (Bear 1972). In this approach, the physical laws governing flow in porous media are represented mathematically on the macroscopic level by a set of partial differential or integral

equations. Fluid flow processes in fracture and matrix systems in the unsaturated zone are described using a macroscopic, dual-permeability continuum approach. In addition to the conservation or continuity equations of mass in fracture and matrix systems, specific relationships or mechanisms are needed that describe how fluid flow occurs in porous and fractured media.

The governing equation for isothermal, unsaturated liquid flow is the Richards equation (Richards 1931; Pruess et al. 1999, Equation A-17, p. 146), based on the conservation of mass (volumetric water content), and Darcy's law (Bear 1972), utilizing capillary pressure and relative permeability concepts to extend Darcy's law to unsaturated conditions. The Richards equation is applied to both the fracture and matrix continua. The fluid exchange between fracture continuum and matrix continuum is the fracture–matrix interaction, which is simulated using the active fracture model in the unsaturated zone flow model (Liu et al. 1998).

The active fracture model was developed within the context of the dual-continuum approach (Liu et al. 1998). It is based on the reasoning that, because of the fingering flow, only a portion of fractures in a connected, unsaturated fracture network contribute to liquid water flow, while other fractures are simply bypassed. The portions of the connected fractures that actively conduct water are called active fractures. In other words, the active fracture model uses a combination of the continuum approach and a simple filtering concept to model fracture flow. Inactive fractures are filtered out in modeling fracture–matrix interaction and flow in the fracture continuum.

The dual-permeability model is also modified by adding additional global fracture–matrix connections at interfaces of TCw–PTn, PTn–TSw, and vitric–nonvitric units to better simulate fracture–matrix flow at these transitions. These additional global fracture–matrix connections do not exist in the original dual-permeability model. Specifically, TCw fractures are vertically connected to the PTn matrix, PTn matrix to TSw fractures, and vitric matrix to nonvitric fractures, respectively, along these interfaces. Vitric units in the CHn are handled as single porosity matrix only (i.e., the effect of fractures on flow and transport within Calico Hills vitric zones is neglected). This conceptual model is supported by observation from the tracer tests (BSC 2001b; BSC 2001c, p. 136).

Model Implementation–The geologic model used for developing the unsaturated zone flow model and its submodels is the geologic framework model (DTN: MO0012MWDGFM02.002). The development and features of the three-dimensional model grids for the unsaturated zone flow model are documented (BSC 2003b). These geologic formations have been organized into layered hydrogeologic units based primarily on the degree of welding (Montazer and Wilson 1984), as follows: the Tiva Canyon welded (TCw) hydrogeologic unit, the Paintbrush nonwelded unit (PTn), the Topopah Spring welded (TSw) unit, the Calico Hills nonwelded (CHn), and the Crater Flat undifferentiated (CFu) units.

The three-dimensional unsaturated zone model domain, as well as the numerical grid for this study, is shown in plan view in Figure G-4, encompassing approximately 40 km^2 of the area over the mountain. The unsaturated zone model grid is referred to as the TSPA-LA grid. It is primarily designed for model calibration and simulations of three-dimensional flow fields delivered for use in TSPA-LA calculations. This three-dimensional model grid uses a refined

mesh in the vicinity of the repository, located near the center of the model domain, covering the region from the Solitario Canyon Fault to Ghost Dance Fault in the west–east direction, and from borehole G-3 in the south to beyond Sever Wash Fault in the north.

Also shown in Figure G-4 are the locations of several boreholes used in model calibrations and analyses. The model domain is selected to focus on the study area of the repository area and to investigate the effects of different infiltration scenarios and major faults on moisture flow around and below the repository. In the model grid, faults are represented in the model by vertical or inclined 30-m-wide zones. The model grid has 2,042 mesh columns of both fracture and matrix continua, and an average of 59 computational grid layers in the vertical direction, resulting in 245,506 gridblocks and 989,375 connections in a dual-permeability grid.

The model simulation results were carried out using TOUGH2 V1.4 (LBNL 2000). The single active liquid-phase flow module (EOS9) of the TOUGH2 code was used to calibrate the unsaturated zone flow model and several submodels and to generate three-dimensional TSPA-LA flow fields. The unsaturated permeability (relative permeability times formation permeability or saturated permeability) is related to both water content (saturation times porosity) and capillary pressure, as described by van Genuchten relationships (van Genuchten 1980).

The ground surface of the mountain (or the tuff-alluvium contact in areas of significant alluvial cover) is taken as the top model boundary; the water table is treated as the bottom model boundary. Both the top and bottom boundaries of the model are treated as Dirichlet-type conditions with specified constant, but spatially varying, temperature and gas pressure. A constant liquid saturation value of 0.99 was set for the bottom boundary. For flow simulations using the EOS9 module, only pressure or saturation values are needed along the top and bottom model boundaries. Surface infiltration is applied using a source term in the fracture gridblocks within the second grid layer from the top. This method was adopted because the first layer is treated as a Dirichlet-type boundary with constant pressure, saturation, and temperature to represent average atmospheric conditions at the mountain. The water table is used as the bottom model boundary, a surface where the water pressure is a fixed, single value. Within the numerical models, only one single set of model primary variables for solving the Richards equations is specified for the bottom boundary, and this is equivalent to specifying a constant saturation. All lateral boundaries, as shown in Figure G-4, are treated as no-flow (closed) boundaries, which allow flow only along the vertical plane.

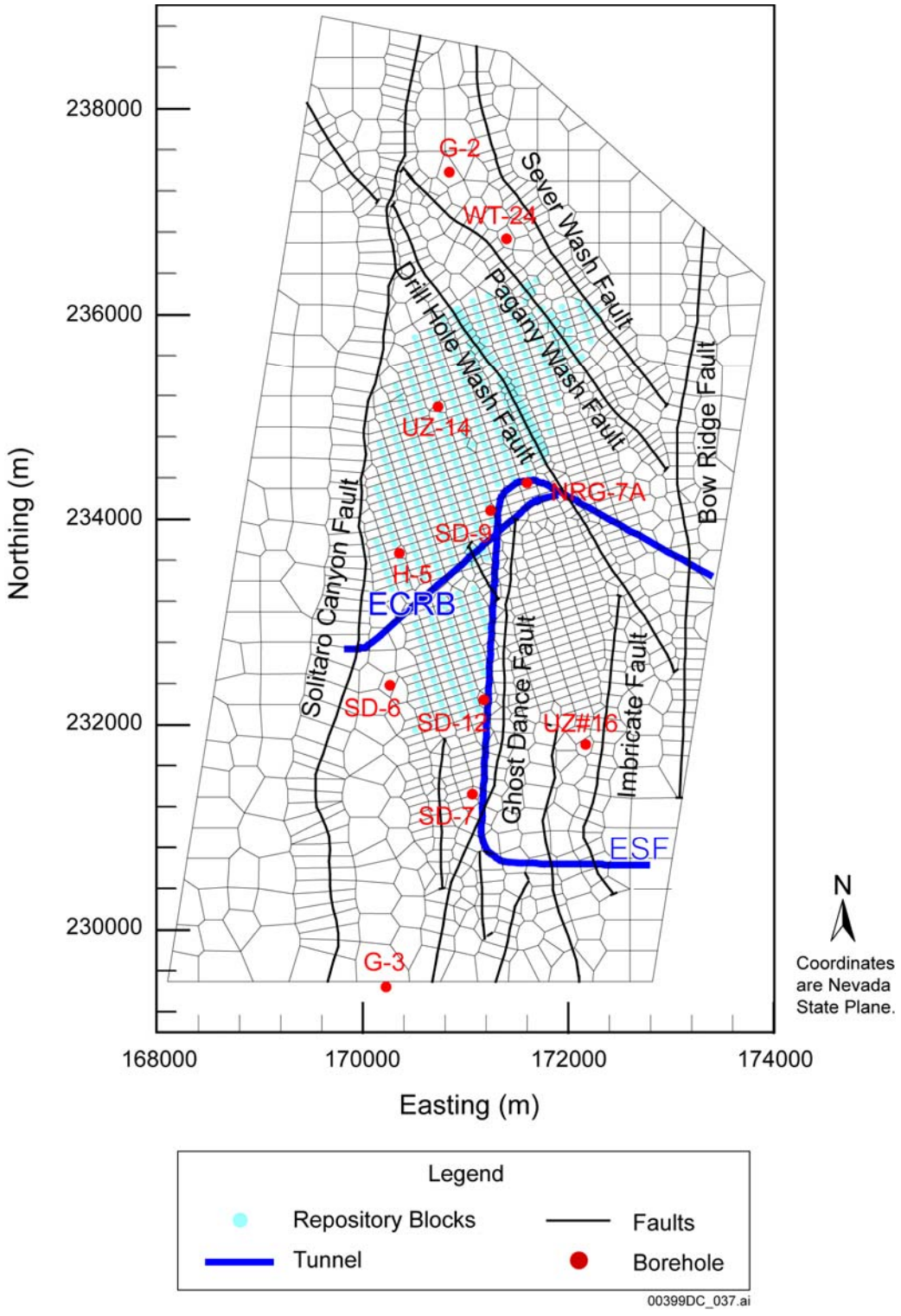

Source: BSC 2003c, Figure 6.1-1.

Figure G-4. Plan View of the Three-Dimensional Unsaturated Zone TSPA-LA Model Grid, Showing the Model Domain, Faults Incorporated, Repository Layout, and Several Borehole Locations

The unsaturated zone model uses net infiltration rates as surface water recharge boundary conditions. The net infiltration rates consist of modern and future scenarios, determined by studies of modern and future climates (USGS 2001c; USGS 2001a). A total of nine net infiltration maps (DTN: GS000308311221.005) are implemented with the unsaturated zone model and its submodels. These infiltration maps are documented in two reports (USGS 2001c; USGS 2001a) for infiltration and climate models. They include modern, monsoon, and glacial transition—three climatic scenarios, each of which consists of lower-bound, mean, and upper-bound rates. The nine infiltration rates are summarized (BSC 2003c, Table 6.1-2) for average values over the model domain. The unsaturated zone flow model is concerned primarily with steady-state flow under each infiltration scenario, while in the climate models reference to future climates means climates are expected to act sequentially over the modeled period: modern, monsoon, and then glacial transition for specific periods.

Calibrated hydrologic properties based on one-, two-, and three-dimensional calibrations were performed for each of the lower-bound, mean, and upper-bound infiltration scenarios for the modern climate. The resulting property sets are used for their respective scenario for each climate. It is well known that permeability is scale-dependent (Neuman 1994). Calibrated properties are necessary on two scales, mountain scale and drift scale. Calibration of the mountain-scale properties considers pneumatic pressure data that reflect the mountain-scale process of barometric pumping. Mountain-scale properties are intended for use in models of processes at the mountain scale. Calibration of the drift-scale properties does not consider the pneumatic pressure data. The drift-scale calibrated properties (DTNs: LB0208UZDSCPMI.002; LB0302UZDSCPUI.002; LB0208UZDSCPLI.002) for the mean, upper-bound, and lower-bound infiltration scenarios, respectively, and mountain-scale calibrated properties (for all infiltration scenarios) (DTN: LB03013DSSCP3I.001) are intended for use in models of processes at the drift scale.

The resulting nine flow fields are the base-case flow fields and have been submitted to TSPA-LA for performance analyses (DTN: LB03023DSSCP9I.001). The flow fields are generated using a dual-permeability model with extra global fracture–matrix connections, which cannot be directly used by the FEHM code in TSPA-LA calculations. These flow fields are converted using the routine flow-con V1.0 (LBNL 2003a), into flow fields on the dual-permeability mesh (mesh_2kb.dkm), which do not have the global fracture–matrix connections. The output-flow field files of flow-con V1.0 (LBNL 2003a) are then used as input files to the routine T2FEHM V4.0 (LBNL 2003b), which converts TOUGH2 files in the format of flow9.dat into files that can be used by FEHM. These converted flow fields were submitted to the Technical Data Management System for the use of the TSPA-LA (DTN: LB0305TSPA18FF.001).

Treatment of Uncertainty–Although the three-dimensional flow fields are based on qualified field-observation data, hydrogeologic conceptual understanding, and integrated modeling studies, significant uncertainties remain. These uncertainties arise from (1) uncertainty in observed parameters and field data; (2) uncertainty in estimated modern and future climates; (3) approximations used in hydrogeologic conceptual models, such as steady-state flow conditions; (4) scale-dependent heterogeneity and model input parameters in the unsaturated zone fracture–matrix system; (5) the complexity of different unsaturated zone coupled processes; and (6) the limitations of current modeling and large volume-average approaches.

A total of six sets of model input parameters are developed, with three base cases and three alternatives, which cover the effect of uncertainties in lower-bound, mean, and upper-bound infiltration rates. Uncertainties with modern and future climates are investigated using three scenarios—present day, monsoon and glacial transition climates—which combine for nine different net infiltration scenarios. In addition, sensitivity and uncertainty with the active fracture model parameter, α, is evaluated for its impact on flow and transport modeling results. The sensitivity analysis shows that α has little effect on simulated percolation fluxes but a large impact on tracer transport. The α value used in the unsaturated zone model produces more conservative transport results.

Uncertainties with unsaturated zone conceptual flow models are studied using two conceptual models of the PTn unit (i.e., base-case and alternative models, and using a permeability-barrier perched-water model). The base-case PTn model is selected for its better predictions of both chloride data and moisture data. Each of the conceptual models uses three different parameter sets for lower-, mean, and upper-bound infiltration rates to cover the uncertainties and possible ranges with model parameters and infiltration rates. This results in nine base-case and nine alternative three-dimensional unsaturated zone flow fields. In general, the nine base-case flow fields show more lateral flow occurring within the PTn than those predicted by the alternative model. Furthermore, analyses have been done for the impact of behavior on tracer or radionuclide transport for the nine base-case and nine alternative flow fields. The results of 40 three-dimensional tracer-transport simulations show a wide range of tracer transport times from the repository to the water table, and the base-case model gives slightly more conservative estimates in general.

Uncertainty may exist in the analysis of lateral flow in the PTn unit because of the choice of approach. Different approaches may yield different conclusions. It has been concluded that lateral flow may occur in the PTn on a smaller scale than found in the unsaturated zone flow model (Flint et al. 2003; BSC 2003c, Figures 6.6-1 to 6.6-3). However, their conclusion is based on a different approach from the one used in the unsaturated zone flow model. First, an analytical solution that is only applicable to single-porosity porous-medium flow with two semi-infinite layers and that may not be suitable to estimate lateral flow for the multilayered fracture–matrix system was used (Flint et al. 2003). Second, the analytical solution uses a Gardner's equation for relative permeability, as compared with the van Genuchten equation used in the unsaturated zone flow model. Third, a two-dimensional modeling study was presented without including three-dimensional effects (Flint et al. 2003). They also acknowledge that no one approach, analysis, or data set can establish whether large-scale lateral flow occurs above the repository.

Interfaces and Integration with Other Models–The unsaturated zone flow model output used for mountain-scale radionuclide transport in the TSPA-LA consists of a set of nine flow fields (three infiltration scenarios for each of the three climate scenarios) and nine alternative flow fields described in *UZ Flow Models and Submodels* (BSC 2003c, Section 6.6 and Attachment IV). The six base-case flow fields under monsoon and glacial transition climates have also been post processed with the software WTRISE V2.0 (LBNL 2003c) using the higher water table expected for future climates, as presented in *UZ Flow Models and Submodels* (BSC 2003c, Section 6.6.3). The unsaturated zone flow model output interfaces with the FEHM particle-tracking algorithm used for mountain-scale radionuclide transport in the TSPA-LA.

This interface requires a flow-field conversion, as discussed above, such that the flow fields are compatible with FEHM.

The unsaturated zone flow model output (DTN: LB03023DSSCP9I.001) is used to establish the percolation flux near waste emplacement drifts in the four emplacement horizons of the TSw hydrogeologic unit (the upper lithophysal or tsw34, middle nonlithophysal or tsw35, lower lithophysal or tsw36, and lower nonlithophysal or tsw36). These flow rates are used to evaluate the fraction of radionuclides released from drifts to the rock fractures and rock matrix (see engineered barrier system radionuclide transport abstraction model).

The unsaturated zone flow model output (DTN: LB0302PTNTSW9I.001) is used to set the flux in the line-averaged heat-source, drift-scale, thermal-hydrologic submodel of the multiscale thermal-hydrologic model, which is a two-dimensional model performed with the software NUFT (LLNL 2002). Although this output is the flux in the unsaturated zone flow model at the PTn–TSw interface, this flux is set at the ground surface in the line-source drift-scale thermal-hydrology submodel (see multiscale thermal-hydrologic model).

The flux boundary condition for the drift seepage abstraction model used in the TSPA-LA is discussed in *Multiscale Thermohydrologic Model* (BSC 2003d, Section 8.3). However, these flux values are taken at the PTn–TSw interface, which is the location used to determine the flux input values for the multiscale thermal-hydrologic model from the unsaturated zone flow model (see above). Therefore, these flux values are nearly identical to the unsaturated zone flow model fluxes determined at this interface, because thermal-hydrologic effects on flow are minimal at this distance from the repository.

As discussed in the conceptual background for the unsaturated zone flow model, the standard dual-permeability model was modified by adding additional global fracture–matrix connections at interfaces of TCw–PTn, PTn–TSw, and vitric-nonvitric units to better simulate fracture–matrix flow at these transitions. As discussed under model implementation, the flow fields are postprocessed such that the standard dual-permeability connection structure used by FEHM will produce the correct flow fields for radionuclide transport. However, the multiscale thermal-hydrologic model, drift-scale thermal-hydrologic seepage model, and the drift-scale thermal-hydrologic-chemical model do not utilize these global connections. These drift-scale models employ drift-scale calibrated properties (rather than the mountain-scale calibrated properties used by the unsaturated zone flow model), which were developed based on the standard dual-permeability connection structure.

G.4.3 Multiscale Thermal-Hydrologic Model

Conceptual Background–The role of the movement of water and heat within the repository is treated by the study of thermal hydrology, which combines the more traditional fields of hydrology and heat transfer. The physical domain is the unsaturated zone of Yucca Mountain, which lies above the groundwater table (i.e., the immediate and near-field location where the emplacement drifts will be constructed and the waste will be disposed). The repository host horizon is the TSw hydrostratigraphic unit, which follows a very gently dipping plane approximately midway between the ground surface and the water table. The repository will accommodate the emplacement of spent nuclear fuel from commercial nuclear power plants and

solidified high-level radioactive waste. Heat output declines exponentially with time, but continues for tens of thousands of years because of the very long half-life of many of the radionuclides.

After the emplacement of heat-generating nuclear waste, the thermally driven flow of water vapor away from the heat source causes a redistribution of the pore fluids within a potentially large volume of rock. Depending on the thermal design of the repository, this volume can extend from the ground surface to some distance below the water table and over an area larger than the repository footprint. Water in the matrix pores evaporates, creating zones of rock dryout (with liquid-phase saturation less than ambient values) around the emplacement drifts. This water vapor is driven (primarily in fractures) away from the heat source in the emplacement drifts to where cooler temperatures cause it to condense, forming condensation zones outside of the dryout zones. The reduction in liquid-phase saturation causes a reduction in relative humidity in both the near-field host rock as well as in the emplacement drifts. Heat pipes can result from the countercurrent flow of water vapor and liquid water between the dryout and condensation zones. The magnitude of the liquid flux in this heat pipe can greatly exceed the magnitude of ambient liquid-phase fluxes. As the heat pulse decays, the system gradually rewets, returning to ambient (humid) preheating conditions.

The multiscale thermal-hydrologic model utilizes a combination of different thermal conduction and thermal-hydrologic submodels. In terms of the treatment of water flow, the line-source drift-scale thermal-hydrology submodel computes the effects of heat transfer (including convection and conduction mechanisms) within a two-dimensional chimney domain (i.e., a two-dimensional model that employs a one-dimensional representation of the hydrogeologic properties). However, because the waste heat is localized (i.e., a two-dimensional heat source) within the model domain, the effects of heat lead to two-dimensional flow and temperature patterns. The other submodels do not include the effects of flow, and heat transfer is limited to thermal conduction.

The treatment of flow phenomena in the multiscale thermal-hydrologic model parallels the approach used in the unsaturated zone flow model (see conceptual background for the unsaturated zone flow model). Both models represent fractured rock as a dual-permeability continuum and flow phenomena using Darcy's law. Both models use the active fracture model for water flow in fractures and fracture–matrix interaction. The multiscale thermal-hydrologic model extends the use of Darcy's law to a two-phase, two-component system to capture the effects of thermal-hydrologic processes such as boiling, condensation, and vapor transport.

Model Implementation–The basis of the multiscale thermal-hydrologic model modeling approach is *UZ Flow Models and Submodels* (BSC 2003c). A three-dimensional definition of hydrostratigraphic units (called unsaturated zone model layers) is incorporated into the multiscale thermal-hydrologic model, including position of the water table and surface topography, thermal-hydrologic properties for these units, and model boundary conditions (BSC 2003b). The model includes 36 unsaturated zone model layers, each of which is considered to be homogeneous with respect to thermal and hydrologic properties. These hydrologic properties are determined through an inverse modeling approach constrained by site hydrologic data; the assumption is made that heterogeneity is captured by the detailed

stratification (Bandurraga and Bodvarsson 1999). Thermal properties are determined on the basis of laboratory measurements (BSC 2002a).

The multiscale thermal-hydrologic model computes thermal-hydrologic behavior through a combination of four component submodels, all using the software NUFT v3.0.1s (LLNL 2002). These submodels are the:

- SMT submodel (the three-dimensional smeared-source mountain-scale thermal-only submodel)
- Line-source drift-scale thermal-hydrology submodel
- SDT submodel (the one-dimensional smeared-source drift-scale thermal-only submodel)
- DDT submodel (the three-dimensional discrete-source drift-scale thermal-only submodel).

The fundamental concept behind the multiscale thermal-hydrologic model is that two-dimensional representations of drift-scale thermal hydrology (the line-source drift-scale thermal-hydrology submodels) can account for mountain-scale edge cooling processes by changing horizontal distance of the adiabatic boundary in the drift-scale model. For locations within an infinite (x and y) expansive repository, the drift-scale model adiabatic boundary distance would be the halfway point between drifts. Edge effects within the model are accommodated by allowing the adiabatic boundaries to extend in time to mimic the cooling process. The measure of the distance to the adiabatic boundary is measured using the areal mass loading factor, which measures the heat input per unit area. As the distance to the adiabatic boundary increases, the areal mass loading decreases.

The relation between the time-varying areal mass loading at any given point in the repository is determined by interpolating the necessary width to the adiabatic boundary needed for an SDT submodel at that particular point to match the SMT submodel predicted temperature. This is a superposition process justified by the linear nature of the conduction-only energy equation. Once this areal mass loading history is established, it is applied to the line-source drift-scale thermal-hydrology submodel, which introduces the dimensionality of the heat source (a waste package) and the hydrology of the system. The final component of multiscale thermal-hydrologic model is the inclusion of thermal-radiative heat transfer with the DDT submodel. Here the temperature redistribution caused by the variation between hotter waste packages, colder waste packages, and gaps between waste packages for one location in the repository is determined. This temperature difference is then applied to the two-dimensional thermal-hydrologic results to give complete thermal-hydrologic histories for all locations and all waste packages within the repository.

The effects of flow are captured in the line-source drift-scale thermal-hydrology submodel. The same mesh, shown in Figure G-5 (BSC 2003d, Figure 6.2-6), is used for the initialization submodel runs, which establish steady-state conditions for the time of emplacement and the submodel runs for the preclosure and postclosure periods. The numerical mesh for the line-source drift-scale thermal-hydrology submodel assumes that the drip shield and waste

package are lumped as a monolithic heat source. This lumped approximation of the drip shield and waste package allows for the representation of thermal-hydrologic behavior down to the surface of the drip shield. The lumped heat source is 1 m in the longitudinal direction along the drift axis. This lumped representation for the waste package and drip shield is applied during both the preclosure and postclosure period.

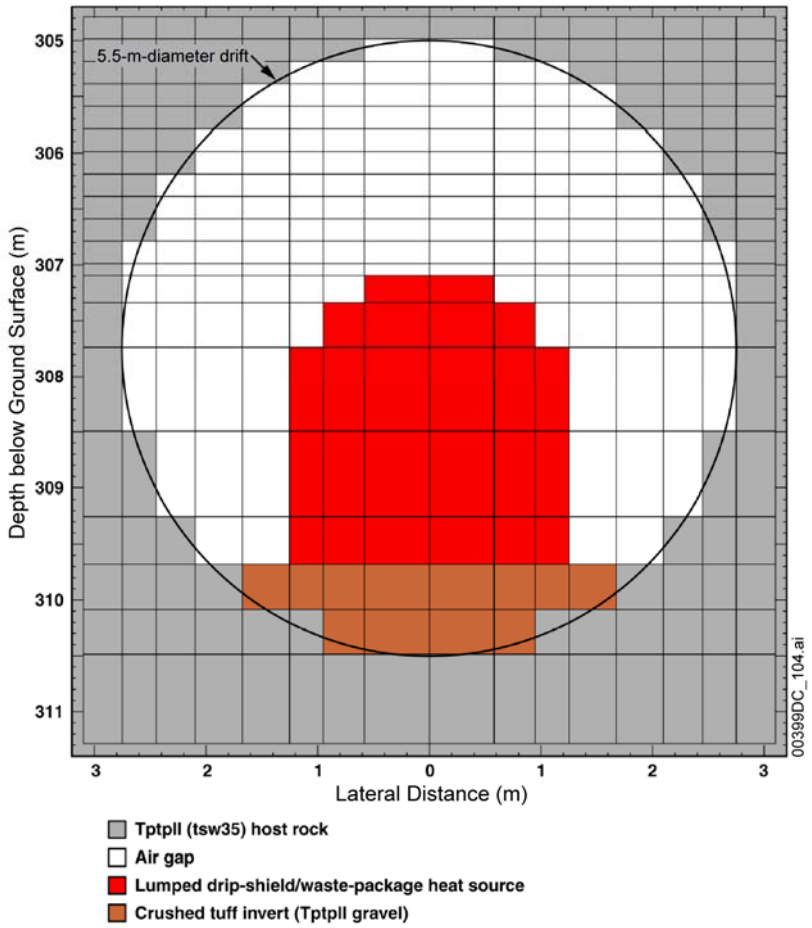

Source: BSC 2003d, Figure 6.2-6.

NOTE: Model domain extends from the ground surface to the water table. LDTH = line-source drift-scale thermal-hydrology.

Figure G-5. Cross-Sectional View of the Numerical Mesh Used in the Vicinity of the Drift for All Line-Source Drift-Scale Thermal-Hydrology Submodels, Including Both of the Initialization Runs and the Preclosure and Postclosure Runs

Because the line-source drift-scale thermal-hydrology submodels are for a symmetry cell between the vertical plane down the center of the drift and the vertical midplane between drifts, the lateral boundaries are adiabatic and no-mass-flow boundaries. The line-source drift-scale thermal-hydrology submodels require temperature, pressure, and gas-phase air–mass fraction at the upper boundary, which represents the ground surface and the lower boundary, which in turn represents the water table. The upper boundary also requires the enthalpy associated with the

infiltration flux at the top of the model. The correct enthalpy is determined from the temperature of the upper boundary. Both the upper and lower boundaries have constant conditions with time. The process of calculating air–mass fraction at the ground surface utilizes the assumption that the atmosphere is at 100% relative humidity (BSC 2003d, Section 5.1.1). A relative humidity of 100% is applied at the upper boundary to ensure that the PTn-to-TSw percolation flux is neither significantly diminished nor increased by virtue of gas-phase moisture flux at this boundary. The effect of this approximation is conservative in that this boundary condition results in a slight increase in moisture flux above the repository horizon.

One hydrologic property set, called the modified mean-infiltration flux hydrologic property set, is used to conduct the line-source drift-scale thermal-hydrology submodel calculations for the low-, mean-, and high-infiltration flux cases. The modified mean-infiltration flux property set is the same as the mean-infiltration flux property set (DTN: LB0208UZDSCPMI.002) with the one modification being that the van Genuchten fracture alpha in the Tptpul (tsw33) is set to be the same (1.02×10^{-4} Pa^{-1}) as that in the Tptpll (tsw35) unit (BSC 2003d, Section 6.3.1). The file dkm-afc-EBS-mi-03 gives the thermal and hydrologic properties of the materials inside the emplacement drift. The thermal properties inside the emplacement drifts, such as the drip shield and invert, are given (BSC 2003d, Table 4-1). The engineered barrier system thermal properties also include the use of an effective thermal conductivity for the gas-filled drift cavity that is based on a correlation (Francis et al. 2003, Table 6) accounting for the influence of natural convection (BSC 2003d, Attachment I). The gas-filled cavity between the drip shield and drift wall is represented as a porous media with 100% porosity and a very large permeability of 11×10^{-8} m^2 (BSC 2003d, Section 5.3.1.7). Because the dual-permeability method is used to represent fracture–matrix flow, it is necessary to partition the gas-filled cavity into the matrix and fracture continuum. This portioning, which is taken to be 50% matrix continuum and 50% fracture continuum, has no effect on flow because conditions in these respective continua are in equilibrium within the gas-filled drift.

The upper boundary of the line-source drift-scale thermal-hydrology submodels must be specified for the liquid-phase flux. For the TSPA-LA base case, the upper-boundary liquid-phase flux corresponds to the distribution of percolation flux just below the base of the PTn unit. This data is generated by the three-dimensional unsaturated zone flow model for the three climate states: modern, monsoon, and glacial transition. Thus, the multiscale thermal-hydrologic model accounts for the influence of lateral diversion in the PTn as represented in the three-dimensional unsaturated zone flow model. Percolation flux is provided for the modern, monsoon, and glacial transition climates for the lower-, mean, and upper-bound infiltration flux cases (DTN: LB0302PTNTSW9I.001), resulting in nine files.

The TSPA-LA discretizes the repository into five bins based on the percolation flux above the repository horizon (BSC 2003e, Figure 5.2-1a). This approach is more transparent and permits improved representation of spatial variability in thermal-hydrologic-chemical processes within the emplacement drifts. The TSPA-LA procedure subdivides the repository into five bins based on values of percolation just above the repository horizon for the medium infiltration scenario during the glacial transition climate.

The multiscale thermal-hydrologic model is implemented in the TSPA-LA through spatial averages over these bins. Time dependent thermal-hydrologic variables will be abstracted from these simulations for each of the repository level bins. Abstracted outputs include:

- Waste package surface temperature and waste package surface relative humidity for seven different package types within discrete environments. These values will be provided to drip shield, waste package, and waste form models in GoldSim (Golder Associates 2003).

- Average waste form temperature and liquid saturation in the invert in each of the five repository level bins. Waste form surface temperature will be assumed to be equal to the waste package surface temperature. These temperature and saturation values will be provided to the waste form degradation and engineered barrier system transport models in the GoldSim (Golder Associates 2003) program.

- Average drift wall temperature, relative humidity, evaporation rate, and liquid saturation in the invert in the repository. These values will be provided to the engineered barrier system chemical environment models. The outputs will be in the form of response surfaces or multidimensional tables.

- Long-term percolation flux above the drift. These values will be used as inputs to the seepage response surface.

Treatment of Uncertainty–For the multiscale thermal-hydrologic model predictions of thermal-hydrologic conditions within the emplacement drifts and in the adjoining host rock, the key uncertain parameters fall into three categories: (1) thermal properties; (2) hydrologic properties; and (3) percolation flux. For thermal and hydrologic properties, the primary focus concerns the properties of the host rock and of the materials within the emplacement drifts and the ambient percolation flux at the repository horizon.

The propagation of parametric uncertainty in the multiscale thermal-hydrologic model involves two key natural-system parameters: host-rock thermal conductivity and percolation flux. A sensitivity study of the influence of hydrologic-property uncertainty supports the conclusion that hydrologic property uncertainty does not need to be propagated in the multiscale thermal-hydrologic model calculations of in-drift temperature and relative humidity. The propagation of percolation flux uncertainty and host-rock thermal-conductivity uncertainty on the multiscale thermal-hydrologic model output is captured with the use of the lower-, mean-, and upper-infiltration flux output data sets for the following reasons. Because the multiscale thermal-hydrologic model captures the influence of repository scale variability, edge cooling effects, the distribution of thermal-hydrologic properties and percolation flux (down to the scale of 20 m along each of the emplacement drifts), and the influence of waste-package-to-waste-package variability of heat-generation output (down to the scale of individual waste packages), and because it captures the wide range in percolation flux (by virtue of incorporating three infiltration-flux cases), the spectrum of calculated thermal-hydrologic conditions is extremely broad. For these three data sets, the range in peak drift-wall temperature resulting from percolation flux uncertainty is from 98.6°C to 154.8°C, with a median drift-wall temperature of 133.0°C; the range in peak waste package temperature is from 108.6°C to 182.9°C, with a

median waste package temperature of 153.3°C (BSC 2003d, Table 6.3-4 and Figure 6.3-37). Another key thermal-hydrologic parameter is the time when boiling ceases at the drift wall because this is an indication of how long seepage into the emplacement drifts is extremely unlikely. For the three data sets, the time when drift-wall boiling ceases ranges from 97.7 to 1,734.6 years, with a median time of 721.0 years (BSC 2003d, Table 6.3-5 and Figure 6.3-37). A sensitivity study of the importance of thermal-conductivity uncertainty on thermal-hydrologic conditions in the emplacement drifts was conducted for selected locations in the repository, which included each of the four host-rock units. It is found that combined influence of percolation flux uncertainty and thermal-conductivity uncertainty results in a peak waste package temperature range of approximately 100°C to 200°C across the repository. The combined influence of percolation flux uncertainty and thermal-conductivity uncertainty results in an approximate range of no boiling at the drift wall to 2,100 years for the time when boiling at the drift wall ceases.

Interfaces and Integration with Other Models–The multiscale thermal-hydrologic model output is used by water flow models inside the waste emplacement drift (see engineered barrier system radionuclide transport abstraction model), providing the invert intragranular flow rates. The flux boundary condition for the drift seepage abstraction model used in the TSPA-LA is given through the output generated by the multiscale thermal-hydrologic model (DTNs: LL030602723122.027; LL030608723122.028; LL030610323122.029). However, these output values are essentially unchanged by the multiscale thermal-hydrologic model from the input values given by the unsaturated zone flow model. The multiscale thermal-hydrologic model receives flow rates from the unsaturated zone flow model at the PTn–TSw interface, but applies these at the ground surface. This is done to allow the multiscale thermal-hydrologic model to include the effects of the units above the TSw and terminate at the ground surface. The approximation invoked is that the ambient percolation flux distribution above the repository horizon is unaffected by mountain-scale repository-heat-driven thermal-hydrologic effects until it reaches the boiling condensation zones surrounding the emplacement drifts. This results from the fact that subboiling evaporation has a negligible influence on the magnitude or direction of liquid-phase flux and that boiling does not occur in units above the TSw.

The multiscale thermal-hydrologic model differs from the unsaturated zone flow model and other unsaturated zone flow models in two areas. The multiscale thermal-hydrologic model does not use the three drift-scale property sets for the lower-bound, mean, and upper-bound scenarios as developed in the calibrated properties model (BSC 2003f). The sensitivity to the variations in hydrologic properties for temperature and humidity in the drift were found to be negligible; therefore, this uncertainty was not propagated through the multiscale thermal-hydrologic model. Furthermore, the multiscale thermal-hydrologic model uses a modified mean property set as compared with the drift-scale mean property set. The modified mean-infiltration flux property set is the same as the mean infiltration-flux property set (DTN: LB0208UZDSCPMI.002), with the one modification being that the van Genuchten fracture alpha in the Tptpul (tsw33) is set to be the same (1.02×10^{-4} Pa^{-1}) as that in the Tptpll (tsw35) unit (BSC 2003d, Section 6.3.1). This modification was used for the multiscale thermal-hydrologic model because it was found that the application of the modified mean-infiltration flux property set to the lower-, mean-, and upper-infiltration flux cases produces more uniform calculated host-rock liquid-phase saturations for the three infiltration-flux cases.

The multiscale thermal-hydrologic model differs from the drift-scale thermal-hydrologic seepage model in terms of the treatment of flow focusing at the drift scale. Flow focusing denotes the potential concentration of flow from the large scale, as simulated with the unsaturated zone flow model, to the drift scale, as simulated by the drift-scale thermal-hydrologic seepage model. Additional sensitivity studies using the multiscale thermal-hydrologic model, considering a similar range of flow focusing as used in the drift-scale thermal-hydrologic seepage model and uncertainty in host-rock thermal conductivity, were performed to investigate the effects of these factors. The results indicate that the range of behavior for peak waste package temperature and duration of boiling captured with the lower-bound, mean, and upper-bound flux scenarios covers roughly 75% of their maximum range when the effects of flow focusing and thermal conductivity uncertainty are included.

G.4.4 Seepage Abstraction Model and Supporting Process Models

Conceptual Background–Drift seepage refers to the flow of liquid water into waste emplacement drifts. The unsaturated rock layers overlying and hosting the repository form a natural barrier that reduces the amount of water entering emplacement drifts by natural subsurface processes. For example, drift seepage is limited by the capillary barrier forming at the drift wall, which decreases or even eliminates water flow from the unsaturated fractured rock into the drift. During the first few hundred years after waste emplacement, when above-boiling rock temperatures will develop as a result of heat generated by the decay of the radioactive waste, vaporization of percolation water is an additional factor preventing seepage. In addition, seepage may be affected from changes in hydrologic properties as a result of mechanical and chemical effects, from changes in the drift shape due to drift degradation, and from the presence of rock bolts used for ground support. Several of these factors are also time dependent, such as percolation flux and thermal effects.

The purpose of the seepage component in TSPA-LA is to calculate the seepage rate (amount of seepage per time) and the seepage fraction (the fraction of waste packages affected by seepage) as a function of time and location in the repository. The calculation is performed using a probabilistic approach that accounts for the spatial and temporal variability and inherent uncertainty of seepage-relevant properties and processes. The resulting information takes the form of probability distributions for seepage events.

Abstraction is defined as the process of purposely simplifying a mathematical model (component, barrier, or subsystem process model) for incorporation into an overall system model of the geologic repository (BSC 2002b, Section 3.1.1). The purpose of the seepage abstraction model is to provide the necessary methodology, tools, parameter distributions, lookup tables, and simplifications to the TSPA-LA, so that the seepage calculations can be performed by the respective TSPA-LA module. The seepage abstraction model is based on various unsaturated zone process models that use similar model concepts, rock properties, and boundary conditions (i.e., water flow rates). Within the abstraction process, the information generated by the seepage process models is modified into a form that can be used in the TSPA-LA. The simplifications and assumptions made in this process are realistic and appropriate. In particular, uncertainties and spatial variabilities of the primary process models for seepage are represented in the abstraction model and propagated to TSPA-LA. Details on the seepage abstraction model are provided (BSC 2003g).

The suite of primary process models providing input to the abstraction model can be categorized as follows. The first three process models explicitly simulate the flow diversion and capillary barrier behavior at the rock–drift interface and provide seepage rates for given parameter cases:

Seepage Calibration Model–This process model provides the conceptual basis for seepage modeling and derives seepage-relevant parameters through calibration of the model against seepage-rate data from liquid-release tests (BSC 2003h). The seepage calibration model is conceptualized as a heterogeneous continuum for the fracture network. Flow in the matrix is not directly represented. The continuum approach can be considered appropriate for seepage studies if it is capable of predicting seepage rates for a drift in a fractured formation. Adopting the continuum approach, water flow under unsaturated conditions is governed by the Richards equation (Richards 1931), which states that isothermal flow of water in a porous medium or rough-walled fracture occurs under the combined effect of gravitational and capillary forces, that flow resistance is a function of saturation, and that (for the purposes of this representation) movement of the nonwetting air phase can be neglected.

Seepage Model for Performance Assessment–This process model predicts drift seepage rates for long-term ambient conditions at Yucca Mountain, for a wide range of seepage-relevant parameters and for potentially important perturbing effects. The model output is in the form of a seepage lookup table, where seepage rates and uncertainties are given as a function of three key parameters (effective capillary-strength parameter, local permeability, and local percolation flux). The seepage model for performance assessment follows the same conceptual model as the seepage calibration model.

Drift-Scale Thermal-Hydrologic Seepage Model–This process model predicts drift seepage during the period when water-flow processes in the drift vicinity are perturbed by heating of the rock (BSC 2003i). The transient, thermally affected seepage rates are given relative to the long-term ambient seepage rates from the seepage model for performance assessment. Flow processes are modeled for thermal seepage using the continuum approach and the extension of Darcy's law for two-phase flow as modified by the active fracture model. Fractured rock is represented using the dual-permeability model, which considers separate but interacting fracture and matrix continua, each with specified hydrogeologic properties.

The second set of models provides information on the percolation flux distributions that are used as an upper boundary to the seepage process models. The main model for this purpose is the unsaturated zone flow model, which provides three-dimensional site-scale flow fields to derive the local percolation flux (BSC 2003c). In addition, flow focusing factors account for intermediate-scale heterogeneity that is not represented in the layer-averaged unsaturated zone flow model. These are estimated from an intermediate-scale flow focusing model (BSC 2001c, Section 6.4.2).

The third set of models provides supporting information on the potential impact of coupled processes on seepage-relevant parameters. These drift-scale models—the coupled thermal-hydrologic-mechanical and the thermal-hydrologic-chemical models—are utilized to assess whether seepage-relevant parameters may be affected by thermally induced mechanical or chemical processes (BSC 2003j; BSC 2003k). These models do not directly calculate seepage rates. Having coupled thermal-hydrologic-mechanical or thermal-hydrologic-chemical models

directly provide seepage rates is desirable but not feasible because of the computational burden involved in such simulations.

The relationship and the information flow between the suite of primary process models important for seepage and the seepage abstraction are schematically illustrated in Figure G-6. It is important that these models are consistent in their use of water flow rates so that the seepage abstraction is based on a suite of consistent process models.

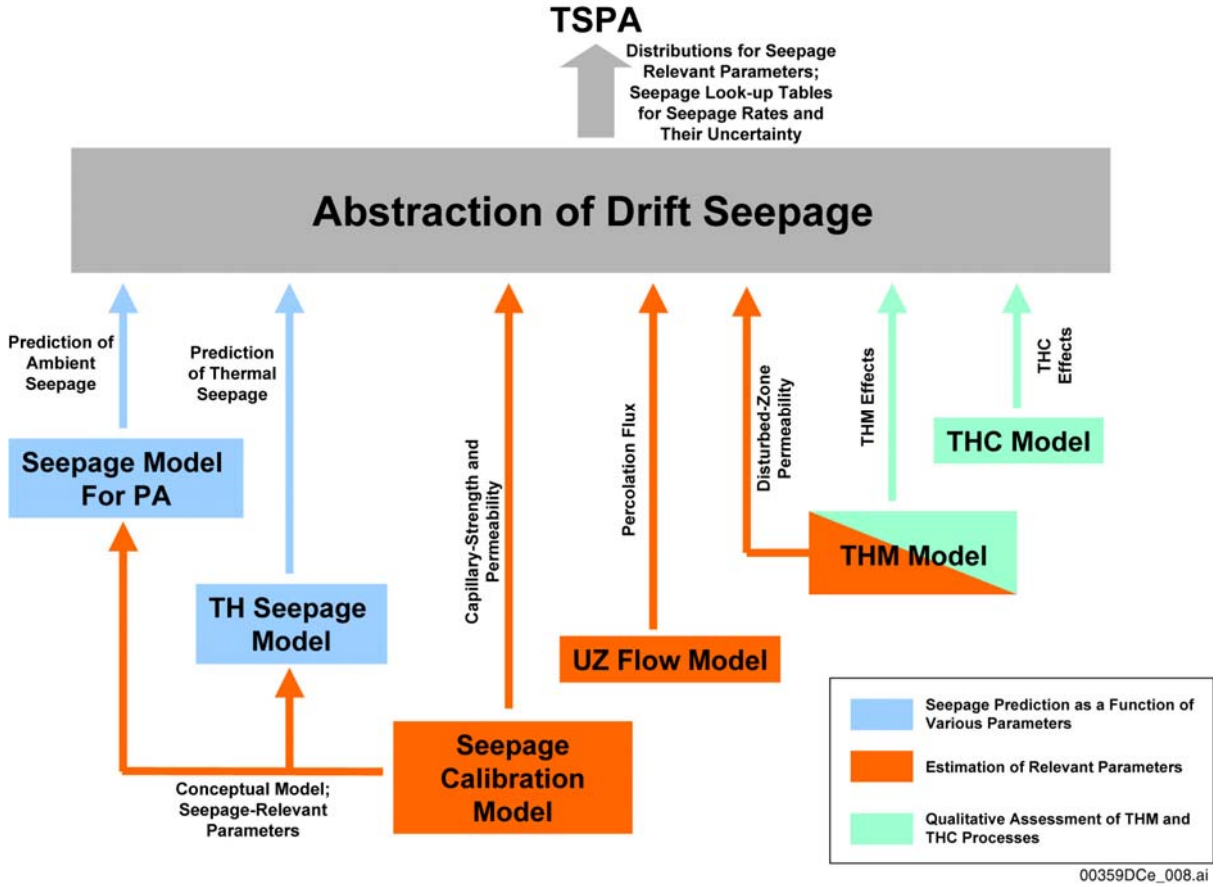

Source: BSC 2003g, Figure 1-1.

NOTE: THC = thermal-hydrologic-chemical; THM = thermal-hydrologic-mechanical; TH = thermal-hydrologic; PA = performance assessment.

Figure G-6. Relationship and Information Flow between Process Models and Seepage Abstraction

Seepage Model for Performance Assessment Implementation–The three-dimensional computational domain for this model (Figure G-7) is chosen to be 10 m high, 4 m wide, and 2.4384 m long, covering the upper left-hand portion of the drift with a diameter of 5.5 m (BSC 2003l, Figure 6-1). Thus, a vertical plane through the axis of the drift forms the right-hand boundary and the drift axis is 0.5 m above the lower boundary. The grid cells in the plane normal to the drift axis are 0.1×0.1 m. The limited size of the computational domain was chosen to allow the use of a fine mesh at the same refinement level as the seepage calibration model and yet contain a reasonable number of grid cells so as not to make the computational time too long. The left-hand boundary is placed equal to 1.25 m (which is the difference

between the model diameter of 4 m and half the drift diameter of 2.75 m) beyond the left-hand limit of the drift to capture the main flow feature (i.e., flow diversion around the drift) (Philip et al. 1989, p. 21, Figure 1). The side boundary conditions are no-flow. The lower boundary condition is gravity drainage, implemented by setting the capillary pressure gradient to zero across the bottom connections. The upper boundary surface is simulated by an extra grid cell with constant percolation flux connected to all the grid cells in the first row. Flow is thus free to move into these cells according to local property parameters. Since all calculations were run to steady state, the initial conditions are not important and are set to zero saturation over the domain.

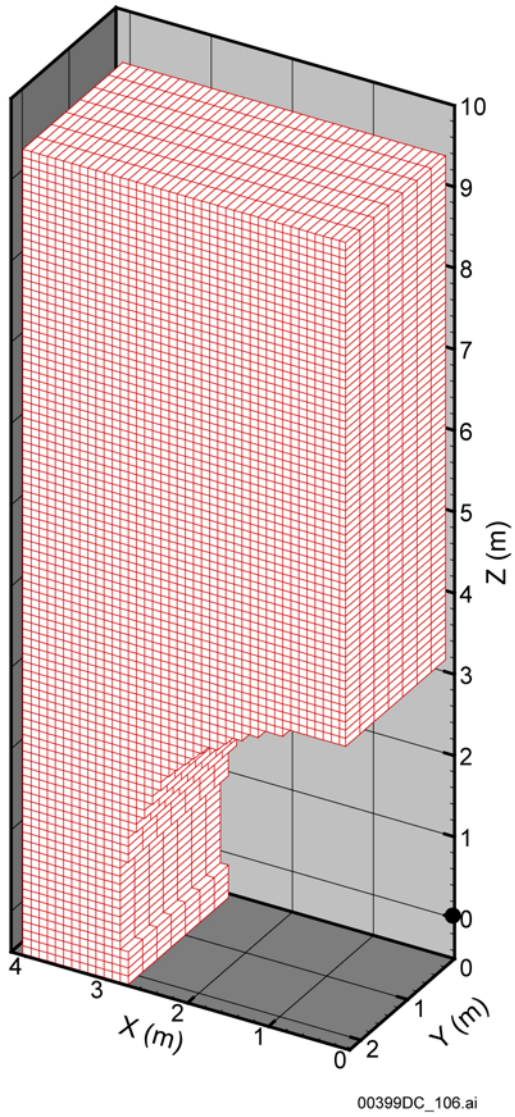

Source: BSC 2003l, Figure 6-1.

NOTE: Z = 0 and X = 0 indicates the axis of the drift.

Figure G-7. Model Domain and Mesh Design

At the drift wall, the nodal distance between the drift surface and the grid cell representing the drift is set to be very small, so that the boundary condition can be applied directly at the drift

wall. The length of the last vertical connection between the drift wall and the neighboring gridblocks representing the formation is set equal to 0.05 m, to make this model consistent with the seepage calibration model (BSC 2003h). The choice of this 0.05-m vertical connection to the drift wall implies a direct gravity-controlled vertical flow, with no horizontal diversion, over this 0.05-m distance.

Flow calculation was performed using iTOUGH2 V5.0 (LBNL 2002). Relative permeability and capillary pressure phenomena in the fracture continuum are represented using the van Genuchten parametric function. The selection of parameter ranges and particular cases to be modeled is based on available relevant data, as discussed in the seepage model for performance assessment. The parameters most likely to affect drift seepage are fracture continuum permeability, van Genuchten $1/\alpha$ value, and the percolation flux. For each combination of these three parameters (i.e., at each grid point in three-dimensional parameter space), seepage model calculations will be made for 20 realizations of the generated heterogeneous permeability field. The percolation fluxes span a range that encompasses any variations caused by climate change.

Drift-Scale Thermal-Hydrologic Seepage Model Implementation–The thermal-hydrologic behavior of the fractured rock is simulated in two-dimensional vertical domains perpendicular to the drift axis. In the vertical direction, the ground surface of Yucca Mountain is taken as the top model boundary. The water table below the repository is used as the bottom boundary of the model area. Symmetry considerations are applied to reduce the model domain in the lateral direction, perpendicular to the drift axis, in order to increase the computational efficiency of the simulation runs. The current repository design of parallel drifts spaced at 81 m can be represented as a series of symmetrical, identical half-drift models with vertical no-flow boundaries between them. Accordingly, the numerical mesh is reduced to a half-drift model with a width of 40.5 m, extending from the drift center to the midpoint between drifts. Both homogeneous and heterogeneous systems are investigated.

To account for the two main host rock units of the repository, two submodels with slightly different numerical gridding and different stratigraphy are studied. The first one, the Tptpmn submodel, considers a drift located in the Topopah Spring Tuff middle nonlithophysal unit (Tptpmn unit). The second one is the Tptpll submodel, assuming a drift located in the Topopah Spring Tuff lower lithophysal unit (Tptpll unit). Figure G-8 (BSC 2003i, Figure 6.2.1.2-3) shows the entire vertical grid and a close-up view with focus on the Tptpll. The discretization of the Tptpmn submodel within the drift and in close vicinity to the drift is identical to the Tptpll submodel (BSC 2003i, Figure 6.2.1.2-2). Unlike the Tptpll submodel, the Tptpmn submodel does not include all geologic layers down to the water table below the modeled drift.

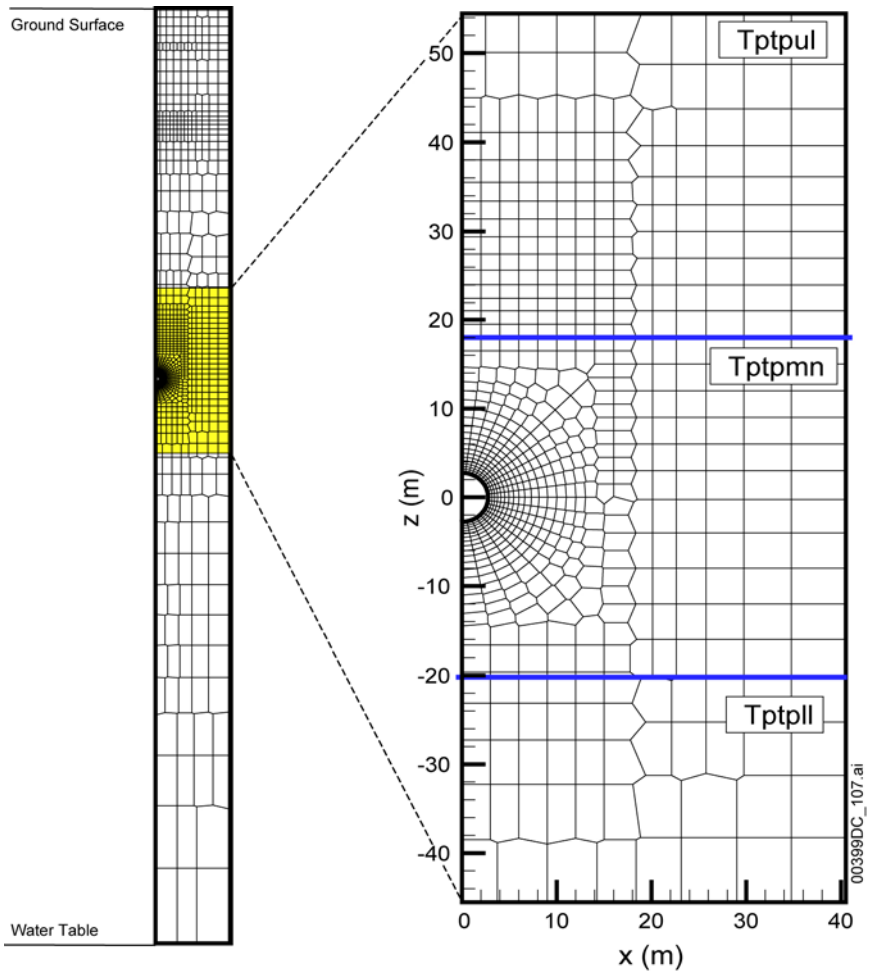

Source: BSC 2003i, Figure 6.2.1.2-3.

NOTE: The top of the entire mesh is at +364 m, the bottom is at –353 m. The blue line shows the interface between the host rock unit Tptpll and the adjacent unit Tptpmn. The top of the Tptpln below the Tptpll is at –52.2 m.

Figure G-8. Tptpll Submodel Mesh with Close-Up View of Drift Vicinity

The ground surface of the mountain is taken as the top model boundary, representing an open atmosphere. The water table as a flat, stable surface is used as the bottom boundary condition. Both the top and bottom boundaries are treated as Dirichlet-type conditions with specified constant temperature, gas pressure, and liquid saturation values. The specific boundary values used for the Tptpmn submodel represent observation at the locations of the USW SD-9 borehole. The Tptpll submodel boundary uses values representative of the center of the repository (DTN: LB991131233129.004; BSC 2003i, Section 4.1.1.2). For the Tptpll unit, the extracted values have been slightly adjusted to make them consistent with the drift-scale thermal-hydrologic-chemical modeling effort (BSC 2002c, Table 11). There is a minor difference of about 0.3% in the boundary temperature and about 0.05% in the boundary pressure between the selected values for the Tptpll (BSC 2003i, Table 6.2.1.3-1) and the values reported in DTN: LB991131233129.004. This discrepancy does not affect the model results. Surface infiltration is applied using a source term in the first rock gridblocks at the top boundary. All lateral boundaries are no-flow boundaries for water, gas, and heat.

The heat load implemented in the drift-scale thermal-hydrologic seepage model is approximately 1.45 kW/m (BSC 2002d). The value of 1.45 kW/m refers to the initial thermal line load that decreases with time as a result of radioactive decay. During the preclosure period, ventilation in the drifts will remove a significant amount of heat. It is estimated that, on average over the 50 years, 86.3% of the time-varying line load is effectively removed from the repository (BSC 2002e, Table 6-6). In other words, only 13.7% of the given line load curve is used for the first 50 years after emplacement. After 50 years, the full line load is implemented.

The mean infiltration scenario was adopted for the simulations (USGS 2001a, Sections 6.9 and 6.11). This scenario considers three long-term periods with different infiltration to account for future climate changes. The infiltration values used as input to the drift-scale thermal-hydrologic seepage model are 6 mm/yr for the modern period (up to 600 years from now), 16 mm/yr for the monsoon period (600 to 2,000 years), and 25 mm/yr for the glacial transition period (more than 2,000 years). These values have been extracted from the respective infiltration map; they represent the average downward percolation over the repository footprint. Averaging was conducted using the values as discussed in *Drift-Scale Coupled Processes (DST and TH Seepage) Models* (BSC 2003i, Section 4.1.1.2. Spatially variable rock properties, lateral flux diversion in the Paintbrush nonwelded unit, and other effects may result in the concentration of flow from the large scale, as simulated with the unsaturated zone flow model, to the drift scale, as simulated by the drift-scale thermal-hydrologic seepage model. These effects are incorporated by multiplying the infiltration rates of the mean infiltration scenario with appropriate factors. Factors of 5, 10, and 20 have been selected that will give rise to maximum percolation values ranging from 125 to 500 mm/yr, respectively, during the glacial transition time period after 2,000 years.

Hydrologic properties (such as permeability, van Genuchten parameters, residual saturation for both the fractures and the matrix, and the active fracture parameter for the fractures) are primarily excerpted from the unsaturated zone drift-scale calibrated property set for the mean infiltration scenario (DTN: LB0208UZDSCPMI.002). The calibration model used to develop these properties is described (BSC 2003f, Section 6.3.2). However, the capillary strength parameter, $1/\alpha$, was chosen to be consistent with the seepage calibration model (CRWMS M&O 2001, Section 6) value that accounts for the effects of permeability changes due to excavation effects, small-scale wall roughness, high-frequency episodicity from small-scale flow processes, film flow, drop formation, discrete fractures that may terminate at the wall, artifacts of finite discretization, and, for the Tptpll unit, effects from lithophysal cavities (BSC 2003i, Section 6.2.1.1.2).

Seepage Abstraction Model Implementation–The TSPA-LA procedure that was developed in the seepage abstraction is schematically illustrated in Figure G-9.

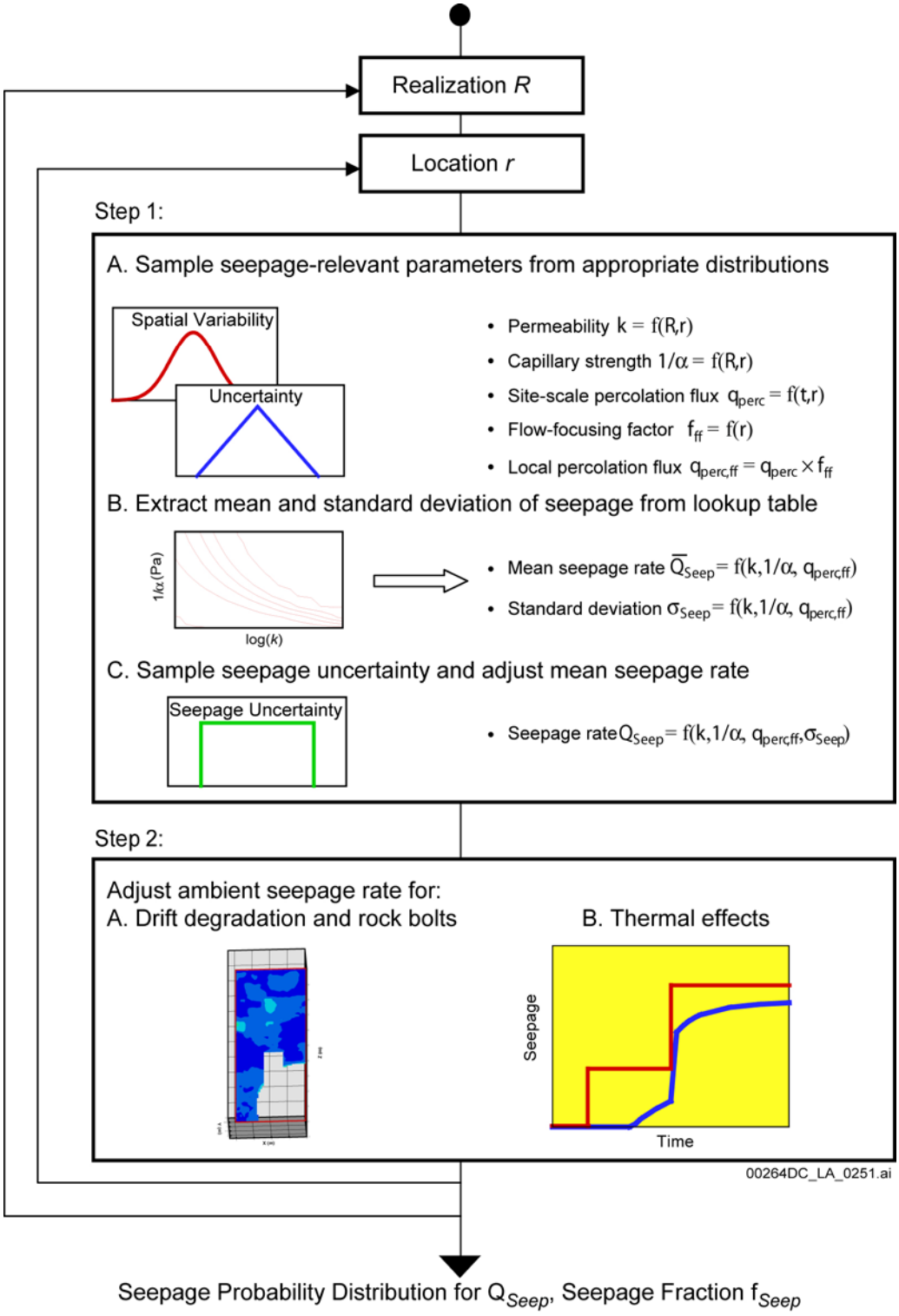

Source: BSC 2003g, Figure 6.5-1.

Figure G-9. Probabilistic Total System Performance Assessment Procedure for Calculating Seepage at Selected Time Steps

The TSPA-LA calculations run over several time steps to account for the temporal variability of relevant processes (e.g., CRWMS M&O 2000, Section 6.3.1.2). Within each time step, random sampling of uncertainty distributions is conducted for a sufficiently large number of realizations *R*. Within each realization *R*, the seepage rate is evaluated at a sufficiently large number of spatial locations *r* in the repository area. As shown in Figure G-9, the general seepage calculation procedure has two main steps:

1. **Probabilistic Evaluation of Ambient Seepage**–The ambient seepage lookup tables derived from the seepage model for performance assessment provide the basis for the quantitative evaluation of seepage as a function of key hydrologic properties. For ambient seepage, these key hydrologic properties are the capillary-strength parameter, permeability, and local percolation flux. One of the main tasks of this seepage abstraction model was to define appropriate probability distributions that represent the spatial variability and uncertainty inherent in these parameters in a cautiously realistic manner.

   Since details on all three key parameters are given (BSC 2003g), the focus here is on the local percolation fluxes (water flow rates). In the ambient seepage abstraction, the spatial and temporal distribution of percolation fluxes in the unsaturated zone is provided by the site-scale unsaturated zone flow and transport model (BSC 2003c). This model derives relevant information on the overall flow and transport fields at Yucca Mountain, accounting for climate changes and related uncertainties, variability in net infiltration, and the effects of different stratigraphic units and faults. Results are given for three different climate stages (modern climate, monsoon climate, and glacial transition climate), during which the unsaturated zone model flow fields are considered steady state. Which one of these flow fields is to be used for sampling depends on the time step considered in the TSPA-LA calculation. For each time step, the local fluxes at the several thousand locations in the repository area are spatially interpolated from the simulated flux distributions. These locations are identical to the locations considered in the multiscale thermal-hydrologic model. Uncertainty inherent in these flux distributions is expressed by using several alternative scenarios of spatial flux distributions, each of them associated with a certain occurrence probability. These scenarios are the mean, the upper-bound and the lower-bound scenario, produced by running the unsaturated zone flow model with the respective mean, upper-bound, and lower-bound infiltration distributions imposed at the upper boundary. The occurrence probability of each climate scenario is provided (BSC 2003a). This will be used in TSPA-LA to assign the appropriate weight to the considered site-scale flow field.

   Seepage abstraction uses the percolation flux distributions across the PTn–TSw boundary. These fluxes incorporate the important effects of flow dampening and lateral flow diversion in the PTn, and they are fairly representative of the fluxes at the repository horizon. The rationale for using the PTn–TSw fluxes, instead of using the flux distribution directly at the repository horizon, is based mainly on consistency considerations. The effect of flow focusing is estimated with a submodel that has the bottom of the PTn as its upper boundary (BSC 2003g, Section 6.6.4.2). The drift

seepage results are averaged over the TSPA-LA repository bins as discussed under the multiscale thermal-hydrologic model.

Because of the large model area covered with the unsaturated zone flow model, the spatial resolution of the model is much larger than the extent of drift-scale seepage models, and layer-averaged properties are used within stratigraphic units. Thus, intermediate-scale heterogeneity is not represented in the unsaturated zone flow model. This heterogeneity may lead to focusing of flow on a scale smaller than the resolution of the site-scale model; that is, it may increase the site-scale fluxes in some areas, while reducing them in other areas. The additional variability and uncertainty of percolation flux stemming from this effect is accounted for in the seepage abstraction by appropriate flow focusing factors, to be multiplied with the percolation flux distribution from the site-scale model. An intermediate-scale flow model was developed to specifically address the issue of spatial flow focusing and to derive a probability distribution for flow focusing factors (BSC 2001d, Section 4.3.2; BSC 2001c, Section 6.4.2; Bodvarsson et al. 2003). The resulting flux distribution represents the local percolation flux distribution needed as input to the predictive drift-scale seepage models (e.g., the seepage model for performance assessment or the drift-scale thermal-hydrologic seepage model).

The seepage calculation samples seepage-relevant parameters (capillary strength, permeability, percolation flux) over R realizations and r locations. For each parameter set, the ambient seepage results are derived using the seepage lookup tables provided by the seepage model for performance assessment results. In particular, the mean seepage rate and its inherent estimation uncertainty, expressed by the standard deviation over the 20 realizations conducted, are linearly interpolated between the table values. The standard deviation is used to define a uniform uncertainty distribution. A seepage uncertainty value is then randomly sampled from this distribution and used to adjust the mean seepage values, giving the final ambient seepage rate for the considered parameter set. Conducting this procedure over a large number of random parameter sets results in the final distribution of ambient seepage.

It is possible that the initially circular-shaped drifts degrade with time as a result of rock fatigue or seismic events. Based on the seepage model for performance assessment modeling results, the impact of drift degradation is accounted for by using separate lookup tables for nondegraded and collapsed drifts. During the TSPA-LA process, the decision will be made as to which is the appropriate lookup table depending on the considered geologic unit, the selected nominal or disruptive scenario, and the assumed rock strength reduction case.

2. **Adjustment of Ambient Seepage Results for Other Relevant Factors**–Since the seepage model for performance assessment lookup tables account for seepage at ambient and somewhat idealized conditions, the impact of additional factors affecting seepage needs to be evaluated in a second step. These factors include the ground support with rock bolts, the expected transient changes in hydrologic properties as a result of thermal-hydrologic-mechanical and thermal-hydrologic-chemical effects as well as parameter changes stemming from drift degradation and drift collapse, and the

thermal perturbation of the flow field as a result of boiling in the rock. The method proposed in the seepage abstraction is to account for these factors in a simplified form, using the ambient seepage results as a basis and adjusting them as suggested by the relative importance of each factor (BSC 2003g). To incorporate uncertainty, the simplifications made in this process are usually conservative yet strive to be as realistic as possible. Conservatism means that the simplified abstractions tend to overestimate seepage compared to the predicted process model results.

The impact of rock bolts, as well as thermal-hydrologic-mechanical, thermal-hydrologic-chemical, and degradation-induced parameter alterations, can be neglected in the abstraction, as demonstrated by drift-scale process models simulating these processes (BSC 2003k; BSC 2003j). Thermal-hydrologic-mechanical simulations, for example, suggested that temperature-induced stress changes give rise to changes in the vertical fracture permeability in the vicinity of waste emplacement drifts (BSC 2003k). It was demonstrated, however, that these permeability changes do not result in significant changes in the flow fields. In particular, the seepage rates calculated for a permeability field including thermal-hydrologic-mechanical permeability changes were similar to, but slightly smaller than, those calculated for a permeability field representative of the initial postexcavation conditions. Thus the ambient seepage model for performance assessment simulation results provide reasonably accurate (slightly conservative) estimates of the expected seepage rates at long-term conditions with coupled thermal-hydrologic-mechanical property changes. Thermal-hydrologic-chemical simulations suggest formation of a precipitation cap about 7 to 8 m above the drift crown (BSC 2003j). The zone of decreased fracture permeability is expected to act as an umbrella that would partially deflect percolating water sideways, limit the amount of flux arriving at the drift crown, and thus reduce seepage. However, because of uncertainties inherent in the thermal-hydrologic-chemical results, the seepage abstraction model uses the ambient seepage rates from the seepage model for performance assessment without accounting for the umbrella effect.

The abstraction methodology for thermal seepage, relative to the ambient seepage results, is based on the consistent trends that were observed in various simulation studies conducted with the drift-scale thermal-hydrologic seepage model (BSC 2003i). Despite different thermal loads, percolation conditions, rock properties, and host rock units studied in various simulation cases, the modeling results from the drift-scale thermal-hydrologic seepage model demonstrated that thermal seepage did not occur at above-boiling temperatures and that the ambient seepage values provide an asymptotic upper limit for thermal seepage. It was concluded that these qualitative trends hold for all relevant TSPA-LA parameter cases (BSC 2003i, Sections 6.2.4 and 8.1). However, the complex transient nature of the thermal-hydrologic coupled processes makes a detailed time-dependent seepage abstraction very tedious. The modeling results demonstrate considerable variability among simulation runs with respect to the duration of the boiling period, the transient rewetting processes, the initiation time of thermal seepage, and the evolution of thermal seepage in comparison with the ambient seepage rates (BSC 2003i, Section 6.2). Thus, implementation of a detailed time-dependent seepage abstraction in the TSPA-LA involves prediction of the transient local thermal-hydrologic conditions throughout the repository, dependent on a number

of spatially varying key parameters. As a result, the benefit of a detailed time-dependent abstraction of thermal seepage may not merit the difficulty of implementing it into the TSPA-LA. Therefore, two alternative abstraction approaches are proposed for the seepage calculation component in the TSPA-LA (BSC 2003i, Section 6.2.4.1). Both approaches define thermal seepage relative to the ambient seepage rates for the respective climate stages. The first model is very simple; it sets thermal seepage equal to the respective ambient seepage throughout the entire TSPA-LA period of 20,000 years; (i.e., it does not incorporate the vaporization barrier that prevents seepage at above-boiling rock temperatures). The second abstraction model is more realistic (less conservative), but requires more complex implementation into the TSPA-LA. In this model, thermal seepage is set to zero for the period of above-boiling rock temperatures in the drift vicinity. For the remaining time period, thermal seepage is set equal to the respective ambient seepage. The decision on which one of the two models should be used will be made during the TSPA-LA process. If the second model is chosen, the information required about the duration of the boiling period in the drift vicinity will be provided by the multiscale thermal-hydrologic model. This boiling period is evaluated over the spatially averaged results for each repository bin.

Treatment of Uncertainty–All sources of uncertainty related to seepage-relevant parameters and seepage simulation results have been characterized in and propagated through the seepage abstraction for the TSPA-LA.

Uncertainty in the key parameters for ambient seepage has been explicitly represented through appropriate probability distributions. The probabilities assigned to these key parameters distinguish between spatial variability (aleatory uncertainty) and uncertainty (epistemic uncertainty), using separate distributions. Spatial variability distributions for the capillary strength parameter and the local permeability have been derived by detailed statistical analysis of the sparsely distributed data (BSC 2003g, Sections 6.6.1 and 6.6.2). Spatial variability distributions for the local percolation flux are provided from site-scale simulations with the unsaturated zone flow and transport model (BSC 2003c, Section 6.6.3). These fluxes are then adjusted to account for intermediate-scale heterogeneity, using a spatial distribution of flow focusing factors. Uncertainty has been characterized by evaluation of all potential sources for uncertainty (i.e., uncertainty in the measurements, the conceptual model, the estimation process, and the spatial variability). Uncertainty inherent in the capillary strength parameter and the local permeability is described by triangular probability distributions (BSC 2003g, Sections 6.6.1 and 6.6.2). Flux distributions are incorporated using three different flow scenarios (BSC 2003g, Section 6.6.4). In addition, an alternative unsaturated zone flow scenario is evaluated (BSC 2003c, Section 6.6.2) but can be neglected in the TSPA-LA because of its limited impact.

Another contribution to uncertainty in the TSPA-LA seepage calculations stems from the simulation results of drift-scale models that describe seepage-relevant processes. These drift-scale models have been introduced and have provided a detailed assessment of the respective model validation and corroboration with alternative conceptual models (BSC 2003g, Section 6.4). As discussed earlier, the treatment of uncertainty in drift-scale simulation results is based on this assessment and considers the respective use of the model in the abstraction. The estimation uncertainty of seepage model for performance assessment simulation results, used

directly in the TSPA-LA as a quantitative measure of seepage, is explicitly incorporated in the seepage abstraction by uniform uncertainty distributions. Other drift-scale models provide quantitative and qualitative information used to adjust the seepage model for performance assessment seepage results for additional factors (thermal-hydrologic-mechanical and thermal-hydrologic-chemical parameter alterations, drift degradation, rock bolts, and thermal seepage). These adjustments are generally based on simplifications of the more complex process-model results. To incorporate uncertainty, these simplifications are chosen to be conservative. This means that the simplified abstractions tend to overestimate the seepage compared to the predicted process model results. Thermal-hydrologic-chemical parameter alterations, for example, were found to decrease the potential of seepage because of a precipitation umbrella forming a few meters above drifts. This process, however, is neglected in the abstraction because of considerable uncertainties in modeling the coupled thermal-hydrologic-chemical processes.

Two different approaches are chosen for ambient seepage estimates in degraded drifts. For noncollapsed drifts, the seepage rates are increased by 20% to account for uncertainty in the prediction. For collapsed drifts, this increase is not necessary because this extreme degree of damage is related to a worst-case scenario that includes sufficient conservatism. Two alternative abstractions have been proposed for thermal seepage. The first approach is simple and conservative; no incorporation of the vaporization barrier in superheated fractured rock takes place, so that the thermal seepage is not different from ambient seepage. The second approach is more realistic; it considers that there is no seepage during the period of above-boiling temperatures. To account for uncertainty, the threshold temperature used to define above-boiling conditions is chosen to be higher than the nominal boiling temperature of water (BSC 2003g, Section 6.5.2.2). For collapsed drifts, only the first approach is recommended (BSC 2003g, Section 6.5.3).

Interfaces and Integration with Other Models–The various process models feeding into the seepage abstraction model and into the TSPA-LA seepage calculation have been introduced earlier in this report. The interfaces between these models are discussed in the following sections, with particular attention to the percolation flux rates (water flow rates) used in these models. The higher the local percolation flux arriving at a drift, the more likely it is that seepage will occur and the higher the expected seepage rate.

Seepage Calibration Model–The seepage calibration model is a small-scale model that is used to calibrate seepage-relevant properties in comparison with liquid release tests. Thus, this model uses the measured water flow rates that were artificially released in these tests. These fluxes were generally much higher than the ambient background percolation flux at the test location, and consequently there is no direct flux interface with other models. A conceptual difference between the seepage calibration model and the seepage model for performance assessment with other unsaturated zone flow models is that the rock is represented as a single continuum and that the representation of fracture flow does not include the active fracture model modification. The bases for these differences are: (1) flow segregation into active and inactive portions of the fracture network is a large-scale effect not engaged during the short-distance liquid-release tests; (2) flow channeling within fractures is partially accounted for through explicit modeling of small-scale heterogeneity; (3) the correction of the fracture–matrix interface area (the main effect captured by the active fracture model) is insignificant for seepage because of insignificant matrix

imbibition during the calibration period (BSC 2003h, Section 6.3.3.2); (4) the potential impact of all active fracture model effects on seepage are automatically reflected in the observed seepage-rate data, which are used to estimate an effective capillary-strength parameter suitable for simulations with a conceptually consistent seepage-prediction model; and (5) matrix permeability is low, and the potential for imbibition of substantial amounts of water into the matrix is limited because of relatively low porosity and relatively high initial liquid saturation.

Seepage Model for Performance Assessment–This process model predicts drift seepage rates for a sufficiently wide range of possible local percolation fluxes imposed at the upper model boundary. See the discussion for the seepage calibration model concerning differences in the conceptual model relative to other unsaturated zone flow models. The percolation fluxes studied with the model range from 1 to 1,000 mm/yr. This range safely covers the possible flux variation within the unsaturated zone at Yucca Mountain (BSC 2003g, Section 6.6.4); thus it is guaranteed that the ambient seepage lookup tables provided by this model include enough parameter cases for seepage abstraction. The mean fluxes at the PTn–TSw interface over the repository domain, as predicted by the unsaturated zone flow and transport model, are 3.8, 11.7, and 17.9 mm/yr, for the modern, monsoon, and the glacial transition climate stages, respectively (BSC 2003g, Table 6.6-11). The respective maximum fluxes are 39.9, 127.9, and 192.4 mm/yr. Including the impact of flow focusing with factors up to 5, this yields maximum values of about 200 mm/yr for the modern climate, about 640 mm/yr for the monsoon climate, and about 960 mm/yr for the glacial transition climate, using the mean climate scenario. For the upper-bound scenario, the theoretical maximum flux during the glacial transition climate is over 1,400 mm/yr, which is beyond the flux range studied with the seepage model for performance assessment. However, these maximum fluxes are extremely unlikely, because of the extremely small probability that two independent events have extreme parameter values at the same time.

Drift-Scale Thermal-Hydrologic Seepage Model–The drift-scale thermal-hydrologic seepage model is applied to demonstrate that the evolution of thermal seepage can be characterized relative to the ambient long-term seepage rates. Therefore, it is important that the percolation flux scenarios studied with the drift-scale model cover the potential flux variability over the repository area. The drift-scale thermal-hydrologic seepage model accounts for the spatial and temporal variation by using appropriate flux boundary conditions at the top of the model domain. Consistent with unsaturated zone flow model, the drift-scale thermal-hydrologic seepage model considers three long-term climate periods with constant net infiltration: the modern climate, the monsoon climate, and the glacial transition climate. The base-case simulation studied with the drift-scale thermal-hydrologic seepage model has assigned percolation fluxes of 6, 16, and 25 mm/yr, respectively, for these three periods (BSC 2003i, Table 6.2.1.4-1). These fluxes are slightly larger than the average fluxes over the repository area for the mean climate scenario (BSC 2003g, Table 6.6-11); thus, they are representative of average percolation conditions within the repository area.

In addition to the average case, three other flux scenarios have been studied with the drift-scale thermal-hydrologic seepage model to cover the expected range of percolation fluxes within the repository units. These scenarios are defined by multiplying the boundary fluxes of the base case using factors of 5, 10, and 20. (Smaller percolation fluxes were not studied because they are too small for seepage to occur at any time.) For the three climate periods, the resulting fluxes are: (1) 30, 80, and 125 mm/yr for a multiplication factor of 5; (2) 60, 160, 250 mm/yr for a

multiplication factor of 10; and (3) 120, 320, and 500 mm/yr for a multiplication factor of 20. Together, these cases cover the major fraction of the parameter distributions for percolation flux developed in seepage abstraction model. As discussed earlier, the probability of local percolation fluxes larger than the range defined by these cases is small. Nevertheless, to test the potential of thermal seepage for extreme cases of percolation flux, two additional flux scenarios—with multiplication factors of 40 and 100, respectively—were considered in simulation studies (BSC 2003g, Section 6.4.3.3). The resulting fluxes for these cases are 240, 640, and 1,000 mm/yr (factor 40) and 600, 1,600, and 2,500 mm/yr (factor 100).

As mentioned above, the percolation-flux boundary condition is applied at the top of the model domain, which represents the ground surface. The ground surface was selected as the top boundary because appropriate boundary conditions for temperature, pressure, and saturation can be easily defined. However, the definition of boundary fluxes at this location faces a conceptual difficulty for a drift-scale model such as the drift-scale thermal-hydrologic seepage model. This is because the percolation flux distribution below the PTn, which defines the thermal-hydrologic conditions in the repository units, is considerably different from the distribution of net infiltration at the ground surface, mainly a result of lateral diversion in the PTn. Since the drift-scale thermal-hydrologic seepage model is essentially a vertical column model, it cannot account for lateral flow diversion in the PTn. Therefore, instead of using the net infiltration rates at the top boundary, the drift-scale thermal-hydrologic seepage model needs to use boundary fluxes representative of the fluxes within the repository units. Thus, the flux boundary conditions at the top of the model domain are designated to represent the range of percolation fluxes below the PTn, rather than the range of net infiltration at the ground surface. (This approach is appropriate because the PTn fluxes are hardly affected by thermal-hydrologic processes.) This is consistent with the probabilistic seepage calculation in the TSPA-LA, which uses the percolation flux distributions across the PTn–TSw boundary to provide input to the seepage lookup tables.

Unsaturated Zone Flow and Transport Model–The percolation fluxes simulated with the unsaturated zone flow and transport model feed directly into the seepage calculation for the TSPA-LA. Spatial variability and uncertainty of percolation fluxes are represented in the seepage abstraction model by sampling from different flux distributions for alternative infiltration scenarios. Spatial heterogeneity below the resolution of the unsaturated zone model is accounted for by an appropriate distribution of flow focusing factors. Flow focusing denotes the possible concentration of downward flow in the unsaturated zone onto a particular drift segment. Multiplication of the local fluxes from the unsaturated zone model with the flow focusing factors gives the local percolation flux to be used in the TSPA-LA calculation.

Drift-Scale Thermal-Hydrologic-Mechanical Model–The drift-scale thermal-hydrologic-mechanical model is applied to assess the magnitude and distribution of stress-induced changes in hydrologic properties and to analyze the impact of such changes on the percolation flux in the rock mass around a repository drift (BSC 2003k). The modeling framework for the thermal-hydrologic processes—boundary conditions and rock properties—is similar to the drift-scale thermal-hydrologic seepage model. However, while the drift-scale thermal-hydrologic seepage model focuses on the thermal-hydrologic conditions to evaluate seepage rates for various seepage-relevant parameter cases, the thermal-hydrologic-mechanical simulations concentrate on the heat-induced stress changes and the resulting impact on the flow field for average percolation flux conditions. Thus, the percolation fluxes applied at the top model boundary are identical to

the base-case simulation studied with the drift-scale thermal-hydrologic seepage model, (i.e., 6, 16, and 25 mm/yr, respectively, for the three climate periods). This is a reasonable approach, as the thermal-hydrologic-mechanical behavior should not be strongly affected by percolation flux boundary conditions. A conservative abstraction approach was chosen for thermal-hydrologic-mechanical effects, neglecting the potentially beneficial effect of thermal-hydrologic-mechanical related property changes.

Drift-Scale Thermal-Hydrologic-Chemical–The drift-scale thermal-hydrologic-chemical model is a drift-scale process model for predicting (1) the composition (not the rate) of gas and water that could enter waste emplacement drifts and (2) the effects of mineral alteration on flow in rocks surrounding drifts (BSC 2003j). The latter effect can be important for seepage abstraction: mineral precipitation is predicted to form "precipitation" caps of calcite, silica, and other minerals above emplacement drifts, leading to changes in fracture porosity, permeability, and local percolation. The modeling framework for the thermal-hydrologic simulations—including grid design, boundary conditions, and rock properties—is similar to the drift-scale thermal-hydrologic seepage model and the drift-scale thermal-hydrologic-mechanical model. However, whereas the drift-scale thermal-hydrologic seepage model focuses on the thermal-hydrologic conditions to evaluate seepage rates for various seepage-relevant parameter cases, the thermal-hydrologic-chemical simulations concentrate on the chemical processes and their related sensitivities for average percolation flux conditions identical to the base-case simulation studied with the drift-scale thermal-hydrologic seepage model (6, 16, and 25 mm/yr). The model includes a wide range of major and minor aqueous species and minerals. Sensitivity studies were performed to evaluate the impact of, for example, alternative geochemical systems, initial water compositions, and reaction rates. The model results indicate that a precipitation cap may form above drifts that could divert fluxes sideways and potentially reduce seepage. In a conservative abstraction approach, this thermal-hydrologic-chemical effect was neglected on account of the considerable model uncertainty, part of which stems from the fact the percolation fluxes were not varied in the study.

G.4.5 Drift-Scale Thermal-Hydrologic-Chemical Model

Conceptual Background–The drift-scale thermal-hydrologic-chemical model computes the evolution of water gas and water chemistry in the rock, which are strongly driven by the waste heat from the repository. Heat conduction from the drift wall into the rock matrix results in vaporization and boiling, with vapor migration out of matrix blocks into fractures. The vapor moves away from the drift through the permeable fracture network by buoyancy, by the increased vapor pressure caused by heating and boiling, and through local convection. In cooler regions, the vapor condenses on fracture walls, where it drains through the fracture network, either down toward the heat source from above or away from the drift into the zone underlying the heat source. Slow imbibition of water from fractures into the matrix gradually leads to increased liquid saturation in the rock matrix. Under conditions of continuous heat loading, a dryout zone may develop closest to the heat source separated from the condensation zone by a nearly isothermal zone maintained at about the boiling temperature. Where this nearly isothermal zone is characterized by a continuous process of boiling, vapor transport, condensation, and migration of water back to the heat source either by capillary forces or gravity drainage), this zone may be termed a heat pipe (Pruess et al. 1990, p. 1235).

Mineral precipitation and dissolution in fractures and matrix have the potential for modifying the porosity, permeability, and unsaturated hydrologic properties of the system. Because the molar volumes of minerals created by hydrolysis reactions (i.e., anhydrous phases, such as feldspars, reacting with aqueous fluids to form hydrous minerals, such as zeolites or clays) are commonly larger than the molar volumes of the primary reactant minerals, dissolution-precipitation reactions commonly lead to porosity reductions. The extent of mineral-water reaction is controlled by the surface areas of the mineral phases in contact with the aqueous fluid, and heterogeneity in the distribution of minerals in the fractures. Therefore, changes in porosity and permeability caused by these processes may also be heterogeneously distributed. Other factors that could lead to heterogeneity in property changes are the distribution of liquid saturation in fractures, the proportion of fractures having actively flowing water, and the rates of evaporative concentration due to boiling, which could change the dominant mechanisms of crystal growth and nucleation.

The rock is described by a dual-permeability model (BSC 2003j, Section 6.2.1.5), which considers separate but interacting fracture and matrix continua, each with specified hydrogeologic properties. Flow processes are modeled using the continuum approach and the extension of Darcy's law for two-phase flow as modified by the active fracture model.

Model Implementation–Simulations were performed on a vertical two-dimensional mesh, using a drift spacing of 81 m (center to center (BSC 2003m)) and a drift diameter of 5.5 m (BSC 2003n). With rock properties laterally homogeneous between drifts (BSC 2003j, Section 6.4.6.1), this setup can be viewed as a series of symmetrical, identical half-drift models with vertical no-flow boundaries between them. Accordingly, the numerical mesh was reduced to a half-drift model with a width of 40.5 m, corresponding to the midpoint between drifts (Figure G-10) (BSC 2003j, Figure 6.7-1). As for the drift-scale thermal-hydrologic seepage model, calculations were performed for drifts in the Tptpmn and Tptpll hydrogeologic units, where most of the waste emplacement drifts are located in the current repository design.

The drift was discretized (BSC 2003j, Figure 6.5-2) to include the design elements and dimensions (BSC 2003j, Figure 4.1-1). The drip shield is not explicitly modeled (BSC 2003j, Section 4.1.7). The gridblock size inside the drift was chosen small enough to provide a realistic drift model. Two in-drift configurations are considered in this model:

1. Preclosure configuration (during the first 50 years): waste package, upper invert, lower invert, and the open space between the waste package and the drift wall

2. Postclosure configuration (after 50 years): waste package, upper invert, lower invert, drip shield, and two open zones: the inner zone, between the waste package and the drip shield; and the outer zone, between the drip shield and drift wall.

The discretization of the drift was kept the same for the two configurations. As such, the preclosure period was simulated by assigning identical open-space properties to gridblocks representing the inner zone and outer zone.

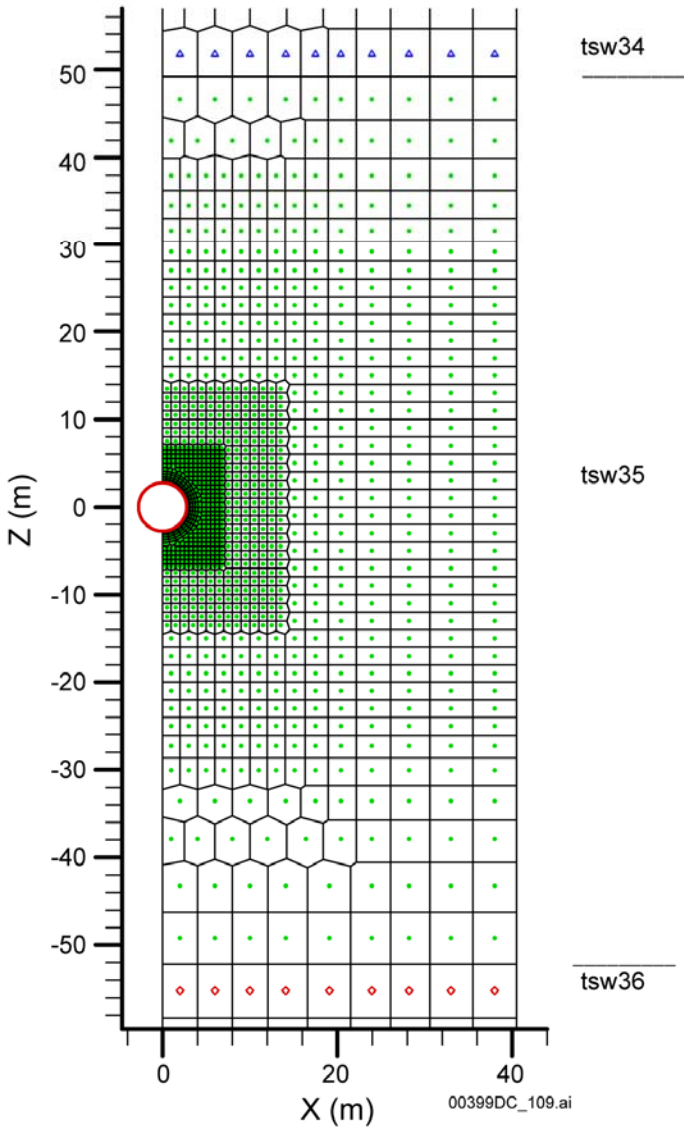

Source: BSC 2003j, Figure 6.7-1.

Note: THC = thermal-hydrologic-chemical. Triangles represent tsw34; dots represent tsw35; diamonds represent tsw36.

Figure G-10. Tptpll Thermal-Hydrologic-Chemical Model Mesh with Hydrogeologic Units Shown in the Vicinity of the Drift: Topopah Spring Tuff Middle Nonlithophysal Lower Lithophysal and Lower Nonlithophysal Units

The following boundary conditions were imposed on the Tptpll thermal-hydrologic-chemical model:

- Top boundary: stepwise changing infiltration rate 6 mm/yr (modern climate, 0 to 600 years); 16 mm/yr (monsoon climate, 600 to 2,000 years) and 25 mm/yr (glacial transition climate after 2,000 years), temperature, pressure, and gas saturation

representing open atmosphere); constant CO_2 partial pressure and composition of infiltrating water

- Bottom boundary: constant temperature, pressure, and liquid saturation (representing the water table). Constant water composition and CO_2 partial pressure at equilibrium
- Side boundaries: no heat, fluid, and chemical fluxes
- Waste package: variable heat load with time, including the effect of 70% heat removal by ventilation for first 50 years (preclosure).
- Drift wall specified open to advective gas and liquid fluxes.

Thermal-hydrologic-chemical simulations were run for an initial period of 50 years, using the preclosure drift configuration and thermal properties (BSC 2003j, Section 4.1.7). The simulations were then restarted using the postclosure drift configuration and properties from 50 years to a total simulation time of 100,000 years. At times corresponding to changes in infiltration rates (at 600 and 2,000 years), the simulations were stopped and then restarted with the new infiltration rate (thus resulting in a stepwise change in infiltration).

Treatment of Uncertainty–The simulations of thermal-hydrologic-chemical processes include coupling between heat, water, and vapor flow, aqueous and gaseous species transport, kinetic and equilibrium mineral-water reactions, and feedback of mineral precipitation/dissolution on porosity, permeability, and capillary pressure (hydrologic properties) for a dual-permeability (fracture–matrix) system. As such, the drift-scale thermal-hydrologic-chemical model takes into account the effects of mineral dissolution and precipitation, the effects of carbon dioxide exsolution and transport in the region surrounding emplacement drifts, and the resulting changes to porosity, permeability, seepage, and chemical composition of percolating waters. The large number of input parameters, the numerical methods implemented in simulating these complex coupled processes, and the simplification and approximations pertaining to the physical setup of the model—all contribute to uncertainties in the predictions from these models.

Of these uncertainties, those directly affecting chemical processes would be most likely to have the most effect on predicted water and gas compositions. The principal hydrologic uncertainties identified are infiltration rate and heterogeneity in hydrologic properties. A range of infiltration rates, corresponding to climate change, was used to represent uncertainty in infiltration. Heterogeneity in fracture hydrologic properties was investigated as a sensitivity case. The conclusions of this sensitivity were that local changes in predicted water compositions around the drift might result from heterogeneity in hydrologic properties. However, the bulk composition of waters around the drift is not expected to be significantly affected because the rock chemical composition and mineralogy in the repository units are fairly homogeneous.

Interfaces and Integration with Other Models–The drift-scale thermal-hydrologic-chemical model is applied to demonstrate that the evolution of seepage chemistry can be characterized. The drift-scale thermal-hydrologic-chemical model accounts for the spatial and temporal variation by using appropriate flux boundary conditions at the top of the model domain. Consistent with unsaturated zone flow and transport model, the drift-scale thermal-hydrologic

seepage model considers three long-term climate periods with constant net infiltration: the modern climate, the monsoon climate, and the glacial transition climate. The base-case simulation studied with the drift-scale thermal-hydrologic-chemical model has assigned percolation fluxes of 6 mm/yr, 16 mm/yr, and 25 mm/yr, respectively, for these three periods (BSC 2003i, Table 6.2.1.4-1). These fluxes are slightly larger than the average fluxes over the repository area for the mean climate scenario (BSC 2003g, Table 6.6-11); they are thus representative of average percolation conditions within the repository area.

Additional flow focusing was not incorporated in the drift-scale thermal-hydrologic-chemical model as used for the drift-scale thermal-hydrologic seepage model. This is due to the results of the drift-scale thermal-hydrologic-chemical model, which indicated that between 6 and 25 mm/yr, there is a small effect on predicted concentrations at the drift wall. The effect would be greater under lower rates of infiltration (when reaction effects start to dominate transport), but such conditions would be less likely to cause in-drift seepage. At high-infiltration rates, most conducive to in-drift seepage, water compositions are more a function of transport than of reaction with host rock minerals, such that the uncertainty regarding the composition of the infiltration water, rather than the rate of mineral dissolution/ precipitation, becomes more important.

As shown in Figure G-2, the drift-scale thermal-hydrologic-chemical model has only one interface with a flow model that is included in the TSPA-LA. That interface being the infiltration model. The more limited interaction between the drift-scale thermal-hydrologic-chemical model and other flow models results from two factors: (1) the drift-scale thermal-hydrologic-chemical model's main product is the chemistry of water and gas that may enter the drift (not water flux) and; (2) the effects of thermal-hydrologic-chemical processes through coupling with hydrologic properties on flow behavior was found to be negligible. The intention of the drift-scale thermal-hydrologic-chemical model is to analyze the effect of thermal-hydrologic-chemical processes in the rock around emplacement drifts (BSC 2003j), including:

- Predicting the composition of waters and gases that could enter the drifts
- Evaluating the effect of thermal-hydrologic-chemical processes on seepage into drifts.

However, the drift-scale thermal-hydrologic-chemical model does not simulate actual seepage of water into drifts, because the range of simulated infiltration rates (including rates for future climate conditions of high infiltration) remains well below the theoretical seepage threshold for rocks around the drift (BSC 2003j, Section 6.2.2.1.2). Instead, the model is used to compute the compositions of pore water and gas in the repository host-rock (matrix and fractures) around a typical drift. Predicted water and gas compositions are then obtained from locations (around the modeled drift) that are deemed the most likely to yield fluids that could seep into the drift. Water and gas compositions predicted at the drift wall are also considered, although, as discussed later, water composition data at the drift wall are not available during the time period when the drift wall remains dry.

Whether to use predicted concentrations from the fracture or matrix continuum is also part of the abstraction used for seepage water chemistry. The permeability of fractures around the drift is several orders of magnitude higher than the permeability of the matrix. Also, fractures have

much lower capillarity than the matrix. Therefore, any water potentially seeping into the drift by gravity is likely to be fracture water, and the composition of that water is used for all areas above the drift.

In contrast, both fracture and matrix water could potentially contribute to in-drift seepage in areas where the drift invert contacts wall rock (by imbibition into the porous invert). For this reason, both fracture and matrix waters are considered in areas below the drift. Predicted concentration gradients near the drift are steep, resulting from steep temperature and liquid saturation gradients. Therefore, abstracted water compositions depend strongly on the location (around the drift) chosen for abstraction. Because of the transient nature of the thermal pulse, predicted water compositions also change significantly through time. Therefore, abstractions in both space and time need to be considered (BSC 2003o, Section 6.2).

G.4.6 Engineered Barrier System Radionuclide Transport Abstraction Model

Conceptual Background–Although this model involves engineered barrier system radionuclide transport abstraction, it also contains the flow model abstraction used for water flow inside the waste emplacement drifts. The source of inflow to the engineered barrier system is the seepage flux that drips from the crown (roof) of the drift. This flux is driven by downward infiltration through the existing fracture system at Yucca Mountain. The seepage flux is conceptualized to flow from discrete fractures above the roof of the drift, falling vertically downward. The inflow from these sources can flow through the engineered barrier system along eight pathways, as shown in Figure G-11. The emplacement pallet is intentionally not shown to reflect the fact that the emplacement pallet is conservatively modeled as failing instantly (BSC 2001e, Table 19, FEP 2.1.06.05.0A).

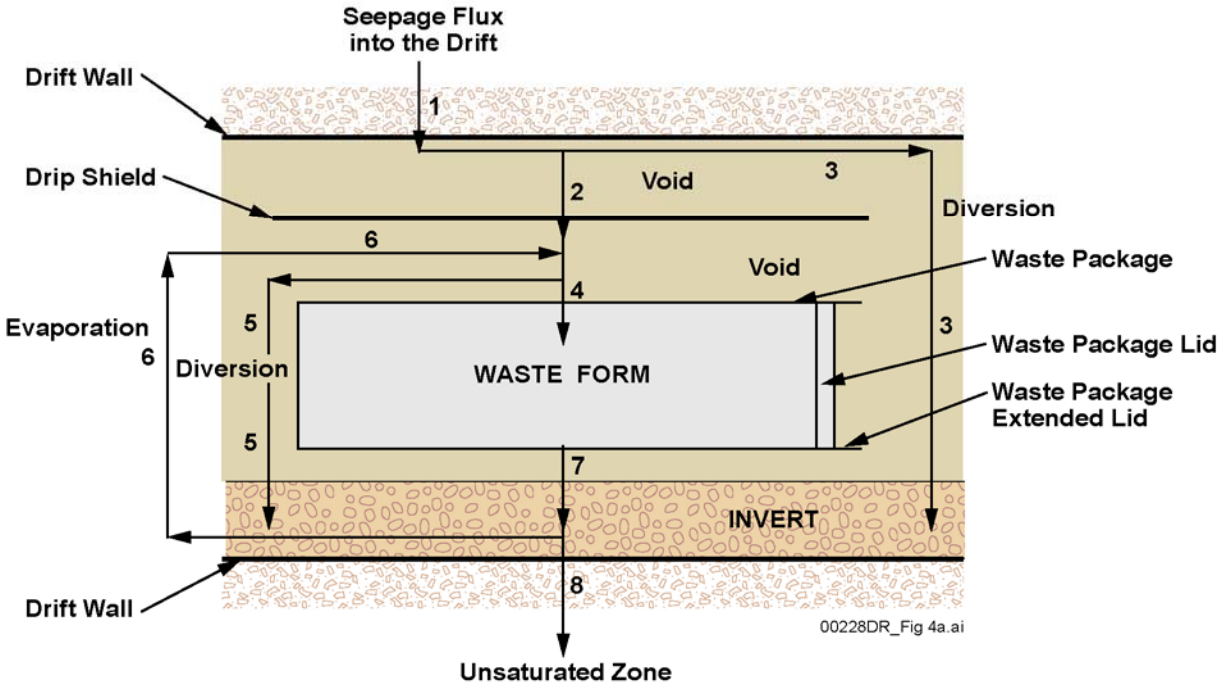

Source: BSC 2001e, Figure 3.

Figure G-11. Schematic of the Potential Flow Pathways in the Engineered Barrier System

The eight pathways are:

1. Seepage flux. This is the dripping flux from the crown (roof) of the drift.

2. Flux through the drip shield. The flux through the drip shield is based on the presence of patches due to general corrosion in the nominal scenario class; localized corrosion (pitting) is not expected to occur (BSC 2003p, Section 8.2). Any stress corrosion cracks that occur in the seismic scenario class are expected to plug from evaporation-induced mineral precipitation preventing advective flux through the drip shield.

3. Diversion around the drip shield. The portion of the flux that does not flow through the drip shield goes straight into the invert.

4. Flux through the waste package. The flux through the waste package is based on the presence of stress corrosion cracks and on patches due to general corrosion; localized corrosion (pitting) is not expected to occur in the waste package outer barrier (BSC 2003p, Section 8.2).

5. Diversion around the waste package. The portion of the flux that does not flow into the waste package bypasses the waste form, going straight into the invert.

6. Evaporative flux. If the drip shield is cooler than the invert, then all the evaporative flux condenses on the underside of the drip shield and then drip onto the waste package. If the drip shield is hotter than the invert, then there is no dripping on the waste package from the evaporative flux.

7. Flux into the invert. All flux from the waste package flows to the invert, independent of patch/pit location on the waste package. In addition, the flux that was diverted around the waste package and the drip shield flows into the invert. The presence of the emplacement pallet is ignored; the flux leaving the waste package flows directly into the invert, with no resistance offered by the pallet. Water also flows directly from the rock in capillary contact with the invert.

8. Flux to the unsaturated zone. All mass flux into the invert, except for the evaporative flux, is released into the unsaturated zone.

These pathways are time-dependent in the sense that drip shield gaps, drip shield penetrations, and waste package penetrations will vary with time and local conditions in the repository. These variations are a function of the development of corrosion patches, pits, and cracks as determined by other models. For example, at early times there may be no penetrations through the drip shield, so liquid can reach the waste package only if pathway 6, evaporation from the invert and condensation on the drip shield, is active.

The conceptual model for the nominal scenario class in TSPA-LA is based on the presence of continuous flow paths through the patches and pits that penetrate the waste package. More specifically, in the TSPA-LA conceptual model, vertical flow of seepage into the waste package, through the waste form, and out of the waste package is not impeded by the location of patches and pits on the surface of the waste package. In other words, there is no long-term build up and

retention of liquid within the waste package for flow and transport. There is also no significant resistance to the flow through the waste form. A similar approach is used for the stress corrosion cracks formed in the seismic scenario class.

The conceptual model for flow through the engineered barrier system also includes three mixing cells: one for the waste form (e.g., fuel rods or defense high-level radioactive waste glass), one for waste package corrosion products, and a third for the invert. The first two mixing cells are conceptualized to have concentric cylindrical geometry for volume calculations, with one-dimensional radial flow. The first cell has a diameter given by the diameter of a fuel rod. The second cell (corrosion products) fills the inside of a waste package within the Alloy 22 outer liner, so its thickness can be as much as the radius of the waste package. The third cell (invert) is in contact with the waste package and is 0.806 m in thickness. This is the maximum thickness of the invert directly beneath the waste package (BSC 2003q). This value is appropriate because flow out of the waste package is primarily vertically downward, centered over the thickest part of the invert. Because the presence of the emplacement pallet is ignored, water and radionuclides pass directly from the waste package to the invert.

All flow pathways except the invert are treated as a single continuum. The invert is a dual continuum, defined by the larger intergranular pore spaces between the crushed tuff grains and the smaller intragranular pore space that was the original porosity of the rock matrix, but is now the microporosity of the tuff grains. The dual-continuum model for the invert does not allow for flow exchange between the inter- and intragranular pore spaces.

Model Implementation–The drift seepage abstraction model provides the method for calculating the seepage flux into the repository, accounting for thermal effects and spatial variability. The fraction of drifts that allow water seepage as a function of infiltration are given as a function of the percolation rate.

The drip shield has been designed to divert liquid water that may enter the drift away from the waste package. If the drip shield works as designed (this issue is discussed in detail below), it then acts as a no-flow boundary. Any seepage that enters the drift moves downward under the force of gravity. As water migrates downward around the drip shield, it encounters the invert. The diversion around the drip shield occurs as droplets or rivulets, and any flow that enters the invert is concentrated at the sides of the drip shield while the drip shield is intact. Once in the invert, water migrates quickly through, probably as fingered flow, into the unsaturated zone host rock at the bottom of the drift.

The advective flow of water into the engineered barrier system has been shown to be effectively segregated from the waste packages as long as the integrity of the drip shield is maintained. Once holes form in the drip shield or adjacent drip shields separate, seepage can drip through the drip shield onto the waste package. The consequence of drip shield failure is that a portion of the seepage water flux now migrates through the drip shield and comes into contact with the waste package. The fraction of seepage that flows around the drip shield is a function of the number of holes in the drip shield and their size. A geometrical model of the interaction of a rivulet with a hole is used to define the flux splitting through and around the drip shield.

Flow through the drip shield intercepts the waste package. As for the drip shield, the flow may penetrate the waste package if holes are present. Similarly, the fraction of flow around the waste package is a function of the number holes in the waste package and their size. A similar geometric formulation is used for the flux splitting of water intercepting the waste package that flows either through or around the waste package.

An additional source of water that may contact the waste package is water that has evaporated from the invert and condensed on the inner surface of the drip shield. This additional water source is zero when the temperature of the drip shield is greater than the temperature of the invert. The potential for condensation is abstracted using the output of the multiscale thermal-hydrologic model. Multiscale thermal-hydrologic model calculations and abstraction provide the average temperature in the invert and the temperature at the crown of the drip shield as a function of time.

The flux leaving the waste package is equal to the flux entering the waste package by the steady-state flow assumption. The total flux entering the invert is equal to the sum of the diversion around the waste package and the flux leaving the waste package, and the diversion around the drip shield. These flow streams, all originating from drift seepage through the crown of the drift, flow exclusively through the intergranular porosity of the invert. Flow from the rock, in capillary contact with the crushed tuff invert, exclusively enters the intragranular porosity of the invert. This flow is defined through the output of the multiscale thermal-hydrologic model. The liquid flux leaving the invert is equal to the total flux entering the invert, minus any evaporative flux leaving the invert.

Treatment of Uncertainty–The uncertainty in the model for flow through the drip shield is expressed through a sampled parameter that is a multiplicative factor in the expression for flow through the drip shield. This results in a probabilistic model, as compared to the deterministic model discussed above. Sources of uncertainty include:

- Drip location with respect to the crown of the drip shield. Drops that fall to either side of the crown will not divide exactly in half, as assumed by this model. The drip location could deviate from the assumed crown location as a result of the drip shield being shifted by seismic events or rockfall, by slight misalignment when the drip shield is emplaced, or simply by the source of the drips being located away from the exact center of the top of the drift.

- Patch location, nominal scenario class. Patches located on the crown will allow the entire dripping flux to pass through, whereas the deterministic model considers all patches to be located off the crown. For a given value of the uncertainty factor, the deterministic model underestimates the flux into crown patches.

- Splattering distribution. Although splattering of drops when they impinge on the drip shield is a random process, preferential directions or distributions could develop, for example, due to surface alteration as a result of corrosion or drift degradation (rockfall).

- Rivulet spread. The breached-drip-shield experiments showed that a range of rivulet spread factors or spread angles can occur even on smooth surfaces. Surface roughness

also affects the rivulet spread angle. Precipitation of salts or accumulation of dust on the drip shield surface could also affect rivulet flow.

- Interference among multiple patches, nominal scenario class. Implicit in this model is that the patches do not interfere with each other, (i.e., that no patch is lower on the drip shield surface than another patch). Patches located below another patch will see reduced or zero flux through the patch.

- Patches outside the footprint of the waste package, nominal scenario class. Flux through these patches will pass directly to the invert. Since the conceptual model dictates that all flow through the drip shield goes onto or into the waste package, the deterministic model will overestimate that flow.

- Evaporation from the surface of the drip shield. Evaporation is neglected; if it occurs, the flux through the drip shield is less than predicted by the deterministic model.

- Size of corrosion patches, nominal scenario class. The WAPDEG model assumes a fixed size and shape for all corrosion patches. In reality, the patches will vary widely in size and shape randomly as well as over time.

Bounds and a distribution for the uncertainty factor must be established for use in the TSPA-LA calculations. Because, under some of these uncertain conditions, the flux through the drip shield may be zero, even when breaches exist, an appropriate lower bound is zero. A range for the uncertainty factor is developed based on data from experiments of flow on breached drip shields. The uncertainty is represented by a uniform distribution over the derived range.

Uncertainty for the flux through or around the waste package is treated in a manner similar to that used for the drip shield, extending the drip shield experiments to define a range for the uncertainty factor for the waste package flow through breaches. The uncertainty is represented by a uniform distribution over the derived range.

Interfaces and Integration with Other Models–The interfaces for the engineered barrier system radionuclide transport abstraction model for water flow are the drift seepage abstraction model and the multiscale thermal-hydrologic model. The water flux into the crown of the drift provided by the drift seepage abstraction model is the boundary condition for flow impinging on the drip shield. This flux also is the defining boundary condition for flow through the intergranular porosity of the invert, because all seepage flow enters this pathway in the invert. The flux into the intragranular porosity of the invert is defined by the multiscale thermal-hydrologic model.

The water flow out of the drift is not used by other models. The water flow through the engineered barrier system is used to compute the radionuclide transport that enters the rock, and furthermore, to compute the fraction of these radionuclide releases that enter the rock matrix versus the fractures. This radionuclide release rate and partitioning is used in the unsaturated zone radionuclide transport model, which uses the output of the unsaturated zone flow model to define the flow field, as discussed previously. At any given location, the flow out of the drift is

only a minor component of the total flow in the unsaturated zone flow model, due to the size of the mountain-scale flow model grid relative to the drift.

The engineered barrier system radionuclide transport abstraction model treats flow through the dual-continuum invert in a manner that differs from the other dual-continuum flow models discussed here. The invert flow model does not account for flow between the intergranular and intragranular pore spaces (i.e., these continua do not interact for water flow). This contrasts with a standard dual-continuum approach that uses the capillary conditions in the two continua to define water flux between the continua.

G.5 REFERENCES

G.5.1 Documents Cited

Bandurraga, T.M. and Bodvarsson, G.S. 1999. "Calibrating Hydrogeologic Parameters for the 3-D Site-Scale Unsaturated Zone Model of Yucca Mountain, Nevada." *Journal of Contaminant Hydrology, 38,* (1-3), 25-46. New York, New York: Elsevier. TIC: 244160.

Bear, J. 1972. *Dynamics of Fluids in Porous Media.* Environmental Science Series. Biswas, A.K., ed. New York, New York: Elsevier. TIC: 217356.

Bodvarsson, G.S.; Wu, Y-S.; and Zhang, K. 2003. "Development of Discrete Flow Paths in Unsaturated Fractures at Yucca Mountain." *Journal of Contaminant Hydrology, 62–63,* 23–42. New York, New York: Elsevier. TIC: 254205.

BSC (Bechtel SAIC Company) 2001a. *Multiscale Thermohydrologic Model.* ANL-EBS-MD-000049 REV 00 ICN 02. Las Vegas, Nevada: Bechtel SAIC Company. ACC: MOL.20020123.0279.

BSC 2001b. *Unsaturated Zone and Saturated Zone Transport Properties (U0100).* ANL-NBS-HS-000019 REV 00 ICN 02. Las Vegas, Nevada: Bechtel SAIC Company. ACC: MOL.20020311.0017.

BSC 2001c. *Unsaturated Zone Flow Patterns and Analysis.* MDL-NBS-HS-000012 REV 00. Las Vegas, Nevada: Bechtel SAIC Company. ACC: MOL.20011029.0315.

BSC 2001d. *FY 01 Supplemental Science and Performance Analyses, Volume 1: Scientific Bases and Analyses.* TDR-MGR-MD-000007 REV 00 ICN 01. Las Vegas, Nevada: Bechtel SAIC Company. ACC: MOL.20010801.0404; MOL.20010712.0062; MOL.20010815.0001.

BSC 2001e. *EBS Radionuclide Transport Abstraction.* ANL-WIS-PA-000001 REV 00 ICN 03. Las Vegas, Nevada: Bechtel SAIC Company. ACC: MOL.20010806.0076.

BSC 2002a. *Thermal Conductivity of the Potential Repository Horizon Model Report.* MDL-NBS-GS-000005 REV 00. Las Vegas, Nevada: Bechtel SAIC Company. ACC: MOL.20020923.0167.

BSC 2002b. *Guidelines for Developing and Documenting Alternative Conceptual Models, Model Abstractions, and Parameter Uncertainty in the Total System Performance Assessment for the License Application.* TDR-WIS-PA-000008 REV 00 ICN 01. Las Vegas, Nevada: Bechtel SAIC Company. ACC: MOL.20020904.0002.

BSC 2002c. *Drift-Scale Coupled Processes (DST and THC Seepage) Models.* MDL-NBS-HS-000001 REV 01 ICN 02. Las Vegas, Nevada: Bechtel SAIC Company. ACC: MOL.20020312.0156.

BSC 2002d. *Repository Design, Repository/PA IED Subsurface Facilities Plan Sht. 1 of 5, Sht. 2 of 5, Sht. 3 of 5, Sht. 4 of 5, and Sht. 5 of 5.* DWG-MGR-MD-000003 REV A. Las Vegas, Nevada: Bechtel SAIC Company. ACC: MOL.20020601.0194.

BSC 2002e. *Ventilation Model.* ANL-EBS-MD-000030 REV 01 ICN 01. Las Vegas, Nevada: Bechtel SAIC Company. ACC: MOL.20021106.0055.

BSC 2003a. *Analysis of Infiltration Uncertainty.* ANL-NBS-HS-000027 REV 01. Las Vegas, Nevada: Bechtel SAIC Company. ACC: DOC.20031030.0003.

BSC 2003b. *Development of Numerical Grids for UZ Flow and Transport Modeling.* ANL-NBS-HS-000015 REV 01. Las Vegas, Nevada: Bechtel SAIC Company. ACC: DOC.20030404.0005.

BSC 2003c. *UZ Flow Models and Submodels.* MDL-NBS-HS-000006 REV 01. Las Vegas, Nevada: Bechtel SAIC Company. ACC: DOC.20030818.0002.

BSC 2003d. *Multiscale Thermohydrologic Model.* ANL-EBS-MD-000049 REV 01. Las Vegas, Nevada: Bechtel SAIC Company. ACC: DOC.20040301.0004.

BSC 2003e. *Total System Performance Assessment-License Application Methods and Approach.* TDR-WIS-PA-000006 REV 00 ICN 01. Las Vegas, Nevada: Bechtel SAIC Company. ACC: DOC.20031215.0001.

BSC 2003f. *Calibrated Properties Model.* MDL-NBS-HS-000003 REV 01. Las Vegas, Nevada: Bechtel SAIC Company. ACC: DOC.20030219.0001.

BSC 2003g. *Abstraction of Drift Seepage.* MDL-NBS-HS-000019 REV 00 ICN 01. Las Vegas, Nevada: Bechtel SAIC Company. ACC: DOC.20031112.0002.

BSC 2003h. *Seepage Calibration Model and Seepage Testing Data.* MDL-NBS-HS-000004 REV 02. Las Vegas, Nevada: Bechtel SAIC Company. ACC: DOC.20030408.0004.

BSC 2003i. *Drift-Scale Coupled Processes (DST and TH Seepage) Models.* MDL-NBS-HS-000015 REV 00C. Las Vegas, Nevada: Bechtel SAIC Company. ACC: MOL.20030910.0160.

BSC 2003j. *Drift-Scale Coupled Processes (DST and THC Seepage) Models.* MDL-NBS-HS-000001 REV 02. Las Vegas, Nevada: Bechtel SAIC Company. ACC: DOC.20030804.0004.

BSC 2003k. *Drift Scale THM Model.* MDL-NBS-HS-000017 REV 00 ICN 01. Las Vegas, Nevada: Bechtel SAIC Company. ACC: DOC.20031014.0009.

BSC 2003l. *Seepage Model for PA Including Drift Collapse.* MDL-NBS-HS-000002 REV 02. Las Vegas, Nevada: Bechtel SAIC Company. ACC: DOC.20030709.0001.

BSC 2003m. *Repository Design, Repository/PA IED Subsurface Facilities.* 800-IED-EBS0-00402-000-00B. Las Vegas, Nevada: Bechtel SAIC Company. ACC: MOL.20030109.0146.

BSC 2003n. *Repository Design Project, Repository/PA IED Emplacement Drift Committed Materials.* 800-IED-EBS0-00301-000-00A. Las Vegas, Nevada: Bechtel SAIC Company. ACC: ENG.20030311.0022.

BSC 2003o. *Abstraction of Drift-Scale Coupled Processes.* MDL-NBS-HS-000018 REV 00. Las Vegas, Nevada: Bechtel SAIC Company. ACC: DOC.20031223.0004.

BSC 2003p. *WAPDEG Analysis of Waste Package and Drip Shield Degradation.* ANL-EBS-PA-000001 REV 01. Las Vegas, Nevada: Bechtel SAIC Company. ACC: DOC.20031208.0004.

BSC 2003q. *Repository Design Project, Repository/PA IED Emplacement Drift Committed Materials (2).* 800-IED-WIS0-00302-000-00A. Las Vegas, Nevada: Bechtel SAIC Company. ACC: ENG.20030627.0004.

CRWMS M&O (Civilian Radioactive Waste Management System Management and Operating Contractor) 2000. *Total System Performance Assessment (TSPA) Model for Site Recommendation.* MDL-WIS-PA-000002 REV 00. Las Vegas, Nevada: CRWMS M&O. ACC: MOL.20001226.0003.

CRWMS M&O 2001. *Seepage Calibration Model and Seepage Testing Data.* MDL-NBS-HS-000004 REV 01. Las Vegas, Nevada: CRWMS M&O. ACC: MOL.20010122.0093.

Flint, A.L. and Childs, S.W. 1991. "Use of the Priestley-Taylor Evaporation Equation for Soil Water Limited Conditions in a Small Forest Clearcut." *Agricultural and Forest Meteorology, 56,* (3–4), 247–260. Amsterdam, The Netherlands: Elsevier. TIC: 241865.

Flint, L.E. 1998. *Characterization of Hydrogeologic Units Using Matrix Properties, Yucca Mountain, Nevada.* Water-Resources Investigations Report 97-4243. Denver, Colorado: U.S. Geological Survey. ACC: MOL.19980429.0512.

Flint, L.E.; Flint, A.L.; and Selker, J.S. 2003. "Influence of Transitional Volcanic Strata on Lateral Diversion at Yucca Mountain, Nevada." *Water Resources Research, 39,* (4), 4-1 to 4-17. Washington, D.C.: American Geophysical Union. TIC: 254439.

Francis, N.D., Jr.; Webb, S.W.; Itamura, M.T.; and James, D.L. 2003. *CFD Modeling of Natural Convection Heat Transfer and Fluid Flow in Yucca Mountain Project (YMP) Enclosures.* SAND2002-4179. Albuquerque, New Mexico: Sandia National Laboratories. ACC: MOL.20030906.0165.

Golder Associates 2003. *Software Code: GoldSim.*. V8.01 Service Pack 1. PC/Windows 2000. 10344-8.01 SP1-00.

LBNL (Lawrence Berkeley National Laboratory) 2000. *Software Code: TOUGH2.* V1.4. Sun Workstation and DEC/ALPHA. 10007-1.4-01.

LBNL 2002. *Software Code: iTOUGH2.* V5.0. SUN UltraSparc., DEC ALPHA, LINUX. 10003-5.0-00.

LBNL 2003a. *Software Code: flow-con.* V1.0. PC/ WINDOWS 95/98(MS-DOS emulation); DEC ALPHA/OSF1 V5.1. 10993-1.0-00.

LBNL 2003b. *Software Code: T2FEHM.* V4.0. DEC ALPHA / OSF1 V4.0/ V5.1. 10997-4.0-00.

LBNL 2003c. *Software Code: WTRISE.* V2.0. PC/WINDOWS 2000/98; DEC ALPHA/OSF1 V5.1. 10537-2.0-00.

Liu, H.H.; Doughty, C.; and Bodvarsson, G.S. 1998. "An Active Fracture Model for Unsaturated Flow and Transport in Fractured Rocks." *Water Resources Research, 34,* (10), 2633–2646. Washington, D.C.: American Geophysical Union. TIC: 243012.

LLNL (Lawrence Livermore National Laboratory) 2002. *Software Code: NUFT.* V3.0.1s. Sun, SUN O.S. 5.8. 10130-3.0.1s-01.

Montazer, P. and Wilson, W.E. 1984. *Conceptual Hydrologic Model of Flow in the Unsaturated Zone, Yucca Mountain, Nevada.* Water-Resources Investigations Report 84-4345. Lakewood, Colorado: U.S. Geological Survey. ACC: NNA.19890327.0051.

Neuman, S.P. 1994. "Generalized Scaling of Permeabilities: Validation and Effect of Support Scale." *Geophysical Research Letters, 21,* (5), 349–352. Washington, D.C.: American Geophysical Union. TIC: 240142.

Philip, J.R.; Knight, J.H.; and Waechter, R.T. 1989. "Unsaturated Seepage and Subterranean Holes: Conspectus, and Exclusion Problem for Circular Cylindrical Cavities." *Water Resources Research, 25,* (1), 16–28. Washington, D.C.: American Geophysical Union. TIC: 239117.

Pruess, K.; Oldenburg, C.; and Moridis, G. 1999. *TOUGH2 User's Guide, Version 2.0.* LBNL-43134. Berkeley, California: Lawrence Berkeley National Laboratory. TIC: 253038.

Pruess, K.; Wang, J.S.Y.; and Tsang, Y.W. 1990. "On Thermohydrologic Conditions Near High-Level Nuclear Wastes Emplaced in Partially Saturated Fractured Tuff, 1. Simulation Studies with Explicit Consideration of Fracture Effects." *Water Resources Research, 26,* (6), 1235–1248. Washington, D.C.: American Geophysical Union. TIC: 221923.

Reamer, C.W. 2001. "U.S. Nuclear Regulatory Commission/U.S. Department of Energy Technical Exchange and Management Meeting on Total System Performance Assessment and Integration (August 6 through 10, 2001)." Letter from C.W. Reamer (NRC) to S. Brocoum (DOE/YMSCO), August 23, 2001, with enclosure. ACC: MOL.20011029.0281.

Richards, L.A. 1931. "Capillary Conduction of Liquids Through Porous Mediums." *Physics, 1,* 318-333. New York, New York: American Physical Society. TIC: 225383.

USGS (U.S. Geological Survey) 2001a. *Simulation of Net Infiltration for Modern and Potential Future Climates.* ANL-NBS-HS-000032 REV 00 ICN 02. Denver, Colorado: U.S. Geological Survey. ACC: MOL.20011119.0334.

USGS 2001b. *Software Code: INFIL.* V2.0. PC. 10307-2.0-00.

USGS 2001c. *Future Climate Analysis.* ANL-NBS-GS-000008 REV 00 ICN 01. Denver, Colorado: U.S. Geological Survey. ACC: MOL.20011107.0004.

van Genuchten, M.T. 1980. "A Closed-Form Equation for Predicting the Hydraulic Conductivity of Unsaturated Soils." *Soil Science Society of America Journal, 44,* (5), 892–898. Madison, Wisconsin: Soil Science Society of America. TIC: 217327.

G.5.2 Data, Listed by Data Tracking Number

GS000208311221.002. Developed Daily Climate Data for Potential Future Monsoon and Glacial Transition Climates Using Records from Selected Analog Sites. Submittal date: 02/28/2000.

GS000308311221.005. Net Infiltration Modeling Results for 3 Climate Scenarios for FY99. Submittal date: 03/01/2000.

GS000308311221.006. Merged USGS Digital Elevation Model from Topopah Spring West and Busted Butte 7.5' DEMS. Submittal date: 03/02/2000.

GS950708312211.003. Fracture/Fault Properties for Fast Pathways Model. Submittal date: 07/24/1995.

LB0208UZDSCPLI.002. Drift-Scale Calibrated Property Sets: Lower Infiltration Data Summary. Submittal date: 08/26/2002.

LB0208UZDSCPMI.002. Drift-Scale Calibrated Property Sets: Mean Infiltration Data Summary. Submittal date: 08/26/2002.

LB03013DSSCP3I.001. 3-D Site Scale Calibrated Properties: Data Summaries. Submittal date: 01/27/2003.

LB03023DSSCP9I.001. 3-D Site Scale UZ Flow Field Simulations for 9 Infiltration Scenarios. Submittal date: 02/28/2003.

LB0302PTNTSW9I.001. PTN/TSW Interface Percolation Flux Maps for 9 Infiltration Scenarios. Submittal date: 02/28/2003.

LB0302UZDSCPUI.002. Drift-Scale Calibrated Property Sets: Upper Infiltration Data Summary. Submittal date: 02/05/2003.

LB0305TSPA18FF.001. Eighteen 3-D Site Scale UZ Flow Fields Converted from TOUGH2 to T2FEHM Format. Submittal date: 05/09/2003.

LB991131233129.004. Modeling of Thermo-Hydrological Data to Simulate Flow, Transport, and Geothermal Conditions of the UZ Model. AMR U0050, "UZ Flow Models and Submodels." Submittal date: 03/11/2000.

LL030602723122.027. Multiscale Thermohydrologic Model Output to TSPA and WAPDEG for the Upper Infiltration Case. Submittal date: 06/25/2003.

LL030608723122.028. Multiscale Thermohydrologic Model Output to TSPA and WAPDEG for the Lower Infiltration Case. Submittal date: 06/27/2003.

LL030610323122.029. Multiscale Thermohydrologic Model Output to TSPA and WAPDEG for the Mean Infiltration Case. Submittal date: 06/27/2003.

MO0012MWDGFM02.002. Geologic Framework Model (GFM2000). Submittal date: 12/18/2000.